The Influence of Naval Warship Experience upon Reliable High-Voltage Pulsed Power Design

*F. J. Agee**

Adamco, Inc. 2223 Watts St., Houston, TX 77030, USA

Abstract - The 11 Megavolt AURORA Flash X-Ray Machine provides an example of how to make high voltage pulsed power machines reliable through design decisions. This versatile pulsed power system was upgraded to provide new capabilities to include new Marx generators. The machine was used for a variety of purposes beyond its original role as a gamma ray simulator. In its high power microwave role, it set a record for energy in a pulse. The achievement of a reliable Marx generator capable of operating at full power with impunity stemmed from naval experience in warship design and operations. This paper relates the advance and its implications for reliable pulsed power design for HPM purposes and other applications.

Keywords: Pulsed Power, High Voltage, Reliability, Naval Warship, High-Power Microwaves, Blumlein, Flash X-Ray, EMP Simulator

1. Introduction

Well designed high voltage pulsed power machines have had the history of working reliably at voltages below their maximum design voltage. However, operating them at full voltage leads to breakdowns in Marx generators and leads to frequent repairs and loss of operational time. This experience has been observed in EMP simulators, such as the TEMPS simulator that operated in the US in tests conducted at a number of commercial and military communications facilities and at Harry Diamond Laboratory. Typically the TEMPS simulator was only operated at full voltage (7 megavolts) at the end of a test period, and then repairs were conducted to get ready for the next test.

Also at the Harry Diamond Laboratories, an 11 megavolt flash X-ray machine, AURORA had similar reliability experience. Both the TEMPS and the AURORA machines were made by Physics International Co. and represented the state of the art when they were built and both had extensive use in testing defense systems. The frequent repairs required posed an inconvenience to customers conducting testing. An opportunity for addressing the unreliable Marx generators at AURORA occurred when an upgrade to produce multiple pulses required changes to the Marx tank to be made. It was also an opportunity to replace the Marx generators with more reliable ones. The AURORA simulator was a flash X-ray machine with four Marx generators that drove four Blumleins. It was a rather large machine, five stories high, weighing 600 tons. Marx insulation was provided by 1.5 million gallons of transformer oil.

2. A New Design for AURORA

Naval ship design and operations influenced the AURORA modernization. The experience in the US Navy has been that ships are designed to meet the specifications mandated by the Bureau of Ships (BUSHIPS, now NAVSEA). The builder would design the ship to meet the specifications including top speed during sea trials. When the specifications had been demonstrated, the ship would be accepted by the Navy. The ship then typically would undergo repairs to fix problems that developed when operating at full speed. For example top speed was 30 knots for a Sumner Class Destroyer of World War II fame. Subsequently during naval service, 30 knots was rarely achieved, as a refit would typically be needed thereafter.

This knowledge guided the specification for the new Marx generators for AURORA. We desired the ability to operate our 11 megavolt machine with impunity at whatever voltage the customer needed, and we elected therefore to specify the new Marx generators at 14 megavolts. The Marx generators were built and operated into a dummy load at 14 megavolts during "sea trials." Although we had no plans to operate above 11 megavolts, due to limitations of the Blumlein system, we anticipated that the new Marx generators would be able to cruise at 11 megavolts without difficulty. This turned out to be the case. Repairs to the Marx generators became comparatively rare. [1]

The AURORA was also used in high-power microwave research that produced the first pulses of microwaves with a kilojoule in a multi-gigawatt pulse at L band. [2]

[1] F. J. Agee, "New Capabilities for the Aurora Flash X-Ray Machine," Nuclear Instrumentation and Methods in Physics Research **B56/57** 1063-1067 (1991).

[2] G. A. Huttlin, M. S. Bushell, D. B. Conrad, D. P. Davis, K. L. Ebersole, D. C. Judy, P. A. Lezcano, M. S. Litz, N. R. Pereira, B. G. Ruth, D. M. Weidenheimer, F. J. Agee "The Reflex-Diode HPM Source on Aurora," IEEE Transactions on Plasma Science **18**, 618-625 (1990).

On the use of XOOPIC for the Simulation of Virtual Cathode Oscillators

E Neira*, F Vega*, F Rachidi †

**EMC-UN Lab, Universidad Nacional de Colombia, Bogota, Colombia, e-mails: eneirac@unal.edu.co, jfvegas@unal.edu.co,*
† Electromagnetic Compability group, Swiss Federal Institute of Technology, Lausanne. EPFL, Switzerland, e-mail: farhad.rachidi@epfl.ch

Abstract

In this paper, a study of the use of XOOPIC code for the simulation of Virtual Cathode Oscillators (Vircators) is presented. Constraints and advantages of XOOPIC code are identified and recommendations to achieve successful simulations are presented.

Keywords: High Power Microwaves, Numerical Simulations, Particles in Cell, Virtual Cathode Oscillator, XOOPIC.

1. Introduction

XOOPIC is an object-oriented, 2-1/2 dimensional plasma particle-in-cell (PIC) simulation code written in C++ [1]. Currently, codes as XOOPIC, KARAT, MAGIC, and CST Particles Studio (CST-PS) are available to execute numerical simulations of Vircators. Each code or software presents advantages and limitations that have generated some contradictories reports. The most common inconsistence reported is the maximum radiation frequency. For example, Clements et al. [2] reported for a specific Vircator setup a maximum radiation frequency simulated by MAGIC in 2.086 GHz and simulated by CST-PS in 2.763 GHz. Other difference in the frequency response can be observed between the works development by E. Choi et al [3], M. Balk [4] and G. Singh [5]. Choi reported for a Vircator setup a maximum radiation frequency simulated by MAGIC in 6.7 GHz. The same geometry was simulated by Balk in CST-PS with a maximum radiation frequency in 6 GHz. For the same geometry, Singh reported the frequency in 6.9 GHz with a modified code based on XOOPIC.

We studied the simulation of Vircators in XOOPIC V2.70, using two experimental setups reported in the literature, [3] and [6]. The results were also compared with the theoretical values. Especially, the behavior of the electron emission models were tested and contrasted with the reported values. Additionally, the time evolution of the frequency content of the radiated wave was performed, using wavelet analysis.

2. Results

In the set of numerical experiments performed, we observed that the high frequency noise reported by Singh [5], disappears when the Poynting vector leaving the extraction surface is calculated. XOOPIC field emission model presents good agreement with the diode current reported in different experiment. Other conclusion found, is the limitation of using XOOPIC when the anode-cathode voltage is time varying. This is due to the fact that the velocity of the particles is calculated just once, at the beginning of the simulation.

References

[1] "OOPIC Pro™ Object-Oriented Particle-in-Cell Simulation, User's Manual." Boulder, 2004.

[2] K. R. Clements, R. D. Curry, R. Druce, W. Carter, M. Kovac, and J. Benford, "Design and Operation of a Dual Vircator HPM Source," vol. 20, no. 4, pp. 1085–1092, 2013.

[3] E. Choi, M. Choi, Y. Jung, M. Chong, J. Ko, Y. Seo, G. Cho, H. S. Uhm, S. Member, and H. Suk, "High-Power Microwave Generation from an Axially Extracted Virtual Cathode Oscillator," *IEEE Trans. PLASMA Sci.*, vol. 28, no. 6, pp. 2128–2134, 2000.

[4] M. Balk, "Simulation of HPM Devices with CST STUDIO SUITE," in *European User Group Meeting*, 2011.

[5] G. Singh and S. Chaturvedi, "PIC simulation of effect of energy-dependent foil transparency in an axially-extracted vircator," *IEEE Transactions on Plasma Science*, vol. 32. pp. 2210–2216, 2004.

[6] R. Verma, R. Shukla, S. K. Sharma, P. Banerjee, R. Das, P. Deb, T. Prabaharan, B. Das, E. Mishra, B. Adhikary, K. Sagar, M. Meena, and A. Shyam, "Characterization of High Power Microwave Radiation by an Axially Extracted Vircator," *Electron Devices, IEEE Transactions on*, vol. 61, no. 1. pp. 141–146, 2014.

Ku-band high power microwave generation from the coaxial foilless transit-time oscillator with low external magnetic field

J P Ling, J D Zhang, J T He, T Jiang

College of Optoelectronic Science and Engineering, National University of Defense Technology, Changsha, 410073，People's Republic of China

Abstract

A non-uniform buncher and a depth-tunable collector have been proposed to improve the power capacity and conversion efficiency of the coaxial foilless transit-time oscillator (TTO) in our previous work. Recently, our Ku-band coaxial TTO with low external magnetic field is improved by employing them, and the related experimentally investigations are carried out on the TORCH-01 accelerator. It is shown that the non-uniform buncher plays key role in the enhancement of microwave pulse duration. The influences of the collector's depth on characteristics of the device indicate that the conversion efficiency can be improved by optimizing the collector's depth in the experiments. With the diode voltage 460 kV, the beam current 8.7 kA, and the guiding magnetic field of 0.6 T, a radiation power of 1GW with the conversion efficiency of 25% at 14.3 GHz is generated by our improved TTO. The output pulse duration is 26 ns and no obvious pulse shortening is observed. The experimental results demonstrate the abilities of this improved Ku-band device to generate high power Ku-band microwave with low guiding magnetic field.

Keywords: Ku-band, high power microwave, transit-time oscillator, pulse duration, conversion efficiency

1 Introduction

A novel Ku-band coaxial foilless transit-time oscillator (TTO) has been proposed in our previous study[1][2]. With the diode voltage 500 kV, the beam current 10 kA, and the guiding magnetic field of 0.6 T, a radiation power of 1GW with the conversion efficiency of 20 % at 14.3 GHz was generated by this device in the experiments. These experimental results demonstrate this device's abilities of generating Ku-band HPM with low guiding magnetic field. However, the output microwave pulse duration was less than 20 ns. Compared with the simulation results, there was obvious pulse shortening, which was probably caused by the limitation of the device's power capacity. In addition, to expand the device's application prospects, its power conversion efficiency still needed to be increased. In Ref.3, we proposed a non-uniform buncher and a depth-tunable collector[3]. Theoretical and simulated investigations have indicated that such a buncher and a collector can increase the power capacity and conversion efficiency, respectively. Recently, our device is improved by employing the non-uniform buncher and depth-tunable collector, and the related experiments are carried out on the TORCH-01 accelerator. This paper briefly describes the improvement of the device and mainly introduces the experimental results.

2 Improvement of the device

The structure of our improved Ku-band coaxial foilless TTO is shown in Fig.1. Compared with the previous one, there are two significant differences in this improved TTO. One is that the non-uniform buncher replaces the uniform one. Another is that a depth-tunable collector is employed in the new structure.

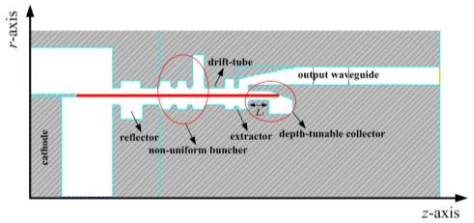

Figure 1. Structure of the improved Ku-band TTO.

Analyses have shown that this non-uniform buncher can effectively improve the power capacity of the device. Our previous uniform buncher is composed of the three cascaded TM_{01} mode resonant cavities, and the maximum surface electric field of the device usually appears in the buncher. By employing a TM_{02} mode resonant cavity instead one of the TM_{01} mode cavities, the non-uniform buncher has a lager cross-sectional area. This means it has a lower power density in the condition of the same energy storage. Therefore, this new buncher has high power capacity and fine electron beam modulation. For the depth-tunable collector, previous research has indicated that changing the depth of it could adjust the resonant frequency of the extractor. Based on the equivalent circuit theory of the transit-time device, the smaller the resonant frequency difference between the extractor and the buncher is, the higher the beam-wave conversion efficiency is. Hence, we can optimize the depth of the collector to obtain a higher conversion efficiency. Usually, there exits distinction between the real resonant frequency and the simulation calculation value, which may change the resonant frequency difference between the extractor and the buncher. This difference could lower the conversion efficiency in the experiments. If the depth of the collector is tunable, we can adjust its depth to eliminate the adverse effects caused by these distinctions, so that the conversion efficiency can be increased in the experiments.

This device is simulated and optimized by the particle in cell (PIC) code CHIPIC, a 2.5D relativistic fully electromagnetic code[4]. To simulate the real experimental condition, based on the voltage waveform in the experiments, a trapezoid voltage with rise time 15 ns, flat top 40 ns, and fall time 15 ns is injected. When the diode voltage is 410 kV, current is 8 kA, and external guiding magnetic field is 0.7 T, a microwave with power of 1 GW, conversion efficiency of 30.5%,

operation frequency of 14.22 GHz, and pulse duration of 27 ns is generated. The output microwave power versus time is shown in Fig. 2. The highest surface electric field of this novel device is 800 kV/cm, which is located at the first cavity of the buncher. This value is lower than the experiential reakdown threshold (1 MV/cm) in vacuum. Figure 3 gives the influences of the collector depth L_1 on characteristics of the device. From the figure, we can find L_1 can greatly affect the resonant frequency of the extractor. As the resonant frequency of the extractor deviates from that of the buncher (14.2 GHz), the output power of the device decreases quickly. This means, to keep high conversion efficiency, we should adjust the resonant frequency of the extractor as close as possible to that of the buncher.

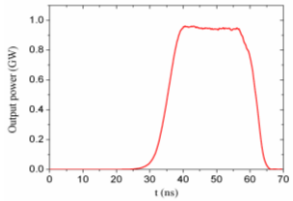

Figure 2. Output power vs time

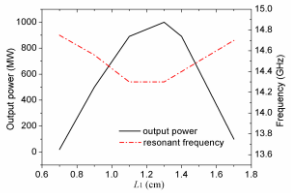

Figure 3. Output power and frequency vs L_1

3 Experimental results

To verify the above analysis, we fabricate the improved Ku-band TTO with the non-uniform buncher and depth-tunable collector and investigate its performance. The experiment is carried out on the TORCH-01 accelerator, which can produce a 55ns duration electron beam in the voltage of 0.3-1MV, and the experimental setup is shown in Fig.4.

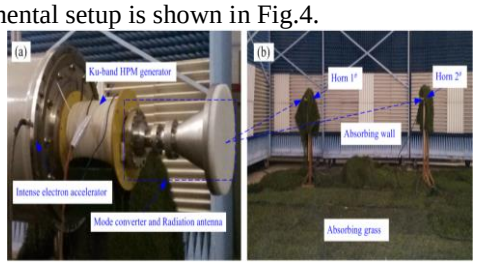

Figure 4. Photograph of the microwave generation system (a) and measurement system (b).

Typical waveforms of the diode voltage, diode current, and microwave are shown in Fig. 5. When the diode voltage is 460 kV, the diode current is 8.7 kA, the guiding magnetic field is 0.6 T and the collector depth L_1 is 1.25cm, the radiated microwave with power of 1GW and conversion efficiency of 25% is generated. Compared with the previous one[3], this improved TTO has a higher conversion. In addition, the output pulse duration is 26 ns and no obvious pulse shortening is observed, which indicates this improved device has higher power capacity. The received microwave signal with its Fast Fourier Transform is given by Fig.6. Only one main frequency 14.3 GHz was observed in the experiment, which is in good agreement with simulation one.

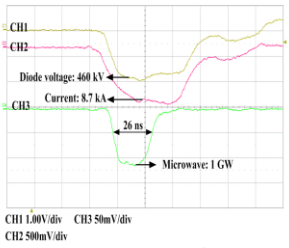

Figure 5. Typical waveforms

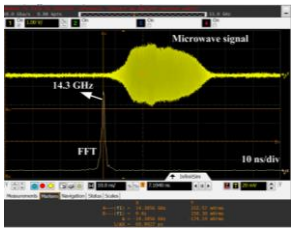

Figure 6. Microwave signal with its FFT.

Furthermore, effects of the coaxial collector depths on the device characteristics are studied in detail. From the Fig.7, we find that the depth of the collector plays important roles in the conversion efficiency of the device and the efficiency has the biggest value when L_1 is equal to 1.25 cm. This experimental optimal value of L_1 is close to the simulation one (1.3 cm), but there still exits distinction between them. This distinction is probable the reason that experimental efficiency is less than that of the simulation. Therefore, by employing the depth-tunable collector, we can optimize its depth to obtain higher efficiency in the experiments.

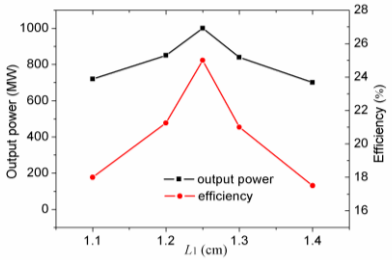

Figure 7. Output power and efficiency vs L_1

4 Conclusion

This paper presents an improved Ku-band coaxial foilless TTO with low external magnetic field. By employing a non-uniform buncher and a depth-tunable collector, this improved device has higher power capacity and conversion efficiency. With an 460 kV, 8.7 kA electron beam guided by an external magnetic field of 0.6T, a radiation power of 1GW with the conversion efficiency of 25% at 14.3 GHz is generated in the experiment, and the conversion efficiency reaches 25%.

References

[1] J. P. Ling, J D. Zhang, and J T. He, et al. "A Ku-band coaxial relativistic transit-time oscillator with low guiding magnetic field", *Laser Part. Beams*, **32**, 295-303, (2014).

[2] J. P. Ling, J T. He, and J D. Zhang, et al. "Suppression of the asymmetric competition mode in the relativistic Ku-band coaxial transit-time oscillator", *Phys. Plasmas*, **21**, 1031081-1031087, (2014).

[3] J. P. Ling, J T. He, and J D. Zhang, et al. Improved foilless Ku-band transit-time oscillator for generating gigawatt level with low guiding magnetic field", *Phys. Plasmas*, **21**, 0931071-0931079, (2014).

[4] J. Zhou, D G. Liu, and C Liao, et al. An efficient code for electromagnetic PIC modelling and simulation", *IEEE Trans. Plasma Sci*,**37**, 2002-2011, (2009).

Lightning direct effect test system of current component A

Xu Wenjun, Yao Xueling, Sun Jinru, Chen Jingliang†

State Key Laboratory of Electrical Insulation and Power Equipment, Xi'an Jiaotong University, Xi'an 710049, China

Abstract

A novel crowbar circuit is designed to produce lightning current component A. A gas triggered switch and triggered vacuum switch are used as main switch can crowbar switch respectively. It is found that the equivalent inductance in the branch of main switch and crowbar switch causes high frequency oscillation at current peak. By connecting a damping resistor in the branch of the main switch, the quality of current waveform can be improved greatly. The designed test system can produce lightning current component A with impulse current amplitude of 200kA, and the load capacity is larger than 50mΩ. The test system can be used for lightning direct effect test of carbon fibre reinforced polymer or structural of airplane.

Keywords: Lightning direct effect, Current component A, Crowbar circuit, Carbon fibre reinforced polymer (CFRP).

1 Introduction

Lightning can cause severe damage to aircraft. The probability for an aircraft of being struck by lightning is related to weather conditions, aircraft type, and flight height. Statistical data show that every commercial plane is struck once for each 3000 flight hours[1]. The direct effects of lightning on an airplane include burning, melting, magnetic force, and acoustic shock at the lightning contact point, the dramatic rise of temperature in the fuselage, and the arcing and sparking at hinges and joints[2]. With advances in aircraft designation and composite material technology, the carbon fibre reinforced polymer (CFRP) composite has been on a continuous rise since the 1960s. The proportion of usage has increased up to more than 53% in the latest aircraft A350XWA [3].

The electrical conductivity thermal conductivity of CFRPs is significantly poor compared to metallic materials. So it is very important for researching the interaction mechanism between the lightning current component and the electrical properties of CFRP specimens. But since CFRPs first appeared several decades ago, their remarkable mechanical properties have been the focus of numerous research and investigation[4, 5], but seldom for its electrical characteristics. May be one of the most important reasons is limitation of the measuring technology and special test apparatus. A Crowbar circuit is designed in this paper for generating lightning current component A, and the factor influencing the waveform accuracy was analysed. The maximum operating voltage is more than 100KV and 200kA lightning current component A can be output. The generator can be used to test CFRP, structural part and airplane.

2 Theoretical circuit for current component A

2.1 General scope for lightning direct effect environment

Fig.1 provides aspects of the lightning environment that are relevant for protection against direct effects [6].

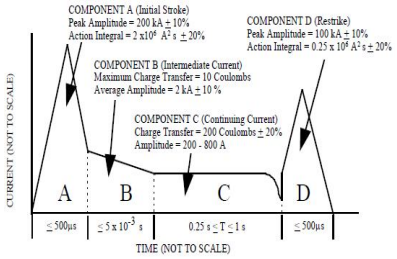

Fig.1 Lightning direct effect environment

The current component A is a unipolar current waveform. Its typical parameters are as followings: peak time $T_p \leq 50\mu s$, duration time $T_w \leq 500\mu s$, peak amplitude $I_m > 200kA$ and the action integral $W_R = 2\times10^6 A^2 s$.

2.2 Novel Crowbar circuit

Because its high working efficiency, crowbar circuit is used to generate current component A. Fig.2 is the equivalent schematic circuit for generating current component A.

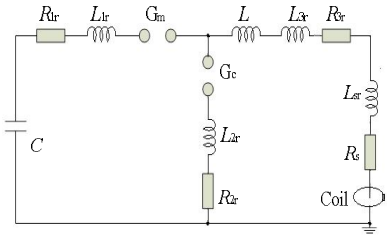

Fig.2 Equivalent circuit of current component A

In Fig.2, C is storage capacitor, L is forming inductor, Rs is test sample, Gm is main switch and Gc is crowbar switch. R_{1r}, R_{2r}, R_{3r}, L_{1r}, L_{2r}, L_{3r}, L_{sr} are equivalent resistor and inductors of connection lead. In general, R_{1r}, R_{2r}, R_{3r} can be ignored. When operating voltage is high, the L_{1r}, L_{2r} can't be omitted. At the time of current peak, the crowbar switch closes, but the magnetic energy stored in L_{1r}, L_{2r} will release through C and Gc, which will make the current component A waveform oscillation after the peak, as shown in Fig.3 (a). In order to improve the current quality, a 200mΩ damping resistor is

connected into the branch of main switch Gm, the improved current waveform is shown in Fig.3 (b).

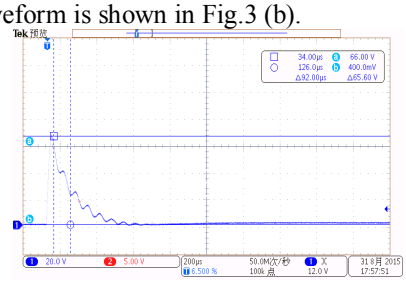

(a)

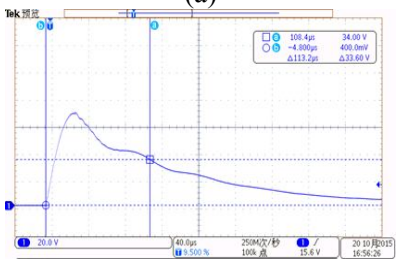

(b)

Fig.3 Current component A waveform

3 Test system of lightning current component A

The test system consists of current generator, control unit, measuring and data processing unit. The main switch is a gas switch and crowbar switch is a triggered vacuum switch. Crowbar switch has obvious advantages such as short delay time and jitter, very wide operating voltage scope. All these features make crowbar switch can be controlled actually to operate at peak time of the current waveform. Figure 4 is impulse current generator. Fig.5 and Table 1 shows the current waveforms.

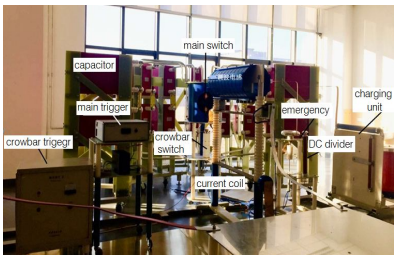

Fig.4 Lightning current component A generator

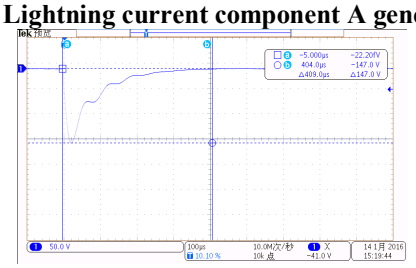

(a) 100kA

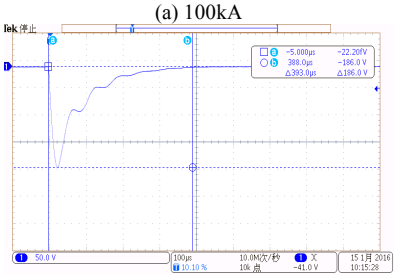

(b) 200kA

Fig.5 Lightning current component A waveform

Table 1: Experimental data

No.	Current peak /kA	Peak time /μs	Action integral /$A^2s(\times10^6)$	Error of Action integral /%
1	75	24	0.24	-14.7
2	110	24	0.55	-9.09
3	150	24	1.02	-9.33
4	207	25	1.88	-12.3

4 Conclusion

A crowbar lightning current test system is designed. A damping resistor is connected in the branch of the main switch to improve the quality of lightning current wave. The peak value of lightning current component A reaches to 200kA, and its parameters content the requirement of the normative standards. The test system can be used for lightning direct effect test of CFRP or structural of airplane.

Acknowledgements

The study was supported by the National Natural Science Foundation of China (No. 51277131, 51477132) and the Funds for the Central Universities (xkjc2014006).

References

[1] Uman, M. A. and Rakov, V. A.,The Interaction of Lightning with Airborne Vehicles, *Progress in Aerospace Sciences,* 39, pp. 61-81(2003).

[2] Plumer, J. A. and Robb, J. D., The Direct Effects of Lightning on Aircraft, *IEEE Transactions on Electromagnetic Compatability,* EMC-24(2), pp. 158-172(1982)

[3]G. Marsch. Airbus A350 XWB update. *Reinforced plastics*, Vol. 45, No. 6, pp 20-24(2010).

[4] Abry, J. C, Bochard, S., Chateauminois, A., Salvia, M. and Giraud, G. In situ Detection of Damage in CFRP Laminates by Electrical Resistance Measurements, *Composites Science and Technology,* 99, pp. 925-935(1999).

[5] Qi Dong, Yunli Guo, Jingliang Chen, Xueling Yao, Xiaosu Yi, Lu Ping, Yuxi Jia. Influencing factor analysis based on electrical-thermal-pyrolytic simulation of carbon fiber composites lightning damage. Composite Structures, 140, pp. 1-10(2016)

[6] MIL-STD-464A, Electromagnetic Environmental Effects Requirements for Systems(2002).

Impulse current test system for lightning direct effect of airplane

Sun Jinru, Yao Xueling, Xu Wenjun, Chen Jingliang*

State Key Laboratory of Electrical Insulation and Power Equipment, Xi'an Jiaotong University, Xi'an 710049, China

Abstract

An impulse current test system carrying the lightning direct effect for testing carbon fiber reinforced polymer or structural part of aircraft is designed and manufactured in the paper. The test system consists of four lightning current generators, controlling unit, measuring unit and computer data processing unit. Four generators produce current component A, B, C, and D respectively. At the same time, coupling and decoupling networks are designed to avoid the interaction between four generators, and ensuring four impulse current waveforms can be applied on the tested object according to the precise timing. The peak altitudes of current component A, B, C and D waveforms are 200kA, 2kA, 800A and 100kA.

Keywords: Multiple current components, coupling and decoupling network, Carbon fiber reinforced polymer.

1 Introduction

Lightning can cause severe damage to aircraft. The probability for an aircraft of being struck by lightning is related to weather conditions, aircraft type, and flight height. Statistical data show that every commercial plane is struck once for each 3000 flight hours in average [1]. The direct effects of lightning on an airplane include burning, melting, magnetic force, and acoustic shock at the lightning contact point, the dramatic rise of temperature in the fuselage, and the arcing and sparking at hinges and joints [2]. With advances in aircraft designation and composite material technology, the carbon fiber reinforced polymer (CFRP) composite has been on a continuous rise in usage since the 1960s. The proportion of usage has increased up to more than 53% in the latest aircraft A350XWA[3].

The electrical and thermal conductivity of CFRPs is significantly poor compared to metallic materials. It is very important for studying the interaction mechanism between the lightning current component and the electrical properties of CFRPs. At present, test technology of lightning direct effect with single current component for test CFRP or structural part of airplane should be no technical problem[4, 5], but the test technology with multiple current components are supplied on the tested object according to a precise timing has not be broken through.

The impulse current test system including current components A, B, C and D is designed and manufactured, and coupling and decoupling networks are also studied. There is no interference between four impulse generator, and multiple current components are applied on sample at pre-set timing.

2 Theoretical circuit of multiple current components of lightning direct effect test

2.1 Lightning direct effect environment

Figure 1 provides aspects and its parameters of the lightning environment that are relevant for protection against direct effects[6]. And Table 1 is the test requirements for different aircraft zones.

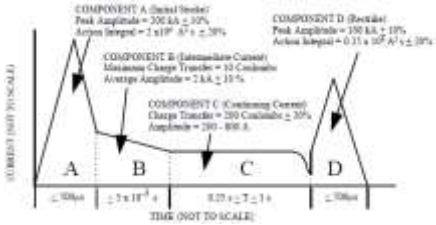

Figure1 Lightning direct effect environment

Table 1 Application of lightning environment to aircraft zones

Aircraft zone	Current component(s)
1A	A, B, C*
1B	A, B, C, D
1C	Ah, B, C*, D
2A	D, B, C*
2B	D, B, C
3(Conducted)	A, B, C, D
3(Direct attachment for new or novel designs)	A/5, B, C

2.2 Theoretical circuit of multiple current components

Figure 2 is the theoretical circuit of test system.

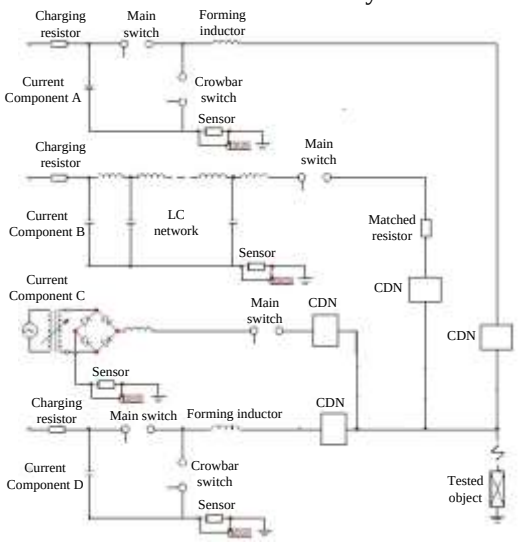

Figure 2 Theoretical circuit of multiple current components

In Figure 2, current components A, Ah and D are realized by crowbar circuit. Component B is realized by LC artificial

transmission line and component *C* by rectification and reactor. Coupling and decoupling networks (CDN) are also designed. The importance of CDN embodies two aspects, one is to ensure the current component applied on the tested object accurately, the other is to prevent the operating impulse current flow into or damage the electrical circuit no work.

3 Test system of multiple lightning current components

The test system consists of current generators, control unit, measuring and data processing unit. The special controlling circuit and software ensures the multiple current component waveforms can be supplied on the tested object according the requirement of normative standards as shown in table 1.
Figure 3 is outlet of the test system. Figure 4 and Figure 5 are the controlling interface and multiple current component waveforms respectively.

Figure 3 Multiple current components generator


Figure 4 Controlling interface of multiple current test system

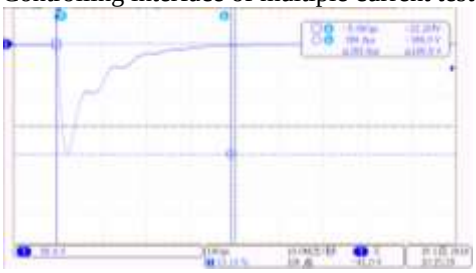
(a) Current component A waveform (200 kA)

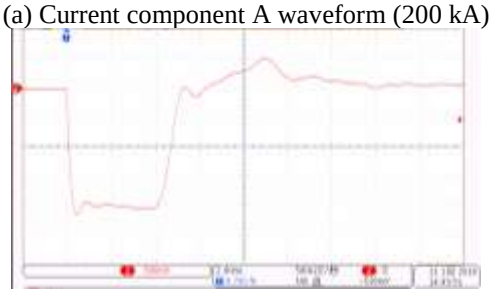
(b) Current component B waveform (2 kA)

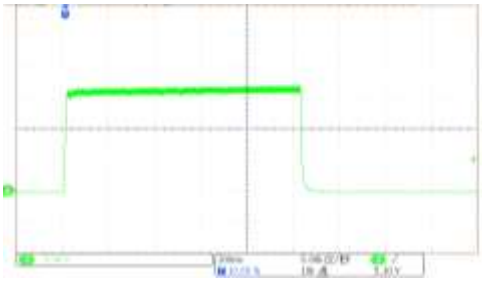
(c) Current component C waveform (200A/1s)

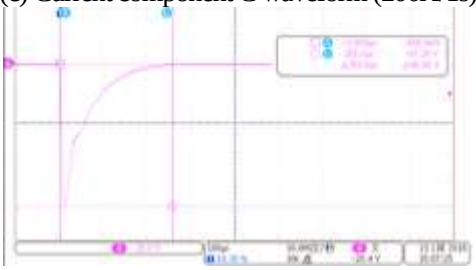
(d) Current component D waveform (100 kA)

4 Conclusion

Multiple lightning current components test system is designed, and CDN, which ensure each current component can be applied on the test object and prevent the operating impulse current flow into or damage the electrical circuit no work, is realized. The special controlling circuit and software are developed to meet the requirements of normative standards. The peak altitudes of current component A, B, C and D waveforms are 200kA, 2kA, 800A and 100kA.

Acknowledgements

The study was supported by the National Natural Science Foundation of China (No. 51477132, 51177131), the Fundamental Research Funds for the Central Universities (xkjc2014006).

References

[1] Uman, M. A. and Rakov, V. A., The Interaction of Lightning with Airborne Vehicles, Progress in Aerospace Sciences, 39, pp. 61-81(2003).
[2] Plumer, J. A. and Robb, J. D., The Direct Effects of Lightning on Aircraft, IEEE Transactions on Electromagnetic Compatability, EMC-24(2), pp. 158-172(1982).
[3] G. Marsch. Airbus A350 XWB update. Reinforced plastics, Vol. 45, No. 6, pp 20-24(2010).
[4] Yao Xueling, Chen Jingliang and Sun Wei. 10/350 μs Crowbar Pulse Current System, IEEE Transactions on Plasma Science, 38(12), pp. 3419-3424(2010).
[5] Y. XueLing, S. Jinru, C. JingLiang and B. DongQiao. Direct current resistance testing methods of carbon fibre reinforced polymer. Materials Research Innovations. 19(5), pp. 64-69(2015).
[6] MIL-STD-464A, Electromagnetic Environmental Effects Requirements for Systems (2002).

Determining the Critical Frequencies for Back- and Frontdoor Coupling into Electronic Devices

Lars Ole Fichte and Marcus Stiemer
Faculty of Electric Engineering
Helmut-Schmidt-University
Hamburg, Germany
lars-ole.fichte@hsu-hh.de

Stefan Potthast and Frank Sabath
Bundeswehr Research Institute for Protective Technologies
and NBC Protection
Munster, Germany

Abstract— **In this paper, a novel procedure that enables the determination of frequencies at which electromagnetic signals can couple into electronic devices is presented. The proposed procedure determines the power absorbed by the device under test (DUT) as a function of the frequency based on the measured values of the power fed into a reverberation chamber and the power losses both empty and loaded chamber. The maxima of the spectral power absorption function indicate critical frequencies for the electromagnetic coupling into the device under test.**.

Keywords-Power absorbed by DUT, Reverberation chamber, frontdoor coupling, backdoor coupling

I. INTRODUCTION

Knowledge of the coupling paths of HPEM into electronic devices is vital information when hardening a system against external threats becomes important. Traditionally, a lot of estimations have to be made, f.i. investigating the dimensions of existing apertures and estimating the corresponding wavelengths. Alas, the final result usually depends heavily on the experience of the designer.

II. MEASUREMENT

We propose a novel method for measuring the critical frequencies. To this end, we set up a mode stirred chamber with a test volume which is big enough for the largest DUT to be analyzed, an oscillator for the excitation of aharmonic electromagnetic field (by a transmitting antenna inside the mode stirred chamber) and a receiving antenna .

In a first step, we measure the average power P_{in} of the exciting field generated by the oscillator, averaged for one full turn of the mode stirrer. At the same time, we measure the average power P_{out} at the footpoint of the receiving antenna inside the mode stirred chamber. By calculating the power difference

$$P_{\text{loss,empty}} = P_{\text{in}} - P_{\text{out,empty}} \qquad (1)$$

we can determine the losses in the empty mode stirred chamber. The biggest part of the losses are caused by the power dissipated in the metallic (non-PEC) walls of the mode stirred chamber. Additionally, the losses in the antennas and the losses stemming from mismatches or nonlinear amplifiers are also included. As a second step, we load the reverberation chamber with the DUT and measure P_{in} and P_{out}, again. As a result we get the total power loss in the loaded reverberation chamber. The difference of the losses in the loaded and unloaded chamber is the power coupling into the DUT at a given frequency:

$$P_{\text{DUT}} = P_{\text{loss}} - P_{\text{loss,empty}}. \qquad (2)$$

Repeating this procedure for a range of frequencies gives the spectral power coupling into a DUT from an external EM field, $P_{\text{DUT}}(f)$. The peaks of the resulting function are the critical frequencies for coupling, and can be used to optimize the hardening process.

To identify the coupling frequencies, we used a parametric model based on Lorentz curves for single resonances. Application of MATLABs fitting tools results in the curve best matched to the data (which suffers from a large amount of statistical niose).

III. EXAMPLE

The proposed method has been successfully applied to a variety of generic DUTs. As an example, the results for a monoresonant device with a resonant frequency at 1.25 GHz is displayed below:

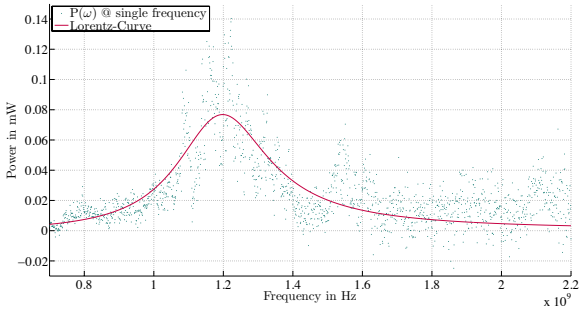

Figure 1. Power absorption by wireless baby monitor

III. CONCLUSION AND OUTLOOK

We are able to estimate the resonant frequencies of known DUTs with a reasonable accuracy. In future work, we will indentify noise sources and eleminate them. Additionally, we will apply advances statistical methods such as Epanechniv kernel density estimation to cope with multi-resonant DUTs.

Re-sampling optimized technique applied to EMC TL issues

C. Kasmi*, S. Lalléchère[#], J. Lopes Esteves*, S. Girard[#], P. Bonnet[#], F. Paladian[#]

**Wireless Security Lab, French Network and Information Security Agency-ANSSI, Paris, France*
[#]Université Clermont Auvergne, Université Blaise Pascal, Institut Pascal, CNRS UMR 6602, 63178 Aubière, France

Abstract

This study refers to the assessment of the confidence interval of the statistical moments of physical quantities such as the induced voltages on a transmission line. A bootstrapping approach has been presented in [1]. In order to extend the published approach, we have been working on the optimization of the number of replications required to estimate the maximum confidence interval of statistical moments under a Gaussian approximation related to the Central Limit Theorem.

Keywords: Statistical Electromagnetics; Re-sampling technique; EMC; Numerical simulation; Transmission Line.

1 Introduction

The electromagnetic compatibility community has shown a high interest in the estimation of the maximum confidence in simulation and measurement results in order to assess accurately the statistical moments of physical observables. Meanwhile, extreme values theory [2] and reliability assessment methods [3] have been introduced to overcome worst case challenges regarding different kind of transmission line issues. Nevertheless, due to their novelty and the required number of experiments (from 1,000 to 100,000), mean contributions with safe margins are still recommended. In this context, the estimation of the averaged contributions of a physical quantity and its related maximum confidence level is still of importance.

2 Re-sampling technique and optimization

The bootstrapping procedure, introduced in 1979 by Elfron [4], is based on the derivation of *new observations* obtained by randomly taking a set of the original data (*sampling with replacement*). It can be mentioned that these methods are based on stochastic process, such as Monte-Carlo, and do not require any additional information. The main lines of this approach have been summarized in [1]. One of the main concerns of the discussed technique is the number of replication required to assess the confidence interval of the statistical moments. We propose here to highlight the benefit of an optimization procedure based on the *Central Limit Theorem* (CLT) in order to reduce the number of the bootstrap replications (1,000 replications given in theory [4]) is proposed. In this study, we focus on the field to line coupling (inside a metallic enclosure through a rectangular aperture) as represented in Fig. 1. Different parameters are assumed randomly defined: load impedances (Z0 and ZL), height of the line (h), and plane wave characteristics (incidence and polarization). The mean current induced at load ZL is represented in Fig. 2 by applying the optimized bootstrapping procedure.

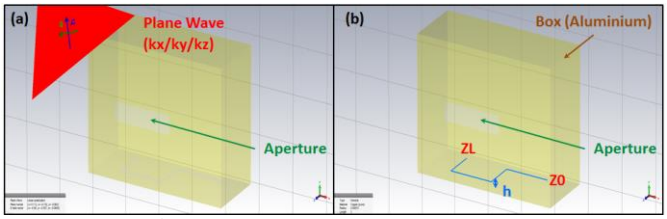

Fig. 1. Mock-up of numerical test case (CST) and assumed random variables.

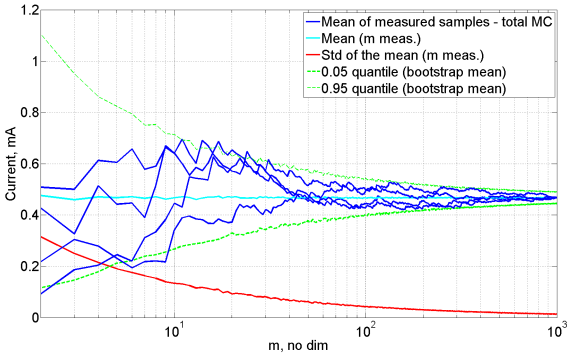

Fig. 2. Mean current (f=297MHz): MC (4 random selections), optimized bootstrap (cyan) and the related 90 % CI (green).

During the presentation, the optimization procedure will be described with the required assumption defined by the CLT. The gain of the procedure will be demonstrated regarding the drastic reduction of 'classically required' replications.

References

[1] C. Kasmi et al. "Optimization of experimental procedure in EMC using re-sampling techniques" , *in Electromagnetic Compatibility (EMC), 2015 IEEE International Symposium on* , vol., no., pp.1238-1242, (2015).

[2] C. Kasmi et al., "Generalised Pareto distribution for extreme value modelling in Electromagnetic Compatibility", *Electronics Letters*, 49, Vol. 5, pp. 334-335, (2013).

[3] A. Kouassi et al. "Safety assessment of a transmission line with EMC requirements", *XXXIth URSI GASS*, Beijing, China, (2014).

[4] B. Efron, R. J. Tibshirani. "An introduction to the bootstrap", Chapman and Hall, London, (1993).

Ultra-Wideband Pulse Propagation in Mode-Stirred Reverberation Chambers

L R Arnaut

School of Electronic Engineering and Computer Science, Queen Mary University of London, London E1 4FZ, U.K.

Abstract

Results are presented on an experimental study and stochastic model for pulse amplitude modulated RF pulsed signals propagating inside a variable-speed mode stirred reverberation chamber. Particular emphasis is on the specific distortion of the pulses caused by the interplay between the nonstationary dynamics of the multipath environment and the field transients of the rising and falling edges of the pulses. It is shown that the stir speed and stir sense of the mechanical rotation characterize the deterministic component of the phase noise and that a nonhomogeneous Poisson process provides a statistical model for the random component of the phase noise.

Keywords: ultra-wideband signals, reverberation chambers, transients, jitter, phase noise.

1 Introduction

Pulse propagation and characterization in continuously time-varying propagation channels are of interest in a variety of EM and more general multi-physics applications. Quasi-static approximations are well established and have served well in modelling open or weakly scattering dynamic environments. However, complex signal modulation schemes (e.g., for multiple-access scenarios in high-mobility multi-scattering environments for broadcasting and machine-to-machine communications) require new models that can efficiently handle the large variability and uncertainty.

Specifically, the large uncertainties associated with pulse jitter (phase noise) and the associated small signal amplitude at the onset of signals are a key concern for achieving adequate synchronization and locking of receivers onto the signal of interest, e.g., in OFDM and generally in live streaming of content where retransmission and error correction in real time are not feasible. Therefore, improving the characterization of strongly variable pulse modulated signal responses in dynamic multipath EM environments is of practical importance.

To this end, measurements and statistical characterization of received pulse-amplitude modulated RF pulses have been performed inside a room-sized reverberation chamber furnished with a continuously rotating mechanical stirrer [1].

2 Phase Noise Statistics of Received Pulse Train

2.1 Experimental set-up

For the measurement campaign, we used a signal generator producing a 2.5 GHz carrier whose amplitude is pulse modulated by a square wave generator with pulse rise time 150 ps, pulse repetition frequency 10 kHz, pulse length 100 μs and 40% duty cycle (Figure 1). Two identical transmitting and receiving dual-ridge horn antennas were separated by 3.4 m that were oriented without a direct line-of-sight coupling path. The received train of 40,000 pulse periods across one full stirrer rotation was sampled and statistically analysed under different conditions of stir velocity Ω (stir speed and clockwise / counterclockwise stir rotation).

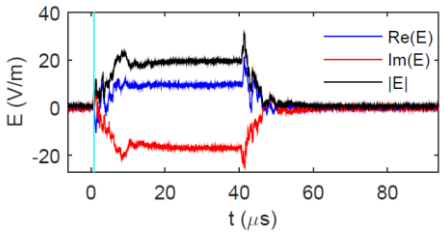

Figure 1. Magnitude, real and imaginary components of typical received single pulse amplitude modulated RF pulse at stir speed 0.25 rps (f_0 = 2.5 GHz, pulse rise time 150 ns, sampling interval 20 ns, pulse period 100 μs).

2.2 Results

Results from the statistical analysis of the measured data show that the random process for the jitter of the leading pulse edges is considerably more intricate than a standard bandlimited white Gaussian noise process. The deterministic part of the process is found to contain information on the rate and sense of the rotation of the stirrer, whereas the randomly fluctuating component represents an evolving (transient) arrivals process associated with the first few reflections from the cavity walls as the onset of wave chaos.

In a simplified model for 1-D translational stirring (projected 2-D rotational stirring) [1], the systematic component of the relative time (or phase) delay $T_d - T_{d,0}$ for the leading edges of the pulse train is found to depend on Ω according to

$$T_d(\Omega t) = T_{d,0} - 2(r_0/c)\,(\Omega t) + (r_0/c)\,(\Omega t)^2 \sin(\Omega t), \qquad (1)$$

shown in Fig.2(a). Its time derivative agrees qualitatively with the measured dependence on Ω, confirming the model (Fig. 2(b)). It was also found that the random component of the phase delay can be modelled with good accuracy as a nonhomogeneous Poisson process (NHP) with time-varying rate of arrival λ(t) (Figs. 3 and 4) [1]. Comparison of the empirical distributions of the random phase noise with a Gauss normal process confirms the significant departure from the latter as an oversimplified white noise process (Fig. 4).

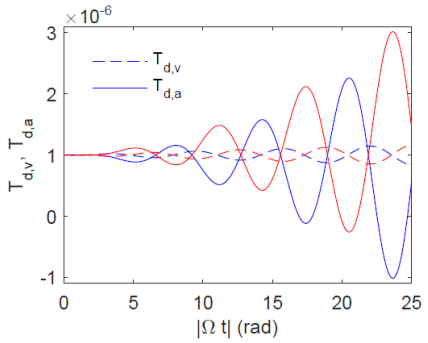

(a)

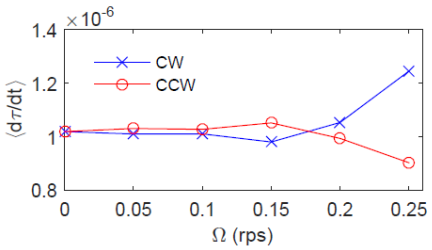

(b)

Figure 2. (a) Relative phase delay for 1-D mode stirring (eq. (1)). (b) Measured average rate of phase delay for 11 stir velocities 0…(0.05)…0.25 rps in clockwise and counterclockwise rotational mechanical stirring.

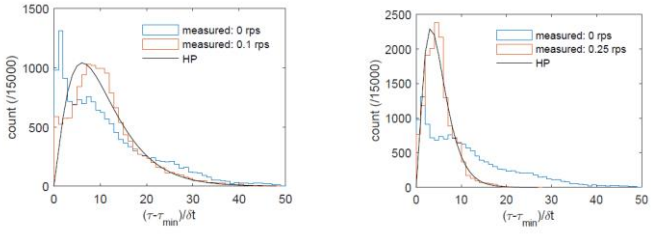

(a) (b)

Figure 3. Histogram of excess delay times (in units sample steps) for static cavity (blue line) and for (a) 0.1 rps and (b) 0.25 rps stirred cavity (brown line), compared with associated logarithmically best-fitting Erlang PMF for homogeneous Poisson process (black line).

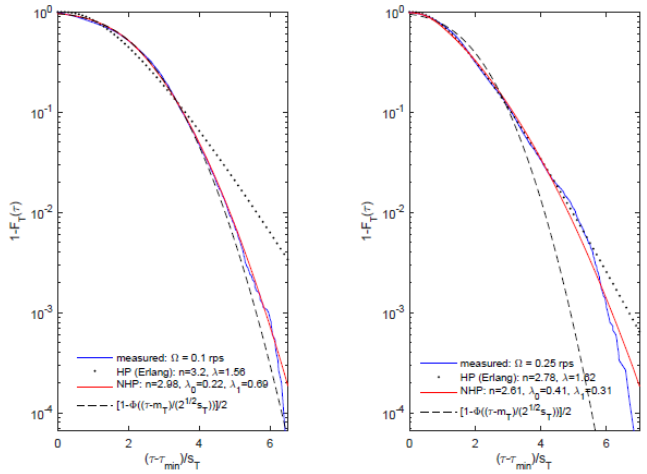

(a) (b)

Figure 4. Empirical complementary cumulative distribution functions for (a) 0.1 rps and (b) 0.25 rps stirred cavity, compared with (i) nonhomogeneous Poisson processes with linear interarrival times $\lambda_0+\lambda_1 t$, (ii) asymptotic Erlang distribution for a homogeneous Poisson process, and (iii) Gaussian process.

3 Conclusion

Pulse modulated signals propagating in continuously time-varying multipath EM environments exhibit complex and considerable pulse-to-pulse variability. While steady-state characteristics of CW and pulsed waves are now well understood from reverberation chamber theory, pulse synchronization for the leading pulse edges is hampered by strong fading and dynamics that have a more complex physical basis. A detailed and systematic stochastic analysis over a large train of sampled pulse periods has shown that a statistical characterization is possible. Ultimately, this should enable prediction of bit error rates more accurately compared to the standard assumption of a white Gaussian noise model for phase jitter.

References

[1] L. R. "Pulse jitter in mode-stirred reverberation", *submitted for publication.*

Scaled Measurements of Realistic Counter-DEW Scenarios

Steven M. Anlage[1,2], Bo Xiao[1], Zach Drikas[3], Jesus Gil Gil[3], T. D. Andreadis[3], Thomas M. Antonsen[1,2], and Edward Ott[1,2]

[1]Department of Electrical and Computer Engineering, University of Maryland (UMD), College Park, Maryland 20742-3285, USA
[2]Department of Physics, University of Maryland, College Park, Maryland 20742-4111, USA
[3]Department of Tactical Electronic Warfare Division, Naval Research Laboratory, Washington, DC 20375 USA

Abstract

The Random Coupling Model (RCM) [1] can treat a fairly wide class of counter-DEW problems of broad interest [2]. We are now extending the RCM to include consideration of more realistic scenarios, including multiple connected enclosures, each of which is ray chaotic [3]. This situation is of particular relevance to ships and aircraft loaded with sophisticated electronics in multiple compartments. These compartments are often interconnected by multiple means, including cable bundles, apertures, air conditioning ducts, and common power supplies. However, to test the RCM under such increasingly realistic scenarios requires experimental facilities currently beyond our means at UMD. To address this problem the UMD group has received a DURIP grant to develop a scaled-down electromagnetic test setup. Tests will be performed on four types of predictions, namely induced voltages on components in chains of connected enclosures [3], and induced voltages for components in enclosures that are illuminated through an irregular aperture [4]. In addition we will study the statistics of induced voltages in the very common situation of enclosures with mixed regular and chaotic behaviour [5], and finally we will consider the transfer of energy through another common situation, one in which the chambers are coupled by means of evanescent waves [6]. We give an update on development of this test facility along with preliminary results.

Keywords: Random Coupling Model, Statistical Electromagnetics, Counter DEW.

Acknowledgements

This work is supported by ONR grants entitled "HPM Effects: Electromagnetic Coupling to Enclosures" grant # N000141512134, and “Wave Chaos Studies for CDE Applications” grant # N000141310474, and the Maryland Center for Nanophysics and Advanced Materials.

References

[1] Gabriele Gradoni, Jen-Hao Yeh, Bo Xiao, Thomas M. Antonsen, Steven M. Anlage, Edward Ott , “Predicting the statistics of wave transport through chaotic cavities by the Random Coupling Model: a review and recent progress,” Wave Motion **51**, 606-621 (2014).

[2] Zachary B. Drikas, Jesus Gil Gil, Hai V. Tran, Sun K. Hong, Tim D. Andreadis, Jen-Hao Yeh, Biniyam T. Taddese and Steven M. Anlage, “Application of the Random Coupling Model to Electromagnetic Statistics in Complex Enclosures,” IEEE Trans. Electromag. Compat. **56**, 1480-1487 (2014).

[3] Gabriele Gradoni, Thomas M. Antonsen, Jr., and Edward Ott, “Impedance and power fluctuations in linear chains of coupled wave chaotic cavities,” Phys. Rev. E **86**, 046204 (2012).

[4] Gabriele Gradoni, Thomas M. Antonsen, Steven M. Anlage, and Edward Ott, “A Statistical Model for the Excitation of Cavities Through Apertures,” IEEE Trans. Electromag. Compat., **57** (5) 1049-1061 (2015).

[5] Ming-Jer Lee, Thomas M. Antonsen, Edward Ott, "Statistical model of short wavelength transport through cavities with coexisting chaotic and regular ray trajectories," Phys. Rev. E **87**, 062906 (2013).

[6] L. M. Pecora, H. Lee, D.-H. Wu, T. Antonsen, M.-J. Lee, E. Ott, "Chaos regularization of quantum tunneling rates," Phys. Rev. E **83**, 065201 (2011).

EMP Environment of High Power Laser Facility

MengCui[1,2], Jin Han Bing[1,2] ,Yang Chao[1,2], Li Xin[1,2],Zheng Wanguo[3]

1 Department of Engineering Physics, Tsinghua University, Beijing, China, 100084
2 Key Laboratory of Particle & Radiation Imaging, Ministry of Education, Beijing, China, 100084
Beijing, China
3 Laser Fusion Research Center, China Academy of Engineering Physics, Miangyang 621900, China

Abstract

In the high power laser-target matter interaction process within the high power laser facility, the movement of hot electron can excite high power electromagnetic pulse with electric field amplitude up to 10,000 V/m and frequency of GHz level. The measurement research and numerical simulation of the EM environment in high power laser facility SG III is introduced in this paper.

Keywords: high power laser ,electromagnetic pulse, PIC, hot electron

1 Introduction

Electromagnetic pulse (EMP) has been found during the interaction of laser pulses and solid targets, which may cause electromagnetic interference problems, such as interfering or damaging electronic equipment and diagnostics and data loss. For example, in experiments of Titan short-pulse laser facility, researchers observed high-level EMP with a broad frequency up to GHz[1]. Energetic electrons are produced in laser p lasma interaction, and a small fraction of these electrons escape the target. It is believed that escaping electrons are the main source of EMP [1,2], the gamma ray radiate EMP is smaller then this one.

2 Numerical Simulation used PIC method

2.1 Simulation of Laser-Plasma Interaction Producing Hot Electrons

The high-intensity laser pulse interaction with plasma is modeled in a two-dimension geometry. Charged particles, mainly electrons, are accelerated by electromagnetic fields. Simulated domain is a rectangle of 10μm×10μm. A p-polarized laser pulse is injected horizontally from the left side and propagates through vacuum and homogeneous copper plasma, with the wavelength at 1.06μm, the intensity at 10^{19}W/cm2, and the duration at the half maximum 50fs. The laser intensity presents a Gaussian shape profile along y axis as well as in time domain. Assume that the plasma density is 1.6×10^{21}/cm3. Lindman absorption boundary condition is used in the left boundary.

We vary the laser intensity from $0.2\times10^{19}$to 10^{19}W/cm^2 and the duration remains 50fs. The simulation results indicate that the temperature of hot electrons depend essentially on the laser intensity,

2.2 Simulation of Escaping Electrons Emission

In this part, 2D cylindrical coordinates are used and variables are simplified into toroidal symmetry. The solid target is in the center of the chamber. The escaping electrons is produced in a 2mm-high，10mm-diam cylinder (red zone), as shown in Fig.3. 10_{11} electrons in total are ejected along positive z axis from the original zone in the earlies 30ps.We record the electromagnetic field at an appropriate position and obtain the electric field as a function of time with a peak filed of order 100kV/m, as shown in Fig.4. And the peak field of magnetic is about 4×10^{-4}T.Based on the Fourier analysis, time domain waveform, electric field in time domain is transformed into signal in frequency domain. EMP has a broad frequency extending up to50GHz and frequency is mostly below 10GHz.

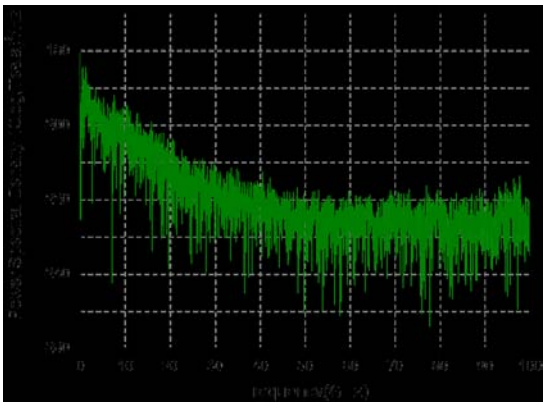

Figure 1. The spectral power density of EMP

2.3 Measurement Results

We developed magnetic field sensor and an electric field sensor, based on the Mobius loop model and the equivalent charge distribution method. They play an important role in high power laser EMP environment measurement. The environment of target chamber and target room are measured using these two kind of sensors.Figure 2 shows the result in target room.

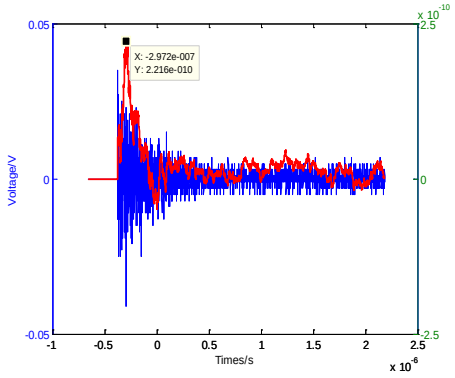

Figure 2. EMP measured in target room

3 Conclusion

The EMP environment is accordance with the format of the power density of high power laser, the target and the interaction format of the laser-target kind. the amplitude of electric field in target chamber is about 10kV/m and the amplitude of electric field in target room is about kV/m when there is window on the chamber. All electric equipment in these areas must be designed specially in order to increase the EMC level.

References

[1] C. G. Brown, E. Bond, T. Clancy, S. Dangi, D. C. Eder, W. Ferguson, etal., "Assessment and Mitigation of Electromagnetic Pulse (EMP) Impacts at Short-pulse Laser Facilities," Sixth International Conference on Inertial Fusion Sciences and Applications, Parts 1-4, vol. 244, p. 4,2010.

[2] J. L. Dubois, F. Lubrano-Lavaderci, D. Raffestin, J. Ribolzi, J. Gazave, A. C. L. Fontaine, et al., "Target charging in short-pulse-laser–plasma experiments," Physical Review E, vol. 89, 2014.

[3] F. N. Beg, A. R. Bell, A. E. Dangor, C. N. Danson, A. P. Fews, M. E. Glinsky, et al., "A study of picosecond laser–solid interactions up to 1019 W_cm−2," Physics of Plasmas, vol. 4, p. 447, 1997.

[4] M. G. Haines, M. S. Wei, F. N. Beg, and R. B. Stephens, "Hot-Electron Temperature and Laser-Light Absorption in Fast Ignition," Physical Review Letters, vol. 102, 2009

Wideband Sources for Vulnerability Tests

Sergey Agafonov, Dmitry Baryshevsky, Vladimir Baryshevsky, Andrey Borisevich, Alexandra Gurinovich

Research Institute for Nuclear Problems, Minsk, Belarus, gur@inp.bsu.by,
Electrophysical Laboratory, Minsk, Belarus, alexandra.gurinovich@ephl.by

Abstract

A family of sources of short high-power electromagnetic pulses dedicated for equipment vulnerability tests is presented. The developed sources are compact and easy-to-use. They allow one to test different systems for electromagnetic pulse effect either in the laboratory or at the testing area, simulating diverse cases of interest.

Keywords: wideband source, short electromagnetic pulse, vulnerability test.

1 Introduction

High-power microwaves have emerged as a new technology allowing new applications and offering innovative approaches to existing applications [1], [2]. Sources of short high-power electromagnetic pulses are of great interest owing to their ability to disrupt or destroy electrical and electronic systems our society is rapidly becoming more and more dependent on. The infrastructure vulnerability (computers, communication systems, electronics of a car, etc.) is suspected, but is not definitely known. Simulators and test facilities for evaluating the electromagnetic pulse effect on electronics could provide the missing data and enable one to explore the protective measures. A range of microwave sources from small autonomous systems [3-6] to large microwave test facilities with varied frequency, pulse and burst length, pulse repetition frequency (PRF), and the output power [7-12] have been developed. The typical electric field strength values at 1 meter distance vary from several kilovolts to several hundreds of kilovolts per meter at frequencies from hundreds of MHz to several GHz. A conventional approach to the vulnerability tests implies either laboratory testing of separate devices and components inside a shielded room [3] or open-air testing of complex multi-component systems with large microwave test facilities [10,11]. Such measurements give data for vulnerability threshold rather than for the behavior of a system in real conditions. This is why testing facilities for in-situ trials are of a certain interest.

2 Concept

Development of the reported family of wideband radiation sources is motivated by numerous tasks for in-situ testing of communication and control systems, computer networks, etc. The sources are compact, easy-to-use, and demonstrative to be used in the laboratory for trials and training. They are capable of radiated electric field strengths from 70 to 800 kV/m at a normalized range of 1m and frequencies from 100 MHz to 2 GHz. Each source includes a pulsed power supply feeding a radiating antenna with an integrated discharge gap. Pulsed power supplies are of two types: a voltage multiplier and a power generator consisting of a capacitor bank and an exploding wire array. Omni-directional antennas of different shapes are designed for operation voltages from 55 to 250kV. The integrated discharge gaps are either gas-filled or oil insulated.

3 The sources

Three types of wideband sources are developed.

3.1. Portable repetitive source of 150 MHz frequency

A repetitive pulsed power source operates with output voltage of about 150 kV and pulse repetition frequencies up to 50 Hz. It is supplied by 24V accumulators. An omni-directional dipole antenna of 30 pF capacity produces "donut shaped" radiation pattern and can be either mounted on a tripod or simply placed on any dielectric surface. It has an integrated nitrogen-filled discharge gap and operates in the range from 150±50 MHz (Fig. 1).

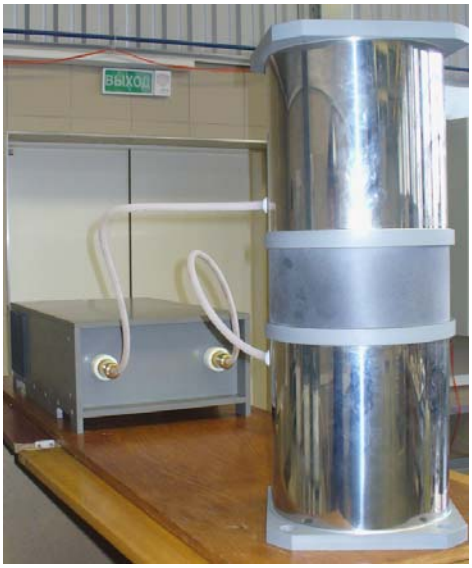

Figure 1. Portable repetitive source of 150MHz frequency

3.2. Portable repetitive source of 1 GHz frequency

An oil insulated voltage multiplier feeds a dipole antenna having a tunable gap and gas pressure. Electric field strength ~80kV/m at a normalized range of 1m in the range from 800 MHz to 1.2 GHz. Use of a dish reflector enables directing and amplifying the signal from the antenna in the prescribed direction to 700kV/m at 1m distance (Fig. 2).

3.3. A high-power single-shot radiation source

A simple circuit with 100kV/3kJ capacitor bank discharging through an array of 100 μm copper wires enables obtaining a single voltage pulse up to 700 kV, whereas use of the additional discharge gap provides shortening of the risetime of the voltage pulse at the antenna gap (Fig. 3). Varying the circuit inductance, the number and length of exploding wires, and the parameters of the discharger switching the voltage pulse to antenna, one gains an incredible assortment of pulse features.

Figure 2. Portable repetitive source of 1GHz frequency with the dish reflector

References

[1] J. Benford, J. A. Swegle, E. Schamiloglu "High Power Microwaves", Taylor& Francis, (2007).

[2] D.V. Giri, "High-Power Electromagnetic Radiators, Non-Lethal Weapons and Applications", Harvard University Press, (2004).

[3] F. Sonnemann, J. Bohl "Susceptibility and Vulnerability of Semiconductor Components and Circuits against HPM" in Proc. XXVIIth General Assembly of the International Union of Radio Science, 2002, Available: http://www.ursi.org Directory: Proceedings/ProcGA02/papers File: p1352.pdf

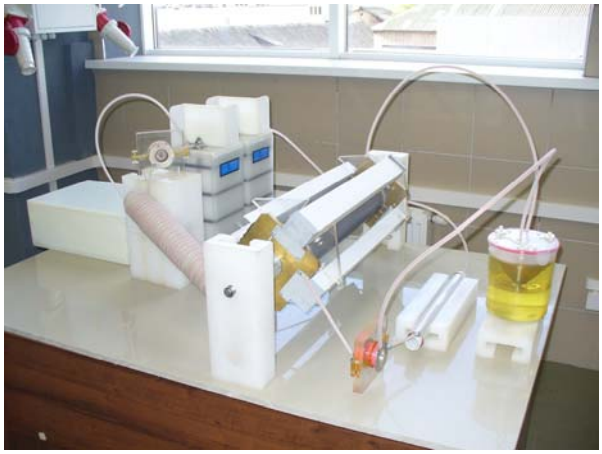

Figure 3. A compact single-shot radiation source

[4] S.M. Hwang, J.I. Hong, and C.S. Huh "Characterization of the susceptibility of integrated circuits with induction caused by high power microwaves", *Progress In Electromagnetics Research*, PIER 81, pp.61-72, (2008).

[5] M. Camp, H. Garbe, D. Nitsch, "UWB and EMP Susceptibility of Modern Electronics", IEEE EMC, Montreal, August 13-17, 2001, ISBN: 0-78036569-0, pp. 1015-1020, (2001).

[6] D. Nitsch, M. Camp, "UWB and EMP Susceptibility of Modern Microprocessorboards", presented at EMC Europe, Brugge, Sept., (2000).

[7] Benot Martin, Philippe Delmote "The GIMLI: a compact High-power UWB radiation source" presented at EUROEM'2008, Lausanne, Switzerland, (2008).

[8] Robert L. Gardner "Methods to Determine the Effect of Pulse Width on Susceptibility Threshold Levels" presented at EUROEM'2008, Lausanne, Switzerland, (2008).

[9] V.B. Carboni, H.J. Kishi,T.M. DaSilva, T.W. Tatman, I.D. Smith, C.C.R. Jones, N.R.M. Ritchie, S.I. Richmond "Full Threat Level Transportable Lightning Simulation System" presented at EUROEM'2008, Lausanne, Switzerland, (2008).

[10] Frank E. Peterkin, James L. Hebert, David C. Stoudt, and John Latess "Modification of an EMP facility to support threshold testing of electronic systems" in Proc. PPC-2005, 2005, p. 759, Available: ftp://ftp.pppl.gov Directory: pub/neumeyer/Pulsed_Power_Conf/data/papers/2005/ File: 2005_187.pdf

[11] Odd Harry Arnesen, Ernst Krogager, Mats Bäckström, Sigbjørn Bø-Sande, Jostein Godø, Seppo Härkönen, Karl G. Lövstrand, Mikko Moisio, Barbro Nordström, Jouni Peltonen, Ole Øystad "High power microwave effects on civilian equipment", Proc. URSI 2005, 2005, p. Available: http://rp.iszf.irk.ru Directory: hawk/URSI2005/pdf File: E03.2(0528).pdf

[12] V.G. Baryshevsky, A.E. Borisevich, A.A. Gurinovich, G.Yu. Drobyshev, P.V. Molchanov, A.V. Senko "A compact high power microwave (HPM) source" presented at EPPC 2009, Geneva, Switzerland, (2009).

VLF Lightning Detection Rate Dependence on Field Strength

J. Ashkenazy[1], A. Lipshtat*, A. S. Kesar**

**Soreq NRC, Yavne, Israel*, [1]joseph@soreq.gov.il

Abstract - VLF lightning detection rate is estimated. The dependence on electric field strength is obtained using the following: calculated field strength vs. distance, empirical scaling of lightning current vs. field strength, lightning distribution function, and global average lightning rate.

Keywords: lightning, VLF, field strength, global rate

Lighting signals dominates the VLF (3-30 kHz) range, and as signal detection threshold is lowered more lightning events are detected. The dependence of detection rate on signal strength could serve in studying lightning distributions. It could help also in discriminating the signal of phenomena of interest, such as meteorites or CTBT (Comprehensive Nuclear Test-Ban Treaty) related events, from the lightning background. We obtain an estimation of lightning detection rate dependence on received signal electric field strength, in four steps:

1. We use a simple analytical model for the current moment of the return stroke [1], $M(t)=I_{00}(v_0/\gamma)[e^{-at}-e^{-bt}][1-e^{-\gamma t}]$, with typical values for I_{00}, v_0, a, b, and γ of 30kA, $8\cdot10^7$m/s, $2\cdot10^4$s^{-1}, $2\cdot10^5$s^{-1}, and $3\cdot10^4$s^{-1} respectively [1]. We then use the long wavelength prediction capability (LWPC) code [2] to calculate the received signal as a function of distance, from which we get the field strength vs. distance for the corresponding peak current of $I_0 \approx 20$ kA, E(r,20).

2. It was found empirically [3] that lightning stroke radiated power scales with the discharge peak current as $I_0^{1.62}$, from which we deduce that $E(r,I_0) \sim I_0^{0.81}$. Then, the peak current that will result in field strength equal or larger than a specific threshold field, E_{th}, at a distance r is equal to or larger than

$$I_{th}(r, E_{th}) = 20 \cdot \left[\frac{E_{th}}{E(r, 20)}\right]^{1.23}. \qquad (1)$$

3. Lightning peak current closely follows a lognormal distribution [3,4]. The cumulative distribution function (CDF) is given by

$$CDF(I_0) = \frac{1}{\sqrt{2\pi}\sigma}\int_{I_0}^{\infty} e^{-\frac{[\ln(I_0)-\mu]^2}{2\sigma^2}}\frac{dI_0}{I_0}, \qquad (2)$$

where e^{μ} is the distribution median. In practice, the upper limit of integration is taken at 500 kA. Based on a comparison of five independent observational studies [4], we take here a median of 30kA for the peak current and $\sigma \approx 0.3$. In fact, the study in [4] refers to first stroke distribution. Nevertheless, since in multiple stroke flashes the first stroke is usually two times or more larger than subsequent stroke [5], we take it here as the distribution of lightning peak current. Substituting $I_{th}(r,E_{th})$ for I_0 we obtain $CDF(r,E_{th})$, which has to be interpreted as the probability of a received lightning signal, from a distance r, to have a field strength higher than the threshold value, E_{th}.

4. Integrating $CDF(r,E_{th})$ over area and multiplying by the global average lightning rate per square kilometer, n_g, we obtain an estimate for the average rate of received lightning signals above E_{th}:

$$N_{av}(E_{th}) = n_g \cdot 2\pi \int_0^{r_{max}} CDF(r, E_{th}) r dr, \qquad (3)$$

where r_{max} is a far enough distance. According to a recent global survey [6] there are close to $1.4\cdot10^9$ flashes per year over the entire Earth (intracloud and cloud to ground combined), corresponding approximately to a global average of $8.6\cdot10^{-8}$ lightning/s/km^2. Although this rate varies strongly with location and time, we assume that the large integration area (in the VLF lightning signals are collected from thousands of kilometer) effectively average over spatial and temporal variations. Typically, intracloud lightning consist about 2/3 of all lightning events although there are large geographical and seasonal variations. On the other hand, intracloud lightning are much weaker than cloud to ground flashes, and as such they will be detected only from a few hundred kilometers at most. To take account for that in estimating n_g, we divide the above global average by a factor of 2.

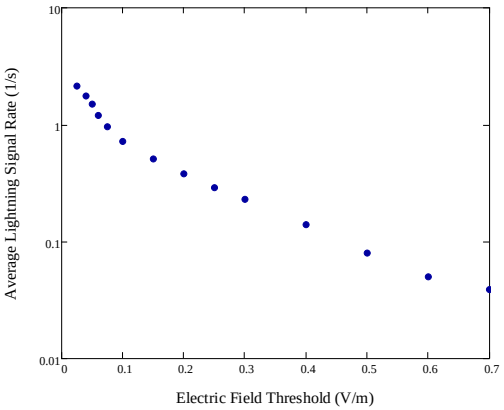

Figure 1: Average lightning signal rate vs. field strength threshold.

$N_{av}(E_{th})$ was calculated for threshold field values in the range 0.025 - 0.7 V/m, and for r_{max} = 4000 km. Fig. 1 shows the

results, demonstrating an appreciable rate increase as the threshold is lowered. It should be mentioned here that at very low threshold values the receiving system may become sensitive also to other sources of noise.

[1] A. S. Dennis, and E. T. Pierce, "The return stroke of the lightning flash to earth as a source of VLF atmospherics", *Radio Sci.*, 68D, 1964.

[2] J. A. Ferguson, "Computer programs for assessment of long wavelength radio communication, version 2.0", Tech. Doc. 3030, Space and Naval Warfare Systems Centre, San Diego, CA, 1998.

[3] M. L. Hutchins, R. H. Holzworth, C. J. Rodger and J. B. Brundell, "Far-field power of lightning strokes as measured by the World Wide Lightning Location Network", *Journal of Atmospheric and Oceanic technology*, vol. 29, pp. 1102-1110, 2012.

[4] J. Takami and S. Okabe, "Observational results of lightning current on transmission towers", *IEEE Trans. Power Delivery* , vol. 22, no. 1, pp. 547-556, 2007.

[5] M. A. Uman and E. P. Krider, "A review of Natural lightning: experimental data and modeling", *IEEE Trans. Electromagnetic Compatability*, vol. EMC-24, no.2, 1982.

[6] H. Christian et al, "Global frequency and distribution of lightning as observed from space by the Optical Transient Detector", *J. of Geophysical Research*, vol. 108, p. 4005, 2003.

Occurrence of Downward and Upward Flashes at the Säntis Tower: Relationship with -10°C Temperature Altitude

M. Azadifar[1], M. Lagasio[2], E. Fiori[2], F. Rachidi[1], M. Rubinstein[3], R. Procopio[4]

1 Swiss Federal Institute of Technology (EPFL), Lausanne, Switzerland
2 CIMA Research Foundation, Savona, Italy
3 University of Applied Sciences of Western Switzerland, Yverdon, Switzerland
4 University of Genoa, Genoa, Italy

Abstract

The negative charge center in thunderclouds is typically located at the -10 °C altitude. Recent studies have suggested that this altitude might be closely related to the initiation of upward flashes from tall structures. In this study, we examine the -10 °C altitude for 37 lightning events occurred at the Säntis tower.

Keywords: ***Lightning, upward flashes, downward flashes, tall towers.***

1 Introduction

The mechanisms of initiation of upward discharges from tall structures are not fully understood (e.g., [1]). Recently, Miki et al. [2] presented an analysis according to which 19 out of 42 downward flashes to the 634-m tall Tokyo Skytree Tower occurred when the -10 °C altitude was higher than 5.5 km. On the other hand, most of the upward flashes occurred when this altitude was below 5.5 km. It is worth noting that negative charges are typically located at altitudes corresponding to a temperature range of -10 to -25 °C [3].
In this study, we examine the -10 °C altitude for lightning events occurred at the Säntis tower.

2 Instrumentation and Observed Lightning Characteristics

The Säntis Tower is located on the top of the 2502-m-tall Mount Säntis in north-eastern Switzerland. The tower is equipped with a lightning current measurement system (see [4,5] for more information on the instrumentation). From June 2010 to January 2015, 427 lightning flashes were successfully recorded at the Säntis Tower, out of which 355 were classified as negative, as positive and 13 as bipolar. Fig. 1 shows the monthly distribution of lightning flashes recorded at the Säntis Tower indicating higher lightning activity during the warm seasons. The great majority of the recorded flashes are of upward type. Indeed, out of 427 recorded flashes, only 4 were classified as downward (3 negative and 1 positive).

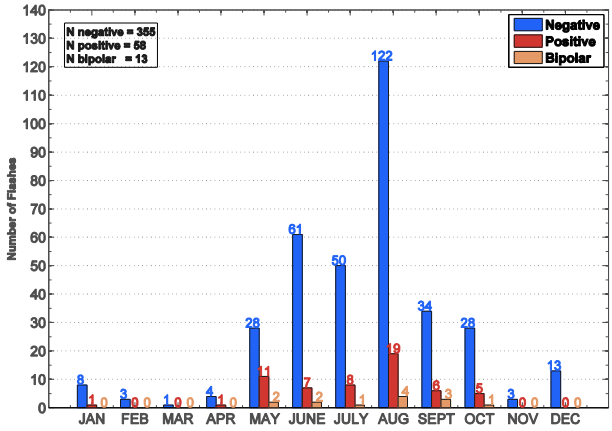

Figure 1. Monthly distribution of lightning flashes recorded at the Säntis Tower

3 Simulation of -10 °C Temperature Altitudes

The numerical weather prediction model used is the Advanced Research Weather Research and Forecast model (WRF-ARW) [6]. The WRF-ARW model calculates the temperature, pressure, all microphysics species, and wind on a discretized three-dimensional grid.
Since in this work the model outputs are available only at each grid point and every 30 minutes, two approximations have been considered in the evaluation of the -10 °C altitude: It is assumed that the Säntis tower is placed in the nearest model grid point and that lightning has occurred at the nearest model time sample without making any interpolation. Since the horizontal grid resolution (1 km x 1 km) and the time sampling for this study are fine enough, the error due to these assumptions is expected to be negligible.
Once the horizontal coordinates and the time sampling are chosen, the required altitude is evaluated performing a linear interpolation between the two consecutive vertical levels whose temperatures contain -10 °C. Such interpolation was used because, while the horizontal grid resolution is uniform ($\Delta x=\Delta y$), a non-uniform sampling is used for the height. Since the most important atmospheric phenomena occur in the atmospheric zone closer to the ground, a higher and not equally distributed number of vertical levels is generally employed in the first kilometres of the atmosphere. A smaller number of

more spatially distributed vertical levels is used to discretize the remaining part of the atmosphere.
To validate the model performance, the temperature data recorded at Payerne station in Switzerland every 12 hours using weather balloons were used. The resulting error in the evaluation of the –10 °C heights at Payerne was found to have a mean value of 95 m and a standard deviation of 300 m.

4 Analysis

The methodology presented in Section 3 was used to evaluate the -10 °C isotherm altitude for the 37 flashes of 6 individual storms. The considered data set includes 3 negative downward flashes, 28 negative upward flashes and 6 positive upward flashes.
Fig. 2 shows the distribution of the -10 °C altitudes for the 37 selected events. It should be noted that all heights are calculated above sea level (ASL).

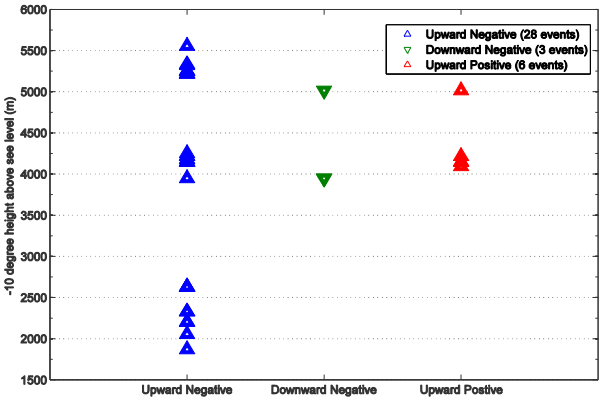

Figure 2. Distribution of -10 °C altitudes (Above Sea Level) as a function of flash type.

For upward negative flashes, the -10 °C ASL altitudes range from about 1.9 to 5.5 km, which is in agreement with the findings of Miki et al. [2]. However, it is also interesting to observe that for the three downward flashes, the -10 °C ASL altitudes were, respectively, 3.9, 4.2 and 5 km. Furthermore, no positive events occurred while the height of the -10 °C isotherm was below 4 km, which is in agreement with the fact that positive charges are generally located in the higher parts of the thunderclouds.
It should be noted, however, that the geographical conditions are very different in the two studies: a 634-m tall tower located on flat terrain in Tokyo (44 m ASL) versus a 124-m tall tower on the top of a 2500 m mountain.

4 Conclusion

Recent studies in Japan suggest that the altitude of the -10 °C temperature level might be related to the initiation of upward discharges from tall structures.
In this study, we examined the -10 °C altitude for 37 lightning events occurred at the Säntis tower. The -10 °C temperature altitudes were determined using the Advanced Research Weather Research and Forecast model (WRF-ARW). The model performance was validated using experimental data of temperature recorded at Payerne station in Switzerland using weather balloons.
Unlike the findings in Japan, the preliminary analysis reveals that the -10 °C altitudes of the three considered downward lightning flashes at Säntis were lower than 5.5 km.
More data are needed before any definitive conclusions can be drawn.

Acknowledgements

Financial support from the Swiss National Science Foundation (Project No. 200021_147058) is acknowledged.

References

[1] A. Smorgonskiy, A. Tajalli, F. Rachidi, M. Rubinstein, G. Diendorfer, and H. Pichler, “An analysis of the initiation of upward flashes from tall towers with particular reference to Gaisberg and Säntis Towers,” *Journal of Atmospheric and Solar-Terrestrial Physics*, *136*, 46-51, 2015.

[2] T. Miki, M. Saito, S. Sugimoto, T. Shindo, H. Motoyama, M. Ishii, H. Taguchi, A. Tajima and A. Fujisawa, “Meteorological condition influencing lightning characteristics hitting Tokyo Skytree,” presented in International Conference on Lightning and Static Electricity, Toulouse, France, 2015.

[3] P.R. Krehbiel, The electrical structure of thunderstorms. In The Earth’s Electrical Environment, eds. E.P. Krider and R.G. Roble, pp. 90-113, National Academy Press, Washington DC, 1986.

[4] C. Romero, M. Paolone, M. Rubinstein, F. Rachidi, A. Rubinstein, G. Diendorfer, W. Schulz, B. Daout, A. Kaelin, and P. Zweiacker, “A system for the measurements of lightning currents at the Säntis Tower,” Elect. Power Syst. Res. J., vol. 82, pp. 34–43, 2012.

[5] M. Azadifar, M. Paolone, D. Pavanello, F. Rachidi, C. Romero, and M. Rubinstein, “An Update on the Instrumentation of the Säntis Tower in Switzerland for Lightning Current Measurements and Obtained Results”, CIGRE International Colloquium on Lightning and Power Systems, Lyon, France, 2014.

[6] W. C. Skamarock, J. B. Klemp, J. Dudhia, D. O. Gill, D. M. Barker, W. Wang, and J. G. Powers, "A description of the advanced research WRF version 2", NCAR Tech. Note TN-468 STR, 88 pp., Natl. Center for Atmos. Res., Boulder, Colo., 2005.

Progress in a statistical topological approach using wave-chaos for electromagnetic effects (STUWEE) studies

G Hadi, S Hemmady, and E Schamiloglu

Dept. of Electrical and Computer Engineering, University of New Mexico, Albuquerque, NM 87131 USA ghadi@unm.edu

Abstract

Predicting the statistical nature of short wavelength reverberation within random interconnections of large complicated cavities finds applications in several fields of physics and engineering. To aide in developing this predictive capability, this paper describes progress in the development of a computational framework that fuses the random coupling model (RCM) with the electromagnetic topology model of Baum-Liu-Tesche. Our simulated results are validated by experimental tests.

Keywords: statistical electromagnetism, wave chaos, Random coupling model; multiconductor transmission lines, BLT equations.

1 Introduction

Predicting the nature of the scattering of short-wavelength waves in random interconnected networks of large chaotic enclosures is routinely encountered in diverse fields such as acoustics, wireless communications, and electromagnetic compatibility engineering. The Random Coupling Model (RCM) [1], based on wave-chaos, is a statistical model describing the scattering of short wavelength waves in large complicated (chaotic) enclosures. The Baum-Liu-Tesche (BLT) EM topology formulation [2] is a hierarchical framework based on the multi-conductor transmission line (MTL) model for describing the flow of energy between different nodes on a network of MTL segments. In this research, we fuse the RCM with the BLT EM topology to create the *"Statistical Topological approach Using Wave-chaos for Electromagnetic Effects"* (STUWEE) for predicting the statistics of the scattering of short-wavelength electromagnetic waves in random interconnected networks of chaotic enclosures. We present experimental results demonstrating the existence of wave-chaotic fluctuations in a large 3D mode stirred chamber (MSC), in accordance with the RCM, and then show how these fluctuations are affected when considering random interconnections of MSCs.

2 Details of the Research

In the context of a very large complicated system, such as the bulkheads of a ship or the fuselage of an airplane exposed to incident electromagnetic energy, analyzing the electromagnetic coupling and interactions is very difficult to model in a deterministic manner. A statistical approach is thus warranted to capture the shapes and scales of the induced fluctuations within the system. To this end, in order to understand the coupling of radiation into an electrically large system, a decomposition of the entire system into subsystems was advocated as the BLT EM topological approach. The BLT equation describes the voltage or current responses on a network of transmission lines [2]. The RCM is a statistical approach based on random matrix theory and wave-chaos. It can predict the induced voltages and currents for objects and components inside complicated enclosures when subjected to electromagnetic fields. This is done by reproducing a large ensemble of the cavity impedance or scattering parameters through a Monte Carlo random matrix theory simulation from the cavity loss parameter and the radiation impedance properties of the coupling ports [3].

Fusing the RCM with the BLT EM topology will enable a rapid assessment of the EM coupling within large complicated systems. This work uses the BLT EM topology to break down the networked cavities and the RCM to study the statistics of each cavity. Li *et al.* [3] took the first steps at this by using two empty computer towers as cavities and connecting them. This research extends their work. In addition to studying the transition from deterministic behavior to wave chaos in a large 3D MSC, we are planning on studying the response of networked 2D Sinai-like cavities.

3 Single Cavity Experiment Setup

The experimental setup consists of a 3D aluminium cavity (Fig. 1a) that acts as a reverberation chamber with paddle-wheel blades. Fig. 1b shows the mode stirrer controlled by a LabVIEW program that rotates it incrementally. The cavity is connected by two transmission lines that hook up to a Keysight E5061B vector network analyzer. The cavity is driven by two ports to measure a large statistical ensemble of a 2x2 cavity scattering matrix $\vec{\vec{S}}$.

In order to generate a very large ensemble of data, the EM configuration inside the cavity changes for each degree rotation as the mode stirrer is incrementally turned. At each increment $\vec{\vec{S}}$ is measured as a function of frequency in 100 MHz increments from 300 MHz to 3 GHz. By rotating the mode stirrer 200 times, an ensemble of 320200 cavity scattering matrices is obtained at each 100 MHz increment.

According to Hemmady et al. [4], once $\vec{\vec{S}}$ is generated, the cavity impedance matrix can be obtained using

$$\overleftrightarrow{Z} = \overleftrightarrow{Z}_0^{1/2}\left(\overleftrightarrow{1} + \overleftrightarrow{S}\right)\left(\overleftrightarrow{1} - \overleftrightarrow{S}\right)\overleftrightarrow{Z}_0^{1/2}. \quad (1)$$

$\overleftrightarrow{Z}$ then has a mean part given by the radiation impedance matrix

$$\overleftrightarrow{Z}_{\text{rad}} = \langle \overleftrightarrow{Z} \rangle. \quad (2)$$

Once we know the radiation impedance we can then easily obtain the normalized impedance matrix $\overleftrightarrow{z}$ and the normalized scattering matrix $\overleftrightarrow{s}$, given by Eqs. (3) and (4), respectively.

$$\overleftrightarrow{z} = \left(\text{Re}\left[\overleftrightarrow{Z}_{\text{rad}}\right]^{-1/2}\left(\overleftrightarrow{Z} - i\,\text{Im}\left[\overleftrightarrow{Z}_{\text{rad}}\right]\right)\left(\text{Re}\left[\overleftrightarrow{Z}_{\text{rad}}\right]\right)^{-1/2}\right) \quad (3)$$

$$\overleftrightarrow{s} = \left(\overleftrightarrow{z} - \overleftrightarrow{1}\right)\left(\overleftrightarrow{z} + \overleftrightarrow{1}\right)^{-1}. \quad (4)$$

Fig. 1a. Photograph of the experimental setup of a single aluminum cavity.

Fig. 1b. Photograph of the mode stirrer inside the cavity.

4 Experimental Chaos Verification for a Single 3D Cavity

We verify the existence of wave-chaotic scattering in our 3D cavity by verifying the statistical independence of the phase and magnitude of the normalized $\overleftrightarrow{s}$ eigenvalues (Dyson's circular ensemble hypothesis). We validated the hypothesis by decomposing the eigenvalues of normalized supervector $\overleftrightarrow{s}$. We then group the eigenvalues into a list of complex eigenvalues (λ_s). Fig. 2 shows the polar contour density plot for {Re[λ_s], Im[λ_s]} in the frequency range of 2.8-2.9 GHz where the loss parameter of the cavity is 1.6. Using Dyson's hypothesis, we were able to confirm that our 3D aluminium cavity is chaotic above 1.6 GHz.

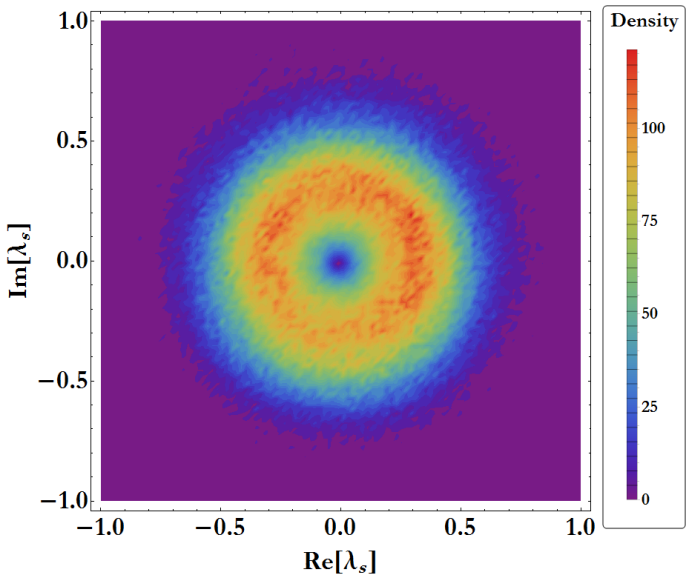

Fig. 2. Polar contour density plot of real λ_s *vs.* imaginary λ_s.

Acknowledgements

This work is supported by ONR Code 35 Grant N00014-14-1-0794, Ryan Hoffman, Program Officer.

References

[1] S. Hemmady, X. Zheng, E. Ott, T.M. Antonsen, and S.M. Anlage, *Phys. Rev. Lett.*, vol. 94, 014102 (2005).

[2] C.E. Baum, Interaction Notes 400 (http://ece-research.unm.edu/summa/notes/In/0400.pdf).

[3] X. Li, C. Meng, Y. Liu, E. Schamiloglu, and S.D. Hemmady, *IEEE Trans. Electromagn. Compat.*, vol. 57, 448 (2015).

[4] S. Hemmady, X. Zheng, T.M. Antonsen, E. Ott, S.M. Anlage, "Universal Properties of 2-Port Scattering, Impedance and Admittance Matrices of Wave Chaotic Systems," *Phys. Rev. E*, vol. 74, 036213 (2006).

Calculation of Electromagnetic Pulse Effect Threshold Probability with Maximum Entropy Model

Kejie LI[#1], Yuhao CHEN[#2], Yanzhao XIE[#3]
[#]State Key Laboratory of Electrical Insulation and Power Equipment
School of Electrical Engineering, Xi'an Jiaotong University
Xi'an, Shaanxi Province, China
[1]kejie.li@hotmail.com, [2]chenyuhao@stu.mail.xjtu.edu.cn, [3]yzxie@mail.xjtu.edu.cn

***Abstract*—Electromagnetic pulse (EMP) does great effects on various electronic devices and systems for its high power and wide band. In order to find the relationship between incident waveform characteristics and caused effects, probability and statistics methods were introduced [1]. The threshold probability model and fit method which is used in our research and experiment, however, needs the assumption of the distribution function usually unknown. This paper proposes a method resulting in the fitted function itself instead of parameters of assumed fitted function. For this reason, the maximum entropy model was introduced and result was verified.**

Keywords-Electromagnetic Pulse Effect; Threshold Probability; Maximum Entropy Model; Lagrange Multipliers; Generalized Iterative Scaling

I. INTRODUCTION

Probability threshold is a proposed bridge to link the "dose" and "response" when objects were put under EMP threaten environment to check the vulnerability of electronic devices and systems. For certain kinds of tested ones, the "does" was continuous as incident electric/magnetic field amplitude, energy or power, and the "response" was discrete as "communication was interrupted or not", which can be classified as case "1"(interrupted) or case "0"(not be interrupted). If we assume every case only happens when input value x is greater than certain inner value, so-called "threshold" T, the result y can be written as:

$$y=\begin{cases}0, & \text{if } x<T\\ 1, & \text{if } x\geq T\end{cases} \tag{1}$$

where $x\in[a,b]$; $a<b$; $a,b\in \mathrm{R}$; $y\in\{0,1\}$.

If the threshold T is random, the model change into probability threshold, which is much more complicated and realistic because systematic and random error make threshold different every time. Given an x, the y may value from {0,1} with different probability, which can be defined by

$$P(Y=0\,|\,X=x)+P(Y=1\,|\,X=x)=1 \tag{2}$$

$$P(Y=1\,|\,X=x)=P(x\geq T)=P(x\leq T)=F(T)\big|_{T=x} \tag{3}$$

where P is probability, F is cumulative distribution function (CDF) of T.

To solve this problem, experimental result data (x_i, y_i) $(i=1,2,\cdots n)$ was used to fit the model. However, when the size of sample is limited or lack the exact information of the population, the fitted function is hard to choose. Although there are amounts of methods which can be used to test the goodness of the fit, only allowing to compare or deny the results after fitting, the result may deeply depends on the assumption of the initial choices.

Instead of making assumption of $F(T)$, we can calculate $P(Y=y\,|\,X=x)$ directly. This paper uses maximum entropy model, trained by the experimental result data, to predict the probability of $P(Y=y\,|\,X=x)$ with entropy maximum, which is the only assumption we need to make, and the result depends on the training data only.

II. MAXIMUM ENTROPY MODEL

A. Probability and Entropy

Based on the Shannon's theory of information entropy, the conditional entropy of our probability is

$$h(p(y\,|\,x))=-\iint_{x,y}p(x)\,p(y\,|\,x)\log(p(y\,|\,x))\mathrm{d}x\mathrm{d}y \tag{4}$$

Because we don't have any information about $p(y\,|\,x)$, which means any subjective assumption (prejudice) might lead to error when estimating the probability. So, the safest way is to regard $p(y\,|\,x)$ as

$$p^{*}(y\,|\,x)=\arg\max h(p(y\,|\,x)) \tag{5},$$

for maximum entropy results in minimum information.

Then there came the experimental result data (x_i, y_i), which the model must admit. Each training data (x_i, y_i) can define a feature function $f_i(x,y)$ itself. In order to satisfy the probability threshold, the feature functions are defined as

$$f_i(x,y)=\begin{cases}1, & \text{if } y=y_i=0, x<x_i \text{ or } y=y_i=1, x\geq x_i\\ 0, & \text{else}\end{cases} \tag{6}$$

The feature function is a kind of weight function valuing "1" only when the condition is satisfied. With the help of

$f_i(x,y)$, all the training data change into weight functions. The constraint condition can be written as:

$$E_{\tilde{P}}(f) = E_P(f) \tag{7}$$

where $E_{\tilde{P}}(f)$ and $E_P(f)$ are expectations of $f_i(x,y)$ based on sample distribution and population distribution, respectively:

Then we can get the maximum entropy model's expression:

$$\begin{aligned} & p^*(y \mid x) = \arg\max h(p(y \mid x)) \\ & s.t. \quad E_{\tilde{P}}(f) = E_P(f), i = 1,2,\cdots,n \\ & \int_y p(y \mid x)\mathrm{d}y = 1 \end{aligned} \tag{8}$$

The Lagrange multipliers $L(p(y \mid x), \lambda)$ are introduced to combine the constraint conditions into one equation:

$$\begin{aligned} & L(p(y \mid x), \lambda) = h(p(y \mid x)) \\ & \quad + \sum_{i=1}^{n} \lambda_i (E_{\tilde{P}}(f) - E_P(f)) + \lambda_0 (\int_y p(y \mid x)\mathrm{d}y - 1) \end{aligned} \tag{9}$$

Finally, we get the model:

$$p^*(y \mid x) = \arg\max_{p(y|x)} \min_{\lambda} L(p(y \mid x), \lambda) \tag{10}$$

B. Generalized Iterative Scaling

An iteration method is used to replace maximum/minimum process above. Set the $\frac{\partial}{\partial \lambda} L(p(y \mid x), \lambda) = 0$,then we get:

$$P^*(y \mid x) = \frac{1}{Z(x)} \exp(\sum_{i=1}^{n} \lambda_i f_i(x,y)) \tag{11}$$

where $Z(x) = \int_y \exp(\sum_{i=1}^{n} \lambda_i f_i(x,y))\mathrm{d}y$.

The $P^*(y \mid x)$ only relies on λ ,which can be iterated by generalized iterative scaling (GIS)[2] method:

$$\begin{aligned} & \lambda_i^0 = 0 \\ & \lambda_i^{k+1} = \lambda_i^k + \frac{1}{C} \log \frac{E_{\tilde{P}}(f_i)}{E_{\tilde{P}}(f_i)} \quad i = 1,2,\cdots,n \end{aligned} \tag{12}$$

where C is constant.

III. Model Verification

Considering a threshold with normal distribution $\Phi(\mu = 25, \sigma = 5)$, from which we draw $n = 100$ samples T with input x ranges from $[a = 5, b = 60]$ uniformly. We can easily get the threshold CDF curves of population and sample. For each x_i, calculate $y_i = \begin{cases} 0, & x_i < T_i \\ 1, & x_i \geq T_i \end{cases}$ and only use (x_i, y_i) as training data. (See Figure 1.)

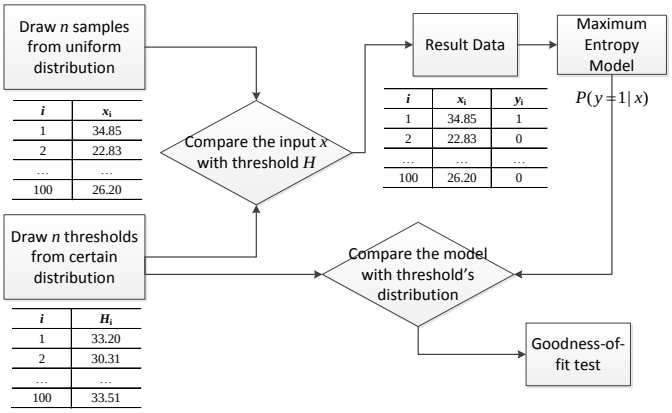

Figure 1. A flowchart showing model verification procedure

The GIS after 50 iterations is shown in the Figure 2.(dash line), compared with the threshold probability's population and sample distribution (solid line and dot dash line respectively)).

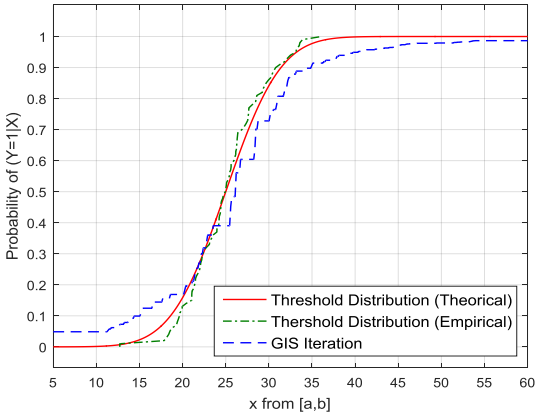

Figure 2. Threshold Probability Comparison

The result shown that the proposed maximum entropy model can give the probability of y $P(y \mid x)$. A Chi-Square test was made to compare the regressed data with threshold's empirical distribution. With the p-value= 0.9252, the null hypothesis cannot be rejected.

IV. Conclusion

EMP effect experimental data was processed based on threshold probability. For single threshold case, when only continues x induced discrete y, the maximum entropy model was proposed to calculate the distribution of threshold regardless the assumption of threshold's function form. With the help of GIS iteration, the model was verified within a simulated example. The result is totally acceptable.

References

[1] Kejie LI, Shaofei WANG, Di WANG, et al. EMP effects statistical analysis based on incident waveform characteristics. The 7th Asia-Pacific Conference on Environmental Electromagnetics (CEEM 2015), Hangzhou, China.

[2] J. N. Darroch, D. Ratcliff. Generalized Iterative Scaling for Log-Linear Models. Annals of Mathematical Statistics, 1972, 43(5):p.1470-148.

Efficient Full-Wave Simulation of the Stochastic Field Coupling to Transmission Line Networks using the Method of Moments

M. Magdowski and R. Vick

Otto-von-Guericke-University, Magdeburg, Germany, Email: mathias.magdowski@ovgu.de

Abstract

An efficient method for the simulation of the stochastic electromagnetic field coupling using the method of moments is exemplary demonstrated for a simple transmission line network of single wires above a conducting ground plane. The coupled voltage at all line terminals is simulated and analyzed statistically. The results are compared to numerical simulations using classical transmission line theory.

Keywords: Transmission Line Theory, Cumulative Distribution Function, BLT Equations, Plane Wave Approximation

1 Introduction

Transmission lines are important coupling paths. Often several lines are connected together forming a network. It is interesting to analyze the excitation by stochastic fields [1], as they are a valuable model for fields in overmoded cavities or reverberation chambers. A simple approach is to simulate one complex field pattern by a superposition of several plane waves.

A simulation model for the stochastic field coupling to transmission line networks based on classical transmission line theory has been presented in [2]. It is also desirable to use the method of moments [3] for such kind of problems, as it is a full-wave method and can handle more general transmission line structures. The usual problem is that the computational effort becomes very large, if several patterns of the stochastic field have to be calculated. A drastic acceleration of the method was presented in [4], where the system matrix has to determined only once.

2 Simulation Example

As an example, the same transmission line network as in [2] will be used. It consists of three lines with a length of $40\,\mathrm{cm}$, $30\,\mathrm{cm}$ and $50\,\mathrm{cm}$ that are connected in a star point. A schematic of this network is shown in Fig. 1. The height of the wires above the ground plane is fixed to $1\,\mathrm{cm}$. The wire radii are $0.6\,\mathrm{mm}$, $0.5\,\mathrm{mm}$ and $0.4\,\mathrm{mm}$ resulting in characteristic impedances of $210.2\,\Omega$, $221.1\,\Omega$ and $234.5\,\Omega$.

According to [2], the coupled voltages at the beginning and end of the ith line are denoted by $U_{\mathrm{L1},i}$ and $U_{\mathrm{L2},i}$. These voltages point from the line to the ground. The voltages for all lines can be represented by two column vectors $[U_{\mathrm{L1}}]$ and $[U_{\mathrm{L2}}]$ with the dimension $L \times 1$, where L denotes the number of lines.

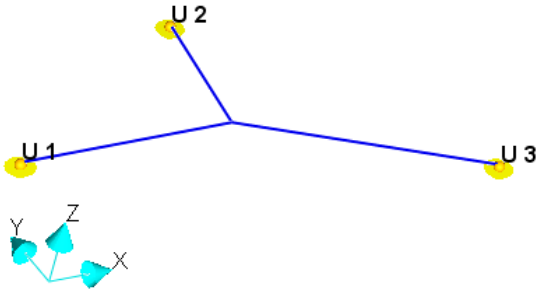

Figure 1: Screenshot of the simulation model of the three-wire transmission line network in CONCEPT-II [5]. The transmission lines are printed in blue. The load resistances are marked by small orange spheres. The conducting ground plane is indicated by small yellow circles. The voltage probes U1, U2 and U3 correspond to the voltages $U_{\mathrm{L1},1}$, $U_{\mathrm{L1},2}$ and $U_{\mathrm{L2},3}$, respectively.

To give a short notation for the entire network, the vectors $[U_{\mathrm{L1}}]$ and $[U_{\mathrm{L2}}]$ can be combined to a single supervector with the dimension $2L \times 1$. Similar to [2, Eq. (13)] all voltages can be calculated using a network BLT equation (named after *Baum*, *Liu* and *Tesche*).

$$[U_L] = \begin{bmatrix}[U_{\mathrm{L1}}] \\ [U_{\mathrm{L2}}]\end{bmatrix} = \big[[E] + [\rho]\big] \cdot \big[[\Gamma] - [\rho]\big]^{-1} \cdot [S] \quad (1)$$

Here, $[E]$ is a $2L \times 2L$ identity matrix. The $2L \times 2L$ reflection matrix $[\rho]$ contains the voltage reflection and transmission coefficients for the whole network. The matrix $[\Gamma]$ is a $2L \times 2L$ propagation matrix and the $2L \times 1$ supervector $[S]$ contains the sources for the field excitation (see [2] for details).

For the BLT calculation as well as for the simulation using the method of moments, a number of 360 field patterns are used as in [2], where each consists of 10 superposed plane waves. The average squared magnitude of the total field strength was normalized to $1\,\mathrm{V}^2/\mathrm{m}^2$.

3 Results and Discussion

Exemplary results for the frequency dependence of the coupled voltage are shown in Fig. 2 and 3. The squared magnitude of the voltage is interesting, as it is proportional to the coupled power. In Fig. 3, smaller load resistances also lead to smaller coupled voltages (but also to higher currents). From both Figs. 2 and 3, transmission line resonances of individual lines and the entire

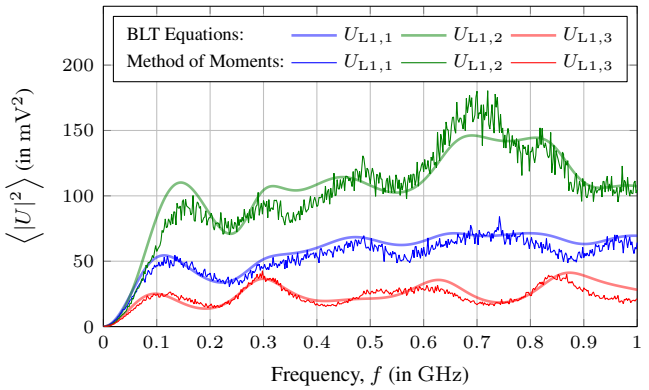

Figure 2: Average squared magnitude of the coupled voltage at the terminals of the transmission line network

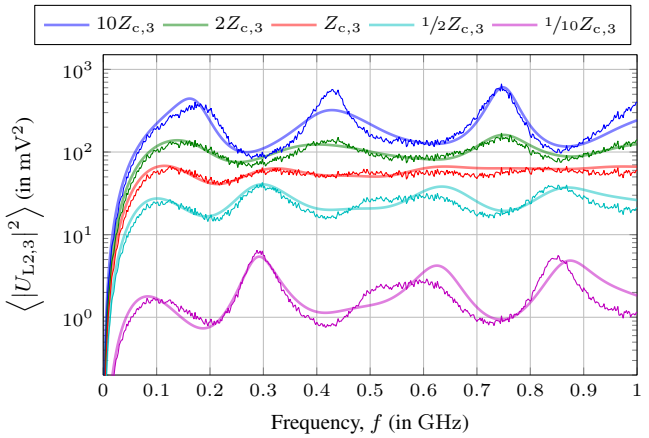

Figure 3: Average squared magnitude of the coupled voltage at the end of transmission line 3 for different load resistances at this line end, which are given as multiples of the characteristic impedance $Z_{c,3}$ of this transmission line (thick lines show the results of the BTL equations, thin lines the results of the method-of-moments simulation).

network are visible. The agreement between both approaches is quite good.

Fig. 4 shows the statistic distribution of the coupled voltage. To obtain a large sample size and smooth distribution functions, all values have been normalized to the corresponding mean value over all field patterns at each frequency. It can be noticed that there is a certain ratio between the prevailing minimum, mean and maximum values. On that condition, the expected maximum value of the coupled voltage can be approximated from the measured or simulated mean for a certain sample size.

4 Conclusion

The field-to-wire coupling has been calculated for a transmission line network using classical transmission line theory and the method of moments. Both methods are comparable in their computational effort, yet the approach using the method of moments can handle more arbitrary transmission line structures like non-uniform lines.

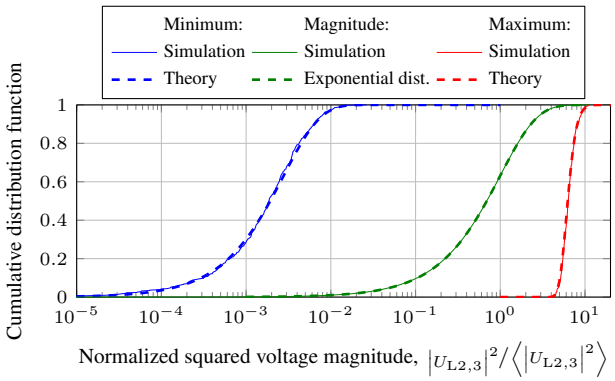

Figure 4: Cumulative distribution function of the squared magnitude of the coupled voltage at the end of transmission line 3 normalized to the mean value. The theoretical distribution function are calculated according to [1, 6].

Acknowledgment

The authors would like to thank Mr. Buddhi Ram Banjade for doing the initial simulations.

References

[1] D. A. Hill, *Electromagnetic Fields in Cavities: Deterministic and Statistical Theories*, 1st ed., ser. IEEE Press Series on Electromagnetic Wave Theory. Piscataway, NJ, USA: IEEE Press, Oct. 2009.

[2] M. Magdowski and R. Vick, "Numerical simulation of the stochastic electromagnetic field coupling to transmission line networks," in *Proceedings of the Joint IEEE International Symposium on Electromagnetic Compatibility and EMC Europe*, Dresden, Germany, Aug. 2015, pp. 818–823, IEEE Catalog Number: CFP15EMC-USB.

[3] R. F. Harrington, *Field Computation by Moment Methods*, 1st ed., ser. IEEE Press Series on Electromagnetic Waves, D. G. Dudley, Ed. Piscataway, NJ, USA: IEEE Press, 1993, originally published by R. E. Krieger Publishing Company Inc., Malabar, FL, USA, 1968.

[4] M. Magdowski, A. Schröder, H. Brüns, and R. Vick, "Effiziente Simulation der Einkopplung statistischer Felder in Leitungsstrukturen mit der Momentenmethode," in *Internationale Fachmesse und Kongress für Elektromagnetische Verträglichkeit*, Heyno Garbe, Leibniz University Hannover, Germany, Ed. emv 2014, Düsseldorf, Germany, 11.–13.03.2014: VDE Verlag GmbH, Berlin & Offenbach, Germany, Mar. 2014, pp. 238 – 245.

[5] Technical University Hamburg-Harburg. CONCEPT-II, version 12.0. [Online]. Available: http://www.tet.tu-harburg.de/concept/?lang=en

[6] J. Galambos, *The Asymptotic Theory of Extreme Order Statistics*, 1st ed., ser. Wiley Series in Probability and Statistics – Applied Probability and Statistics Section. New York, USA: Wiley, May 1978.

Statistical Significance and Reliability of HEPM Field Tests

Lars Ole Fichte*,Sven Knoth†, Stefan Potthast#, Frank Sabath#, Marcus Stiemer*

**Helmut Schmidt University, Faculty of Electrical Engineering, Hamburg, Germany*
† Helmut Schmidt University, Faculty of Economics, Hamburg, Germany
#Bundeswehr Research Institute for Protective Technologgies – NBC-Protection, Munster, Germany

Abstract

In this paper, several statistical approaches to assess the quality of HEMP field tests are presented and compared to the test protocol specified by a German standard. The proposed schemes are based on acceptance sampling and confidence intervals and improve the significance of the derived conclusions. In addition, more advanced techniques are discussed.

Keywords: HEMP field tests, Statistical Evaluation

1 Introduction

Several national and international standards on how to perform HEMP field test exist, and have been reviewed in numerous papers in the past [1]. Yet, employing statistical models can lead to a better understanding of the test's validity.

A device under test (DUT) which fails to pass a HEMP test with a non-zero probability **might**, but **need not** fail in the next test run. If we consider, e.g., a DUT with a probability of failure p_{FA} = 0.1$, and perform a test sequence of five single exposures on it, the probability for at least one failure is *1-(1-0.1)^5 = 0.41*, which is remarkably high.
This means that a satisfactory device with a sufficiently small failure probability has a good chance to fail the test. This gives rise to the question how reliable and significant test results are and how they should be validated.

To deal with this problem, limits for `sturdy' and `vulnerable' DUTs can be introduced, e.g. a DUT with p_{FA}=0.1 would be classified as sturdy, whereas p_{FA}=0.5 would mean that it is vulnerable. The aim of any statistical method proposed in this paper is to ensure that the chances for misclassification are as small as possible (i.e., that a vulnerable devices is tested and classified as sturdy, or vice versa).
Tab.~1 shows the four possible combinations. While in the cases marked with `ok' the test results correctly predict the system vulnerability in the real world, `case 1' means that a vulnerable DUT was not detected by the test sequence. This is the worst case from an operational viewpoint. The last combination, `case 2', is undesirable from an economic viewpoint because `sturdy' DUTs are falsely rejected.

Table 1: Classification of a DUT after test sequence

	passed	failed
"vulnerable"	Case 1	Ok
"sturdy"	ok	Case 2

2 Acceptance testing

Acceptance sampling is a common tool in statistical quality control [6]; here, a randomly selected sample of items (of size *N*) out of a finite lot consisting of ***N*** items is evaluated to make a decision regarding the lot disposition, that is, to accept or to reject the lot. This is usually based on the criterion that the number of items that fail the test does not exceed a predefined level *c*. Note that in economical scenarios the test procedures can be very sophisticated and are usually multi-stage procedures; yet we will investigated simple single stage tests in this paper only.
For setting up our procedure, we employ the operation characteristic function -- see, for instance, Section 15.2.2 `The OC Curve` in [6]on page 637 ff.:

$$L(p) = P\_p\left(\Sigma_{i=1}^{N} X_i \le c\right),$$

which defines the probability of accepting the lot for a given (but unknown) reject rate p.
This rate p is added as subscript to the probability measures here, and X_i indicates that sample $_i$ meets the specification (X_i =0) or not (X_i =1).

The operation characteristic function *L* is governed by a hyper geometric distribution but can be approximated by a binomial distribution for ***N*** » N, which is met by the HEMP test design through ***N***=∞. The simple acceptance sampling plan is defined by two numbers *(N,c)* (*N* is the number of independent tests, *c* is the maximum number of allowed rejects within the *N* tests for accepting the lot). Using this notation, the test plan given in [2].is characterized by *(N,1)*, and the probability for rejecting the DUT can be expressed by the operation characteristic function $p_{Fail}(p_{FA}) = 1 - L(p_{FA})$.
Now, we apply design ideas known from acceptance sampling to design a better test procedure by using [3].
We choose the two probabilities p_{FA}^{good} and p_{FA}^{bad} and define limits for *L(p):*

$L(p_{FA}^{good};N,c) \ge 1-\alpha$ and $L(p_{FA}^{bad} N,c) \le \beta$.

An exemplary R-Code shows the simple setup of the test:

```
p.good <- 0.1; p.bad <- 0.5
L.good <- 0.95; L.bad <- 0.05

cG <- -1
repeat {
cG <- cG+1
NG <- cG
while ( pbinom(cG, NG, p.bad) > L.bad ) NG <- NG + 1
if ( pbinom(cG, NG, p.good) >= L.good ) break
```

The function `pbinom(q,N,p)` computes the cumulative distribution function of a binomial distribution.
For the discussed example the result is the following sequence for *N*:

cG = 0, NG = 5, L.bad = 0.0312, L.good = 0.5905
cG = 1, NG = 8, L.bad = 0.0352, L.good = 0.8131
cG = 2, NG = 11, L.bad = 0.0327, L.good = 0.9104
cG = 3, NG = 13, L.bad = 0.0461, L.good = 0.9658

This shows that the test procedure meets the defined criteria and can be used for testing.

3 Confidence intervalls

Besides the design described in [1,2] and the acceptance sampling approach discussed in the previous section, one could derive design rules based on confidence intervals for success probabilities (or proportions). Essentially we are interested in upper bounds for the unknown probability p_{FA}. See [4] for a comparison of seven different concepts to construct such an interval. Here we focus on the classic one by [5] and two designs relying on normal approximation (known as Wald and Wilson intervals, respectively). Before we will describe these three approaches in more detail, we recall the framework. We assume that *N* HEMP tests were performed and $0 \le x \le N$ failures were registered. Given these two numbers, we determine an upper bound π^{upper} so that

$$P_{p_{FA}}(p_{FA} \le \pi^{upper}) \ge 1 - \alpha.$$

We applied several well known approaches to estimate the confidence intervalls, i.e. Clopper-Pearson intervals, Wald intervall, Wilson and Agresti-Coell intervals; the results are displayed in fig.1.
The **R** package `binom` provides functions to calculate the three intervals described above as well as some further constructions of confidence intervals. Besides these three we consider the Agresti-Coull intervall [7] whose performance is in between those of Clopper-Pearson and of Wilson [8].
By calling `binom.confin(x, N, conf.level = 1-α)` we obtain the two bounds for *N* trials, *X=x* failures and confidence level $1-\alpha$.
In Figure 1 we present the upper bounds π^{upper} for $N \in \{2,3,...,20\}$, $x \in \{0,1\}$ and $1-\alpha = 95\ \%$.
Obviously the Wald interval is rather useless *x=0* is not defined and for *x=1* and $N \ge 5$ the resulting values are definitely too small).
The other three perform similarly. It is not surprising that the Clopper-Pearson bounds are the largest ones (they comply with the level $1-\alpha$ by construction). Wilson- and Agresti-Coull bounds are really close to each other, while Wilson provides always smaller values. For *x=0* and *N>12*, Clopper-Pearson and Agresti-Coull bounds are nearly the same. To give a recommendation for the choice of *N* we deduce that $N \approx 10$ provides a reasonable performance. Then, no failure (*x=0*) would yield $\pi^{upper} \approx 0.2$, which is a reasonable upper bound for practice. If one would allow *x=1* (one failure), then one should use a much larger *N* or has to cope with upper bounds of size $\pi^{upper} > 0.3$.

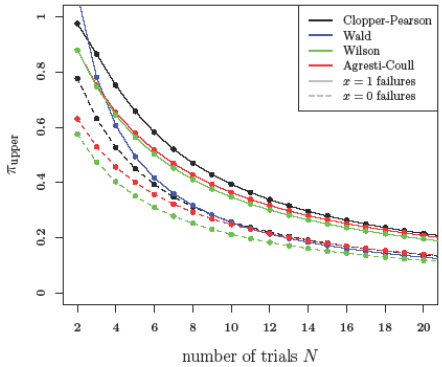

Figure 1 Various confidence intervals for HEMP tests.

4 Conclusions

We employed statistical methods to evaluate the HEMP field test procedure in [1] and [2]. As a result, we propose three different ways to determine the number of single tests N and the corresponding success rates:

1. choosing a test procedure from the Guenther algorithm [3] (acceptance sampling) to determine *N* --- here *X*>1 may be possible or
2. calculation of *N* by evaluating the confidence interval for p_{FA}, again for *X=0*.

The method of generalized linear models (binary regression in particular) will be investigated in our future work, and can probably be employed if certain covariates failure relationships are known for DUTs.

References

[1] Sabath, F.; Potthast, S. (2013). "Tolerance Values and the Confidence Level for High-Altitude Electromagnetic Pulse (HEMP) Field Tests". IEEE Transactions on Electromagnetic Compatibility, 55(3), pp. 518 -- “525.

[2] VG 96903-50 Beiblatt 1, Normenstelle Elektrotechnik (NE) im DIN (2012). "Nuclear electromagnetic pulse (NEMP) and lightning protection, Test methods, test equipment and limiting values".

[3] Guenther, W. C. (1977). "Sampling Inspection in Statistical Quality Control", Griffin, London, UK.

[4] Newcombe, R.G. (1998). "Two-sided confidence intervals for the single proportion: comparison of seven methods". Statistics in Medicine}, 17(8), pp. 857 - 872.

[5] Clopper, C.J.; Pearson, E.S. (1934). "The use of confidence or fiducial limits illustrated in the case of the binomial". Biometrika, 26(4), pp. 404-413.

[6] Montgomery, D. C. (2009). 'Statistical quality control: A Modern Introduction", 6th ed., John Wiley & Sons (Asia), Pte. Ltd.

[7] Agresti, A. (2013). "Categorical Data Analysis". Wiley, Hoboken, N. J., 3rd ed.

[8] Agresti, A.; Coull, B.A. (1998). "Approximate Is Better than ``Exact" for Interval Estimation of Binomial Proportions". The American Statistician, 52(2), pp. 119.

Marx Generator Design for Narrow-Width Pulse Generation

Jiafeng Zhou*, Yi Huang*, He Jiang*, Q. Xu*, C. Song*, L. Xing[#] and Jan Nalborczyk [†]

**Univeristy of Liverpool, UK, jiafeng.zhou@liverpool.ac.uk, yi.huang@liverpool.ac.uk,*
[#]Nanjing University of Aeronautics and Astronautics, China
[†]MPE Limited,UK, JNalborczyk@mpe.co.uk

Abstract

This paper introduces the design of a Marx generator that can generate high amplitude pulses up to 25 kV and 2.5 kA. The rise time is 20 ns and the pulse width is 230 ns on a 10 Ω resistor.

In the design, it was found that parasitic effect of circuit components could significantly affect the performance of the generator. This is mainly because the pulse width is very narrow and its frequency spectrum is very wideband. The high-frequency circuit models of the components used in the generator were obtained by calculation and optimization, and then further verified by experiment. The verified circuit modes were then used to design a three-stage generator. The measured performance agrees very well with the simulated one.

Keywords: Spark Gap, Parasitic, Pulse, Circuit Model, Marx Generator.

1 Introduction

High-altitude ElectroMagnetic Pulse (HEMP) filters help safeguard equipment and systems against the potentially devastating effects of HEMP generated in the atmosphere [1]. Military computer and communications networks as well as civil and commercial infrastructure can be knocked out by HEMP if they are not adequately protected by filters. In the design of such filters, a HEMP generator is usually needed to test them.

A Marx generator is a high-voltage pulse generator first described by Erwin Otto Marx in 1924. It has many scientific uses such as HEMP protection system testing, insulation and lightning safety testing [2][3][4]. The basic operation of the generator is to charge capacitors in parallel and then discharge them in series. Hence a high voltage pulse can be generated. This paper describes the design of a Marx generator that can be used for HEMP filter testing. The three-stage generator can produce pulses with a peak voltage of 25 kV on a 10 Ω resistor. The rise time is 20 ns and the pulse width is 230 ns.

Since the pulse width is very narrow, its frequency spectrum is very wideband. Parasitic effects of those components used in the generator cannot be ignored. The paper will describe how to establish a circuit model for each component and use the circuit models to design a Marx generator.

2 Theoretical Marx Generator Design

The Marx generator circuit generates high voltage pulses by charging a number of capacitors in parallel first as shown in Figure 1. At the beginning the capacitors C_{charge} are charged by the DC power supply through charging resistors R_{charge}. When the spark gaps are triggered, the capacitors will be discharged simultaneously in series to generate a high-voltage pulse.

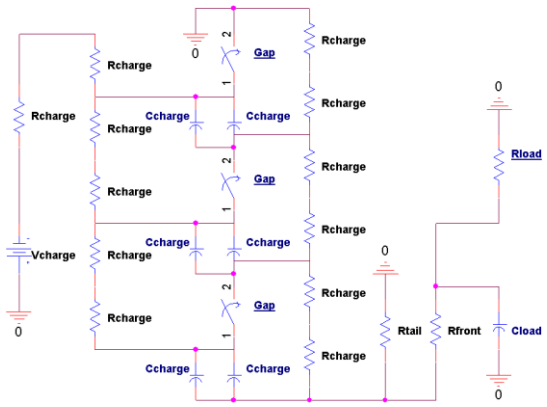

Figure 1. A circuit diagram of a typical Marx generator

To meet HEMP protection specifications, such as MIL-STD 188-125 [5], the generated pulses should have a rise time of less than 20 ns and a Full-Width at Half-Maximum amplitude (FWHM) of 500 ns. The pulses should have a double exponential waveform. While a simple resistor-capacitor circuit generates a single exponential waveform, the double exponential waveform can be obtained by the addition of another resistor and capacitor.

Based on the circuit shown in Figure 1, a Marx generator was designed and assembled as shown in Figure 2. When the generator was first tested, the measured response was quite different from the ideal response. The magnitude of the measured voltage, hence the current as well, is much higher than the theoretical value. The width was much narrower. The main reason is because the parasitic effect of the wires and other components significantly affect the circuit performance. Therefore, the design of the generator needs to be improved by taking account of the parasitic effect, to be discussed in the next section.

3 Improved Design and Experimental Results

The response of the Marx generator should be a double exponential waveform. The rise time of the pulse is less than 100 ns, so the bandwidth of the spectrum is from DC up to tens of MHz. The parasitic parameters of the parts and wires cannot be neglected and the circuit simulation should be improved.

In the design, the parasitic inductance of the wires, and both parasitic inductance and capacitance of the resistors should be taken into account. A PSpice circuit model is established for each of the components and each section of the wires [6][7][8][9]. Then a one-stage Marx generator was constructed and measured to verify and tune the proposed circuit models without using the waveform shaping circuit. The circuit models were then used to design a second-stage Marx Generator. The circuit models are further optimized and tweaked by measuring the two-stage generator. Eventually the three-stage prototype Marx generator was designed using the verified circuit models.

(a)

Figure 2. A photograph of the assembled generator.

The measured pulse waveform generated by the three-stage generator is shown in Figure 3. The pulse has an FWHM of 230 ns. The rise time is about 20 ns. Except for the front spikes [8], the peak voltage is about 25 kV on a 10 Ω resistor, which is in very good agreement with simulation. It should be noted that the output voltages have negative values. If desired, positive voltages can be generated by either changing how the capacitors are connected or simply changing the polarity of the power supply.

4 Conclusions

The design of a Marx Generator is introduced in this paper. The generator can generate high altitude pulses up to 25 kV on a 10 Ω resistor. The rise time is 20 ns and the pulse width is about 230 ns. Since the pulse width is very narrow and its frequency spectrum is very wideband, it was necessary to consider parasitic effect of components in the design. In the design, the circuit model of each component in the generator is proposed and verified by experiment on a one-stage generator. The verified circuit models were then used to construct the three-stage Marx generator. The measured response of the generator was in very good agreement with the simulated one using the proposed circuit models.

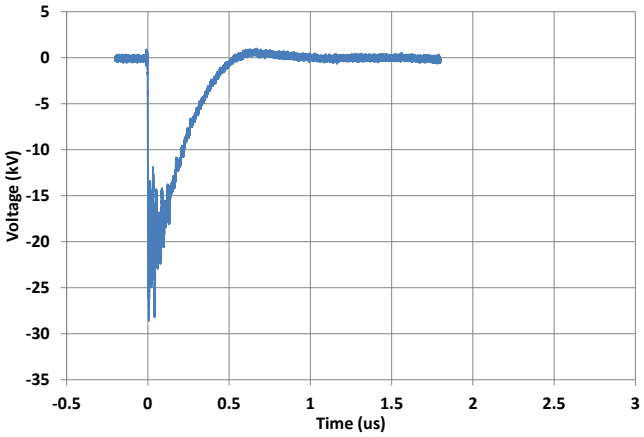

Figure 3. The measured waveform of a pulse.

References

[1] A. J. Nalborczyk, "HEMP filter design to meet MIL-STD-188-125 PCI test requirements," Electromagnetic Interference & Compatibility, INCEMIC 2008. 10th International Conference on , vol., no., pp.205-209, 26-27 Nov. 2008.

[2] Hongtao Li, Hong-Je Ryoo, Jong-Soo Kim, Geun-Hie Rim, Young-Bae Kim, and Jianjun Deng, "Development of Rectangle-Pulse Marx Generator Based on PFN", IEEE Transactions on Plasma Science, VOL. 37, NO. 1, JANUARY 2009.

[3] A. A. Neuber, Y. J. Chen, J. C. Dickens, M. Kristiansen, "A Compact, Repetitive, 500kv, 500 J, Marx Generator", Pulsed Power Conference, 2005 IEEE

[4] Archana Sharma, Senthil Kumar, Sabyasachi Mitra, Vishnu Sharma, Ankur Patel, Amitava Roy, Rakhee Menon, K. V. Nagesh, and D. P. Chakravarthy, "Development and Characterization of Repetitive 1-kJ Marx-Generator-Driven Reflex Triode System for High-Power Microwave Generation", IEEE Transactions On Plasma Science, VOL. 39, NO. 5, MAY 2011.

[5] MIL-STD-188-125-1, *High-Altitude Electromagnetic Pulse (Hemp) Protection For Ground-Based C4I Facilities Performing Critical, Time-Urgent Missions*, Department of Defence, Interface Standard, USA, 17 July 1998.

[6] J. R. Mayes and C. W. Hatfield, "Development of a sequentially switched Marx generator for HPM loads," Pulsed Power Conference, 2009. PPC '09. IEEE, pp.934-937, Jun. 2009.

[7] Muhammad Saufi Kamarudin, Erwan Sulaiman, Md Zarafi Ahmad, Shamsul Aizam Zulkifli and Ainul Faiza Othman, "Impulse Generator and Lightning Characteristics Simulation using Orcad PSpice Software", Proceedings of EnCon 2008, pp. 1032-1037, Dec., Malaysia, 2008

[8] Y. E. Kolyada, O. N. Bulanchuk and V. I. Fedun, "Numerical simulation of the Marx-generator behavior on nonlinear load-high-current vaccum diode," Vopr. At. Nauki Teh., Âd.-Fiz. Issled. 5 pp.27-29, 2001.

[9] R. Sheeba, M. Jayaraju, T. K. N. Shanavas, "Simulation of impulse voltage generator and impulse testing of insulator using MATLAB Simulink," Word Journal of Modelling and Simulaiton, vol. 8, no. 4, pp. 302-209, 2012.

[10] W. J. Carey and J. R. Mayes, "Marx Generator Design And Performance", Power Modulator Symposium, 2002 and 2002 High-Voltage Workshop.

Optimization of a long range anechoic chamber for IEMI tests

Jean-Christophe Joly[1], Nicolas Albuisson[1], Jean-Pierre Adam[1], Pierrick Hamel[2],Yannick Beniguel[2], Gwenaël Dun[3]

[1] CEA, DAM, Gramat, F-46500 Gramat, France
[2] IEEA, Courbevoie, France
[3] Siepel, F-56470 La Trinité sur Mer, France

Abstract

In 2006, CEA-Gramat decided to build a long range anechoic chamber to perform IEMI tests on the microwave band.
This facility called MELUSINE has been realized in a 100 meters long tunnel. The anechoic specifications of the chamber had been respected thanks to a succession of arches supporting pyramidal absorbers.
In 2006, the location and the design of those arches had been studied with analytical and optic numerical methods.
In 2015, it is now possible to mesh and simulate the whole tunnel with exact 3D methods, such as a FDTD codes.
Cea-Gramat intends here to increase the anechoic performances of such a tunnel by optimizing the arches design and the arches location.

Keywords: Anechoic, tunnel, fdtd, IEMI.

1 Introduction

For high power microwave tests, the Melusine long range anechoic chamber has been built at CEA-Gramat in 2006.

The solution of a 100 meters tunnel was interesting for several reasons :

- The length allows real size demonstrations,
- The length respects the far field conditions in terms of impedance and wave front,

For the respect of the anechoic properties, a simple lateral covering of the inner surface of the tunnel with classical pyramidal absorbers was not a chosen solution. The reflectivity of such radio frequency absorbers is only correct when the angles of the incident fields are close to the normal (see figure 1).

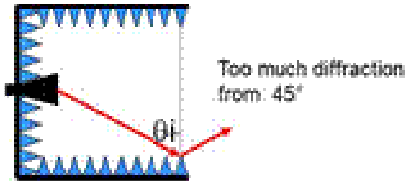

Figure 1 : reflection in case of lateral covering of the tunnel

In that way, too much diffraction would have generated non-homogenous fields at the extremity of the tunnel (see figure 2).

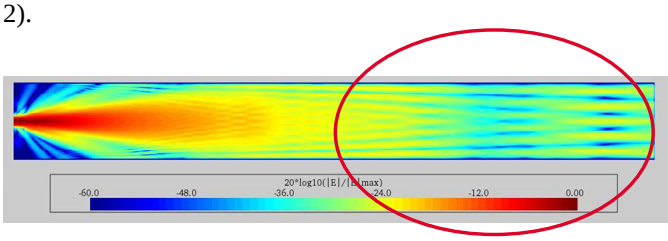

Figure 2 : non homogeneous field at the extremity of the tunnel in case of total lateral covering with absorbers

As a consequence, the chosen solution is a clever succession of arches all along the tunnel. Pyramidal absorbers are then located on the arches surface in order to face the incident field (see figure 3)

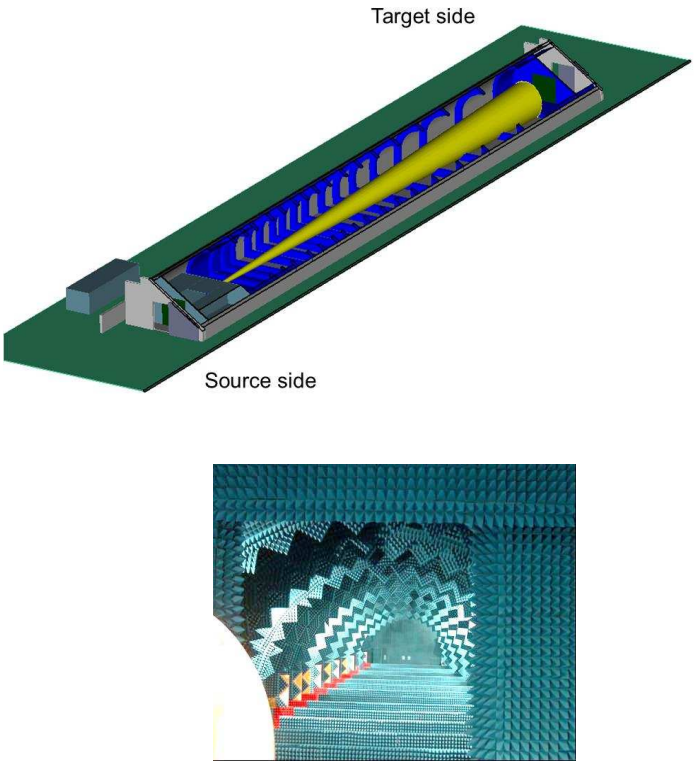

Figure 3 : succession of arches along the tunnel

The succession of arches is not only interesting for performances reasons but also for cost reasons. The quantity of absorbers is then limited because metallic surfaces in the back and in the shadow of each arches are not recovered with absorbers.

The location of the arches had been chosen with an optic approach. The “shadow zone” of each arch is not seen by the direct incident beam. (see figure 4).

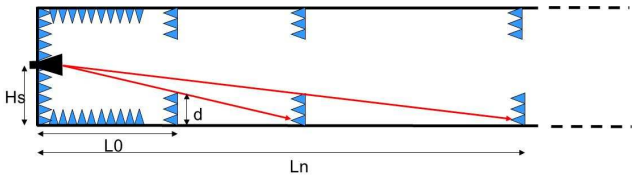

Figure 4 : optic principle of the arches placement in Melusine in 2006

In 2015, based on this experience, CEA-Gramat analyzes the opportunity to improve the anechoic quality of such a tunnel. The idea is to take benefit of the newest computational performances.

2 Optimization of the arches shape

For the beginning, the shape of a single arch is studied in order to limit the diffraction at the edge of the arch.
Several rolled shapes are simulated (see figure 5). The incident field is a plane wave.

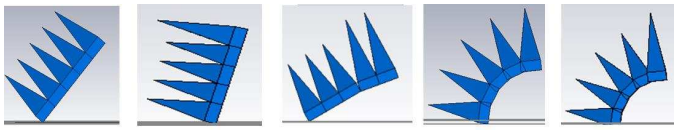

Figure 5 : example of rolled shapes

The chosen criteria in a given quiet zone is :

$$Qz = 20\log\left(\frac{E_{\max} - E_{\min}}{E_{\max} + E_{\min}}\right)$$

3 Simultaneous optimization of the arches shape and location in 2D FDTD

For this task, a genetic algorithm is applied. A huge number of configurations are simulated versus various parameters (shape, position, number of arches, absorber charge…). A 2D FDTD code is required as a consequence.
The figure below illustrates the convergence toward an optimized configuration.

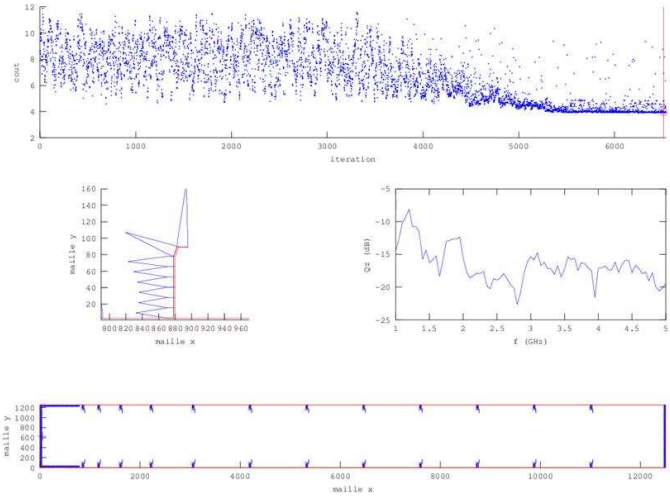

Figure 6 : illustration of the genetic algorithm and the convergence toward an optimized design and location of the arches

4 Verification of the optimization in 3D FDTD

The conclusions of the previous step in 2D are verified now in 3D with a FDTD code (called GORF). The whole tunnel is meshed with 4 billons of cells. The cell size is 1.6 cm. In the source zone, a horn at 1 GHz is also meshed.
For a practical and financial point of view, a compromise has been chosen to limit the diversity of absorbers (only one charge of carbon, all the pyramids have the same dimensions…).

5 Conclusion

Diffraction due to the arches of such a solution for this anechoic tunnel is unescapable. Nevertheless, the methodology which has been chosen here limits the diffraction and improves the homogeneity of the electric field in the quiet zone.
The optimization has simultaneously affected the shape and the location of the arches.
The advanced computational performances have allowed an exact 3D numerical simulation of the whole tunnel with a FDTD code. The diffraction due to the arches is taken into account, which was not the case with the initial optic design of the Melusine tunnel.

References

[1] J APPEL-HANSEN. “Reflectivity level of radio anechoic chambers”, *IEEE Trans. on antennas and propagation”*, AP-21, no. 4, (July 1973).

Perturbation by glass-encased Cs cell of electromagnetic-field sensor based on quantum phenomena

Masanori Ishii and Moto Kinoshita

National Institute of Advanced Industrial Science and Technology, National Metrology Institute of Japan, Research Institute for Physical Measurement
AIST Tsukuba Central 3, 1-1-1, Umezono, Tsukuba, Ibaraki 305-8563, Japan
masanori-ishii@aist.go.jp

Abstract

We developed a new type of electromagnetic-field sensor based on quantum phenomena. The new sensor has a glass cell containing a gas of cesium-133 atoms instead of metal antenna elements usually required by electromagnetic-field sensors. Here, we report an initial study on the effects of the glass cell on electromagnetic field measurements by using numerical simulations based on the method of moments.

Keywords: Magnetic-field sensor, Cesium-133 atoms, Glass cell, Antenna measurement.

1 Introduction

Sensors of electromagnetic fields traditionally consist of antenna elements that are made of metal. Since the operating principle of these sensors is based on Maxwell's equations, a common concern is perturbation of the electromagnetic field by the measurements.

We have recently developed and reported an initial examination of a new type of electromagnetic-field sensor based on quantum phenomena, in which metal antenna elements are not employed [1]. This new sensor has a glass cell that holds a gas of cesium-133 atoms instead of the metal antenna elements ordinarily required by electromagnetic-field sensors. The perturbation of an electromagnetic field being measured by the ^{133}Cs-based sensor is thus expected to be lower than that by a metal-antenna-based sensor. This paper reports the results of numerical simulations based on the method of moments (MoM), which were carried out as a preliminary investigation of the hypothesized reduction in electromagnetic perturbation.

2 Glass cell containing gas of cesium-133 atoms

A glass cell containing a gas of cesium-133 atoms is shown in Fig. 1. This cell was designed to accommodate a WR-90 rectangular waveguide [2]. The size of the cell was 40 mm × 22.5 mm × 10 mm, and the thickness of the glass was 1.5 mm. A relative permittivity of 3.575 was obtained for the cell in a separate experiment. The frequency was 9.19 GHz.

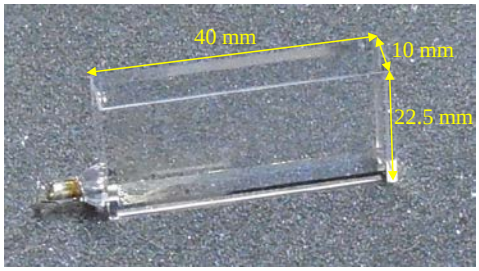

Figure 1. A glass cell enclosing Cesium-133 gas.

3 Comparison of perturbations by the MoM

In the simulations, a glass cell, a loop antenna made of copper sheets, or nothing (free space) was placed at a distance of 80 mm from the aperture plane of a horn antenna, as shown in Fig. 2. Fig. 3 shows distributions of the magnetic field strength at 80 mm from the aperture plane and parallel to the aperture plane (i.e., parallel to the *y* axis in Fig. 2).

4 Discussion

Fig. 3 shows that the glass cell had the largest effect on the magnetic field being measured. However, resonance was expected to occur inside the glass cell as its size matched that of the WR-90 rectangular waveguide in the current design. Therefore, in order to avoid the resonance, the shape and the size of the glass cell will be investigated in the next phase of the study.

Acknowledgements

This work was supported by JSPS KAKENHI (grant no. 26630117).

References

[1] M. Ishii and M. Kinoshita, "Electromagnetic measurement based on the Rabi frequency in free space," Eighth 2015 Korea-Japan Joint Conference on EMT/EMC/BE (KJJC-2015), November 2015.

[2] M. Kinoshita et al., "Atomic microwave power standard based on the Rabi frequency," IEEE Trans. Instrum. Meas., 60(7), 2696–2701, 2011.

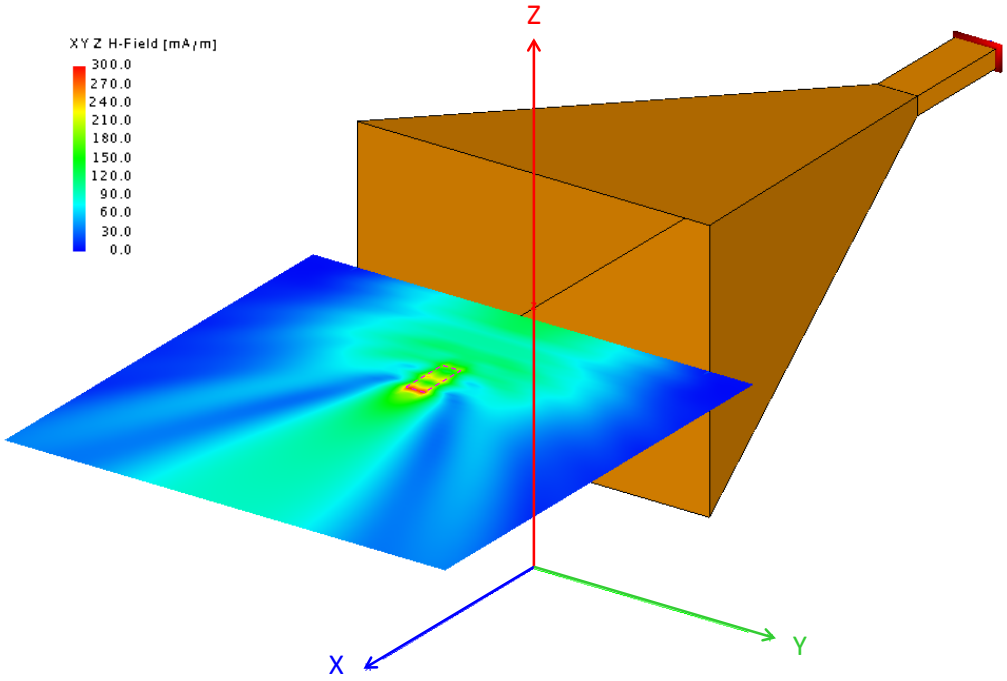

Figure 2. Schematic view of the simulation setup. The rectangle enclosed by the dotted red line on the distribution map of magnetic field strength shows the position of the cross-sectional plan of the glass cell.

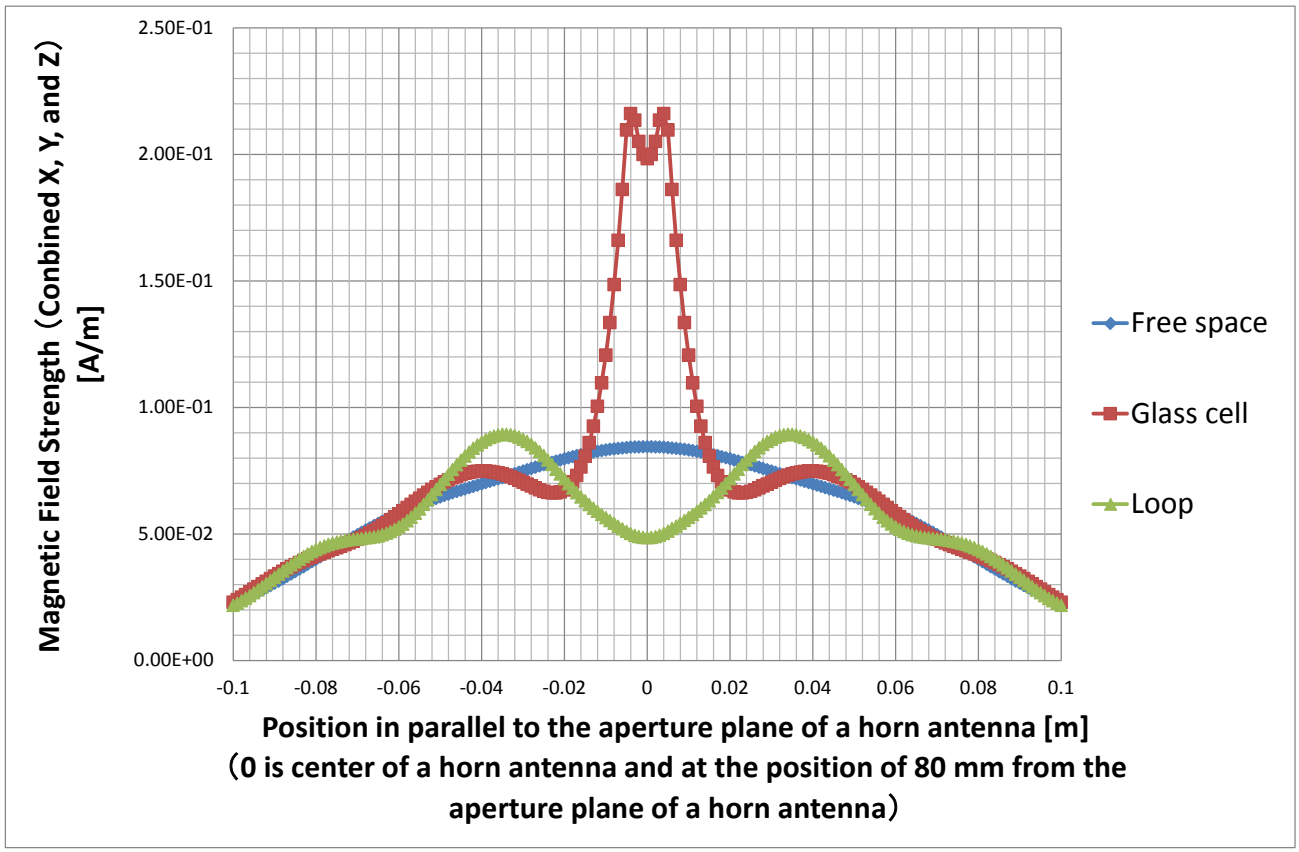

Figure 3. Comparison of the distributions of magnetic field strength, $H = (H_x^2 + H_y^2 + H_z^2)^{1/2}$, in the presence of free space, a Cs-containing glass cell, and a copper loop. Position 0 is defined as the center of the horn antenna at a distance of 80 mm from its aperture plane.

3-Axis optical sensor for real time and vectorial analysis of UWB electric field

G Gaborit[†], L. Gillette*[†], Jean Dahdah[†], A. Bazin[‡], J. Tarayre[‡], J. Luc[‡], Lionel Duvillaret[†]*

**Laboratoire IMEP-LAHC, Université Savoie Mont Blanc, 73376 Le Bourget du Lac Cedex, France , [†]Kapteos S.A.S., 354 Voie Magellan, Bât. Cleanspace, 73 800 Ste Hélène du Lac, France, [‡]CEA, DAM, Gramat – F-46500 Gramat*

Abstract

This paper describes latest improvements concerning optical probe dedicated to electric field characterization. The presented optical sensors are pigtailed and can be located at a few tens meter from the data acquisition. Their tiny size together with their fully dielectric composition ensure a minimum disturbance on the field to be measured. The field analysis can be performed in real time and the covered frequency bandwidth spreads up to 20 GHz. The minimum detectable field is weaker than 100 $mV.m^{-1}.Hz^{-1/2}$ and the probe dynamics reaches more than 130 dB. Finally the field can be assessed in various fluids such as gazes, liquids or even cold plasmas.

Keywords: Electric field measurement, vectorial analysis, fiber optics sensor, UWB characterization.

1 Introduction

Pigtailed electric (E) field sensors, based on electro-optic (EO) effect, have been developed since early 21st century [1]. This E-field measurement technique present many advantages comparatively to classical metallic antennas. Their intrinsic frequency bandwidth reaches even terahertz frequencies in the case of time equivalent sampling. The developed sub-centimeter sized probes are made of non-conductive material and allows a non-perturbative E-field mapping in the very near field region of a device (such as a patch antenna). EO transducer gives a vector component selective measurement leading to the magnitude and the phase of the E-field [2]. The dynamics of the EO system is greater than 130 dB and E-field strength greater than the disruptive field in the air can be analysed in real time [3]. Nevertheless, these optical sensors exhibit a sensitivity which remains lower than antennas.

2 The 3-Axis optical sensor

The E-field measurement probe consists in an optical arrangement involving an EO crystal. The crystal acts as an electric to optical converter between the field vector component to be measured and the induced polarisation state modulation (PSM) of a laser beam (Low noise pigtailed DFB Laser).

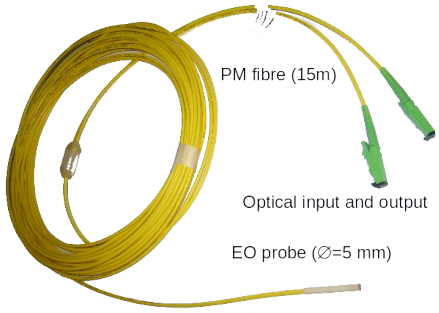

Figure 1. Photography of a packaged EO probe.

The bare EO probe is a dielectric cylinder (diameter of 1.8 mm, length of 15 mm) with a relative permittivity of 42. A picture of a single axis optical probe is given in Fig. 1. Due to a complete absence of coupling between adjacent probes (even spaced by less than 2 mm), several probes can be packaged together to access to the 3 components of the E-field vector. The PSM induced by the field components is carried through a polarizing maintaining fiber up to an instrument. This latter one includes a high speed photodiode, allowing to retrieve an electrical signal directly proportional to the E-field vector components.

3 Thermal influence, and real time compensation

The temperature variation leads to a drift of the optimal working point of the probe and also of PSM analysis parameters. This lack of stability has been solved using a proper arrangement of fixed wave plates. The output response of the whole EO system to the field remains identical whatever the environmental temperature variations. The realized probes have been used in harsh environment and have demonstrated a stable behaviour: in the closest vicinity of a cold plasma with temperature variation as fast as 10°C/s, in vacuum environment, in the presence of soft X-rays, immersed in biological submitted to intense RF field, ...

4 Sensitivity improvements

The EO technique is perfectly suitable for intense field vectorial analysis. However, the minimum detectable field E_{min} usually lies in the range of the $V.m^{-1}.Hz^{-1/2}$. This value is too poor in the case of single shot and ultrawide bandwidth E-field temporal analysis. Indeed, actual minimal value of E-field is given by the product of the sensitivity in $V.m^{-1}.Hz^{-1/2}$ by the square root of the instantaneous frequency band which is analysed.

We here propose to enhance the interaction efficiency between the field to be measured and the optical probe beam PSM. In fact, the optical modulation is rigorously induced by the inner crystal field which can be different than the outer relevant E-field. A proper packaging protects mechanical and optical integrity of the probe. It can also acts as an adaptive electromagnetic transition between the media in which the field have to be measured and the crystal transducer. For air and water, we have developed a multilayer adaptive coating of the probe increasing the field penetration up to the crystal. The sensitivity have be improved of 6 dB in the air and of 20 dB for field in water or biological solution. This improvement of the signal to noise ratio is in agreement theoretical expectations and with predictive numerical simulations (2D Finite Difference Time Domain technique).

5 Experiments

As an example, we here propose a comparison between an EO probe (linear) and an D-Dot sensor (derivative). The two sensors are submitted to a single shot pulse. The peak field strength is estimated to be 400 kV/m. The two sensors are located in the near field region of the radiating antenna. The measurements are performed simultaneously and recorded with a sampling time of 100 picoseconds. The result is presented in Fig. 2. The results are in a good agreement and both spectrograms exhibit the same transient evolution of the spectral distribution.

6 Conclusion

The recent advances in the EO technique lead to a relevant and reliable analysis of the E-field. Indeed, temperature influence has been overcome thanks to a specific optical arrangement. Such EO sensor can be suitable for numerous applications (defense, bioelectromagnism, plasma diagnostic, energy monitoring, …). The principle of the EO technique, together with practical optimisation of their sensitivity will be explained during the conference. A wide range of experimental results will also be presented.

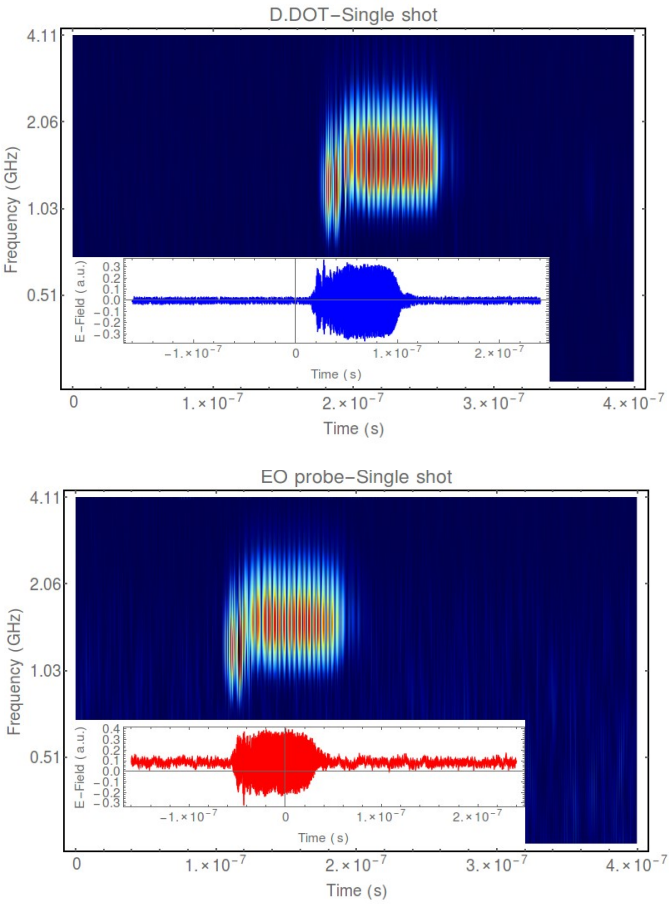

Figure 2. Wavelet transform of the measured transient signals (given in inset) for the D-Dot Sensor (top) and the EO probe (bottom)

Acknowledgements

The authors would like to acknowledge the DGA (French Military Programs Management and Procurement Agency) for the funded SNIFER project (program RAPID), DGCIS for financial support. They also would like to thank the French National Research Program for Environmental and Occupational Health of Anses (2013/2/20).

References

[1] K. Yang, L. P. B. Katehi, J. F. Whitaker, “Electro-optic field mapping system utilizing external gallium arsenide probes”, *Appl. Phys. Lett.*, 77(4), pp. 486-488, (2000).

[2] G. Gaborit, J.-L. Coutaz, L. Duvillaret, “Vectorial electric field measurement using isotropic electro-optic crystals”, *Appl. Phys. Lett.*,90, 241118, (2007).

[3] G. Gaborit, P. Jarrige, F. Lecoche, J. Dahdah, E. Duraz, C. Volat, L. Duvillaret, “Single Shot and Vectorial Characterization of Intense Electric Field in Various Environments with Pigtailed Electro-optic Probe”, IEEE *Trans. Plas. Sci.*, 42, 5, pp. 1265-1273, (2014).

New susceptibility and immunity figures of PWM patterns and circuits with temperature impacts

J.M. Dienot*

**LGP-Labceem, University P. Sabatier, France – jm.dienot@iut-tarbes.fr*

Abstract

This paper deals with susceptibility studies combined with temperature on electronic devices used to control power and transmissions. Specific dual thermal-electromagnetic test set-up developed for this are presented. Temperature dependant susceptibility and sensitivity of the PWM parameters on dedicated digital PCB are compared and analyzed.

Keywords: Susceptibility, Immunity, Thermal impacts; PWM; Near-field aggression;

1 Introduction

Previous experimental and simulation works try to estimate the realistic impact of external temperature on emissions and susceptibility cases of electronic devices[1][2][3]. EMC effects and High temperature can be inherently generated around electronic devices, in technology as Smart Power ICs, High Power modules and Driver Chips[4][5]. EMC characterizations can be performed over Printed Circuit Board(PCB) and Integrated Circuits(IC) with Near-Field scan table and/or Transverse Electro-Magnetic(TEM)Cells [6][7]. We propose the insertion of a warming plate solution, up to 300°C. Pulse Width Modulation (PWM) pattern characteristics in both time/frequency domains are representative of significant and critical immunity cases. For example, in driving DC/AC currents in converters, transformers and motors, a slight shift in nominal duty cycle rate (α) less than 1%, can induce a severe fail in the command tasks and current injection. We present susceptibility responses of PWM circuits to both harmonic and temperature aggressions, and try to identify the impacts on main PWM signals characteristics.

2 New Thermal-Immunity methods

2.1 Near-Field aggression test bench

Separate E-Field and H-field measurement or injection, considered as Near-Field approach, is realized over different areas of PCB with dedicated probe's set like H-spires and E-dipoles, associated to a motorized table system. Electromagnetic probes have been fabricated with high-frequency semi-rigid coaxial cable to inject RF power from MHz until 3GHz. A warming plate, using inductive heating, can generate temperature until 300-350°C over a fixed glass area. It is placed under the PCB, with a specific conductive test support. A thermal contact probe, with a touch end of 0.1mm diameter, and a thin body support of 8cm long, has been coupled on the same scan table moving fixture, with a different Z-axis reference. When moving and positioning the measurement point, thermal probe stays in with the body of the electric element, as near-field probes are just over. As at high temperature, we observe shifts in RF level injected about 1.2 to 1.5 dB, correction factor for RF injection Level are determined and complete the calibration of the test set-up.

2.2 TEM Cell aggression test bench

Transverse Electrical-Magnetic Cell (Crawford TEM cell) is commonly used for EMC characterization, from 1MHz up to 3GHz, at PCB and Integrated Circuits levels [8][9]. Specific PPCB have to be designed to comply with the dimension of the aperture cell and the completion of shielding quality of the system. Starting from this configuration, a special fixture arm has been realized, so to maintain the PCB-TEM Cell device over the warming plate at a 4cm height to keep efficient heating action. The new constraint is to report electrical and thermal connections very close to the PCB, and with 90° angle so as to not touch the hot warming plate (Fig. 1). Acquisition of real external temperature close on board is realized by thin thermal resistor in SMD or Thin Film technology. A special attention has been made, for pertinent immunity measurements, with the thermal routing network [10]. A specific roadmap procedure and computational algorithm has been developed to drive the experiment and all the post-processing data's.

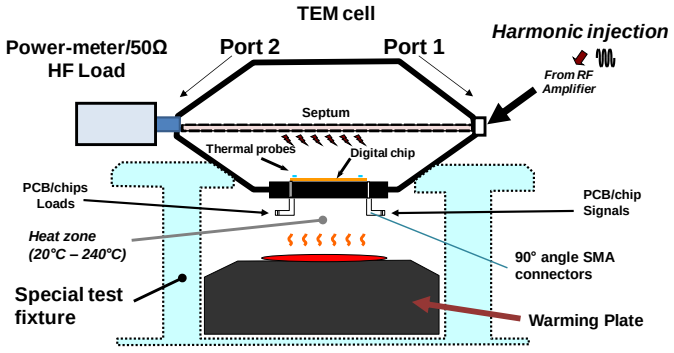

Figure 1. Schematic of Heated TEM-Cell configuration for immunity testing on 10cmx10cm PCB.

3 Application on PWM circuit boards

3.1 First demonstrator: Integrated PWM Circuit

The first study concerns a PWM demonstrator using a Programmable IC, that operates in synchronous mode, with a clock reference of 5MHz. Two inputs are used to modulate the output square signal, with an absolute cyclic rate from 5% to 94%. Main susceptibility aspects are generally, for digital mode device, the modifications of thresholds levels and switching times, due to the couplings of external parasitic signals on supply and I/O ports. Results show that mainly relative amplitude of waveform of current switching device, I_{VDD}, has significant shifts with both harmonic frequency and temperature aggression.

3.2 Second demonstrator: two discrete PWM circuits

The second study concerns a dual PWM generator, dedicated for driving DC brushless motors. The PCB is compliant with TEM Cell aperture (10cm*10cm) but the area of the overall SMD circuit is about 3cm*3cm. Four main default criteria are defined for these test the shift on duty cycle rate α, on frequency f_0, on switching margins VDD-GND, and on the mean value VMEAN. Susceptibility tests are repeated with steps of temperature of 20°. We present main significant and pertinent results in fig.2 and fig. 3.

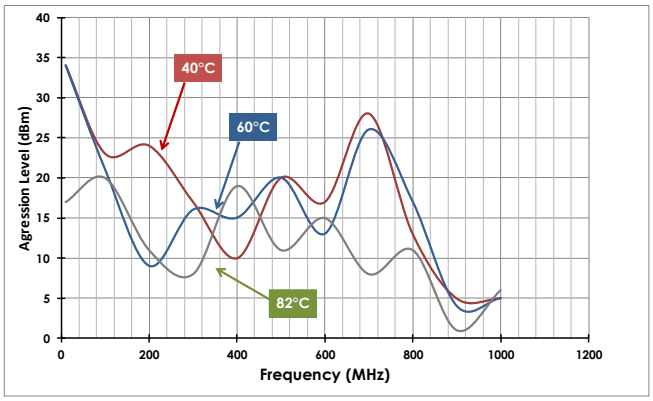

Figure 2. Immunity table at temperature steps of 20°C for criteria "1%" on duty cycle α.

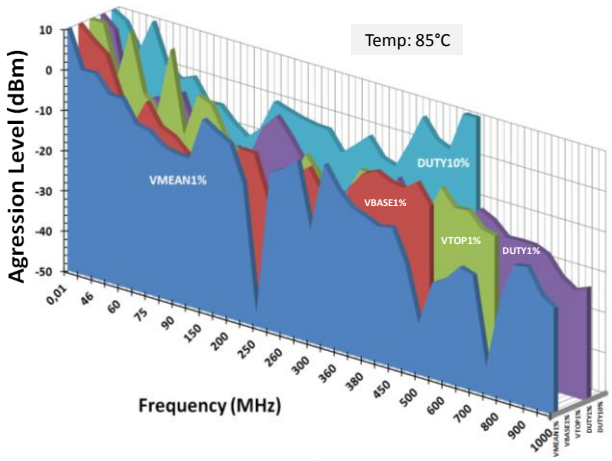

Figure 3: 3D table representation of worst-case's immunity with PCB temperature of 85°C, for 5 criteria's of the PWM

4 Conclusion

With these works, new modified EMC characterization approach is in progress, for real-case EMC investigations. Specific test benches have been developed, based on conventional Near-Field and TEM cell immunity test setups. External aggression of light range of temperature (20°-100°) has been correctly added, so to combine both EM-Thermal effects on susceptibility of electronic chips on PCB. A focus has been made on immunity cases on PWM signals, which need to be well driven for main applications. After a measurement campaign with a wide range of different susceptibility responses of the demonstrators, main significant results are synthesized in this work. These results confirm a main influence of temperature on susceptibility levels of programmable or discrete chips: some critical defaults, as the shift of more than 1% of the duty cycle rate or Mean value VMEAN, are very sensitive with a non-ambient temperature, and critical for immunity of these applications.

References

[1] J.M. Dienot, G. Lourdel, "Experimental study of thermal influence on EMC emission of digital circuit on PCB", Proceedings of the 16th International Symposium on Electromagnetic Compatibility, pp. 299-302, Zurich, February 13-18, 2005.

[2] S. Ben Dhia, E. Sicard, A. Boyer, Y. Mequignon, J.M. Dienot, " Thermal Influence on 16 bits Microcontroller Emission", In Proc. of 2007 IEEE International Symposium on Electromagnetic Compatibility, EMC for IC session, Honolulu (USA), July 9-13, 2007.

[3] J.M. Dienot, "Characterization and simulation of digital device electromagnetic noise under non-ambient temperature conditions.", Electronics Letters Volume 43, Issue 20, pp 1073-1074, September, 2007, DOI 10.1049/el:20070495

[4] E. Hoene and al., "Simulating electromagnetic interactions in high power density converters", in Proc. of 36th IEEE Power Electronics Specialists Conference, pp. 1665-1670, Recife(BRA), 2005.

[5] S. Weber, S. Guttowski, E. Hoene, W. John and H. Reichl, " EMI Couplings from Automotive Traction Systems", In Proc. of IEEE Symposium on Electromagnetic Compatibility, Vol. 1, pp. 591-594 , Istanbul(TUR), May 11-16, 2003.

[6] D. Baudry, C. Arcambal, A. Louis, B. Mazari, and P. Eudeline, " Applications of the Near-Field Techniques in EMC Investigations", IEEE Trans. On Electromagnetic Compatibility, Vol. 49, N° 3, pp. 485-493, August 2007.

[7] K.P. Slattery, J. Neal, and W. Cui, "Near-field measurements of VLSI devices", IEEE Transactions on Electromagnetic Compatibility, vol.41, n°4, pp 374-384, November 1999.

[8] P-M. Nicolae, I-D. Nicolae, D-G. Stănescu, "Using GTEM Cells for Immunity Tests on Electronic Boards with Microcontroller", In Proc. of IEEE 2012 Symposium on EMC, pp. 44 49, Pittsburgh(USA), August 5-10, 2012

[9] X. K. Gao, E. K. Chua, and E. P. Li, "Integrated EM immunity design and diagnosis system for electronic devices", in Proc. of 2009 International Symposium on Electromagnetic Compatibility, pp. 329-332, Kyoto, Japan, July 20-24, 2009.

[10] J.M. Dienot, E. Batista, "Real-Cases of Electromagnetic Immunity and Reliability in Embedded Electronics Architectures", in Book of Abstract of EUROEM 2012, pp 87, European Electromagnetic Symposium, Toulouse, France, 2-6 July, 2012.

Development of Multi-channel Norm Detector

Xu Kong, Yan-zhao Xie

State Key Laboratory of Electrical Insulation and Power Equipment,
School of Electrical Engineering, Xi'an Jiaotong University,
Xi'an,China
Email: Yanzhao.xie@gmail.com

***Abstract* - This paper reports a multi-channel norm detector based on high speed digital acquisition technology. The multi-channel norm detector can measure the current and voltage signals on the multi-port synchronously without the need of cable or fiber-optic link. So, the corresponding norms, such as power, energy, etc. can be calculated.**

Keywords: EMP, digital measurement, FPGA, wireless, norm.

1 Introduction

During the high altitude electromagnetic pulse (HEMP) effect experiments, one often has to measure the coupled current or voltage signals on the multi-port, such as the port of multi-transmission line [1, 2]. Although the current and voltage probe has been well developed, they still need cables or fiber-optic links to transmit the measured signals to the distant oscilloscope. For the coupled signals measurement inside a hermetically sealed cavity such as the cavity of a cockpit, the present measuring method cannot be used directly [3, 4].
Now, the rapid development of analogue to digital data converter (ADC) and field programmable gate array (FPGA) promotes the development of high speed data acquisition and storage technology. This makes the digital measurement system realizable. Digital measurement system can directly output digitized signal of the measured physical quantity and therefore, meet many special measurement requirements [5, 6]. So, a multi-channel norm detector technology is designed based on high speed digital acquisition technology in this paper.

2 System design and fabrication of the multi-channel norms detector

The schematic drawing of the multi-channel norm detector is shown in Fig.1. Each channel is composed of a conditioning circuit, an ADC chip and a FPGA chip. The analogue signal from current or voltage probe is first amplified or attenuated by the conditioning circuit to be able to input into the ADC. The ADC completes the analog-to-digital conversion and its output digital signal is received and stored by the FPGA. All the channels use a common clock signal to be synchronous. The FPGAs can communicate with each other to be synchronous triggered and transmit data. The measured data can be uploaded to the computer by a USB port after the experiment.

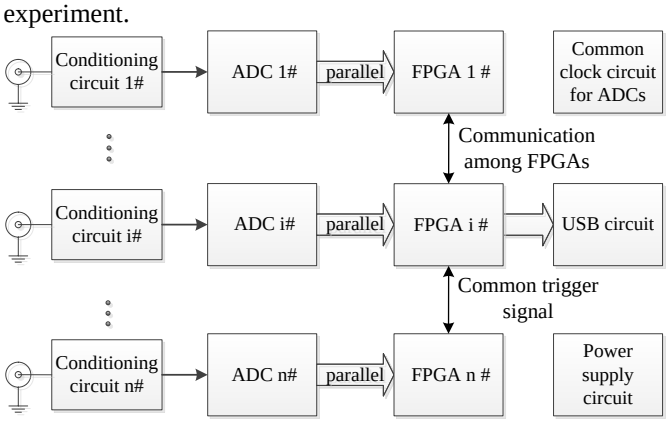

Figure 1. Schematic drawing of the multi-channel norm detector

The working process of the multi-channel norm detector is shown in Fig.2. The system starts data sampling and storage once powered up. When the stored data reach pre-trigger depth, the trigger function will be activated. Then the stored data will update in real time and its amount will maintain invariable until trigger signal arrived. After triggered, the pre-set memory space will be filled and then waiting for data uploading. So, it is designed for single pulse signal measurement.

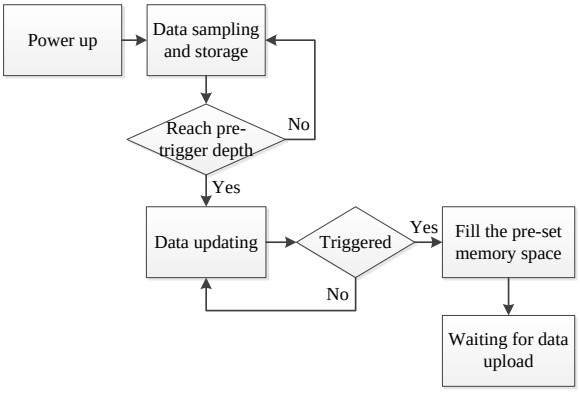

Figure 2. Working process of the multi-channel norm detector

The multi-channel norm detector has a sampling rate of 500 Msps and a storage depth of 2 K bytes. Measuring result

comparison between the multi-channel norm detector and the E-field sensor based on fiber-optic link system [7, 8] is shown in Fig.3. The measured signal is a 50 ns square-wave pulse with a rising time of 5 ns. The measuring result shows that the multi-channel norm detector has high signal to noise ratio (SNR) and can be used for the induced transient signal measurement.

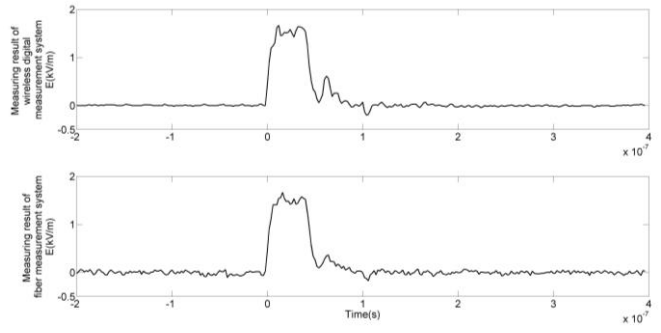

Figure 3. Measuring result comparison between the multi-channel norm detector and the fiber measurement system

The most commonly used norms such as the peak value, the integral of square value and the peak rate of rise can be calculated after the physical quantity is measured and stored. Moreover, as the current and voltage signal can be measured synchronously, the coupled energy and power signal can be calculated.

3 Conclusion

A multi-channel wireless digital measurement system is designed based on high speed digital acquisition technology. It can be used to measure the transient coupled signals inside a hermetically sealed cavity. Since the current and voltage signals on a multi-port can be measured synchronously, the coupled power or energy can be calculated and the equivalent module of the multi-port can be deduced as well. The FPGA has powerful signal processing ability, so the norms and super-norms of the measured signals can be acquired by multi-channel norm detector.

References

[1] Carl E. Baum, “From the electromagnetic pulse to high-power electromagnetics,” Proceedings of the IEEE, vol. 80, no. 6, pp. 789-817, Jun. 1992.

[2] Carl E. Baum, Norm detectors for multiple signals, Measurement Notes, Note 40, Oct. 1991.

[3] William D. Prather, Dave V. Giri, Robert L. Gardner, Fred M. Tesche, Robert L. Hutchins and Joseph C. Giles, “Early developments in sensors and simulators at the air force weapons laboratory,” IEEE transactions on electromagnetic compatibility, vol. 55, no. 3, pp. 431-439, Jun. 2013.

[4] William A. Radasky, Carl E. Baum and Manuem W. Wik. Introduction to the Special Issue on High-Power Electromagnetics (HPEM) and Intentional Electromagnetic Interference (IEMI)[J]. IEEE Trans. Electromagn. Compat., vol. 46, no. 3, pp. 314-321, Aug. 2004.

[5] Xiao-lei Cheng, Xiao-xia Tian, Ming Zeng and Xiao-xue Han, “The design of 1 Gsps real-time sampling system for transient pulsed signal,” IEEE transactions on nuclear science, vol. 57, no. 2, pp. 539-542, Apr. 2010.

[6] Stephan Braun, Thomas Donauer and Peter Russer, “A real-time time-domain EMI measurement system for full-compliance measurements according to CISPR 16-1-1,” IEEE transactions on electromagnetic compatibility, vol. 50, no. 2, pp. 259-267, May. 2008.

[7] Xu Kong and Yan-zhao Xie, "An Active E-field Sensor Based on Laser Diode for EMP Measurement," presented at The XXXI General Assembly and Scientific Symposium of the International Union of Radio Science, Beijing, China, Aug. 18-23, 2014.

[8] Xu Kong and Yan-zhao Xie, “Measurement Uncertainty Analysis of the Electro-Optical E-field Measurement System,” presented at the Asia-Pacific Conf. on Environmental Electromagnetics, Hangzhou, China, Nov. 4-7, 2015.

Wide band resistive sensors

P. Ragulis*, Ž. Kancleris, R. Simniškis and M. Dagys

* *Microwave Laboratory of Physical Technology Department, Centre for Physical Sciences and Technology*
Vilnius, Lithuania, paulius.ragulis@ftmc.ltt

Abstract

Resistive sensors for WRD840 and WRD250 double ridged waveguides were developed. The flat frequency response of the sensors was achieved by changing the parameters of the sensing element. The measurement system comprised of the resistive sensors connected to corresponding wide band horn antenna for measurements in free space covering frequency ranges 0.84 – 2.0 and 2.6 – 7.8 GHz was implemented.

Keywords: resistive sensor; high power microwaves.

1 Introduction

A resistive sensor (RS) is a device based on electron heating effect in semiconductors. It found applications for high power microwave (HPM) pulse measurements [1]. Some advantages of the RS can be mentioned when comparing it with a semiconductor diode, which is also sometimes used for HPM pulse measurement. The RS measures HPM pulses directly, is overload resistant and demonstrates perfect long-term stability [1]. Operating frequency range of the RS is limited by the waveguide in which RS is mounted. Therefore for the measurement of HPM pulses in a wide frequency range a set of sensors mounted in the rectangular waveguides of different cross-section size has to be used.

In this study, the RS mounted in a double ridged waveguides WRD840 and WRD250 was investigated. Pass bands of these waveguides are from 0.84 to 2.0 GHz and from 2.6 to 7.8 GHz. It is seen that by using double ridged waveguide, the frequency range of the RS can be more than doubled comparing it with a standard rectangular waveguide. The RS is made of two sensing elements, which are separated from each other. On a top of them there is a dielectric concentrator [2]. This configuration was chosen since it allowed us to achieve smaller sensitivity variation on frequency.

2 Sensitivity of the sensors

Sensitivity of the resistive sensors can be written as:

$$\zeta = \frac{\Delta R}{R}/P \ , \qquad (1)$$

where $\Delta R/R$ is a relative resistance change in the microwave field, and P power of the microwaves in the waveguide. Finite-difference time-domain method was used to solve electromagnetic field scattering problem and optimize sensor's frequency response. From the simulation results, shown in

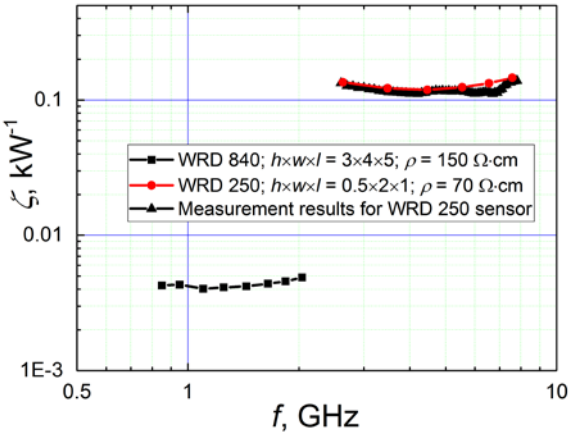

Figure 1. Sensitivity dependences on frequency of resistive sensors for WRD840 and WRD250 waveguides.

Fig. 1, it is seen that sensitivity variation is only ±9.6% and ±9.4% for sensors mounted in WRD840 and WRD250 waveguides respectively. A few sensors for WRD250 were investigated experimentally by measuring their output signal dependences on pulse power propagating in a waveguide, frequency response, and reflection coefficient. Reasonable agreement between measured and calculated frequency responses of the RS was obtained. Sensitivity variation measured experimentally was ±10.8%. We have also tested the RS connected to a wide band horn antenna and matched load for the measurement of electric field strength in free space. It is shown that accounting for the antennas parameters when engineering sensor's frequency response, the RS integrated with antenna for the measurement of electric field strength in free space with flat frequency response can be developed.

Acknowledgements

This research was funded by EU project No 284802 "Protection of Critical Infrastructures against High Power Microwave Threats" (HIPOW)

References

[1] M. Dagys, Z. Kancleris, R. Simniskis, E. Schamiloglu, and F. J. Agee, "The resistive sensor: a device for high-power microwave pulsed measurements," *Antennas and Propagation Magazine, IEEE*, vol. 43, pp. 64-79, 2001.

[2] Ž. Kancleris, P. Ragulis, R. Simniškis, and M. Dagys, "Resistive Sensor for High-Power Microwave Pulse Measurement in Double-Ridged Waveguide," in *Ultra-Wideband, Short-Pulse Electromagnetics 10*, ed: Springer, 2014, pp. 369-377.

Design and manufacturing of a high power L-band helical antenna

N. Albuisson*, J.-C. Joly*, J.-M. Lopez*, J.-P. Adam*

**CEA, DAM, Gramat, France*
jean-pierre.adam@cea.fr

Abstract

This paper presents a helical antenna able to radiate 60 kW at the L-band frequencies. This presentation ranges from the design to the measurements. Two ways to simulate the antenna feeding were tested in a FDTD solver.

Keywords: High power antenna, L-band, helical antenna, FDTD.

1 Introduction

In order to study the effect of electromagnetic waves on electronic devices, an antenna able to handle high power levels is required. Table 1 summarized the typical characteristics of such an antenna. Helical antennas design and manufacturing are easily performed. In addition, this kind of antenna has been reported to be able to manage high power (for example in [1]).

Table 1: Antenna specifications

Description	Objective
bandwidth	1.1 GHz - 1.5 GHz
S11	< -10 dB
Directivity	> 10 dBi
Polarization	circular
Power handling	60 kW pulsed power
Size	< 1 m

2 Design and simulations

2.1 Antenna geometry

The main difficulty in the design of this antenna is its input section. A horizontal line is used to connect the core conductor of the input coaxial line to the helical wire. The height of this horizontal line sets the input impedance. If it is chosen for a good input matching, it is unacceptably low : the electric field is locally high enough for dielectric breakdown of the air. To overcome this problem, the height of this section is increased and the input impedance is lowered with a metal plate inspired by [2]. Fig. 1 presents the details of this geometry.

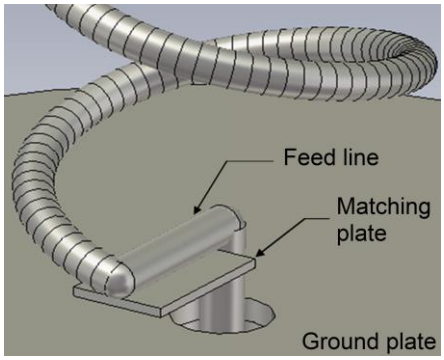

Figure 1. View of the matching plate used to modify the input impedance of the helical antenna.

2.2 FDTD simulation

CST Microwave Studio was mainly used for the design of this antenna. However, a FDTD simulation with an in-house solver called Gorf3D ([3]) was required. This solver is able to run simulations of few billions of cells, enabling the study of the antenna within a complex environment.

Reasonable results were obtained if the antenna was fed with a voltage source on a thin wire in the FDTD simulation. However, this kind of source introduces an unwanted wire inductance. A better source model was implemented in Gorf3D. This wave port source accurately simulates the coaxial feed line by applying the actual TEM mode electromagnetic field distribution on a meshed coaxial waveguide.

3 Manufacturing and measurements

The antenna has been manufactured in order to measure the input impedance and the radiation pattern of this prototype. Fig. 2 presents the obtained antenna and Fig. 3 shows the excellent agreement between the measured and the simulated performances. The final version of this paper will contain measured and simulated radiation patterns.

Figure 2. Manufactured helical antenna.

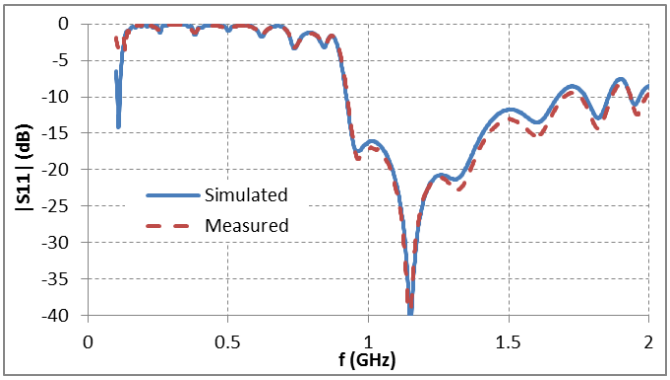

Figure 3. Comparison of the simulated (Gorf3D, with wave port) and the measured input matching of the antenna.

Finally, this antenna was successfully tested with a 60 kW pulsed power input.

References

[1] J.R. Mayes, M.G. Mayes, W.C. Nunnally, C.W. Hatfield, "Helical Antennas for high powered RF", IEEE, 2009

[2] J. D. Kraus, "A 50-Ohm Input Impedance for Helical Beam Antennas", IEEE Transactions on Antennas and Propagation, vol. ap-25, NO. 6, 1977, p913.

[3] L. Morel, B. Pecqueux, R. Vézinet, "Notice d'installation et d'utilisation de la version exportable du code GORF3D", Note interne CEG I94-28, October 1994.

Analysis of Folded Feed Half Impulse Radiating Antenna for High-Power Impulse Radiation

Sachin B. Umbarkar[*1], H. A. Mangalvedekar[2], Archana Sharma[3], Ramesh Vasappanavara[1], R. Agrawal, M.D. Patil[1], S. Kulkarni[1], S. Petkar[1]

[1]Ramrao Adik Institute of Technology, D Y Patil Group, Nerul Navi Mumbai-706,
[2]Veermata Jijabai Technological Institute, Matunga, Mumbai-019,
[3]Bhabha Atomic Research Centre, APPD, Mumbai-085, India.
[*]sachin.umb@gmail.com

Abstract

This paper gives the brief analysis of Folded Feed Half Impulse Radiating Antenna (FF-HIRA) for high power impulse radiation, mounted over a Marx generator of 20 stages, 64 J, 300 kV. To achieve maximum E far field radiation intensity the feed arms and the reflector of antenna are designed so as to increase the illumination on the reflector and reduce the field blockage. The mathematical calculation using wavelet transform, simulation and experimentation are discussed in this paper.

Keywords: Antenna, HIRA, Impulse, Marx Generator.

1 Introduction

Impulse Radiating Antenna (IRA) plays an important role in the high power electromagnetics impulse radiator. To achieve this, the reflector and feed arms of the IRA has been designed, simulated and experimented. These IRA systems has very high bandwidth; 10`s of MHz to several GHz. The low frequency cut off for the system is determined by the reflector size. The high frequency cut off is determined by the rise time of the input feeding pulse [1]. This system has useful applications in waste water treatment, development and strengthening of electronics, underground inspection, nonlethal weapons and radar systems etc. [2].

Half Impulse radiating Antenna (HIRA) was first proposed by Capt. Carl E. Baum in the 1989, wherein they concluded that the paraboloidal reflector fed by TEM transmission line have extremely wide bandwidth properties [3]. The terminating impedance of feed plates can be tuned to reduce the reflections, and to balance the late time electric and magnetic dipole moments of such an IRA [4,5]. The ratio of electric and magnetic dipole moments have to be such as to maximize lower frequency radiation to make radiator as broad-band as possible. This feed impedance should be lower to get the higher gain of antenna. But lower feed impedance gives more field blockage [6]. A single ended pulse generator driving a full IRA results in differential and common mode currents on the feed plates. Hence full IRA requires high voltage balun [6,7]. The geometry of the reflector is parabolic in nature and there are two folded-feed arms resulting in half reflector type antenna [8]. To radiate high intensity pulse in a bore sight direction, we need to harness EM field diffraction. This diffraction is obtained by optimally designing (i) parabolic reflector and (ii) the shape and inclination of the feeder arms [1, 9].

This paper simulates field blocking and its effect in reducing the E far field intensity. Using this, the feeding arms are modified so as to have curvilinear shape at the terminating (feed) point. This gives rise to a uniform field distribution between the arms and the reflector. This also increases the illumination level and hence the fill factor. The existing mathematical model [3] was used to design and fabricate the Folded Feed Half Impulse Radiating Antenna (FF-HIRA). This antenna is mounted co-centric on the peaking switch with the coplanar feeder arms projecting vertically and has an offset. The terminating ends of the feeder arms have curvilinear shape. It is observed in simulation that this arrangement reduces the reflections and increases the fill factor. Fill factor indicates the quantum of uniformity of illumination on the reflector [2]. The arm is terminated with matched load resistance to avoid the resonance effect of the feeder plates in the far field and to get the clean radiated far field spectrum. This terminating resistor gives the balance wave transmission and also reduces the reflections. Hence to obtain clean radiated spectrum, it is desirable to have resistive termination. The resistor used was of carbon composite type/carbon film type to reduce inductance. The disadvantage of the curvilinear nature of the arm leads is the high capacitance and lower voltage stand-off capability at the termination end. To avoid this, the termination of the arm was trimmed and insulated with Teflon coating of 1 mm thickness. The experiment using this system is given in detail in this paper.

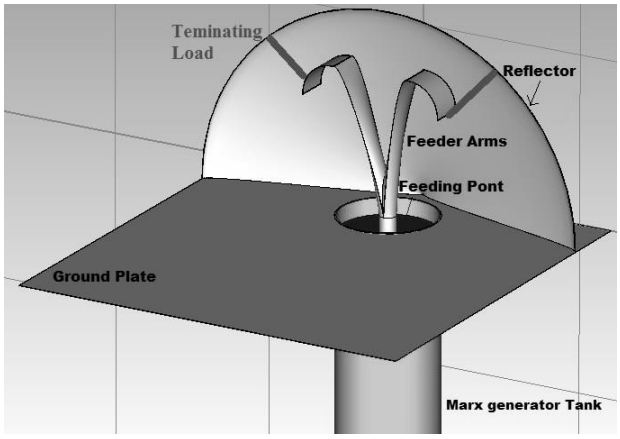

Fig. 1 3 D CST Model of HIRA-2

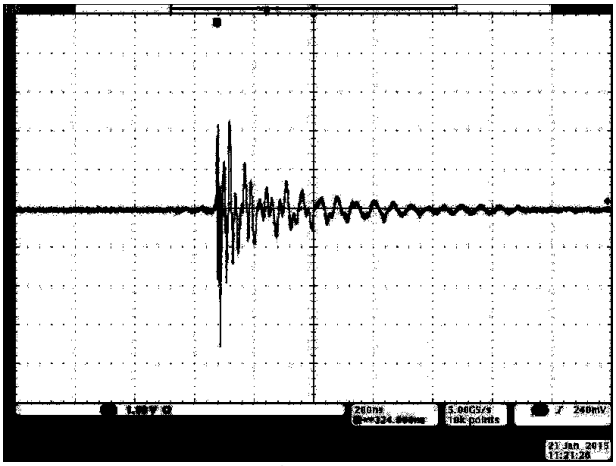

Fig. 2 Measured at 15 m, 0^o

5 CONCLUSION

In this paper brief mathematical analysis, simulation and experiments on FF-HIRA is carried out. The novel folded feed arrangement is brought out. It is felt that this has more potential to improve the performance of the antenna. The FF-HIRA with uniform reflector illumination (fill-factor) has been designed so as to give higher fill-factor. This is achieved by using the folded feed and vertical arrangement. The radiated field has far field intensity 14.4 kV/m at 15 m distance. Thus it is observed that, this antenna is more directive than the half transverse electromagnetics (HTEM) antenna reported in [12].

ACKNOWLEDGMENT

The authors thank to Dr. Vijay D. Patil (President, DY Patil Group), Prof. O.G. Kakde (Director-VJTI), Mr. R. K. Rajawat (Head, APPD, BARC), Dr. N.M. Singh, Dr. Sushma W., Prof. F.S. Kazi, Dr. R.N. Awale, of V.J.T.I, Mumbai, and Mr. Sandip Singh, Dr. A. K. Ray, Mr. D P Chakravarthy, for their encouragement and fabrication support. Authors would like to acknowledge Board of Research in Nuclear Science (BRNS) and Centre of Excellence, Control and Nonlinear Dynamic System, (CoE-CNDS), VJTI for financial support.

REFERENCES

[1] J. B. Keller and A. Blank, "Diffraction and Reflected of Pulse by wedges and corners", Communications on Pure and Applied Mathematics, Volume 4, 1951, pp. 75–94.

[2] D. V. Giri (2004), book on 'High-Power Electromagnetic Radiators-Nonleathal Weapons and Other Applications', Harvard University Press.

[3] E Carl E. Baum, "Radiation of Impulse-Like Fields", Sensor and Simulation note 321.

[4] D. V. Giri, H. Lackner, I. D. Smith, D. W. Morton, C. E. Baum, J. R. Marek, W. D. Prather, and D. W. Schofield, "Design Fabrication and Testing of a Paraboloidal Reflector Antenna and Pulser System for Impulse Like Waveforms ", IEEE Transaction on Plasma Science, Volume 25, Number 2, pp. 318-326, April 1997.

[5] O. V. Mikheev et.al., "New Method for calculating Pulse radiation From an Antenna with a reflector", IEEE Transactions on Electromagnetic Compatibility, Volume 39, number 1,February 1997, pp.48-54.

[6] Everett G. Farr "Optimizing the feed impedance of Impulse Radiating Antennas Part I: Reflector IRAs", Summa Foundation Sensor and Simulation Notes series No. 354, Nov. 1997.

[7] Everett G. Farr, Carl E. Baum, William D. Prather "Multifunction Impulse Radiating Antennas: Theory and Experiment", Summa Foundation Sensor and Simulation Notes series No. 413, Nov. 1997.

[8] S. V. Tewari, Sachin B. Umbarkar, Ritu A, P C Saroj, A Sharma, K C Mittal, H A Mangalvedekar, "Development and analysis of PFN based Marx generator finite integration technique for an antenna load" IEEE Transaction on Plasma Science, Vol. 41, No.10, OCT.2013.

[9] Carl E Baum, "Aperture Efficiencies for IRAs", Sensor and Simulation note 328.

[10] M. Abramowitz, and I. A. Stegun [1967], "Handbook of Mathematical Functions", National Bureau of standards, AMS-55, Chapters 16 and 17.

[11] Sachin B Umbarkar, S. Bindu, H A Mangalvedekar, Ayush Saxena, N M Singh, Archana Sharma, P C saroj, K C Mittal (2014), "Particle in cell simulation of Peaking Switch for Breakdown Evaluation" IEEE, International Symposium on Discharges and Electrical Insulation in Vaccume, (ISDEIV).

[12] Sachin B. Umbarkar, S.Bindu, H.A Mangalvedeker, Archana Sharma, P C Saroj, K C Mittal (2014) "Analysis of HTEM horn type Antenna for High-Power Impulse Radiation" *IEEE, Transaction on Plasma Science,* Vol.42, No. 10, pp.3288-3294.

Object detection by three-channel antenna system of ultrawideband borehole radar

V. I. Koshelev, E. V. Balzovsky, Yu. I. Buyanov, E. S. Nekrasov

Institute of High Current Electronics SB RAS, 2/3, Akademichesky ave., Tomsk, 634055, Russia
koshelev@lhfe.hcei.tsc.ru

Abstract

A three-channel antenna system for ultrawideband pulse borehole radar has been developed and investigated. It consists of three identical transceivers arranged one after another along the borehole length with successive rotation of 120 degrees. Each transceiver includes separate receiving and transmitting combined antennas and runs its own angular sector. The antennas are optimized to excite by a bipolar voltage pulse of the length 3.5 ns. Possibility to detect objects under the ground with the angular and space resolution was demonstrated experimentally.

Keywords: Detection, borehole, radar, ultrawideband.

1 Introduction

Short pulses of ultrawideband (UWB) radiation are used in borehole radar to provide range space resolution when detecting objects near a borehole. While using dipole antennas, the angular resolution in the plane perpendicular to the borehole axis is absent. Development of borehole radar with the space and angular resolution is of interest for applications.

2 Design and measurement results

The antenna system of radar consists of three transceivers. The transceivers are spaced to the distance of 60 cm from each other and turned through 120 degrees. The transmitting and receiving antennas are identical being created basing on the combination of electric and magnetic type of radiators. The applied approach allows creating antennas with decreased dimensions and directed radiation pattern. Using the FDTD method, the antennas are designed to operate in the medium with relative dielectric permittivity of four. The diameter and the length of the antennas are 115 and 330 mm, respectively. The lower matching frequency by the level of VSWR = 2 is 140 MHz. The space near the antenna electrodes is filled with solid dielectric which can separate from the antenna. Two antennas of the transceiver are connected to a dielectric tube. For convenient movement of the antenna system inside the measuring bench, each antenna had three rubbered wheels at its end.

To investigate a three-channel antenna system, a test bench has been created. The base of the bench is a polyethylene tube of the length 6 m with the external diameter of 160 mm and wall thickness of 9.5 mm. The tube was placed horizontally in the ground at a depth of 1 m. For access to the tube edges, two pits of the length 2 m, width and depth of 1.5 m each were made. Three transceivers were placed inside the tube. A generator and an oscilloscope were located near the tube edge. An ultrawideband receiving antenna used for recording radiated pulses or a sounded object were placed on the surface of the ground.

The transmitting antennas were excited by bipolar voltage pulses of the length 3.5 ns and amplitude 100 V. The time window for recording the signal reflected from the object was 55 ns. Initially, frequency and time domain characteristics of one transmitting antenna were investigated. The obtained results of measurements were in agreement with the results of numerical simulation.

Then the radar sensitivity to the presence of the reflecting object was studied depending on the antenna orientation. In the experiments, the difference of the signals at the presence and absence of the object (metal plate) was recorded. The signal amplitude in the vertical plane was three times higher than the signals from the antennas rotated by 120 and 240 degrees.

Steering of an object lying on the surface of the ground was made. A metal plate of the dimension 0.95×0.7 m moved along the borehole axis with the step of 5 cm. The estimation of the plate length obtained in the experiments corresponds to the real one.

3 Conclusion

A three-channel antenna system for ultrawideband borehole radar has been created. To test the radar, a bench simulating the medium in the borehole and a reflecting object was used. The radar is capable to run three sectors of 120 degrees each in the azimuthal plane, while a dipole antenna radar is omnidirectional in this plane.

Acknowledgements

The work was supported by the grant of Russian Foundation for Basic Research No. 13-08-98069.

Retrieving metal objects in multi-receiver FDEM data through signal matching

M Smetryns*, P De Smedt*, J De Pue†, T Saey*, N Note*, M Van Meirvenne*

**Research Group Soil Spational Inventory Techniques, Department of Soil Management, Ghent University, Belgium,*
†Research Group Soil Physics SoPHy, Department of Soil Management, Ghent University, Belgium
Marthe.Smetryns@UGent.be

Abstract

This paper addresses the problem of identifying buried metal objects with a frequency domain electromagnetic induction (FDEM) sensor. While the use of single-receiver time domain or multi-frequency FDEM sensors has become common in metal detection, the possibilities of a multi-receiver single-frequency FDEM sensor are less explored. The multiple receivers allow to make an exhaustive analysis of the subsurface and detected objects. The proposed procedure was calibrated on a terrain where metal objects were buried, and thereafter tested on a former World War 1 (WW1) battlefield in Belgium.

Keywords: electromagnetic induction, metal detection, FDEM, signal matching

1 Introduction

Multi-receiver FDEM sensors are often used in soil science, environmental applications and archaeology to map electrical and magnetic variations in the subsurface [1]. Despite the known sensitivity of FDEM instruments to metal objects [2], use of this technique in metal detection has remained limited compared to the application of more conventional methods [3]. However, through using multi-receiver instruments, information with different spatial sensitivities can be integrated into one single survey, facilitating data analysis and interpretation.

In demining, the reliable detection of metallic objects in geophysical datasets is of great importance. Time is less important than accuracy [4]. In this presentation we propose a pattern matching procedure based on theoretical electromagnetic response models of metal objects to allow robust metal detection in multi-receiver FDEM data.

2 Materials and methods

2.1 Soil survey

The operated FDEM sensor (DUALEM-21S) consists of one transmitter and four receiver coils, alternating in horizontal co-planar (HCP) and perpendicular (PRP) configuration at varying distances from the transmitter coil (1 m, 1.1 m, 2 m and 2.1 m, respectively). The sensor is towed behind an all-terrain vehicle to allow swift large-area surveys. Both the quadrature- and in-phase part of the received magnetic field are recorded for every coil configuration.

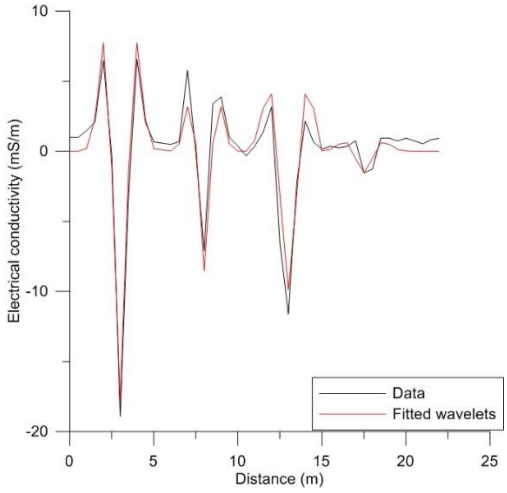

Figure 1. Wavelet basis fitted to data from a terrain with buried metal objects.

2.2 Signal matching procedure

Detecting metallic objects in the geophysical data is not always straightforward because background effects affect the capacity to delineate the metallic objects on the sensor's output. Therefore in a first step unwanted variation in the data is eliminated by detrending and denoising, using Hampel filtering [5] and moving median.

The following steps are based on a matching pursuit algorithm developed by Mallat & Zhang [6], who obtained signal decomposition using a wavelet matching algorithm. In the first step a wavelet basis is chosen based on a theoretical model that calculated the electromagnetic response of a metal sphere. Next, the wavelet basis is fitted to the electromagnetic signal by scaling and shifting it over the signal. In every step a coefficient of correlation between the signal and the fitted wavelet basis is calculated. A high correlation coefficient indicates the pattern is matching that specific part of the signal.

This procedure is performed on both the in- and quadrature-phase recordings of each coil configuration. The theoretical model proves that the in- and quadrature-phase response for a

metal sphere show the same pattern. Since a multi-receiver configuration is used, it is possible to apply the signal decomposition to all datachannels. If the signal in all channels matches with the theoretical fingerprint of a metal object, it can be marked as a potential unexploded object with a higher accuracy.

The procedure was calibrated on a terrain where metal objects were buried. Figure 1 shows the data with fitted wavelet where metal objects are present. Afterwards it was tested on fields in the former WW1 front region in Belgium where the remains of WW1 ammunition still pose a threat to the local inhabitants.

3 Conclusion

The proposed procedure shows potential to locate buried metal objects in multi-receiver FDEM data. The multiple coil configurations provide a more exhaustive analysis of the subsurface and detected objects. A theoretical model calculated the specific response of a metal sphere for each coil configuration. However, practical results deviate from the theoretically calculated results, warranting caution when choosing the wavelet basis for subsequent signal matching.

References

[1] M. E. Everett. "Theoretical developments in electromagnetic induction geophysics with selected applications in the near surface", *Surveys in Geophysics*, **33**, pp. 22-63 (2012).

[2] T. Saey, M. Van Meirvenne, M. Dewilde, F. Wyffels, P. De Smedt, E. Meerschman, M. M. Islam, F. Meeuws, L. Cockx. "Combining multiple signals of an electromagnetic induction sensor to prospect land for metal objects", *Near Surface Geophysics*, **9**, pp. 309-317 (2011).

[3] C. Bruschini. "A multidisciplinary analysis of frequency domain metal detectors for humanitarian demining", University of Brussels, (2002).

[4] M. K. Habib. "Humanitarian demining: the problem, difficulties, priorities, demining technology and the challenge for robotics", I-Tech Education and Publishing, Vienna, Austria, pp. 392 (2008).

[5] Pearson, R.K., Outliers in process modeling and identification. *Control Systems Technology, IEEE Transactions on*, **10**: p. 55-63 (2002).

[6] S. Mallat, Z. Zhang. "Adaptive time-frequency decomposition with matching pursuits", *IEEE Transactions SP*, **41**, No. 12, pp. 3397-3415, (1993).

Utilization and enhancement of early-time diffusion component of short pulses in imaging through obscuring random media

E H Bleszynski, M K Bleszynski, T Jaroszewicz

Monopole Research, Thousand Oaks, CA 91360, USA
elizabeth@ monopoleresearch.com

Abstract

We examine the possibility of utilizing the "early-time" diffusion component of the time-resolved intensity of short pulses in range imaging and communication through particulate obscuring random media composed of scatterers large compared to the wavelength. The early-time diffusion phenomenon, manifesting itself as a rapidly rising intensity enhancement closely following the ballistic signal, is due to multiple scattering on individual scatterers characterized by a strongly forward-peaked differential cross-section.

The early time diffusion phenomenon can be described by the radiative transfer equation (RTE), and attributed to the existence of the specific RTE eigenmodes characterized by relatively low attenuation and a narrow angular distribution of the energy flux.b In contrast, the ordinary "late-time" diffusion is dominated by the eigenmodes having a broad temporal, spatial, and angular distribution.

We investigate means of enhancing the early-time relative to late-time diffusion intensity components by an appropriate beamforming and an appropriate filtering of the measured time-resolved specific intensity: both the source and the filter should be matched to the dominant early-time diffusion eigenmodes and should be, as much as possible, "orthogonal" to the late-time diffusion modes.

Keywords: propagation in obscuring random media, early-time diffusion, short pulses, target detection, imaging, radiative transfer equation

1 Introduction

Scattering-induced diffusion is known to cause significant spatial and temporal spreading of optical pulses propagating in random particulate media (such as atmospheric clouds or fog) and thus to seriously hinder their application in imaging and communication. Mitigation of these detrimental effects may be possible by exploiting properties of the recently described [1] "early-time diffusion" of short pulses. This phenomenon, observed in solutions of the radiative transfer equation (RTE) for the time-resolved specific intensity, manifests itself as the appearance of a sharply rising structure bimmediately following the ballistic signal, but attenuated at a significantly lower rate and characterized by a time scale much (orders of magnitude) shorter than the ordinary "late-time" diffusion. The early-time signal can be separated (e.g., by means of high-pass filtering of the time-resolved intensity) from the long diffusive tail and utilized in range imaging or in communication.

2 Physical origin and eigenmode description of early- and late-time diffusion

Early-time diffusion arises in random media composed of scatterers sufficiently large compared to the wavelength and is due to multiple scattering with forward-peaked differential cross-section. This process, described by the RTE, can be interpreted probabilistically as a persistent random walk, leading to diffusion in the transverse directions relative to the overall propagation direction.

At the same time, however, the specific intensity can be represented in terms of the *eigenmodes* of the RTE. In particular, one may consider the RTE Green function $\Gamma(t, \boldsymbol{R}; \hat{\boldsymbol{s}}, \hat{\boldsymbol{s}}')$, representing the probability density for the energy flux emitted in the direction $\hat{\boldsymbol{s}}'$ at the origin at time $t = 0$ and arriving in the direction $\hat{\boldsymbol{s}}$ observed at the space-time point $(t, \boldsymbol{R})$. It follows from the properties of the RTE that Γ can be expressed as a sum of products $W_k(\boldsymbol{P}, \hat{\boldsymbol{s}}; t, \boldsymbol{R})\, W_k{}^{\mathrm{T}}(\boldsymbol{P}, \hat{\boldsymbol{s}}'; t, \boldsymbol{R})$ of eigenmodes. Each eigenmode $W_k(\boldsymbol{P}, \hat{\boldsymbol{s}}; t, \boldsymbol{R})$, labelled by a discrete or continuous index k, has a plane-wave dependence on $(t, \boldsymbol{R})$, characterized by a wave vector $\boldsymbol{P}$ and a certain frequency $\Omega_k(\boldsymbol{P})$, as well as a specific distribution in the energy flux direction $\hat{\boldsymbol{s}}$. The usefulness of this representation lies in the fact that, at propagation distances R large compared to the mean free path, the contribution of every $\boldsymbol{P}$ to the Green function is dominated by only a few least unattenuated eigenmodes, responsible for either early- or late-time diffusion. The first appear for small $P = |\boldsymbol{P}|$ and have a wide (nearly isotropic) $\hat{\boldsymbol{s}}$ distribution, while the latter, arising mostly at large P, have a narrow distribution in $\hat{\boldsymbol{s}}$ (of the width comparable to that of the differential cross-section).

3 Enhancing early-time diffusion by matched source and filtering

The purpose of the effort reported here is to find means of enhancing the early-time relative to late-time diffusion intensity components by an appropriate beamforming as well as filtering of the measured time-resolved specific intensity. Such an enhancement is of significant interest in a variety of applications in the context of detection and imaging of objects

hidden behind a medium composed of randomly distributed scatterers of sizes large compared to the probing pulse carrier wavelength. At a given propagation distance, it would significantly improve the temporal (range) and angular resolution; alternatively, for a desired resolution, it would allow increasing the imaging distance.

The observed specific intensity $I(t, \boldsymbol{R}; \hat{\boldsymbol{s}})$ at a propagation distance $\boldsymbol{R}$, due to a given source, can be represented as a convolution, over space time points and over the initial flux direction $\hat{\boldsymbol{s}}'$, of the Green function $\Gamma(t, \boldsymbol{R}; \hat{\boldsymbol{s}}, \hat{\boldsymbol{s}}')$ with a certain intensity source function S, sesquilinear in the amplitudes of the field source. In view of the eigenmode representation of the Green function, the convolution involves a generalized "inner product" (W_k , S). Similarly, filtering the measured specific intensity $I(t, \boldsymbol{R}; \hat{\boldsymbol{s}})$, i.e., integrating it with a certain t- and $\boldsymbol{R}$-dependent function U, results in a generalized inner product (U, W_k). It follows that, in order to enhance the early-time relative to the late-time diffusion modes, both the source S and the filter U should be matched to the dominant early-time diffusion eigenmodes W_k and should be, as much as possible, "orthogonal" to the late-time diffusion modes.

4 Representative results

Preliminary results of our analysis indicate that the design of suitable filters is relatively straightforward, provided processing can be performed numerically on digitized measured data. Within the available amount of data (e.g., the available angular ($\hat{\boldsymbol{s}}$) field of view) one can isolate the contributions of the leading early-time diffusion modes and, depending on the choice of the filter, achieve a significant improvement in the temporal or angular resolution. As an example, a typical time- and angle-resolved intensity is shown in Fig. 1. The effect of angular filtering is illustrated in Fig. 2, which shows a strong suppression of late-time diffusion.

The task of matching the source to the early-time diffusion eigenmodes is more difficult, in view of the physical constraints, such as positive semi-definiteness of the energy density, etc. In particular, it is not possible to arbitrarily suppress contributions of small P values (responsible for late-time diffusion), since the effective source intensity is, essentially, the autocorrelation function of the field sources and thus must have a maximum at $P = 0$. Nevertheless, a modulation of the time-dependence of the source can reduce contributions of intermediate P values, partly overlapping the P interval associated with the late-time diffusion, but lower than the values responsible for the early-time diffusion signal. Similarly, modulation of the $\hat{\boldsymbol{s}}$-distribution of the beam may enhance the contents of the early-time diffusion modes.

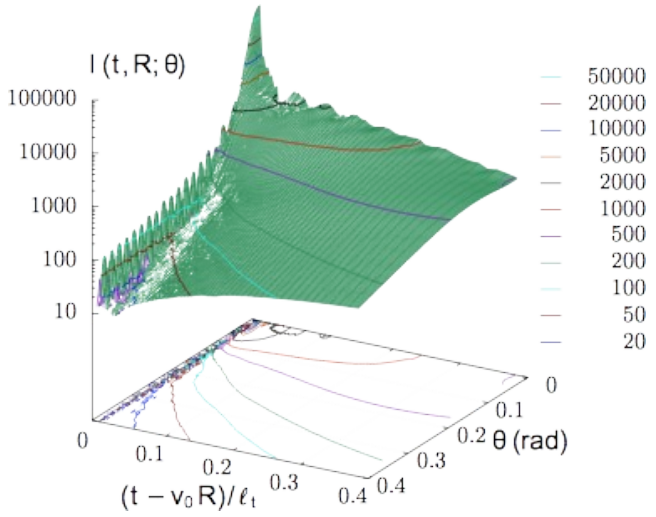

Fig. 1. The time-and angle-resolved specific intensity at the observation distance of 12 mean free paths in a typical atmospheric cloud, obtained by solving the time-dependentRTE. Here θ is the angle between the flux direction $\hat{\boldsymbol{s}}$ and the observation direction. The angular dependence is narrow at small time delay (the early-time diffusion region) and nearly flat at larger times, in the ordinary diffusion regime.

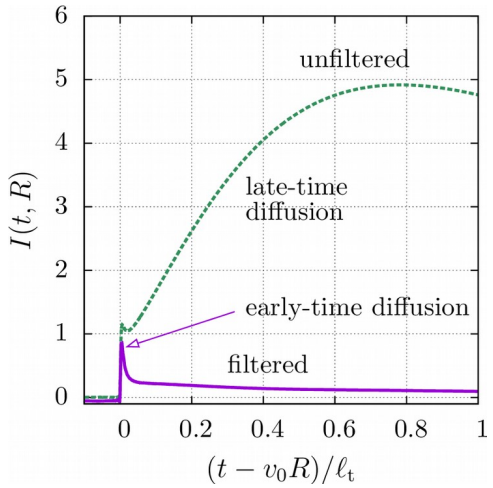

Fig. 2. Effects of angular filtering applied to the time-resolved intensity of Fig. 1.

Acknowledgements

This work is supported by the Air Force Office for Scientific Research.

References

[1] E. Bleszynski, M. Bleszynski, and T. Jaroszewicz, *Optics Letters*, **39**, pp. 5862-5865 (2014).

[2] L. Mandel and E. Wolf, "*Optical Coherence and Quantum Optics*", Cambridge University Press (1995).

An Overview of the Natural Frequencies of a Straight Wire by Various Methods

D. V. Giri* and F. M. Tesche †

**Pro-Tech, 11-C Orchard Court, Alamo, CA 94507, USA , † EMConsultant (Retired)*

Abstract - ***There are a number of different methods for computing the natural frequencies of a straight wire antenna or scatterer. The most accurate method is that derived from a numerical solution to the integral equation for the wire current. Due to the relative difficulty in obtaining this solution, however, several different approximations to natural frequencies have been developed and used in the past. Most recently, a paper by Meyers, et al. has described a variational approach for computing these natural frequencies. This paper provides a brief description of each of these methods for determining the natural frequencies of a straight wire, and then presents a comparison of the result of each method for a wire of diameter to length ratio (d / L) ranging from 0 to 0.1.***

Keywords: Wire scatterers, Wire antennas, Natural resonances, Antenna transient analysis, Singularity expansion method.

1 Introduction

Expansions based on natural frequencies are well established in the literature of mathematical physics. Later, Baum's singularity expansion method (SEM) formulation [1] exploited these earlier investigations. In his work, Baum introduced the SEM in electromagnetics and generalized its formulation to integro-differential and integral operators instead of particularly differential operators related to Sturm-Liouville theory. SEM is useful in evaluating the response of complex objects such as an aircraft to an incoming electromagnetic pulse, via natural frequencies, coupling coefficients, and natural modes. Coupling coefficients are described as the "transfer function" between the incident waves and the natural modes. The determination of the coupling coefficients was an important step on the path to synthesizing the responses.

A key element to the SEM analysis is the determination of the natural resonances of the antenna. In this paper, we are focusing on reviewing various ways of evaluating the natural frequencies of a straight wire. Early work discussed the resonances of a straight wire and developed approximate expressions for the principal natural frequencies of the wire. In 1973 Tesche [2] showed through a numerical solution of the Pocklington integro-differential equation that the straight wire has complex natural resonances, much like those of the spherical antenna. The corresponding natural frequencies of the wire occur in layers in the complex frequency plane, arranged with an increasing imaginary part ($j\omega$), at approximately equal intervals. A similar study was conducted by Singaraju, et al. [3] using a different method for searching for the resonances of the integral equation solution.

More recently, a novel variational method that is completely different from the previous approaches, but which stems from an integral equation analysis of the wire, has been developed by Meyers, Sandler and Wu [4]. With these differing methods for determining the natural frequencies of the wire, it is interesting to evaluate which is most accurate when compared with the numerically determined values.

2 Illustrative Results

Figure 1 shows a comparison of three different methods of evaluating the natural frequencies of a straight wire

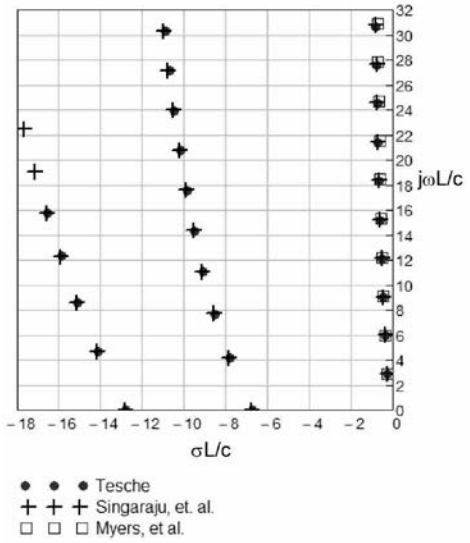

Figure 1. Overlay plots of the normalized natural frequencies

[1] C. E. Baum, "On the Singularity Expansion Method for the Solution of Electromagnetic Interaction Problems, *Interaction Notes, Note 88, 1971.*

[2] F. M. Tesche, "On the Analysis of Scattering and Antenna Problems Using the Singularity Expansion Technique," IEEE Transactions on AP, vol. AP-21, pp. 53–62, January 1973.

[3] B. K. Singaraju, D. V. Giri, and C. E. Baum, "Further Developments in the Application of Contour Integration to the Evaluation of the Zeros of Analytic Functions and Relevant Computer Programs", Mathematics Notes, Note 42, Air Force Weapons Laboratory, March 1976.

[4] Meyers, J. M., S. S. Sandler and T. T. Wu, "Electromagnetic Resonances in a Straight Wire", IEEE Trans AP, vol. 59, No. 1, Jan. 2011.

Power-balance in the time-domain for IEMI coupling prediction

J F Dawson, I D Flintoft*, A C Marvin*, M P Robinson*, L Dawson**

**University of York, UK, e-mail: john.dawson@york.ac.uk*

Abstract

In this paper we describe the use of the power-balance technique to estimate coupling into enclosures in the time domain for the prediction of coupling of Intentional Electromagnetic Interference (IEMI). The time domain method allows the peak fields for pulsed waveforms to be estimated.

Keywords: Power balance, IEMI, time-domain, shielding.

1 Introduction

The origins of the Power Balance (PWB) approach are in the work of Hill et. al. in a paper that showed how to divide the power loss in a cavity into four component parts: power lost through apertures; power absorbed by receiving antennas in the cavity; power absorbed in lossy objects and power absorbed in the cavity walls [1]. This frequency-domain PWB approach was developed further by NIST and the method was developed into a systematic high-frequency simulation technique overlaid on the Electromagnetic Topology (EMT) methodology by Parmantier and Junqua at ONERA [2].

Here we describe a time-domain solution inspired by [3] and compare the results with a finite-difference time domain (FDTD) solution.

2 The time-domain power balance method

Within the assumptions of PWB analysis the decay of the average energy, $\langle U \rangle$, in an enclosure is described by a first-order ordinary differential equation

$$\frac{\mathrm{d}\langle U \rangle}{\mathrm{d}t} + \Lambda_{\mathrm{enc}} \langle U \rangle = P^{\mathrm{t}}(t), \qquad (1)$$

where $\Lambda_{\mathrm{enc}} = 1/\tau_{\mathrm{enc}}$ is the total energy loss rate and $P^{\mathrm{t}}(t)$ is the instantaneous average power injected into the enclosure. This equation has a simple analytical solution. The power coupled into a cavity via an aperture can be determined using an approximate time response derived from a dispersion function of the form $\left(s/\left(s+\omega_{\mathrm{ap}}\right)\right)^2$, where ω_{ap} is the aperture's angular cut-off frequency and s is the Laplace variable. For a pulse waveform incident on an aperture the aperture response can be used to modify the incident pulse shape, which is then used as the excitation term in (1). The scalar power density in the enclosure is $c_0\langle U \rangle/V$, where V is the enclosure volume and c_0 is the velocity of light.

3 Pulse illuminated enclosure with aperture

In Fig. 1 the time evolution of the power density in an enclosure illuminated with a 60 kV/m, 180 ps, pulse from a JOLT source is shown and compared with the FDTD solution.

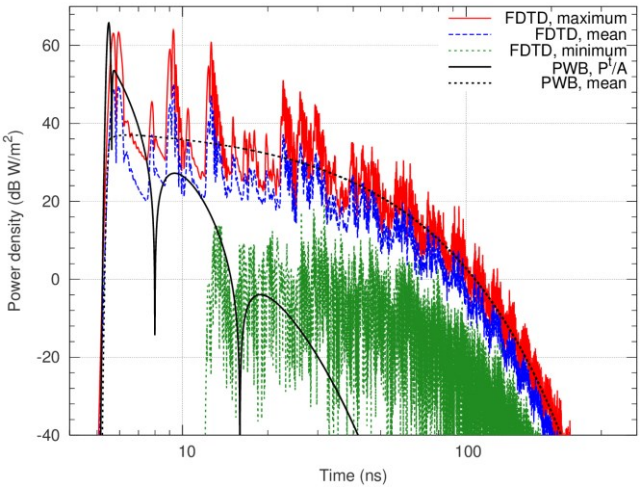

Figure 1. Power density decay as a function of time for a 3 m × 4 m × 5 m enclosure with a Q-factor of about 100 illuminated by a short pulse via a 1 m square aperture.

The power density of the initial pulse inside the enclosure is estimated as $P^{\mathrm{t}}(t)/A$, where A is the aperture area. The PWB mean value, is that predicted by (1). This is compared with the maximum, mean and minimum found in the volume by a FDTD simulation. The time-domain PWB model provides a good prediction of the initial peak amplitude (within 2 dB) and the envelope of the mean power density decay with minimal computational effort compared to the FDTD solution.

Acknowledgements

This work has been supported by the European Union Seventh Framework Programme under grant agreement number FP7-SEC-2011-285257.

References

[1] D. A. Hill, M. T. Ma, A. R. Ondrejka, B. F. Riddle, M. L. Crawford and R. T. Johnk, "Aperture excitation of electrically large, lossy cavities", *IEEE Transactions on Electromagnetic Compatibility*, vol. 36, pp. 169-178, 1994.

[2] I. Junqua, J.-P. Parmantier and F. Issac, "A network formulation of the power balance method for high-frequency coupling", *Electromagnetics*, vol. 25, pp. 603–622, 2005.

[3] G. B. Tait, R. E. Richardson, M. B. Slocum, M. O. Hatfield and M. J. Rodriguez, "Reverberant microwave propagation in coupled complex cavities", *IEEE Transactions on Electromagnetic Compatibility*, vol. 53, pp. 229–232, 2011.

Quick numerical approach for specific absorption rate determination in a reverberating environment - Application to an EM stopping vehicle project

N. Albuisson, J-C. Joly**

** CEA, DAM, GRAMAT, F-46500 Gramat, France, nicolas.albuisson@cea.fr, jean-christophe.joly@cea.fr*

Abstract

This paper presents a quick approach to assess a human SAR by numerical simulation. The application concerned is an EM stopping vehicle project. A driver is seated in a car illuminated by a plane wave at 1 GHz. For this frequency, the car compartment can be approximated as a reverberating cavity. In order to reduce CPU and memory resources, we propose to explore a quick methodology for whole body SAR calculation.

Keywords: SAR, Bio EM, numerical simulation, FDTD.

1. Introduction

For frequencies from 100 kHz to 10 GHz, EM waves cause temperature elevation of human body. In order to limit this thermal effect, standards define thresholds of EM power absorbed in body tissues by mass unity (expressed in W/kg), averaged on 6 minutes exposure time, locally or for the whole body [1].

SAR is calculated with the following relation (1):

$$DAS = \frac{\sigma \left| E_{eff} \right|^2}{\rho} \qquad (1)$$

Where σ is the conductivity of biological tissue (S/m), ρ is volumic mass (kg/m^3) and $|E_{eff}|$ is the RMS value of electric field (V/m).

For an IEMI stop vehicle project, CEA-Gramat needs SAR values of the car driver for numerous configurations (several frequencies, antennas, E-field incident angles…). A quick and simple method of SAR simulation with a FDTD code is presented here.

2. Context and methodology

In the context of a stopping vehicle project with electromagnetic waves, a plane wave incident field illuminates the vehicle and its driver. The frequency is 1 GHz. The vehicle is approximated as a reverberating cavity. EM fields inside such a cavity are supposed to be homogeneous and isotropic for a statistical point of view.

SAR simulation in reverberant environment implies two major difficulties:

- Difficulties due to the reverberating properties of the cavity. Calculation volume is important compared to the wavelength. Furthermore, calculation durations are very long in order to take multi-reflections inside the cavity into account.
- Difficulties due to the short wavelengths in biological tissue. The total number of meshes for a meshing of a driver in a car is about 520 millions.

Such an exact method simulation is thus long in time and requires large CPU and memory resources. For this reason, we propose here to explore the accuracy of a quicker alternative method in 3 steps.

3. SAR reference with the exact method

The driver and the vehicle are meshed together with $\lambda_0 / (10.\sqrt{\varepsilon_r})$ = **5 mm cells** (Cf. Figure 1).

Figure 1: Driver and car meshing obtained with the "Nash" FDTD mesher in the Quercy2 simulation platform

The whole body SAR of the driver versus the azimuth angle of the incident field is represented in green in Figure 2.

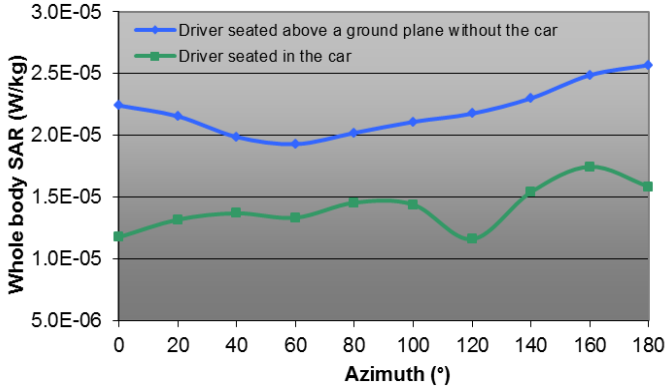

Figure 2: Green line: whole body SAR of driver inside vehicle. *(Blue line for comparison, whole body SAR of the driver in the same position above the ground plane but without the car)*

4. SAR obtained with the quick method

The 3 steps of the quick method for whole body SAR assessment are presented below:

Step 1: The whole body SAR of the driver **alone** is simulated with a λ_0 **/70 mesh size.** The illumination is a plane wave with azimuth from 0° to 180°.

Step 2: The shielding effectiveness of the vehicle **without the driver** is simulated. In this case mesh size is only λ_0 **/10** because the driver is not in the car**.** Same configurations as the first step are explored (same plane wave and same azimuths). The E-field average attenuations in the volume englobing the space let by the driver are obtained (Figure 3).

Step 3: For each incidences, SAR of the driver is immediately obtained with the next formula (2):

$$SAR_{car} = SAR_{free\,space} \times Att^2 \quad (2)$$

"Att" is the average E-field attenuation at the driver location in the car compartment (simulated at step 2).

Between the exact and the quick method, the cell dimension is **divided by 7** (λ_0 /10 instead of λ_0 /70). The total meshing size is thus divided by $\mathbf{7^3 = 343.}$ Calculation time is consequently reduced.

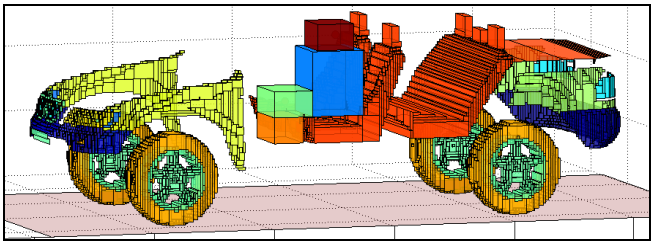

Figure 3: Step 2 - Vehicle mesh without driver, in λ_0 /10 (3 cm); cubic volumes are representing the driver seat (metallic parts are not represented on this view).

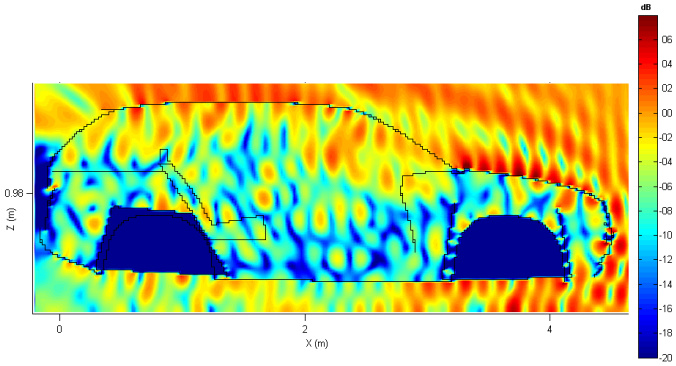

Figure 4: Step 2 - Visualization of fields inside the car (in dBV/m) for 2 V/m incident plane wave above a PEC ground plane (azimuth 160°).

5. Comparison of SAR from the exact method and from the quick method

Figure 5 shows the SAR obtained from the 2 methods. Results are similar.

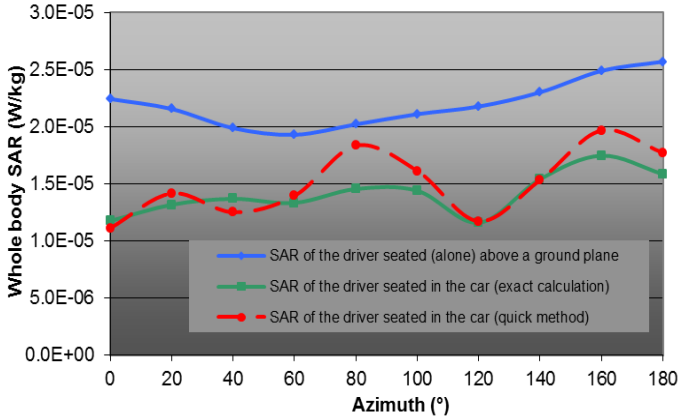

Figure 5: Comparison of SAR values obtained with quick method (Step 3) and exact calculation for different azimuths of plane wave around the car.

The influence of other parameters (polarization and elevation angles, frequency, environment…) can be now explored with this quick method.

6. Conclusion

Whole body SAR values have been obtained with the exact and the quick methods. It is interesting because the resources in time and in memory are reduced. A gain of 343 is obtained in cells number and 630 in Cpu-time.

References

[1] European Parliament and Council of the European Union, "Directive 2013/35/EU of 26 June 2013 on the minimum health and safety requirements regarding the exposure of workers to the risks arising from physical agents (electromagnetic fields) and repealing Directive 2004/40/EC", *Official Journal of the European Union*, L 179, 29 June 2013, pp 1-21

Analytical Evaluation of the Per-Unit-Length Conductance of a Coated Two-Wire Transmission Line

N. Mora, I. Junqua†, F. Rachidi*, J. P. Parmantier†*

**EMC Laboratory, Swiss Federal Institute of Technology (EPFL), Switzerland, nicolas.mora@epfl.ch*
† EMC group, Department of Electromagnetism and Radar, ONERA, France

Abstract

This work presents the derivation of analytical and semi-analytical expressions that approximate the p.u.l. conductance of coated two-wire transmission lines. The presented formulas are shown to be accurate when the separation distance between the wires exceeds about 4 times the coating radius. The proposed analytical and semi-analytical methods were validated by comparing the results of several stochastically generated cross sections with the numerical calculation of the parameters obtained using an electrostatic numerical code based on the method of moments.

Keywords: Transmission lines, cable insulation, per-unit-length electrical parameters

1 Introduction

The study of the propagation properties of transmission lines (TLs) composed of coated wires has been a subject of research for at least four decades (see Chapter 3 of [1]). Particularly, the case of a coated two-wire TL is of special interest in the assessment of the differential mode propagation of low voltage signals. Simple assessment methods of the EMC performance of such TLs require the evaluation of the propagation speed and characteristic impedance of the TL. Such quantities can themselves be estimated from the calculation of the per-unit-length (p.u.l.) inductance and capacitance, assuming a lossless line. At high frequencies, resistive and dielectric losses may become significant and could no longer be disregarded. In this case, impedance and admittance have to be considered, requiring the inclusion of p.u.l. resistance and conductance.

This paper presents an analytical method for the evaluation of the p.u.l. conductance of a coated two-wire line. Unlike the case of homogeneous TLs or microstrip lines for which analytical expressions for these parameters are readily available in the literature, to the best of the authors' knowledge, no analytical solutions have been proposed when it comes to inhomogeneous lines involving coated lines, especially for the line conductance.

2 Calculation of the equivalent p.u.l. conductance of a coated two-wire transmission line

Consider the coated two-wire line of Fig. 1. The two wires are assumed to be identical and the separation distance between the centers of the wires is *s*.

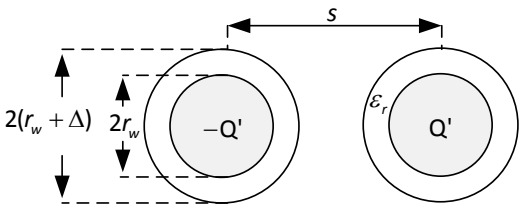

Fig. 1 Schematic diagram of a coated two-wire line

We suggest approximating the p.u.l. capacitance of the line as schematically illustrated in Fig. 2. C'_1 is the capacitance of two identical 'internal' coaxial transmission lines with internal and external radii r_w and $(r_w+\Delta)$, respectively, filled up with a dielectric exhibiting a relative permittivity ε_r. And C'_2 is the capacitance of an 'external' transmission line composed by two bare wires of radii $(r_w+\Delta)$ in free space.

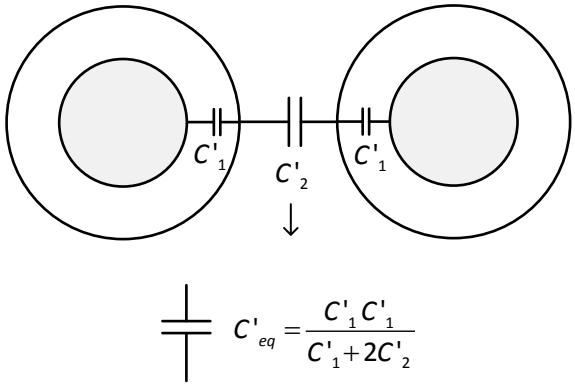

Fig. 2 Decomposition of the total capacitance as the 'internal' capacitances *C'₁* in series with the capacitance between the equivalent external wires *C'₂*.

We use the concept of complex p.u.l. capacitance [1] to obtain the p.u.l. conductance of the line as will be shown in what follows. The procedure is inspired by a method that was

originally proposed in [2] for deriving the equivalent complex p.u.l. capacitance of a coaxial line with two dielectric coatings.

Making reference to Fig. 2, one can define the complex p.u.l. capacitance of the internal lines as $\hat{C}_1 = C_1(1 - j\tan\delta)$ and use the procedure illustrated in Fig. 3 to derive the equivalent complex p.u.l. capacitance $\hat{C}'_{eq}$ [2].

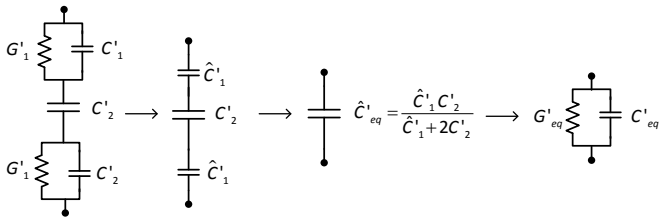

Fig. 3 Schematic illustration of the procedure for calculating the equivalent p.u.l. conductance of the line.

The equivalent capacitance can be calculated as:

$$\hat{C}'_{\text{eq}} = \frac{\hat{C}'_1 C'_2}{\hat{C}'_1 + 2C'_2} = C'_{\text{eq}} - j\frac{G'_{\text{eq}}}{\omega} \tag{1}$$

It can readily be shown that if $\tan\delta << 1$:

$$C'_{\text{eq}} \approx \frac{C'_1 C'_2}{C'_1 + 2C'_2}$$
$$\frac{G'_{\text{eq}}}{\omega} \approx 2\tan\delta \frac{C'_1 C'^2_2}{(C'_1 + 2C'_2)^2} = 2\tan\delta \frac{C'^2_{\text{eq}}}{C'_1} \tag{2}$$

3 Method Validation

In order to validate the accuracy of the method, a Monte Carlo analysis was carried out in which the p.u.l. conductance of 10,000 cross-sections was calculated and compared to the p.u.l. condutance obtained with the LAPLACE tool [3]. The cross-sections' parameters, were randomly chosen according to a standard normal distribution bounded by the limits specified in Table 1.

The capacitance C'$_1$ was estimated by the capacitance of a coaxial line, and C'$_2$ by the capacitance of a bare two-wire line.

A scatter plot showing the absolute percentage error for each of the Monte Carlo simulations is presented in Fig. 4. It can be seen that the resulting errors are below 10%, for distances exceeding about 4 times the coating radius. This suggests that as the separation distance gets shorter, the 'internal' wires do not behave as ideal coaxial lines due to the off-centering of the punctual charge

Table 1 Monte Carlo Analysis setup (10,000 cross sections)

Parameter	Variable	Min.	Max.
wire radius	r_w	0.1 mm	1 mm
coating thickness/wire ratio	Δ / r_w	0.5	2
separation/coating radius ratio	s/ ($r_w + \Delta$)	2	10
relative permittivity	ε_r	2	6
Tangent Loss	$\tan\delta$	10^{-5}	10^{-1}

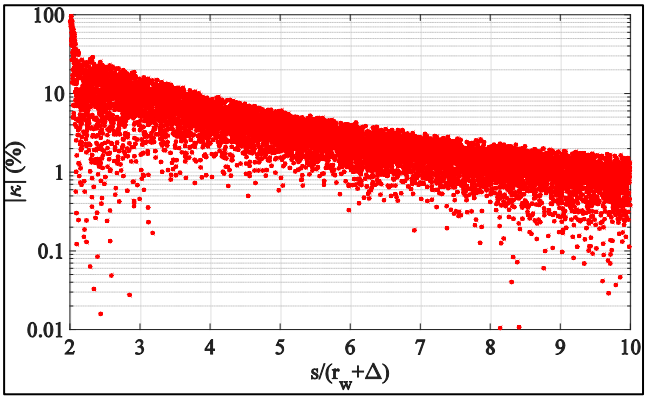

Fig. 4 Scatter plot of the absolute percentage error in the evaluation of the p.u.l conductance using (2).

3 Conclusion and Prospects

In this paper, an analytical formulation of p.u.l conductance of coated two-wire transmission line was developed and validated. The next step will consist in introducing this conductance in the computation, via the transmission line theory, and evaluating the effect of such losses on the propagation of high frequency interferences along cable networks.

References

[1] R. F. Harrington, "Losses on Multiconductor Transmission Lines in Multilayered Dielectric Media," *Microwave Theory and Techniques, IEEE Transactions on*, vol. 32, pp. 705-710, 1984.

[2] C. R. Paul, *Analysis of multiconductor transmission lines*. Hoboken, N.J.: Wiley-Interscience : IEEE Press, 2008.

[3] J. P. Parmantier, S. Bertuol, and I. Junqua, "CRIPTE : Code de réseaux de lignes de transmission multiconducteur - USER'S GUIDE – Version 5.1," ONERA/DEMR/T-N119/10 - CRIPTE 5.1 2010.

Comparison of Active and Passive Shielding Effectiveness Measurement Techniques

G. Eastwood, T. Rees, B. Petit & R. Hoad

QinetiQ Ltd.

Cody Technology Park, Farnborough, Hampshire, GU14 0LX, UK

gaestwood@qinetiq.com

***Abstract*— The Shielding Effectiveness (SE) or attenuation of facility structures (i.e. fences, gates and buildings) is an important factor in determining the levels of protection that a facility may have from Intentional Electromagnetic Interference (IEMI). This paper compares and analyses two methods, active and passive methods, of making shielding effectiveness measurements. Both methods use the simple A minus B approach to determine the shielding effectiveness of a structure. A is the E-field reference signal free space measurement and B is the E-field reference measured with the structure in the line of sight of the reference signal. The paper discusses the relative merits and limitations of each method.**

Keywords- IEMI, Shielding Effectiveness, Attenuation

1. Introduction

Today within Critical National Infrastructure (CNI) sites there is increasing levels of integration of embedded electronic systems for control and diagnostic purposes. In parallel there is an increasing availability of capable Intentional Electromagnetic Interference (IEMI) sources. When these facts are considered together it means that CNI asset owners and operators must now consider their vulnerability to IEMI. The Shielding Effectiveness (SE) or attenuation of the facility structures (i.e. fences, gates and buildings) is an important factor in determining the levels of protection that a facility may have from IEMI.

Within this paper two methods of making SE measurements are analysed and compared. The passive SE measurement method uses existing (non-controllable) external RF sources, such as AM / FM radio transmissions, and signals from mobile (cellular) phone base stations [1], in broad accordance with IEEE 473:1985, 'IEEE Recommended Practice for an Electromagnetic Site Survey (10 kHz to 10 GHz)' [2]. The active SE measurement method uses a controllable external RF source to provide a known RF reference signal, in accordance with standard test procedures such as IEEE 299 [3].

2. Passive SE measurement methods

The passive SE measurement method makes use of RF transmissions that are already present and part of the ambient environment for example, AM / FM radio; and mobile phone transmissions. The number of frequency points able to be measured is highly dependent upon the location that the measurements are being made. For example in a city there is likely to be multiple mobile phone users using 2G, 3G and 4G plus multiple radio stations, however in a rural area there may be limited mobile phone coverage say only 2G and only a limited number transmitter stations. Figure 1 shows a typical 'ambient' RF environment at a rural CNI site.

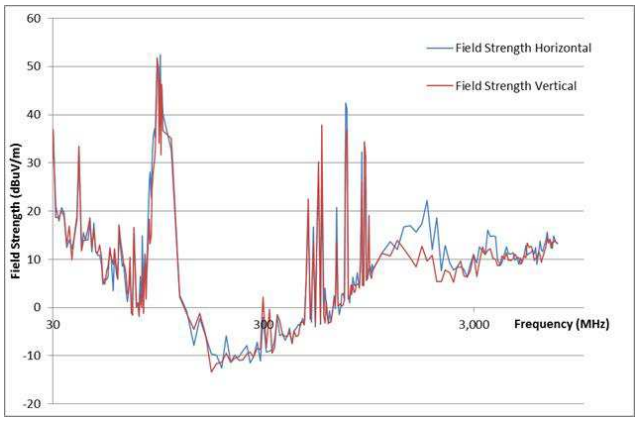

Figure 1: Typical ambient RF environment at a rural CNI site

For this method a measurement made of the 'ambient' environment either side of the structure to be evaluated.

3. Active SE measurement methods

The active method is based on IEEE 299:2006 [3]. The active method requires the controlled transmission of RF signals. Invariably, when transmitting RF in the open, compliance with spectrum management regulations is necessary, e.g. OFCOM in the UK [4] and FCC in the US [5]. QinetiQ has developed a low powered SE Measurement System (SEMS) comprising a low power transmitter, a receiver, and two matched antennas that cover the frequency range to be tested whilst maintaining full compliance with the non-licence low power aspects of the spectrum regulations. A photograph of the SEMS antennas deployed at a CNI site is shown in Figure 2.

The active technique requires two measurements to be made, a Free Space Reference Measurement, typically referred to as measurement A and Radio Frequency Attenuation Measurement typically referred to as measurement B. These measurements are E-field measurements made at a number of spot frequencies across the required frequency range. The separation between the antennas is normally 2 m and the antenna height is typically 1.2 m in accordance with IEEE 473:1985. [2]

4. Discussion

Following a series of measurements made at a rural CNI site using the passive and active SE methods we have identified and will discuss the relative merits and limitations of each method.

Figure 2: SEMS antennas measuring the SE of a perimeter fence

For both methods we have found that it is very important to control (prohibit) the use of Transmitting Portable Electronic Devices (T-PEDS), e.g. cellular phones, handheld radios etc. within 20 metres of the test-setup.

For the passive SE measurement we have found that only very limited frequency points across the frequency range of interest (our interest covers the range 30MHz to 6 GHz) can be relied upon to provide consistent results. It is important and necessary to identify the location of the distant transmitting antenna so that it can be identified whether the measured signal is being reflected, refracted or obscured by structures on the site. In our experience the AM and FM bands provide useful and comparative data to the active measurement method for building structures but do not correspond well with active measurements of fence structures (largely due to the relative heights of the transmitting antennas). We have found that it is practically very difficult to distinguish and manage cellular up-link signals, which are generated by mobile handsets and Machine 2 Machine (M2M) embedded transmitters from valid base station down-link transmission signals, particularly on CNI sites in urban areas.

Further examples and discussion will be provided in the paper.

References

[1] International Commission on Non-Ionizing Radiation Protection, “GUIDELINES FOR LIMITING EXPOSURE TO TIME-VARYING ELECTRIC, MAGNETIC, AND ELECTROMAGNETIC FIELDS (UP TO 300 GHz),” 1997.

[2] Federal Aviation Administration, DEPARTMENT OF TRANSPORTATION, “High-Intensity Radiated Fields (HIRF) Protection for Aircraft Electrical and Electronic Systems,” vol. 72, no. 150, 2007.

[3] W. A. Radasky, “Protection of Commercial Installations from the High-Frequency Electromagnetic Threats of HEMP and IEMI Using IEC Standards,” in *Asia-Pacific International Symposium on Electromagnetic Compatibility*, Beijing, 2010.

Comparison of Active and Passive Shielding Effectiveness Measurement Techniques

G. Eastwood, T. Rees, B. Petit & R. Hoad

QinetiQ Ltd.

Cody Technology Park, Farnborough, Hampshire, GU14 0LX, UK

gaestwood@qinetiq.com

***Abstract*— The Shielding Effectiveness (SE) or attenuation of facility structures (i.e. fences, gates and buildings) is an important factor in determining the levels of protection that a facility may have from Intentional Electromagnetic Interference (IEMI). This paper compares and analyses two methods, active and passive methods, of making shielding effectiveness measurements. Both methods use the simple A minus B approach to determine the shielding effectiveness of a structure. A is the E-field reference signal free space measurement and B is the E-field reference measured with the structure in the line of sight of the reference signal. The paper discusses the relative merits and limitations of each method.**

Keywords- IEMI, Shielding Effectiveness, Attenuation

1. Introduction

Today within Critical National Infrastructure (CNI) sites there is increasing levels of integration of embedded electronic systems for control and diagnostic purposes. In parallel there is an increasing availability of capable Intentional Electromagnetic Interference (IEMI) sources. When these facts are considered together it means that CNI asset owners and operators must now consider their vulnerability to IEMI. The Shielding Effectiveness (SE) or attenuation of the facility structures (i.e. fences, gates and buildings) is an important factor in determining the levels of protection that a facility may have from IEMI.

Within this paper two methods of making SE measurements are analysed and compared. The passive SE measurement method uses existing (non-controllable) external RF sources, such as AM / FM radio transmissions, and signals from mobile (cellular) phone base stations [1], in broad accordance with IEEE 473:1985, 'IEEE Recommended Practice for an Electromagnetic Site Survey (10 kHz to 10 GHz)' [2]. The active SE measurement method uses a controllable external RF source to provide a known RF reference signal, in accordance with standard test procedures such as IEEE 299 [3].

2. Passive SE measurement methods

The passive SE measurement method makes use of RF transmissions that are already present and part of the ambient environment for example, AM / FM radio; and mobile phone transmissions. The number of frequency points able to be measured is highly dependent upon the location that the measurements are being made. For example in a city there is likely to be multiple mobile phone users using 2G, 3G and 4G plus multiple radio stations, however in a rural area there may be limited mobile phone coverage say only 2G and only a limited number transmitter stations. Figure 1 shows a typical 'ambient' RF environment at a rural CNI site.

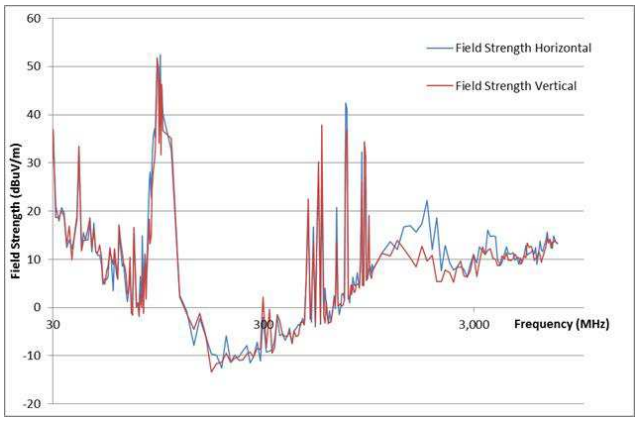

Figure 1: Typical ambient RF environment at a rural CNI site

For this method a measurement made of the 'ambient' environment either side of the structure to be evaluated.

3. Active SE measurement methods

The active method is based on IEEE 299:2006 [3]. The active method requires the controlled transmission of RF signals. Invariably, when transmitting RF in the open, compliance with spectrum management regulations is necessary, e.g. OFCOM in the UK [4] and FCC in the US [5]. QinetiQ has developed a low powered SE Measurement System (SEMS) comprising a low power transmitter, a receiver, and two matched antennas that cover the frequency range to be tested whilst maintaining full compliance with the non-licence low power aspects of the spectrum regulations. A photograph of the SEMS antennas deployed at a CNI site is shown in Figure 2.

The active technique requires two measurements to be made, a Free Space Reference Measurement, typically referred to as measurement A and Radio Frequency Attenuation Measurement typically referred to as measurement B. These measurements are E-field measurements made at a number of spot frequencies across the required frequency range. The separation between the antennas is normally 2 m and the antenna height is typically 1.2 m in accordance with IEEE 473:1985. [2]

4. Discussion

Following a series of measurements made at a rural CNI site using the passive and active SE methods we have identified and will discuss the relative merits and limitations of each method.

Figure 2: SEMS antennas measuring the SE of a perimeter fence

For both methods we have found that it is very important to control (prohibit) the use of Transmitting Portable Electronic Devices (T-PEDS), e.g. cellular phones, handheld radios etc. within 20 metres of the test-setup.

For the passive SE measurement we have found that only very limited frequency points across the frequency range of interest (our interest covers the range 30MHz to 6 GHz) can be relied upon to provide consistent results. It is important and necessary to identify the location of the distant transmitting antenna so that it can be identified whether the measured signal is being reflected, refracted or obscured by structures on the site. In our experience the AM and FM bands provide useful and comparative data to the active measurement method for building structures but do not correspond well with active measurements of fence structures (largely due to the relative heights of the transmitting antennas). We have found that it is practically very difficult to distinguish and manage cellular up-link signals, which are generated by mobile handsets and Machine 2 Machine (M2M) embedded transmitters from valid base station down-link transmission signals, particularly on CNI sites in urban areas.

Further examples and discussion will be provided in the paper.

References

[1] International Commission on Non-Ionizing Radiation Protection, “GUIDELINES FOR LIMITING EXPOSURE TO TIME-VARYING ELECTRIC, MAGNETIC, AND ELECTROMAGNETIC FIELDS (UP TO 300 GHz),” 1997.

[2] Federal Aviation Administration, DEPARTMENT OF TRANSPORTATION, “High-Intensity Radiated Fields (HIRF) Protection for Aircraft Electrical and Electronic Systems,” vol. 72, no. 150, 2007.

[3] W. A. Radasky, “Protection of Commercial Installations from the High-Frequency Electromagnetic Threats of HEMP and IEMI Using IEC Standards,” in *Asia-Pacific International Symposium on Electromagnetic Compatibility*, Beijing, 2010.

The Uncertainty of Measurement in NEMP Testing

Matthias Kreitlow*, Gernot Schmidt*, Frank Sabath*

**Bundeswehr Research Institute for Protective Technologie and NBC Protection (WIS)*
Munster, Germany 29633
Email: wis320hpem@bundeswehr

Abstract

Qualification of electronic equipment and systems against the threat of a nuclear electromagnetic pulse (NEMP) is a standard procedure for military systems. There are several standards for performing such tests that describe the methods, limits and threats, but the test facilities are always a very custom environment. Therefore it is up to the test laboratory to establish a test procedure that meets all the requirements of the standards. The test procedure used at the Bundeswehr Research Institute for Protective Technologies and NBC Protection (WIS) has been accredited for NEMP qualification tests. One fundamental aspect for an accreditation is to provide an uncertainty budget for the measured field quantities. In this paper the approach for the measurement technique is presented and an appropriate uncertainty budget is determined.

Keywords: NEMP, accreditation, uncertainty.

1 Introduction

The Bundeswehr Research Institute for Protective Technologies and NBC Protection (WIS) is responsible for the evaluation of the hardness of the German armed forces systems and devices against the threats from a nuclear electromagnetic pulse (NEMP). Although the likelihood of such an event has decreased within in the last years, the consequences would be dramatic. This leads to a still considerably high risk and therefore a high demand for qualification tests.

For this purpose the Bundeswehr Research Institute for Protective Technologies and NBC Protection (WIS) operates an NEMP testing procedure in accordance to DIN EN ISO/IEC 17025 [1] to provide reliable and repeatable NEMP qualification tests. In 2015 the "Testing Procedure for Protection against Radiated HEMP Disturbances" has been accredited by the DAkkS (Deutsche Akkreditierungsstelle). The procedure covers the testing standards VG 95371-10 [2] in conjunction with VG 96903-50 [3] which describe the methods, limits and the test environment

2 Metrological Approach

By measuring the field quantities applied field strength to the equipment under test (EUT) it is proved that requirements of the test standards are satisfied. But the measurement of very high transient field quantities differs quite a lot to typical electromagnetic compatibility (EMC) testing.

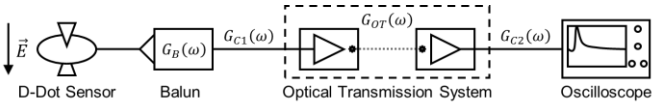

Figure 1. Measurement chain for a D-dot probe.

The main difference is that the NEMP has to be measured in time domain as it is a single event and mainly characterised by its rise time and peak amplitude. Therefore oscilloscopes are often used together with so called D-dot probes which measure in fact the time derivative of the electric displacement current. The result is not a single value but a complete waveform with all its characteristics.

In real test set-ups the complete measurement chain consists of the D-dot probe which is connected via coaxial cables, optical transmission systems and attenuators to the input of the oscilloscope (Fig. 1). In theory the sampled signal could then be integrated and the sensor factor could be applied to calculate the waveform of the electrical field strength. In practise the measurement chain will have a significant frequency dependent influence denoted by $G_x(\omega)$ on the sensor signal which has to be dealt with.

A simple of application of gain factors for each element is not sufficient as a NEMP covers a wide frequency spectrum. A more sophisticated way is to consider each element's influence in the frequency domain which can easily be measured as S_{21} parameter by a vector network analyser (VNA). From this data the frequency dependent amplitude response and the linear phase deviation can be calculated which corresponds to the complex $G_x(\omega)$ in Fig. 1. These transfer functions can be applied as correction functions to the discrete Fourier (DFT) transform of the sampled oscilloscope data. So the first step is to transform the sampled data into frequency domain by using the DFT:

$$\hat{a}_k = \mathcal{F}\big(a(t_n)\big) \text{ with } a(t_n) = (a_0, \dots, a_N) \qquad (1)$$

Then the complex transfer functions of the measurement chain have to be interpolated and expanded to the frequency steps and symmetry of the DFT. This leads to complex symmetric corrections vectors $g_{x,sym}$ which can be applied to correct $\hat{a}$:

$$\hat{a}_{k,corr} = \hat{a}_k \cdot \prod_{x=1}^{n} \frac{1}{g_{x,sym}} \qquad (2)$$

Afterwards the inverse DFT is used to calculate the corrected discrete sensor output $V_o(t_n)$:

Table 2: Uncertainty Budget

Symbol		Source of uncertainty	Value	Probability distribution	Divisor	c_i	$u_i(y)$	$(u_i(y))^2$
$E_{calc}(t)$	[dB]	Estimation	0.5	rectangular	1.732	1	0.289	0.083
dV_{scope}	[dB]	Calibration Certificate of the oscilloscope	0.5	rectangular	1.732	1	0.289	0.083
dV_{sensor}	[dB]	Estimation from reference measurement	2.0	normal, $k = 2$	2	1	1.000	1.000
R_s	[dB]	Verification measurement	2.0	normal, $k = 2$	2	1	1.000	1.000
dM_B	[dB]	Calibration Certificate of the VNA	0.3	rectangular	1.732	1	0.173	0.030
dM_{OT}	[dB]	Calibration Certificate of the VNA	0.3	rectangular	1.732	1	0.173	0.030
dM_{C1}	[dB]	Calibration Certificate of the VNA	0.3	rectangular	1.732	1	0.173	0.030
dM_{C2}	[dB]	Calibration Certificate of the VNA	0.3	rectangular	1.732	1	0.173	0.030
$u_c(E(t))$	[dB]			normal			1.512	2.287
$\boldsymbol{U(E(t))}$	**[dB]**	**Expanded uncertainty**		**normal, $k = 2.1$**	**2.1**		**3.2**	

$$V_o(t_n) = \mathcal{F}^{-1}(\hat{a}_{k,corr}) \quad (3)$$

As a last step the integration respectively the summation can be performed for calculating the electrical field strength:

$$E_{calc}(t_n) = \frac{1}{R \cdot A_{eq} \cdot \varepsilon_0} \cdot \sum_{n=0}^{N} V_o(t_n) \cdot \Delta t \quad (4)$$

A more comprehensive explanation of this approach will be published at the 2016 IEEE International Symposium on Electromagnetic Compatibility. Using this approach the uncertainty of measurement can be determined.

3 Uncertainty of Measurement

Traceability of the measurement quantities is very important for an accredited test procedure. The accuracy and the confidence in the measurement results are based on the uncertainty budget. The model equation for the described measurement chain is as follows:

$$E(t) = E_{calc}(t) + dV_{scope} + dV_{sensor} + R_s + \sum dM_x \quad (5)$$

Table 1 describes the contributions. Due to a complete consideration of the measurement chain's complex transfer functions the uncertainty contributions for these parts reduce to the contributions from S_{21} measurements. It is very common for this type of measurements to use logarithmic quantities.

Table 2 shows the complete calculation of the expanded uncertainty including the sources uncertainty and the assumed distributions. The calculation is done on the basis of the "Guide to the Expression of Uncertainty in Measurement" (GUM) [4]. For the presented NEMP testing method an expanded uncertainty of appropriately 3.2 dB with an expansion factor of $k = 2.1$ can be determined.

3 Conclusion

In this paper the basic principles for measuring the transient waveform of a NEMP with a mathematical correction for the measurement chain's influence is presented. In doing so an exact uncertainty budget can be calculated which leads to an expanded uncertainty of 3.2 dB.

Table 1: Uncertainty Contributions

Symbol	Quantity	Unit	Description
$E(t)$	Electrical field strength	dBV/m	This is the result of the measurement
$E_{calc}(t)$	Calculated electrical field strength	dBV/m	This is the value calculated from the sampled data after post processing
dV_{scope}	Amplitude error of the oscilloscope	dB	Amplitude error of the oscilloscope
dV_{sensor}	Output error of the D-dot probe	dB	This value summarizes all the imperfections of the field probe
R_s	Measurement repeatability	dB	This value is an estimation for the repeatability of the measurement, e.g. the placement of the sensor
$\sum dM_x$	Sum of errors of the measurement chain	dB	This value is the overall gain error from the S_{21} measurement of the measurement chain's elements

References

[1] General requirements for the competence of testing and calibration laboratories, International Organization for Standardization (ISO) Std. ISO 17025:2005, August 2005.

[2] Electromagnetic compatibility (EMC) including electromagnetic pulse (EMP) and lightning protection, DIN Deutsches Institut für Normung e.V. (DIN) Std. VG 95 371-10, September 2011.

[3] Nuclear electromagnetic pulse (NEMP) and lightning protection, DIN Deutsches Institut fürr Normung e.V. (DIN) Std. VG 96 903-50, October 2012.

[4] Evaluation of measurement data - Guide to the expression of uncertainty in measurement (GUM), Joint Committee for Guides in Metrology (JCGM/WG 1), September 2008

Shielded cable leakage measured in the time domain

E. B. Savage*, W. A. Radasky[†], R. Williamson[‡]

**[†]Metatech Corporation, U.S.A, savagee@cox.net*, wradasky@aol.com[†];*
Aetna Insulated Wire and Cable, rwilliamson@aetnawire.com[‡]

Abstract

A major concern in hardening a building to IEMI/HEMP is the external cabling. For critical systems, the US military standard requires solid metal conduits, welded to the building metal shield. For less critical situations, other cable shielding approaches might be considered. This paper considers flexible conduits that use non-welded connections; and uses a time domain approach to measure the EM leakage into the cable.

Keywords: shielded cable, transfer impedance, time domain.

1 Introduction

For linear time-independent systems, time and frequency domains are fully equivalent, in theory. Either domain can be used to measure the leakage of a shielded cable, as long as nonlinear effects do not occur. Often cable leakage for EMC studies use the frequency domain, but for transient situations such as HEMP and IEMI the time domain can be useful.

For very critical systems, the US standard MIL-STD-188-125-1 [1] requires solid metal conduits that are welded to the building shield. The conduit is required to keep residuals below certain levels when the outer shield is driven with specified current pulses. Our measurements replicate this situation for a set of nine cables, as shown in Fig. 1. The cables use non-welded connectors. The measurement approach is similar to the shield evaluation method in [2].

2 Sample measurement result

Fig. 2 shows the measurement concept. The cable is held a fixed distance above a ground plane. One end of the cable is sealed off – in this case a metal plate is welded across the end of the shield, with the inner wires on this end floating. The other end uses a connector - the evaluation of this connector is part of the measurement. The connector is attached to a closed termination box, using the same attachment as would connect the cable to a building's shield wall. Inside the box the internal wires are connected together, and connected to a BNC feed-thru in the box wall. An oscilloscope connects to the feed-thru, to measure the internal voltage. On the other end of the cable a fast transient pulser is connected between the cable shield end plate and ground plane, and the oscilloscope measures the injected current with a current probe. Fig. 3 shows a sample result. The green line is the external current, and the red line is the internal wires signal. High frequencies dominate, as expected [3].

Figure 1. Cable samples.

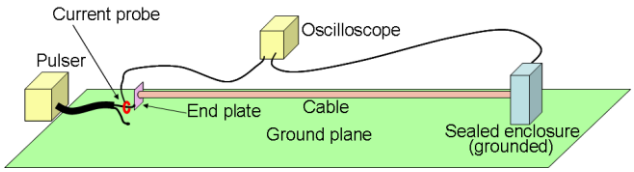

Figure 2. The measurement concept.

References

[1] MIL-STD-188-125-1, "Department of Defense Interface Standard, High-Altitude Electromagnetic Pulse (HEMP) Protection for Ground-Based C4I Facilities Performing Critical, Time-Urgent Missions, Part 1, Fixed Facilities", 7 April 2005.

[2] [8] IEC 61000-4-24, "Electromagnetic compatibility (EMC) - Part 4-24: Testing and measurement techniques - Test methods for protective devices for HEMP conducted disturbance", International Electrotechnical Commission, 2015, Geneva.

[3] Edward F. Vance, "Coupling to Shielded Cables:, Robert E. Krieger Publishing Company, 1987, Florida.

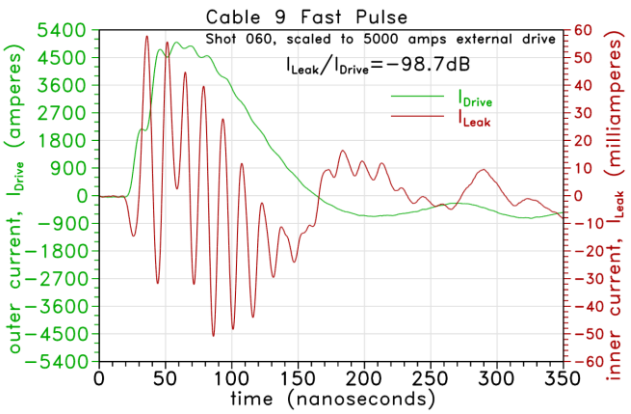

Figure 3. Sample cable measurement.

Lithium Niobate ($LiNbO_3$) Waveguides for Sensing of High Powered and Short Duration Electromagnetic Pulses (EMP).

Adrian Dzipalski, Andrew Waddie*, Mohammad Taghizadeh*, Iain Thurston†, Micheal Moutrie †*

* *Institute of Photonics and Quantum Sciences, School of Engineering and Physical Sciences, Heriot-Watt University, Riccarton, Edinburgh, EH14 4AS, United Kingdom,* † *Atomic Weapons Establishment, Aldermaston, Reading, Berkshire, RG7 4PR United Kingdom* .

Abstract

In this paper we present an all optical Lithium Niobate ($LiNbO_3$) waveguide sensor for RF electromagnetic pulse detection. This sensor is capable of measuring both the peak field strength and the temporal pulse shape of the EMP. The waveguides are 1µm wide, 1µm deep and are spaced by 900nm. The waveguide geometry is optimised for operation at a wavelength of 1550nm and the sensors are capable of measuring electric field strengths in excess of 500kV/m with minimum perturbation to the electric field. An algorithm based on the short time Fourier Transform (STFT) has been developed to aid with the signal processing of the sensor output.

Keywords: Electromagnetic Fields, Optical Waveguides, Coupled Mode Analysis, Lithium Compounds.

1 Introduction

The detection of electromagnetic pulses (EMP) with a double Gaussian temporal profile of up to a few hundred nanoseconds duration and GHz centre frequencies, such as those produced in a typical lightning discharge event, is typically achieved using an electrical antenna based sensor[1]. These sensors which are capable of accurately measuring both the peak electric field strength of the EMP and the temporal profile of the pulse are macroscopic systems (with sizes comparable to several wavelengths of the central RF frequency) and can introduce significant perturbation of the EMP during measurement. The commercially available d-dot sensors measure the time derivative of the electric flux density on the surface of a conductor allowing for the electric field profile to be calculated by integration of the measured signal. These sensors, which are capable of measuring the typical temporal electric field profiles under consideration, are subject to a number of limitations in performance and usage, most significantly in the bandwidth, sensitivity, perturbation of the measured field and overall sensor size.

The upper frequency bandwidth of a d-dot sensor is proportional to the reciprocal of the time constant of the complete electrical circuit of the sensor. In order to have a sensor capable of high frequency operation, the low voltage capacitance of the sensor has to be minimised, leading to reduced sensitivity at lower frequencies. By exploiting an all optical device based around electro-optical materials and optical detection methods, a small form factor, high bandwidth sensor can be designed offering the possibility of a significantly smaller sensor package with minimal potential for EMP perturbation.

Lithium Niobate ($LiNbO_3$), a man made material widely used in the optoelectronic industry, possesses a large electro-optic tensor and hence offers a potential route for coupling the incident radio frequency(RF) EMP to an optical sensing system. It can be used as a bulk electro-optic modulator, but integrated optical devices have a number of inherent benefits such as reduced device size, increased non linear interaction due to small mode confinement volume and longer interaction lengths. They also offer the greatest potential for high sensitivity and miniaturization of the system.

There exist a number of different methods for the fabrication of waveguides in Lithium Niobate. Doping processes, employing either titanium in-diffusion or annealed proton exchange, have been present since the 1970's and have been used to create both planar or channel waveguides [2]. During in-diffusion the electro- optical properties of the crystal are maintained and the final structure provides good optical confinement. Typical waveguide widths range from 5-10 µm and overall waveguide depths from 30-100nm. During this process both the ordinary and extra ordinary refractive indices are altered making the in-diffused waveguides insensitive to the incident light polarisation [3]. Proton exchange followed by annealing to recover the non-linear coefficients compromised during the proton exchange process has been used to fabricate waveguides with depths of up to 500nm. This method provides a much larger change in the extraordinary refractive index when compared to in-diffusion [4], but suffers from being highly sensitive to the polarisation of the incident light. More recently it has been demonstrated that waveguides may be fabricated by translating the transparent $LiNbO_3$ substrate through the focus of a femtosecond pulse train through which changes in the refractive index of the substrate are induced through stress in the crystal matrix [5]. The waveguides produced using this approach are limited by the optics of the laser exposure system and the accuracy of the translation stage. Smart Cut or crystal ion slicing[6] devices are formed from a thin (up to 1 µm) $LiNbO_3$ film bonded to a SiO2 layer of 50-100µm thickness which can then be attached to a carrier wafer to facilitate mechanical handing and processing. Waveguides with widths of up to 800nm have been demonstrated also offering a high degree of optical confinement. Optical grade dicing has also shown potential for the formation of waveguides [7] leading to the fabrication of

waveguides with widths and depths of 6 µm and 10 µm respectively. The major limitation of this technique is that the spacing between waveguides is limited by the width of the dicing saw blade used (~200µm).

In this paper we present a novel and highly compact electro-optic EMP sensor based around leaky channel waveguides etched into Lithium Niobate base substrates. The waveguides used in this paper are fabricated through a combination of electron beam lithography, reactive ion etching, backfilling deposition and lift-off. A number of fabrication limitations caused by the structure of Lithium Niobate, were identified and overcome during the development of the fabrication process. The waveguide EMP sensor is capable of measuring both the peak EMP field strength and the temporal pulse shape of the incident EMP. A robust noise removal algorithm based on the short time Fourier transform (STFT) is also presented which aids with the removal of the excess high frequency noise encountered during testing.

2 Sensing Mechanism

The structure used to perform the EMP sensing is based around three waveguides placed in close proximity to permit evanescent coupling [8] between the central input waveguide and the two side waveguides. The evanescent coupling is highly sensitive to the refractive index changes of the cladding material between the waveguides and, by using a material ($LiNbO_3$) with a large electro-optic non linear refractive index, a device with an output that is a function of the applied electric field has been created.

The light propagating through the waveguide has most of the power concentrated in the central core of the waveguide. In the cladding region the light intensity decays exponentially with distance from the core. The presence of the additional waveguides on either side of the central waveguide introduces a perturbation to the mode shape of the central waveguide and vice versa [9].

Instead of having two independent modes with the same effective index, one of which is localised in the central waveguide and the other two are in the adjacent sides, the modes and their effective indices couple and two super modes are created with effective indices slightly larger and slightly lower than the effective index of the unperturbed central waveguide mode. For the precise device geometry under consideration in this paper, the waveguide cladding is $LiNbO_3$ (n=2.2111 @ 1550nm) and the core is a-Si (n=2.3343 @ 1550nm). The core cross section is square with total size of 1µm X 1µm. The three waveguides are separated by a distance of 900nm. The supermodes are both solutions to the wave equation and upon excitation will propagate through the waveguide unperturbed. When both the symmetric and anti-symmetric modes are excited a beating effect is observed between the two modes and the power distribution between the individual waveguides changes as the incident light propagates through the structure. The length of the waveguide structure can be adjusted to ensure a specific level of coupling from the central waveguide to the adjacent waveguides. Due to the typical propagation length (300-850µm) being much longer than the wavelength of the incident light propagated, the beam envelope method can be used to model the waveguide coupling as the computational mesh does not need to resolve on the wavelength scale but rather on the inter-super mode beating length scale[10]. The total electric field can be written as the sum of the electric fields of the two super modes;

$$\mathrm{E}(z) = [\mathrm{E}_1 + \mathrm{E}_2\exp(-i(\beta_A - \beta_S)y]\exp(-i\beta_S y) \quad (1)$$

Where E_1 and E_2 are the amplitudes of the two supermodes (and can be assumed to be identical), β_A and β_S are the propagation constants of the antisymmetric and symmetric supermodes respectively and y is the propagation distance along the waveguide.

The expression within the square parenthesis can be solved giving an expression for the coupling length (L) of

$$(\beta_A - \beta_S)\mathrm{L} = 2\pi \quad (2)$$

Therefore;

$$\mathrm{L} = \frac{2\pi}{(\beta_A - \beta_S)} \quad (3)$$

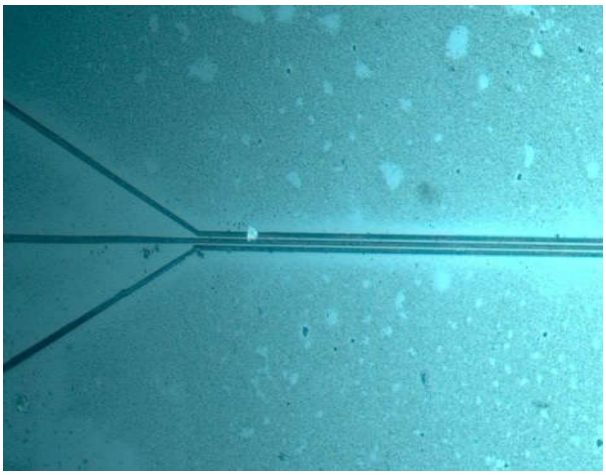

Figure 1. Micrograph of part of the waveguide microstructure after processing under a phase contrast microscope at 50X magnification.

Figure 1 above shows a micrograph of the waveguides after fabrication as seen under a phase contrast microscope. The sensing mechanism of these sensors relies on the Pockels effect, in which a refractive index change is induced in the cladding of the waveguides by the incident EMP. This results in a reduction of the modal confinement in the central input waveguide and increasing the coupling to the adjacent side waveguides as a function of the applied electric field calculated from;

$$\mathrm{n(E)} = \mathrm{n_o} + \frac{1}{2}\mathrm{r_{33}n_o{}^3E_z} \quad (4)$$

Where n_0 is the ordinary refractive index of $LiNbO_3$ in the absence of external electric field, r_{33} is the z-field, z-directed

component of the electro-optic tensor of $LiNbO_3$ (r_{33}=30.9 pm/V) and E_z is the applied RF electric field. For the field strengths required to be measured (50kV/m – 500 kV/m) Eq. 4 results in a change in refractive index on the order of 10^{-4} to 10^{-5}.

Table 1 below compares the operating parameters for a PRODYN free space d-dot electric field sensor with those for the waveguide sensor. The complete assembly of the waveguide sensor can be seen from **Figure 2** below. The waveguide sensor is limited in terms of bandwidth and rise time by the detection electronics, in particular the photodiode used to convert the optical signal into an electrical signal.

Sensor	AD-20 (free space d-dot)	$LiNbO_3$ waveguide
Response	>10GHz	>0.63GHz
Rise Time	<.029ns	<1.57ns
Maximum Output	150V	1-5V
Mass	40 g	6.6g
Length	390.4mm	25mm
Breath	25.4mm	15mm
Height	10.9mm	8mm

Table 1: Comparison between commercially available d-dot sensor and fabricated $LiNbO_3$ waveguide sensor.

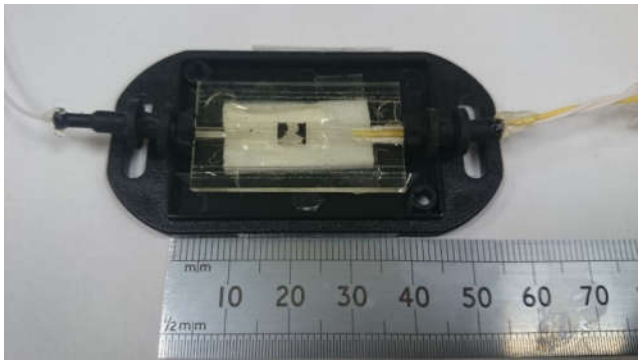

Figure 2. Assembly of Complete Sensor Package.

3 Results and Discussion

The completed sensors were tested using an RF pulse generation system capable of producing pulses of up to 500kV/m with a double Gaussian profile of 50-200ns duration. By placing the sensors at different locations within the tapered region of the pulse generation system, different peak field strengths were achieved and the response of the sensor to these different fields could be assessed. The sensor worked as designed, although some issues regarding the amplification of the detected optical signal are still being addressed. The overall loss of the optical system (from laser source to detector) is in the order of 60dB primarily due to mode field mismatch between the single mode optical fibre and the a-Si/$LiNbO_3$ waveguides. The optical signal from the waveguides was detected by using an off the shelf InGaAs High speed photodiode (ThorLabs DET08CFC) with a sub-ns (<70ps) rise time and a peak responsivity of 0.9A/W. A typical response of the sensor to an EMP is shown in **Figure 3** in which case the peak field strength, was ~500kV/m although EMP detection was observed at each of the different peak field strengths investigated. The red trace is the triggering EMP and the blue trace is the detected optical signal from one of the waveguide output channels. The delay between the initial triggering pulse and the observed optical signal is 60ns corresponding to the path difference between the direct free space path of the EMP trigger and the longer guided optical path of the sensor signal.

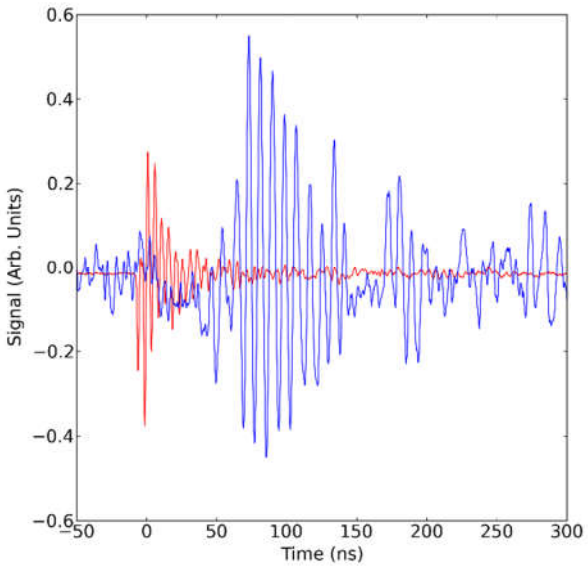

Figure 3. Temporal response of the sensor under 500kV/m EMP. The red trace is the triggering EMP pulse as measured by a wire loop antenna and the blue trace is the output from one of the side channels of the waveguides.

The significant noise levels in the measured signal has necessitated for the development of a data processing algorithm that allows for the removal of most of noise in the signal wihout significantly impacting the waveform produced by the sensor. The algorithm used for the noise removal is a thresholded short time fourier transform (STFT). The thresholding is carried out on the 90th percentile of the signal which removes most of the high frequency noise without impacting the overall waveform as seen in **Figure 4**. The short time fourier transform is a fourier related transform used in the determination of the sinosoidal frequency and phase contents of local sections of a signal as it changes over time. The long

time signal is divided into shorter segments of equal length and the fourier transform is applied on each of these short segments. The signal to be transformed is multiplied by a window function which is non zero for only a short period of time. The fourier transform of the resulting signal is taken as the window is slid along the time axis, resulting in a two dimensional representation of the signal. This is described by Eq. 5 below.

$$STFT\big(x(t)\big)(\tau,\omega) \equiv X(\tau,\omega) = \int_{-\infty}^{\infty} x(t)\omega(t-\tau)e^{-i\omega t}dt \quad (5)$$

Where x(t) is the signal to be transformed, ω(t) is the window function centred around zero and X(τ,ω) is the Fourier transform of x (t)ω(τ,ω), represented over time and frequency. This method is similar in concept to the wavelet transform and produces a time frequency spectrogram[11]. **Figure 5** which shows the clear existance of the EMP induced variation separated from the background noise.

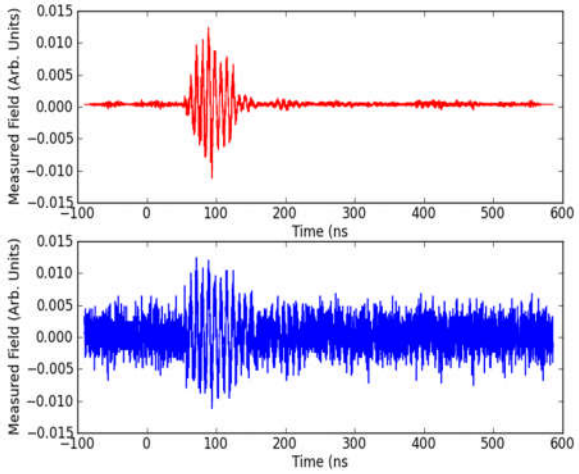

Figure 4. The temporal response of the sensor under 500kV/m EMP as seen in Figure 3. The red trace is the signal after STFT signal processing to remove the noise and the blue trace is the detected optical signal.

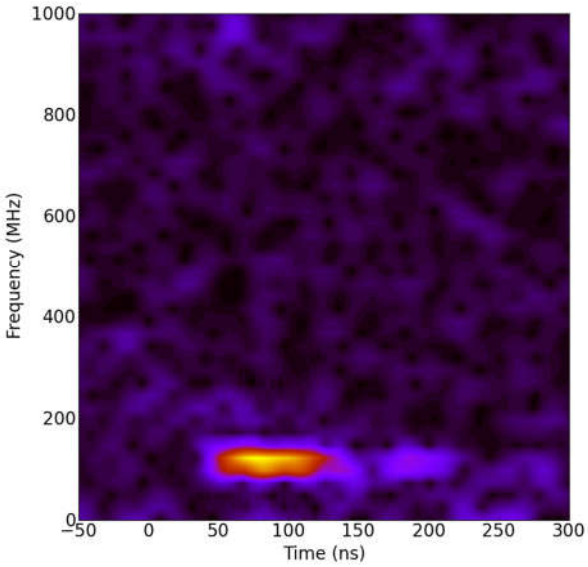

Figure 5. Time-Frequency Spectrogram for the pulse shown in Figure 4.

The response of the sensor to peak EMP field strength was determined by plotting the peak measured voltage of two different coupling length sensors (450µm and 850µm) as a function of the nominal EMP field strength (calculated by reference to the measured pulse strength). The results of these measurements can be seen in **Figure 6**. Here the peak voltage is normalised by the detected optical power passing through the central waveguide channel as different sensors had different base levels of transmitted power. It can be seen that the trend of the measured sensor response appears to follow a generally sinusoidal pattern- primarily due to the existence of a low finesse cavity formed between the end facets of the waveguide structure and the optical fibres used to transport the signal to and from the sensor. Regions in the response curves exist where the monotonically increasing response would allow for the determination of the peak EMP field strength over a limited range of field strengths. The replacement of the orthogonal waveguide facets with angled facets is a potential way to eliminate the low finesse cavity and improve the operational range of the sensor. In addition, the deployment of two sensors with different coupling lengths in parallel would allow for the identification of the peak field strength over a much larger range of EMP field strengths.

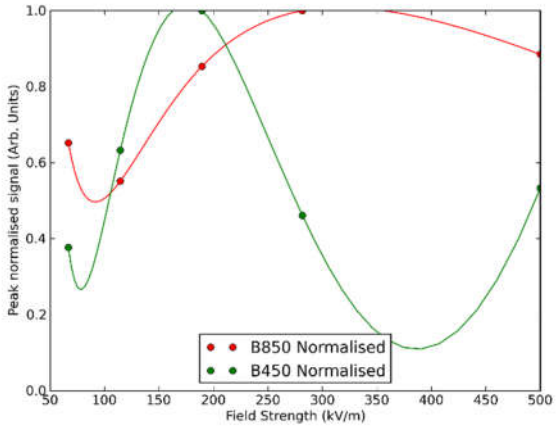

Figure 6. Variation of the peak measured sensor response as a function of peak EMP field strength.

The measured response from the waveguide sensor provides a reconstruction of the EMP temporal pulse as measured by the wire loop antenna. The signal measured optically is generally similar to the signal measured by the wire loop antenna. There exists a temporal expansion of features due to the frequency response of the detector used.

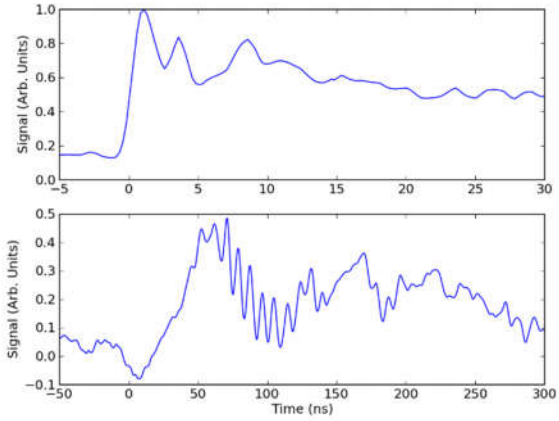

Figure 7. Temporal Shape analysis of the EMP signal from Figure 3 . The Top trace shows the pulse shape as measured by the wire loop antenna and the bottom trace shows the reconstructed signal as measured by the waveguide sensor.

4 Conclusion

We have presented the theory and the testing of an optical EMP sensor capable of determining both the temporal shape of the EMP as well as the peak field strength of the measured pulse. The use of $LiNbO_3$ as the substrate material has allowed for the development of a compact sensor head which is compatible with powerful readily available laser sources and optoelectronic detection equipment. The fabrication processes needed to produce the desired waveguide structures has been characterised and optimised with the aim of producing large numbers of sensors with standardized responses to the incident EMP. The processing of off the shelf $LiNbO_3$ substrates using an electron beam lithography micro fabrication technique allows for the creation of highly novel optically non-linear devices without the need for time consuming doping or expensive femtosecond machining. The integration of the sensor heads with optical fibres is still a relatively time consuming process as each assembly must be performed individually. From the experimental testing it has been concluded that only a single output channel needs to be directly monitored and therefore only two fibres will need to be integrated with the sensor head rather than the current four.

References

[1] H.-M. Shen, "New sensors for measuring very short electromagnetic pulses," *IEEE Trans. Antennas Propag.*, vol. 38, no. 6, pp. 838–846, 1990.

[2] H .Hu, A.P Milenin, R.B. Wehrspohn, H. Hermann "Plasma etching of proton exchanged lithium niobate*." J. Vac. Sci. Tech A*. 24(4), pp.1012-1015, Jun. 2006.

[3] R.V. Schmidt and I.P. Kaminov. "Metal diffused optical waveguides in $LiNbO_3$ " *Appl. Phys. Lett.*. 25(18), pp.458-460, Jun. 1974.

[4] M. L. Bortz and M.M. Fejer. "Annealed Proton-exchanged $LiNbO_3$ Waveguides." *Opt. Lett.* 16(23) pp.1844-1846, Dec. 1991.

[5] R.R.Thomson, S. Campbell, I.J. Blewett, A.K. Kar and D.T. Reid.. "Optical waveguide fabrication in z-cut lithium niobate (LiNbO3) using femtosecond pulses in the low repetition rate regime." *Appl. Phys. Lett.* 88(11), pp. 111109-111109-3, Mar. 2006.

[6] H. Lu, B. Sadani, N. Courjal, G. Ulliac. "Enhanced electro-optical Lithium Niobate photonic crystal wire waveguide on a smart cut thin film." *Opt. Express.* 20(3), pp. 2974-2981, Jan. 2012.

[7] N. Courjal, F. Devaux, A. Gerthoffer, C.Guyot. "Low-loss $LiNbO_3$ tapered-ridge waveguides made by optical-grade dicing." *Opt. Express.* 23(11), pp. 13983-13990, Mar. 2015.

[8] W-P Huang. "Coupled Mode Theory For Optical Waveguides: an Overview." *J.Opt.Soc.Am.A* 11(3), pp. 963-983, Mar. 1994.

[9] M. Lohmeyer.. "Wave-matching-method for mode analysis of dielectric waveguides." *Opt. and Quant. Elec.* 29(9), pp. 907-922, Sep.1997.

[10] S. Somekh, E. Garmire, A. Yariv, H.L. Garvin, and R.G. Hunsperger. "Channel Optical Waveguides and Directional Couplers in GaAs-lmbedded and Ridged*". Appl. Opt.* 13(2), pp.327-330, Feb. 1974.

[11] S. Qian, "Introduction to Time-Frequency and

Wavelet Transforms", 1st ed., Prentice Hall, 2002.

Calibration of Transient (sub-ns) Field Sensors using a Half TEM Antenna Radiator

[1]Vijay H Bhosale, [2]M. Joy Thomas, [3]Shiva S Rai, [4]D C Pande and [5]Sachin B. Umbarkar

[1] O/o Director General (ECS), DRDO, Bangalore, Karnataka, India; [2] IISc, Bangalore, Karnataka, India ; [3,4] LRDE, DRDO, Bangalore, Karnataka, India; [5]VJTI, Mumbai, India

[1] imvijayb@yahoo.com, [2] jtm@ee.iisc.ernet.in, [3]shivasrai@gmail.com, [4]pande.dc@gmail.com, [5]sachin.b.umbarkar@gmail.com

Abstract- Since the last few decades the Ultra Wide Band (UWB) systems have been found suitable for many commercial, industrial and defence applications due to their extremely wide bandwidth. Bandwidth of such systems depends principally on the rise time of the excitation voltage pulse from a pulsed power source which is typically in the sub-ns regime. This paper discusses a simple method for the calibration of sensors for characterization of such sub-ns rise time pulsed radiated field from UWB systems. The method uses a fast high voltage sub-ns rise time UWB source to feed a calibrated Half Transverse Electromagnetic (HTEM) antenna radiator. The test set up can be used to calibrate a variety of D dot and B dot sensors.

Keywords: *Calibration, Field Sensors, UWB, HTEM*

I. Introduction

The UWB type impulse radiating system generates radiation of an intense, short duration Electro Magnetic (EM) pulse in a desired direction. Many researchers have developed different UWB systems worldwide [1]. Characterization of such intense and ultra wide band field is necessary to find the suitability of the UWB system for a particular application. Derivative type electric and magnetic field sensors (D dot and B dot) are used to characterize such fast sub-ns duration fields. The authors have developed a 50kV Ultra Wide Band system [2] which was proposed to be validated by using the D dot and B dot sensors. Before usage it was necessary to characterize these sensors by calibrating them. For the calibration various methods were tried but the results of the method using the illumination of the sensor by the plane wave radiation from a Half TEM antenna radiator fed by a fast UWB excitation source were found to be reliable.

II. Calibration Method Used and Results

To calibrate the sensor it is necessary to evaluate its performance for a known field. Though the use of TEM wave guide/GTEM cell has been prescribed for this as per [3], due to the compatibility/availability issues, a characterized Half TEM antenna has been used for the present work. The sensor under calibration was placed in the far field plane wave main lobe region of the calibrated half TEM antenna. A fast voltage source FPG 10-P from M/s FID GmbH, Germany with output peak voltage of up to 10 kV (variable), sub ns rise time of 300 ps and pulse duration of 1-3 ns was used. The source was capable of generating a planar TEM field from a HTEM antenna radiator where the D dot sensor to be calibrated was kept [4]. The calibration test set up developed is as shown in Fig.1. The HTEM antenna is fed from the UWB pulse source of FID, GmbH. The field profile at variable distances from the HTEM antenna can be found analytically/by simulation [5]. The sensor to be calibrated was placed at distances ranging from 0.5 m to 2 m from the antenna. The field profile recorded by the measurement system consisting of sensor, balun and oscilloscope is as shown in Fig. 1.

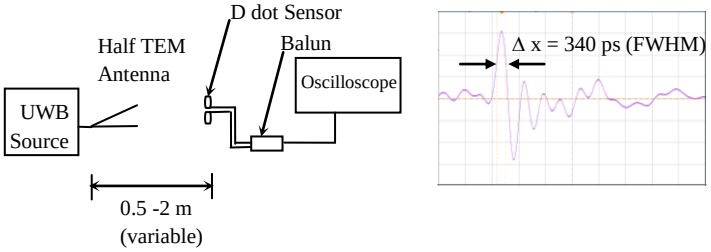

Fig. 1. Calibration set up and the recorded field waveform

Table 1: Calibration error for sensors

Sensor Type with Sensitivity	Percentage calibration error for the rise time measurement
D dot of $10^{-3}m^2$	2.85
B dot of $10^{-3}m^2$	3.62

III. Conclusion

For the experimental evaluation of UWB systems it is necessary to use calibrated field sensors. This paper has proposed a method of characterization and calibration of various types of sub-ns field sensors using a HTEM antenna radiator. The method has the advantage of simplicity with the feasibility of upgrading the test up for even faster systems.

IV. References

[1] C. E. Baum, et al., "JOLT: A highly Directive, Very Intensive and Impulse like Radiator," *Sensor and Simulation Notes*, Note 480, Nov 2003.

[2] Vijay H. Bhosale, M. Joy Thomas and D. C. Pande, "Design and Analysis of a Fast UWB Pulse Generating System", *International Conference on Electromagnetic Interference and compatibility*, Bangalore, India, Dec 2012 pp 393-398.

[3] IEEE Std. for Calibration of Electromagnetic Field Sensors and Probes (Excluding Antennas) from 9 kHz to 40 GHz.

[4] Sensor catalogue from M/s Pulse Power Measurement, Ltd., Wiltshire, UK.

[5] Sachin B. Umbarkar, et al., "Analysis of Half TEM Horn Antenna for High Power UWB System," *Pulse Power and Plasma Sci. Conference*, Jun. 2013.

Belgium's World War 1 front zone today: a sleeping UXO problem characterised by frequency domain EMI

N. Note, T. Saey, M. Smetryns, M. Van Meirvenne

Research Group Soil Spational Inventory Techniques, Department of Soil Management, Ghent University, Belgium
nicolas.note@ugent.be

Abstract

Without any demining regulation or active search approach mission, the Belgian WW1 front zone produces each year a minimum of 100 tons unexploded ordnances. In this area, multi-receiver EMI as a large scale mapping technique, showed that high percentages of the remains of the 1914-18 war are still present beneath the surface. Because of the complexity and the scale of the problem, the current situation can be compared with an uncontrolled landfill for which an adapted methodology is needed. Multi-receiver EMI as mapping technique proved successful in characterizing the buried remains. An integration with other techniques could lead to a thoughtful approach of the post-WW1 landscape where the costs of conventional UXO search approaches can be reduced.

Keywords: Belgian World War 1 front zone, soil mapping, UXO, frequency domain EMI

1 Introduction

Today, the cemeteries and monuments makes us remember the cruel battles that were held in the period of 1914-18 at the former Western front in Belgium. More than a hundred years after the outbreak of WW1, the war still poses some serious threats to society. The current problem is located beneath the surface: high concentrations of exploded and unexploded projectiles, ammunition dumps and depots are still buried in within Flanders fields. On a (inter-)national level, this situation is not well known but inhabitants of the front region, especially farmers, archaeologists and construction workers are faced daily with the consequences of WW1.

In 2012, 140 tons of unexploded ammunition was collected mainly from the Ypres region by DOVO, the Belgian army mine-clearing service [1]. Because of the absence of a legal framework that encourages active unexploded ordnance (UXO) detection in former war zones, this number only points out to accidentally finds. If there was a regulation similar to the ones in neighbour countries Germany and The Netherlands, the number of findings would be several orders larger. Establishing an active detection regulation can be introduced by politicians, procedures and committees, but this will involve a difficult process.

A larger challenge is the development of methods, to distinguish possible UXO from the omnipresent shrapnel within these fields. After scanning more than 170 ha in the former Belgian front zone with frequency domain electromagnetic induction (FDEM) and to lesser extent fluxgate gradiometers, a complex situation appears. Because of the stationarity of the western front, the fights and bombings were extremely concentrated across a relative long period of time within a small area. Not only a high concentration of possible ammunition appears within the geophysical data but also trenches, communication cables, dug-out systems, bunkers and other structures. Moreover, soil of the region is covered by iron clutter, originating from heavy shelling during WW1. After the war, the poorly cleared front was immediately released to allow the development of infrastructural, industrial and agricultural practices [2]. In 2015, a Dutch demining company tested their detection and demining approach within the Ypres region. They aimed at clearing an area of 2 ha with five people in five days. Metal detectors (TDEM) and fluxgate gradiometers were employed as survey techniques to localize the possible UXO. At the end of the project, the Dutch demining company could only clear a small part of the proposed area. The main difficulty was to distinguish the UXO from the iron clutter. To allow for an effective clearance of areas at the Western WW1 front zone, an improved approach deemed necessary.

Therefore, we proposed to integrate the multiple signals of a multi-receiver EMI instrument at the heavily shelled study site. To give an insight in the complex situation at the Western front, the survey results of an EMI multi-frequency domain sensor were outlined within the next paragraph. This technique already proved successful for mapping WW1 archaeology at the Western front [3,4]. Today, a basis for metal localisation, classification and filtering already exists but improvements to this sensing technique and discrimination algorithms would increase the usability of frequency domain EMI for UXO detection. The combination with other commonly applied sensing techniques could lead to an adapted and efficient methodology.

2 Electromagnetic induction survey

In order to map the subsoil, the DUALEM-21S EMI sensor (DUALEM, Milton, Canada) was used. This sensor incorporates horizontal coplanar (HCP) and perpendicular (PRP) coil configurations that operate at a frequency of 9

kHz. This instrument is pulled by an all-terrain vehicle within a HDPE sled at a speed between 6-10 km h-1, crossing the field at parallel lines 1.4 m apart. The instrument is aligned parallel with the direction of travel. All measurements are georeferenced by an RTK-GPS and integrally logged onto a rugged field computer at a frequency of 8 Hz. The DUALEM-21S instrument consists of one transmitter coil and four receiver coils, located at distances of 1.0, 1.1, 2.0 and 2.1 m from the transmitter coil. The 1.0 m and 2.0 m transmitter-receiver pairs form a vertical dipole mode (1HCP and 2HCP), while the 1.1 m and 2.1 m pairs form a perpendicular dipole mode (1PRP and 2PRP). The advantage of this sensor is that it simultaneously produces 8 maps (4 magnetic susceptibility and 4 electrical conductivity maps) with complementary information about the subsoil (electrical conductivity compared to magnetic susceptibility) which relate to four different soil volumes.

2.1 Metal classification and filtering

By integrating data layers from the DUALEM-21S coil configurations, *Saey et al.* [5] proved that metal objects can be localised and classified within different depth intervals between the surface up to 1 m depth employing the FEMP-calculation (fused electromagnetic metal prediction). This classification is a first step in localising and distinguishing UXO and other metal objects from metal shrapnel. The planar precision of designating objects is comparable to traditional fluxgate gradiometer surveys. Using the 1HCP data, near surface metal can be separated from the FEMP-indicated objects [3].

2.2 Case: Mont de la Hutte

Mont de la Hutte is a hamlet in the city of Comines-Warneton, 12 km to the south of Ypres. At this location, an arable field of 11.7 ha was surveyed in September 2014. A comparative study was made on historical aerial photographs and the finds by electromagnetic induction [3]. The results showed that 73% of all linear structures (trenches, military roads, communication cables and narrow-gaugerailway) visible on the historical aerial photographs, were detected by EMI survey. Other surveyed sites indicate comparable results (between 65-71%) [3]. Using the FEMP-formula, around 7% of this field is classified as metal-containing.

The geophysical data and archaeological analysis were derived from the 'Non-Invasive Landscape Archaeology of the Great War' project, funded by Ghent University's Special Research Fund – Concerted Research Action 2014-2018 (grant number 01G00214).

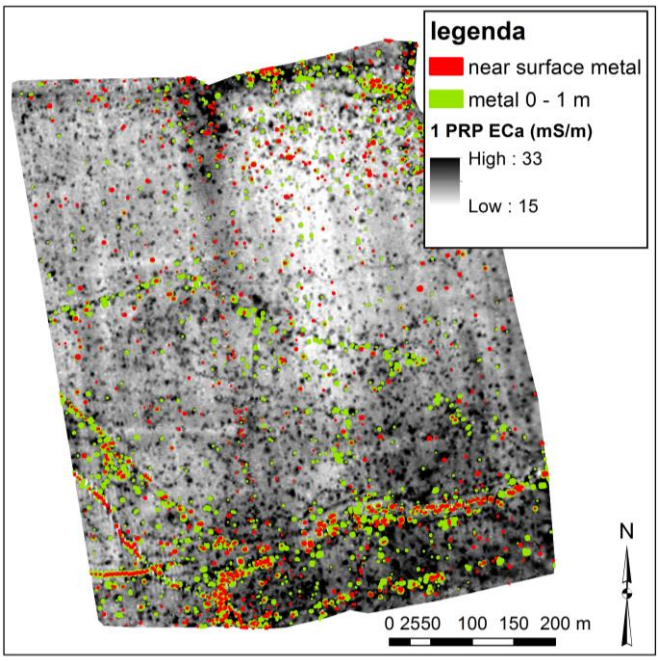

Figure 1. The 1PRP ECa data showing the WW1 remains combined with a metal analysis.

3. Conclusions

Integrating the multiple signals from a multi-receiver EMI sensor showed potential to characterize structures and UXO within soil saturated with small metallic objects. Moreover, multi-receiver EMI has the advantage to map also non-metallic features which improves the interpretation of the detected features. Compared to multi-receiver EMI, magnetometry has the advantage to scan at a high resolution and frequency. Fine-tuning the EMI method for detecting smaller features and developing more discrimination options, would lead to an increased usability for UXO detection within soils full of metal shrapnel like the Western WW1 front zone.

References

[1] "2012 was een druk jaar voor DOVO en de Sea Kings van Defensie." Retrieved from http://www.belgium.be/nl/nieuws/2013/news_2012_druk_jaar_dovo_sea_king.jsp (2016, January 8)

[2] Debaeke, S. "Oud ijzer. De frontstreek bedolven onder levensgevaarlijke oorlogsmunitie." *Uitgeverij de Klaproos, Bruges, Belgium.* (2013)

[3] Saey, T., Gheyle, W., Stichelbaut, B., Bourgeois, J., Verplaetse, S., Van Eetvelde, V., Note, N., Van Meirvenne M. "The characterization of a former World War I battlefield by integrating multiple signals from multi-receiver EMI soil sensor." *Geoderma*, (accepted 15/11/2015)

[4] Saey T., Stichelbaut B., Bourgeois J., Van Eetvelde, V., Van Meirvenne M., "An interdisciplinary non-invasive approach to landscape archaeology of the Great War." *Archaeological Prospection*, 20: 39-44 (2013)

[5] Saey T., Van Meirvenne, M., Dewilde M., Wyffels, F., De Smedt, P., Meerschman, E., Islam, M.M., Meeuws, F., Cockx, L. "Combining multiple signals of an electromagnetic induction sensor to prospect land for metal objects." *Near Surface Geophysics*, 9:309-317 (2011)

Humanitarian Microwave Detection of Improvised Explosive Devices in Colombia (Project MEDICI)

J Sachs, R Bustamante**, F. Vega‡, C Baer†*

**Technische Universität Ilmenau, Germany, Email: juergen.sachs@tu-ilmenau.de*
*** Universidad de los Andes, Colombia, Email: rbustama@uniandes.edu.co*
‡Universidad Nacional de Colombia, Colombia, Email jfvegas@unal.edu.co
†Ruhr-Universität Bochum,Germany, Email: christoph.baer@rub.de

Abstract

This paper presents project MEDICI, (Humanitarian Microwave Detection of Improvised Explosive Devices in Colombia), a German-Colombian scientific cooperation initiative, aimed to the detection of Improvised Explosive Devices (IEDs) using polarimetric, ground penetrating radar detection techniques.

Keywords: Improvised explosive devices detection, polarimetric radar, UWB Radar, landmines.

1 Introduction

Colombia is the only country in Latin America where anti personal landmines and improvised explosive devices (IED) continue to be planted regularly. 10253 people of Colombian nationality have been victims of these devices between 1990 and 2013, 2126 of which deceased, as a result of the injuries received.

Differently from conventional landmines, IEDs are fabricated in a nonstandard way, having variable shape, triggering mechanism, explosive content and low content of metallic parts. This variability reduces the usefulness of traditional methods of detection, based on metal detectors or in the recognition of the regular and standard pattern that conventional, mass produced antipersonnel landmines represent.

Classical mine detection techniques by ground penetrating radar (GPR) try to extract the radar signature of a mine from the gathered data. If these signatures (reflectivity, time-frequency-parameters, etc.) are verifiable, a mine is to be considered as detected. This approach implies some knowledge and some assumptions about the electromagnetic scattering behavior of the mine and the soil which is embedding the mine. This technique will however fail in Colombia due to the variability of the IEDs and due to the diversity of soils that can be found in the country.

2. Project MEDICI

Project MEDICI (Humanitarian Microwave Detection of Improvised Explosive Devices in Colombia) is scientific cooperation initiative financed by the German foundation for scientific research, DFG (Deutsche Forschungsgemeinschaft) and the Colombian agency for science, technology and innovation (Colciencias). The project is developed by the Technical University of Ilmenau (Germany), the Ruhr University at Bochum, (Germany), Andes University (Colombia) and National University of Colombia.

The project is aimed to the development of new technologies for the detection of IEDs in Colombia. The project takes into account the non-standardized manufacturing techniques of IEDs and the challenging soil and environmental conditions. It's expected that the result of this project will be applied in humanitarian clearance operations in Colombia, especially for the clearing of roads, crop fields, and other civilian infrastructures.

The project will focus on radar detection techniques. However, it is proposed to switch the sensing philosophy to an approach called: "*Foreign Object Detection in a Heterogeneous Environment*". Here, it's assumed that the statistical properties of the soil are perturbed by the mine and the hole in which the mine was placed. In order to get a pattern/picture/comprehension as complete as possible from the scenario under test, it's necessary to gather the whole set of electrically accessible data of the mine affected area. In order to achieve this, an ultra-wideband (UWB) polarimetric multiple-input multiple-output (MIMO) radar (Figure 1) will be developed, calibrated and tested in laboratory and in operational conditions [1].

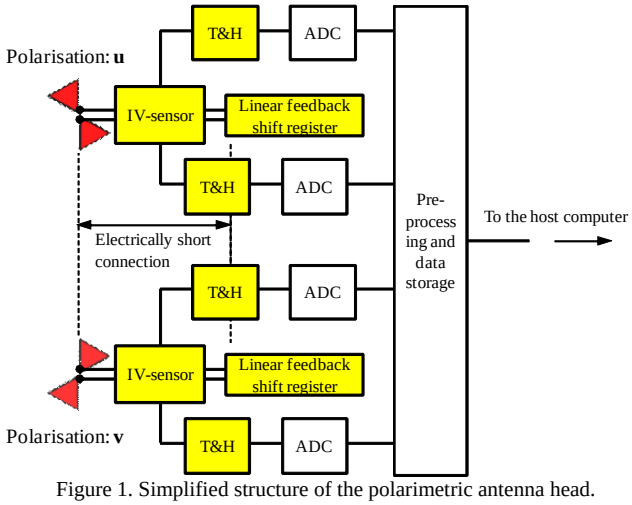

Figure 1. Simplified structure of the polarimetric antenna head.

References

[1] J. Sachs, *Handbook of Ultra-Wideband Short-Range Sensing - Theory, Sensors, Applications*. Berlin: Wiley-VCH, 2012.

On the applicability of search coils used in commercial handheld metal detectors for metallic target characterization

Davorin Ambruš, Darko Vasić, Vedran Bilas*,
Liam A Marsh, John L Davidson, Anthony J Peyton†

**University of Zagreb, Faculty of Electrical Engineering and Computing, Unska 3, Zagreb, Croatia, davorin.ambrus@fer.hr,*
† School of Electrical and Electronic Engineering, The University of Manchester, Manchester M13 9PL, UK

Abstract

Search coils of handheld metal detectors (HMD) employed for detection of buried landmines typically feature planar designs, normally based on single transmitter and one or more receiver coils. Such designs are usually optimized with respect to detector sensitivity to small metallic targets in a single (e.g. vertical) direction only. Capturing a target's induced responses corresponding to all possible directions of transmitted/received magnetic fields opens up a possibility of reconstructing the target's magnetic polarizability tensor. The elements of this tensor are closely related to target's geometrical and material properties. In effect, an HMD could be considered as a potential target characterization tool, which is important for improving target discrimination capabilities of current HMD technology. In this paper, we analyze directional sensitivities of three different search coil designs, typically found in the humanitarian demining industry, and asses their applicability for target characterization.

Keywords: metal detectors, landmine detection, metal target characterization, directional target polarizabilities

1 Theoretical background

We analyze a scenario in which the elements of a magnetic polarizability tensor of a buried metallic target need to be estimated using voltage measurements from a search coil, Fig. 1, taken at multiple positions above the target. For the purpose of our analysis, we assume the scanning positions of the search head and the target location as *a priori* known.

Sensor response to a target modeled as an induced magnetic dipole with six independent directional polarizabilities m_{ij} is given by (1). The sensitivity matrix $\mathbf{S}$ contains cross-coupled contributions of *x*-, *y*- and *z*-components of the transmitter field $\mathbf{H}_{TX}$, and a field that would be generated by the receiver if it was used as a transmitter, $\mathbf{H}_{RX}$ [1].

$$\mathbf{u}_{ind} = \begin{bmatrix} \mathbf{H}_{x\_TX} \circ \mathbf{H}_{x\_RX} \\ \mathbf{H}_{x\_TX} \circ \mathbf{H}_{y\_RX} + \mathbf{H}_{y\_TX} \circ \mathbf{H}_{x\_RX} \\ \mathbf{H}_{x\_TX} \circ \mathbf{H}_{z\_RX} + \mathbf{H}_{z\_TX} \circ \mathbf{H}_{x\_RX} \\ \mathbf{H}_{y\_TX} \circ \mathbf{H}_{y\_RX} \\ \mathbf{H}_{y\_TX} \circ \mathbf{H}_{z\_RX} + \mathbf{H}_{z\_TX} \circ \mathbf{H}_{y\_RX} \\ \mathbf{H}_{z\_TX} \circ \mathbf{H}_{z\_RX} \end{bmatrix}^{T} \begin{bmatrix} m_{xx} \\ m_{xy} \\ m_{xz} \\ m_{yy} \\ m_{yz} \\ m_{zz} \end{bmatrix} k = \mathbf{S}\,\mathbf{M}_v\,k \quad (1)$$

For search coil designs given in Fig. 1, we have calculated their corresponding directional sensitivity maps, Fig. 2. The maps are calculated for three characteristic directions that correspond to three principal magnetic polarizabilities of a normally oriented target (i.e. *xx*-, *yy*- and *zz*-directions).

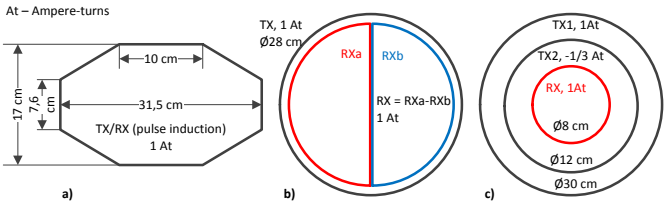

Fig. 1. Search coil designs analyzed. a) octagonal mono-coil, b) "double-D" gradiometer, c) magnetic cavity coil design.

2 Results and conclusions

The sensitivity maps reveal that *z*-direction sensitivities dominate over *x*- and *y*-direction sensitivities, as expected for planar sensors. For a mono-coil and double-D gradiometer case, commensurable sensitivities in *x*- any *y*-directions can be obtained near the coil edges. Lower sensitivities of a magnetic cavity design are due to smaller receiver area.

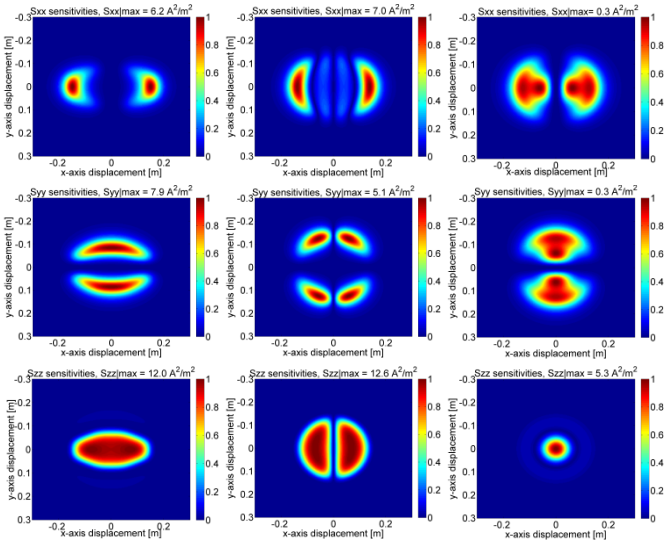

Fig. 2. Normalized sensitivity maps corresponding to m_{xx} (1st row), m_{yy} (2nd row) and m_{zz} (3rd row) for octagonal mono-coil, double-D gradiometer and magnetic cavity design (col. 1-3, resp.), 5 cm depth.

Acknowledgements

This work was supported by the Find a Better Way charity (www.findabetterway.org.uk/).

References

[1] B Dekdouk, C Ktistis, L A Marsh, D W Armitage, A J Peyton, "Towards metal detection and identification for humanitarian demining using magnetic polarizability tensor spectroscopy", *Meas. Sci. Tech.*, 26 (11), 2015.

Delivery of Picosecond Pulses to Subcutaneous Tissues

Shu Xiao*†, Ross Petrella,† Karl H. Schoenbach

**Department of Electrical and Computer Engineering, †Frank Reidy Research Center for Bioelectrics, Old Dominion University, Norfolk, VA 23508 USA*

Abstract

A dielectrically loaded rod antenna has been studied as a pulse delivery system to subcutaneous tissues. Simulation results of applying 100 ps electrical pulse show that the antenna allows us to generate critical electric field for biological effects, such as brain stimulation, in the range of several centimeters. In order to reach the critical electric field for biological effects, which is approximately 20 kV/cm, at a depth of 2 cm, the input voltage needs to be 175 kV. The electric field spot size in the brain at this position is approximately 1 cm^2. These results set the foundation for high voltage, in situ experiments on the complete antenna system and the delivery of pulses to biological tissue.

Keywords: picosecond pulses, dielectrically loaded antenna.

1 Introduction

The efforts to utilize wideband antennas for the delivery of intense pulsed electric fields into tissue have led to the development of focusing wideband antennas [1,2]. For example, the prolate spheroid antenna designed by Baum et al. [3,4] has the potential to generate large electric fields in tissue. It has been shown using pulses with a rise time of 200 ps and pulse width [full-width at half-maximum (FWHM)] of 400 ps, that it is possible to generate a peak electric field of 68 kV/m at 10 m if the voltage fed into the antenna is 1 MV [5]. At closer distance, electrical fields in air could be much higher and close to the required field strength for biostimulation: 20 kV/cm. Yet, the electric field in biological targets is strongly reduced compared to that in air by the reflection at the interface of air and tissue, which is due to the large difference in permittivity. The relative permittivity of brain matter for example is approximately 50 at a frequency of 1 GHz [6]. As a result, the antenna-based delivery of subnanosecond electric pulses still has not found therapeutic applications.

An approach that can overcome the problem of losses at the interface of air and tissue is the use of a dielectric antenna. With such an antenna, the coupling of the radiation to the tissue can be strongly increased by making direct contact to the tissue. As will be shown, although it is not as efficient as large antennas, it permits the delivery of pulses to targets that are 1-2 cm in depth. Also, because the antenna is dielectrically loaded, it can be much smaller than a prolate-spheroidal antenna.

2 Antenna Structure

The dielectric antenna consists of three sections (Fig.1): 1) a hollow conical TEM waveguide, which is loaded with a dielectric. Such a structure is commonly used for launching waves to a dielectric lens [7]. In principle it is an aperture antenna but has a small aperture area. In order to preserve the pulse shape of the incident pulse in the cylindrical wave guide, the incident waves in Section 2 should ideally be planar waves. This can be achieved by using a small slope launcher (small θ_0), which resembles to some degree two parallel plates; 2) a dielectric rod, i.e., a cylindrical wave guide, which is used to confine the electromagnetic waves and guide them to the emitting section. When determining the diameter of the rod, a rule of thumb is that the radius R should be greater than the pulse spatial width. This means that the pulse reflected from the rod-air interface will be temporally separated from the existing pulse on the axis; and 3) a dielectric cone as the wave emitting section. The impinging ray should be reflected at the surface of the cone and then exit from the cone apex. The angle of the cone can be chosen as α_0, the critical angle for total internal reflection. This ensures the rays that are in parallel with the axis reach the cone apex and radiate into the tissue.

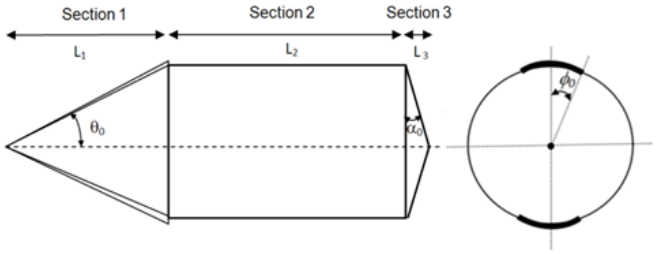

Figure 1. A conical antenna that is loaded with a dielectric. In Section 1, the wave is launched by a conical waveguide centered on the y axis and is characterized by two angles: θ_0 and ϕ_0. In Section 2, the waves emitted from the launching section are guided by a dielectric rod to the emitting section. In Section 3, the waves are detached from the antenna and propagate in the +z direction.

Such an antenna could be used to stimulate neurological tissue. We have therefore used CST Microwave Studio® to simulate the electric field distribution in a partial human head voxel model. The model consists of seven dielectrics with dielectric properties of skin, fat, bone, blood, optical nerve, and brain (grey and white matter). Aluminum Nitride (AlN)

with a relative permittivity, ε_r, of 7.3 was selected as the antenna dielectric material.

3 Results

The wave launched from the apex is guided to the emitting section, as shown in several snap shots (Fig.2). The electric field travels down the wave launching section in a spherical wave form at 0.75 ns. The pulse is scattered at the joint between Section 1 and Section 2. Three scattered waves can be clearly observed at 1 ns: a reflected wave which bounces back to the source, an evanescent wave on the rod surface, and the waves confined in the rod. The last part refracts into the brain tissue at 1.25 ns and reaches the brain tissue at 2 cm depth at 1.5 ns.

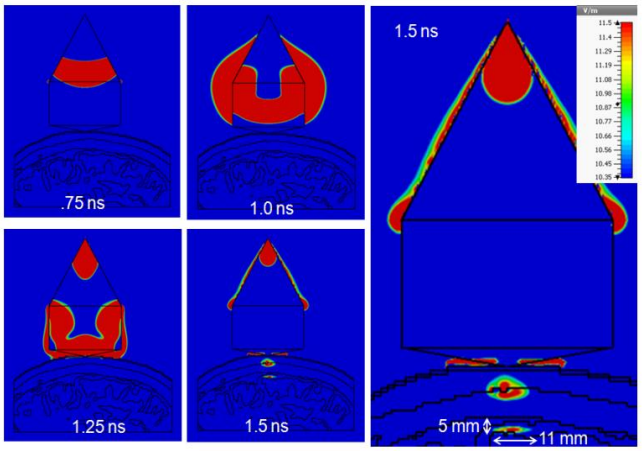

Figure 2. The transient propagation of the electric field shows an excitation of the brain tissue at 11.5 V/m with a diameter of approximately 11 mm.

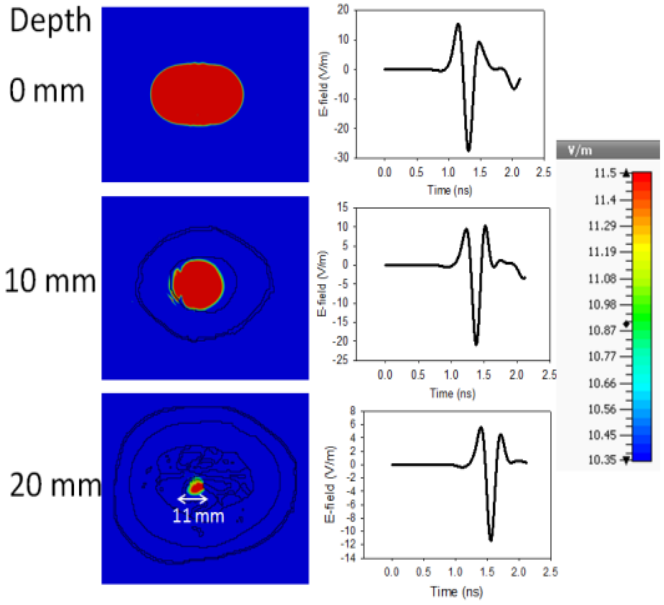

Figure 3. Cross sectional view of the brain tissue at three depths shows the field decreasing in magnitude and size with increasing depth.

If we define the stimulation spot size as the area that has the electric field value greater than 90% of the peak value, the thickness and width of the stimulation spot can be estimated to be 5 mm by 11 mm (Fig.3). At the surface the spot size is on the order of the diameter of the waveguide and shrinks until reaching 11 mm in width in the brain tissue (2 cm deep). This field concentration is caused by the tissue attenuation. Since the electric field is highest at the center and it remains to be so at deeper regions in the brain.

4 Conclusion

In a simulation, electric pulses in the hundred picosecond range were successfully delivered to the subcutaneous region of the brain using a conical dielectrically loaded antenna. The antenna makes a direct contact to the tissue, without air gap, thus reducing the large reflection losses due to the difference in the permittivity of air and tissue. For the dielectrically loaded antenna ($\varepsilon = 7.3$), the electric field at a depth of 20 mm (inside brain tissue) was shown to be 11.5 V/m for a 1V input. In order to stimulate tissue, the critical electric field needs to be on the order of 20 kV/cm, as found in our previous study [8]. This critical field corresponds to an input voltage of 175 kV. This voltage is achievable with current pulsed power systems. The spot size in the brain is estimated to be 5 mm × 11 mm × 11 mm and is better than that created by other neural stimulation modalities, specifically repetitive transcranial magnetic stimulation (rTMS) [9]. For this spot volume, the electric field at the skin is 2.4 times greater than the field in the brain tissue. Future work will be focused on the experimental verification of the design. One improvement of the design is to use a lens in the joint between Section 1 and Section 2 to collimate the waves so that the intensity at the Section 3 can be increased.

Acknowledgements

This project was sponsored by NIH with a R21 project (1R21EB016912-01A1).

References

[1] C. E. Baum, “Focal waveform of a prolate- spheroidal impulse-radiating antenna,” Radio Science, 42, RS6S27, doi:10.1029/2006RS003556, 2007.

[2] S. Xiao, S. Altunc, P. Kumar, C. E. Baum and K. H. Schoenbach, “A reflector antenna for focusing in the near field," IEEE Antennas and Wireless Propagation Letters,Vol. 9, pp.12-15, Mar. 2010.

[3] P. Kumar, C. E. Baum, S. Altunc, J. Buchenauer, S. Xiao, C. G. Christodoulou,E. Schamiloglu, and K. H. Schoenbach, "A hyperband antenna to launch and focus fast high-voltage pulses onto biological targets," IEEE Trans. Microwave Theory and Techniques, Vol.59, No. 4, p.1090-1101, April, 2011.

[4] F. Guo, C. Yao, C. Bajracharya, S. Polisetty , K. H. Schoenbach and S. Xiao, “Simulation of delivery of subnanosecond pulses to biological tissues with impulse radiating antenna,” Bioelectromagnetics, 6 Nov 2013DOI: 10.1002/bem.21825.

[5] W. D. Prather, C. E. Baum, R. J. Torres, F. Sabath and D. Nitsch, “Survey of worldwide high-power wideband capabilities,” IEEE Trans. Electromagnetic Compatibility, 46(3), 2003. 335-344.

[6] K.R. Foster, J.L. Schepps, R.D. Stoy, H.P. Schwan, "Dielectric properties of brain tissue between 0.01 and 10 GHz,"Phys Med Biol. 1979 Nov;24(6):1177-87.

[7] C. E. Baum, "Emerging technology for transient and broad-band analysis and synthesis of antennas and scatterers," Proc. IEEE, 64(11), 1976, pp.1598-1616.

[8] S. Xiao, A Pakhomov, F. Gou, S. Polisetty, and K. Schoenbach, “Neurostimulation using subnanosecond electric pulses,” Progress in Biomedical Optics and Imaging: Terahertz and Ultrashort Electromagnetic Pulses for Biomedical Applications, vol. 14, no. 21, February 2013.

[9] Z. Deng, S.H. Lisanby and A. V. Peterchev, "Electric field depth–focality tradeoff in transcranial magnetic stimulation: simulation comparison of 50 coil designs," Brain Stimulation, 6(1):1-13,2013.

The acute UWB pulse exposure induced the temporary hyperglycaemia and hepatic injury of KM mouse

Xiao-yun LU*, Kai-hong GUO*, Yan-zhao XIE †

** Xi'an Jiaotong University, School of Life Science and Technology, Xi'an 710049, Shaanxi, China.*
† Xi'an Jiaotong University, School of Electrical Engineering, Xi'an 710049, Shaanxi, China.

Abstract

KM mice were treated with UWB radiation of 2 ns duration and 100 Hz repetition rate at 120 kV/m for 60 min. The acute exposure resulted in the increase of AST, ALT, glucose and Cys-C, which reflected the temporary hyperglycaemia, hepatic injury and slight dysfunction of kidney. The histological characteristic of hepatic tissue revealed the accumulation of intracellular lipid drops and over expression of NF-kB 24h after exposure.

Keywords: UWB pulse, hepatic injury, hyperglycaemia, KM mice.

1 Introduction

The increased use of ultra-wideband (UWB) technology in many applications has raised concerns about potential influences on the scientists and engineers when doing test, thereby motivating a number of recent UWB electromagnetic pulse (EMP) exposure studies [1]–[4]. Nevertheless, the potential health risk of UWB radiation exposure is far from fully revealed.

Recently, a UWB radiation system was established in our lab with 2 ns pulse duration and 100 Hz repetition rate. We evaluated the effect of UWB electromagnetic pulses exposure on the KM mice at the field intensity of 120 kV/m by analyzing some general physiological parameters such as the blood routine examination, the liver and the kidney function test. The pilot results demonstrated that the acute exposure of 60 min induced the temporary hyperglycaemia and hepatic injury of KM mice.

2 Material and method

16 KM mice were divided into four groups randomly with 4 mice in each group. The three treating groups were exposure to the UWB pulses of 2 ns duration and 100 Hz repetition rate at the field intensity of 120 kV/m for 60 min. The sham group was place in the same environment but without UWB radiation. Mice of the three treating groups were sacrificed at 6h, 24h and 72h after exposure, respectively, and the blood samples and tissue samples were prepared according to the corresponding standard protocols. The blood routine examination, the liver function and the kidney function were detected with blood samples by blood biochemical analyzer. Histological characteristic of hepatic tissue was studied by the conventional paraffin method combined with hematoxylin-eosin staining. The hepatic expression of stress induced transcription factor NF-κB was evaluated with immunehisto-chemistry staining.

3 Results

3.1 The effect of UWB pulses exposure on the liver functions and kidney functions of KM mice

The liver function and kidney function of KM mice were analyzed 6h, 24h and 72h after the UWB pulses treatment and the results were shown in figure 1. The increase of AST and ALT at 6-24h revealed the temporary hepatic injury. The increase of Cys-C also suggested the decrease of glomerular filtration rate. At the same time, the glucose level was significantly increased after UWB pulses exposure which indicated the dysfunction of energy metabolism.

3.2 Histological characteristic of hepatic tissue

We then observed the hepatic tissue slices prepared by paraffin method and stained with hematoxylin-eosin. From figure 2 we could see that there are many lipid droplets inside the hepatic cells 24h after UWB pulses exposure. This might also due to the dysfunction of energy metabolism especially the failure of fatty acid β-oxidation pathway after hepatic cell damages. But whether it was resulted from the thermal effect due to UWB pulses radiation or not is still an open problem to be further investigated.

The expression of oxidative and other stress induced transcription factor NF-κB was analyzed by immunehisto-chemistry method and the results was shown in figure 3. The expression of NF-κB after UWB pulses exposure was significantly increased but the accumulation of NF-kB is mainly in the cytoplasm but not in the nucleus.

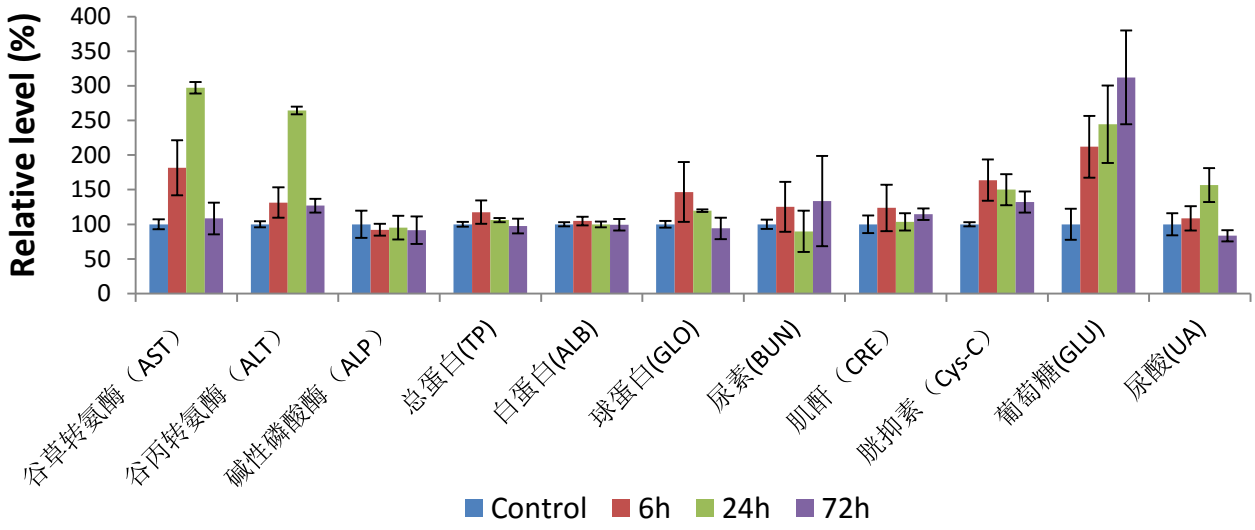

Figure 1. Parts of biochemical parameters indicating liver functions and kidney functions

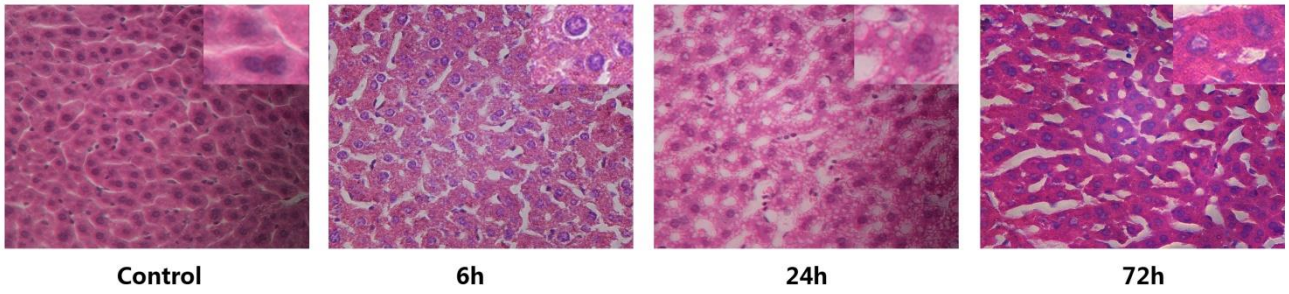

Figure 2. Hepatic tissue slices of KM mice after UWB pulses exposure

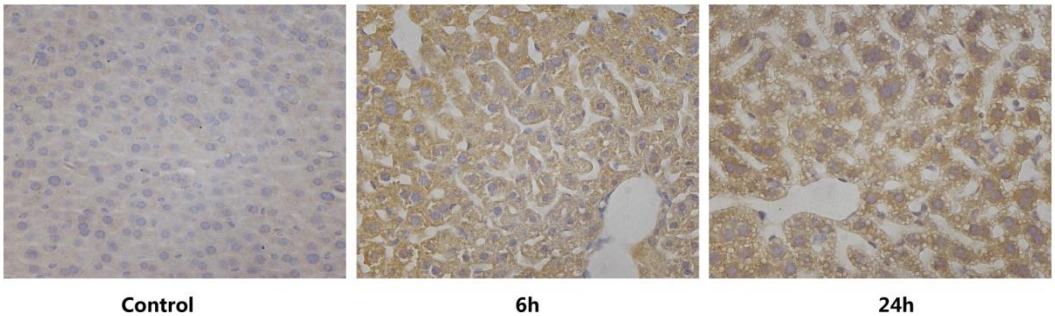

Figure 3. The expression of NF-kB in the tepatic cells after UWB pulses exposure

References

[1] M. Natarajan, B. K. Nayak, C. Galindo, S. P. Mathur, F. N. Roldan, and M. L. Meltz, "Nuclear translocation and DNA-binding activity of NF-kB upon pulsed ultra-wideband electromagnetic field exposure fails to transactivate kB-dependent gene expression in human monocytes", *Radiat. Res.*, **165**, pp. 645-654,(2006)

[2] R. L. Seaman, J. E. Parker, J. L. Kiel, S. P. Mathur, T. R. Grubbs, and K. Prol, "Ultra-wideband pulses increase nitric oxide production by RAW 274.7 macrophages incubated in nitrate", *Bioelectromagnetics*, vol. 23, pp. 83–87, 2002.

[3] Vijayalaxmi, R. L. Seaman, M. L. Belt, J. M. Doyle, S. P. Mathur, and T. J. Prehode, "Frequency of micronuclei in the blood and bone marrow cells of mice exposed to ultra-wideband electromagnetic radiation", *Int. J. Radiat. Biol.*, 75, pp. 115–120, (1999).

[4] R. L. Seaman, "Effects of exposure of animals to ultra-wideband pulses", *Health Physics*, **92**, 629-634,(2007)

An Automated Test System for assessing Aircraft for radiated effects from Transmitting Portable Electronic Devices (T-PEDs)

G. D. M. Barber, T. Noad and R. F. Marson

QinetiQ Ltd. Farnborough, Hampshire, UK
gdbarber@qinetiq.com

Abstract

With the emergence and rapid proliferation of Portable Electronic Devices (PEDs) and their increased use on-board commercial aircraft, a standards committee was formed that developed and published a test standard specifically aimed at testing aircraft systems to the radiated effects of Transmitting PED (T-PED) devices. This paper details an approach and development of a 'bespoke' automated test method for assessing the effects of transmissions on aircraft systems when T-PEDs are used on-board. The techniques have been used in the evaluation of both commercial and military aircraft.

Keywords: T-PED, ED-130, Aircraft, EMC

1 Introduction

Transmitting Portable Electronic Devices (T-PEDs) comprise a wide range of intentional transmitting personal equipment that encompasses mobile phones, wireless networking technology and radio transceivers. In many instances of portable electronics the transmitting element is not the primary function; for example the remote control of a toy and Wi-Fi equipped laptops and tablets. Although these are essentially low power devices, as with any source of Radio Frequency (RF) energy, T-PEDs may potentially pose a source of interference to other electronic systems that are present within the same operating environment. Of particular concern is the effect of T-PED transmissions on safety critical or safety involved systems, and particularly those associated with the flight control or navigation functions of an aircraft.

Guidance on the approval of T-PED technologies new to aircraft and the general procedures accepted by aviation authorities for demonstrating that no interference will be caused by the use of T-PEDs is provided in Section 4 of ED-130 [1]. Evaluation methods include analysis and aircraft test. Typically analysis is considered where similarity to previous aircraft or integrated system rig test can be demonstrated.

2 Overview of Test Methods

The QinetiQ T-PED automated test system is based on the 'Net Power method' of ED-130 [1]. UK Military Standards [2] do not currently include procedures for T-PED assessment. The 'Net Power method' is considered to present a thorough approach, eliminating the uncertainty of an Electric Field reference. Using the Multiple Equipment Factor (MEF) of ED-130 [1], the combined transmission of multiple devices operating a common transmission standard can be simulated from a single omnidirectional test antenna by scaling the Net Power. QinetiQ's automated test system is based around a configuration file set-up, simplifying test parameter entry, and a Graphical User Interface (GUI), shown in Fig.1, that provides the following functionality:

- Automatic frequency increment with selectable stepped test level increase and maximum power limit.
- Manual override and control for threshold assessment.
- Real time Frequency, Forward, Reflected and Net Power indication.
- User comment entry fields for susceptibility recording.

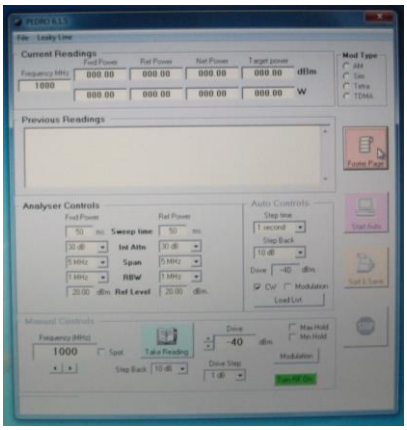

Figure 1. GUI – Automated Test System.

This paper will discuss the latest requirements for T-PED testing on aircraft, describe the test methods and share insight of the testing conducted on civil and military aircraft over the last 10 years

References

[1] EUROCAE ED-130, "Guidance for the use of Portable Electronic Devices (PEDs) On Board Aircraft", December 2006.

[2] DEF STAN 59-411, UK MOD Defence Standard Electromagnetic Compatibility, issue 2, 31 March 2014

The development and use of Analogue Fibre Optic Links for HIRF Testing

P W Surman*, D Bromley*

**Pulse Power and Measurement Ltd, UK. 65 Shrivenham Hundred Business Park, Watchfield, SN6 8TY. psurman@ppm.co.uk*

Abstract

This paper explores the key requirements for an analogue fibre link (FOL) which is specifically designed to support HIRF, lightning and EMP testing. All civil and military platforms need to demonstrate safe and reliable operation in various environments, including strong electromagnetic fields from manmade or natural events. Factors such as fibre choice, noise figure, dynamic range, group delay, gain stability, shielding effectiveness and the way in which fibre is deployed will be discussed in detail.

Keywords: Fibre, Shielding, Sensitivity, HIRF, EMP, Lighning

1 Introduction

The fibre optic link in a HIRF, Lightning or EMP test set up is a critical link between the sensor and measurement instrument. As it contains active electronics and is in effect a bandpass filter it introduces noise, gain and phase variation. Importantly, a FOL does deliver RF performance which is independent of the length of the signal path and a galvanic free connection which minimises disruption to the unit under test. The objective of the FOL designer is to manage noise, group delay and gain variation. There are also opportunities to enhance the entire test by optimising the RF performance and layout.

2 Overview of Tests

Frequency domain techniques, such as LLSF (low level swept frequency) [1,2] and LLSC (low level swept current) have been developed to establish the transfer function of a platform. This is done by putting a sensor inside the platform and exposing it to a known EM field and measuring the sensor response. FOLs contribute to a more reliable, repeatable and representative measurement of the transfer function by reducing the impact the measurement equipment has on the platform. Providing galvanic isolation helps to maintain the shield integrity of the platform being tested. A high sensitivity FOL input reduces the radiated power to meet a required SNR.

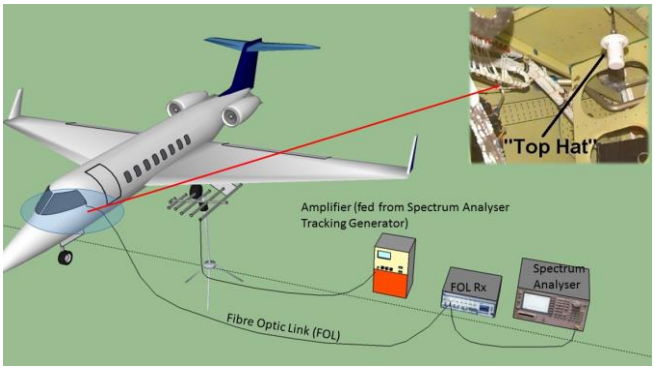

Figure 1. Example LLSF Layout

Time domain testing techniques, such as full threat indirect lightning testing, requires very high magnetic fields which are generated using high voltage capacitor banks. These are coupled to a large TEM or elaborate set of return conductors, an example shown in Fig.2, carefully arranged to provide specific impedance to the HV source and manage entry and exit points. The large field strength puts more emphasis on the shielding effectiveness of the FOL itself. The use of galvanic free fibre allows connections to the platform without affecting the return conductor, or introducing unwanted return paths back to the measurement equipment, which could be catastrophic. The signals from the sensors in this case can be 10 orders of magnitude higher than in the frequency domain tests. The FOL needs to maintain linearity under these conditions, and the usual definition of compression point (P1dB point) is not suitable for time domain measurements.

Figure 2. Example of return conductor setup

The following parameters will be discussed including the trade-offs and the impact on the measurement and the wider set up implications.

RF Parameters	Physical parameters
• Passband (3dB/1dB points and flatness) • Gain • Sensitivity • Noise figure • Dynamic range • Max instantaneous input • Linearity (P1dB/P0.1dB) • Input Impedance	• Fibre choice • Laser choice • Modulation choice • Distance • Battery life • Mechanical design • Size • User interface • Automated test

References

[1] Def Stan 59-411, Part 4, Issue 2, dated March 2014
[2] EUROCAE ED-107A/SAE ARP5583A, dated July 2010

The Development of a High Intensity Radiated Field (HIRF) Aircraft HF Test facility

T. Hague*, G. D. M. Barber[†] and T J Duggan[††]

**AR Europe Ltd, Milton Keynes, UK, [†]QinetiQ Ltd., Farnborough, Hants, UK , [††]QinetiQ Ltd., Boscombe Down, Wilts, UK*
thague@arworld.us

Abstract

The Radio Frequency Environment Generator (REG) facility located at MOD Boscombe Down in Wiltshire simulates the typical RF environment and provides High Intensity Radiated Field (HIRF) immunity testing for military aircraft. The REG provides an RF environment simulation from the High Frequency (HF) end of the spectrum up to microwave frequencies. The HF simulation aspect of the REG (2 MHz to 32 MHz) was originally based around a Marconi broadcast transmitter and dipole antenna. Due largely to component obsolescence issues the HF capability has recently been upgraded. This paper describes the planning and upgrade of the HF capability in the REG facility to bring it into the 21st century.

Keywords: EMC, HIRF, HF Antenna

1 Introduction

MOD Boscombe Down in Wiltshire, UK has been the main centre for the Test and Evaluation (T&E) of military aircraft since it was established (initially as RAF Boscombe Down) in 1939. Significant milestones of British aviation history have been witnessed here including the first flights of the English Electric P1 (forerunner of the Lightning) and the BAC TSR2. QinetiQ now manage and operate Boscombe Down under the Long Term Partnering Agreement (LTPA) contract with the MoD to deliver T&E and training support services to the UK and her allies.

With the increasing use of electronic systems in safety and mission critical areas of avionics it is vital that the UK has a modern HIRF test facility with a capability to meet the RF Environments defined in Def Stan 59-411[1] and similar military standards such as Mil Std 464[2].

Because of the RF field levels required and the location of the test facility, the HF capability upgrade had to be designed within strict constraints. For example, it was decreed early in the requirements setting phase that the Radiated Field hazard area or footprint should not exceed the hazard area for the obsolete HF capability. It was also specified that the new HF amplifier should be able to be limited in forward power to match the existing unit, and that the output of the amplifier should be switchable to various antennas and test points around the facility. The new HF system itself should be integrated into the existing bespoke operating software which has been developed over many years on site.

2 Design Goals

The HF upgrade encompassed the following subsystems:

- Provision of new High Power Broadband RF Power Amplifier
- Provision of new Broadband horizontally polarised HF Antenna
- Provision of RF Switching Exchange.

The Amplifier specification was articulated as follows:

- Operating Band: 100kHz – 80MHz (min)
- Power Output: 30kW CW
- Air Cooled
- Solid State
- Full power into 6.1:1 VSWR

Fig. 1 shows the Amplifier installation.

Figure 1. HF Amplifier installed in the REG

The HF Antenna specification was articulated as follows:

- Operating Band 2 to 32MHz
- 30 kW CW Power handling, upgradeable to 100kW
- Strict environmental requirements, wind, ice etc

- Height restrictions due to location
- Performance to exceed existing antenna
- VSWR better than 3.1:1 over operating bandwidth

Figure 2 shows the horizontal dipole antenna in-situ at the REG facility.

Figure 2. HF horizontal dipole antenna

The RF Switching Exchange Specification included the following requirements:

- Rated to 100% reverse power
- 2 Channels in, 5 Channels out
- Remote and Local Control
- Fail Safe

The complete system has subsequently been delivered, installed and is now in the final stages of commissioning. The presentation will discuss the amplifier design, antenna selection process and system testing including results.

References

[1] Defence Standard 59-411, 'Electromagnetic Compatibility', issue 2, 31 March 2014

[2] Department of Defense, "Interface Standard Electromagnetic Environmental Effects Requirements for Systems" MIL_STD 464C, December 2010

Test and Simulation on the Lightning Indirect Effects of Helicopter

GUO Fei, GAO Cheng

National Key laboratory on Electromagnetic Environment and Electro-optical Engineering
PLA University of Science and Technology, Nanjing, China

Abstract

To improve the protection performance of helicopter against lightning, this paper presents an indirect effects test and simulation to simulate helicopter struck by high current pulse and study its lightning indirect effects according to the SAE-ARP 5416A. The distributions of the electromagnetic field and the surface current of the helicopter stroke by the lightning are discussed. The results indicate that test results are in good agreement with the simulation; those methods can effectively analyze the helicopter indirect effects stroke by lightning and guide the lightning protection design of the helicopter.

Keywords: helicopter; lightning indirect effects; numerical simulation

1 Introduction

Due to the lightning electromagnetic (EM) fields penetrated inside the aircraft, and induce currents and voltages in the bundles of wires that connect the electrical and electronic equipment, thus generating damages that can be a threat to the aircraft safety [1]. Aircraft must meet the requirements bearing the damage caused by the lightning strike without catastrophic accidents according to the standards [2]-[4]. Thus, it is of great importance to study the lightning indirect effects on aircraft [5]. The scope of the research activity is to describe the test and the simulation approaches developed to accurately predict the induced effect of the direct lightning stroke to a helicopter, validate those by comparison with numerical and experimental test cases, and use those for lightning protection design of helicopter.

2 Test configurations

2.1 Test setup

The test setup includes the aircraft, a suitable return conductor arrangement, the current generator, and current generator controls and monitoring instruments, and induced transient measurement instruments. Lightning interaction with a helicopter depends on the lightning attachment points. The lightning attachment points are represented by the current generator and return conductor attachments to the aircraft. A simplified helicopter model on the scale of 1:3.5 is used in the study. Figure 1 gives a typical attachment configuration from the tail rotor blade to the landing skid based on the SAE-ARP5416. The test configuration is shown in Fig. 2.

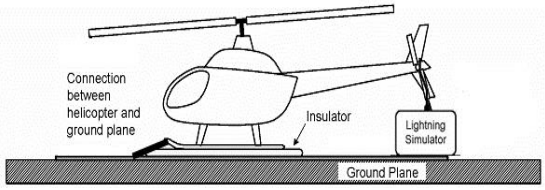

Fig. 1. Helicopter and ground plane arrangement

Fig. 2. Test configuration

2.2 Measurement methods

Current is pulsed into the helicopter and returned conductor by a current generator. The waveform of lightning injection current used in the test is the current component A [6], representing the characteristic of the natural lightning according to the standard.

The injection current is measured by Rofowski coil, and the electric fields and magnetic fields in the cabin are measured by three-dimensional field sensors simultaneously, as shown in Fig.3.

(a) 3D electric field sensor (b) 3D magnetic field sensor

Fig. 3. Measurement of transient electromagnetic field

The surface currents at critical points of floor are measured by a 2D giant magnetoresistance sensor.

3 Modelling and simulation of the test

The simulation uses the same simplified model of helicopter by CST based on TLM [7]. The models of the test including the current generator, return conductor, ground plane and monitoring instruments also are established. The 3-D model of helicopter is shown in Fig.4.

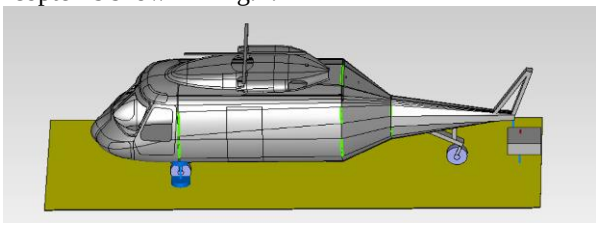

Fig. 4. 3-D model of helicopter

4 Results

4.1 The internal electromagnetic fields of the helicopter

The waveforms of the coupling electromagnetic field inside the cabin are shown in Fig.5. Compared to the test data, the rising edge of the simulation magnetic field is faster, and the decay time is shorter. The simulation waveform of the electric field has a large reflection, and the peak value is later than that of the measured waveform. But the maximum amplitude of both is similar.

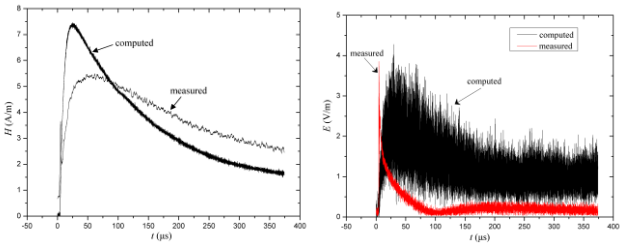

(a) magnetic field (b) electric field

Fig. 5. comparision between measured and computed

4.2 The surface current of The Helicopter

The comparison of the measured surface current and the source is shown in Fig.6. GMR-X represents the measured waveform of the surface current from X axial probe; GMR-Y represents the measured waveform from Y axial probe. The waveforms show that the trend of the surface current is fundamentally coincident with the injection current waveform. Table.1 shows the maximum intensity of the surface current at different points. H_m is a synthesized surface current from the two components of GMR-X and GMR-Y, and H_c is a computed surface current. It shows that the measured results are somewhat similar with the computed results from Table 1. The surface currents at different points shows that the distribution of the surface currents has the basic same rule.

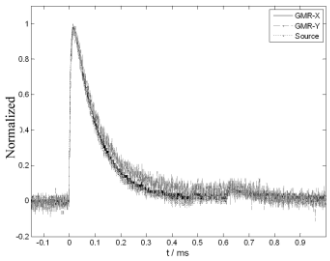

Fig. 6. The normalized waveforms of the surface current and the injection source

Table 1 Maximum of the measured and computed results

	Point 1	**Point 2**	**Point 3**
H_m (A/m)	13.4539	4.2522	20.6060
H_c (A/m)	8.4	5	16.2
20log(H_m/H_c) (dB)	4.0914	-1.4071	2.0896

5 Conclusions

This paper discusses the test and simulation about the indirect effects of an simplified helicopter stroke by the lightning. By contrasting the simulation results with the test, it shows that these methods can effectively analyze the indirect effects on the helicopter. The numerical prediction of the EM effects produced by a lightning stroke to an aircraft has the advantage of higher flexibility and lower costs with respect to the experimental approach. However, the complexity of the system requires the implementation of accurate simulation models, and at the same time, of simplifying hypotheses that lead to reasonable required computational efforts.

Acknowledgment

This work is supported by the Chinese National Science Foundation (No.60971063) and the National Key Laboratory Foundation (FD2015003).

References

[1] C. GAO, S. SONG, Z.H. SHI, et al. “Impact of composite tructure of aircraft on lightning attachment points”, *Journal of PLA University of Science and Technology Natural Science Edition*, vol. 14, pp. 227-231, 2013

[2] USDOD. “MIL-STD-464C, Electromagnetic environment effects requirements for systems”, *United States Department of Defense*, 2010.

[3] USDOD. “MIL-STD-1757, Lightning qualification test techniques for aerospace vehicle and hardware:, *United States Department of Defense*, 1980.

[4] SAE. ARP5416A. “Aircraft lightningtest methods”, *Warrendale: Society of Automotive Engineers*, 2013.

[5] F.A. Fisher, J.A. Plummer. “Aircraft lightning protection handbook”, Atlantic City: *Federal Aviation Administration Technical Center*, 1989.

[6] SAE. ARP5412A. “Aircraftlightning environment and related test waveforms”, *Warrendale:Society of Automotive Engineers*, 2005.

[7] F. Guo, B.H. Zhou, C. GAO, “Analysis for lightning indirect effects of the aircraft by numerical simulation,” *Chinese Journal of Radio Science*, vol. 27, pp. 1129-1135, 2012.

[8] SAE. ARP5414A. “Aircraft lightning zoning”, *Warrendale: Society of Automotive Engineers*, 2005.

UWB Backscattering Characterization of Improvised Explosives Devices

D Martinez[‡], S Gutierrez[‡], S Rodriguez[‡], F Vega[‡], R Bustamante**, J Sachs*, C Baer[†]

[‡]Universidad Nacional de Colombia, Colombia, Email drmartinezhe@unal.edu.co, sagutierrezd@unal.edu.co, sirodriguezr@unal.edu.co, jfvegas@unal.edu.co
**Technische Universität Ilmenau, Germany, Email: juergen.sachs@tu-ilmenau.de*
[†]Ruhr-Universität Bochum,Germany, Email: christoph.baer@rub.de
*** Universidad de los Andes, Colombia, Email: rbustama@uniandes.edu.co*

Abstract

In recent years, Colombian government has worked hard on a demining process across the country. As a result, it has opened new opportunities for researching and developing new techniques for detection, neutralization and destruction of Improvised Explosive Devices (IEDs). The Colombian IEDs have a high variability in terms of materials, shapes and methods of activation. We show in this paper a measurement technique aimed to extract the UWB polarimetry backscattering of IEDs, based on M-sequence technology. This procedure is aimed to construct a database of characteristic features associated with different IED typologies, for future detection algorithms.

Keywords: Backscattering, Improvised explosive devices, M-sequence technology, Polarimetry, UWB Radar.

1 Introduction

The Improvised Explosive Devices (IEDs) have a particular and non-standardized way of construction. Basically, it is a bomb, fabricated in an artisanal manner, which include chemicals, non-military components and compounds that are commercially available. They have variable shape, size, triggering mechanism and explosive content with little to no metal parts. This strong dependence on building features reduces the usefulness of traditional methods of detection, for instance, metal detectors or by recognition of regular and standard patterns.

Classical mine detection techniques, by radar, try to extract the electromagnetic signature of a mine from the gathered data. If these signatures (reflectivity, time-frequency parameters, etc.) are verified on the field, the mine can be considered as detected. With this in mind, backscattering measurements are of interest for the aim of collecting target information to meet specific Colombian non-standardized IEDs constraints.

In a previous paper, a group of 22 IEDs were experimentally characterized [1]. The challenge here is to collect more information about the target to improve IED identification by a classification approach. It is expected that the results of this work will be applied on near field radar processing of buried objects based on polarimetry MiMo-radar.

We carried out a measurement procedure in order to find the backscattering behaviour of IEDs under test, by means of M-sequence based technology. This experiment will allow the extraction of Radar Cross-Section (RCS) information, and a further statistical analysis, that leads to the identification of common features of these devices. The test was performed in an anechoic chamber and also in an indoor, non-anechoic chamber environment.

The test setup, shown in Fig. 1, allows the parallel measurement of the polarimetry RCS for backscattering at two-bistatic-angles. Measurements are performed with computer-controlled M-sequence radar platform. Three dual-polarized Vivaldi antennas, working at lower GHz range, are mounted on tripod. One of the antennas is used as polarimetric transmitter and the two others as polarimetric receivers. The turntable for the target is a Styrofoam support which is essentially transparent at microwave frequencies.

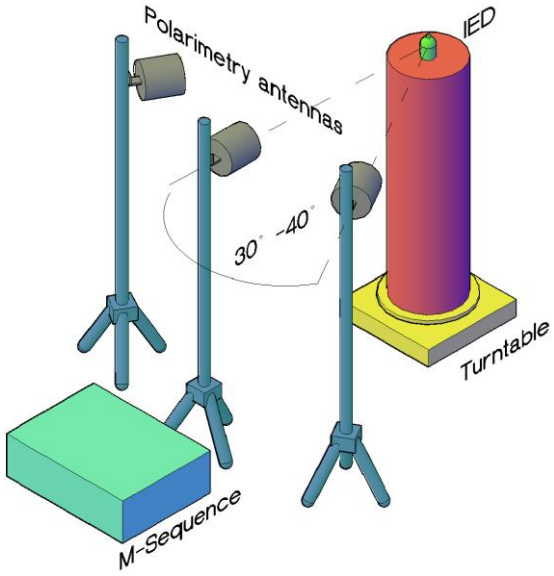

Figure 1. Array of UWB polarimetric antennas and target.

The paper reports the scattering measurements and the statistical analysis of the measurement, looking for common features that can be used by future work on detection algorithms.

References

[1] Pantoja, J.J.; Pena, N.; Rachidi, F.; Vega, F.; Roman, F., "Characterization, Modelling, and Statistical Analysis of the Electromagnetic Response of Inert Improvised Explosive Devices," in Electromagnetic Compatibility, IEEE Transactions on vol.56, no.2, pp.393-403, April 2014.

Permittivity of Improvised Explosives made of Ammonium Nitrate and Fuel Oil

T Just*, S Gutierrez[‡], J Sachs*, C Baer[†], F Vega[‡], R Bustamante**

**Technische Universität Ilmenau, Germany, Email: thomas.just@tu-ilmenau.de, juergen.sachs@tu-ilmenau.de*
[†]Ruhr-Universität Bochum,Germany, Email: christoph.baer@rub.de
[‡]Universidad Nacional de Colombia, Colombia, Email: sagutierrezd@unal.edu.co, jfvegas@unal.edu.co
*** Universidad de los Andes, Colombia, Email: rbustama@uniandes.edu.co*

Abstract

Colombia is the only country in Latin America where improvised explosive devices (IED) are still planted regularly. Major challenges of Colombia IED detection are difficult environmental conditions as well as the huge diversity of the IED's shapes and materials. Currently, big efforts are made to expedite the demining of the country. In this context, a scientific cooperation project between Colombian and German Universities was established, with the objective of accompany the demining activities. One of the research aims is to provide a field-grad method for the determination of the electric permittivity within the lower GHz-range of the explosives used in IED's.

Keywords: Permittivity, Improvised explosive devices, Homemade explosives, Ultra-wideband M-sequences.

1 Introduction

Due to the long lasting internal conflict in Colombia, countless IEDs of different shapes and mechanisms have been planted throughout the country. Despite the huge diversity, a typical Colombian IED is composed of a main explosive, an electric detonator, a switch (made to be accidentally operated by victims), and a casing (that can be a plastic pipe, a wooden case, a glass bottle or a plastic can). Usually the main explosive is homemade with ammonium nitrate extracted from fertilizers and mixed with fuel oil to produce ammonium nitrate and fuel oil (ANFO). Therefore, permittivity measurements of ANFO are of interest for calibration of detection devices (e.g. ground penetrating radar) and to find a fingerprint of the explosives. Additionally, this knowledge is required to elaborate safety surrogate materials for laboratory tests and IED RCS-measurements as well as for deminers training.

The permittivity estimation of bulk material within the microwave range is typically done via S-parameter measurements of waveguide specimen holders [1]. Here, we use a detachable coaxial line as depicted in **Error! Reference source not found.**, in which the space between inner and outer conductor is filled with the material under test.

The standard device for S-parameter measurements is the network analyzer. It is however quite expensive and less suited for field measurements. Hence, we apply an M-sequence based S-parameter measurement setup [2] and compare its performance with the classical network analyzer approach.

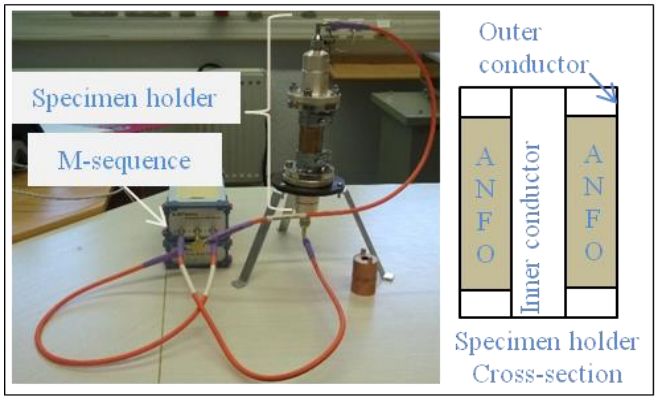

Figure 1 M-sequence measurement head and simplified cross section of the specimen holder.

Two measurement concepts will be investigated. One exploits directional couplers for wave separation as it is done in network analyzers and the second deals with wave separation via time isolation as used in time domain reflectometry. The wanted permittivity values of the explosive under test are finally extracted from the measured S-Parameters of the specimen holder.

Permittivity measurements of explosives with ultra-wideband M-sequences will be presented and compared with traditional measurement methods using a vector network analyzer.

References

[1] J. Baker-Jarvis, M. D. Janzic, B. F. Riddle, R. T. Johnk, P. Kabos, C. L. Holloway, R. G. Geyer, and C. A. Grosvenor, "Measuring the Permittivity and Permeability of Lossy Materials: Solids, Liquids, Metals, Building Materials, and Negative-Index Materials " NIST2005.

[2] J. Sachs, M. Helbig, M. Kmec, R. Herrmann, K. Schilling, and P. Rauschenbach, "Integrated dielectric spectrometer for wideband and highspeed measurements using pseudo-noise codes," 2013 J. Phys.: Conf. Ser. 434 012032 (http://iopscience.iop.org/article/10.1088/1742-6596/434/1/012032)

Susceptibility testing for detecting IEMI-based covert channels

C. Kasmi, J. Lopes Esteves, P. Valembois

Wireless Security Lab, French Network and Information Security Agency - ANSSI, *Paris, France*

Abstract

Many studies were devoted for the analysis and the classification of the susceptibility of electronic devices to parasitic fields. Recent researches were focusing on a way of characterizing possible failure of the system through the inspection of resources available to embedded operating systems. Based on these observables, it has been noticed that failures can be directly correlated with the parasitic waveform. We propose to highlight the possibility of designing a covert channel for controlling malicious software (e.g. malware) by exploiting the susceptibility of the host computer. In supplement, it is shown that the proposed characterization approach of the susceptibility combined with related dedicated health monitoring software allows for detecting possible covert channels.

Keywords: Electromagnetic security; Information security; Electromagnetic Interference; Cyber-electromagnetics; Covert channels.

1 Introduction

Information Security aims at hardening networks and systems in critical infrastructures for ensuring the *confidentiality*, the *integrity* and the *availability* of sensitive information. In some specific cases (e.g. military facilities, country vital resources providers), the air-gap technique which consists in a physical isolation the critical infrastructure from the outside world (e.g. Internet) is applied. Recent studies, as [1-4] for example, have been focusing on air-gap bypass techniques by creating physical covert communication channels between the trusted environment and the unsecured world. Recently, we have been working on a fine-grain analysis of the effects induced by parasitic field on consumer-of-the-shelf (COTS) computers by involving the operating system logs and data recorded by the enclosed sensors (ex. fan speed, temperature sensor). From the obtained results, real-time monitoring software was proposed in [5] in order to detect malicious electromagnetic activity. Going one step further, it was observed that the emitted signal waveform and the effects were highly correlated. This lead us to consider the possibility of using intentional electromagnetic interferences (IEMI) and the related effects as a covert communication channel. A proof-of-concept was recently proposed in [4] using the perturbations induced on an isolated computer's temperature sensor by an On-Off keying modulated waveform for air-gap bridging.

2 EM Susceptibility and physical covert channels

For bridging an air-gap through a physical covert channel, the target isolated system has to host a malware that is able to access information related to the physical layer activity and to understand the communication protocol. In [4], the use of IEMI and back-door coupling as physical layer for covert channels has been introduced. It has been shown in [5] that some IEMI effects can be detected at the operating system level. These software accessible observables can thus be used by the receiver malware as an inbound covert communication interface. This means that the analysis of the EM susceptibility of a device, and more specifically the impacts at the software level, can allow for the detection of possible EM physical covert channels.

3 Discussions

During the presentations, we propose to summarize the main lines of the air-gap bridging techniques and a focus on the design of IEMI based covert channels will be made. Some results will be presented and the possibility of using a health monitoring software for this class of covert channels will be emphasised. Moreover, it will be argued that it becomes necessary to provide the susceptibility tests results to Information Security experts in order to provide valuable information about possible security vulnerabilities related to EMC/EMI issues.

References

[1] S. J. O'Malley, K. K. R. Choo, "Bridging the Air Gap: Inaudible Data Exfiltration by Insiders", 20th Americas Conference on Information Systems (2014).

[2] D. Goodin, "Meet "badBIOS", the mysterious Mac and PC malware that jumps airgaps", Arstechnica, http://arstechnica.com/security/2013/10/meet-badbios-the-mysterious-mac-and-pc-malware-that-jumps-airgaps (2013).

[3] M. Guri, G. Kedma, A. Kachlon, Y. Elovici, "AirHopper: Bridging the Air-Gap between Isolated Networks and Mobile Phones using Radio Frequencies", 9th IEEE International Conference on Malicious and Unwanted Software (2014).

[4] C. Kasmi, J. Lopes Esteves, P. Valembois, "Air-gap Limitations and Bypass Techniques: "Command and Control" using Smart Electromagnetic Interferences", The 3rd Botnet Fighting Conference, Paris, France (2015).

[5] C. Kasmi, J. Lopes Esteves, M. Renard, "Automation of the Immunity testing of COTS computers by the instrumentation of the internal sensors and involving the operating system logs – Technical report ", System Design and Assessment Note SDAN 044 (2014).

Identifying Some Radiated EMSEC Vulnerabilities of Tablet Personal Computers

S. R. Patient, A. L. Macintyre, M. D. Thomas and R. Hoad

QinetiQ Ltd., Farnborough, Hants, UK
almacintyre@qinetiq.com

Abstract

Tablet Personal Computers (PCs) are becoming ubiquitous and there is a temptation to use Tablet PCs to process sensitive e-mails or documents. Several Commercial Off the Shelf Tablet PCs have been tested to identify if they produce radiated compromising emanations which could pose an Electromagnetic Security (EMSEC) risk from electronic eavesdropping. This paper discusses the result of a preliminary evaluation of the EMSEC of two brands of Tablet PC.

Keywords: Compromising Emanations, EMSEC, electronic eavesdropping

1 Introduction

Tablet PCs are finding widespread use and are a particularly powerful form of mobile computing. There have been reports in the media of high profile politicians using tablet PCs to handle sensitive e-mails and to produce and read documents. Traditionally Electromagnetic Security (EMSEC) [1] has focussed on the electronic eavesdropping risk to fixed installations, typically processing security classified or other sensitive information, however, the temptation to use mobile computing/information processing equipment for sensitive work is of growing concern. We have undertaken a limited study to investigate the radiated compromising emanations from two brands of tablet PC, similar to [2] which use different operating systems. Both Tablets were 7 inch display screen sized.

2 Investigation Outline

All testing was carried out within a 3m Semi Anechoic Chamber, although some measurements were subsequently verified in the open laboratory environment. For all tests, the Tablet was set up on a conductive ground plane, though wooden standoffs placed on rubber mats were used to provide separation and isolation from the ground plane and allow positioning of the tablet through various orientations. During radiated tests the battery was always above 50% charge. The following variables associated with the configuration/use of the Tablet were identified and evaluated during testing:

- Physical orientation (Vertical/horizontal/front/back/sides)
- Screen orientation (Landscape/portrait)
- Transmitters (Bluetooth, WiFi, NFC)
- Screen brightness (Minimum/maximum)
- Physical connections (power/headphone connections)

The testing considered radiated Radio Frequency (RF) emanations and in particular addressed the following potential risk areas;

- Video – can the tablet screen image be reproduced from information recovered from radiated emanations
- Speech – With a microphone input can speech information be recovered from radiated emanations
- Audio – Can audio information be recovered from the headphone output via radiated emanations
- Touchscreen fingerprinting – Can the use of the touchscreen keyboard be recovered from the radiated emanations

3 Preliminary Results

It was found to be difficult to recover meaningful speech or audio information from radiated RF emanations from the tablet PCs tested in any configuration.

The video or screen image was recoverable. Figure 1 shows the typical home screen ‘App’ view of one of the tablets investigated and the video image recovered from the radiated emanation.

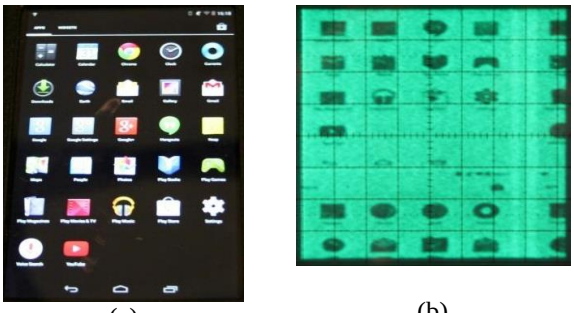

(a) (b)

Figure 1. (a) App screen (b) recovered video image

Near field probing revealed the source of the video bearing emanations to be located where the processor/LCD screen driver chip is located. It may also be coincidence, but at the time of probing the clearest radiated emanations were found

at a similar frequency to the clock of the integrated graphics card (located within the processor).

The act of turning the tablet through 90 degrees caused drastic changes in the quality of the recovered image from radiated emanations. When the screen was rotated through 90 degrees, the recovered image also rotated through 90 degrees. This suggests that when the screen orientation is changed, the X and Y axis are shifted.

When the tablet transmitters were toggled through the different configurations, there was no observed difference in the quality of the recovered image, it was also found that adjusting the tablet screen brightness had no effect on the quality of the recovered image.

In terms of touchscreen fingerprinting, we were able to recover information relating to the position on the Y axis being touched on the touchscreen at a significant level. It was possible to detect very small amounts of movement from the recovered emanations. Figure 2 shows the signal recovered from the radiated emanation.

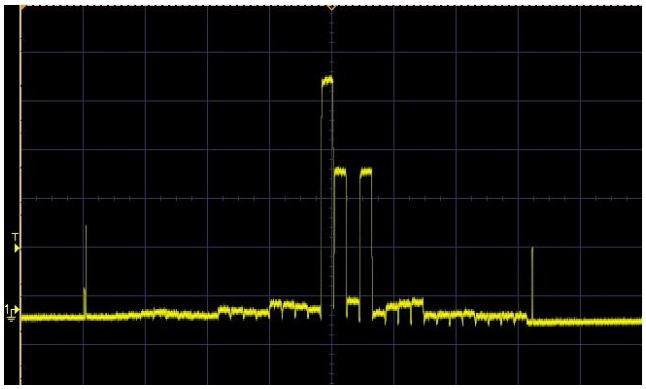

Figure 2. Recovered information relating to the touch position on the touchscreen

The signal is made up of 32 bits which are enclosed within a 'start' and 'stop' pulse. The pulse on the far left relates to the bottom of the screen and the pulse at the far right relates to the top of the screen. The signal relates to touch activity in the Y direction only.

The worst case configuration was identified as when the user and tablet are isolated from each other i.e. no direct contact with the device other than the screen. The use of cosmetic cases to protect tablet PCs is commonplace and these generally provide galvanic isolation.

Using these recovered emanations it is considered that it would not be beyond current technical limitations to produce a best-guess algorithm which could recover text input via the touchscreen keyboard.

The presentation will discuss the test set-up, the tablet PC configurations evaluated and provide more detail on the results and observations made from the testing.

References

[1] NACSIM 5000: Tempest Fundamentals. National Security Agency, Fort George G. Meade, Maryland, February 1982. Partially declassified transcript: http://cryptome.org/nacsim-5000.htm

[2] Hayashi Y., Homma N., Miura M. Aoki T. and Sone H., 'A Threat for Tablet PCs in Public Space: Remote Visualization of Screen Images Using EM Emanation', Proceedings of the 2014 ACM SIGSAC Conference on Computer and Communications Security, Pages 954-965

Momentum in magnetic clouds before sudden impulse observations on ground magnetometers

J L Gilbert*

**Metatech, Goleta,California,USA, james.gilbert@metatechcorp.com*

Abstract

This presentation discusses the mechanisms responsible for the sudden impulses seen in the geomagnetic field and shows the correlation between the time history of the observation of the particle momentum flux at a spacecraft located at a stationary point the earth and the sun and the observed sudden impulse geomagnetic disturbances associated with the onset of magnetic storms.

Keywords: sudden impulse, geomagnetic disturbance, sudden storm commencement

1 Introduction

In this presentation we describe how the particle momentum flux seen at the ACE (Advanced Composition Explorer) spacecraft located at the L1 Lagrange point at 1.5×10^6 km sunward from the earth correlates with surface geomagnetic field measurements for sudden magnetic storm commencement or sudden impulse. A magnetic cloud consists of a collection of particles held together by local surrounding magnetic field. An abrupt increase in the momentum per unit time carried by the flow of these particles is seen within an hour of sudden impulsea in the ground magnetometer data.

2 Particle momentum flux

The particle momentum flux per unit time at the ACE spacecraft is given by the particle density times the square of the earthward velocity. This is readily seen as the non-relativistic forward momentum per unit volume is given by the mass per unit volume times the forward velocity. The momentum flux per unit time is given by the momentum per unit volume times the velocity so the momentum flux is given by Equation 1

$$F_p = \rho v_f^2 \qquad (1)$$

where F_p is the momentum flow per unit area, ρ is the mass density and v_f is the earthward velocity. F_p is equal to the pressure per unit area if the particles were to impinge and stick to a solid collector. In terms of the proton density n_{H+} (#/cm3) and proton speed v_{H+} (km/s) available in the ACE data, F_p is given in Newtons/m^2 by Equation 2.

$$F_p = 1.75\times10^{-15} n_{H+} v_{H+}^2 \qquad (2)$$

for a typical ratio for He^{4+} to H^+ ions. The magnetic field associated with the magnetic cloud also contains momentum, but it is negligible compared to the particle momentum. Dimensionally, this appears to be the appropriate parameter of interest in the compression of the geomagnetic field seen in SI magnetometer measurements, however it is not apparent that the peak value of the flux or some time convolution of the momentum flux is the appropriate quantity to compare – this would depend on the physics of the slowing down of the particle flow and possible compression of the front at lower altitudes than ACE, and this convolution could well depend on the northward component of the magnetic field in the magnetic cloud.

Figure 1 shows the particle momentum flux calculated for the two hours before the observed sudden impulse magnetic field observed at Boulder on July 30, 1999.

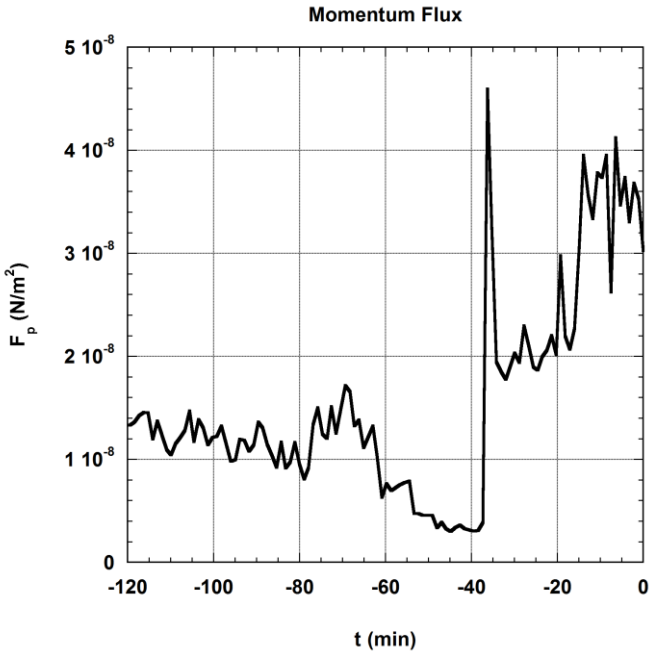

Figure 1. Particle momentum flux calculated from ACE hydrogen ion data.

The time scale in the figure is minutes before the observed sudden impulse on the ground. Note the sudden spike in the

momentum flux 37 minutes before the observed geomagnetic disturbance on the ground.

3 Interplanetary magnetic field

In addition to the hydrogen ion velocity and density, the ACE spacecraft contains a magnetometer for measurement of the interplanetary magnetic field. The northward component is of greatest importance and is shown in Figure 2.

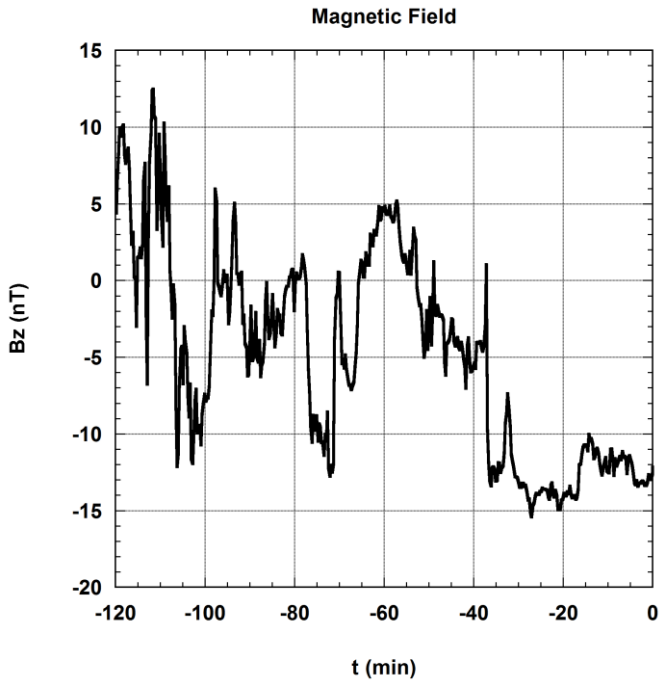

Figure 2. Northward interplanetary magnetic field component at the ACE spacecraft.

The reader should note that there is nothing remarkable evident in the north-south magnetic fields at the time that there is the sudden spike in the particle momentum flux.

Additional cases will be shown including the time histories of the sudden impulse geomagnetic fields after initial arrival. The ACE instrumentation measuring either the particle velocity or density often failed during magnetic cloud arrival. A new spacecraft, the Deep Space Climate Observatory (DSCOVR) has similar instrumentation. At the time of writing this spacecraft is on station but still in the testing phase and data has not been publicly released. It is hoped that data from DSCOVR for sudden impulse disturbances will be available for this presentation.

Acknowledgement

This work was supported by Metatech Corporation under IR&D.

Frequency Spectrum Analysis of Radiated Partial Discharge Signals

A Jaber[1], P Lazaridis[1], Y Zhang[1], B Saeed[1], U Khan[1], D Upton[1], H Ahmed[1], P Mather[1], M F Q Vieira[2], R Atkinson[3], M Judd[4], R Seviour[1] and I A Glover[1]

[1]*Department of Engineering & Technology, University of Huddersfield, Huddersfield HD1 3DH, UK*
[2]*Department of Electrical Engineering, Universidade Federal de Campina Grande, Campina Grande, Brazil*
[3]*Department of Electronic and Electrical Engineering, University of Strathclyde, Glasgow G1 1XW, UK*
[4]*High Frequency Diagnostics & Engineering Ltd, Glasgow G2 6HJ, UK*
E-mail: Adel.Jaber@hud.ac.uk

Abstract

Partial discharge is measured simultaneously using free-space radiometry (FSR) and a contact measurement approach based on the IEC 60270 standard. The PD source is a specially constructed emulator of the floating-electrode type. The power supply applied to the source is DC. A biconical antenna is used to capture the radiated signal and the frequency spectrum is obtained by FFT analysis of time-domain pulses. The relative spectral densities in the frequency bands 50 MHz - 290 MHz, 290 MHz - 470 MHz and 470 MHz – 800 MHz are determined.

Keywords: Partial discharge; free space radiometric measurement; IEC 60270; PD spectral density.

1 Introduction

Measurement of partial discharge (PD) is an important tool to avoid catastrophic failure of high voltage (HV) equipment. PD can be monitored using optical, chemical, acoustic and/or electrical methods. A major problem in HV power systems is breakdown and degradation of insulators [1]. PD measurement has been used to diagnose substation insulation faults and predict imminent equipment failure with consequent reduction in system outage [2].

Traditional electrical methods of measuring PD use high frequency current transformers (HFCTs) and transient earth voltage (TEV) sensors to collect PD pulses. These methods involve the physical attachment of a sensor to a particular item of plant. The radiometric method of measuring PD uses an antenna to receive the signals radiated by the transient PD pulses. Some diagnostic techniques depend on the spectrum of the PD pulse energy.

In this paper the frequency spectrum of radiated PD energy is compared with the spectrum of energies measured using the electrical contact method described in the IEC 60270 standard. The PD source used for the comparison is a floating electrode PD emulator. The measurements were carried out in a laboratory environment.

2 Experimental devices

Figure 1 demonstrates the devices used to simultaneously capture contact and FSR measurements from the same PD event.

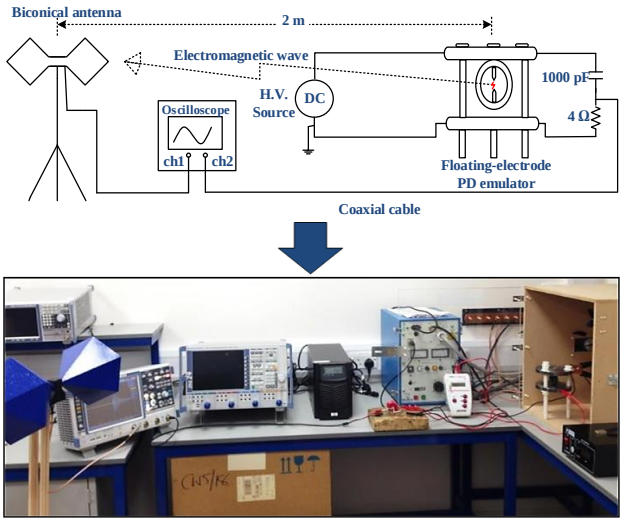

Figure 1. PD measurement apparatus.

PD is created by applying a HV DC to the artificial PD source which is a floating-electrode PD emulator with a 0.50 mm gap from the floating electrodes to the HV. The radiometric measurements were made with a biconical antenna connected a 4 GHz, 20 GSa/s, digital sampling oscilloscope (DSO). A biconical antenna was located 2m from the PD emulator source, and was horizontally polarised. The voltage rating of the coupling capacitor is 40 kV in contact measurement technique. For detecting PD, a coupling capacitor was connected parallel with the artificial PD source [3].

3 Experimental results

The two measurements captured by contact measurement and the FSR techniques, are shown in Figure 2. The PD event occurred at a HV of 6.2 kV. This event is illustrative of many similar measurements.

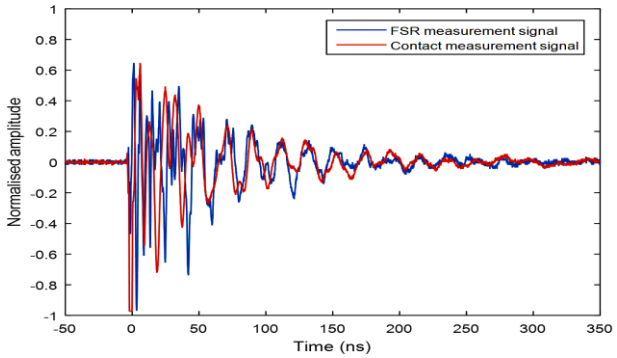

Figure 2. FSR and contact measurements comparison.

There is an approximate similarity between the temporal decay of the two signals in the two measurements, which was more similar than expected. For the FSR measurement, severe band limiting caused by the electromagnetic radiation and reception processes was expected. In contrast, the contact measurement was expected to produce less severe band limiting – this should, in principle, result in a less pronounced ringing. The conclusion is that band limiting is controlled by the capacitive and inductive features of the floating-electrode PD emulator and the connecting cables, rather than the frequency response of the antenna that receives the FSR measurement. Frequency spectra demonstrate that the PD discharge central frequency is located in the frequency range of 50 - 290 MHz. However, frequency spectra of FSR and contact measurements can be seen not to be identical, with differences in their energy distribution as shown in Figure 3.

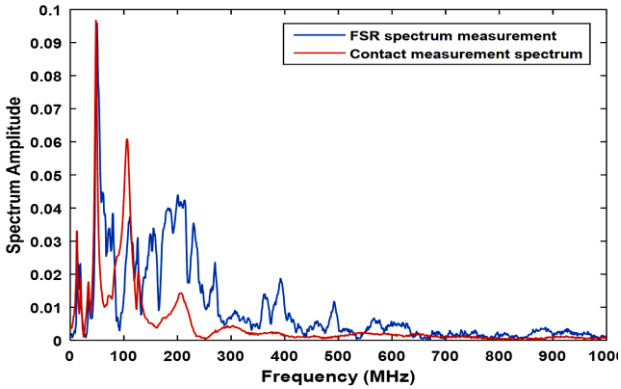

Figure 3. Normalised frequency spectra of FSR and contact measurements.

Most of the power in the PD radiation is contained in the band 50 MHz to 800 MHz. Figures 4 and 5 depict the three measurements of PD pulse energy for the FSR and contact measurement, in which a clear distinction is seen between the two techniques. The frequency spectrum was separated into three bands, and the energy contained within each band is plotted. The frequency spectrum in the 50 - 290 MHz, 290 - 470 MHz and 470 - 800 MHz bands is observed on a linear scale amplitude. The total energy and the percentage of energy present in the frequency bands is also shown.

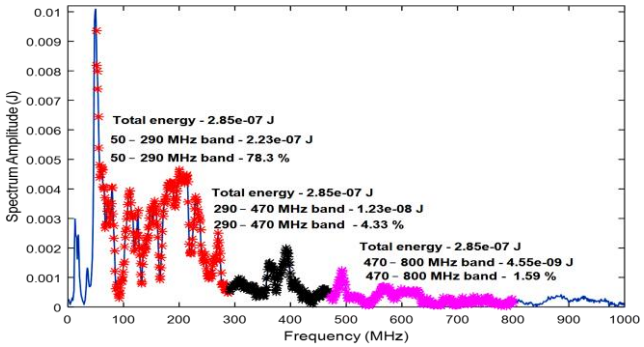

Figure 4. Frequency bands energy content for the FSR measurement method.

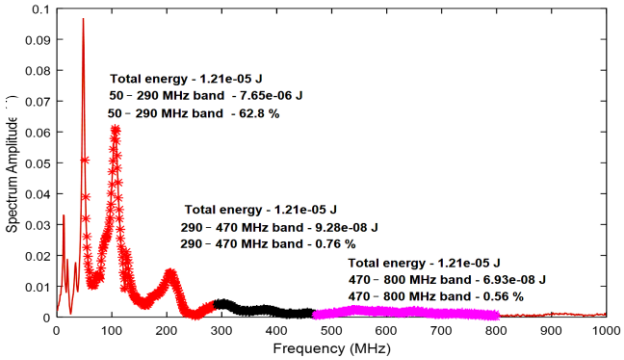

Figure 5. Frequency bands energy content for contact measurement method.

4 Conclusions

PD signals were captured using FSR and contact measurement techniques. The signals were analysed in the time and frequency domains. The results show an optical similarity in the time domain signals. Frequency spectra demonstrate that the PD discharge central frequency is located in the low frequency band, in particular the frequency range of 50 - 290 MHz. However, frequency spectra of FSR and contact measurements are not identical, with differences in their energy distribution. FSR and contact measurement techniques confirm that, the energy concentration of the PD signal in the frequency band of 50 MHz - 290 MHz is higher than the energy in the other frequency bands.

Acknowledgements

The authors acknowledge the Engineering and Physical Sciences Research Council for their support of this work under grant EP/J015873/1.

References

[1] E. A. G. Stone, Boulter, I. Culbert, H. Dhirani, "Electrical Insulation for Rotating Machines," IEEE Press, 2004.

[2] I. E. Portugues, P. J. Moore, I. A. Glover, C. Johnstone, R. H. McKosky, M. B. Goff, et al., "RF-Based Partial Discharge Early Warning System for Air-Insulated Substations," IEEE Transactions on Power Delivery, vol. 24, pp. 20-29, 2009.

[3] A. Jaber, P. Lazaridis, Y Zhang, D Upton, H Ahmed, U Khan, B Saeed, P Mather, M F Q Vieira, R Atkinson, M Judd, and I A Glover, "Comparison of contact measurement and free-space radiation measurement of partial discharge signals," in Automation and Computing (ICAC), 2015 21st International Conference on, 2015, pp. 1-4.

UWB radiation source location based on the electromagnetic time reversal method

Shaoyin He, Yanzhao Xie, Mingxiang Gao, Shaofei Wang, Xu Kong

State Key laboratory of Electrical Insulation and Power Equipment
Electrical Engineering College, Xi'an Jiaotong University
Xi'an, Shannxi, China

Abstract

This paper presents a three dimensions (3D) numerical simulation model basing on the electromagnetic time reversal (EMTR) method for locating the Ultra Wide Band (UWB) radiation source. The electromagnetic (EM) pulse of UWB radiation source has extremely fast front which could reach nanosecond or sub-nanosecond level. The key problem of UWB radiation source location is the difficulty in the rigorously precise time arrival of received signals on the condition of multipath transmission, and many methods are trying to improve the time arrival resolution. The EMTR uses the complete recorded waveform and performs an extraordinarily high spatial resolution. The result of simulation proved validity of the method.

Keywords: Electromagnetic time reversal, UWB radiation source, location, simulation.

1 Introduction

Different detection and location techniques such as time-of-arrival (TOA), time-difference-of-arrival (TDOA), and the hyperboloid-genetic algorithm have been developed in the application of location for many years. These methods based on the measurements of travel time between emitter and receivers and was actually a special case of EMTR [1]. But EMTR is not involved the problem of time delay selection of signal and have a good performance in multipath transmission circumstance, which is different from the TOA/TDOA method. Recently, a novel location and detection method basing EMTR has been introduced and considered in the lightning [1] and faults location of power networks [2]. The time reversal technique was first introduced and used in the field of acoustic in 1992 [3], and then developed in electromagnetic [4] and applied to objection detection and imaging. In this paper, we apply electromagnetic time reversal (EMTR) technique to locate the UWB pulsed EM radiation source.

2 EMTR theory and simulation model

2.1 The EMTR principle

In the basic theory of EMTR，the direction of time has been changed :

$$t \rightarrow -t . \quad (1)$$

Apply the time reversal transformation to Maxwell's equations and introduce the time reversal operator T, we get the following results due to the intrinsic definition of the electric and magnetic field [4]:

$$TE(r,t) = E(r,-t) \qquad T\rho(r,t) = p(r,-t) \quad (2a)$$

$$TH(r,t) = -H(r,-t) \qquad TJ(r,t) = -J(r,-t) \quad (2b)$$

If (2) is substituted into Maxwell's equations, the equations being mathematical manipulated are still valid. In the other words, Maxwell's equations is time reverse invariant when the time reversed solution are also valid for physical equations.

2.2 The simulation model

Because EMTR technique requires at least three field sensors, we set three dipole antennas (r_1, r_2, r_3) consisting a receiving array, as the time reversal mirror(TRM). In Cartesian coordinate, mm in unit, coordinates of r_1, r_2, r_3 are respectively (1000, 1000, 0), (-1000, 1000, 0), (-1000, -1000, 0) and r_s is (100, 100, 200) which is 200mm higher than TRM plane. Each arm of dipole is 2mm in length, and background parameters are ε_0 and μ_0 which is the electric permittivity and the magnetic permeability of the free space. 3D model is presented to locate the discharge point with CST and MATLAB software. The discharge source is approximated as a short line current source, and the Gaussian pulse is employed to be the excitation source.

2.3 The steps of the simulation

The simulation model to locate the discharge point consists 4 steps as following:

1) Radiate the signal by a line current source.
2) Record the induction signals of three receiving dipole antennas.
3) Reverse the signals. In practical implementations, T is the duration of the signal, apply the transformation, $t \rightarrow T-t$, and emit time reversal (TR) signals in the same simulation model.

4) Search the maximum value of |E| at the proper time step to find the source location.

In the model, the electric field measured by the sensor can be seen as far field, the E-field at arbitrary location $\vec{r}$ is:

$$\vec{E}(\vec{r},t)=\frac{\vec{\psi}(t-\frac{\|\vec{r}-\vec{r}_s\|}{c})}{\|\vec{r}-\vec{r}_s\|} \quad (3)$$

where $\vec{\psi}(t)$ is the electric field generated at the source and *c* is the speed of light. Here we are only interested in the far field, so we can see that source produce the plane waves.

Apply TR operator to this electric field at sensor n using expression:

$$\vec{E}_n(\vec{r},T-t)=\frac{\vec{\psi}(T-t+\frac{\|\vec{r}_n-\vec{r}_s\|}{c})}{\|\vec{r}_n-\vec{r}_s\|} \quad (4)$$

Hence time reversed electric field of each antenna n at location $\vec{r}$ is:

$$\vec{E}_{TR_n}(\vec{r},t)=\frac{\vec{\psi}(T-t+\frac{\|\vec{r}_n-\vec{r}_s\|}{c}-\frac{\|\vec{r}-\vec{r}_n\|}{c})}{\|\vec{r}-\vec{r}_n\|\|\vec{r}_s-\vec{r}_n\|} \quad (5)$$

We multiply by $\|\vec{r}-\vec{r}_n\|$ in both sides of (6) to offset the attenuation of electric field's amplitude, and calculate the superposition of the contribution of N TRM sensors:

$$\sum_{n=1}^{N}\vec{E}_{TR_n}(\vec{r},t)\times\|\vec{r}-\vec{r}_n\|=\sum_{n=1}^{N}\frac{\vec{\psi}(T-t+\frac{\|\vec{r}_n-\vec{r}_s\|}{c}-\frac{\|\vec{r}-\vec{r}_n\|}{c})}{\|\vec{r}_s-\vec{r}_n\|} \quad (6)$$

From equation (6), the field is back propagated without attenuation, and the superposition of fields will arrive with very high amplitude in source position at proper time step.

2.4 Simulation results

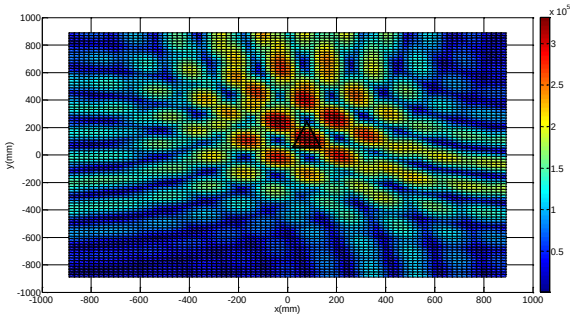

Figure 1. The superposition of time reversed field

In the colour graph, different colour present the field of each point. The back propagated waves produce constructive interference in several points which is shown as red colour and the size of the discrete elements is 10 mm × 10 mm. Nevertheless, there is only one position where all the waves arrive in same phase and superposition the field reaches maximum amplitude. It can be seen that calculated location point consists source position very well which shows darkest red.

2.5 Verification experiment

For validate the actual result of EMTR method used in location, we set up a system base impulse radiating (IRA) antenna and TEM receiving antenna, which can produce sub-nanosecond EM pulse radiation. The IRA antenna emits the EM signals and will be received by TEM antennas. We estimate the source location by EMTR method and assess the location accuracy. The experiment results will be provided in the presentation of conference.

3 Conclusions and future outlook

The time reversed technique is applied to locate the circuit breaker discharge and yield good results under the ideal conditions of perfectly conducing ground. However, this is a basic validation for the EMTR method and the following subjects need to be investigated in future for the real cases:

1) The relationship between the insulation fault and its corresponding discharge electric field characteristics should be investigated for the insulation fault detection.
2) The attenuation and distortion in wave propagation models in practical location needs to be further investigated as well.

What is deserved to mention is max value of the amplitude (or absolute value of amplitude) is the main criterion to determine the source location now. Combining the norm detection theory, the multiple EM norm characteristics including gradient of pulse front, pulse peak, action integral and others, the criterion of their application in the spatial location focus should be studied.

References

[1] G. Lugrin, N. M. Parra, F. Rachidi, M. Rubinstein, and G. Diendorfer, "On the Location of Lightning Discharges Using Time Reversal of Electromagnetic Fields," *Electromagnetic Compatibility, IEEE Transactions on*, vol. 56, pp. 149-158, 2014.

[2] R. Razzaghi, G. Lugrin, H. M. Manesh, C. Romero, M. Paolone, and F. Rachidi, "An Efficient Method Based on the Electromagnetic Time Reversal to Locate Faults in Power Networks," *Power Delivery, IEEE Transactions on*, vol. 28, pp. 1663-1673, 2013.

[3] M. Fink, "Time reversal of ultrasonic fields. I. Basic principles," *Ultrasonics, Ferroelectrics, and Frequency Control, IEEE Transactions on*, vol. 39, pp. 555-566, 1992.

[4] J. de Rosny, G. Lerosey, and M. Fink, "Theory of Electromagnetic Time-Reversal Mirrors," *Antennas and Propagation, IEEE Transactions on*, vol. 58, pp. 3139-3149, 2010.

Worldwide correlation study of geomagnetic sudden storm commencements (SSCs)

W. A. Radasky†, E. B. Savage, J. L. Gilbert^*

†^Metatech Corporation, U.S.A, wradasky@aol.com†, savagee@cox.net*, quantum_mechanic@alum.mit.edu^*

Abstract

In this paper we evaluate sudden storm commencement (SSC) B-field measurements due to solar activity. Samples of magnetometer data at 12 locations are examined in this paper along with particle data measured at the ACE satellite in order to correlate the arrival of these SSC B-fields at diverse locations on the Earth's surface.

Keywords: sudden storm commencement; sudden impulse; geomagnetic storms; SSC; SI

1 Introduction

Geomagnetic storms, and their effects on our critical infrastructures, can be important. It is well known that B-fields generated by a severe storm can adversely affect the electric power system, through generation of horizontal E-fields in the Earth and through their subsequent coupling to power transmission lines to create quasi-DC currents that can cause half-cycle saturation in large AC transformers [1]. During the initial phase of a geomagnetic storm, caused by a coronal mass ejection (CME) at the Sun, a sudden storm commencement (SSC) signal is observed and depending on the latitude of the observer, it may be followed by a long lasting high-level B-field. The focus of this paper is on the initial measured SSC waveform on the Earth to understand its behavior in time and location on the Earth.

2 Ground-based measurements

Table I describes the locations of the magnetometers used in this study.

Table 1: Data measurement locations

ID	Code	Site	Location	Cadence	GeomagLat
F	FFF	Forbes, Minnesota	47.3717N, 92.6042W	2 sec	56.5°
V	VSS	Vassouras, Brazil	22.400S, 43.601W	1 min	-13.6°
K	KAK	Kakioka, Japan	36.23N, 140.19E	1 sec	27.7°
J	HTY	Hatizyo, Japan	33.07N, 139.82E	1 sec	24.5°
N	KNY	Kanoya, Japan	31.42N, 130.88E	1 sec	22.2°
M	MMB	Memambetsu, Japan	43.910N, 144.19E	1 sec	35.7°
W	WMQ	Urumqi, China	43.800N, 87.700E	1 sec	34.4°
Y	YCB	Yinchuan, China	38.500N, 106.300E	1 sec	28.6°
H	HON	Honolulu, Hawaii	21.320N, 158.000W	1 min	21.7°
O	TRO	Tromso, Norway	69.6617N, 18.9400E	10 sec	67.3°
T	TRO	Tromso, Norway	69.6617N, 18.9400E	1 min	67.3°
D	DOB	Dombas, Norway	62.0728N, 9.1114E	10 sec	61.9°

It should be noted that there is a strong variation in magnetic latitude and geographic longitude included in this set of measurement locations. Also most of the data locations have a "fast" time cadence for their measurements, which is important to resolve the often rapid rise of the SSC waveforms, which are often on the order of 1 minute.

3 Examples of B-field SSCs

One example of an SSC time-of-arrival and waveshape correlation are shown in this section. Figure 1 illustrates 7 B-field SSC measurements at geomagnetic latitudes between 36 and -14 degrees and for longitude variations extending from Brazil to China. The waveforms are the horizontal B-fields, and the legend indicates the 3-letter observatory code, followed by the peak value, the sun location at the observation point (0 – 0.5 is the sun-side, while 0.5 – 1 indicates the dark side of the Earth at the time of the event), and the magnetic latitude.

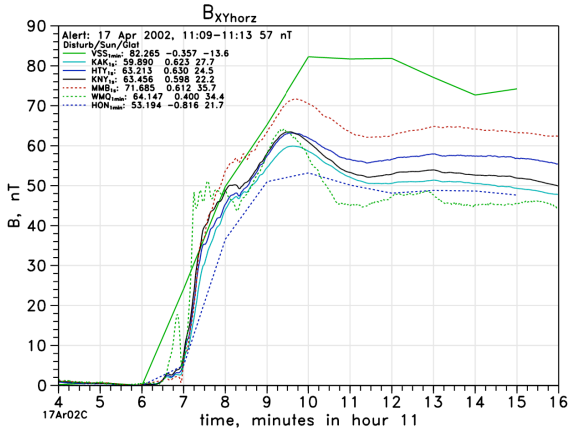

Figure 1. Horizontal SSC B-fields measured 17 April 2002

During the presentation, several examples of the time correlation of SSC waveforms will be shown as well as whether there are any significant variations in longitude relative to "high noon" of the arrival of the SSC. Particle arrival data at the ACE satellite will be also discussed.

References

[1] W. A. Radasky: "Overview of the impact of intense geomagnetic Storms on the U.S. high voltage power grid," 2011 IEEE International Symposium on EMC, Long Beach, August 2011, pp. 300-305.

A Comparison of EED Radiated Susceptibility Test Methods

P. P. Meekums, N. J. Carter, T. Noad, G. D. M. Barber and R. Hoad

QinetiQ Ltd., Farnborough, Hampshire, UK, ppmeekums@qinetiq.com

Abstract

Radiated susceptibility testing has been performed within QinetiQ's anechoic and reverberation chambers on a PW11 Electro-Explosive Device configured with temperature sensor instrumentation. The anechoic chamber radiated susceptibility testing was based on Def-Stan 59-411 whilst the reverberation chamber testing followed the mode stirred test method defined within RTCA DO-160G. The comparison between these two tests has been used to ascertain if Electro-Explosive Device electromagnetic compatibility testing is feasible within a reverberation chamber.

Keywords: EED, Reverberation Chamber, Anechoic Chamber, DO-160G, Def-Stan 59-411, NFT

1 Introduction

Electro-Explosive Devices (EEDs) have been known to initiate prematurely when subjected to high power Radio Frequency (RF) fields. Therefore, Def-Stan 59-114 [1] references Def-Stan 59-411 part 3 [2] in order to undertake radiated susceptibility testing, in an anechoic chamber, to qualify a system structure fitted with EEDs.

The conventional antenna illumination method's radiated susceptibility technique requires the Equipment Under Test (EUT) to be rotated to several angles and polarisations in order to represent the Electromagnetic (EM) environment that EEDs are exposed to when operational. The reverberation chamber subjects an EUT to the peak field levels in a multitude of polarisations and aspect angles over one paddle rotation, removing the need to rotate the EUT. This test is therefore a more thorough test and the field has the greatest probability of coupling to the EED without the need to reposition the EUT.

2 Test Method Considerations

The testing has been performed to DO-160G [3] which utilises a mode stirred method of testing. DO-160G suggests a method for determining the required tuner speed. As illustrated in Figure 1 the EED and instrumentation functional response time must be lower than the period over which the field remains higher than half (3dB) the maximum value of the peak field, over 1 tuner rotation. Experimental results of QinetiQ's reverberation chamber paddle show that the 3dB peak amplitude duration decreases with increasing frequency for a given paddle speed.

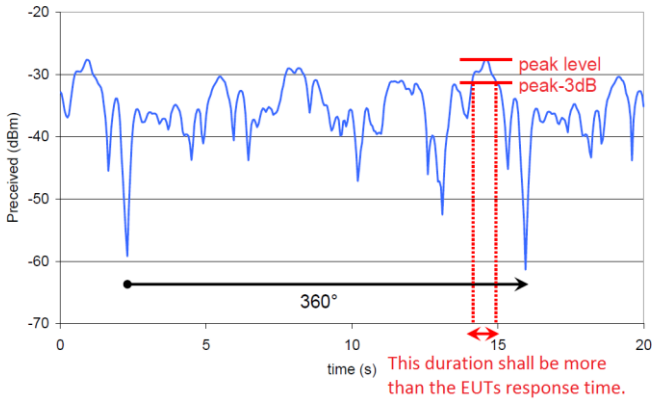

Figure 1. Measurement of 3dB point over one tuner rotation

Two common instrumentation systems have been used to monitor the induced bridge wire current in order to make sure the induced pick-up does not exceed a suitable margin below the No Fire Threshold (NFT) power of the EED. OpSens's OTG-R has a response time of 65ms [4] which is compatible with our tuner's minimum rotation speed; however, the Hazard Measuring Equipment's (HME's) 750ms [4] response time requires paddle rotation times of hours instead of minutes and becomes unpractical. Testing has been performed between the minimum speed of the paddle, 0.1249 RPM, and 4RPM. Therefore, the HME was not relied upon to determine the trigger level but was monitored in parallel with the OpSens OTG-R.

The results from the anechoic and reverberation chambers have been compared for continuous wave (CW) and varying pulse widths in order to ascertain if it is possible to certify electro-explosive devices within a reverberation chamber. This could lead to more thorough and faster testing cutting costs and time whilst improving the safety of EED operation.

References

[1] MOD Def-Stan 59-114, Safety Principles for Electrical Circuits in Systems Incorporating Explosive Components, (2012)

[2] MOD Def-Stan 59-411 part 3, Electromagnetic Compatibility, (2014)

[3] RTCA, DO-160G, Environmental Conditions and Test Procedure for Airborne Equipment, Revision G, pp. 20-A6 (2010)

[4] K. Skelton, Assessment of the OpSens 'RadSens' Measurement System, (2007)

Aspects of the shielding effectiveness of wire-meshes

R Gunnarsson*, M Bäckström*

**Saab Aeronautics, Linköping, Sweden, ronny.gunnarsson@saabgroup.com*

Abstract

Measurement and simulation results are presented illustrating that the shielding effectiveness of wire-meshes depend only slightly on whether or not there is electrical contact at the wire junctions.

Keywords: Wire-mesh; shielding effectiveness; numerical simulations; measurements.

1 Introduction

A simple and cost-efficient way of improving the shielding effectiveness (SE) of an enclosure with apertures (e.g. ventilation holes) is to cover the apertures with a metallic wire-mesh. Experimental, numerical and analytical results are presented in order to illustrate some aspects of the shielding performance of wire-mesh covered apertures.

2 Is electrical contact at wire junctions required to achieve good shielding?

It is sometimes claimed that good electrical contact at the wire junctions is required to obtain good shielding. To verify or disprove this claim, measurements and numerical simulations were performed on a 10×10 cm^2 aperture covered by wire-meshes with or without electrical contact at wire junctions. A wire-mesh was constructed consisting of 9+9 equally spaced circular wires with diameter 1.5 mm. Measured and simulated isotropic SE, <SE>, is presented in Fig.1 and is seen to be in reasonably good agreement. Essentially, the same shielding is provided by non-connected and connected wire-meshes. Measurements were performed in a reverberation chamber while simulated results were obtained using the methodology presented in [1].

3 The need for prediction tools to ensure that intended SE is obtained

Simple analytic or numerical models for the prediction of the shielding performance of wire-meshes are valuable. Fig.2 presents SE (plane wave) for a 30×30 cm^2 aperture covered by a commercially available wire-mesh with diameter 25.4 μm and subaperture separation 254 μm. Measured, simulated and analytic results are in good agreement while the data stated by the supplier differs substantially at 10 GHz. Note that the agreement between simulated and analytic results [2] can be improved if the expression for the sheet inductance in [2] is replaced by Equation (29) and (30) in [4].

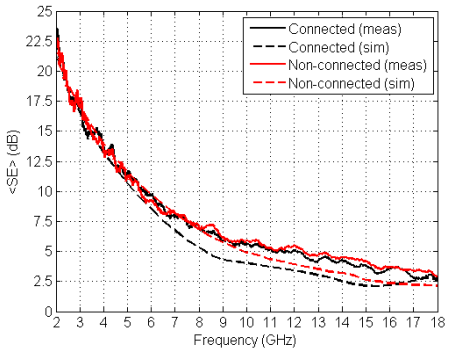

Figure 1. Measured (solid) and simulated (dashed) <SE> of wire-mesh covered aperture with and without (black/red) electrical contact at wire junctions.

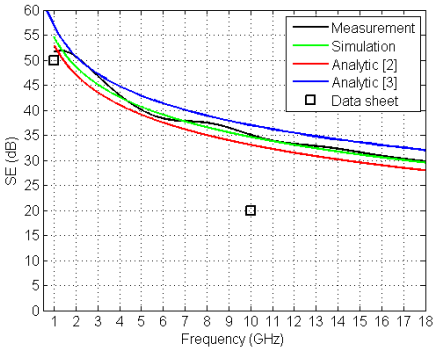

Figure 2. SE of a wire-mesh covered aperture for a normally incident plane wave. Measured (black), simulated (green) and analytic according to [2] (red) and [3] (blue). Data sheet values (black rectangles).

References

[1] R. Gunnarsson, M. Bäckström. "A methodology for numerical calculation of isotropic transmission cross section", *ASIAEM 2015*, Jeju, South Korea, 2 – 7 August 2015.

[2] Kenneth F. Casey, "Electromagnetic shielding behavior of wire-mesh screens", *IEEE Trans. on EMC*, Vol.30, No.3, August 1988, pp.298-306.

[3] R. Gunnarsson, M. Bäckström, "A heuristic model for the transmission cross section of wire-mesh covered apertures", EMC Europe 2015, Dresden, Germany, 16 – 22 August 2015.

[4] Larry K. Warne et al., "Approximations to wire grid inductance", Sandia National Laboratories, SAND2007-0816, January 2008, pp.1-15.

Random Coupling Model Applied to the Irradiation of Buildings

G Gradoni[#], D Micheli*, S M Anlage [†], E Ott [†], T M Antonsen [†]

[#]University of Nottingham, United Kingdom gabriele.gradoni@nottingham.ac.uk,
**Telecom Italia Lab, Italy and contact details,*
[†]University of Maryland, United States of America {anlage, edott, antonsen}@umd.edu

Abstract

We present applications of a statistical model, the Random Coupling Model (RCM), to the penetration of electromagnetic energy through the walls and apertures of a reverberant chamber. An approach based on the principle of reciprocity is discussed, for which the far field radiation pattern of a source inside the room is calculated. The power received by a terminal operating inside a cavity when the cavity is illuminated by external radiation in presence of arbitrary absorption losses, apertures, and walls can then be calculated. Results are of interest for characterizing the field propagation in the outdoor-to-indoor wireless channel transition.

Keywords: Chaos, Aperture, Coupling, Reciprocity, Building, Outdoor-to-Indoor

1 Introduction

Extending the coverage of actual mobile telecommunication networks necessarily involve describing the propagation between the outdoor and the indoor electromagnetic environments. This is the so-called outdoor-to-indoor transition. The mechanisms for which outdoor radiation couples to indoor environments, e.g., buildings, are mainly two: one involving the leakage through apertures, i.e., windows and doors, and one involving the transmission through walls, e.g., made of concrete, of the electromagnetic energy. The fractions of power related to the two mechanisms are highly dependent on geometry and material loading the aperture/wall [1]. In the high frequency irradiation of buildings, the coupling is extremely sensitive to geometrical details and it can be thought of as occurring in three steps: a free-space (outdoor) step where the field impinging in the building comes from the base station in the form of a plane wave, a step in which the wall or aperture is penetrated, and a closed-space (indoor) step in which the waves reverberate and interfere in the chamber. The RCM helps us to understand how the penetration and reverberation steps interact and interfere [2].

2 Statistical model

For a building with an arbitrary boundary geometry, we solve Maxwell's equations with boundary conditions modelling the presence of opaque walls with apertures to arrive at a reciprocity relation. The reciprocity relates antenna voltages and currents given a field incident on the wall. This is achieved by evaluating the radiation pattern of an antenna radiating through the building into the free-space. We expand the field at the cavity surface – either in presence of wall or aperture – in a basis of eigen-functions. Then, we approximate the propagation through the wall or aperture by assuming that each basis mode propagates independently. The fields on the inside surface of the wall or aperture are related by the RCM model for the cavity [2], which in this case is the room. Specifically, in order to calculate the radiation pattern of the antenna radiating in presence of the cavity, the transmission through the wall is derived by solving for the voltage on the outside of the wall in terms of the voltage on the inside. The reciprocity is thus used to work out an expression for the scattered voltages when the building is irradiated from the outside. If we assume that the cavity has an irregular geometry, in the high frequency limit, the voltage induced to an antenna inside a building can be predicted statistically by replacing actual cavity modes with chaotic modes. This is encoded in the statistical prescriptions leading to the RCM. This way allows for deriving the average shielding effectiveness $\left\langle h_{eff} \right\rangle$ of the building against an external radiation for arbitrary distributed losses a in the environment. In the high loss limit, this expression is consistent with the power balance approach, leading to

$$\left\langle h_{eff} \right\rangle \propto \frac{k^2 A}{a G_p(\mathsf{W})} \left\langle T_w \right\rangle \qquad (1)$$

where A is the irradiated area, k the wavenumber, G_p the gain of the receiving antenna, and $\left\langle T_w \right\rangle$ the average wall transmittance.

Acknowledgements

Financial support from Telecom Italia Grant N142005, ONR Grant N00014130474, and AFOSR CoE Grant FA9550-15-1-0171.

References

[1] P. Ragulis *et al*, ``Transmission and Reflection of Microwave Radiation from Novel Window Panes'', *AMEREM 2014*, Albuquerque NM, USA.

[2] G. Gradoni, *et al* "A Statistical Model for the Excitation of Cavities Through Apertures," in *Electromagnetic Compatibility, IEEE Transactions on* , vol.57, no.5, pp.1049-1061, (2015).

Electromagnetic coupling to thin wire structures inside resonators

S V Tkachenko*, J B Nitsch*, R Rambousky†, R Vick*

**Otto-von-Guericke University, Magdeburg, Germany, e-mail: Sergey.Tkachenko.ovgu.de*
†Bundeswehr Research Institute for Protective Technologies and NBC Protection (WIS), Munster, Germany

Abstract

In this paper we shortly summarize some research results about the interaction of different thin-wire structures in resonators with the resonator walls. Different methods such as the approximate Method of Small Antennas, the Method of Thin Wire Lines as well as an exact Method of Symmetrical Lines are used to describe the interactions in rectangular and cylindrical cavities. The used analytical techniques can also be applied to investigate stochastic transmission lines in resonators.

Keywords: Resonators, Transmission Lines, Thin Wires.

1 Introduction

In practice one can find different transmission-line configurations in resonators. These are, e.g., small dipoles and loops as well as lines connecting devices. All these antennas couple with natural and intentional electromagnetic fields penetrating inside cavities. Those cavities may be an aircraft fuselage, a computer rack or car chassis, to name only a few.
Another important problem is the coupling with DUTs including their connecting transmission lines in mode-stirred chambers. Such a cavity environment can change the coupling dramatically due to the interaction of the transmission line and resonator modes. Furthermore, the exact geometrical and electrical parameters of transmission lines, which define such interactions, are unknown in practical applications. As a result, one can only talk about the probability of one or another parameter and, correspondingly, of induced currents and voltages.
One way to consider such problems is the use of direct numerical methods as MoM, TLT, etc. However, these methods describe only specific cases and do not describe general features of interaction. Moreover, they are quite time consuming which circumstance leads to difficulties of statistical modeling. This is the reason to develop analytical methods. As usual in mathematical physics these methods are based on the method of small parameters or on the symmetry of the system.

2 Analytical methods.

2.1 Method of Small antenna (MSA) [1,2].

In the method of small antennas it is assumed that the linear dimension of the antennas is small in comparison to the wavelength. In this case one can evaluate the scattered current in an antenna in a resonator from the scattered data of the antenna (scattered amplitude, or polarisability, or an admittance function in free space). In other words, as an equivalent circuit describing a small antenna in free space. Instead of the parameter of radiation resistance appears an impedance of the system "antenna in resonator" which depends on parameters of the antenna, the parameters of the resonator and also depends from the position of the antenna in the resonator.
The developed general theory is applied for the solution of specific problems: as for the calculation of the input impedance of a small dipole (monopole) or a loop antenna in a resonator and for the mutual impedance of two antennas in rectangular or cylindrical resonators [1,2,3], as well as for the calculation of the penetration of radiation into the resonator [2], including also the consideration of scattering by many small antennas in a resonator [4].
In this paper we present general equations for the polarisability tensor of electrical and magnetic dipoles inside the resonator.

2.2 Method of Thin Wire Line [5].

Another small parameter that can be used to solve the coupling problem for electrically long objects inside a resonator is the ratio of the thickness of the wire compared to other geometrical parameters of the problem (wavelength, height of the wire above ground, etc.) [5]. Here the relevant mathematical technique is the method of analytical regularization [6] which allows coupling of EM fields with electrically long antennas and transmission lines inside a resonator, if the considered frequency is close to one of the resonance frequencies and all the other modes of the resonator contribute to form the singular part of the cavity's Green's function. In the ref. [5] this method was applied for a horizontal transmission line in resonator. In this paper we apply this method for the transmission line with vertical loaded elements in a rectangular resonator.
However, this method uses approximate representations of the singular and regular parts of the Green's function and an approximate resolution operator (TL approximation) and is valid for undermoded cavities. It is interesting to compare these results with results of an exact solution.

2.3 Method of Symmetrical Line [7].

As usual in theoretical physics, an exact solution for the system "transmission line in resonator" can be found for a high-symmetrical system where wire and cavity have the same symmetry. For a rectangular resonator the wire is conducted parallely to four walls of the resonator and connects two opposite walls. This system allows an exact analytical solution by spatial Fourier transformation for any kind of excitation, including lumped sources (or loads, which can be considered as controlled voltage sources) [7]. This method is quite general and can be applied to symmetrical wires inside cylinders of general form, including the most practical case of the right circular cylinder [8].

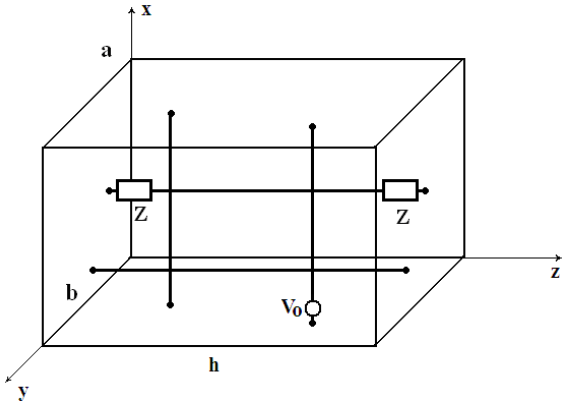

Figure 1: Set of transmission lines with symmetrical geometry inside a rectangular cavity.

Also the method can be applied to more complicated wire configurations conserving the symmetry of the system: several parallel wires, wire with arbitrary multi-loads [9,10].
In the present paper we consider the problem of electromagnetic field coupling to mutually perpendicular wires in a rectangular resonator (see Fig. 1) which can be solved by the Method of Symmetrical Lines. The current in the wires again is determined using spatial Fourier series. Due to the symmetry of wires the basic functions (cosines) of the series coincide with the Green's function of the empty cavity. Therefore it is possible to build an exact fast analytical "solver" for arbitrary excitation (lumped or distributed) for this problem. The loads at the terminals of the line can be introduced as controlled voltage sources. The knowledge of the current can be used to calculate the scattered electromagnetic field inside the resonator.
Using the developed method one can investigate (within a reasonable time) the statistical properties of induced currents and fields for the case of stochastically arranged symmetrical lines in rectangular resonators.

3 Conclusion

In this paper we presented a review of results of our investigation of thin-wire systems in resonators. The fast analytical techniques were also applied to investigate stochastically arranged TLs in resonators. Further applications to TLs with stochastic geometries in resonators were discussed.

Acknowledgements

This work was supported by the German Research Foundation (DFG), Contract Number: VI 207/6-1 .

References

[1] S.Tkachenko, H.-G.Krauthäuser, F.Gronwald, J.Nitsch, „High Frequency Electromagnetic Field Coupling to Small Antennas in Rectangular Resonator", *Int. Conf. on Electromagnetics in Adv. Appl. ICEAA'09*, Sept. 14-18, 2009, Torino, Italy, pp.188-191. (ISBN: 978-1-4244-3386-5).

[2] S. Tkachenko, J.Nitsch, M.Al-Hamid, „High-Frequency Electromagnetic Field Coupling to Small Antennae in a Rectangular Resonator", *International Journal of Antennas and Propagation*, **volume** 2012, Article ID 897074, doi:10.1155/2012/897074.

[3] S.Tkachenko, J.Nitsch, R.Rambousky, „Electromagnetic field coupling to an electrically small axial dipole antenna in a cylindrical cavity", *EMC Europe*, Goteborg, Sweden, Sept. 2014, pp.175-180. doi: 10.1109/EMCEurope.2014.6930898

[4] S.Tkachenko, J.Nitsch, R.Vick, G.Vodopianov, „Simulation of Mode Stirred Chambers by Small Antenna Method", *Proc. of 8th Int. Sym. on EMC and Electromagnetic Ecology*, June 16-19 2009, St-Petersburg, Russia. Conf. Proceed., pp. 192-195.

[5] S.Tkachenko, J.Nitsch, R.Vick, "HF Coupling to a Transmission Line inside a Rectangular Cavity", *URSI International Symposia on Electromagnetic Theory, Berlin, Germany, August 16-19*, 2010 (ISBN: 978-1-4244-5154-8), pp. 41-44.

[6] N.I. Nosich, "The method of analytical regularization in wave-scattering and eigen-value problems: foundations and review of solutions", *IEEE AP Mag*., **volume** 41, pp.34-39, June 1999.

[7] S.V.Tkachenko, R.Rambousky, J.B.Nitsch, "Electro-magnetic Field Coupling to a Thin Wire Located Symmetrically Inside a Rectangular Enclosure", *IEEE Trans. on EMC*, **volume** 55, No. 2, 2013, pp. 334-341.

[8] S.Tkachenko, R.Rambousky, J.Nitsch, "Analysis of Induced Currents on a Thin Wire Located Symmetrically Inside a Cylinder", *IEEE Trans. on EMC*, **volume** 56, Nr.6, 2014, pp. 1649-1656.

[9] S.Tkachenko, J.Nitsch, R.Rambousky, "Electromagnetic Coupling to Transmission Lines with Symmetric Geometry Inside Rectangular Resonators", F. Sabath and E.L. Mokole (eds.), Ultra-Wideband, Short-Pulse Electromagnetics **volume** 10, Springer, 2014. pp. 31-48.

[10] R.Rambousky, S.Tkachenko, J.B. Nitsch, "Calculation of Currents Induced in a Long Transmission Line Placed Symmetrically Inside a Rectangular Cavity", IEEE Int. Sym. on EMC Denver, 5-9 Aug. 2013, pp. 796 – 801.

High Power Radio Frequency Risk/Hazard Assessment Tool

L. Chatt, B. Petit & Dr R. Hoad

QinetiQ Ltd.

Cody Technology Park, Farnborough, Hampshire, GU14 0LX, UK

lmchatt@qinetiq.com

***Abstract*—This paper describes the development of a software tool for visualising the electric fields generated by Radio Frequency Disruptive Technologies (RF DT) and Intentional Electromagnetic Interference (IEMI) devices. These visualisations are used to identify regions at a site where susceptible equipment can be affected by a known level of IEMI, accounting for propagation and attenuation of electric fields due to intermediate structures. The tool can also be used to visualise the Electromagnetic (EM) footprint from a specific RF DT or IEMI system. These visualisations can be used to inform minimum separation requirements for personnel, ordnance, flammable atmospheres and safety critical equipment, in addition to advising on the potential need for any additional EM hardening and illustrating the efficacy of shielding for susceptible systems.**

Keywords- RF DT, IEMI, Susceptibility,

1. Introduction

Due to the perceived rising threat from Intentional Electromagnetic Interference (IEMI) devices the capability of modelling and in particular visualising the propagation of the output from these systems at a site level is critical. To this end QinetiQ has developed a software tool known as PhoS. Threats from different IEMI systems can be evaluated and the insight gained can be used to identify systems most at risk as well as the locations where a hazard/threat would have maximum impact. The visualisation software combines both Electromagnetic (EM) immunity and susceptibility information and knowledge of RF DT/IEMI threat levels, which subsequently can be used to inform the augmentation of EM security measures where it is needed the most.

Where simple propagation through free space is assumed, the magnitude of the electric field generated during an EM attack is proportional to the inverse distance between source and victim system. A slightly more complex model can include the effects of ground reflections. In reality, additional phenomena can contribute to losses such as scattering, diffraction, interference and absorption. Either of the two simple models can be visualised by PhoS, however propagation through free space is often assumed to be the worst case scenario.

PhoS visualisations account for the attenuation of incident RF radiation due to intermediate physical structures such as fences and buildings. These losses can be approximated using typical values associated with certain materials, e.g. a concrete wall provides roughly 15 dB attenuation [1]. However more accurate attenuation readings can be provided for a specific site, for example, using values from the output of QinetiQ's Shielding Effectiveness Measurement System (SEMS) [2].

2. EM Risk Plot

Using PhoS a vulnerable region/system can be defined within a site using the electric fields associated with levels such as immunity, upset and damage if they are known. For specific IEMI sources PhoS can display the electric field patterns or power densities as they propagate through a site. This information can be used to identify areas where the source can be placed in order to cause upset or damage as well as specifying positions where the susceptible system would be immune (Figure 1). This model, as seen in Figure 1, accounts for the attenuation of intermediate structures. Whilst the site shielding prevents an attack from outside of the fenced perimeter from damaging susceptible equipment, there is a region to the north where the IEMI source could cause upset. This information together with an understanding of the physical accessibility of the location can be used to inform requirements for additional EM hardening of a site and subsequently visualise the effectiveness of the proposed shielding prior to installation.

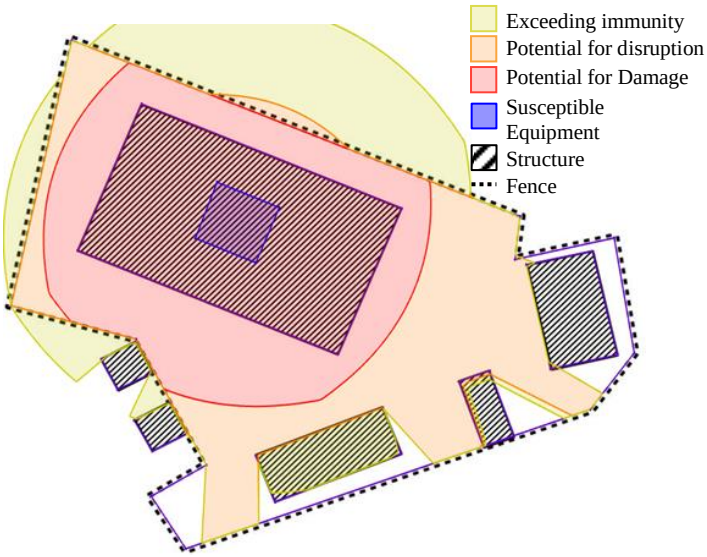

Figure 1: PhoS risk model of a Vulnerable Area at a Secure Site

3. Source Footprint Plot

Secondly PhoS can visualise the EM environment from the perspective of a known IEMI source at a specific position (Figure 2). These models can be used to plot the safe/hazard regions for personnel, ordnance, flammable atmosphere and safety critical equipment, for example personnel exposure limits specified by ICNIRP [3] or commercial aircraft limits specified by HIRF environments [4]. This can advise safety

measures to be taken when an IEMI system is to be tested outdoors.

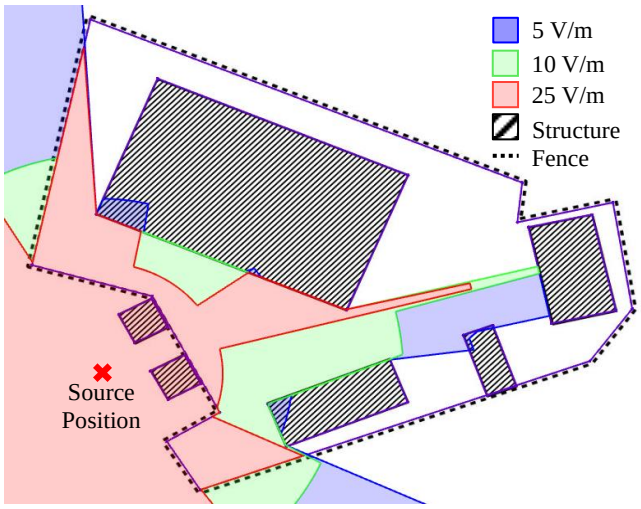

Figure 2: PhoS model of the Source Footprint at a Secure Site

The modelling basis is simplified and does not include details such as terrain or edge diffraction. However the tool has been validated and found to agree with measurements to an acceptable level of fidelity. Most importantly the tool helps customers and others who have limited understanding of RF DT and IEMI to visualise the complexity of the problem.

References

[1] W. A. Radasky, "Protection of Commercial Installations from the High-Frequency Electromagnetic Threats of HEMP and IEMI Using IEC Standards," in *Asia-Pacific International Symposium on Electromagnetic Compatibility*, Beijing, 2010.

[2] R. Hoad, B. Petit, S. P. Watkins, A. Wraight, A. Lambourne and A. Leaver, "Measurement of the attenuation of buildings and structures and comparison with published data", AMEREM 2010, Ottawa, Ontario, Canada, 7th to 10th July 2010

[3] International Commission on Non-Ionizing Radiation Protection, "GUIDELINES FOR LIMITING EXPOSURE TO TIME-VARYING ELECTRIC, MAGNETIC, AND ELECTROMAGNETIC FIELDS (UP TO 300 GHz)," 1997.

[4] Federal Aviation Administration, DEPARTMENT OF TRANSPORTATION, "High-Intensity Radiated Fields (HIRF) Protection for Aircraft Electrical and Electronic Systems," vol. 72, no. 150, 2007.

Shielding Effectiveness Studies of Energy Saving Windows and Coated Window Panes – a Summary

***P Ängskog*[*†], *M Bäckström*[*#], *C Samuelsson*[#], *B Vallhagen*[#]**

[*]*Electromagnetic Engineering Lab, KTH Royal Institute of Technology, Sweden, pangskog@kth.se,*
[†]*Department of Electronics, Mathematics and Natural Sciences, University of Gävle, Sweden*
[#]*SAAB Aeronautics, SAAB AB, Sweden, mats.backstrom@saabgroup.com*

Abstract—**In recent decades, window panes and windows have undergone a virtual revolution with respect to energy saving. Along with this revolution a strong reduction of radio transmission capability through windows has followed. It has been observed that radio communication (e.g. mobile telephony) in newly built or renovated buildings has become increasingly difficult to accomplish due to the higher attenuation in these energy-saving windows. On the upside though, the increased attenuation can help in the protection against intentional electromagnetic interference (IEMI) and compromising emanations from activities inside the building.**
In this paper we summarize shielding effectiveness (SE) measurements conducted on window panes and window modules during 2014 and 2015 and give some conclusions drawn regarding do's and don'ts when installing windows.

Keywords: *Shielding Effectiveness; Energy saving windows; Coated window panes; IEMI*

1 Introduction

With the purpose to determine the shielding effectiveness of energy saving windows and the window panes they are composed of, a series of measurements have been carried out at the EMC laboratory of Saab Aeronautics in Linköping, Sweden.

2 Testing

Measurements were made using two complementary methods; in a nested reverberation chamber (RC) [1] - [2], and in a semi-anechoic chamber (SAC), both covering the range 1 – 18 GHz.
A few of the window panes were also tested for HPM irradiation effects on the L-band with the field strength 28 kV/m at the Swedish MTF range in Linköping [3].

2.1 Test Methods

In the RC the sample covered an aperture in the wall of an internal nested RC, fields being stirred in both chambers.
The tests in the SAC where traditional comparative "hatch-on/hatch-off" type, carried out with a standard plane wave irradiation with normal incidence.
The HPM test was conducted as a "before/after" test where the panes were tested in the RC before and after being subject to the high-power irradiation.

2.2 Test Objects

The objects tested were four energy saving windows representing four generation of windows, and five different window panes whereof four had different coatings [4].

3 Results

An important observation among the conclusions drawn from the tests is the generation dependence of windows, where the most modern types may give an SE of on average 20 to 30 dB, potentially reaching 50 to 60 dB in the upper part of the measured frequency range while traditional two- or three-pane windows only give a few dB [4].
Other conclusions drawn are the importance of how the panes are mounted in the sashes, e.g. on which side the coating is placed, the importance of using aluminium spacerbars rather than the energy saving "warm-edge" insulating cavity spacer to avoid RF leakage.
From the HPM testing the conclusion was drawn that the type of coating determines the capability to withstand high-power irradiation without thermal break-down of the coating where soft-coated panes showed visually observable cracks while hard-coated panes survived without deterioration [3].

References

[1] M. Bäckström, T. Nilsson and B. Vallhagen, "Guideline for HPM protection and verification based on the method of power balance," in *Electromagnetic Compatibility (EMC Europe), 2014 International Symposium on*, Gothenburg, Sweden, 2014.

[2] D. A. Hill, M. T. Ma, A. R. Ondrejka, B. F. Riddle, M. L. Crawford and R. T. Johnk, "Aperture Excitation of Electrically Large, Lossy Cavities," *IEEE Trans. Electromagn. Compat.*, vol. 36, no. 3, pp. 169-178, August 1994.

[3] P. Ängskog, M. Bäckström and B. Vallhagen, "High Power Microwave Effects on Coated Window Panes," in *Asia Electromagnetics Conference (ASIAEM) 2015*, Jeju, South Korea, 2015.

[4] P. Ängskog, M. Bäckström and B. Vallhagen, "Measurement of Radio Signal Propagation through Window Panes and Energy Saving Windows," in *Proceedings of Electromagnetic Compatibility (EMC), 2015 IEEE International Symposium on*, Dresden, Germany,2015, p. 74-79.

Shielding effectiveness of screens from polypyrrole conducting layers

R Simniškis*, Ž. Kancleris*, and M. Kirsnytė†

*Laboratories of *Microwave and †Bio-nanotechnology of Centre for Physical Sciences and Technology, Vilnius Lithuania*
e-mail rimantas.simniskis@ftmc.lt

Abstract

The shielding effectiveness and conductive properties of organic conductor polypyrrole were experimentally investigated in a frequency range from 10 to 40 GHz, the analytical model of shielding properties of conductive layer on dielectric substrate was proposed and compared with experimental results.

Keywords: organic conductor, polypyrrole, electromagnetic shielding.

1 Introduction

Nowadays a lot of new shielding materials and structures are investigated, developed and commercially available. One promising trend is the application of organic conductors with tunable properties [1]. The structures and composites containing polypyrrole (PPY) are convenient in application as shielding additive material in fabrics, or layers on different dielectric materials.
The aim of this work was to investigate properties of PPY layers in a frequency range 10-40 GHz optimizing their absorbing features.

2 Investigation of PPY shielding properties in Ku and Ka bands

Using analytical model proposed in [2] reflectance, transmittance and absorption was calculated of the thin conductive layer deposited on a glass surface. Calculated dependencies of these parameters on sheet resistance of the conductive layer at 31.5 GHz are shown in Figure 1. It is seen that transmittance and absorption strongly depends on the side from which radiation falls on the investigated structure.

PPY films were made on a glass substrate with a polyvinyl alcohol (PVA) underlayer. PPY film was synthesized on top of PVA with dropwise addition of $FeCl_3$ into pyrrole and water solution. Measured PPY layer thickness was in the range from 15 to 40 μm. The chemical synthesis process does not ensure the regular structure and reproductive properties of layers, but it shields protected area and suppresses the resonances inside the protected volume. The properties of PPY samples were investigated by mounting samples in to Ku

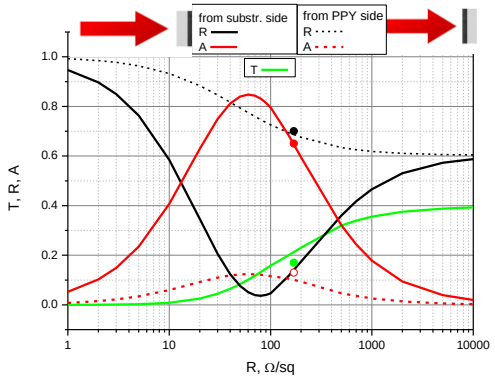

Figure 1. Dependence of absorption (A), reflectance (R) and transmittance (T) on sheet resistance of conductive PPY layer on 1mm glass substrate at f=31.5 GHz. Solid lines represent calculated values when radiation falls from substrate side, dashed lines – from PPY side, points correspond to experimental measurements.

(WR62) and Ka (WR28) waveguides. The reflectance and transmittance were measured, from their values absorption in the PPY layer was determined. The calculated and measured values of absorption, transmittance and reflectance of conductive layer on 1 mm glass substrate at 31.5 GHz is shown in Figure 1. It is seen, that transmittance is independent of the side from which radiation is falling on the investigated structure, whereas reflection and absorption depends on the side of radiation. The maximum absorption is observed at R_{sq}=80 Ω/sq when radiation falls from the substrate side. Experimental measurements have revealed that sheet resistance of PPY was R_{sq}=170 Ω/sq, and measured reflectance and transmittance are close to calculated values.

3 Conclusions

Electromagnetic properties of PPY layers were investigated in the frequency range 10-40 GHz. It was shown that by changing substrate properties and side, from which it is radiated layer absorption can be maximized.

References

[1] A. Kaynak, et al, *The Journal of Applied Polymer Science*, **v 54**, pp. 269-278, 1994
[2] P.Ragulis, et al, *The Journal of Applied Physics*, **v 117**, 2015

RF propagation to targets in maritime environments

F. Sonnemann, J. Urban, R. Stark

Diehl BGT Defence GmbH & CoKG, 90552 Roethenbach a d Pegnitz, Fischbachstr. 16, Germany

Abstract

This paper presents RF propagation measurements on water to determine optimum radiation parameters (frequency, polarisation, transmitter height and source-target distance) for electromagnetic boat stop scenarios. A comparison is made between measured propagation attenuation and numerical TERPEM simulations. A validation of code has been performed by propagation measurements on a perfectly conductive surface.

Keywords: RF propagation, maritime environment, TERPEM, parabolic equation method, HPEM, boat stop

1 Introduction

The parabolic equation (PE) method [1] is a useful numerical method to calculate the electromagnetic field over sea or irregular terrain. Because of the very large size of the domains of interest relative to the wavelength, the exact computation of Maxwell's equation is very time consuming and use of approximations is very beneficial. The PE method goes back to the 1940s and is based on an approximation of the wave equation which models the energy radiated by an antenna in a certain cone of direction, the paraxial direction. Originally, the method was formulated in the frequency domain. However, a transformation in the time domain can easily be performed. The method calculates the 2-dimensional field along the surface for all antenna heights of interest. A commercial software package based on this method is called TERPEM by Signal Science Limited. It includes the effects of atmospheric refraction, terrain diffraction and swell of sea which are especially important for the propagation of radiowaves in the VHF-band and mm-range. The method is often used for long-range radar applications in the km-range. However, for short range applications, e.g., boat stop scenarios, the paraxial beam approximation is less well fulfilled, especially if low-gain antennas are used.

2 Reference measurement

A reference measurement over "perfectly" conductive ground has been performed with a HPEM mesoband test source. (Figure 1). The HPEM source was modelled in TERPEM as a dipole antenna and a normalised radiated peak field of 1 MV/m (pk-pk/2) @ 1m. As an example, the (normalised) measured and the computed field for the parameters h_1 = 2m, r = 15 m and h_2 = 0.3 m are shown in Figure 2. Remark: The calculated transfer function in TERPEM (called complex propagation factor), given in amplitude and phase, has been used to calculate the time domain response of the propagated HPEM mesoband pulse.

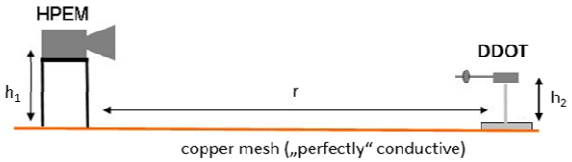

Figure 1. Reference measurement set up

A good agreement between TERPEM simulation and measurement for this "ideal" propagation condition can be noted. It is clear, that the horizontal polarised (HP) E-field is much lower in amplitude than the vertical polarised (VP) E-field close over ground. Note that the constructive superposition for vertical polarisation results in higher electrical field strength compared to free-space propagation.

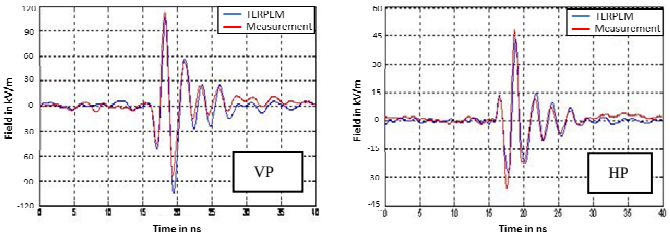

Figure 2. Propagated HPEM pulse measured and simulated close over perfectly conductive ground (h_1 = 2m, r = 15m, h_2 = 0.3m), (normalised values)

2 Water propagation measurements

The propagation measurement has been performed on an artificial lake at the maritime test range WTD 71, Germany located at the North Sea. The transmitter source is positioned on the landside and can be lifted with a crane on different heights. The receiving antenna is located on a swimming wooden platform (Figure 3).

Figure 3. Measurement setup for HPEM propagation over water

The water is weakly salty with a salinity of 0.4 %. For comparison: The North Sea has a salinity of 3.5 %. The water is mainly flat and smooth.

A low-level swept frequency measurement has been performed with a CW frequency generator and connected Log-Per antenna. The frequency range was chosen to 100 MHz – 900 MHz. As an example, Figure 4 shows the measured and simulated E-field propagation factor for horizontal polarisation for two different transmitter heights (h_1 = 5 m and h_1 = 15 m), r = 33 m, h_2 = 1 m. Note, that the propagation factor does not include the free-space 1/r E-field decay over distance. The simulation shows a reasonable result in comparison with the measurement. Discrepancies may be caused by uncertainties in the measurement set-up, wavering of the swimming platform and the small water waves. Also, the paraxial beam approximation is not really fulfilled for the Log-Per antenna with the propagation parameter used.

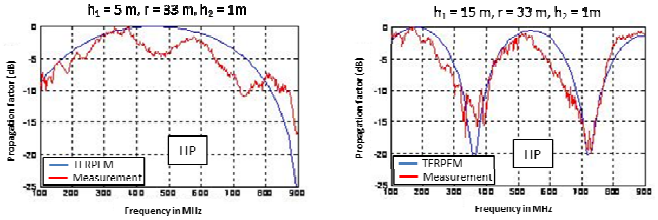

Figure 4. Propagation factor for horizontal E-polarisation

In Figure 5, the propagation factor for vertical polarisation is depicted. All other parameters remain the same. Similar as for horizontal polarisation, the discrepancy between measurement and simulation is in the range of 0 - 5 dB. It can be noted that resonance minima and maxima have been changed for horizontal and vertical polarisation.

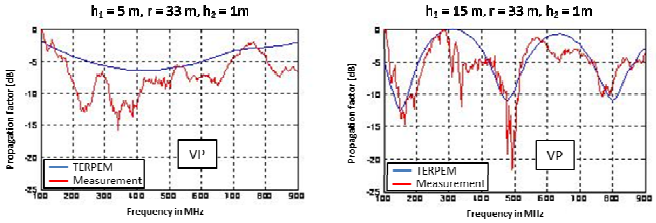

Figure 5. Propagation factor for vertical E-polarisation

For HPEM propagation test, a dipole-based mesoband test source with a normalised radiated peak field of 1 MV/m (pk-pk/2) @ 1 m and a center frequency of 350 MHz has been used. The source-target distance and receiver height remain the same (r = 33 m, h_2 = 1 m). Figure 6 left shows the influence of the transmitter height. It can be noticed that at horizontal polarisation the electric field is more than two times higher for a transmitter height of h_1 = 5 m compared to h_1 = 15 m. The time domain result is in accordance to the frequency plots in Figure 4. Figure 6 right shows the influence of the polarisation for a transmitter height of h_1 = 5 m. The picture shows that for the given propagation parameters, a horizontal polarised field give approximately two times more field amplitude than a vertical polarised field – a result which is again in accordance to Figure 4 and Figure 5 (left pictures).

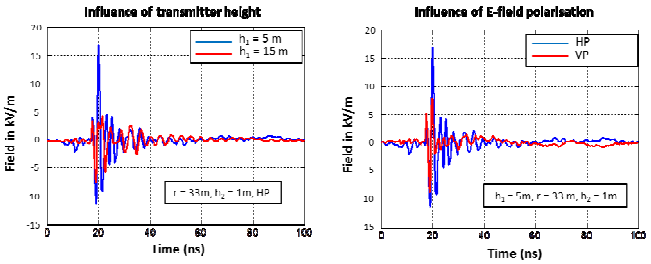

Figure 6. Influence of transmitter height and polarisation (measurement, normalised values)

Figure 7 shows a TERPEM simulation of the electric field amplitude vs. distance radiated by a HPEM mesoband source at center frequency 350 MHz and horizontal polarisation. The radiated peak field was normalized to 1 MV/m (pk-pk/2) @ 1m. Propagation parameters: wind velocity: 0m/s (flat surface), salinity: 0.4%, electrical conductivity: 0.625 S/m, dielectric constant 60. Low transmitter heights are preferred for short source-target distances (< 50 meter) and high transmitter heights for large source-target distances (> 50 meter). For comparison, the free space propagation decay (1/r) is also depicted.

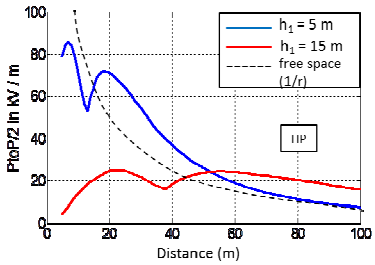

Figure 7. E-Field (pk-Pk/2) vs. distance (HP) for two transmitter heights

3 Summary

TERPEM propagation simulations over water show in general a good agreement with measurements. However, discrepancies between 0 – 5 dB can occur. Constructive superposition can lead to increased field strength levels compared to free space propagation (maximum 6 dB).

For boat stop scenario wave propagation and constructive interference with respect to swell and salinity have been taken into account in order to ensure effective target interaction. First results have been presented for smooth water surface and low salinity water.

References

[1] M. Levy, “Parabolic equation methods for electromagnetic wave propagation”

Stratified ground effects in the land-ocean geoelectric field during magnetic storms

J L Gilbert*

**Metatech Corporation, Goleta,California,USA, james.gilbert@metatechcorp.com*

Abstract

This presentation discusses the enhancement of the geoelectric field on the landward side of ocean boundaries during magnetic storms for layered conductivities. Previous work developed models for homogenous soil and it was found that a simple analytic form was useful for a wide range of cases. This work is extended to layered soils with finite difference methods.

Keywords: Geomagnetically induced current, GIC, magnetic storms, Geomagnetic induction

1 Introduction

In this presentation we will discuss the enhancement of the geoelectric field on the landward side of ocean boundaries during magnetic storms for layered conductivities. In [1] the basic theory was developed for homogenous soil by the use of integral equation techniques and it was found that the enhancement had a particularly simple form for typical land and ocean conductivities and continental shelf slopes. The extension to layered conductivities cannot be made using the same techniques and requires the use of finite difference techniques. The form for the fitting is based on dimensionless forms so that frequency-distance scaling is preserved.

2 The boundary enhancement effect

In [1] it was shown that when the ocean was thick compared to skin depths the surface electric field E_{surf} on the landward side for a uniform exponentially rising magnetic field $H_{inc}\, e^{st}$ was given by Equation (1)

$$E_{surf} = H_{inc}\sqrt{\frac{s\mu_0}{\sigma}} \times\left[\sqrt{\frac{1}{\pi x\sqrt{s\mu_0\sigma}}}e^{-x\sqrt{\mu_0\sigma}} + \mathrm{erf}\left(\sqrt{x\sqrt{s\mu_0\sigma}}\right)\right] \quad (1)$$

where x is the distance landward from the edge of the ocean, σ is the ground conductivity and μ_0 is the magnetic permeability. This solution has the surprising property that the integral of the landward electric field less the field that occurs over homogenous soil has a spatial integral that is independent of frequency and is given by Equation (2)

$$\Delta V = \int_0^\infty dx\,(E_{surf} - \sqrt{\frac{s\mu_0}{\sigma}}H_{inc}) = \frac{H_{inc}}{2\sigma} \quad (2)$$

3 Calculation of stratification effects

When we examine the case where we have a stratified ground with near surface conductivity σ_1 and a different conductivity σ_2 below some depth d, we introduce two additional parameters into the solution. These can be taken to be the ratio of the conductivities $p_1=\sigma_{1/}\,\sigma_2$ and the ratio of the depth d to the skin depth in the upper region given in Equation (3)

$$p_2 = d\sqrt{s\mu_0\sigma_1} \quad (1)$$

The form of the additional voltage should be given in the form given by Equation (3)

$$\Delta V = \int_0^\infty dx\,[E_{surf} - \sqrt{\frac{s\mu_0}{\sigma_1}}g(p_1,p_2)H_{inc}] = f(p_1,p_2)\frac{H_{inc}}{2\sigma_1} \quad (3)$$

where $f(p_1,p_2)$ approaches unity for large values of p_2. Note that the factor f is applied to the enhancement in the upper region and the field far from the interface uses the upper layer impedance multiplied by a function $g(p_1,p_2)$ (which is straightforward) so as to include the effect of both layers. An earlier attempt by the author to examine this behaviour by the same integral equation techniques used to derive Equations (1) and (2) was unsuccessful as the kernels of the integral equations no longer had closed forms. For this reason, we now turn to the use of numerical solution of the fields in two dimensions.

An example of the magnetic field in the two dimensional calculation for a stratified soil is shown in Figure 1. This calculation was performed with the lower layer having a factor of 10 times less conductivity below 50 km.

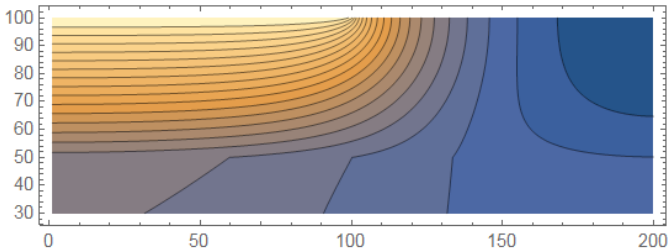

Figure 1. Contour plot of the magnetic field of a calculation with stratified ground conductivity.

and the corresponding plot with a uniform ground conductivity is shown in Figure 2.

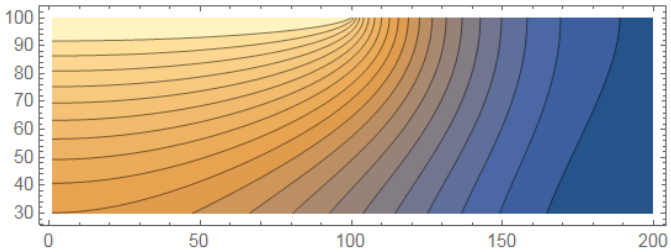

Figure 2. Contour plot of the magnetic field of a calculation with uniform ground conductivity.

Plots of the horizontal electric fields in the two calculations are shown in Figure 3.

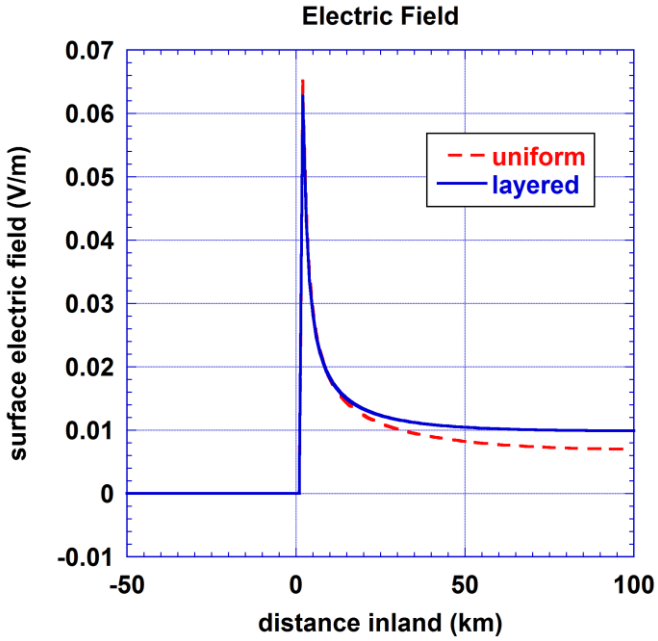

Figure 3. Spatial plots of the surface horizontal electric field.

In the presentation, we will show families of curves for additional cases and an analytic fit to the parameterization.

Acknowledgement

This work was supported by Metatech Corporation under IR&D.

References

[1] J. L. Gilbert, "Modeling the effect of the ocean-land interface on induced electric fields during geomagnetic storms" *Space Weather*, **volume 3**, no 4. S04A03, doi: 10.1029/2004SW000120, 2005

Hypothesis Testing for Verification of Electromagnetic Simulation

William N. Reynolds*, Andrew D. Greenwood†

**Stellar Science Ltd. Co., †Air Force Research Laboratory, Directed Energy Directorate, New Mexico, USA*

Abstract

We present a novel technique for the validation of numerical simulation based on the technique of *Hypothesis Testing*. The approach is based on the idea of stochastically stimulating a simulation by selecting random inputs from a known distribution. With appropriate input distributions, suitable approximations to the simulation outputs can be made. Given these output distributions, quantitative tests can be made of the null hypothesis that the outputs of a baseline simulation are drawn from the same distribution as the outputs from a test simulation. The procedure presents a number of advantages over standard approaches, including the ability to ignore approximation errors while catching verification errors and combining multiple simultaneous verification checks. The technique is demonstrated on a US Government-developed finite-element boundary-integral (FEBI) computational electromagnetics (CEM) code. The approach suffers from the requirement of performing multiple runs of the simulation. Mitigation of this requirement through the use of stochastic inversion and other areas for future study are discussed.

Keywords: V&V, CEM, Hypothesis testing, multiple testing, stochastic inversion.

1 Introduction

Verification of complex numerical simulations presents a number of practical difficulties [1]. One challenge arises when performing numerical comparisons of outputs between a new simulation and some *baseline* source (either an analytic calculation or a known-correct simulation). Typical simulation outputs are approximations to exact solutions; thus, naïve numerical comparison of the outputs is insufficient – values are only approximately the same. A standard means of testing such outputs is *interval testing*, in which values from the test simulation are deemed correct if they fall within an interval $\pm\epsilon$ of the values of the test simulation. The problem with this approach is determining the appropriate values of ϵ, which will depend on the quantity being tested. One approach to address this issue is through the use of *Hypothesis Testing* [2], in which multiple samples are generated from the baseline and test simulation, and statistical tests are performed to see if the tests are identical.

In this work, we extend this approach by carefully monitoring the *effect size* of the test [3]. This extension enables the test to be calibrated to detect errors in outputs of a specified size, while ignoring output differences due to numerical approximation. We further extend the approach using multiple testing methodologies to simultaneously perform multiple verification tests, providing an overall check of a simulation's correctness.

2 Hypothesis Testing

2.1 Testing Samples from Distribution

A classic problem in frequentist statistics is testing whether two samples come from the same statistical distribution. A number of tests have been developed in the last century to test whether this null hypothesis is true or not. These include the Kolmogorov-Smirnov (KS), the Mann-Whitely (or U) test, and the two sample *t*-test [4] [5]. These tests, given a tolerable *false positive* rate, α, give a concrete procedure for determining whether two samples arise from the same distribution. If the null hypothesis is true, the tests will correctly infer this result $1 - \alpha$ percent of the time.

2.2 Verification of CEM Codes

We demonstrate the testing approach on a US Government-developed FEBI CEM simulation code (USCEM). For the test, we use the USCEM to simulate a plane electromagnetic wave incident upon a perfect-electric conducting (PEC) sphere of radius 1M. For input values, we use random wavelengths drawn from a Normal distribution centered at 1M, with a standard deviation (SD) of γ, where γ is a parameter to be calibrated. For a baseline, we use an analytic code based on Mie scattering theory [6]. We collect N samples from the test and baseline code and compute the RCS value [7] on a 100x100 angular grid surrounding the sphere. This gives us 2xN samples at each of the 10,000 grid points. For each pair of samples, we perform a *t*-test, which yields a *p*-value. In this way, we obtain 10,000 *p*-values. We test these values using a standard multiple testing approach [8]. If the null hypothesis is true, namely that the baseline and test code are identical, then these *p*-values will have been generated by a uniform distribution. If we sort these *p*-values and plot them, we will obtain a linear plot if the null hypothesis is true. We then use a Holm step-down procedure to test departure from linearity [9].

2.3 Effect Size Calibration

Standard hypothesis testing controls the rate of false positives, α. Another important error is the possibility of *false negatives.* For this case, an important quantity is the *effect size* [3], a quantity that can be computed from a pair of samples. For the *t*-test, effect sizes below 0.2 are "small" and unlikely to be detected, while effect sizes greater than 0.8 are "large" and likely will not lead to a false positive. A novel aspect of this work is being able to calibrate the effect size

due to the stochastic stimulus such that "true" errors will be detected, while errors associated with approximations of the USCEM to the Mie result will not be. Calibration can be effected by adjusting the SD of the Normal distribution used for the inputs. For small enough input variances, outputs will be approximately Normal-distributed with a SD proportional to the input SD [10].

In Figure 1, we plot the effect size of approximation errors (the blue lines) and of "true" errors (RCS differences of 0.1, the gold lines) as a function of the incident standard deviation (in units of the incident wavelength) for 100 samples. For reference, we also plot "small" and "large" effect sizes. We see that for an input SD of 0.015, effect sizes for the approximation are much smaller than "small", and those for true errors are much larger than large. Thus, tests using this input SD value should detect true errors rather than approximation errors.

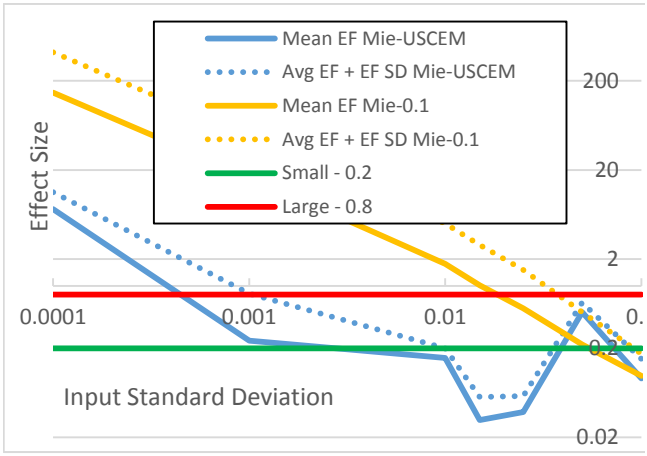

Figure 1. Effect Size as function of input standard deviation

We note that we have not specified a specific rate of false positive, β, since effect sizes will vary over the target; however, the false positive rate for a "large" effect of 0.8, with α=0.05 and 100 samples is $O(10^{-4})$, and our typical effect sizes for "true" errors are greater than "large." Note that the sample size is an additional free variable that could be calibrated to control the effect size. This can be used reduce the number of simulations necessary to run the test.

2.4 CEM Solver Areas Addressed By the Test

Because the USCEM has been applied to plane wave scattering of a PEC sphere, the BI portion of the code, but not the FE portion is exercised. Further, the near-to-far-field transformation to compute RCS has a known smoothing effect on the output data. Further work involves looking at computation of cavity problems to exercise the FE portion of the code, computation of scattering problems using the full FEBI capability of the code, and application to scattered near fields.

3 Challenges and Future Work

As mentioned, we are currently modifying the test to monitor other aspects of the USCEM solver.

The current approach requires multiple simulation runs to conduct the test, but this method can be a disadvantage for computationally-intensive codes. One way to address this concern would be to consider a sample over the surface of the target. The challenge is that this approach would require a non-parametric test, for which effect calibration is not available. A promising approach would be to use stochastic inversion [11] to identify sampling distributions over the surface, which would lead to known output distributions, thus enabling parametric tests.

Acknowledgements

WNR acknowledges the support of the United States Air Force, contract FA9451-14-C-0223.

References

[1] Department of Defense Modeling and Simulation Coordination Office, "Verification, Validation and Accreditation Recommended Practice Guide," 31 January 2011. [Online]. Available: http://www.msco.mil/vva_rpg.html. [Accessed 7 December 2015].

[2] R. G. Sargent, "VERIFICATION AND VALIDATION OF SIMULATION MODELS.," in *Proceedings of the 2011 Winter Simulation Conference*, Phoenix, AZ, 2011.

[3] J. Cohen, Statistical Power Analysis for the Behavioral Sciences, San Diego, CA: Academic Press, 1969.

[4] J. H. McDonald, Handbook of Biological Statistics, Baltimore, Maryland: Sparky House Publishing, , 2014.

[5] R. R. Sokal and F. J. Rohlf, Biometry, San Francisco: W.H. Freeman and Company, 1969.

[6] G. Mie, "Beiträge zur Optik trüber Medien, speziell kolloidaler Metallösungen," *Annalen der Physik*, vol. 30, no. 3, p. 377–445., 1908.

[7] C. A. Balanis, Advanced Engineering Electromagnetics, Wiley, 2012.

[8] R. G. Miller, Simultaneous Statistical Inference, 2nd Ed., New York: Springer Verlag, 1981.

[9] S. Holm, "A simple sequentially rejective multiple test procedure," *Scandinavian Journal of Statistics* , vol. 6, no. 2, pp. 65-70, 1979.

[10] K. O. Arras, "An Introduction To Error Propagation: CY FX CX FX," Autonomous Systems Lab, Institute of Robotic Systems,, Lausanne, 1998.

[11] J. Breidt, T. Butler and D. Estep, "A Measure-Theoretic Computational Method for Inverse Sensitivity Problems I: Method and Analysis," *SIAM J. Numer. Anal.*, vol. 49, no. 5, pp. 1836-1859, 2011.

Software and hardware assessment of FDTD simulations for very large and complex scenes

B. Pecqueux*, P. Leyde*, C. Gonzalez*, J.-P. Adam*

**CEA, DAM, Gramat, France*
jean-pierre.adam@cea.fr

Abstract

This paper presents tools recently developed at CEA/Gramat to analyse the transient EM field on large targets. It focuses on the peripheral software around a FDTD solver : the mesh generation and the result visualisation.

Keywords: FDTD, large simulation, mesh generation, result visualization.

1 Introduction

The Finite-Difference Time-Domain Method (FDTD) is widely used to solve electromagnetic problems. As described in [1], this algorithm can be efficiently implemented on massively parallel computers. An example of such implementation is Gorf3D. It is developed at CEA/Gramat for many years ([2]) and is able to use the computation power of the TERA 100 machine described in [3]. While problems of few billions of cells are routinely solved, the generation of such huge meshes can be challenging. At the other end of the simulation process, while extracting the transient response at a given point of a large structure can be trivial, the visualization of the EM field over the entire target may require a significant amount of computational resources. This kind of output is desirable as it provides a valuable insight into the coupling phenomenon and as it is usually difficult to choose at first sight a point of interest in a complex scene.

2 Method and tools

2.2 Mesh generation

The starting point of the example presented here is an existing city part. The buildings have been scanned with a laser. The obtained cloud of points has been processed into a CAD model. This model was meshed with triangles. The last step was the conversion of this set of triangles into a cartesian grid mesh, also called staircase model. Fig. 1 presents an example of that kind of mesh.

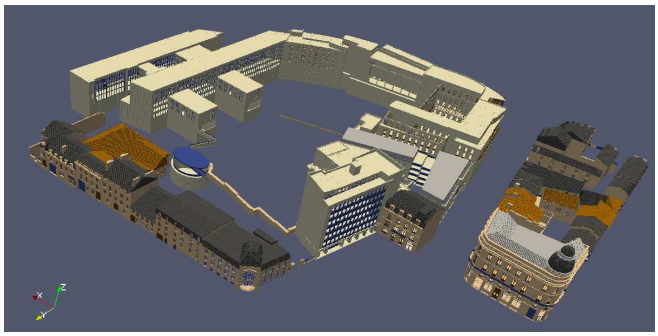

Figure 1. Cartesian mesh of an entire city part. The cell size is 10 cm, resulting in a total of 2 billions of cells.

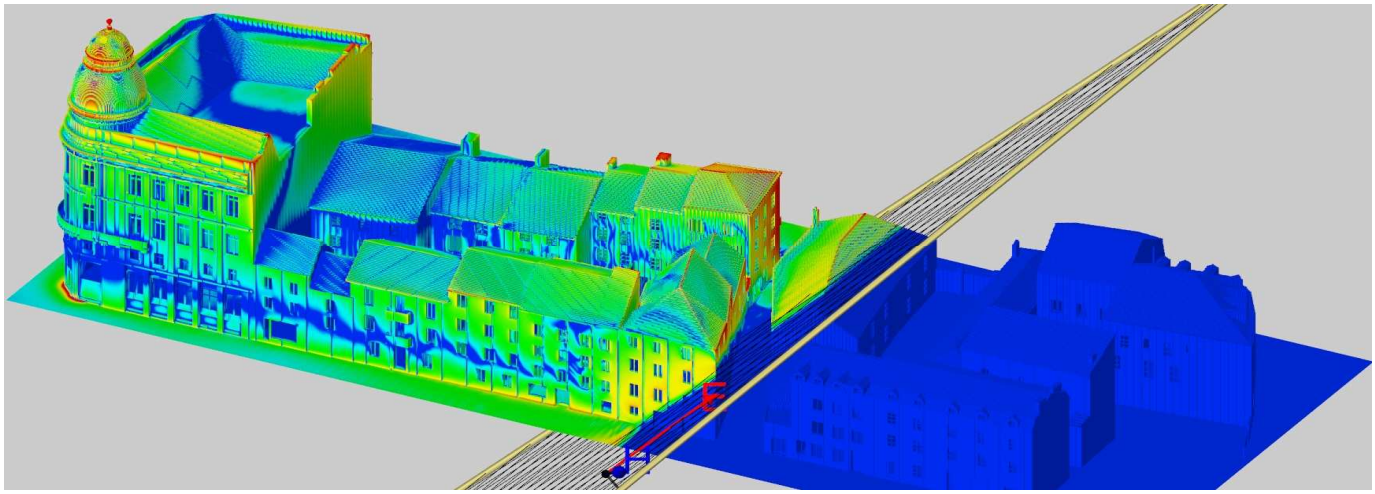

Figure 2. Surface field at a given time step of the propagation of an incident plane wave.

2.2 Result visualisation

An in-house software tool based on VTK [4] has been used to post process the considerable amount of data produced by the FDTD simulation of large objects. As illustrated on Fig. 2, this tool is able to display the transient electromagnetic field over the entire simulated domain, enabling the user to generate a video for example.

3 Example of results

The described software toolchain can be applied in many ways by the end user. A simple example of results is presented on Fig. 3. It compares the coupling of an element of the complex scene, extracted from its actual environment. The comparison is useful to estimate the shadowing or enhancing effects of the surrounding buildings and to decide if the study can be simplified into the building alone.

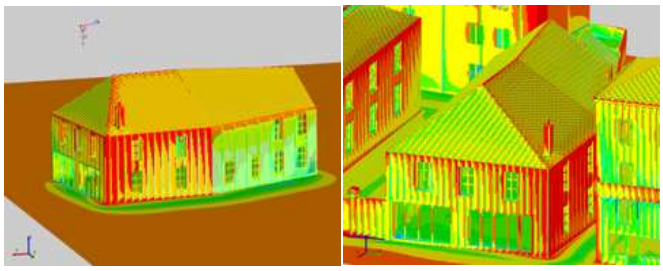

Figure 3. Maximal surface field on the same building alone (left) and within its actual environment (right).

Acknowledgements

This study has been carried out for the DGA.

References

[1] Allen Taflove, Computational Electrodynamics, The Finite-Difference Time-Domain Method, Artech House, 1995.

[2] L. Morel, B. Pecqueux, R. Vézinet, ”Notice d’installation et d’utilisation de la version exportable du code GORF3D”, Note interne CEG I94-28, October 1994.

[3] http://www-hpc.cea.fr/en/complexe/pages/29-T100.htm

[4] Visualization Toolkit (VTK): http://www.vtk.org/

JEMS-FDTD and Its Applications in Electromagnetic Scattering and Coupling by Large Complex Object

Li Hanyu *, Zhou Haijing*, Bao Xianfeng †

** Institute of Applied Physics and Computational Mathematics, Beijing, China, 100094*
† Software Center for High Performance Numerical Simulation, CAEP, Beijing, China,100088

Abstract

A massively parallel electromagnetic field simulation software named JEMS-FDTD (J Electromagnetic Solver-Finite Difference Time Domain) is presented. JEMS-FDTD uses FDTD-related methods to solve the Maxwell equations in time domain. JEMS-FDTD has the capability of solving electric-large problems of thousands wavelengths with hundreds of billions mesh cells, which makes it a suitable tool to simulate electromagnetic scattering and coupling by large complex objects. In this paper, the characteristics of JEMS-FDTD is discussed, as well as some numerical examples.

Keywords: computational electromagnetics; FDTD; parallel computation; coupling, scattering

1 Introduction

The FDTD method, which is a simple and direct way to solve the transient Maxwell equations, has been widely employed to solve various electromagnetic problems for decades. FDTD requires a finer mesh compared to other numerical methods such as Method of Moment, thus limits its application. However, as the development of parallel computation, FDTD solving electric-large problems becomes possible.

2 A Brief introduction to JEMS-FDTD

We have been developing a massively parallel electromagnetic field simulation program named JEMS-FDTD [1-2]. JEMS-FDTD is a universal massively parallel electromagnetic field simulation program, which is capable of simulating transient high frequency electromagnetic problems, such as transmitting, propagation, scattering and coupling. JEMS-FDTD adopts FDTD-related methods, including conventional FDTD method, high-order FDTD, AMR-FDTD. JEMS-FDTD is designed oriented to using numerous processors on HPCs (High Performance Computers), with MPI (Message Passing Interface) and OPENMP (Open Multi-Processing) hybrid-parallel techniques.

Usually, there are two key issues constraining the parallel computation performance, the load balance and computer memory access latency. JEMS-FDTD adopts a four-level *cell-patch-level-domain* hierarchical data structure strategy to deal with these problems. When performing computation, all the data on the currently computing patch can be loaded into CPU's data cache from RAM (Random Access Memory) by choosing the patch size slightly smaller than data cache, thus fragmentally RAM access is avoided, and memory access efficiency is guaranteed. For load balancing, JEMS-FDTD periodically checks the computation load on each processor, translates patches from heavy-load processors to light-load ones to obtain a balanced computation load distribution.

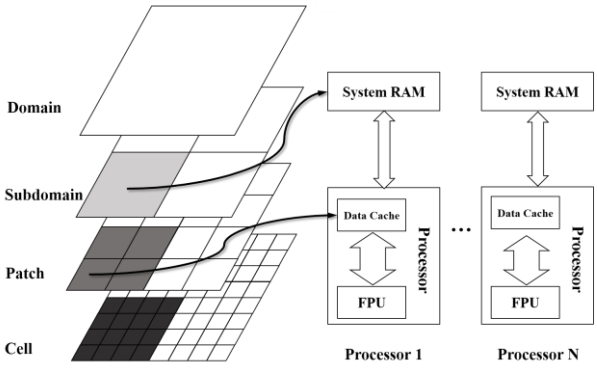

Figure 1. Four-level hierarchical data structure strategy.

An efficiency test is performed on TIANHE-2 super computer. The test started from one computation node (24 processors) and successfully scaled to 8192 nodes (196,608 processors) with parallel efficiency of 30%.

3 Validation of JEMS-FDTD

To verify JEMS-FDTD, the coupled fields of a metallic enclosure are measured and compared to results computed by JEMS-FDTD. The enclosure is a rectangular metallic box with slots and apertures on the side walls. The box is radiated from each direction from 0.3GHz to 2.5GHz. A wideband sensor is located at the geometric centre of the box to measure the electric field. Some results are presented.

The FSV (Feature Selective Validation) method [3] and criteria are used to assess the results of computation. The ADM (Amplitude Difference Measure), FDM (Feature Difference Measure) and GDM (Global Difference Measure) value is 0.419, 0.334, 0.588 respectively. The GDM grade is 4, which means *fair* according to IEEE std. 1597 [4].

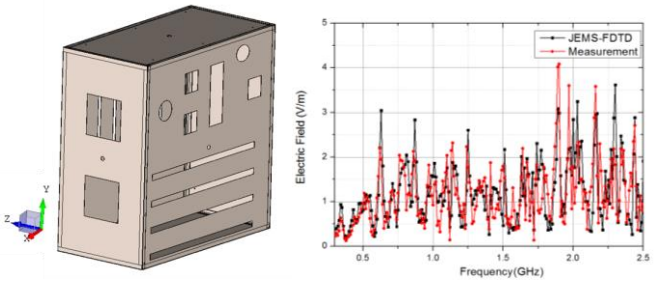

Figure 2. Diagram of the enclosure and electric field at the geometric center, the propagation and polarization of the incident wave is -X and Y.

4 Applications in Large Complex Object Scattering and Coupling

4.1 Electromagnetic pulse coupled by building

In this example, the scattering and coupling by a real building is simulated. The dimension of the building is 15m × 7.5m × 13.27m. The electric properties of materials are obtained by field test. The incident wave is set to a wideband pulse from 1 to 3 GHz. A fine mesh of 12.5 billion cells is generated to describe this model. The computation takes approximate 30 hours on 5760 processors.

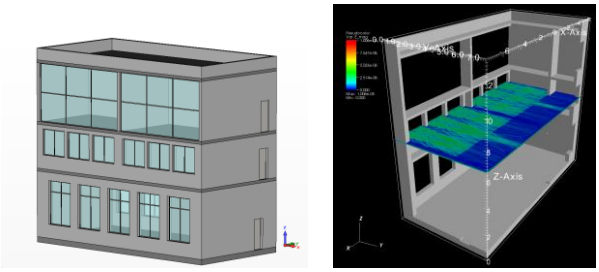

Figure 3. Building model and electric field distribution on horizontal slice.

4.2 Electromagnetic pulse coupled by aircraft

Aircraft may face extreme electromagnetic environment e.g. lighting, HIRF (High Intensity Radiated Field) during the flight. To analyse the electromagnetic environmental effect on avionic system, the distribution of fields or currents coupled by the aircraft is needed [5]. In this example, the coupled filed of a middle size cargo aircraft impacted by electromagnetic pulse is computed. The aircraft is modelled with full size of 35 meters in length, 38 meters in width and 12 meters in height. A non-uniform fine mesh of 29.6 billion cells is generated to represent the complex structure. A Gaussian pulsed plane wave with frequency range of 0.5-1.5 GHz hits the aircraft right from the nose. JEMS-FDTD computes this model with 10800 processors in approximate 500 minutes. The computation provides the transient electric field distribution of coupled and scattered by the aircraft.

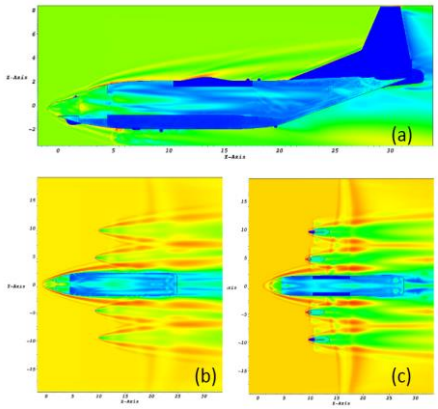

Figure 4. Electric field distribution at (a) y=0 m, (b) z=0 m, (c) z=1 m

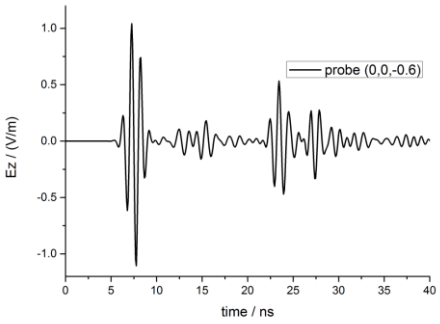

Figure 5. Transient electric field at position of (0, 0 -0.6)

References

[1] Li Hanyu, Zhou Haijing, Liao Cheng, "Parallel performance test of JEMS-FDTD on massively parallel processor", *High Power Laser and Particle Beams*, Vol. 23, pp. 3003-3006, 2011.

[2] Hanyu. Li, Haijing Zhou, et al., "Massively parallel FDTD program JEMS-FDTD and its applications in platform coupling simulation", *Electromagnetic Compatibility (EMC Europe), 2014 International Symposium on, Gothenburg*, 2014, pp. 229-233.

[3] Duffy, Alistair P., et al., "Feature selective validation (FSV) for validation of computational electromagnetics (CEM). part I-the FSV method", *Electromagnetic Compatibility, IEEE Transactions on* 48.3 (2006): 449-459.

[4] *IEEE Standard for Validation of Computational Electromagnetics Computer Modeling and Simulations*, IEEE Std. 1597.1, 2008.

[5] Perrin E., Tristant F., et al., "A 3D model to compute lightning and HIRF coupling effects on avionic equipment of an aircraft", *Proc. ESA Workshop on Aerospace EMC*, Venice, 2012.

The implementation of CPML absorbing boundary for split-field radial point interpolation meshless method

Hui Zhu, Cheng Gao, Hai-lin Chen

PLA University of Science and Technology, Nanjing, China, zhuhuiblog@gmail.com

Abstract

The convolutional perfectly matched layer (CPML) can truncate the computational domain and efficiently absorb outgoing electromagnetic waves. This paper introduces the implementation of CPML for the split-filed radial point interpolation meshless (RPIM) method. Numerical example is designed to verify the effectiveness of this absorbing boundary condition.

Keywords: Periodic structures, perfectly matched layer (PML), radial point interpolation meshless method (RPIM), split-field method.

1 Introduction

RPIM method [1-3] falls into the category of meshless method, which means that this method does not need to deal with mesh topology. Instead of using various cells in those mesh-based methods, scattered nodes are employed in this method to approximate a computational domain. Thus complex geometries can be modeled more accurately than traditional methods such as finite difference time domain (FDTD) and finite element method (FEM). Another advantage of this method is that the time-consuming mesh-generating process is removed, which will accelerate simulations.

The analysis of periodic structures, such as metamaterials, antenna arrays, and frequency selective surface (FSS), have increasingly attracted the interest of researchers. In our previous work [3], a split-field RPIM method is proposed to analyze periodic structures at oblique incidence. In this method, the time delay in the transverse plane is removed by field transformation [4]. Then the split-field technology [5] is used to solve the transformed equations. In addition, The periodic boundary condition (PBC) is employed to characterize the periodicity, thus only one unit cell is required to simulate the whole structures.

CPML can truncate the computational domain and efficiently absorb outgoing electromagnetic waves [6]. Though CPML is used in [3] to simulate open regions, the implementation is not introduced. In this paper, we will details the implementation of CPML for the split-field RPIM method.

2 Formulation

In linear, isotropic, nondispersive, and lossless media and the stretched coordination system, the transformed Maxwell's equations [4] are given in stretched coordinate system as

$$j\omega\varepsilon\frac{\mu_r}{c}Q_{xa}=-\frac{1}{s_y}\frac{\partial P_z}{\partial y} \tag{1a}$$

$$j\omega\varepsilon\frac{\mu_r}{c}Q_y=\frac{1}{s_x}\frac{\partial P_z}{\partial x} \tag{1b}$$

$$j\omega\varepsilon\frac{\varepsilon_r}{c}P_{za}=\frac{1}{s_x}\frac{\partial Q_y}{\partial x}-\frac{1}{s_y}\frac{\partial Q_x}{\partial y} \tag{1c}$$

$$Q_x=Q_{xa}+\frac{\sin\varphi}{\mu_r}P_z \tag{1d}$$

$$P_z=P_{za}+\frac{\sin\varphi}{\varepsilon_r}Q_x \tag{1e}$$

where $s_i=\kappa_i+\sigma_i/\left(\alpha_i+j\omega\varepsilon_0\right), i=x,y,z$.

The time-domain nature of the method requires that Equation (1) should be transformed to time domain, which will lead to the computation of convolution.

$$\frac{\mu_r}{c}\frac{Q_{xa}}{t}=-\bar{s}_y*\frac{\partial P_z}{\partial y} \tag{2a}$$

$$\frac{\mu_r}{c}\frac{Q_y}{t}=\bar{s}_x*\frac{\partial P_z}{\partial x} \tag{2b}$$

$$\frac{\varepsilon_r}{c}\frac{P_{za}}{t}=\bar{s}_x*\frac{\partial Q_y}{\partial x}-\bar{s}_y*\frac{\partial Q_x}{\partial y} \tag{2c}$$

where $\bar{s}_i$ is the inverse fourier transform of s_i^{-1} and satisfies

$$\bar{s}_i\left(t\right)=F^{-1}(\frac{1}{s_i})=\frac{\delta\left(t\right)}{\kappa_i}-A_i e^{-\beta_i t}U\left(t\right), i=x,y,z \tag{3}$$

Here, $A_i=\sigma_i/\left(\kappa_i^2\varepsilon_0\right)$ and $\beta_i=\sigma_i/\left(\kappa_i\varepsilon_0\right)+\alpha_i/\left(\varepsilon_0\right)$.

Substitution of (3) into (2) gives

$$\frac{\mu_r}{c}\frac{Q_{xa}}{t}=-\frac{1}{\kappa_y}\frac{\partial P_z}{\partial y}+\psi_{xz} \tag{4a}$$

$$\frac{\mu_r}{c}\frac{Q_y}{t}=\frac{1}{\kappa_x}\frac{\partial P_z}{\partial x}-\psi_{yz} \tag{4b}$$

$$\frac{\varepsilon_r}{c}\frac{P_{za}}{t}=\frac{1}{\kappa_x}\frac{\partial Q_y}{\partial x}-\frac{1}{\kappa_y}\frac{\partial Q_x}{\partial y}-\psi_{zy}+\psi_{zx} \tag{4c}$$

where ψ is auxiliary variable introduced to deal with convolution.

By employing the space interpolation scheme in [1] for fields and their derivatives, the updating equations can be expressed as the first sub-step

$$Q_{xa,i}^{n+1/2} = Q_{xa,i}^{n-1/2} + \frac{c\Delta t}{\mu_r}\left(-\frac{1}{\kappa_{y,i}} \sum_j P_{z,j}^n \partial y \Phi_j + \psi_{xz,i}^n \right) \quad (5a)$$

$$Q_{y,i}^{n+1/2} = Q_{y,i}^{n-1/2} + \frac{c\Delta t}{\mu_r}\left(\frac{1}{\kappa_{x,i}} \sum_j P_{z,j}^n \partial x \Phi_j - \psi_{yz,i}^n \right) \quad (5b)$$

$$P_{za,i}^{n+1/2} = P_{za,i}^{n-1/2} + \frac{c\Delta t}{\varepsilon_r}\left(\begin{array}{l} \frac{1}{\kappa_{x,i}} \sum_j Q_{y,j}^n \partial x \Phi_j - \psi_{zy,i}^n \\ -\frac{1}{\kappa_{y,i}} \sum_j Q_{x,j}^n \partial y \Phi_j + \psi_{zx,i}^n \end{array} \right) \quad (5c)$$

$$Q_{x,i}^{n+1/2} = \mu_r \varepsilon_r A Q_{xa,i}^{n+1/2} + \varepsilon_r A \sin\varphi \sum_j P_{za,j}^{n+1/2} \Phi_j \quad (5d)$$

$$P_{z,i}^{n+1/2} = P_{za,i}^{n+1/2} + \frac{\sin\varphi}{\varepsilon_r} \sum_j Q_{x,j}^{n+1/2} \Phi_j \quad (5e)$$

and second step

$$Q_{xa,i}^{n+1} = Q_{xa,i}^{n} + \frac{c\Delta t}{\mu_r}\left(-\frac{1}{\kappa_{y,i}} \sum_j P_{z,j}^{n+1/2} \partial y \Phi_j + \psi_{xz,i}^{n+1/2} \right) \quad (6a)$$

$$Q_{y,i}^{n+1} = Q_{y,i}^{n} + \frac{c\Delta t}{\mu_r}\left(\frac{1}{\kappa_{x,i}} \sum_j P_{z,j}^{n+1/2} \partial x \Phi_j - \psi_{yz,i}^{n+1/2} \right) \quad (6b)$$

$$P_{za,i}^{n+1} = P_{za,i}^{n} + \frac{c\Delta t}{\varepsilon_r}\left(\begin{array}{l} \frac{1}{\kappa_{x,i}} \sum_j Q_{y,j}^{n+1/2} \partial x \Phi_j - \psi_{zy,i}^{n+1/2} \\ -\frac{1}{\kappa_{y,i}} \sum_j Q_{x,j}^{n+1/2} \partial y \Phi_j + \psi_{zx,i}^{n+1/2} \end{array} \right) \quad (6c)$$

$$Q_{x,i}^{n+1} = \mu_r \varepsilon_r A Q_{xa,i}^{n+1} + \varepsilon_r A \sin\varphi \sum_j P_{za,j}^{n+1} \Phi_j \quad (6d)$$

$$P_{z,i}^{n+1} = P_{za,i}^{n+1} + \frac{\sin\varphi}{\varepsilon_r} \sum_j Q_{x,j}^{n+1} \Phi_j \quad (6e)$$

where the subscript i represents the i -th node and j stands for the j -th node in its support domain.

The auxiliary ψ should be updated at each sub-step. The updating equation for ψ_{xz} is

$$\psi_{xz,i}^{n+1/2} = b_{z,i} \psi_{xz,i}^{n} + a_{z,i} \sum_j P_{z,j}^{n+1/2} \partial y \Phi_j \quad (7e)$$

$$\psi_{xz,i}^{n+1} = b_{z,i} \psi_{xz,i}^{n+1/2} + a_{z,i} \sum_j P_{z,j}^{n+1} \partial y \Phi_j \quad (7e)$$

where

$$b_{z,i} = e^{-\left(\sigma_{z,i}/\kappa_{z,i} + \alpha_{z,i}\right)\left(\Delta t/\varepsilon_0\right)} \quad (8)$$

$$a_{z,i} = \frac{\sigma_{z,i}}{\sigma_{z,i}\kappa_{z,i} + \kappa_{z,i}^2 \sigma_{z,i}} \left(b_{z,i} - 1 \right) \quad (9)$$

Here, $\kappa_{z,i}$ and $\sigma_{z,i}$ varies with polynomial grading, as is used in FDTD method [5]. The updation of other auxiliary variables at each sub-step can be achieved in a similar way.

2 Numerical example

An electromagnetic bandgap (EBG) structure is designed to validate the effectiveness of CPML. The geometry of this structures is depicted in the left part of Fig. 1, with $a = 2\text{mm}$ and $b = 9\text{mm}$. The relative permittivity of the dielectric rods are $\varepsilon_r = 4.2$.

The plane wave is excited via TF/SF boundary and excitation signal is sinusoidal modulated Gaussian pulse. CPML is set at both ends along x-direction P_z field at the observation point is recorded with incident angle $\theta = 30^\circ$. In addition, FDTD with fine mesh is used as reference.

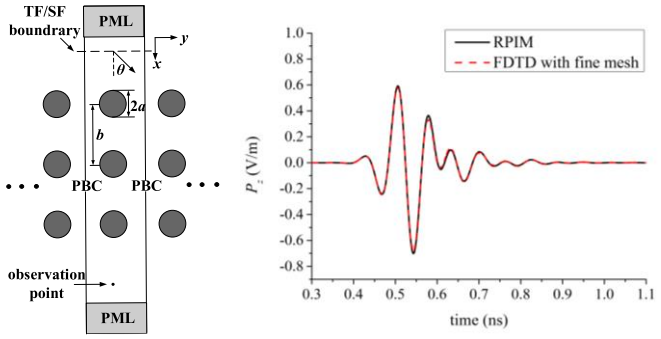

Fig 1. Geometry configuration of the EBG structure and the recorded P_z field at the observation point.

Acknowledgements

The authors would like to acknowledge the financial supports for this work by the National Natural Science Fund of China under Grants 51277182 and 51407199.

References

[1] J. G. Wang and G. R. Liu. "A point interpolation meshless method based on radial basis functions", Int. J. Numer. Methods Eng., vol. 54, pp. 1626–1648, (2002).

[2] Y. Yu and Z. D. Chen. "A 3-D radial point interpolation method for meshless time-domain electromagnetics", IEEE Trans. Microw. Theory Techn., vol. 57, no. 8, pp. 2015-2020, (2009).

[3] Hui Zhu, Hailin Chen, Cheng Gao, etc.. "Study of Periodic Structures at Oblique Incidence by Radial Point Interpolation Meshless Method", IEEE Antennas Wireless Propag. Lett., vol. 14, pp. 982–985, (2015).

[4] A. Taflove and S. C. Hagness. "Computational Electrodynamics: The Finite-Difference Time-Domain Method", 2nd ed. Norwood, MA: Artech House, (2000).

[5] J. A. Roden, S. D. Gedney, M. P. Kesler, J. G. Maloney, and P. H. Harms. "Time-domain analysis of periodic structures at oblique incidence: orthogonal and nonorthogonal FDTD implementations", IEEE Trans. Microw. Theory Tech., vol. 46, no. 4, pp. 420-427, (1998).

[6] A. Roden and S. D. Gedney, "Convolution PML (CPML): An efficient FDTD implementation of the CFS-PML for arbitrary media", Microwave and Optical Technology Letters, Vd .27, No. 5, pp. 334-339,

(2000).

Transient Thermal Analysis of MOSFET in Metallic Enclosure Illuminated by Electromagnetic Pulse

Yuna Kim, Jongwon Lee†, Jin Soo Choi†, Doo-Soo Kim†, and Jong-Gwan Yook**

**Dept. Of Electrical and Electric Engineering, Yonsei university, Seoul, Republic of Korea, jgyook@yonsei.ac.kr*
, †Agency of Defense Development, Daejeon, Republic of Korea, jwlee@add.re.kr, jschoi@add.re.kr, dsoo@add.re.kr

Abstract

This paper performs transient thermal analysis of MOSFET installed in multi-layered PCB in metallic enclosure. Firstly, we calculate the waveform of input pulse distorted by resonant characteristics of PCB and enclosure. Then the coupled voltage is assumed to be applied to drain node of MOSFET. Secondly, the amount of induced current is obtained, which enables to generate Joule heat. Based on the analysis of accumulated and radiated heat in the MOSFET, it is possible to predict the effects of external pulse on the device operation by transient thermal process. As a result, it is observed that the electromagnetic pulse on an electric device is significantly weakened by the enclosure and aperture. Despite the low level of coupled voltage, malfunction and breakdown are predicted from numerical investigation because of thermal accumulation.

Keywords: Electromagnetic transients; EMP radiation effects; Printed circuits; Electromagnetic pulse, Thermal analysis

1 Introduction

When electromagnetic pulse is propagated toward the target, devices suffer from undesirable effects due to various transient phenomena. The coupled voltage or current may cause self-heating effect in the device, which increases temperature within it. Thermal response is considered as the key to the analysis of breakdown and malfunction, because the heat radiation takes a long time[1]. After the duration of incident pulse is finished, target is still exposed to the harmful effect of high temperature. It may lead to thermal accumulation that intensifies threats of the external pulse[1-2]. Despite low level of coupling into the device, the accumulated heat may destroy the device.

There are several researches related malfunction and breakdown under the impact of electromagnetic pulse[3-4]. Previous researches have dealt with target device which is directly exposed to the external field. However, devices are usually installed in printed circuit board (PCB) covered by the enclosure. Thus the coupling effect is totally different including levels of voltage and current. Therefore, this study concentrates on the thermal analysis of MOSFET with the transient voltage response distorted by the structures of PCB and enclosure.

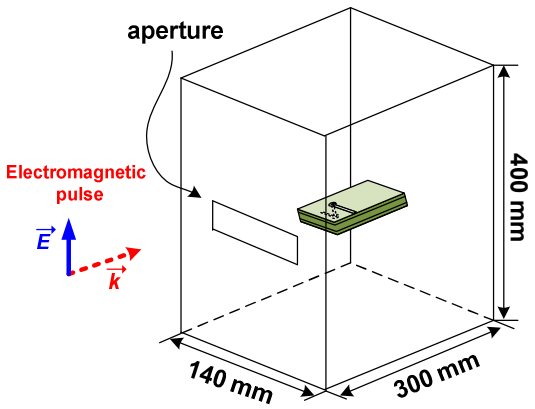

Figure 1. Multi-layered PCB in metallic enclosure

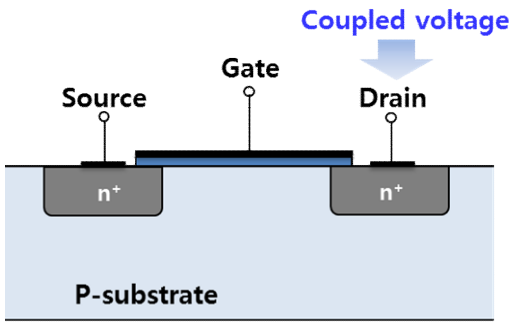

Figure 2. MOSFET with coupled voltage to drain

2 Analysis target

In figure 1, metallic rectangular enclosure with aperture contains multi-layered PCB that consists of 6 layers including two power planes and ground planes. Incident field is assigned as the measurement from previous research[5]. The aperture allows electromagnetic pulse to penetrate and to have influence on the PCB. Because the target PCB has several via-holes, the coupling effect from incident field is enhanced. The coupling tendency strongly depends on the resonance frequencies of PCB and enclosure[6]. For the reason, the transient coupling response is totally distorted. It is assumed that target trace is connected to drain node of MOSFET

installed in the PCB. The coupled transient voltage response induces self-heating effect in the device. The heat can be accumulated within it, which increases internal temperature.

3 Methodology

When the coupled voltage is applied to drain of MOSFET as shown in figure 2, it induces current flow in the device. The current density $\boldsymbol{J}$ generates Joule heat based on Equation (1) with internal electric field $\boldsymbol{E}$. Joule heat Q_{Joule} is considered as the major heat source of MOSFET alongside heat radiated from electron-hole recombination process. Q_{recom} . With electromagnetic pulse coupling, Joule heat is the most influential factor on total heat source Q_{total} . The heat source is constituted into Equation (3), which describes the heat transfer in solid:

$$\boldsymbol{E} \cdot \boldsymbol{J} = Q_{Joule} \tag{1}$$

$$Q_{Joule} + Q_{recom} = Q_{total} \tag{2}$$

$$\rho C_p \frac{\partial T}{\partial t} - \nabla \cdot (k \nabla T) = Q_{total} \tag{3}$$

where ρ is density, C_p is heat capacity, k is thermal conductivity.

4 Summary and conclusion

Time-varying coupling characteristics are investigated when electromagnetic pulse propagates toward a MOSFET installed in multi-layered PCB in metallic enclosure. Figure (3) represents the incident electric field measured in previous experimental research[5]. As shown in figure (4), the calculation result reveals that the level of incident wave drops sharply because of the shielding effect of enclosure and aperture. Simultaneously, the shape of pulse is completely distorted by the resonance characteristics of the structure. At the same time, the duration of the harmful effect is prolonged. The coupled voltage is assumed to be applied to the drain of MOSFET, which causes current flow. In figure (5), it is observed that thermal accumulation leads to high temperature within the device. When the temperature exceeds 450℃, thermal breakdown occurs. Consequently, thermal process intensifies the threat of voltage coupling with relatively low amplitude.

Acknowledgements

This work was supported by Agency for Defense Development, Daejeon, Republic of Korea

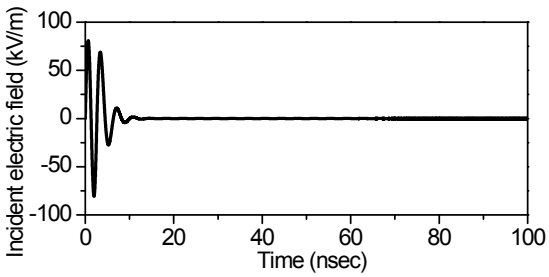

Figure 3. Incident electric field toward target

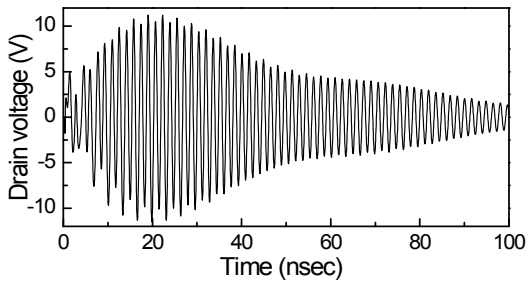

Figure 4. Transient voltage coupled to drain

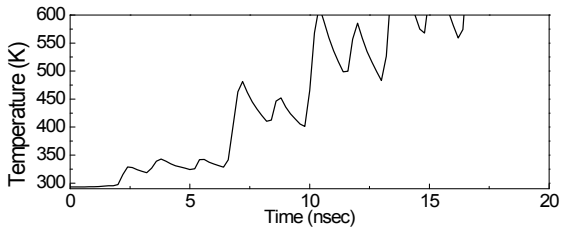

Figure 5. Temperature in MOSET

References

[1] Z. Ren, W.-Y. Yin, Y.-B. Shi, and Q. H. Liu, "Thermal accumulation effects on the transient temperature responses in LDMOSFETs under the impact of a periodic electromagnetic pulse," *Electron Devices, IEEE Transactions on*, vol. 57, pp. 345-352. (2010)

[2] S. V. Georgakopoulos, C. R. Birtcher, and C. A. Balanis, "HIRF penetration through apertures: FDTD versus measurements," *IEEE Transactions on Electromagnetic Compatibility*, vol. 43, no. 3, pp. 282–294, Aug. (2001)

[3] Hwang, Sun-Mook, Joo-Il Hong, and Chang-Su Huh. "Characterization of the susceptibility of integrated circuits with induction caused by high power microwaves." *Progress In Electromagnetics Research 81*, pp. 61-72. (2008)

[4] Camp, M., H. Garbe, and F. Sabath. "Coupling of transient ultra wide band electromagnetic fields to complex electronic systems." *IEEE international symposium on electromagnetic compatibility*, vol. 2. (2005)

[5] J. Ryu and J. Lee, "An integrated antenna-source system of very high ultra wide-band gain for radiating high-power wide-band pulses," *Plasma Science, IEEE Transactions on,* vol. 40, pp. 1019-1026. (2012)

[6] Yuna Kim, Jin-Kyoung Du, Se-Young Hyun, Jong-Gwan Yook, Jongwon Lee, and Jin Soo Choi, "Transient Voltage Responses of Multilayered PCBs in Metallic Enclosure Illuminated by Periodic Electromagnetic Pulse." *Asia Electromagnetics International Symposium* (2015)

Car-stopping concept based on an airborne HPM source

F. Christophe, D. Prost, L. Guibert, C. Martel, J-P. Parmantier*

**ONERA, France, jean-philippe.parmantier@onera.fr*

Abstract

This paper describes a study carried out in the frame of the "Aeroceptor" project in order to stop a car with an EM source installed onboard an UAV. The paper describes the different steps of the study in order to design the source. First a susceptibility analysis has been carried out in MSRC on a fuel injection system alone in order to assess orders of magnitude and waveforms required to induce vulnerability. Then transfer functions have been assessed in order to evaluate suitable levels to be generated by the EM source at car-engine level. Finally the source was designed taking into account operational and installation constraints on a large size UAV. Demonstration of the vulnerability of the car has been made on ground with an equivalent waveform delivered by a laboratory source connected to a purposely designed antenna.

Keywords: HPM, Car-stopping, Car ignition system

1 Introduction

This study has been carried out from 2012 to 2015 in the frame of the "Aeroceptor" project of the FP7 security call of the European Commission (http://www.aeroceptor.eu/). The goal of this still running project is to investigate several techniques to stop a fast-moving vehicle using specific payloads embarked onboard a UAV (nets, painting, electronic nails…). In this approach the UAV offers several advantages in terms of pursuit and agility for positioning the UAV with respect to a fast-moving target. Especially, High Power Microwave was considered as a potential device because of its capability to trigger interference on the car electronic equipment. In the project, the objective was limited to the design of the source and the demonstration of its effects in laboratory conditions.

2 EM susceptibility analysis

At a first step the EM susceptibility analysis of the ignition system was studied. A whole system was thereby tested inside ONERA's 30 m^3 Mode Steering Reverberating Chamber (MSRC) in Toulouse, France with CW pulses of various repetition rates and duration, between 100 MHz and several GHz. The activity of the engine control unit and the various error messages were monitored. Susceptibility proved to essentially depend on the amplitude of the EM field generated in the chamber. Most serious errors were obtained under 1 GHz range with field levels of some 100 V/m but anticipation of the design of the source to be embarked on a drone implied considering effects at higher frequencies. Hopefully, triggering of errors was observed above 1 GHz but required larger EM field amplitudes of some kV/m.

The transfer function of the car body was then assessed and open area tests carried out at INTA laboratory (Spain) resulted in a 15 dB averaged attenuation under the car bonnet. Effect tests carried out in INTA's 60 m^3 MSRC also demonstrated the strong influence of the car attenuation since no reproducible effect could be observed without leaving the car's bonnet open with the sources available at the time of the test.

2 EM source design

Weight and volume constraints for installation onboard a UAV led to the choice of a S-band magnetron solution delivering peak power in the MW range. Weight of the full payload including modulator, antenna, radome and positioning motor was estimated at 120 kg in total and was considered as acceptable for currently available large-size rotary wing UAVs (6-8 meters long). Specific attention was also paid to the antenna design: a slotted waveguide array provided the required illumination spot with fair efficiency, sidelobe control and peak power handling (Figure 1).

Figure 1The airborne HPM concept and live demonstration of effects

3 EM effect demonstration

Demonstration of effects expected with the amplitude, position and distance of the source with respect to the car was made at DGA-TA (France) using their laboratory high peak power amplifier and the slotted waveguide array antenna specifically designed for the application (Figure 1). The test confirmed the amplitude threshold required in the S-band to obtain definitive car stopping and not only transient errors.

Acknowledgements

This work has received funding from the European Union's Seventh Programme for research, technological development and demonstration under grant agreement No 285144

Generation dependence of ICT device IEMI vulnerability

C. Adami, B. Jörres, M. Jöster, T. Pusch, M. Suhrke, A. Taenzer*

**Fraunhofer INT, Euskirchen, Germany, thorsten.pusch@int.fraunhofer.de*

Abstract

Immunity of electronic devices against (I)EMI may be subject to generational changes since baseline technologies constantly evolve. We submitted mobile phones from time frames spanning sixteen years in total as well as two succeeding generations of tablet computers to HPM pulses in order to probe their robustness. Such devices are widely used in critical infrastructures, thus risking to present targets for IEMI attacks. While rising device complexity and miniaturization may imply problems, average immunity of newer devices has in parts even improved, possibly due to inner EMC concerns.

Keywords: IEMI, HPM, susceptibility, cell phone, tablet.

1 Introduction

Critical infrastructure operation relies in many parts on modern communication technology, while device functionality rapidly evolved over the last decades. In practice, e.g. industrial SCADA systems are controlled by tablet-like devices, fire fighters resort to smartphone apps helping to forecast propagation of noxious gas clouds, while the military procures commercial-off-the-shelf hardware in order to provide soldiers with accrued situational awareness. We set out to investigate what effects evolutionary steps in design and technology might have on the vulnerability of such systems against IEMI, more specifically High Power Microwave (HPM) exposure.

In this vein, we identified a few development areas where important changes occurred over the last few years:

- Device functionality is continuously added upon
- Hardware and IC structures are shrinking
- Touchscreen interfaces replace mechanical keys
- Basic wireless network technology is supplemented by new standards (3G, 4G, etc., as well as 5 GHz WiFi), increasing the number of frequency bands
- Globalized markets call for universal hardware solutions, operational in all local frequency bands

2 Test devices and experimental programme

Our approach to Device Under Test (DUT) selection has been the following: Nine mobile phones from manufacturing years 1997-2000 had previously been tested onsite according to our standard methodology, featuring just 2G mobile network technology. We decided to make a comparison with a similar batch of contemporary devices, specifically subsequent hardware generations of medium-class smartphones dating from 2012/13. These operate on additional frequency bands, pertaining to 3G and WiFi networks as well as satellite navigation services. We included tablet computers as well, the lines being blurred between device categories. Some of these 2013/14 specimen include 4G technology. All in all, we started our investigations with at least 5 devices in each group.

We performed vulnerability tests on all DUT within a tapered open TEM waveguide, test frequencies ranging from 150 MHz to 3450 MHz. Pulsed signals of 1 µs length and 1 kHz repetition rate were applied, the field strength ranging well above standard EMC. We recorded failure thresholds as evidenced under monitoring during a power ramp.

3 Results and discussion

We observed some instances of permanent damage, almost universally tied to front door coupling, i.e. the test frequency lying in one of the communication bands. The touch screen as input interface has proven a weak spot on modern devices, many phantom touches were observed. With the tablets, significant failure clustering in frequency ranges delimited by basic enclosure resonances could be observed.

In general, the newer phones performed at least on par, if not better than the older ones when averaging over well-defined frequency bins, compare Fig.1. We conclude that design measures meant to improve inner EMC and being imperative due to the plethora of supported (and surrounding) wireless services possibly account for this effect, as evidenced by a particular robustness *within* communication bands. Above 2.5 GHz, the tablet devices were less immune on average than the other two device groups.

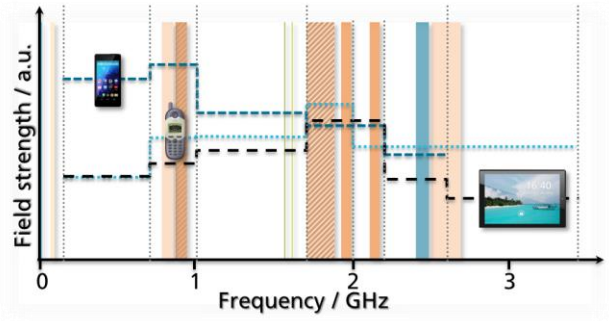

Figure 1. Failure thresholds averaged over bins covering in-band and out-of-band frequencies.

Further investigations into additional device generations provide even deeper insight into generation dependency of IEMI susceptibility.

E-learning tool for introduction to IEMI risk and techniques for mitigation

J Godø, I Junqua* [†]

**Forsvarsbygg, Norway, jostein.godo@forsvarsbygg.no, [†]Onera, France, Isabelle.Junqua@onera.fr*

Abstract

The HIPOW project has studied threats and vulnerabilities of critical infrastructure concerning High Power Microwaves threats. Multiple reports have been written, dealing with different aspects of the problem.

In many cases, people responsible for security of critical infrastructure are not familiar with electromagnetic threats. Reading all the reports from the project would not be an easy introduction to the theme. Presenting the basic information in an e-learning tool gives the possibility to present information in an easy accessible way, and at the same time provide the possibility for the more interested or sceptical reader to find more detailed information.

Keywords: Education, IEMI.

1 Introduction

Security officers with the responsibility to handle a broad variety of threats may find the threat from electromagnetic sources somewhat exotic. The basic understanding of other physical threats, like bombs and other weapons are more easily pictured. Although these threats also require proper understanding in order to do correct design, dimensioning and maintenance of protective measures. This course is an attempt to give a basic understanding of the electromagnetic threat to professionals dealing with other threats.

2 The course

The course presented here is an introduction to IEMI, which attempt to cover many aspects of IEMI threats and mitigation. Some external links in the course can give quite detailed information. In some cases the links will help the reader to find additional information on his own. Other issues are more briefly explained.

The various parts of the course can be useful when assessing the threat, others for deciding location of the facility or specific parts of the installation. A major part of the course is technical solutions to protection. Detailed design will require more detailed knowledge which can be found in other guidelines or handbooks.

The course is at present time divided in 9 sub chapters. Fig. 1 show a screen shot of a page in the course, where you can see the list of chapters on the left side. Depending on your position, some chapters may be less interesting than others.

The first chapters establish the threat, explaining why high power electromagnetics is interesting as a weapon, their effects onto potential targets. One can also find a link towards guidelines for human exposure. A chapter is also dedicated to risk analysis. The last chapters are concerned with how to protect your assets against the threat and maintenance of the protection. Different approaches, which can be combined, are explained. In the chapter "Power balance model" a tool, as an excel file, is provided, in order to calculate impact in a building from a threat, or to calculate safety distance for that threat, given a potential external weapon.

Figure 1. Screen shot from e-learning program.

Acknowledgements

Calculation tool for power balance model is developed by Onera.

This work has been carried out in the HIPOW project under the seventh framework programme (grant agreement n° 284802).

Aircraft EMP Hardening in the 21st Century

-- EMP Hardening as a part of an Integrated E3 Design --

William D. Prather

Air Force Research Laboratory, Albuquerque, NM, USA, william.d.prather@ieee.org

Abstract

The EMI/EMC, HIRF, ESD, and Lightning requirements placed on new military and commercial aircraft are significant. Modern aircraft are built around an integrated Electromagnetic Environment Effects (E3) design that can significantly influence the electromagnetic pulse (EMP) hardening, making it more straightforward and less costly than it was when the first EMP-hardened aircraft were built. In addition, tools exist today to measure the hardening components in situ, something that did not previously exist. This paper discusses the hardening standards, test methods, and EMP simulators we have today and their effect on design, verification, and life-cycle maintenance.

Keywords: aircraft, EMP, hardening, integrated design

1 Integrated E3 designs

The external electromagnetic requirements levied on new military and commercial aircraft have significantly increased over the past 40 years. These include EMI/EMC, high intensity radio frequency (HIRF), ESD, and Lightning. As a result, new aircraft designed to meet all of these E3 requirements have a solid foundation upon which to build an EMP hardening design [1-3]. Many of the cable shields, filter boxes, and terminal protection devices are already designed into the airframe, their space and weight already accounted for. *These are needed whether there is an EMP requirement or not*. This is in stark contrast to the 1970s and 1980s, when the cost to EMP harden, test, and maintain an aircraft added substantially to the cost and complexity of the system.

2 Life cycle maintenance

We now have tools available to measure virtually all the hardening features in situ during design, verification and maintenance, including CW illuminators, cable shield and aperture testers, as well as CW fuselage drive and pulse current injection techniques [4]. In addition, much of the maintenance time and cost is mixed in with the rest of the E3 program and does not stand out as something separate.

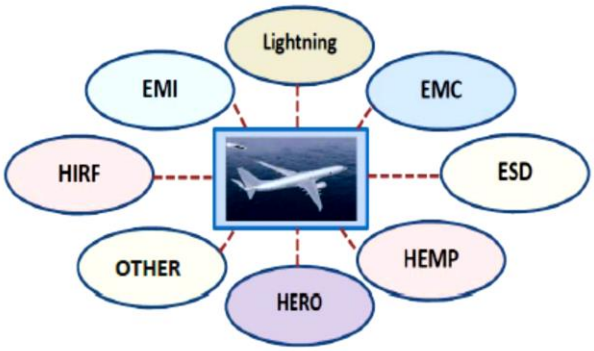

Figure 1. Integrated E3 design.

3 EMP hardening verification

The time and cost required for EMP hardness verification tests today is considerably less than what it was during the 1970s and 80s, and the new Military Standards have made this more straightforward and unambiguous than ever before. There are qualified facilities available, and modern transient digitizers, network analyzers, fiber optics, and computers are faster and much more capable. The test time is shorter, and the recorded data more accurate.

Acknowledgements

This work has been supported by the US Air Force, the US Navy, and the Defense Threat Reduction Agency.

References

[1] MIL-STD-464C, "Electromagnetic Environmental Effects Requirements for Systems," (December 2010).

[2] RTCA/DO-160G, "Environmental Conditions and Test Procedures for Airborne Equipment," (Dec 2010).

[3] "System Lightning Protection," Federal Aviation Regulations (FAR), Code of Federal Regulations (1994).

[4] W.D. Prather, J. Cafferky, L. Ortiz, and J. Anderson, "CW Measurements of Electromagnetic Shields," *IEEE Trans. on EMC, Special Issue on HEMP*, (March 2013).

Mission-Critical Systems Electromagnetic Pulse Immunity Testing For MIL-STD-4023 Shipboard Applications

Walter J. Scott, Engility Corporation
Michael R. Rooney, Defense Threat Reduction Agency

Abstract

U.S military ships designed and constructed to operate during and after exposure to intense electromagnetic fields from a high-altitude nuclear electromagnetic pulse (HEMP) must demonstrate their hardness through a rigorous test program on their mission-critical systems (MCS), subsystems and equipment. The first threat-level, full ship HEMP test was performed on the Anzio in 1993 using the EMPRESS II threat-level HEMP simulator [1]. This test demonstrated that a modern warship design, together with HEMP-specific platform, rack and equipment-level hardening techniques could be used to effectively protect the ship from the adverse effects of an HEMP event. Using the EMPRESS II experience as a baseline, the U.S. Department of Defense's Defense Threat Reduction Agency, in collaboration with the U.S. Navy, has developed protection and testing protocols contained in MIL-STD-4023 HEMP Protection of Military Surface Ships.

Keywords: HEMP, MCS, immunity, ship

1 Introduction

The ability of ships to perform their missions during and after exposure to a high-altitude electromagnetic pulse (HEMP) event is directly dependent on the HEMP immunity of onboard mission-critical systems, subsystems and equipment, and on the HEMP-induced stresses that appear at MCS entry points. A ship can be considered a mobile platform consisting of multiple systems performing critical functions such as navigation, propulsion, communications, detection, weapons deployment and so forth. Systems are generally composed of one or more subsystems, which in turn contain electrical and electronics-based equipment. This paper focuses on necessary and sufficient testing protocols to ensure, with low-risk, the HEMP survivability of MCS onboard ships.

2 Discussion

Ships having a low-risk HEMP survivability requirement are required to demonstrate their operability during and after full-ship exposure to simulated threat-level HEMP fields. For typical U.S. military shipboard applications, below-deck MCS are required to meet MIL-STD-461 CS116 and RS103 testing requirements. Above-deck MCS are required to meet both CS116 and RS105 requirements, since they can be exposed to the full radiated HEMP environment. MIL-STD-461 testing is generally performed on MCS prior to their installation on the ship. For MCS passing these MIL-STD-461 tests, a known operational immunity level, or strength is established. This immunity level can then be used as a strength baseline for comparisons with HEMP-induced conducted currents and radiated electromagnetic (EM) field stresses that the MCS could be subjected to during a high-altitude EMP event as shown in Fig. 1. A margin is

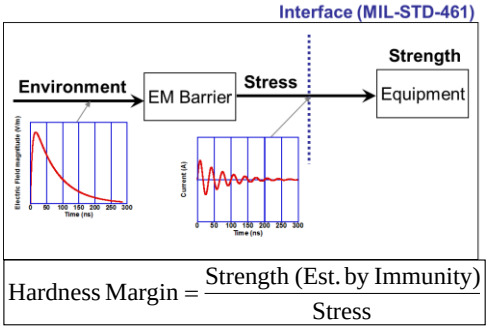

Figure 1. Relationship of margin to stress and strength.

added to the stresses to account for uncertainties in the design and testing processes. Margins can be used as pass/fail criteria to demonstrate that uncertainties have been met (bounded). The nature of these measurement and testing uncertainties will be discussed in detail in the paper presentation

MIL-STD-4023 High-altitude EMP Protection of Military Surface Ships requires that full ships, including all installed MCS, be tested in an HEMP threat-level simulator with illuminating fields representative of the threat environment in MIL-STD-2169 (see Fig. 2).

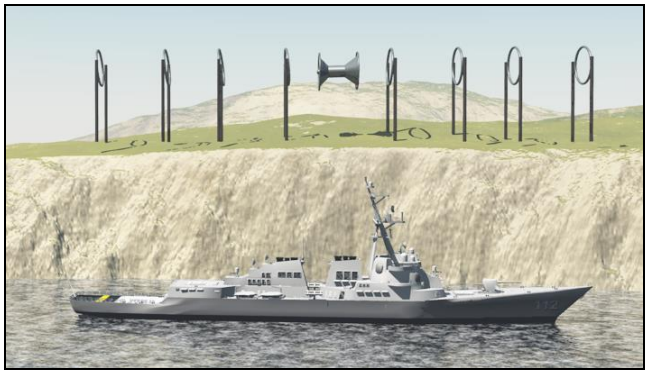

Figure 2. Full ship HEMP test (notional simulator).

A key element of this test is illuminating the full ship while measurements are taken on EMP-induced current stresses at MCS entry points, as well as on localized residual HEMP fields in vicinity of MCS. These conducted stresses are then extrapolated to the MIL-STD-2169 HEMP threat environment to account for any waveform fidelity differences between the simulator and the threat. Next a hardness margin is added to the extrapolated current waveform to account for uncertainties in the ship design and testing processes. (The larger the demonstrated hardness margin, the lower the risk that the MCS will not operate normally both during and after exposure to the HEMP threat.) Finally the measured threat-extrapolated current stress, increased by the hardness margin, is pulse current injected into each operational MCS cable entry point to verify its conducted immunity to the HEMP threat environment. This current is injected at the same MCS location as was used for the MIL-STD-461 CS116 baseline immunity testing. A stress vs. strength comparison is facilitated by first taking the norm attributes of the disparate waveforms as will be discussed in the paper presentation. Confidence in the HEMP survivability of the in-situ MCS is enhanced when the norms of the MIL-STD-461 CS116 waveform (MCS estimated strength) exceed those of the threat-extrapolated injected current waveform plus margin at each MCS port.

3 Summary

This paper provides a test methodology and criteria designed to establish confidence that a ship's mission-critical systems when exposed to a high-altitude electromagnetic pulse event will continue to operate normally during and after the event.

Acknowledgements

The authors wish to thank the members of the MIL-STD-4023 and MIL-STD-3023 Tri-Service Technical Working Groups who contributed to the development of this test methodology.

References

[1] John M. Nelson et al, "USS *Anzio* EMPRESS II Trial," Naval Engineering Journal, May 1996

Protection of Commercial Infrastructure against HEMP and IEMI

Jan Nalborczyk, David Rimmer, William Turner

MPE Ltd, Liverpool, UK, jnalborczyk@mpe.co.uk, drimmer@mpe.co.uk, wturner@mpe.co.uk

Abstract

Most existing HEMP protection is aimed at critical military infrastructure and assumes that the immunity level of equipment to be protected is not known so the maximum level of protection is required. In a more commercial environment, it can be assumed that equipment will already have some immunity due to compliance with EMC standards. Also, some shielding is provided by buildings and equipment housings. It is therefore possible to reduce the requirements for protection of commercial infrastructure compared to military standards. This paper gives examples of how this can be achieved using commercial performance HEMP filters and local supplementary shielding to offer a reduced cost solution.

Keywords: HEMP filters, IEMI, Commercial Infrastructure

1 Introduction

When considering protection of commercial installations, as well as taking into account the intrinsic immunity of the equipment and existing natural shielding, the installation can often tolerate some damage or disruption if normal operation can be restored within an acceptable time period. This means that the protection requirements can normally be reduced compared to military requirements as long as the risk is acceptable. IEC61000-4-24 defines a residual current requirement of 50A max from a power line HEMP filter for critical commercial applications compared to the normal10A for military applications. This means that a lower performance commercial HEMP filter can be used.

2 Protection requirements

It is necessary to protect against both radiated fields and conducted pulses on cables so both shielding and filtering requirements must be addressed at the same time.

2.1 For new build protection of commercial infrastructure

Where several items of equipment need protection, the most cost-effective approach may be to put them all in a single shielded room with filters at each point of entry, in the traditional manner. The shielding need not be to the normal military requirement of 80dB but could be 60dB or even 40dB in less critical applications. A reduced performance HEMP filter can also be used as long as it meets the residual current performance of 50A max (for critical infrastructure applications) as defined in IEC61000-4-24.

2.2 For retrofit or localised protection

For retrofit protection, it may not be practical or cost – effective to fit a full shield. After surveying the existing installation, it may be possible to supplement existing building shielding with additional local shielding around equipment requiring protection. To complement this, a commercial performance HEMP filter should be used at the local shield to protect against conducted pulses. However, a better solution is to employ staged protection with filters both where power enters the building and at the equipment as shown in Fig. 1. The first filter will reduce pulses from cables before they enter the building leaving only lower energy pulses to be addressed by the filter local to the equipment.

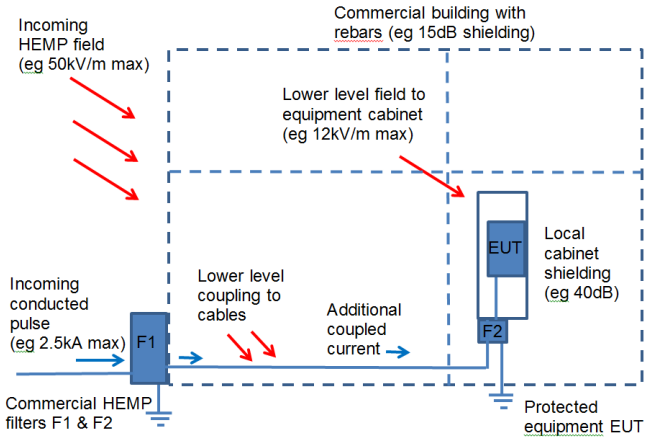

Figure 1 Example of staged HEMP protection

2.3 IEMI requirements

IEMI protection requires a similar approach to HEMP protection except the threat is localised and confined to higher frequencies from around 100kHz to 20GHz. HEMP filters and shielding will also work for IEMI protection as long as their filtering, shielding and transient suppression response time extends to 20GHz. For IEMI protection alone, smaller filters and lower performance shielding could be used without the need for performance below about 10MHz

3 Summary

New guidance from IEC61000-4-24 suggests lower levels of filtering which permits lower cost solutions for HEMP and IEMI protection of critical commercial infrastructure using commercial performance HEMP filters and simple shielding.

Electromagnetic pulse (EMP) mitigation devices in short-pulse laser experiments

M Bardon[*], F Lubrano[*], J L Dubois[#], J Ribolzi[*], D Gontier[†], S Depierreux[†], A Compant La Fontaine[†], C Rubbelynck[†], S Champeaux[†], O Cessenat[*], S Hulin[#], V Tikhonchuk[#]

[*]CEA/CESTA, Le Barp 33114, France
[†]CEA/DIF, Bruyères-le-Châtel 91297, France
[#]CELIA-University of Bordeaux-CNRS-CEA, Talence 33405, France
matthieu.bardon@cea.fr

Keywords: EMP, Mitigation, Laser experiments.

1 Introduction

Significant electromagnetic pulse (EMP) can be generated during laser-plasma experiments [1]. Recent works [2] have demonstrated that short-pulse laser experiments on flat metallic targets produced the strongest EMP. These kinds of experiments on new power-laser facilities such as PETAL (Pétawatt Aquitaine Laser in the LMJ facility – CEA/CESTA – France) may lead to the generation of electric field exceeding 1 MV/m. Such a field might damage diagnostics and facility equipment and will produce spurious signals in detectors.

A classical way to protect from this EMP consists in shielding each facility's equipment [3]. The drawback of this solution is that you must protect several equipments, which can be very expensive and very difficult to set up. We have worked on a different concept whose goal is to mitigate EMP generation from the beginning of this process.

The first conception step has consisted in understanding and identifying the mechanism of EMP generation [4-5-6]. Then, a 3D, multi-scale, multi-physics, calculation chain has been developed [4]. Simulations have been performed in order to define new EMP mitigation devices. Finally, these concepts have been validated on two experimental campaigns called Popsicle 1 and 2, in 2014 and 2015, at the CEA/DIF EQUINOX laser facility in France. Magnetic field mitigation factors between 5 and 10 have been measured.

2 Physics of EMP generation in short-pulse laser-plasma experiments

The basic principles are described in references [4-5-6]. The laser-pulse accelerates plasma's electrons at the target surface. They spread in and out of the target creating an electric potential at the surface. This potential is a barrier that the electrons must overcome to escape. The number of escaped electrons defines the net positive charge left on the target. The return to balance is achieved through a discharge in the target holder. Finally, the set [target + target holder] acts as a dipole antenna.

3 Development of a 3D numerical simulation chain

EMP generation in a laser chamber is a multi-physics and multi-scale process. The simulation is performed in four subsequent steps with a suite of numerical codes. First, the effect of laser pre-pulse on the solid target is simulated with a hydrodynamic code developed at CEA/DIF. Second, the main laser pulse interaction with plasma, which accelerates hot electrons, is simulated with particle-in-cell (PIC) code developed at CEA/DIF. The electrons are carried in the target by a Monte-Carlo code. Finally the escape of electrons from the target and their propagation to the laser chamber is simulated by another PIC code developed at CEA/CESTA.

4 Experimental set up

Two diagnostics are used. The first one is a Bdot probe which measures the magnetic field radiation. The second one measures the discharge current in the target holder by connecting a coaxial cable between an oscilloscope and the target holder. Integrating the discharge current provides the ejected charge.

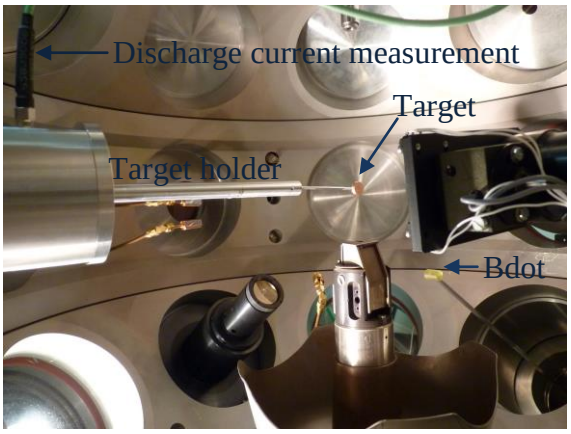

Figure 1. Experimental set up.

The laser parameters for the two campaigns were: energy on target of 100 mJ, pulse duration of 80 fs, focal spot diameter (FWHM) of 10 µm. These parameters lead to a laser intensity of 10^{18} W/cm^2.

5 Results

The goal of the EMP mitigation concepts is to damp the discharge current which is the source of the antenna formed by the set [target + target holder]. These devices act on the target holder.

All the EMP mitigation devices are compared to a reference without any mitigation concept. Fig. 2 represents the radiated magnetic field measured by the Bdot probe versus time. A significant mitigation is observed, according to numerical simulations.

Higher laser energy (100 J) tests are planned on the LULI 2000 laser facility (Ecole Polytechnique – France).

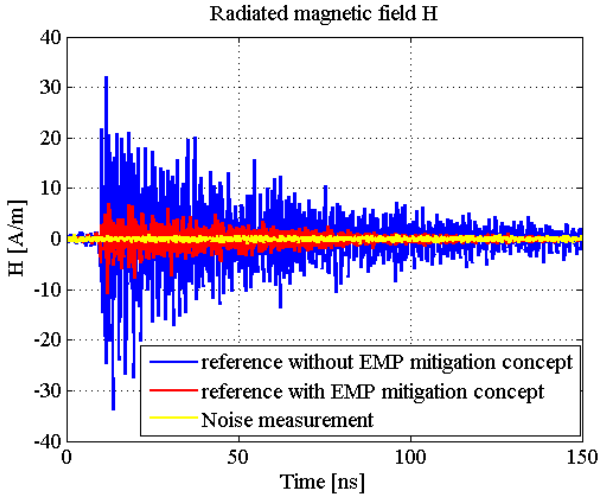

Figure 2. Measurement of the radiated magnetic field.

References

[1] M. J. Mead et al., "Electromagnetic pulse generation within a petawatt laser target chamber", *Rev. Sci. Instrum.*, **75**, 4225, (2004).

[2] C. J. Brown et al., "Analysis of electromagnetic pulse (EMP) measurements in the National Ignition Facility's target bay and chamber", *EPJ Web of Conf.*, **59**, 08012, (2013).

[3] J. L. Bourgade et al., "Diagnostic hardening for harsh environment in Laser Mégajoule", *Rev. of Sci. Instrum.*, **79**, 10F301, (2008).

[4] J. L. Dubois et al., "Target charging in short-pulse-laser-plasma experiments", *Phys. Rev. E*, **89**, 013102, (2014).

[5] A. Poyé et al., "Physics of giant electromagnetic pulse generation in short-pulse laser experiments", *Phys. Rev. E*, **91**, 043106, (2015).

[6] A. Poyé et al., "Dynamic model of target charging by short laser pulse interactions", *Phys. Rev. E*, **92**, 043107, (2015).

High Performance Conducted Filtering to 50GHz

William Turner

MPE Ltd, Liverpool, UK wturner@mpe.co.uk

Abstract

As transmission frequencies and clock speeds are constantly increasing, proliferation of wireless telecommunications continues, the threat of EMI, IEMI and EMP will grow exponentially. Conducted filtering has to keep pace providing clean signals, protection and security. This paper investigates the performance of a selection of high frequency high performance filters up to 50GHz.

Keywords: Intentional Electromagnetic Interference (IEMI), High Altitude Electromagnetic Pulse (HEMP), Protection, Filter, TEMPEST

1 Introduction

High performance high frequency filtering has existed for decades; many electromagnetic protection products on the market today will perform well up to 10GHz including MPE's own Powerline product range. But with the continual march of technology both EMI and IEMI can be generated in significant levels at frequencies 2, 3 or even 4 times this frequency. To combat this filtering at higher frequencies than before is required.

2 Test Setup and Limitations

Working from a known baseline several ranges of MPE products were gathered together for the test, covering EMI and EMP single phase and three phase mains filters, control and telecommunications filters and AC and DC feedthrough capacitors. The tests performed were all insertion loss tests applied in accordance with BS EN 55017 (CISPR 17). For the signal generator and receiver a 50GHz Vector Network Analyser was employed with a >100dB dynamic range across the 1GHz to 50GHz band. This was vital as many of the products being tested were known to already provide rated >100dB of protection from 100kHz to 10GHz. It is important to note that this was a conducted test and does not guarantee shielding performance, although at the higher frequencies they are intrinsically linked so there is a strong correlation to it. These tests are still valid as it fundamentally measures how well a signal propagates from one end of a filter to the other regardless of how it passes through the intervening filtered space. It should be noted that the power levels of the injected signal were in the +5 to -10 dBm range so for high power threats additional higher power handling may be required.

3 Feedthrough Capacitors

Feedthrough capacitors, in contrast with two terminal capacitors, are one of the critical building blocks for high frequency filtering due to their near ideal capacitor behaviour. All capacitors were tested within the same shielded enclosure to ensure consistency. It was demonstrated that very high performance of 100dB from 1GHz to 25GHz and above is possible with only a single capacitor; however it also shows installation, capacitor internal construction, mounting arrangement and capacitor quality are all critical to this. Poor choice of gasket or bad practice in the mounting arrangement will quickly diminish this to 60dB or even less. This may appear as a sudden loss of performance in a particular band, say 5-10GHz, but still perform at much higher frequencies.

4 Multistage and Multiline Filters

Multiline filters demonstrated impressive performance, to 100dB at 50GHz in some cases. Filters designed for 10GHz all performed well to 40GHz, with those containing more high frequency stages consistently performing even better. By high frequency stages it is meant fully sealed barriers with high frequency feedthrough capacitors, not variations based on 2 terminal capacitors or partially sealed barriers.

A surprise result was that filters with stainless steel construction performed well, giving practical benefit beyond 10GHz despite the inherently poor conductivity of stainless steel.

The use of high integrity sealing of the output compartments ensured good performance in this critical area, with gaskets, mounting holes and cable glands also being primary concerns.

5 Recommendations for 1GHz to 50GHz

In conclusion a simple feedthrough capacitor can provide acceptable filtering benefits but to guarantee high performance above 1GHz a multi-element filter is the preferred choice.

Cost-effectively managing Functional Safety and other risks which could be caused by electromagnetic disturbances

Keith Armstrong

Cherry Clough Consultants Ltd, UK, keith.armstrong@cherryclough.com

Abstract

Where critical systems or installations rely on the correct operation of modern electronics, errors, malfunctions or failures in the electronics could cause unacceptable levels of Functional Safety or other risks.
High Power Electromagnetic disturbances (HPEM) can cause actual damage to critical electronics, and can also cause electromagnetic interference (EMI) with any/all electronic signals and power supplies. Both these possibilities must be taken into account where Functional Safety or other types of risk must be managed.
However, it is impossible to do enough electromagnetic immunity testing to achieve sufficient confidence that modern electronics will maintain low-enough risks, despite the electromagnetic (EM) disturbances that could occur throughout their lifecycles.
This paper describes the IET's recent guidance on how to cost-effectively deal with this problem.

Keywords: Functional safety, risk management

1 Introduction to "EM Resilience"

Where an electronic system is used in an application where its incorrect functioning could increase safety risks, and where those safety risks must maintain acceptably low levels all throughout their lifecycles, we say that the incorrect electronic functioning can cause Functional Safety risks.

To an ever-increasing degree, human safety relies on the correct functioning of programmable digital electronics (microprocessors running software programs), but it has been impossible to fully test even a modest microprocessor or software program for at least the last 20 years [1] [2].

This impossibility arises because hardware and software became so complex that they had too many possible digital states to allow full testing in any reasonable time-scale [1] [2] [3]. In addition, all digital systems are discontinuous (i.e. non-linear) which means that even if a very large percentage of their states are tested, this does not allow any predictions to be made about the untested ones [3].

One result of this is that all digital systems can malfunction as the direct result of untested combinations of perfectly correct inputs (i.e. all inputs lying within their specified ranges).

Safety and product liability laws/regulations generally require an item of equipment not to expose a member of the public to a risk of much more than one in a million chance of death per year. Where higher risks are required, these laws generally require analyses prove that they are justified. The UK's Health and Safety Executive (HSE) provides a wide range of guidance on these issues [4].

The problem of having to achieve such low risk levels whilst being unable to thoroughly test modern electronics was first recognized in the 1970s, and by the 1980s a huge international effort was underway to try to establish suitable Functional Safety methods, resulting in the first international standard on Functional Safety, IEC 61508 [5], being published in 2000 as an IEC Basic Safety Standard.

A family of application-related Functional Safety standards have been developed based on IEC 61508, including:

- IEC 61511 (Process Control)
- IEC 62061 (Machinery)
- IEC 62278, EN 50126, IEC/EN 50128/9 (Railways)
- IEC 61513 (Nuclear Power)
- RTCA DO-178B & -254, EUROCAE ED-12B (Avionics)
- ISO 26262 (Automobiles)

This IEC 61508 family of Functional Safety standards deals with the impossibility of fully testing a digital system, by determining the level of acceptable risk, and using it to guide the application of a range of well-proven techniques and measures (T&Ms) in design, verification and validation. This work is all described in a 'Safety Case' which is independently assessed, then the design, verification and validation is iterated as required to satisfy the assessor.

Complex equipment is split into two parts: the 'Equipment Under Control' (EUC) and the much smaller 'Safety-Related System' (SRS) which manages the EUC's Functional Safety.

A powerful technique in Functional Safety is for an SRS to switch its EUC into one of its 'safe states', when it detects that a hazard might occur. For example, upon opening a machine guard, the machine's SRS stops the machine before any part of a human body can come into contact with the hazard being guarded. Some applications (e.g. life-support) have no safe states, and so must keep operating well-enough to prevent unacceptable risks at all times, and IEC 61508 also includes T&Ms suitable for such applications.

All electronics can suffer from errors, malfunctions and/or failures due to EMI, which must therefore be taken into account for Functional Safety. When applying IEC 61508 or its related standards it is usual to allocate one-tenth of the overall risk level to EMI causes. So if a digital system should maintain a less than one-in-a million risk of death per person per year, then EMI should not cause a risk of death greater than one in 10 million.

Electromagnetic compatibility (EMC) is traditionally assured by laboratory testing. Where there are safety risks it is usual to achieve a (so-called!) 'Safety Margin' by increasing test levels. This approach has been shown to be inadequate, on its own, for Functional Safety since 2004 [7] [8].

As previously discussed, it is impossible to test a sufficient number of states of a digital system to prove Functional Safety, so it must also be impossible to test sufficient states whilst exposing the system to EM disturbances, one at a time.

Furthermore, safety risks must be low enough over the whole lifecycle of an SRS, so proving Functional Safety by EMC immunity testing alone would also have to consider the effects on the equipment's EM immunity of:

- Corrosion, aging, wear, contamination, etc.
- Faults (e.g., a broken filter ground wire)
- Foreseeable use/misuse (opening a shield door, replacing shielded cables with unshielded, etc.)
- Mechanical stresses and strains that can degrade the performance of shielding and filtering
- EM disturbances that exceed the tested levels
- Different EM disturbances occurring simultaneously or in some critical time sequence
- Reasonably foreseeable combinations of at least all of the above, because they are all independent variables.

Even if an EM test plan was possible (which it is not), extending it to cover this (non-exhaustive) list of issues would cause it to become impossibly large [7].

The traditional way of achieving Functional Safety despite EM disturbances that could foreseeably arise over its lifecycle, and any internal electronic faults, is to use ruggedized 'high-spec' EM mitigation (shielding, filtering, surge protection, galvanic isolation, etc.) so the SRS is only exposed to an insignificant proportion of the external EM disturbances. But this approach is too large, heavy or costly for many modern SRSs, especially in avionics, automobiles, portable or implantable medical devices, etc.

For this reason, the IEE/IET's Working Group on EMC for Functional Safety developed a practical alternative, [9] published in August 2013 after considerable input from a large number of Functional Safety and EMC experts. [9] builds on existing expertize in EMC testing and Functional Safety design/assessment by developing IEC 61508's 'T&M' methodology to achieve "EMI Resilience," see Figure 1.

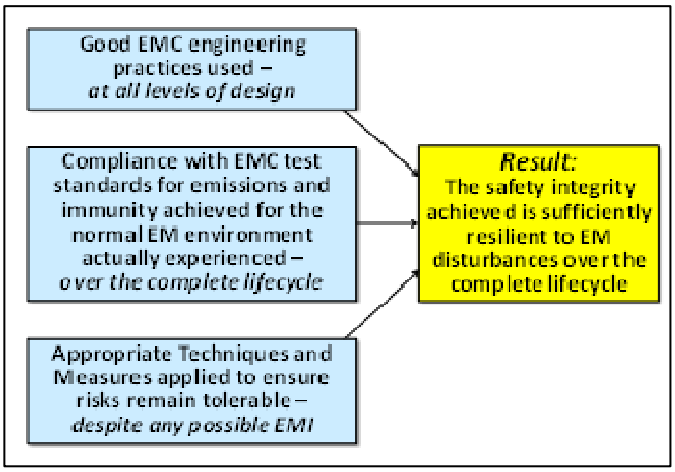

Figure 1. Overview of the IET's 2013 guidance [9]

EMI can only affect electrical data, control, signals and power supplies, so IEC 61508's T&Ms turn out to be quite effective in dealing with the effects of EMI.

Accordingly, the IET's 2013 guidance [9] recommends some of IEC 61508's existing T&Ms are good for dealing with EMI, as well as describing how to improve them to better achieve EM resilience.

The functional safety standards applied to medical/healthcare equipment and systems are based on ISO 14971 instead of IEC 61508.

ISO 14971 uses different terminology from IEC 61508, and does not provide a practical process for achieving or assessing compliance. Nevertheless, [9] may still be used to manage the safety risks that can be caused by EM disturbances [6].

The above discussion has only concerned safety risks, but the methodology described by the relevant Functional Safety standards and [9], can readily be adapted for helping to manage any other type of risk that must not exceed acceptable levels over the lifecycle.

2 EM resilience T&Ms for design

Electronic hardware, software and system designers are generally knowledgeable about the T&Ms used by IEC 61508, many of which were in use long before 61508 was first published. For example, the use of multiple 'redundant channels', using two or more sensors to sense the same parameters, storing two or more copies of data, communicating via two or more communication channels, processing the same data with two or more processors, etc.

Comparing one channel's output with another's can detect many types of errors, and 'voting' (e.g. any two channels that agree out of three) can correct errors.

[9] recommends that these well-known multi-channel techniques are used with diverse technologies and techniques for their individual channel to improve their effectiveness against the common-cause errors typically caused by EM disturbances.

For example, in a redundant system with two identical channels, simply inverting the data in one of the channels makes EMI more likely to be detected, at no extra cost.

Better detection and/or correction of errors in digital communications caused by EM disturbances might require applying error detection and/or error correction coding (ECC) T&Ms in a slightly different way from usual.

Static and dynamic self-testing are also useful T&Ms for detecting the effects of EM disturbances. Static self-testing checks hardware and/or software before operation begins, preventing start-up if necessary. Dynamic self-testing checks the correct operation of hardware and software during operation, and critical aspects of data processing might be checked once every second, perhaps even more often.

Examples of T&Ms for power supplies includes the use of window comparators to check power supplies are within design limits; energy storage (e.g. batteries) for when external power supplies are outside design limits; multiply-redundant power sources and power converters so that the failure of one or more does not cause unsafe operation of the EUC, etc.

Many more EM Resilience T&Ms are briefly discussed in [10] [11], but for more detail see [9]. Some of EM Resilience T&Ms will be chosen by designers for non-EM reasons, and some of them will be able to have their EM Resilience effectiveness improved. Additional EM Resilience T&Ms might then need to be applied to achieve EM Functional Safety over the lifecycle.

It is possible to rely solely on T&Ms in an SRS to create a functionally safe EUC, but they can suffer too much down-time (i.e., have unacceptably low availability) because EM disturbances can make them fail to start up, or switch to a safe state, too frequently. Such systems can be expected to be modified to improve availability, by disabling the SRS, so relying solely on T&Ms cannot be considered safe enough.

Achieving adequate availability simply needs compliance with the relevant EMC immunity test standards, which have been developed over time, and are still developing, for specific applications and/or specific types of EM environments.

The EMC community is of course very familiar with such testing, however EM Functional Safety requires that an SRS be capable of passing these tests throughout its entire lifecycle, which is new to most EMC testing practitioners.

3 T&Ms for verification and validation

No single verification/validation method is comprehensive enough to prove Functional Safety, so IEC 61508 requires the use of several different well-known methods, including: demonstrations; checklists; inspections; ‘walk-throughs’, reviews; assessments; audits and others.

Each of these methods can employ one or more of the following standardized analysis T&Ms: inductive, deductive and ‘brainstorming’; validated mathematical or computer modelling; testing, and others. As most of these were never developed to deal with EM disturbances, to help verify/validate adequate EM resilience they generally need to be competently modified and/or extended, to take into account that EM disturbances can cause:

- One or more signals, data and/or controls to suffer an almost infinite variety of degraded, distorted, delayed, re-prioritized, intermittent and/or false values;
- One or more power supplies to suffer from an almost infinite variety of waveform distortions, overvoltages, undervoltages (dips, dropouts, interruptions, etc.);
- The above effects to happen simultaneously for any critical duration, or in any critical time sequence.

Standard EMC immunity tests can usefully be modified, and ad hoc EM tests developed on a case-by-case basis to help verify/validate sufficient EM Resilience for a given SRS.

For example, standard EMC immunity tests can have their frequency ranges extended higher (and lower); have their test levels increased [12]; use more radiated angles/polarizations, and the SRS can be exposed to frequencies that its design is especially susceptible to, either by the carrier wave itself, by demodulation, or by intermodulation (e.g. twin-tone testing, see [13]). The author has documented two cases in which a certain modulation frequency resulted in over 80dB worse susceptibility to radiated/conducted disturbances, and of course no-one can predict when those modulation frequencies will occur in real life.

During any immunity testing, all variations in functional performance should be recorded and analysed afterwards to see if they could have any possible relevance for the Functional Safety risks of the SRS. This is especially important when constructing an SRS from individual items of equipment that are only ever tested alone or in sub-systems.
Another good verification and validation T&M for EM resilience is to repeat the standard or extended EMC immunity tests on units during and after accelerated aging to simulate the effects of the foreseeable physical, climatic and user environments over the lifecycle.

4. Summary and conclusions

The management of Functional Safety or other risks so as to ensure they remain at or below acceptable levels throughout the lifecycle of any system or installation that relies upon the correct functioning of modern electronics cannot be assured by immunity testing alone [7], however high the test levels are set [8].

The only practical techniques that, at the time of writing, can be used to demonstrate that no possible EM disturbances can cause unacceptable Functional Safety or other risks are:

- Ruggedized 'high-spec' EM mitigation
- 'EM resilience' as described in [9], or other techniques and measures that provide the same resilience having regard to EM disturbances, over the lifecycle.

References

[1] Watts S. Humphrey, "The Quality Attitude," Software Engineering Institute, Carnegie Mellon University, in "News at SEI," March 1, 2004: www.sei.cmu.edu/library/abstracts/news-at-sei/wattsnew20043.cfm

[2] Nancy Leveson, Professor of Aeronautics and Astronautics, Professor of Engineering Systems, "A New Accident Model for Engineering Safer Systems," Massachusetts Institute of Technology, in "Safety Science," Vol. 42, No. 4, April 2004: http://sunnyday.mit.edu/accidents/safetyscience-single.pdf

[3] The IET, "Computer Based Safety-Critical Systems", 2009 updated 2013: www.theiet.org/factfiles/it/comp-scs-page.cfm?type=pdf

[4] Many very useful free HSE publications on Risk Assessment from www.hse.gov.uk/pubns, search by "ALARP risk assessment," the most relevant documents will appear on the first and second pages of results and can be downloaded as PDFs

[5] IEC 61508 "Functional Safety of Electrical/Electronic/Programmable Electronic Safety-Related Systems, Parts 1-7", www.webstore.iec.ch

[6] Keith Armstrong, "Why few (if any) medical devices comply with their EMC standard, and what can be done about it," IEEE 2014 International EMC Symposium, Raleigh, NC, ISBN: 978-1-4799-5543-5

[7] Keith Armstrong, "Why EMC Immunity Testing is Inadequate for Functional Safety," IEEE 2004 International EMC Symposium, Santa Clara, CA, ISBN: 0-7803-8444-X

[8] Keith Armstrong, "Why increasing immunity test levels is not sufficient for high-reliability and critical equipment," IEEE 2009 International EMC Symposium, Austin, TX, ISBN: 978-1-4244-4285-0

[9] The IET, "Overview of techniques and measures related to EMC for Functional Safety," UK, August 2013, free from: www.theiet.org/factfiles/emc/emc-overview.cfm

[10] Jeffrey Silberberg and Keith Armstrong, "EMC Risk Management", a half-day workshop at the IEEE 2015 Symposium on EMC&SI, March 2015, Santa Clara, CA, ISBN: 978-1-4799-1991-8

[11] Prof. Davy Pissoort and Keith Armstrong, "EMC for Functional Safety or Risk-Managing EMC — Practical Methods", a half-day tutorial at IEEE Int. EMC Symp. and EMC Europe, EMC 2015, Dresden, Germany, August 2015, ISBN: 978-1-4799-6615-8

[12] Keith Armstrong, "Testing for immunity to simultaneous disturbances and similar issues for risk managing EMC," IEEE 2012 International EMC Symposium, Pittsburgh, PA, ISBN: 978-1-4673-2059-7

[13] Dipl. Ing. (FH) Werner. Grommes and Keith Armstrong, "Developing Immunity Testing to Cover Intermodulation," IEEE 2011 Int. EMC Symp., Long Beach, CA, ISBN: 978-1-45770810-7

Semi-analytical Model for predicting the Electromagnetic Field around a NEMP Simulator

N. Mora, B. Daout, M. Sallin, F. Trotti, C. Romero

Montena Technology, Switzerland, nicolas.mora@montena.com

Abstract

We present a semi-analytical procedure for the analysis of the electromagnetic field distribution around a Nuclear Electromagnetic Pulse (NEMP) test installation. The method has been validated through measurements performed with a reduced scale model of a NEMP generator.

Keywords: NEMP simulator, Sommerfeld integrals

1 Introduction

There are concerns about the exposure of human beings and equipment to EM fields radiated by Nuclear Electromagnetic Pulse (NEMP) simulators. This has led to the interest of determining the exposure levels for the personnel working around the facility and evaluating the likelihood of relevant electromagnetic interferences in the neighboring equipment due to coupling to the wirings.

In a previous work [1], we discussed methods for the numerical and analytical prediction of the near and far fields around NEMP installations. In this work, we present an update of the analytical model in which the currents generated in the surface of the conical transmission line are evaluated through full wave simulation instead of transmission line theory [2]. The simulation model has been validated with measurements performed around a reduced scale model of a NEMP generator.

2 Structure under study

A picture illustrating the small NEMP simulator under study is presented in Fig. 1.

Fig. 1 Picture of the Montena Technology EMP25K-2-23 small NEMP simulator

The Montena Technology EMP25K-2-23 simulator is composed of a wired conical transmission line [3] terminated with a distributed resistive load. The line height h=50 cm and width W=69 cm are chosen to obtain the desired characteristic impedance of Z_c=110 ohm that will be matched with the resistive termination. The total horizontal length from the apex of the conical transmission line up to the end of the termination lines is L= 124 cm.

3 Electromagnetic model

In order to calculate the fields around the structure, we assume that the structure shown in Fig. 1 is located outdoor above a lossy ground that is characterized with conductivity σ and relative permittivity ε_r . The evaluation of the fields is performed in a two-step procedure.

First, the induced currents along the wires are calculated with NEC4 by injecting a unitary voltage source at the input of the conical transmission line. The calculation is simplified by assuming a perfectly conducting ground, thus leading to shorter simulation time.

Secondly, the EM fields are evaluated by using the approximated solution of Sommerfeld's integrals derived by Norton [2, 4, 5] relating the electric field at an observation point above a lossy ground due to a vertical and horizontal current element. The total field is recovered as the superposition of the Green's functions of the space wave and the surface wave around the structure.

Close to the ground, the far fields are governed by the surface wave. At several meters above the ground, the space wave dominates the response. Both, the space wave and the surface wave are affected by the properties of the lossy ground.

4 Experimental validation

The simulator in Fig. 1 was located outdoor above a field recovered with grass and soil. Several measurements of the E field inside the working volume and around the structure were made by using a Ddot sensor connected to a measurement oscilloscope through a fiber optic link. A 28 kV pulser with a risetime of 2 ns and 23 ns duration was used to excite the line. The average measured field in the working volume was a 50 kV/m pulse with similar risetime and duration as the injected pulse.

An example showing the comparison of the numerically predicted and measured vertical electric field at a distance of 10 m from the apex, at an angle of 45 ° from the symmetry axis, is presented in Fig. 2. The simulation results were

obtained with a soil conductivity of $\sigma = 1$ mS/m and relative permittivity $\varepsilon_r = 10$.

The simulation results were found in good agreement with the measurements; provided that the soil parameters were unknown and could change depending on the moisture level.

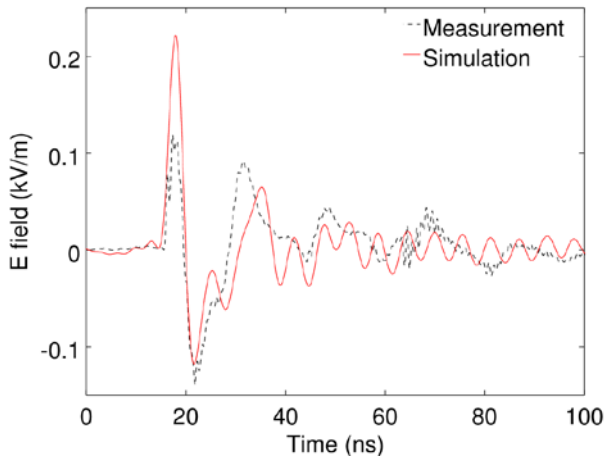

Fig. 2 Comparison of the measured and simulated E-field waveform at 10 m from the apex of the conical transmission line

The proposed EM model can be used to generate field plots of the maximum expected field around the simulator by using different values of the soil conductivity and permittivity.

5 References

[1] B. Daout, N. Mora, M. Sallin, C. Romero, F. Vega, and F. Rachidi, "Analysis of the Induced Electromagnetic Field in the Surroundings of a NEMP Simulator," presented at the Asia Electromagnetics International Symsposium (ASIAEM), Jeju, Republic of Korea, 2015.

[2] F. M. Tesche, C. Mo, and R. W. Shoup, "Determination of the electromagnetic fields radiated from the ARES EMP simulator," *Electromagnetic Compatibility, IEEE Transactions on*, vol. 36, pp. 331-341, 1994.

[3] C. E. Baum, "The Conical Transmission Line as a Wave Launcher and Terminator for a Cylindrical Transmission Line," *Sensor and Simulation Notes*, vol. 31, 16 Jan 1967.

[4] K. Norton, "The physical reality of space and surface waves in the radiation field of radio antennas," *Radio Engineers, Proceedings of the Institute of*, vol. 25, pp. 1192-1202, 1937.

[5] E. C. Jordan and K. G. Balmain, *Electromagnetic waves and radiating systems* vol. 4: Prentice-Hall Englewood Cliffs, NJ, 1968.

Analytical Iterative Solution of the EMP Coupling to Lossless Multi-conductor Transmission Lines in Time Domain

Jun Guo, Yan-zhao Xie, Yan-ming Li

State Key laboratory of Electrical Insulation and Power Equipment
Electrical Engineering College, Xi'an Jiaotong University
Xi'an, Shannxi, China
gjgjgj@stu.xjtu.edu.cn, yzxie@mail.xjtu.edu.cn.

Abstract

The distributed analytical representation and iterative technique (DARIT) Jacobi iteration (Jacobi-DARIT-field) method in frequency domain has been proposed for the calculation of electromagnetic pulse (EMP) radiated field coupling to multi-conductor transmission lines (MTLs). This paper extends Jacobi-DARIT-field method to the time domain in order to handle the case with nonlinear loads. The validation examples show that the proposed method could efficiently handle the case of lossless multiconductor transmission line with nonlinear loads.

Keywords: analytical solution; time-domain method; nonlinear loads; transmission line modelling; waveform relaxation.

1 Introduction

To predict the effects of EMP coupling to multi-conductor transmission lines (MTLs), many researchers have proposed the method of modelling of EMP coupling to MTLs [1]. In 2013, Y.-Z. Xie, J. Guo and F. Canavero proposed an approach using the distributed analytical representation and iterative technique (DARIT) method for the response calculation of multi-conductor transmission lines illuminated by the incident EMP field [2]. Hereafter, this algorithm named Jacobi iterative method of DARIT-field (Jacobi-DARIT-field). The algorithm can avoid the need for inversing the matrix when solving MTLs equations and leading to high computational efficiency.

However, the Jacobi-DARIT-field method is a frequency domain method which could not handle the nonlinear problem. This paper extends Jacobi-DARIT-field method to time domain for the case of lossless multiconductor transmission lines with nonlinear loads.

2 Outline of the method

The problem to be investigated is shown in Fig. 1. It consists of MTLs of length *L* and the number of conductors *N* (the reference conductor is not included), with loads at each end of the lines. All the lines are excited by the incoming EMP plane wave. For this problem, the load responses of voltages and currents at each line end are to be determined.

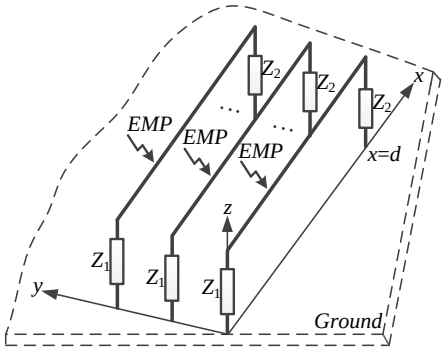

Figure 1. The configuration of MTLs to be investigated.

The Telegrapher's equations of the MTLs in the time domain are described by a set of differential equations in the following form:

$$\begin{aligned}\frac{\partial \mathbf{v}(x,t)}{\partial x}+\mathbf{L_w}'\frac{\partial \mathbf{i}(x,t)}{\partial t}&=\mathbf{v_s}'(x,t)\\ \frac{\partial \mathbf{i}(x,t)}{\partial x}+\mathbf{C_w}'\frac{\partial \mathbf{v}(x,t)}{\partial t}&=\mathbf{i_s}'(x,t)\end{aligned} \tag{1}$$

where $\mathbf{v}(x,t)$ and $\mathbf{i}(x,t)$ are the vectors of the N voltages and currents on the lines. $\mathbf{v_s}'(x,t)$ and $\mathbf{i_s}'(x,t)$ are the source terms which detailed expressions depending upon the coupling model used, e.g. Taylor model (used in this paper), Agrawal Model and Rachidi Model. $\mathbf{L_w}'$ and $\mathbf{C_w}'$ are the $N*N$ matrices of the line impedances and admittances.

The Telegrapher's equations in (1) for line i could be expressed as follows:

$$\begin{aligned}\frac{\partial v_i(x,t)}{\partial x}+L_{w,ii}'\frac{\partial i_i(x,t)}{\partial t}&=v_{s,i}'(x,t)-\sum_{\substack{j=1\\ j\neq i}}^{N}L_{w,ij}'\frac{\partial i_j(x,t)}{\partial t}\\ \frac{\partial i_i(x,t)}{\partial x}+C_{w,ii}'\frac{\partial v_i(x,t)}{\partial t}&=i_{s,i}'(x,t)-\sum_{\substack{j=1\\ j\neq i}}^{N}C_{w,ij}'\frac{\partial v_j(x,t)}{\partial t}\end{aligned} \tag{2}$$

where $v_i'(x,t)$ and $i_i'(x,t)$ are the general source terms of line i due to the incoming EMP wave. The summation terms in (2) are the neighbouring effects on line i due to the coupling of other adjacent lines. By applying waveform relaxation

techniques to (2), we obtain a recursive set of decoupled differential equations based on Jacobi iteration in the time domain, and then it is transformed into the combined voltage form as:

$$\frac{\partial w_+^{(r+1)}(x,t)}{\partial x} + k_w \frac{\partial w_+^{(r+1)}(x,t)}{\partial t} = w_+'^{(r)}(x,t)$$
$$\frac{\partial w_-^{(r+1)}(x,t)}{\partial x} + k_w \frac{\partial w_-^{(r+1)}(x,t)}{\partial t} = w_-'^{(r)}(x,t) \quad (3)$$

where

$$w_+^{(r+1)} = v^{(r+1)} + Z_c i^{(r+1)}, \quad w_-^{(r+1)} = v^{(r+1)} - Z_c i^{(r+1)}$$
$$w_+'^{(r)} = v_s' + Z_c i_s'^{(r)}, \quad w_-'^{(r)} = v_s' - Z_c i_s'^{(r)} \quad (4)$$
$$k_w = \sqrt{L_w' C_w'}$$

In order to solve the voltages and currents at the terminals step by step, the main task of each iteration step is to determine the source vector and the distribution of induced voltage and current along the line.

2.1 Iteration 1

At this iteration, there are no coupling effects due to the neighbouring line since the initial states of the lines are zeros. The only exciting source is from the illuminating EMP wave. The load responses could be solved analytically.

2.2 Iteration 2

From iteration 2 on, each line is excited by the incoming EMP wave and the coupling effects of all the other adjacent lines.

3 Validation of the proposed algorithm

In order to demonstrate the validity of the proposed time-domain Jacobi-DARIT-field algorithm for the calculation of EMP coupling to MTLs, this section mainly gives two examples which with the linear loads and nonlinear loads, respectively.

In the first example, a symmetrical and three conductors microstrip structure with the length of 1 m, height of 0.1 m, diameter of 1 mm distance between lines of 0.15 m which above the perfect ground is considered. The loads on both sides are 50 Ω. Figure 2 shows the comparison of the results from the proposed method and from the chain matrix parameter method. It can be seen that the result from the proposed method agree well with the conventional method.

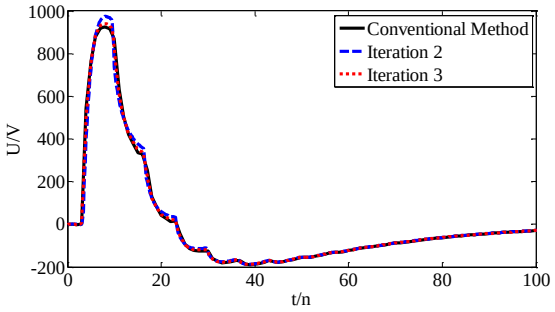

Figure 2. The result of the proposed method.

In the second example, a symmetrical and three conductors microstrip structure with the length of 0.1 m, height of 1 cm, diameter of 1 mm distance between lines of 1.5 cm which above the perfect ground is considered. The load on near-end is 50 Ω. The loads on far-end are 50Ω and a nonlinear load in parallel. The nonlinear characteristic is shown in Figure 3. Figure 4 shows the comparison of the results from the proposed method and from the SPICE software. It can be seen that the result from the proposed method agree well with the SPICE method.

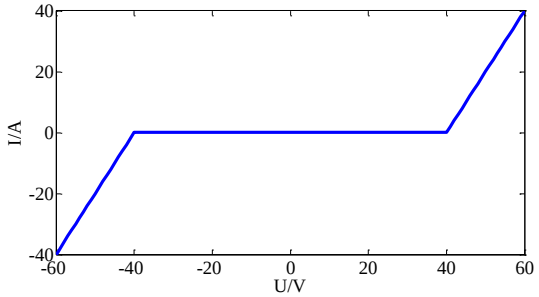

Figure 3. The U-I curve of the nonlinear load.

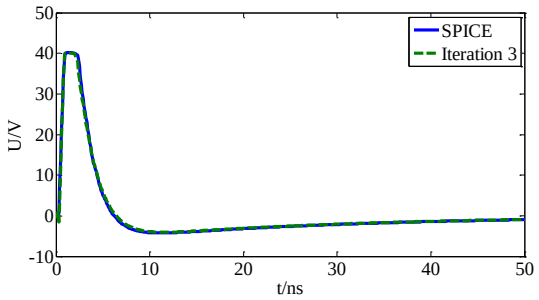

Figure 4. The configuration of MTLs to be investigated.

4 Conclusion

This paper proposed the time-domain Jacobi-DARIT-field method for lossless multiconductor transmission lines. The two validation examples show that the method could efficiently handle both the case with the linear loads and the case with nonlinear loads. However, it is worthy to note that the proposed method could not handle the case with frequency dependent parameter, therefore, how to solve the case both have nonlinear loads and frequency dependent parameter in an analytical iterative way is still an open question.

References

[1] C. R. Paul. Analysis of Multiconductor Transmission Lines, Second Edition, New York: John Wiley \& Sons, 2008.

[2] Y. Z. Xie, J. Guo and F. Canavero, ``Analytic iterative solution of electromagnetic pulse coupling to multiconductor transmission lines," IEEE Transactions on Electromagnetic Compatibility, vol.55, no.3, pp.451-466, June 2013.

Application of Singularity Expansion Method (SEM) to non-uniform transmission lines

S V Tkachenko*, J B Nitsch*, F Middelstaedt*, M Magdowski*, D Hellge-Theune*, H-J Sheibe*, R Rambousky†, R Vick*

** Otto-von-Guericke University, Magdeburg, Germany, e-mail: Sergey.Tkachenko@ovgu.de*
†Bundeswehr Research Institute for Protective Technologies and NBC Protection (WIS), Munster, Germany

Abstract

This work deals with the calculation of SEM poles of thin-wire transmission lines above perfectly conducting ground. This set of poles yields the main contribution to the response function of the transmission line to an excitation. It also defines the scattering amplitude, the response in time domain, etc. Moreover, the SEM poles can be used for the identification of systems. In this paper we consider two different methods to derive the SEM poles: the method of asymptotic approach and the method of modal parameters. The results are compared with NEC calculations as well as with measurements. The essential difference between SEM poles for systems of different geometric form was shown.

Keywords: SEM, Transmission Lines, Thin wires.

1 Introduction

Transmission lines play an important role in EMC. They serve for the transmission of the desired signals between electronic devises of different kind. On the other hand, they are subject of different kind of electronic interferences. Induced voltages are often the reason for the failure of electronic devises. Different numerical methods (as MoM, FDTD, etc.) can be applied to calculate induced currents and voltages but they are not very helpful to gain insight into the physics of the coupling phenomena.

In contrast, the analytical Singularity Expansion Method (SEM) [1] represents the scattering object as a set of oscillators, helpful to understand the underlying physics of the coupling phenomena, both in the frequency domain and in the time domain. Recently, this method has attracted an increased interest [2,3] in connection with the problem of target identification.

The SEM poles in the complex frequency plane depend only on the geometry of the wiring system and terminal loads and do not depend on the point of definition of the current and on the way of excitation of the system. In another words, they own a natural property, the "signature" of the system. The knowledge of the SEM poles help to find the main contribution to the response function (strictly speaking, the functional) of transmission line to excitation, they define the scattering amplitude, the response in time domain, etc. Moreover, the SEM poles can be used for the identification of systems. Thus, the definition of SEM poles is an important problem for the study of transmission lines.

In our recent papers [4,5,6] SEM was applied for the analysis of loaded transmission lines above conducting ground using the classical transmission-line theory as well as the asymptotic approach [7]. In this paper we describe previous and new results using different methods to investigate SEM poles: the method of asymptotic approach and the method of modal parameters. Comparison of the obtained results with data of a numerical simulation and data of measurement will be presented.

2 Theory

2.1 SEM and asymptotic approach

We consider a long loaded line above perfectly conducting ground (L, h and r0 is a length, height and radius of the wire, correspondingly) illuminated by an incident plane wave. The line also can have a bent in the central part [10].

To obtain the frequency domain solution in the main, central part of the wire, the so-called asymptotic region [7] is used. This approach is applicable for the long line and evaluates the current(s) in the central asymptotic region(s) from the reflection (and transmission for the bent) coefficients for TEM current waves and the scattering coefficients for forced waves (current waves induced by the plane wave in the infinite line). Formally the solution in the asymptotic region looks like a classical TL solution, but the reflection and transmission coefficients have to be calculated in the high-frequency case, when the wavelength can be about or small as the height of the wire above ground. These coefficients can be calculated using the perturbation theory for thin wires [7,8,9], or by an analysis of numerical results. The formula for the current includes the resonance denominator, which contains only reflection coefficients. The zeros of the denominator yield the SEM poles of the first layer. Furthermore, SEM poles are obtained in explicit form in three canonical cases: (i) an open circuit straight horizontal wire [6], (ii) a straight horizontal wire short-circuited by vertical risers [5,9], (iii) a horizontal wire with horizontal bent, open or short - circuited [10]. It was shown that these different systems yield different type of poles which allow to make a rough identification of the systems.

2.2 SEM and method of modal parameters

The method of modal parameters is described in [11]. In this method the exact integro-differential equations describing the coupling problem is reduced to the system of two matrix equations with infinite inductance and capacitance matrices by a spatial Fourier series transformation. The inductance and capacitance matrices are matrix elements of the kern of the first and second integral equation, correspondingly, for the spatial Fourier series. The solution for the induced current column can be found by the product of the column of the initial tangential electric field with the inverse infinite impedance matrix, which can be obtained from the inductance and capacitance matrix by the usual way. Thus, the poles of the induced currents in the complex plane are given by the eigen - values of the infinite impedance matrix.

3 Numerical simulation

The frequency response of the line was simulated using MoM NEC (Numerical Electromagnetic Code) software. The SEM poles can be extracted from numerical data using a Padé approximation as described in [12]. The comparison of the poles obtained by the solution in the asymptotic approximation and NEC calculation is shown in Fig. 1.

4 Measurements

The measurement of the field coupling with a transmission line was conducted in a GTEM cell. With the aid of a vector network analyzer (VNA) the scattering parameters between the base point of the wire (port 1 of the VNA) and the feeding port of the GTEM cell (port 2 of the VNA) were measured.
Then, the obtained response function is treated by the same manner using the Pade approximation. Corresponding results are presented in Fig. 1. One can see an excellent agreement between measurements and NEC and a satisfactory agreement with modal and asymptotic theory.

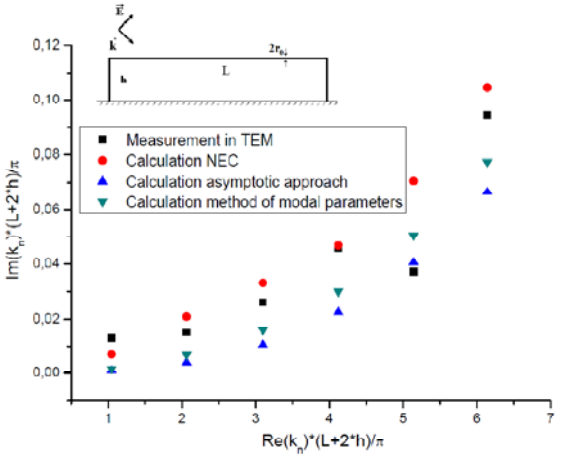

Figure 1. SEM poles for short-circuit line. Comparison of the measurement with NEC, asymptotic method and method of modal parameters. L=10 m, h=0.5 m, r0=1 cm.

5 Conclusion

In this paper we presented different analytical techniques to define SEM poles of the thin-wires structures. The comparison of numerical simulations with measurements was done. In future research we intend to apply these methods to multiconductor transmission lines.

Acknowledgements

This work was supported by the Bundeswehr Research Institute for Protective Technologies and NBS Protection, Munster, Germany.

References

[1] C.E. Baum, "The Singularity Expansion Method in Electromagnetics", D.V.Giri and F.M. Tesche (editors), Lulu Enterprises 2012.

[2] F.M. Tesche and D.V. Giri, "On the natural oscillation frequencies of a straight wire", *Interaction Notes*, **Note 621**, June 2011.

[3] J.M.Myer, S.S.Sandler and T.T.Wu, "Electro-magnetic resonances of a straight wire", *IEEE Trans. Ant. Prop.*, **volume 59**, Jan.2011, pp.129-134.

[4] J. Nitsch, S. Tkachenko, R. Vick, F. Rachidi, D. Poljak, „Coupling of Pulsed EM Fields to TL*", 2012 Int. European Symp. on EMC* (Rome 2012).

[5] S.Tkachenko, F. Middelstaedt, J.Nitsch, R.Vick, G.Lugrin and F.Rachidi, "Application of Singularity Expansion Method (SEM) to Long Transmission Lines", *AMEREM 2014,* Albuquerque.

[6] S.Tkachenko, J.Nitsch, R.Vick, F.Rachidi, D.Poljak, "Singularity expansion method (SEM) for long terminated transmission lines", 2013 Int. Conf. on EM in Adv. Appl. (ICEAA), Torino, 2013.

[7] F.Rachidi, S.Tkachenko (editors), "*EM Field Interaction with TL. From Classical Theory to HF Radiation Effects"*, WIT Press 2008. Ch. 4 and 5.

[8] S.Tkachenko, F.Middelstaedt, J.Nitsch, R.Vick, G.Lugrin, F.Rachidi, "High–Frequency Electromagnetic Field Coupling to a Long Finite Line with Vertical Risers", *GA URSI 2014* Beijing.

[9] F .Middelstaedt, S.V. Tkachenko, R.Rambousky and R. Vick, "High-Frequency Electromagnetic Field Coupling with Vertical Risers Above Ground", accepted for publication in *IEEE Trans. on EMC.*

[10] F .Middelstaedt, S.V. Tkachenko, R.Rambousky and R. Vick, "Analytic Approximation of Bent Wire Structures above Ground", *IEEE EMC Symposium 2015*, Dresden, pp.812-817.

[11] J.B.Nitsch, S.V.Tkachenko, "Global and Modal Parameters in the Generalized Transmission Line Theory and Their Physical Meaning", *Radio Science Bulletin*, **312**, March 2005, pp.21-31.

[12] T.B.A. Senior and J.M. Pond, "Pole Extraction in the Frequency Domain", ", *Interaction Notes*, **Note 411**, December 1981.

Propagation of high-frequency current waves along transmission lines with stochastic geometry

S V Tkachenko*, J B Nitsch*, R Vick*

** Otto-von-Guericke University, Magdeburg, Germany, e-mail: Sergey.Tkachenko.ovgu.de*

Abstract

On the basis of different analytical approaches we investigate the propagation of high frequency current waves along transmission lines with stochastic geometry.

Keywords: Transmission lines, stochastic geometry, high frequencies.

1 Introduction

Investigation of the propagation of voltage and current waves along different wiring structures constitutes one of the main topics in electromagnetic compatibility. In practice, often electrical parameters of such transmission lines are known only statistically (e.g., in cars, aircraft, etc.). A usual engineering approach to solve such problems includes the following three steps: (1) numerical generating of the stochastic geometry, (2) numerical solution of the corresponding TL or full-wave equations for each configuration and (3) averaging of the statistical ensemble. On the other hand, the application of direct numerical methods to solve stochastic problems is very time consuming and only describes a specific case of a distribution with fixed parameters. Therefore, it appears to be necessary to develop different analytical and semi-analytical approaches.

One of such approaches was developed in our previous work [1-3]. The current in the line is described by the system of telegrapher's equations. On the another hand this system can be reduced to a Schrödinger - like equation of second order (for the "wave function" which is connected with the current up to a known factor) with a "potential" that can be calculated from the transmission line parameters applying a differential operator of second order. We have assumed the geometry of the line (function h(z)) as a Gaussian delta - correlated process. Then, the parameters of the Telegrapher's equation and the "potential" in Schrödinger's equation also are Gaussian delta - correlated processes. Then, for the solution of such problems we have used a schema known in quantum mechanics and radio physics [4-6]. As a value still under study we considered the reflection coefficient for current waves which is a physical value connected with a usual scattering matrix in electrical engineering.

On the first step, the non-linear equations of Riccati type for the reflection coefficient from the finite region of the potential were obtained (using so-named method of invariant embedding). This equation includes the stochastic "potential" as parameter. Then, on the basis of this differential equation, corresponding to the Fokker-Planck equation for the PDF, the reflection coefficient was obtained. One interesting effect was observed: the current wave cannot pass the stochastic system (the transmission coefficients exponentially approached to zero with the length of the system). The analytical solution was compared with numerical results, obtained by the usual way, and a good agreement was observed.

2 Description of obtained results

In this work we improved the method in order to obtain, to generalize, and geometrically represent these results by a different way. The equation for the reflection coefficient for the current wave in a single-wire problem was obtained by means of a simple Feynman diagram technique from the system of Telegrapher's equations. The advantage of this approach in comparison with the previous one is that it does not require a derivation of the Schrödinger-like equation from the Telegrapher's equations which procedure contains double differentiation and is not convenient for numerical calculations. Then this equation can be rewritten by a way which makes the picture of the scattering phenomenon physically more clear. Using the substitution of [7], it can be represented in a form, where the one-dimensional lossless scattering is considered as a motion on the Lobachevski plane (in the representation of the hyperboloid model of the hyperbolic geometry, also known as the Minkowski model or the Lorentz model). In turn, the scattering in the stochastic wire corresponds to the diffusion on the Lobachevski plane [8]. Here one has to distinguish two limiting cases: weak and strong scattering. In the first case, when the absolute value of the reflection coefficient is much smaller that one, the diffusion looks like diffusion on the Euclidean plane and the reflection coefficient (real and imaginary parts) has a Gaussian distribution for the PDF [8,3]. Note that the results for this case can be obtained in the first order of perturbation theory. The second limiting case of strong scattering corresponds to an absolute value of the reflection coefficient about one. The average absolute value of the transmission coefficient damps exponentially with the length of the stochastic region (see Fig. 1) . In this case the PDF of the reflection coefficient is much more complicated [4,5,6].

The developed approach can be applied for the description of propagation of high-frequency current waves along transmission lines with stochastic geometry. In this case, when the radiation of transmission line can be essential, the

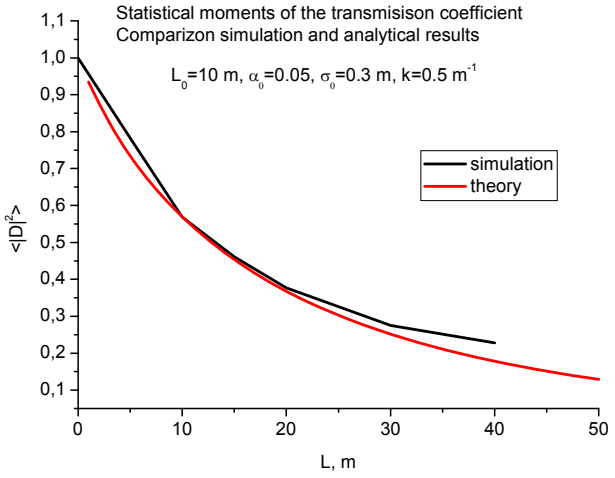

Figure 1: Length dependence of the average square value of the transmission coefficient through the line with stochastic geometry calculated using general theory and numerical simulation. Case of strong scattering.

propagation of the current wave for a given non-uniform geometry of the line is described by the so called Super Transmission Line Theory (see, for example, [9]). In this theory, propagation of currents and potentials along the transmission line with lumped source(s) and load(s) are described by a system of two differential equations of the first order - generalized Telegrapher's equations. The parameter matrix of this system, instead of the case of classical TL, is complex-valued, length dependent and contains diagonal elements. Non-classical elements of this matrix are: the imaginary parts of non-diagonal elements and the diagonal elements. These are responsible for radiation. This parameter matrix can be obtained, if one knows the geometry of the transmission line. As in the case of classical TL equations the equation for the reflection coefficient for the current wave in a single-wire problem can be obtained by means of a simple Feynman diagram technique from the system of generalized Telegrapher's equation. In the case of a stochastic transmission line this equation contains stochastic parameters which are connected with the geometry of the system. Then the usual technique is applied: we obtain the Fokker-Plank equation for the PDF of the reflection coefficient (absolute value). The solution of this equation for the PDF can be obtained by a numerical method, and gives a picture of competition between stochastic reflection and radiation during the propagation of current waves along the transmission line. For the case of stochastically arranged lumped loads such phenomena was investigated in [2].

The derivation procedure of the equation for the reflection coefficient can also be generalized for the case of multiconductor lines (many channel case in quantum mechanics) again by means of Feynman diagram techniques (by consideration of the diagram of lowest order in infinitesimal distance). Corresponding Fokker-Planck equations can be derived. One can show, that for the case of weak scattering the PDF of the reflection coefficient is multidimensional Gaussian. However, the solution of these equations for a general case currently remains a challenge.

Acknowledgements

This work was supported by the German Research Foundation (DFG), Contract Numbers: VI 207/3-1 and VI 207/6-1.

References

[1] S. Tkachenko, J. Nitsch and R. Vick, "Propagation of Current Waves along a Transmission Line with Stochastic Geometry", *Book of Abstracts EUROEM 2012*, Toulouse, p.46.

[2] S. Tkachenko, H.-J. Scheibe, X. Wang, R. Vick, „Propagation of Current Waves along a Transmission Line with Randomly Located Non-Uniformities", *Proc. of 10th Int. Conf. on Electro-magnetics in Advanced Applications* (ICEAA 13), September 9-13, 2013 - Torino, Italy.

[3] R. Vick, "High Frequency Stochastic Properties of Transmission Lines", Final Report for DFG Project Nr. VI 207/3-1. 2014, Magdeburg.

[4] G.C.Papanicolaou, "Wave Propagation in a One-Dimensional Random Medium", *SIAM J. Appl. Math.*, **volume 21**, No. 1, July 1971, pp. 13-18.

[5] I.M. Lifshits, S.A. Gredeskul, L.A.Pastur, *Introduction to the Theory of Disordered Systems*, NY: Wiley, 1988.

[6] V.I. Klyatskin, V.I. Tatarskii, "On the statistical theory of waves propagation in random media", *Transactions of High Schools, Radio physics*, 1977, **volume 20**, p. 1040 (Rus.).

[7] A.M. Peres „Transfer Matrices for One-dimensional potential", *J. Math. Phys.*, **volume 24**(5), May 1983, pp.1110-1119.

[8] M.E. Herzenstein, V.B. Vasiljev, „Diffusion Equation for the Statistically Nonuniform Waveguide", *Radiotechnic and Electronics*, 1959, N4, pp.611-617 (Rus.)

[9] J.B. Nitsch, S.V. Tkachenko „Propagation of Current Waves along Quasi-Periodical Thin-Wire Structures: Taking Radiation Losses into Account", *Radio Science Bulletin*, No **322**, September 2007, pp. 19-40.

Bianisotropic Scalar Potential Formulation and Depolarizing Dyad Anomaly

M J Havrilla*

**Air Force Institute of Technology, ECE Dept., 2950 Hobson Way, WPAFB, OH, 45433, USA, Michael.Havrilla@afit.edu*

Abstract

A scalar potential formulation for gyrotropic bianisotropic media is developed. It is shown that this formulation has two major advantages compared to working directly with Maxwell's field-based equations. It is discussed that both an expected and unexpected depolarizing dyad arises in the scalar potential technique. The unexpected depolarizing dyad is removable through careful application of Leibnitz's rule, which is often overlooked in analysis. The important implications of this work and future goals will also be discussed.

Keywords: Bianisotropic, gyrotropic, potential, dyad.

1 Introduction

Recent advances in material fabrication capability have had a profound influence on the investigation of the phenomena associated with complex (e.g., bianisotropic, hyperbolic, etc.) media. Gyrotropic media, for example, hold great interest due to their Faraday rotation and non-reciprocal properties. When solving problems involving complex media, Maxwell's equations are typically employed in a direct manner using, for example, the six-vector formalism [1]. This formulation is concise and can accommodate generic bianisotropic media (i.e., fully populated material tensors), however, a block 3×3 matrix must be inverted during the solution process. This inversion can be mathematically tedious and can obscure physical insight. It will be shown in the next section that, if the generic media is specialized to gyrotropic bianisotropic media, then a scalar potential formulation can be successfully employed. The advantages, limitations and care that must be taken with this formulation will also be discussed.

2 Scalar potential formulation

Consider Maxwell's curl equations for bianisotropic gyrotropic media ($e^{j\omega t}$ assumed and supressed)

$$\begin{aligned}\nabla\times\vec{E} &= -\vec{J}_h - j\omega\ddot{\mu}\cdot\vec{H} - j\omega\ddot{\zeta}\cdot\vec{E}\\ \nabla\times\vec{H} &= \vec{J}_e + j\omega\ddot{\varepsilon}\cdot\vec{E} + j\omega\ddot{\xi}\cdot\vec{H}\end{aligned}, \tag{1}$$

where the material tensor matrices have the specialized form $\ddot{\kappa}=\kappa_t\ddot{I}_t + j\kappa_g\hat{z}\times\ddot{I}_t + \hat{z}\hat{z}\kappa_z$, $\ddot{I}_t=\hat{x}\hat{x}+\hat{y}\hat{y}$ for $\ddot{\kappa}=\ddot{\varepsilon},\ddot{\mu},\ddot{\xi},\ddot{\zeta}$. Decomposing Maxwell's curl equations into transverse and longitudinal relations and utilizing the 2D Helmholtz expansion for the transverse fields and currents, namely

$$\begin{aligned}\vec{E}_t &= \nabla_t\Phi + \nabla_t\times\hat{z}\theta \;,\; \vec{H}_t = \nabla_t\pi + \nabla_t\times\hat{z}\psi\\ \vec{J}_{et} &= \nabla_t u_e + \nabla_t\times\hat{z}v_e \;,\; \vec{J}_{ht} = \nabla_t u_h + \nabla_t\times\hat{z}v_h\end{aligned}, \tag{2}$$

leads to the following scalar potential formulation

$$\begin{bmatrix}L_1 & L_2\\ L_3 & L_4\end{bmatrix}\begin{bmatrix}\psi\\ \theta\end{bmatrix}=\begin{bmatrix}s_1\\ s_2\end{bmatrix},\quad \begin{aligned}\Phi &= f\left(\tfrac{\partial\psi}{\partial z},\tfrac{\partial\theta}{\partial z}\right)\\ \pi &= g\left(\tfrac{\partial\psi}{\partial z},\tfrac{\partial\theta}{\partial z}\right)\end{aligned}, \tag{3}$$

where Φ,π have dependence on longitudinal derivatives, the terms L_1,L_2,L_3,L_4 are second-order differential operators and s_1,s_2 are source terms (details omitted for the sake of brevity).

One major advantage of this formalism is that only a block 1×1 matrix requires inversion, substantially easing mathematical effort. The other advantage is the enhanced physical insight due to the 2D Helmholtz expansion into lamellar and circulating components. The overall limitation of this technique is it accommodates gyrotropic media only.

Although the technique substantially reduces mathematical effort, great care must be taken in the field recovery process. As mentioned above, derivatives with respect to the $z-$variable must be taken in the solution process, resulting in terms of the form

$$\frac{\partial}{\partial z}\int_{a(z)}^{b(z)} h(z,z')dz'. \tag{4}$$

A commonly-encountered error is the passing of the derivative operator through the integral without regard to the functional dependence of the limits of integration. Rigorously, Leibnitz's rule must be employed in calculating the derivative, namely

$$\begin{aligned}&\frac{\partial}{\partial z}\int_{a(z)}^{b(z)} h(z,z')dz' =\\ &\qquad\int_{a(z)}^{b(z)}\frac{\partial h(z,z')}{\partial z}dz' + h(z,b)\frac{\partial b}{\partial z} - h(z,a)\frac{\partial a}{\partial z}\end{aligned}. \tag{5}$$

Although omitted here for the sake of brevity, it will be shown in the presentation that the additional Leibnitz terms do indeed produce a vital contribution. It turns out that this contribution exactly cancels an unexpected and unphysical depolarizing dyad term encountered in the scalar potential development. Without this vital contribution, the analysis would produce mathematically inconsistent and physically incorrect results.

3 Conclusion

A scalar potential formulation was developed and advantages and limitations were discussed and compared to a direct field-based formulation. The major advantages of the scalar potential formalism is the significant reduction in mathematical analysis and enhanced physical insight resulting from the 2D Helmholtz field expansion into lamellar and rotational parts. This insight can greatly aid the design of feed structures in practical problems. The limitation, although not too severe, of the scalar potential development is its ability to only accommodate bianisotropic gyrotropic media. It was also discussed that great care, via correct application of Leibnitz's rule, must be taken when employing the scalar potential formulation. In this case, the additional Leibnitz terms produce a vital contribution that must be properly handled in order to obtain a mathematically and physically consistent theory. Future work will include the analysis of radiating and propagation environments involving bianisotropic gyrotropic media, that includes as a subset, hyperbolic media [2], which is presently of great interest.

Acknowledgements

The views expressed in this article are those of the author and do not reflect the official policy or position of the United States Air Force, Department of Defense, or the U.S. Government.

References

[1] I.V. Lindell, A.H. Sihvola and K. Suchy, "Six-vector formalism in electromagnetics on bi-anisotropic media," *Journal of Electromagnetic Waves and Applications*, vol. 9, no. 7/8, pp. 887-903 (1995).

[2] A. Poddubny, I. Iorsh, P. Belov, and Y. Kivshar, "Hyperbolic metamaterials," *Nature Photonics*, vol. 7, pp. 958-967 (2013).

Impact evaluation of conducted UWB transients on terminal loads in a network

Bing Li and Daniel Månsson

KTH Royal Institute of Technology, School of Electrical Engineering
Department of Electromagnetic Engineering
Stockholm, Sweden
libing@kth.se, manssond@kth.se

Abstract

In this paper, we consider a conducted UWB disturbance due to intentional electromagnetic interference (IEMI), and evaluate impact quantifiers at the loads of a network. Through FFT, we characterize the time-domain transient and apply a Baum-Liu-Tesche (BLT) approach. The EMI received at the loads, which can be inductive, capacitive or resistive, is calculated and via the inverse FFT, we get the load responses in time-domain. To perform an impact evaluation of the loads, five quantifiers, i.e., time-domain peak, total signal energy, peak signal power, peak time rate of change and peak time integral of the pulse, are employed. It is seen that the impact evaluation of different kinds of loads, in a particular network, should be based on different attributes depending upon the characteristics of the transient.

Keywords: conducted UWB transient, IEMI, galvanic network, impact evaluation.

1 Introduction

In modern society, the terminal loads connected to a power line network are not limited to simple electrical loads. With the development of smart grids and techniques of power line communication, more diverse loads, such as power line modems, smart meters, and other modern electronics, are also able to directly access to the power line network. This increases the vulnerability of the power line system when it is exposed to an electromagnetic disturbance.

Intentional electromagnetic interference (IEMI) is a particular high power EM threat to civilian society. In [1], the IEMI-cube is provided for evaluating IEMI vulnerability. Having a complete impact evaluation helps a lot to reinforce the robustness of the systems. To perform the evaluation, several metrics can be utilized. In [2], five common quantifiers, which differ in different aspects, such as the dielectric breakdown, heating effects, etc., are proposed. According to distinct characteristics of resistive, inductive and capacitive terminal loads, the situations of being affected by IEMI may differ a lot. The definitions of those five common and important criteria are given as follows:

- Time-domain peak, $\sup_{0<t<\infty} \left|x(t)\right|$
- Total signal energy, $\int_0^\infty \left|x(t)\right|^2 dt$
- Peak signal power, $\sup_{0<t<\infty} \left|x(t)\right|^2$
- Peak time rate of change, $\sup_{0<t<\infty} \left|\frac{d}{dt}x(t)\right|$
- Peak time integral of the pulse, $\sup_{0<t<\infty} \int_0^t x(t)\,dt$

In this paper, we consider a load, whose impedance varies from inductive to capacitive, placed in a multi-junction power line network. With an injected IEMI, we calculate the transient response of the targeted load, and obtain results in terms of five quantifiers.

2 Analytical Model

A network that consists of two junctions and four branches is studied in our work, as shown in Fig. 1. A conducted IEMI disturbance is injected into the network from the end of one branch and other branches have loads connected. For the sake of simplicity, we assume load 1 and load 2 are resistive, while load 3 varies in both amplitude and phase (of course any load arrangement can be made to better suit a specific situation). Regarding load 3 ($Z_3 = R \pm jX = |Z|\angle\varphi$), the ranges of amplitude (i.e., $|Z|$) and phase (i.e., φ) are given by 1 to 1000 Ω and $-\pi/2$ to $\pi/2$, respectively. Furthermore, we assume that branch lines are of the same length L and characteristic parameters Z_c. Parameters of the model are summarized in Table 1. Here, a double-exponential UWB transient is considered for the IEMI source, and expressed by

$$a(t) = A_0\left(e^{-\alpha t} - e^{-\beta t}\right), \tag{1}$$

where A_0 is the peak value, α and β relate to the full width at half maximum (FWHM) and rise-time, respectively (however any waveform could be used in the investigation).

In the calculation, the duration of the UWB transient is 10 ns and the rise-time is 0.1 ns. FFT is used to characterize the double exponential pulse in the frequency domain, and the number of sampling points for FFT is 1024.

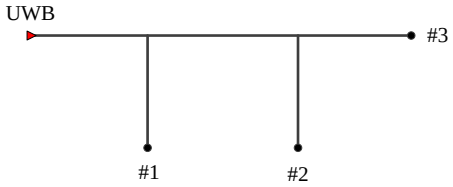

Figure 1. Example of a power line network.

By using the developed method [3] based on the BLT equation [4, 5], we subsequently calculate the voltage received at each load for different frequencies. Afterwards, the transient responses of the loads (in time domain) are obtained through the inverse FFT.

Table 1: Parameters in the model.

Parameter	Z_1	Z_2	$\|Z\|$	φ	Z_c
Value	100 Ω	100 Ω	1 ~ 1000 Ω	-π/2 ~ π/2	50 Ω
Parameter	A_0	α	β	**NFFT**	L
Value	1 kV	10^9	10^{10}	1024	3 m

3 Results and Analyses

Based on the analytical model established in Section 2, we can obtain numerical results for each load, with respect to the mentioned five quantifiers. Regarding load 3, results varying in the amplitude-phase plane, are shown in Fig. 2, and we can see that:

- From Fig. 2a) to 2d), in the region of low amplitudes (<= 400 Ω), there are two peaks occurring in each figure, at dominantly inductive and capacitive behaviour and around 50 Ω (which was seen to be, but not shown, a function of Z_c). It indicates that dominantly inductive or capacitive loads, with certain amplitudes, may suffer most from conducted UWB transients. However, in high amplitude region (> 400 Ω), with respect to amplitude or phase, the impacts of IEMI on five quantifiers are not significant.

- In Fig. 2e), for all phase values, the quantifier increases monotonically with amplitude, and the reason is that the transient voltage response of load 3 keeps positive in this case. Similarly to the first observation, when the amplitude is less than 200 Ω, especially around 50 Ω, the peak time integral of the pulse will faster achieve the highest value, when the load tends to be dominantly inductive or capacitive.

4 Conclusions

In this paper, we consider a specific multi-junction multi-branch power line network and investigate, with the aid of FFT and developed BLT method, the impact of IEMI on a targeted load in time domain.

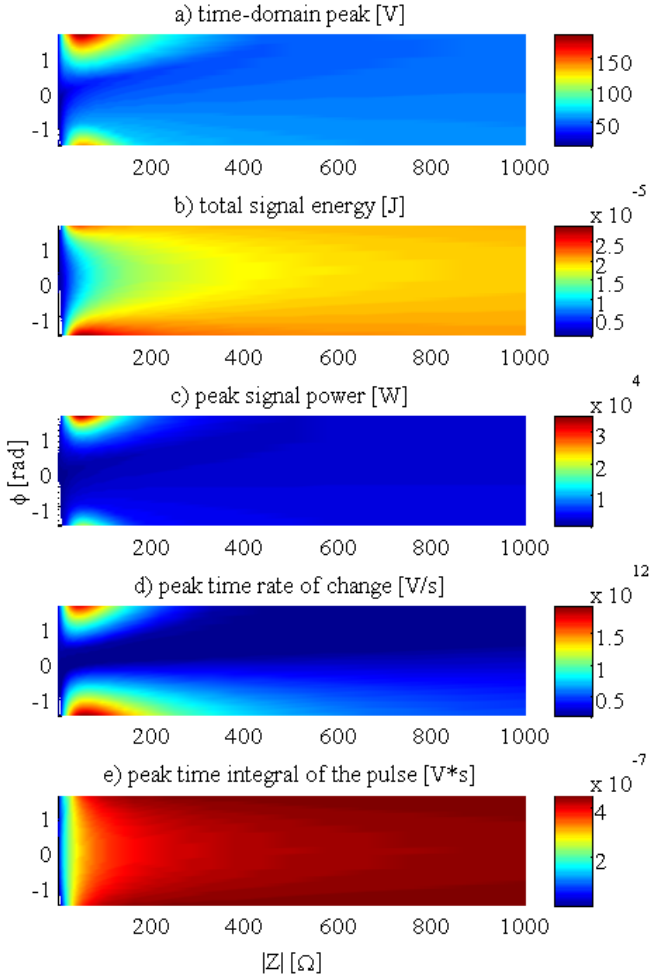

Figure 2. Calculation results of five quantifiers.

Results show that, in terms of the five common distinct evaluation quantifiers, a UWB source has a significant impact on a dominantly inductive or capacitive load with, here, a low amplitude (≈ 50 Ω). Thus, a system can be made less vulnerable by adapting the input impedance accordingly.

References

[1] D. Månsson, R. Thottappillil, and M. Bäckström, "Methodology for classifying facilities with respect to intentional EMI", *Electromagnetic Compatibility, IEEE Transactions on*, **vol. 51**, pp. 46-52, (2009).

[2] C. D. Taylor, and D. V. Giri, *High-power microwave systems and effects*, Taylor & Francis, (1994).

[3] B. Li, D. Månsson, and G. Yang, "An Efficient Method for Solving Frequency Responses of Power-Line Networks", *Progress in Electromagnetics Research B*, **vol. 62**, pp. 303–317, (2015).

[4] C. E. Baum, T. K. Liu, and F. M. Tesche, "On the analysis of general multiconductor transmission line networks", *Interaction Note 350*, pp. 467–547, (1978).

[5] C. E. Baum, "Generalization of the BLT equation", *Proc. 13th Zurich EMC Symp.*, pp. 131-136, (1999).

Intentional EMI mechanisms on a wireless receiver

S. van de Beek*, H. Schipper [†], and F. Leferink* [†]

**University of Twente, Netherlands, Email: g.s.vandebeek@utwente.nl, [†]Thales Nederland B.V., Netherlands*

Abstract

In this extended abstract, the different interference mechanisms on a wireless receiver are discussed. Front door coupled IEMI can result in a Denial-of-Service in three different ways: damage, saturation, and jamming. The mechanisms are fundamentally different and protection strategies should be approached from different disciplines.

Keywords: electromagnetic interference, wireless receiver, IEMI.

1 Introduction

In this extended abstract, it will be shown that the analysis of the robustness of a terrestrial trunked radio (TETRA) base station against intentional electromagnetic interference (IEMI) in [1] can be extended to any wireless receiver. The focus has been put on the front end of a receiver, since this is directly connected to the antenna and, as such, is the most vulnerable subsystem against front door coupled intentional EMI. From analysis [1] it is concluded that for a full investigation of IEMI vulnerability it is necessary to study three fundamentally different interference mechanisms.

2 Typical wireless receiver

In Fig. 1, an overview is given of a common receiver architecture. An RF signal received by the antenna is filtered by the front door filter which selects an entire band (the bandwidth is mostly a few MHz up to 20 MHz). The signal is fed to the low noise amplifier (LNA) and the mixer converts the RF signal to a lower intermediate frequency (IF). The selectivity of the receiver is dominated by the filtering at IF frequencies and not by the filter at RF.

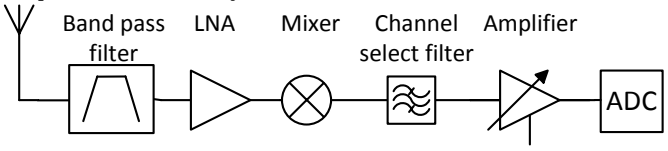

Figure 1. Typical receiver architecture

3 Interference Mechanisms

Research revealed that three mechanisms can be recognized in which front door coupled IEMI can result in a denial-of-service (DoS) of the wireless communication: damage, saturation, and jamming [1].

Firstly, high-power interference can damage the LNA [2], leading to a permanent DoS. Typical destruction levels of LNAs are summarized in [2] to be 34 dBm. Out-of-band (OoB) interference can be attenuated by the front door filter. In-band interference cannot be filtered out, but the electronics can be protected by a limiter.

Secondly, a high-power interferer (below damage levels) can saturate the receiver and as a result desensitize the receiver for the desired signal [3]. A high selective receiver is not more robust against this interference mechanism, since the degradation happens at the RF stage and the selectivity is at the IF stages. A high dynamic range of a receiver does improve the robustness against saturation.

Finally, the third interference mechanism is what is defined as jamming [4]. A low-power interferer, i.e. comparable power levels as the desired signal, can mask the desired signal. If the signal-to-noise ratio is too low the receiver will not be able to detect and decode the signal. A highly selective receiver improves robustness against jamming. For interference that is exactly in-channel, protection strategies can be found in spread spectrum techniques, smart antennas, and error coding schemes.

4 Conclusion

The previous discussed interference mechanisms are fundamentally different and it is necessary to have involved experts in different disciplines for developing protection strategies.

References

[1] S. van de Beek, F. Leferink. “Robustness of a TETRA Base Station Receiver Against Intentional EMI”, *Electromagnetic Compatibility, IEEE Transactions on*, **vol. 57**, pp. 461-469, (2015).

[2] T. Nilsson, R. Jonsson. “Investigation of HPM front-door protection devices and component susceptibility”, FOI-R-1771-SE, 2005.

[3] J.J. Gavan, M.B. Shulman. "Effects of desensitization on mobile radio system performance, part I: Qualitative analysis," in *Vehicular Technology, IEEE Transactions on* , **vol.33**, no.4, pp.285-290, Nov. 1984.

[4] K. Pelechrinis, M. Iliofotou, and S. V. Krishnamurthy, “Denial of service attacks in wireless networks: The case of jammers,” *IEEE Commun. Surveys Tuts.*, **vol. 13**, no. 2, pp. 245–257, 2011.

Predicting and Modelling High Power Electromagnetic Effects on Electronics

T Clarke, J Lawrance, H Pohle, J MacGillivray, D Guillette, E Landreth

Air Force Research Labarotory
Kirtland Air Force Base, New Mexico, USA
clarketj@ieee.org

Abstract

Characterizing the response of electronics systems to high power electromagnetic (HPEM) fields is critical to ensuring that they will continue to function correctly in extreme electromagnetic environments. Developing such a predictive capability represents an extremely challenging technical problem, and until recently limited progress has been made. We will describe a new approach to this problem, based on combining coupling and circuit interaction experiments with high fidelity simulations, as well as presenting results of this research.

Keywords: High power electromagnetics, intentional EMI

1 Introduction

The ability to understand and predict high power electromagnetic (HPEM) effects on electronics is critical to ensuring that electronic systems will continue to function correctly in high intensity electromagnetic environments, as well as to guaranteeing their continued operation in the face of intentional EMI threats. Unfortunately, developing such a predictive capability represents an extremely challenging technical problem, and until recently limited progress has been made. In the last few years we have initiated a new approach, attacking this problem by combining electromagnetic coupling measurements and high fidelity finite difference time domain electromagnetic simulations with an investigation of the electronic response at the device, circuit and system levels, and we will describe this general approach as well as presenting results of our research.

2 Results and Discussion

We will describe our work in a number of areas, including collaborative work with the University of New Mexico and the University of Maryland under a newly established University Center of Excellence with the title "The Science of Electronics in Extreme Electromagnetic Environments". This work includes an investigation of how high-intensity electromagnetic fields interact with basic CMOS devices, as well as a study of how these interactions change as electronics evolves.

Next, we will present results of our research to understand and predict the response of a microcontroller to a high-power electromagnetic waveform [1]. This work was motivated by an earlier German study into the immunity of digital electronics to transient pulses [2], which investigated how a burst of 50ns electrical transient pulses affected a simple 8-bit 80C51 microcontroller, while it performed a single assembler instruction repeatedly. Our research is based on the observation that a microcontroller is a complete digital system (a full, self-contained computer implemented on a single integrated circuit), but without many of the additional features (metal enclosure, multiple printed circuit boards each containing multiple chips and interconnects, peripherals connected via cables, etc.) that make predicting the response of a digital system such as a standard desktop PC so challenging. In this sense, a microcontroller represents an intermediate level of complexity between a single CMOS device and a complete digital system such as a personal computer.

Finally, we will describe how our results shed light on the broader problem of predicting the response of a general digital system to a high-power electromagnetic waveform.

Acknowledgements

The work described was supported in part by the Air Force Office of Scientific Research.

References

[1] T. Clarke, A. Taylor, N. Estep, S. Yakura, D. Brumit, D. Dietz, S. Hemmady, and J. Duffey, "Predictive Modeling of High-Power Electromagnetic Effects on Electronics", 2011 International Conference on Electromagnetics in Advanced Applications, 429, DOI: 10.1109/ICEAA.2011.6046377, 2011.

[2] Vick, R. and E. Habiger. The Dependence of the Immunity of Digital Equipment on the Hardware and Software Structure. Proceedings of International Symposium on Electromagnetic Susceptibility, ed. L. Zhang and K. Zhou, 383-386, 1997.

Developing Predictive Capability for Upset of Digital Systems in HPEM Environments

J Lawrance, T Clarke, H Pohle, J MacGillivray, D Guillette, E Landreth

**Air Force Research Laboratory,*
Kirtland Air Force Base, NM
char@unm.edu

Abstract

It is desirable to develop a capability that would allow one to predict the upset threshold of a digital electronic system for any high power electromagnetic (HPEM) waveform. Developing this capability depends largely on understanding how HPEM energy penetrates into a system and couples into internal electronics. This paper focuses on our efforts to understand this process, through analysis, experiment and simulation.

Keywords: Upset in digital systems, HPEM, EMI induced upset.

1 Introduction

Upset of digital electronic systems when illuminated with HPEM excitation has been investigated experimentally for over 30 years. Past attempts were made to develop an analytic understanding of the problem of coupling into these systems and the exact mechanism(s) of the resulting upset. The results of these past efforts are perhaps best summarized in [1].

However, due to the complexity of the problem, confounded by the continuous evolution of digital systems, not much progress was made in past years. Progress in this area was also impeded in the past by the lack of today's computing power.

The most important first step in developing this predictive capability is in understanding how HPEM energy pentrates into the system housing and subsequently couples into internal electronics; certainly if the frequency content of an incident HPEM waveform prevents it from penetrating a system, it cannot interfere with normal operation of the target system. Conversely, if the incident HPEM waveform comprises frequencies that penetrate easily and which couple into electronics easily, there is a significantly increased probability that the excitation will interfere with normal operation of the system under test.

To first order, understanding the penetration/coupling portion of this problem alone would give us significant predictive capability.

At high frequencies, where the wavelength of the incident HPEM wave is much smaller than the dimensions of the system, the Random Coupling Model [2] has proven to be effective. However, at frequencies where the wavelength approaches the dimension of the system, this model is not valid.

2 Results

In recent years, we have begun methodical exploration of the penetration/coupling aspect of the problem through analysis, experiment and simulation, focusing on the frequency range from 1-10GHz and a single personal computer (PC). Simulations were run using TMAX [3], a finite difference time domain code, on a detailed model of the computer housing and results were compared with experimental measurements made to explore penetration and coupling into the PC.

3 Discussion

Through these efforts, we have begun to understand and quantify: penetration of HPEM into a cavity; the magnitude of electric fields that are induced internally (often enhanced by resonant modes of the structure); and how these electromagnetic fields couple into the internal electronics.

Acknowledgements

This work was funded in part by the Air Force Office of Scientific Research (AFOSR).

References

[1] K.S.H. Lee, G Hoffer and D.P.McLemore,. "Trend and Bound Approach to Transfer Functions and Application to Interpolation/Extraction of System Level Results", *DCTR-0328.120-3*, **December 2002**

[2] S. Hemmady, X. Zheng, E. Ott, T. M. Antonsen and S. M. Anlage,"Universal Statistics of the Scattering Coefficient of Chaotic Microwave Cavities. *Phys. Rev.* E 71, 056215, 2005.

[3] J. MacGilligray, J. Schwarzmeier, M. Abdalla "TMAX Electromagnetic Finite Difference Time Domain Simulation Cray X1 of the Impulse Radiating Antenna", *IEEE Computer Society*, ISBN: 0-7695-2496-6 **June 2005**

Quality Criteria for NEMP Test Environments

F. Sabath, S. Potthast

Bundeswehr Research Institute for Protective Technologies and NBC-Protection (WIS),
29633 Munster, Germany, email: WIS300Physik@bundeswehr.org

Abstract

This paper discusses tolerance values for NEMP field tests. A NEMP simulator provides the NEMP environment with various degrees of completeness. Deviations from the analytical waveform occur due to the simulator structure and concept. In this paper we review tolerance values for pulse parameters specified in civil and military standards.

Keywords: Electromagnetic Pulse, NEMP, Test Methods, Tolerance Specification

1 Introduction

Due to physical characteristics of the high voltage pulse source as well as limitations and characteristics of the simulator design, the environment simulated by an NEMP simulator deviates from the specified waveform. Generally, NEMP environment standards do not specify limits for acceptable deviations of the simulated environment from the analytically specified waveforms. In this paper, we will discuss how quality criteria for NEMP test environments are specified in various test standards.

2 NEMP Environment

Standards on NEMP testing employ various mathematical formulations to describe the electromagnetic environment. Commonly, the most important parameters of the waveform are the rise time $\tau_{10\%\text{-}90\%}$, the pulse width at half maximum T_{FWHM}, and the peak amplitude of the electric field E_0. A very popular mathematical model for the NEMP waveform is the difference of double exponentials with the unit step function [1, 2]:

$$E(t) = kE_0\left(e^{-\alpha t} - e^{-\beta t}\right)u(t) \qquad (1)$$

where the value of the peak amplitude of electric field is generally E_0 = 50 kV/m and the unitary factor k=1.33. The waveform characteristics $\tau_{10\%\text{-}90\%}$ and T_{FWHM} are determined by the model parameter α, β and E_0 in (1).

3 Quality Criteria

NEMP environment specifications do not provide any information on the assessment of deviations from the analytical waveforms. Due to the impact of these deviations on the coupling and interaction of the simulated NEMP environment with the system under NEMP test specifications are required to close this lack of information. The usual way this aspect is addressed in standards on NEMP field tests is to define tolerance values for the time domain waveform characteristics.

The test values specified by most military standards and by IEC 61000-4-25 [1] tolerate a 6 dB overshooting of the peak amplitude (Table 1). In these cases an over test is tolerated as it provides an additional safety margin. With regard to the short development cycles of commercial electronics and the relatively low likelihood of an NEMP event this practice has been questioned by manufacturer and user.

The German VG 96903-50 [3], which was updated recently, enhanced this approach by adding some more details on time domain characteristics. In addition this standard defines tolerance values for the time integral and the energy flux rate. The primary intent was to set a limit on over- and under-tests with regard to the applied energy [4].

Table 1: Test parameter and tolerances of selected civil and military NEMP test environments.

	IEC 61000-4-25 [1]		**VG 95371-10 [2]**	**VG 96903-50 [3]**
	test parameter	***tolerance value***	***test parameter***	***tolerance value***
E_0	50 kV/m	+0 - +6dB	50 kV/m	±10%
$\tau_{10\%-90\%}$	2.5 ns	± 1.5 ns	2.5 ns	±10%
T_{FWHM}	25 ns	25 – 75 ns	23 ns	±20%
$\int_0^\infty E(t)\cdot dt$	NA	NA	1.25 10^{-3} Vs/m	±20%
$\frac{1}{\eta_0}\int_0^\infty E^2(t)\cdot dt$	NA	NA	0.114 J/m^2	±30%

NA: not applicable

References

[1] IEC 61000-4-25:2001, Electromagnetic compatibility (EMC) - Part 4: Testing and measurement techniques – Section 25: HEMP immunity test methods for equipment and Systems. Basic EMC publication, November 2001.

[2] VG 95371-10:2011, Electromagnetic compatibility (EMC) including electromagnetic pulse (EMP) and lightning protection — Fundamentals — Part 10: Threat levels for NEMP and lightning, September 2011.

[3] VG 96903-50:2012, Nuclear electromagnetic pulse (NEMP) and lightning protection — Test methods, test equipment and limiting values — Part 50: Field test with NEMP simulators (Test procedure SF 50), October 2012.

[4] Sabath, F.; Potthast, S., "Tolerance Values and the Confidence Level for High-Altitude Electromagnetic Pulse (HEMP) Field Tests," in IEEE Transactions on Electromagnetic Compatibility, vol.55, no.3, pp.518-525, June 2013

Alternative treatments of shielded cables entering a shielded building

E. B. Savage*, W. A. Radasky†

**†Metatech Corporation, U.S.A, savagee@cox.net*, wradasky@aol.com†*

Abstract

For IEMI/HEMP hardening, system cables outside a shielded building should be shielded to lessen coupling to their wires that connect inside the building. However any coupled current on that shield should be dumped off outside before entering the shielded building. In this paper we present measurements of several techniques for this current "wipe-off".

Keywords: current wipe-off, shielded cables.

1 Introduction

In general an IEMI/HEMP hardened building should use a whole-building shield and shielded external cabling. The best practice is to have the cable shield 360° circumferentially bonded to the building shield on entry. This 360° requirement is not just to avoid apertures, per se, but because the very high current dumped off the shield would be very close to any such aperture. Many types of feed-thru connectors are manufactured that make such full-shielded bonds, however it still is not convenient to implement this requirement in all cases. In this paper we look at alternative approaches in which there is an open aperture through the building wall, and the shield current is dumped off outside before the cable goes through the aperture.

Given that we need to accept having a cable feed-thru aperture, it still is good to short out the current outside before coming through the aperture. This current wipe-off should not be right at the aperture, because then the fields associated with the high current could leak through the aperture, nor should it be too far from the aperture, because the cable between the grounding point and aperture would have coupling to the external field. We also want the wipe-off method to have low impedance to ground, especially with regard to the very high frequencies of IEMI and HEMP.

Figure 1. Current wipe-off clamp.

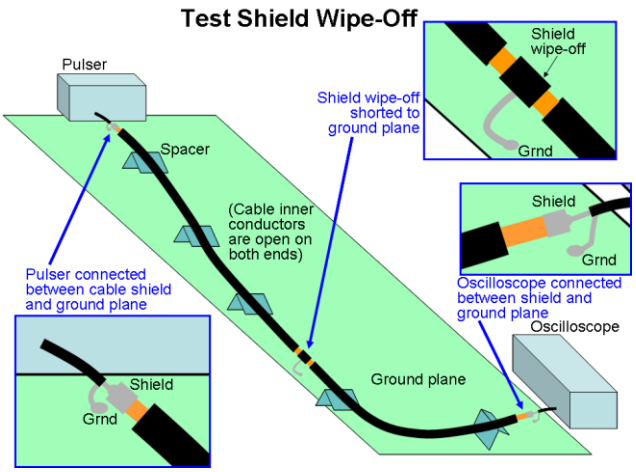

Figure 2. The measurement approach.

2 Current wipe-off measurements

Fig. 1 shows a sample wipe-off method. It uses a commercial clamp; possibly designed for lightning considerations. It has a simple snap-on clamp, and lead wire to connect to ground. Fig. 2 shows the measurement concept. A long sample of shielded cable is laid out a fixed distance above a ground plane. On one end of the cable a pulser is connected between the cable shield and the ground plane. On the other end the cable shield is connected to an oscilloscope. Fig. 3 shows a result for this case, using normalized scaling. The red line is the voltage at the pulser end (only used for reference). The green line is the voltage at the other end, with the wipe-off clamp grounded to the ground plane. It is normalized so the amplitude of 1.0 is the peak when the wipe-off clamp's ground lead is disconnected from the ground plane. Many other sample results will be given in the presentation.

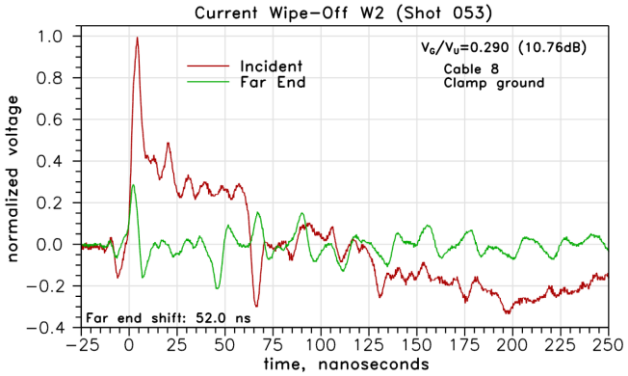

Figure 3. Sample wipe-off current measurement.

UWB-IEMI laboratory tests of single-stage and multi-stage lightning and HEMP-protection devices

A. W. Kaelin*, M. Nyffeler†

**EMProtec GmbH, Switzerland, armin.kaelin@emprotec.ch*
†armasuisse Science and Technology, Switzerland, markus.nyffeler@armasuisse.ch

Abstract

Devices that protect against conducted threats of lightning- and HEMP-induced currents are readily available on the market for a variety of applications. Typical UWB-IEMI-pulses may have a rise-time that is up to 1000 times shorter compared to HEMP and the question is, if such protection devices can survive such IEMI attacks and if they can also provide sufficient protection to subsequent electronics. In this paper we describe UWB-tests of single-stage and multi-stage HEMP-protection devices. For the test nine different protection devices were investigated. UWB-pulses with amplitudes up to 12kV and rise-times as short as 100ps have been injected and the output voltages have been measured for various input amplitudes.

Keywords: IEMI, UWP pulse test, PCI, HEMP-protection

1 Introduction

Protection devices to protect electronic equipment against conducted transient overvoltages are available on the market for many years and from a variety of manufacturers. While some products protect only against lightning surges and others only against HEMP transients, there are also some that provide combined protection for both lightning and HEMP transients. There is an increasing concern about IEMI attacks on critical infrastructure, and this raises the question, if such protection devices can also provide sufficient protection against IEMI-like transients, such as repetitive and very fast rising Ultra-Wide Band (UWB) pulses.
Giri and Tesche [1] classified IEMI environments by their bandwidth. More recently the availability of powerful conducted and radiated IEMI sources was added to the classification [2] criteria. Until now a few investigations of the behaviour of HEMP protection devices under IEMI-like conditions have been published. In a first experiment UWB pulses with 150ps rise-time and peak voltages up to 1.5kV were used [3]. Then IEMI tests of network protectors were done by using EFT-pulses (Electric Fast Transients) with risetimes of 5ns and amplitudes up to 8kV [4]. In this work an Ultra-wide band solid-state source with output voltages up to 12kV was used and the range of devices under test (DUT) has been extended from various network protectors to lower speed dataline protectors and a DC-powerline protector.

2 DUT's and Measurement Setup

In total 9 different protection devices numbered as #1 to #9 have been investigated (see Table 1). #1 to #3 are coaxial RF-protectors with exchangable GDT's, providing only single-stage coarse protection. The GDT's had a DC-breakdown voltage of 90V, 230V and 900V respectively.
DUT #4 to #9 are all advertised for both lightning and HEMP-protection. DUT #4 is for the protection of analog or digital (up to 2Mbit/s) telephone lines. DUT #5 protects a single wire of a DC-power line for max. 30VDC and 3A. DUT #6 protects a Gigabit-Ethernet cable (4 wire pairs) and also works in PoE (Power over Ethernet) applications. DUT #7 protects a Fast-Ethernet cable (2 wire pairs only), it cannot be used for PoE. DUT #8 also protects a Gigabit-Ethernet cable, but doesn't work with PoE. Finally DUT #9 protects a Gigabit-Ethernet cable and permits use of PoE+, which is currently the latest standard for Power over Ethernet use.
As an UWB-source a Kentech PBG3/D/V solid-state generator was used. It generates pulses of typically 100ps rise-time and a pulse duration of approximately 3ns. The pulse repetition frequency (PRF) can be adjusted from single pulse to 1 kHz. The pulse amplitude into a load of 50 Ohms is adjustable from approx. 1.8kV to 12kV.
Fig.1 shows the typical test setup scheme for direct pulsed current injection (PCI) into the DUT. The electrical wiring scheme is as suggested in the newly updated IEC-standard [5] and the unused cable of the twisted wire pair is grounded only on one side to avoid shortening of possible current-compensated chokes inside the protector.

DUT	Protection Device		
	Model / S =single-stage, M=multi-stage		*Manufacturer*
#1	3402.17A with 90V GDT for RF cable	S	Huber & Suhner
#2	3402.17A with 230V GDT (73Z-0-0-4)	S	Huber & Suhner
#3	3402.17A with 900V GDT (73Z-0-0-52)	S	Huber & Suhner
#4	USS-2-2048-F (digital telephone)	M	Meteolabor®
#5	USS-2-3A-30V (DC power)	M	Meteolabor®
#6	USN-80001 Gigabit Ethernet, PoE	M	Meteolabor®
#7	USN-40001 Fast Ethernet (no PoE)	M	Meteolabor®
#8	EMP-843000 Gigabit Ethernet (no PoE)	M	EMProtec
#9	EMP-843110 Gigabit Ethernet, PoE+	M	EMProtec

Table 1: List of DUT's (Device under Test).

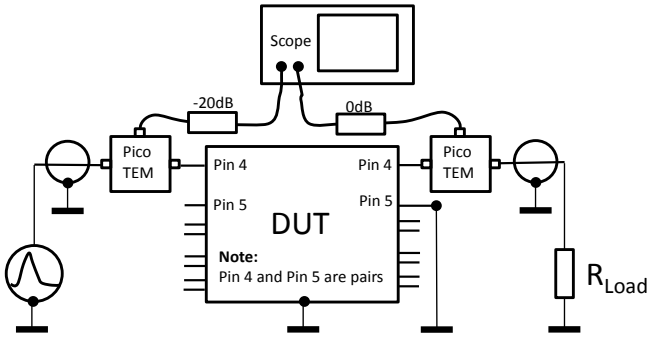

Figure 1. Typical PCI-Test Setup for multi-line DUT's.

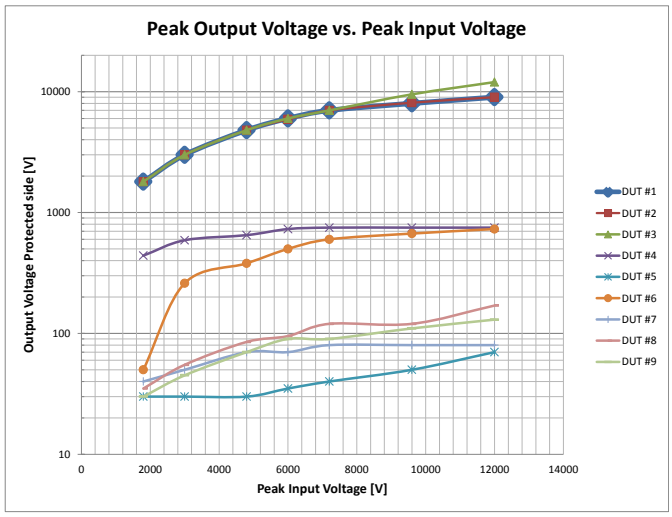

Figure 2. Summary and comparison of the peak output voltages of all tested DUT's vs. the input peak voltage. Note that the vertical axis has a logarithmic scale.

The DUT is installed as feed-through device into a shield wall of a Faraday's cage. The pulse is applied through a 50 Ohms coaxial cable and the output of the DUT is terminated by a 5m long coaxial cable, which is long enough to eliminate unwanted reflections from the termination within the time of interest. The setup is shielded on both sides of the DUT and unwanted coupling outside of the DUT is minimized.
The applied voltage on the unprotected side as well as the output voltage on the protected side is measured by two derivative voltage sensors Montena VDOT8G. These voltage sensors are pico-TEM-cells [6] that are suited to measure very fast pulses while having almost no insertion loss. The output is fed into a digital scope LeCroy SDA 11000, which is capable to record two channels simultaneously with a bandwidth of 11 GHz. Each DUT is tested with a series of pulses with increasing peak voltages of 1.8kV, 3kV, 4.8kV, 6kV, 7.2kV, 9.6kV and 12kV.

3 Measurement Results

Fig.2 shows a summary of the measured peak voltages of all DUT's. The well-known dynamic behaviour of GDT's can be observed in all three single-stage protection devices. Although the GDT breaks down after a finite time (approx. 1 ns) the peak of the UWB-pulses is fully transmitted for most amplitudes, but the tail of the pulse is truncated.
The multi-stage DUT's responded to all tested levels and they all had residual voltages clearly below 1000V for all input amplitudes, thus clearly reducing the peak amplitude.

4 Conclusions

Due to their finite response time single-stage protections show relatively high residual voltages when exposed to UWB-pulses. Although they may provide some protection by truncating the incoming pulse, for many applications this might be not sufficient protection from such IEM-like pulses.
All tested multi-stage protectors provide protection levels clearly below 1000V, which is a quite safe level for electronics tested by standard EMC-tests including ESD (ElectroStatic Discharge) and EFT-pulses.
In the oral presentation we will show more results and also give some considerations to repetitive UWB-pulses. Since the DUT's investigated here are designed for both lightning and HEMP-protection they are capable to both, respond quickly and absorb relatively large pulse energies.
Nevertheless, it is important to keep in mind, that such protectors can reliably prevent physical damage to electronics, but by there working principle they will not be able to avoid loss of information when a data line is exposed to an IEMI-attack with repetitive pulses.

References

[1] D. V. Giri and F. M. Tesche, "Classification of intentional electromagnetic environments (IEME)," *IEEE Transactions on Electromagnetic Compatibility*, vol. 46, pp. 322-328, (2004).

[2] G. Lugrin, N. Mora, S. Sliman, F. Rachidi, M. Rubinstein, R. Cherkaoui, "Overview of IEMI Conducted and Radiated Sources: Characteristics and Trends", *Proc. of the 2013 International Symposium on Electromagnetic Compatibility (EMC Europe 2013)*, Brugge, Belgium, (2013).

[3] M. Nyffeler, A. W. Kaelin, D. Rolle, P. F. Bertholet, and A. Jaquier, "Behavior of combined Lightning and HEMP Protection Devices to HPEM Overvoltage Input Signals," *AMEREM 2010 conference, Ottawa*, Canada.

[4] E B Savage, W A Radasky, "IEMI laboratory tests of network line protectors: vulnerability and protection ability", *ASIAEM 2015 conference in Jeju do*, Korea, paper 56, (2015).

[5] IEC 61000-4-24, ed. 2.0, Nov. 2015, Electromagnetic compatibility (EMC) – Part 4-24: Testing and measurement techniques – Test methods for protective devices for HEMP conducted disturbance, IEC, Geneva, ISBN 978-2-8322-2971-2.

[6] T. Weber and J. L. ter Haseborg, "Measurement Techniques for Conducted HPEM Signals", IEEE Transactions on Electromagnetic Compatibility, Vol. 46, No. 3, August 2004

Lessons Learnt From IEMI Detector Deployments

D. Herke, L. Chatt, B. Petit and R. Hoad

QinetiQ Ltd., Cody Technology Park, Farnborough, Hampshire, UK,
rhoad@qinetiq.com

Abstract

Detection of Intentional Electromagnetic Interference (IEMI) is clearly an important step in understanding and quantifying the site based risk from IEMI and for providing a cue for an appropriate response, recovery plan. Several prototype IEMI detectors have been developed but information on the challenges involved in actually deploying detectors on to Critical National Infrastructure (CNI) sites has not been widely discussed to date. This paper summarises some lessons learned from a recent trial deployment of an IEMI detection system.

Keywords: High Power RF, IEMI, Detection

1 Introduction

It has been well documented that IEMI detection is very likely to be important in understanding the risk posed to a site from IEMI and as a cue for a site recovery strategy [1]. Several groups have developed hardware [2, 3, 4] and software solutions [5] for IEMI event detection. Presently we are undertaking a trial based deployment of several IEMI detectors, working name 'TotEM™', shown in Figure 1, at four Critical National Infrastructure sites within the UK.

Figure 1. TotEM™ IEMI Detector.

This paper discusses some of the challenges experienced in deploying the detectors and summarises the findings to date.

2 IEMI Detector Deployment Challenges

2.1 Identifying where to site the detector(s)

The physical location of the detector(s) on the site has to be selected with care. Siting the detector on the outside façade of a facility may seem optimal, however, practically speaking the detector must be available 24 hours a day, 7 days a week, 365 days a year and therefore is likely to require an external power supply. Providing an external supply to the façade or to the site perimeter to power the detector could, if not managed with care, compromise the intrinsic IEMI resilience of the facility.

The setting of an appropriate threshold or thresholds which appropriately reflects an IEMI 'threat' level event for critical equipment inside a facility from an IEMI generator outside of the facility as is highly complicated. There are many factors that need to be considered including the magnitude (an uncertainty) of the facility façade structural attenuation and other factors influencing the propagation of the threat from outside of the facility to inside,. Our preferred strategy for the optimum siting of detectors is to locate them as close to the critical equipment as possible and preferably aligned to the most likely direction that the threat could emanate from.

Fortunately QinetiQ has conducted site surveys and developed tools to visualise where the most likely risk (from a vehicle or hand emplaced IEMI device) might occur [6] and can therefore optimise detector location for those specific sites. However, the final location is often a compromise between the optimum location from the threat perspective and the availability of a space with appropriate power and which does not compromise building regulations. Additionally, positioning the detector away from electrically noisy systems is preferred to allow better sensitivity and therefore a greater chance of detecting IEMI.

2.2 Logging events, retrieving events and controlling the detector(s)

A permanent log of IEMI events is required to enable evidence collection. We have found that simple non-volatile memory can be used to provide this functionality. The site owner/operator has to provide agreement that the log file can be recovered by an appropriate external agency in the circumstance where an IEMI event occurs and evidence collection is necessary. Of course IEMI event information or alerts must also be available to the site owner/operator in a

timely manner so that appropriate preventative or remedial/recovery actions can be taken. This immediate indication is achieved in the first instance by visual indicators on the unit. A second method for event notification to a remote off-site terminal is provided via GPRS SMS text messaging. Status information and limited command control functionality can be provided via this messaging system. This messaging system is dependent upon mobile/cellular coverage but we have found that by pre-interrogating the mobile/cellular coverage at a site we can identify the best local provider.

2.3 Managing and discriminating against false alarms

From our recent experience it has become apparent that detectors may be located in an environment where electromagnetic interference (EMI) events, particularly transients, routinely occur. For example EMI events such as those generated by arcs, corona, partial discharge and circuit breaker transients are very common, particularly on High Voltage Sub-station sites. In order to deal with and discriminate 'ambient' EMI events from IEMI events, the detector is equipped with an ambient survey mode allowing full characterization of the ambient environment over a user determined survey period. Further, it has been found to be important to correlate 'events' recorded by the detector with an actual functional disturbance of the site critical equipment.

3 Summary

This paper summarises some lessons learned from a recent trial deployment of an IEMI detection system. It is hoped that this information will help those planning to implement similar systems on other sites.

References

[1] R. Hoad and A. Blyth, "Electromagnetic (EM) susceptibility of information systems – The need for EM detection", *Proceedings of the 4th European Conference on Information warfare (ECIW) and security*, University of Glamorgan, July (2005)

[2] D. B. Jackson, T. R. Noe, G. H. Baker III, "High Dynamic Range, Wide Bandwidth Electromagnetic Field Threat Detector", *Ultra-Wideband, Short-Pulse Electromagnetics 10*, pp 355-368, 28 November (2013)

[3] M. Suhrke, "Threat and Detection of High Power Microwaves", *Progress In Electromagnetics Research Symposium Abstracts, Stockholm, Sweden*, Aug. 12-15, (2013)

[4] J. F. Dawson, I. D. Flintoft, P. Kortoci, L. Dawson, A.C. Marvin, M. P. Robinson, "A Cost-Efficient System for Detecting an Intentional Electromagnetic Interference (IEMI) Attack", *International Symposium on Electromagnetic Compatibility (EMC Europe 2014), At Gothenburg, Sweden,* September (2014)

[5] C. Kasmi, J. Lopes-Esteves, M. Renard, "Autonomous Electromagnetic Attacks Detection considering a COTS Computer as a Multi-Sensor System", *General Assembly and Scientific Symposium (URSI GASS), 2014 XXXIth URSI*, Page(s):1 – 4, 16-23 Aug. (2014)

[6] B. Petit, R. Hoad and A. Fernandes, 'An Overview of Some Site Specific IEMI Risk Assessment Tools', *AMEREM 2014, Albuquerque, NM, USA,* 27th July to 1st August (2014)

The IEMI Threat and a Practical Response

William Turner

MPE Ltd, Liverpool, UK wturner@mpe.co.uk

Abstract

With the increasing use of electronics to control every aspect of modern life, IEMI is a growing risk. This paper presents several methodologies for asset protection and provides analysis of their benefit against an attack.

Keywords: Intentional Electromagnetic Interference (IEMI), High Altitude Electromagnetic Pulse (HEMP), Protection, Filter

1 Introduction

Although various market specific initiatives have been setup and new standards are being worked on, for effective protection it is worth understanding what is being protected against and how that compares and contrasts with other electromagnetic protection standards.

2 Methods of Threat Delivery

To protect against a threat one must first understand the nature of it. IEMI attacks can take many forms however Fig. 1 shows the simplified frequency / magnitude nature of possible threats. IEMI differs from most other EM threats in that it typically occupies a narrow frequency band dependent upon the specific malicious source being used. This contrasts with other threats such as lightning and HEMP (high altitude EMP) which are very broadband in nature.

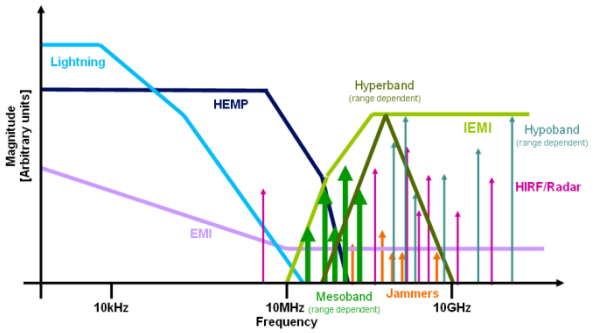

Figure 1. Comparison of IEMI and other EM disturbances

3 Asset Protection

3.1 Classical Approach

Dismissing the flawed argument of existing EMC Directive compliance or similar the obvious protection methodology is to place everything to be protected in a Faraday cage using shielding and filters on all penetrating conductors. This is the method employed by the nuclear EMP protection (HEMP) standard for critical military infrastructure Mil-Std 188-125. As confirmation of this principle MPE recently tested their HEMP filters against a Diehl pulser providing a 350MHz damped sine wave source capable of 120kV/m at 1m. The results demonstrated that the principle still holds true.

3.2 Staged Protection

An alternative approach is to assess the likely threats and focus protection against them, taking advantage of existing, even incidental, protection. Fig. 2 shows an example of this approach.

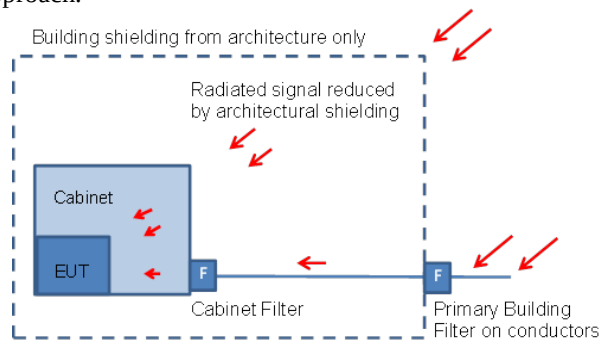

Figure 2. Staged Protection

4 Threat Detection

With the arrival of lower cost IEMI detection equipment, detection of attacks as an intermediary or complementary step to protection is economically viable. By logging the disturbance in enough detail in the time domain offline analysis can be performed, removing the need for complex and protected analysis, and thus cost, within the detector. With multiple detectors deployed information that could be available through analysis includes triangulation of the threat source, attenuation provided by existing buildings, infrastructure or shielding. This solution gives the two desired outcomes from detection: an evidence trail for any cost/benefit assessments for stakeholders to invest in further protection; time stamping of disturbances to be correlated with any CCTV or other evidence in legal proceedings.

Acknowledgements

I would like to thank Radiotechnika and Warsaw University for the use of their Diehl pulser and test facilities. I would also like to thank Dr Richard Hoad for supplying Figure 1.

PROGRESS project: Vulnerability and protection of GNSS ground-based infrastructures

N Ribière-Tharaud[1], J-C Joly[1], A. Rouquand[1], S Schopferer[2], C Michalski[2], M Schimmerohn[2], S Crabbe[3]

[1]CEA, DAM, F-46500 Gramat, France (nicolas.ribiere-tharaud@cea.fr), [2]Fraunhofer EMI, Eckerstraße 4, 79104 Freiburg, Germany, [3]Crabbe Consulting Ltd, Allerheiligenstr. 17, 99084 Erfurt, Germany

Abstract

PROGRESS is a FP7 project focussing on the detection and mitigation of attacks to GNSS infrastructures from highly educated attackers whose numbers may increase in the near future. This paper presents the work achieved in this framework considering the High Power Microwaves (HPM) threats. The main project objectives are presented as well as the work carried out during the first phase of the project in terms of threat detection and in terms of infrastructure protection.

Keywords: Critical Infrastructure, HPM, Vulnerability, Detection, Protection, GNSS

1 Introduction

PROGRESS focuses on improving the security and resilience of Global Navigation Satellite Systems (GNSS) and its results are also applicable to earth observation infrastructure and assets [1]. At the start of the project a generic GNSS system has been designed and has been assessed with regards to vulnerability from intentional malicious threats. In focus are threats, which are generally considered to have a low risk of occurrence but potentially very large impacts. PROGRESS will concentrate on threats that have the potential to increase in the coming years (Ground facility physical attacks, including explosive attacks and High Power Microwaves attacks, RF spoofing and jamming, Cyber-attacks).
The resulting prioritization of threats and scenarios is used as input to develop a prototype Security Management Solution (SMS). PROGRESS SMS (Fig. 1) is a centralized solution able to automatically detect malicious actions with a built-in reconfiguration capability to ensure the overall system Quality of Service. A major concern is to address different types of threats on a single large-scale infrastructure. This paper focuses on the detection and mitigation of HPM threats but also gives some examples related to the work carried out in the same way on the impact analysis of blast waves in case of explosive attacks.

2 PROGRESS Concept

The PROGRESS SMS is composed of an Integrated Ground Station Security Monitoring System (IGSSMS) and a Security Control Centre (SCC). The IGSSMS is an innovative monitoring solution for the detection of specific malicious types of attacks. The Security Control Centre role is to analyse the impact of the reported disturbances to the system performance and Quality of Service (QoS) and to propose mitigation strategies, including automatic system reconfiguration.
The SMS is developed with full consideration of present methods and measures for the security and resilience of complex interconnected space control ground station networks by present operators.

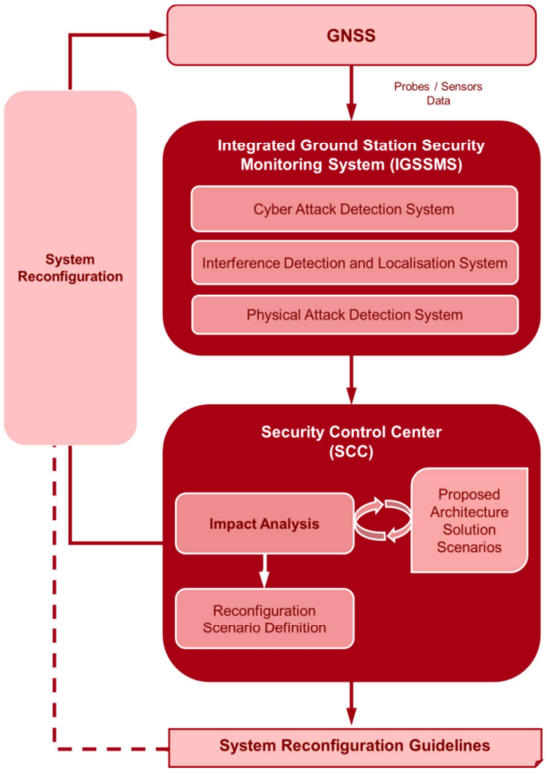

Figure 1. PROGRESS Security Management Prototype.

3 Threat detection

3.1 HPM detector

The IGSSMS includes a detection system dedicated to physical attacks (HPM and explosive attacks), the so-called Physical Attack Detection System (PADS). Suitable detection techniques developed within the PROGRESS framework

have been integrated into an autonomous sensor node (Fig. 2). In the case of HPM threats, the detection appears as a first protection level in order to ensure appropriate reactions in case of such events. In this context, detection systems have already been studied [2] and the PROGRESS HPM detection solution is based on a similar approach.

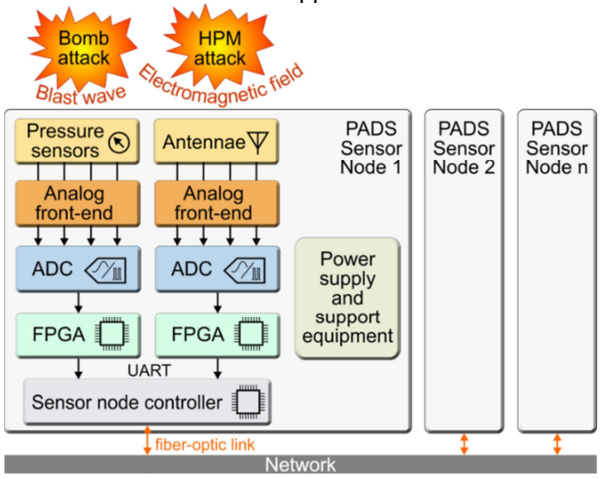

Figure 2. PROGRESS Physical Attack Detection System sensor node. Several autonomous nodes can be distributed across the monitored site, connected via fiber-optic links (detection of explosions is also performed within this sensor node).

3.2 HPM detector characterization

In order to assess the HPM detector prototype developed by Fraunhofer EMI, tests have been carried out in the CEA test facilities. The purpose of the measurement campaign was to test the HPM detection system under realistic conditions, i.e. in an intense electromagnetic environment. The following points were targeted to be verified / achieved:

- The system shall be able to detect IEMI threats produced by various types of HPM sources [3].
- The system shall be able to measure the intensity of the HPM attack, and to estimate the direction to the source.
- The system shall be robust against the detected threats, i.e. it must not be damaged even at very high field strength.

The measurements and assessments showed that the expected performances were met.

4 Protection by design

The detection system in connection with the Security Control Centre and its associated capabilities for system reconfiguration is answering partly to the protection needs. In order to reduce risk and to improve the GNSS system resilience, a set of complementary protection tools is studied in the project, for instance tools leading to strengthened design of infrastructures, applicable to new ones but also to existing ones.

HPM back-door attacks are assessed in the PROGRESS project through numerical simulations based on a finite differences in time domain code. The main objective is to define protection that can be easily implemented on existing and future buildings. The simulations are carried out on an actual building. A numerical model has been established from it including details such as the hardware implemented in server rooms dedicated to operations similar to those used for GNSS. The results show that the improvement of protection can be derived from the implementation of simple rules such as adding a conducting grid mesh between the car park/road and building, using glasses with embedded thermal protection, using reinforced concrete walls with a high density of metal bars, increasing the distance between car park/road and building.

The approach has also been carried out considering the explosive threat, on the same actual building. The impacts of the blast waves resulting from scenarios related to various explosive loads are simulated using the Conwep module based on US tabulated data [4] (tool implemented in the ABAQUS finite element code). This approach allows again providing rules for designing a strengthened building. Moreover this work leads to protection by design compliant with what has been derived in the case of the HPM threat.

Further work in the PROGRESS project will focus on the integration and the evaluation of the whole SMS prototype.

Acknowledgements

PROGRESS has received funding from EU FP7 under grant agreement Contract No. 607679. The information appearing in this document has been prepared in good faith and represents the opinions of the authors. The authors are solely responsible for this publication and it does not represent the opinion of the European Commission. Neither the authors nor the European Commission are responsible or any use that might be made of data including opinions appearing herein.
The project started on 1st May 2014 and is due to be completed by 30th April 2017.

References

[1] N. Ribière-Tharaud, “PROGRESS: Protection and Resilience Of Ground based infRastructures for European Space Systems”, *European CIIP Newsletter Volume 9 issue 1* (2015).

[2] C. Adami, C. Braun, P. Clemens, M. Suhrke, H.U. Schmidt, A. Taenzer, “HPM detection system for mobile and stationary use”, *Proceedings of the 10th International Symposium on Electromagnetic Compatibility, York, UK, September 26* (2011).

[3] A. Kreth, T. Peikert, B. Menssen and H. Garbe, “Characteristic HPEM Signals for the Detection of IEMI Threats”, *Ultra-Wideband Short-Pulse Electromagnetics, Springer*, Vol. 10, pp. 379-392, (2014).

[4] J. Petes, “Handbook of HE explosion effects, Kaman Tempo”, *Technical report prepared for Defence Nuclear Agency*, DASIAC-TN-86-15, (1986).

Validation of a Simple Propagation Model for High Power Mesoband Pulsed Sources

B. Petit, L. Chatt & R. Hoad

QinetiQ Ltd.

Cody Technology Park, Farnborough, Hampshire, GU14 0LX, UK

bjpetit@qinetiq.com

***Abstract*— An increasing number of High Power Radio Frequency (HP RF) systems are being developed for a wide variety of applications. Part of the development process is the requirement to operate these systems safely outdoors. Intentional Electromagnetic Interference (IEMI) sources are also a growing concern and understanding the risk posed to infrastructure is important. HP RF and IEMI systems can be deployed on or near to the ground. When these systems operate in the VHF frequency range (generally Mesoband systems) the line of sight propagation of the waveform is strongly influenced by the ground and terrain at low elevation angles. Using over simplifications of electric field propagation can lead to prohibitive safety distance requirements or overestimates of risk. This paper examines two simple propagation modelling approaches and describes the results of a simple experiment used to validate the models.**

Keywords- High Power Radio Frequency, IEMI, Hazard, Propagation Modelling

1. Introduction

High Power Radio Frequency (HP RF) sources are being developed for a wide variety of applications, including, but not limited to vehicle, vessel and Unmanned Ariel Vehicle (UAV) stopping/defeat. Operating these systems outside comes with a number of inherent hazards that must be considered and mitigated if operation is to be permitted in accordance with the applicable laws, regulations and standards.

IEMI sources are also of concern. Briefcase or Man portable Mesoband sources operating in the VHF frequency range pose a risk to electrical/electronic systems such as those used within Critical National Infrastructure (CNI). For the applications described above the HPRF and IEMI sources are generally considered to be deployed within 1 to 2 metres of the ground. At these deployment heights and at these frequencies, ground interaction (the ground reflected wave) will have a large bearing on the magnitude of the E-field at a distance from the source.

Different techniques exist to model electromagnetic (EM) fields as they propagate over distance. It is important to apply the correct model for calculating the field levels that will be seen at different locations so that the hazard/risk can be appropriately managed.

There are a very wide variety of different propagation models that can be used to predict how EM fields may interact with the environment and terrain. Two of the simplest examples are discussed within this paper – the Free Space Path Loss (FSPL) **[1]** model and the Ground Plane Reflection (GPR) model **[2]**.

2. Simple Propagation Model Description

The FSPL model follows the simplest form of propagation for EM waves. It assumes that the Electric field (E-Field) will decrease proportionally to distance. Thus, the power density decreases proportionally to distance squared as described in Equation 1.

$$FSPL = \left(\frac{4\pi d}{\lambda}\right)^2$$

Equation 1: Free Space Propagation Equation

This equation does not support information which has a profound effect on the E-field at distance such as; the height of transmit and receive antennas above a ground plane, the conductivity of the ground plane, the effects of absorption, dispersion or scattering. The model is most applicable for identifying how transmissions might propagate through the air between a source and an aircraft at altitude. It may be used as quick guidance to identify the worst case.

The GPR model is a very simple propagation model which accounts for the direct path from the source to a receiver or target, as well as the ground reflected path and associated interactions. Figure 1 shows the typical characteristic of the GPR model compared with the FSPL model.

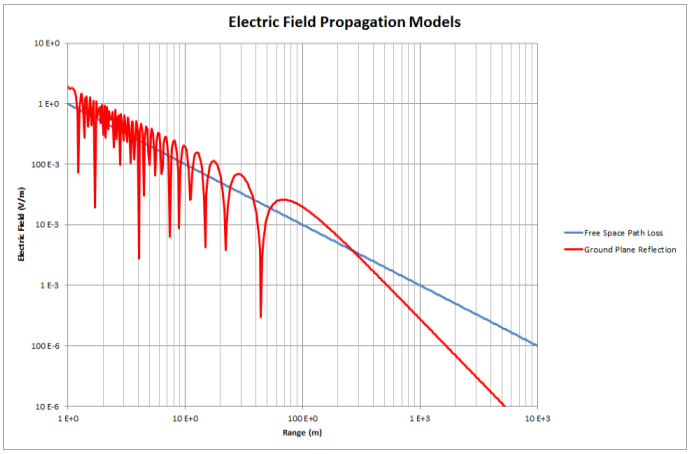

Figure 1: Free Space Path Loss and Ground Plane Reflection Models for a Simple Scenario

This model allows the identification of the near field/far field boundary and the point at which (in the far field) the E-field departs from the FSPL model due to ground reflected ray interactions.

The output of the model is affected by the different heights of the transmitter and the receiver as well as the wavelength of the signal and uses an assumption of perfect ground conductivity for simplicity. It is also a 2D model and therefore does not take terrain effects into account. It should be noted that the GPR model is primarily concerned with single frequencies and cannot therefore account for frequency dispersion of pulsed sources. The GPR model is, however, a simplified step towards understanding how antenna height and the presence of a ground plane affect propagation.

The simple GPR model can be easily integrated together with test instrumentation to provide a very fast, though approximate, estimation of propagation loss.

3. Model Validation

QinetiQ's simple EM visualisation tool known as PhoS has both the FSPL model and the GPR model built in, allowing the user to select either for different scenarios. Additionally, standardised limits are included in PhoS (such as the International Commission on Non-Ionising Radiation Protection human exposure guidelines).

A key requirement was to validate the model and understand the limitations of the model with measurements. To this end a series of experiments were conducted using a low power Mesoband source in the open and measuring the pulse characteristics at a series of distances from the source over varying terrain **[3]**.

Initially the test location was selected based upon the worst case (highest possible) E-field emissions from the source, often with an added margin, to ensure safety. The first set of measurements was required to verify that the initial safety calculations were correct. This was done by taking a measurement on boresight of the transmitting antenna in the far field at a distance that has been modelled.

Once all safety measurements were completed, measurements were made to ensure compliance with any regulations, such as those of OfCom (UK communications regulator), as well as any other transmission limits that may have been placed upon the experiment. This involved measurements at the test range boundary to confirm compliance.

The next stage of the testing was to do field mapping. This process had several stages including proving the symmetry of the field pattern (thus allowing measurements to be made on one side of the antenna in the knowledge that the transmission pattern should be a mirror image on the other side). This was done by picking a few key points in the field pattern in the far field and confirming that the measurements on the other side of the antenna at the same distance were at the same levels (within a predefined acceptance margin). After that, the emitted fields were measured at key distances around the antenna to confirm that the pattern was as expected, in accordance with the EM model. Finally, measurements were taken at significant features in the terrain to validate the transmission pattern. Key features included at the peak of local hills, on banks at the other sides of bodies of water, or at range boundaries. Careful analysis of the terrain, models and results indicated where the transmissions have followed the FSPL model (typically when the transmission path is significantly removed from the terrain) and when the transmissions have followed the GPR model.

4. Summary

There are a few basic models available for creating simple models of EM propagation. The simpler tools are useful for quick calculations for predicting field levels at different distances. All EM models must be validated through real measurements.

QinetiQ have a tool known as PhoS with built in models for EM propagation. This tool has been validated through various trials of High Power RF sources. Generally speaking, the validation has shown that the different EM models provide good approximations of the predicted fields, but tend to over-estimate values. This is favourable from a safety context.

References

[1] Bernard Sklar, January 2001, Digital Communications: Fundamentals and Applications (Prentice Hall Communications Engineering and Emerging Techno), 2nd Edition, Communications Engineering Services.

[2] Andrea Goldsmith, September 2005, Wireless Communications, 1st Edition, Cambridge, UK, Cambridge University Press.

[3] Unpublished QinetiQ Report

Double-Positive Metamaterial Composites with High Dielectric Strength

R D Curry, K M Noel, A M Pearson

**Center for Physical and Power Electronics, University of Missouri, Columbia, MO*

Abstract

Metamaterial composites with both ferroelectric and ferromagnetic phases have promising applications in the field of applied electromagnetics and directed energy. Two new procedures have been developed to produce double-positive metamaterials by combining ferrite powders with a dielectric binder. The resulting composites are machinable bulk materials produced at significantly lower temperatures than sintered components. One of the metamaterials integrates the dielectric-ferromagnetic properties into a single composite using a hydrothermal process and the other composite uses a binder as the dielectric. The dielectric and magnetic constants have been measured with an airline waveguide, and the high voltage breakdown of the material was determined using nanosecond pulses from a PA-80, 100 KV pulser.

Keywords: Electromagnetic metamaterials, nanocomposites, electric breakdown, high power microwaves, pulsed power

1 Introduction

Metamaterials are currently under development to reduce the size of high power antennas. These materials may also have applications in other high power, dielectric-loaded components, including nonlinear transmission lines, filters and high power oscillators. Multiferroic metamaterials with tailored permittivity ε_r, and permeability μ_r, can be used to shrink antenna sizes and match impedances. Antenna size can be determined by the wavelength in the material as seen in Equation 1, where λ_0 is the free space wavelength. By increasing the ε_r and μ_r of the material used in an antenna the size can be reduced substantially for similar wavelengths. [1].

$$\lambda_D = \frac{\lambda_0}{\sqrt{\epsilon_r \mu_r}} \qquad (1)$$

The impedance of a material is also affected by its dielectric properties, as seen in Equation 2. When using materials with high dielectric constants, the impedance of the material becomes mismatched to free space [2]. Multiferroic metamaterials with near equal ε_r and μ_r values, over a wide frequency band, will aid in impedance matching.

$$Z_m = Z_0 \sqrt{\frac{\mu_e}{\varepsilon_r}} \qquad (2)$$

An important factor determining the survivability of a material for use in a high power antenna system is its dielectric strength. The ability of a material to withstand extremely high electric fields is often a limiting factor in the power handling capability of these types of antennae. Also, since the desired application is to hasten the development of compact systems in which the energy density is high, as compared to the system volume, measurement and characterization of the materials ability to withstand such fields is of the utmost interest.

2 Material Characterization

Two metamaterial composites have been designed, one composite uses ferrite particles coated in a polymer binder, the other material composite is synthesized using a hydrothermal process. The hydrothermal reaction process is designed for growth of barium titanate layers around the surface of the ferrite particles. A binder is then used to create a polymer network around the particles in both composites removing the need for sintering.

2.1 Permittivity and Permeability

The multiferroic properties of the composite were measured using an Agilent 50 Ohm, Type N airline, an Agilent network analyzer, and dielectric measurement software. The software uses S parameters to calculate the ε_r and μ_r using the Ross-Nicolson method [3]. To use the airline, the samples were machined into toroids with an inner diameter of 0.3 cm and the outer diameter of 0.7 cm. The ferrite and barium titanate-ferrite composites were tested from 200 MHz to 2 GHz and compared.

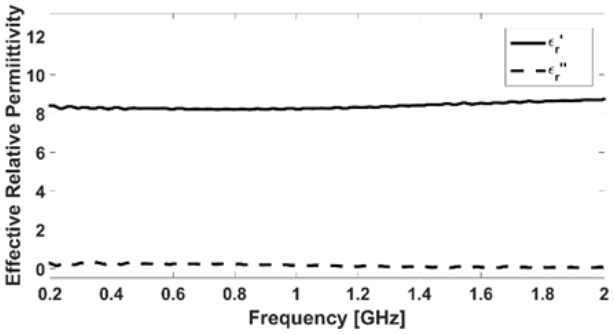

Figure 1: Relative permeability of ferrite composites

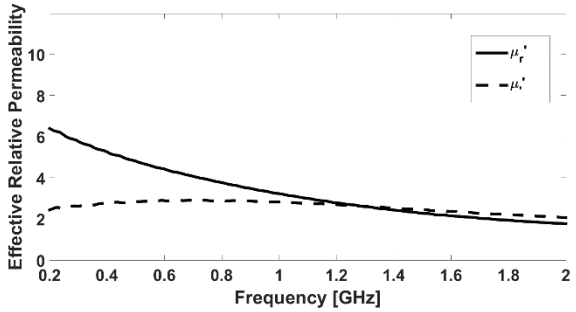

Figure 2: Relative Permeability of Ferrite Composites

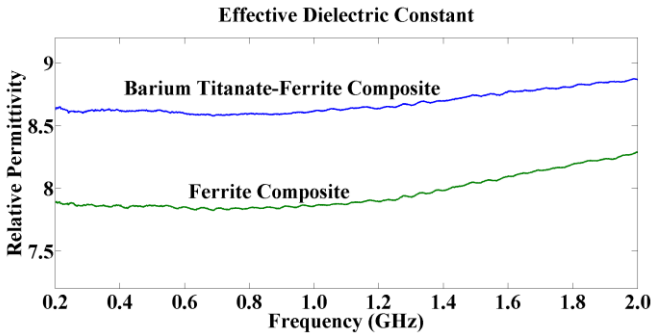

Figure 3: Relative Permittivity of Barium-Titanate Ferrite Composites

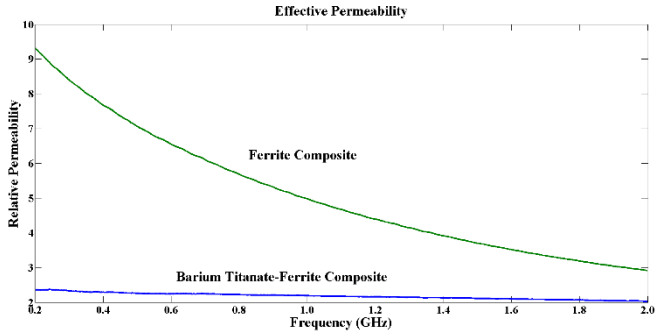

Figure 4: Relative Permeability of Barium-Titanate Ferrite Composites

2.2 Voltage Strength

The dielectric strength of the metamaterial was tested using a PA-80, 100 kV pulser. The pulses had a 10% to 90% rise time of 60 ns. North Star voltage probes with a 1000:1 voltage ratio were used to measure the voltage difference across the electrodes on the sample. The breakdown voltage of each of the materials were measured using a Tektronix oscilloscope.

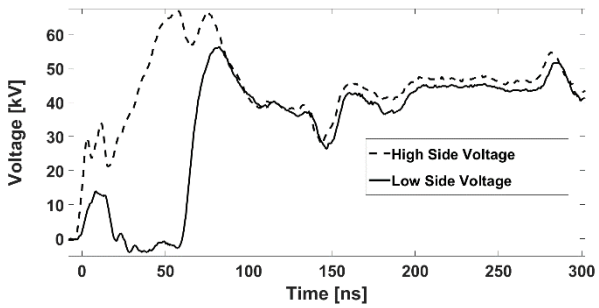

Figure 5: Voltage Breakdown of Ferrite Composites

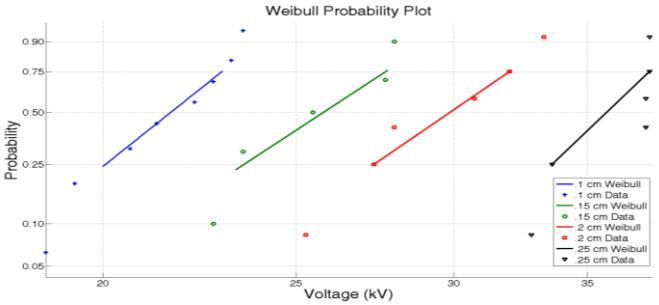

Figure 6: Voltage Breakdown of Barium-Titanate Ferrite Composites

3 Conclusions

Ferrite powder in a bimodal distribution was combined with a low-dielectric constant binder to form a metamaterial. Another composite was engineered with barium titanate layers bonded to ferrite particles. These composites are specifically designed to present positive values of both permittivity and permeability greater than unity while also demonstrating high dielectric strength. Between 20 MHz to 2 GHz the bimodal ferrite composites allow for a maximum antenna a size reduction of 6. The highest observed electric field sustained before breakdown was 309.5 kV/cm. The barium titanate-ferrite composites show an increased permittivity but a decreased permeability when compared to the ferrite composites.

Acknowledgements

These projects are supported by the Office of Naval Research (Code 30) contract N0001413-1-0516.

References

[1] Schileo, "Recent developments in ceramic multiferroic composites based on core/shell and other heterostructures obtained by sol–gel routes", Progress in Solid State Chemistry, Volume 41, Issue 4, December 2013, Pages 87-98, (http://www.sciencedirect.com/science/article/pii/S0079678613000186)

[2] K. A. O'Connor and R. Curry, "High dielectric constant composite for high power antennas," IEEE Pulsed Power Conference, 2011

[3] A. M. Nicolson and G. F. Ross. "Measurement of the Intrinsic Properties of Materials by Time-Domain Techniques" IEEE Transactions on Instrumentation and Measurement. 19(4) 377-382. November 1970.

Artificial Material Design for High Power Microwave Applications

A. Hopper, R. Seviour

University of Huddersfield, UK
aimee.hopper@hud.ac.uk

Abstract

In this paper we explore the application of Artificial Materials (AMs) to vacuum electronics, and the power limitations are presented. We present numerical and experimental results that show how the dispersion relation can be engineered and the effects of relative high power operation.
We also present results from numerical simulations low-loss AM unit cells, focussing on their electromagnetic and thermal characteristics, demonstrating that the dispersion relation of the material can be tailored to interact with a charged particle beam over several regimes.

Keywords: Artificial Material, Microwave, Simulation.

1 Introduction

Artificial materials (AMs) are structures whose characteristic properties are determined by their sub-wavelength, periodic unit cell composition, creating an effective media [1]. These materials can produce novel electromagnetic effects such as an arbitrary phase shift of an incident electromagnetic wave over the material where the dispersion relation of the material can be engineered by altering the geometric design of the unit cells. This enables an optimisation of the material to maximise regions of energy transfer between a charged particle beam and an incident EM wave, a condition required in certain high power vacuum devices, such as a Travelling Wave Tube (TWT).

The interaction of an EM wave with a material can be described through the constitutive relations

$$\mathbf{D} = \varepsilon\mathbf{E} \quad (1)$$
$$\mathbf{B} = \mu\mathbf{H} \quad (2)$$

where **D** and **B** represent the electric and magnetic flux densities, **E** and **H** represent the electric and magnetic fields, ε and μ represent the permittivity and permeability. These can be defined through a Drude-Lorentz model [2] as

$$\varepsilon(\omega) = \varepsilon_\infty - \frac{\varepsilon_\infty \omega_p^2}{\omega(\omega - i\nu_c)} \quad (3)$$

$$\mu(\omega) = \mu_\infty + \frac{(\mu_s - \mu_\infty)\omega_0^2}{\omega_0^2 - \omega^2 + i\omega\delta} \quad (4)$$

where ε_∞ is the permittivity in the high frequency limit, ω_p is the radial plasma frequency, ν_c is the collision frequency, μ_s (μ_∞) is the permeability in the low (high) frequency limit, ω_0 is the radial resonant frequency, and δ is the damping frequency.

2 Previous Work

To test the ability of AMs in a high power environment, simulations determining the thermal characteristics of the material were run [3]. Using COMSOL [4], simulations of an AM consisting of two copper square SRRs on an FR4 PCB backplate with a copper strip-line along the reverse were run. Fig. 1 (left) shows the predicted heat map for one of the unit cells in the simulation. The simulation predicted that for 1W of incident RF at 10GHz (the resonant frequency of the SRRs in the unit cells) temperatures exceeding 600°C, the combustion point of FR4, were expected.

To determine the validity of this simulation, an experiment was set up and the AM was fabricated to the specifications used in the simulation. After 15 seconds of exposure to 1W of RF at 10GHz, the material was found to combust. Fig. 1 (right) shows the combustion pattern of the unit cell corresponding to that predicted, validating the simulation methodology, and showing that conventional techniques using AMs are not suitable for high power environments. This is caused by energy from the incident wave being stored in the resonators resulting in breakdown. A number of other unit cell geometries and compositions were also tested, all showing that operation at the resonant frequency of the SRRs resulted in catastrophic failure.

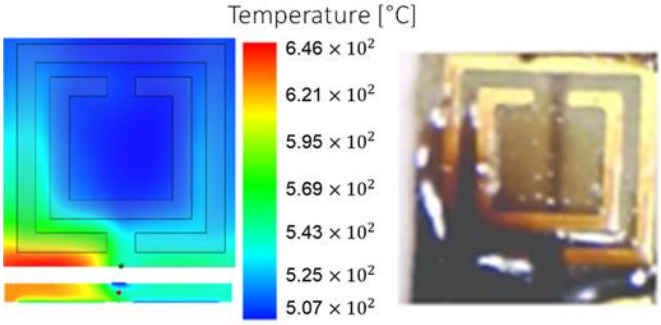

Figure 1: (Left) Heat map for one of the unit cells simulated in COMSOL. (Right) Experimental outcome after 15 seconds from exposing structure to 1W of RF at 10GHz, validating the simulation [3].

3 Results

By operating away from the resonance of the SRRs, in regions of low ε and μ, we aim to reduce the absorption of energy into the AM whilst maintaining the ability to arbitrarily engineer its EM characteristics.

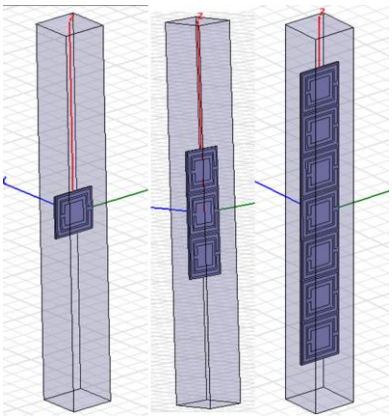

Figure 2: HFSS Simulations, wave travels from the bottom of the vacuum in the z direction.

HFSS [5] was used to simulate these AMs and the scattering parameters were extracted for differing numbers of unit cells in the direction of wave propagation (z), see Fig. 2. The copper was replaced with PEC to reduce computing time. By using established techniques [6, 7, 8] we can relate the scattering parameters to the effective ε and μ of the AM, determining the dispersion relation. The unit cell size was 2.4mm x 2.4mm, the thickness of the FR4 substrate is 0.1mm. The PEC tracks had a width of 0.2mm.

The resulting dispersion curves are shown in Fig. 3 where lines corresponding to electron beams of 20, 25 and 30 keV are included, along with the light line. We can see that there are a number of frequencies where the beam lines and the dispersion curves intersect, suggesting several regimes for interactions are possible. Interaction regions around 10GHz would result in large absorptions (see Fig. 4), though the 7 Cell simulations predict relatively low absorptions around 12GHz.

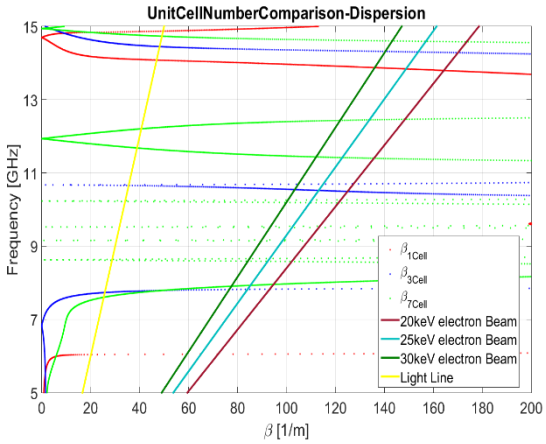

Figure 3: Dispersion curves for 1, 3 and 7 unit cells in the direction of wave propagation.

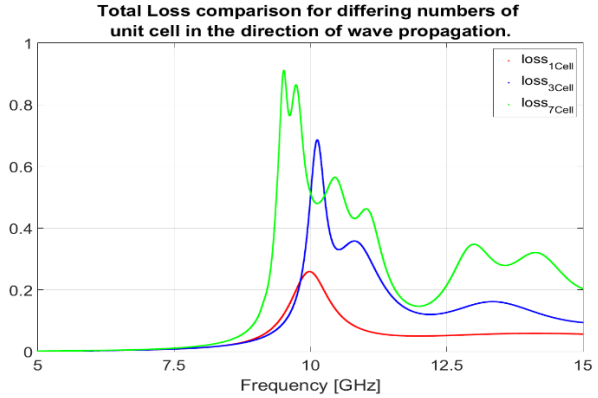

Figure 4: Loss plot for differing numbers of unit cells.

4 Conclusions

Previous work has shown that existing AMs cannot withstand relative high power when operating at resonance; absorption of the energy from the incident wave results in breakdown of the material. This demonstrates AMs inability to operate in high power vacuum electronic devices at resonance.

To investigate regions of low absorption, simulations of AMs with varying numbers of unit cells in the direction of wave propagation have been conducted in HFSS. We see that regions of possible beam-wave interactions occur away from resonance, showing that the dispersion relation can be tailored to interact with a charged particle beam over several regimes with low absorption.

Acknowledgements

The Authors thank the Airforce Office of Scientific Research and the EPSRC for their financial support.

References

[1] C. Caloz, "Perspectives on EM Metamaterials", *Materials Today*, **12**(3), pp 12-20, (2009)

[2] F. Qureshi *et al*, "A Compact and Low-Profile Metamaterial Ring Antenna With Vertical Polarization", *IEEE Antennas Wireless Propagation Lett.2*, **7,** pp 103-106, (2003)

[3] R. Seviour, *et al*, "Effects of High Power on Microwave Metamaterials", *8th International Conference on Advanced Electromagnetic Materials in Microwaves and Optics (METAMATERIALS)*, IEEE, pp 142-144, (2014)

[4] ANSYS Workbench, ANSYS Inc., Canonsburg, PA.Ver.12.1, (2009)

[5] HFSS, Ansoft Corporation, Pittsburgh, PA.Ver.12.1, (2010).

[6] A.M. Nicholson, G.F. Ross, "Measurement of the Intrinsic Properties of Materials by Time-Domain Techniques", *IEEE Transactions on Instrumentation and Measurement*, **19**(4) pp 377-382, (1970)

[7] W.B. Weir, "Automatic Measurements of Complex Dielectric Constant and Permeability at Microwave Frequencies", *Proceedings of the IEEE*, **62**(1) pp 33-36, (1974)

[8] D.R. Smith *et al*, "Determination of Effective Permittivity and Permeability of Metamaterials from Reflection and Transmission Coefficients", *Phys. Rev. B*, **65**(19):195104, (2002)

Effects of RF Electromagnetic Fields on Optically Non-linear Nanostructured Plasmonic Surfaces.

Andrew J. Waddie*, Adrian Dzipalski*, Iain Thurston†, Michael Moutrie† and Mohammad R. Taghizadeh*

**Institute of Photonics and Quantum Sciences, School of Engineering and Physical Sciences, Heriot-Watt University, Riccarton, Edinburgh, EH14 4AS, United Kingdom. †EMP Team, Radiation Science, AWE, Aldermaston, RG7 4PR, United Kingdom.*

Abstract

In this paper we present the results of a study into the application of both static and dynamic electromagnetic fields to a nanostructured plasmonic surface formed on a Lithium Niobate substrate. The nanostructured plasmonic surface is composed of periodic arrays of sub-wavelength (<400nm) holes in a thin semi-transparent layer of gold. The gold layer supports the creation of both bulk and surface plasmons, resulting in a transmission spectrum that is highly sensitive to the electro-optic changes induced in the substrate by orthogonally applied static and RF electromagnetic fields.

Keywords: Surface Plasmons, Lithium Niobate, Non-linear Optics.

1 Introduction

Surface plasmons [1] are a class of electromagnetic surface wave arising from the interaction of an incident optical-frequency electromagnetic wave with a thin noble metal surface containing a periodic array of sub-wavelength holes. These surface waves provide the mechanism for the transmission of energy above that supported by classical scattering and diffraction theory. This extra-ordinary transmission (EOT) has been exploited in many applications such as surface enhanced Raman spectroscopy (SERS) [2], surface enhanced fluorescence spectroscopy [3] and as a biosensor[4]. Each of these applications relies on the sensitivity of the EOT to very small changes in the refractive index of the material above the nanohole array. In this paper, we present the design, fabrication and experimental verification of a nanohole array on an optically non-linear substrate with a large electro-optic coefficient. The chosen substrate material was Lithium Niobate ($LiNbO_3$) and the nanostructured surface was fabricated such that an orthogonally applied EM field would induce a refractive index change through the largest (d_{33}=-31.5pm/V) component of the electro-optic tensor. The modified refractive index of the substrate under an electric field strength of E_z is given by

$$n(E)=n_o+\frac{1}{2}d_{33}n_o^{\,3}E_z \qquad (1)$$

where the base refractive index of the $LiNbO_3$ n_0 = 2.2773. Detailed EM modelling by means of the Finite Difference Time Domain (FDTD) method allows theoretical transmission spectrum of the device to be calculated. The modelling used Drude-Lorentz dispersive models [5]for both the substrate and the metallic layers and was modified in light of the results of the fabrication process to more accurately reflect the fabricated structures. The fabricated devices were tested experimentally using both static and dynamic electromagnetic fields and shown to produce good agreement with the theory. The dynamic response of the nanostructured array to a fast RF electromagnetic pulse suggests the suitability of the device as a sensor for high speed electromagnetic discharge events such as lightning strikes.

2 Modelling and Design of Nanostructured Plasmonic Surface.

The plasmonic device was simulated using a periodic FDTD with perfectly matched layer boundary conditions in the direction of light propagation. The unit cell of the simulations had a periodicity in the transverse directions of 600nm, a gold thickness of 100nm and hole diameters of between 240nm and 350nm. The transmission spectra for the nanostructured surface for different hole sizes and the same metal layer thickness and periodicity are shown in Figure 1.

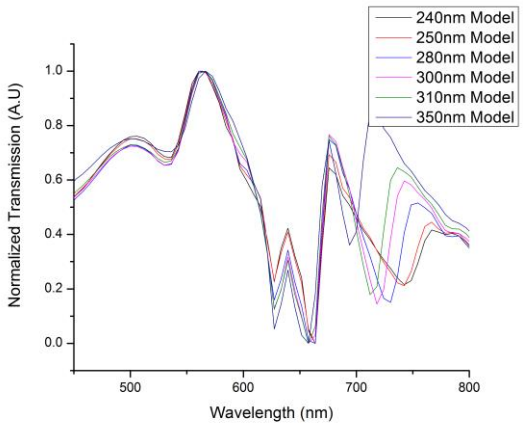

Figure 1: Modelled Transmission Spectra for the nanostructured surface with varying hole diameter.

A number of distinct transmission peaks can be seen in the spectra. The leftmost two peaks (at ~500nm and ~560nm) correspond to the bulk plasmons that exist in an unperturbed thin layer of gold – they are insensitive to hole size in both transmission and peak wavelength. The rightmost two peaks (at ~670nm and 710nm-780nm) are those associated with the (1,1) and (1,0) surface plasmons respectively – the (1,0) plasmon exhibits no blue shift of peak wavelength while the (1,1) shows a strong blue shift.

3 Fabrication and Measurement.

A total of six nanohole arrays with hole sizes of 240, 250, 280, 300, 310 and 350nm were fabricated using direct e-beam writing, RF sputtering and lift-off. The fabricated nanoholes showed good uniformity across a total area of 500µm x 500µm with an overall gold thickness of 100nm. A spectroscopic scan of the 280nm hole array (Figure 2) shows good agreement between theory and experiment.

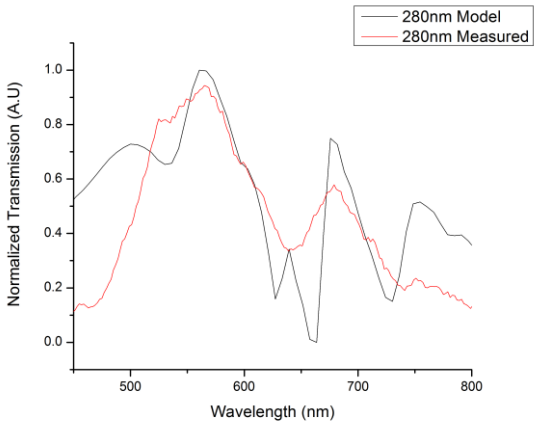

Figure 2: Comparison between theory and experiment for 280nm hole diameter nanohole array.

The (1,0) surface plasmon is clearly visible and comparison between the theory and each of the other hole diameter arrays shows similarly good agreement. The decrease of the short wavelength bulk and long wavelength surface plasmonic peaks is due to the limited spectral bandwidth of the white light source used in the fibre-coupled photospectrometer. The nanostructured plasmonic device was integrated with multimode GIF-625 optical fibre and illuminated by a 3mW laser diode. Three different levels of static electric field were applied to the device (0kVm^{-1}, 312.5 kVm^{-1} and 625 kVm^{-1}) and the resultant output power measured using a calibrated Si photodiode. In order to account for any power fluctuations in the laser output, the measurement was repeated 2000 times at a frequency of 4Hz. The results of the static field measurements can be seen in Figure 3 where a clear variation in the measured optical transmission can be seen between the different applied electric field strengths.

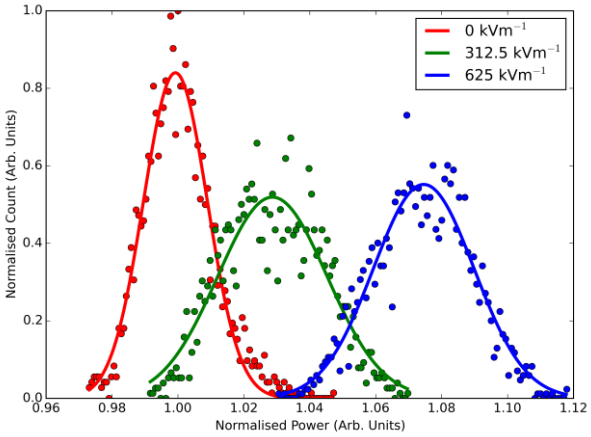

Figure 3: Output power distribution for 280nm nanohole array for three different applied electric field strengths. The normalisation factors for the power and count are the 0kVm^{-1} mean power and peak count respectively.

The response of the nanohole array to a pulsed RF EM field was also measured using a high speed Si photodiode. The EM pulse was provided by a 5kV Pockel cell driver feeding into two plane parallel electrodes within a Faraday cage. This crude arrangement leads to a significant level of noise within the measured signal due to scattering and back-reflection of the EM pulse. From Figure 4 it can be seen that the nanohole array has a different response for differing levels of applied peak power.

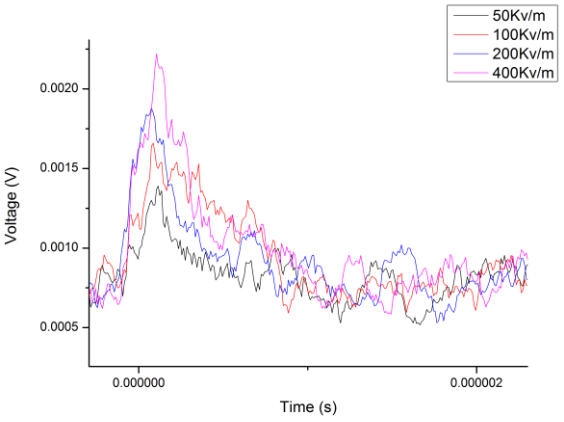

Figure 4: Measured response of 280nm nanohole plasmonic array to applied pulsed electromagnetic field.

References

[1] J.A.Polo Jr., T.G.MacKay and A.Lakhtakia, Electromagnetic Surface Waves : A Modern Perspective, Elsevier Insights, 2013

[2] A. G. Brolo, S. C. Kwok, M. G. Moffitt, R. Gordon, J. Riordon, and K. L. Kavanagh, "Enhanced fluorescence from arrays of nanoholes in a gold film," *J. Am. Chem. Soc.*, vol. 127, no. 42, pp. 14936–

14941, 2005.
[3] Y. B. Zheng, B. K. Juluri, X. Mao, T. R. Walker, and T. J. Huang, "Systematic investigation of localized surface plasmon resonance of long-range ordered Au nanodisk arrays," *J. Appl. Phys.*, vol. 103, no. 1, pp. 1–9, 2008.
[4] G. M. Hwang, L. P. L. Pang, E. H. Mullen, and Y. Fainman, "Plasmonic Sensing of Biological Analytes Through Nanoholes," *IEEE Sens. J.*, vol. 8, no. 12, pp. 2074–2079, 2008.
[5] A. Taflove, S. Hagness, W. Gwarek, M. Fujii and S.-H. Chang, "Dispersive, Nonlinear and Gain Materials" in Computational Electrodynamics 3rd Ed., Artech House, 2005.

Single helical antenna and linear arrays excited by nanosecond bipolar pulses

V. I. Koshelev, Yu. A. Andreev, A. A. Petkun, M. Yu. Zorkaltseva

Institute of High Current Electronics SB RAS, 2/3, Akademichesky ave., Tomsk 634055, Russia
koshelev@lhfe.hcei.tsc.ru

Abstract

A computer code based on the finite-difference time domain (FDTD) method has been developed for numerical simulation of single helical antennas. Results of the numerical simulation and measurements were compared. Four-element linear arrays with different distances between antennas have been developed and studied experimentally. The antennas were excited by bipolar voltage pulses of the length 1 ns. The investigations were carried out in the modes of synchronous excitation of the array elements and pattern steering. The main attention was given to the polarization characteristic of radiation.

Keywords: Helical antenna, array, ultrawideband radiation.

1 Introduction

Short pulses of elliptically polarized ultrawideband (UWB) radiation are used in radar and in the investigations of electronic system susceptibility. To radiate elliptically polarized UWB pulses, the cylindrical helical antennas in the mode of axial radiation are widely used. It was of interest to study the polarization structure of radiation at different linear array parameters and modes of antenna excitation.

2 Investigation results

To simulate a single helical antenna, a computer code based on the FDTD method has been developed. Creation of the program used to calculate VSWR in the antenna feeder required much effort. Different variants of setting the excitation source and geometry of the antenna input have been investigated.

Based on the numerical simulation, a cylindrical helical antenna with the number of coils N = 4.5 has been developed. The antenna geometry was optimized to excite by a 1-ns length bipolar pulse. The mode of axial radiation corresponded to the frequencies near 1 GHz. The obtained results of the calculations and measurements are in good agreement.

The four-element linear arrays of helical antennas with N = 4.5 were studied. The distance between the elements was 15, 21, and 30 cm at the central wavelength of the radiation spectrum equal to 30 cm. The measurements were carried out in the frequency and time domains.

VSWR of the array elements versus the distance between them as well as the positioning of the helixes in the array were measured in the frequency domain. To study the interaction of the array elements, we have obtained frequency dependences of the ratio of signal transmission from one element to another. Significant influence of the positions of the ends of the array helixes on the measured characteristics is an interesting result.

Initially, time-domain measurements were made at the synchronous excitation of the array elements. Increase of the distance between the array elements resulted practically in the twofold decrease of the pattern FWHM by the peak power. The axial ratio for radiation in the pattern center increases slightly from 1.7 to 2.

Pattern steering was realized due to the time delays of the array element excitation. Deviation of the array pattern maximum was chosen to be equal approximately to 20 degrees which corresponded to the pattern angle of a single antenna at FWHM. The steering was carried out towards positive and negative angles. The studies have shown that the axial ratio for radiation in the pattern maximum is practically independent on the distance between the array elements and somewhat (17 %) different for positive and negative steering angles.

3 Conclusion

A FDTD code has been created and a single helical antenna optimized to excite by 1-ns length bipolar pulses has been developed. The four-element linear arrays have been developed and studied at the synchronous excitation of the elements and the pattern steering. The polarization characteristic of the UWB radiation was shown to depend weakly on the distance between the array elements and the steering angle.

Acknowledgements

The work was partially supported by the grant of Russian Foundation for Basic Research No. 16-08-00297.

Development of Impulse Radiating Antenna

Shao-fei Wang, Yan-zhao Xie, Ming-xiang Gao

State Key laboratory of Electrical Insulation and Power Equipment
Electrical Engineering College, Xi'an Jiaotong University
Xi'an, Shannxi, China
Xi'an Jiaotong University, China
wsf2013@stu.xjtu.edu.cn; yzxie@mail.xjtu.edu.cn; gaomingxiang1025@stu.xjtu.edu.cn

Abstract

One high pulse repetition frequency Impulse Radiating Antenna (IRA), CHIRA-I was developed for the buried objects detection. The system consists of a pulser, a balun, four feeding arms and a parabolic reflector. The diameter of the reflector is 1.2 m. The electric field of CHIRA-I was measured by a TEM horn antenna. The rise time of electric field on the boresight at 21 m from the aperture is 130ps, effective potential is about 12 kV and the maximum pulse repetition frequency is 100 kHz, which are quite good for the detection application of buried objects.

Keywords: IRA; fast rise time; high pulse repetition frequency; buried objects detection.

1 Introduction

Ultrawideband (UWB) radiating systems have many useful applications, such as electromagnetic disrupter, buried objects detection, electromagnetic vulnerability tests, study of electrical characterization of materials and detection of leaky or defective pipes etc. [1]. With high PRF, the UWB system could work better for the applications mentioned above.

In this paper, a kind of UWB radiating system with high PRF is developed based on Impulse Radiating Antenna for the detection of buried object.

2 Design of CHIRA-I

CHIRA-I consists of a pulser, a balun, 4 feeding arms and a parabolic reflector, whose diagram is shown as Figure 1. In practice, the pulser is set behind the reflector to avoid electromagnetic interference and blockage.
The pulser is of fast rise time and high repetition frequency, and the output impedance of the pulser is 50 Ω. The feeding arms consist of two pairs of coplanar conical transmission lines, and the impedance of each is designed as 400Ω according to stereographic projection and conformal mapping [2]. And the two pairs of arms are connected in parallel at the head, which makes the impedance 200 Ω. And at the end, the feeding arms are connected to the reflector via matched load.

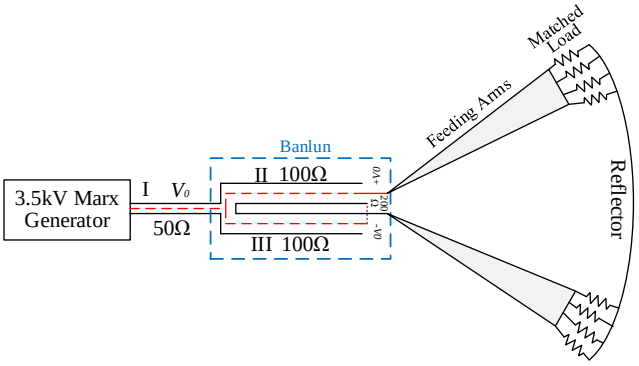

Figure 1. Diagram of CHIRA-I

A balun module is designed to connect the pulser and the antenna. At the head of the balun, two pieces of 100 Ω cable are connected in parallel, while at the end the two cables are connected in series. Thus, the one-side pulse with impedance of 50 Ω is transformed into differential pulse with impedance of 200 Ω, so that the pulser and the antenna could be well connected without impedance mismatch.

3 Performance of CHIRA-I

The picture of CHIRA-I is shown as Figure 2. Diameter of the reflector is 1.2 m and the focal length is 0.384 m.

Figure 2. The picture of CHIRA-I

The waveform of the output pulsed voltage from the pulser is shown in Figure.3.

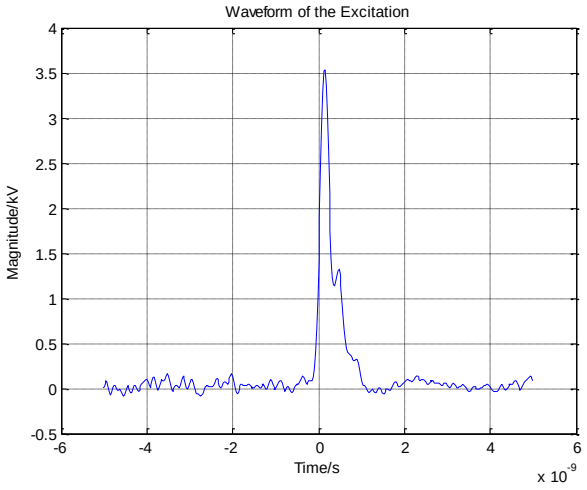

Figure 3. The waveform of the output voltage of the pulser

The amplitude of the pulsed voltage is 3.5 kV, and the rise time is 160ps, the pulse duration is 270 ps, the maximum PRF is 100 kHz.

The VSWR of the antenna is measured with vector network analyzer whose frequency range is 0.3-3 GHz, and the results is shown in Figure 4.

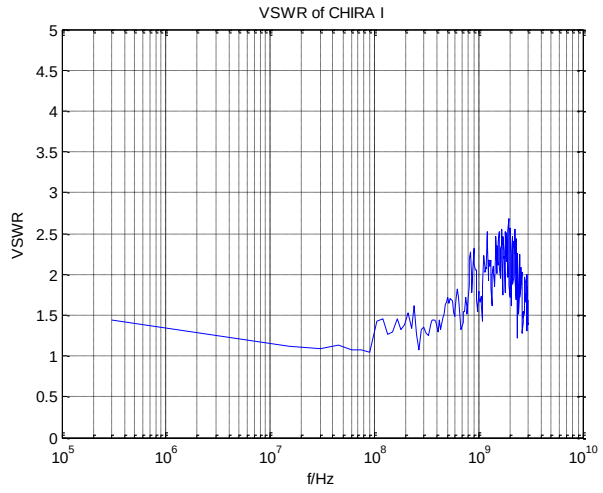

Figure 4. VSWR of the antenna

According to Figure 4, the VSWR of the antenna is 2 around at the frequency range from 300 kHz to 3GHz, which means the antenna could effectively radiate the pulsed voltage generated by the pulser.

The electric field is measured at the point which is 21m from the aperture on the boresight. The waveform of the electric field is shown in Figure 5.

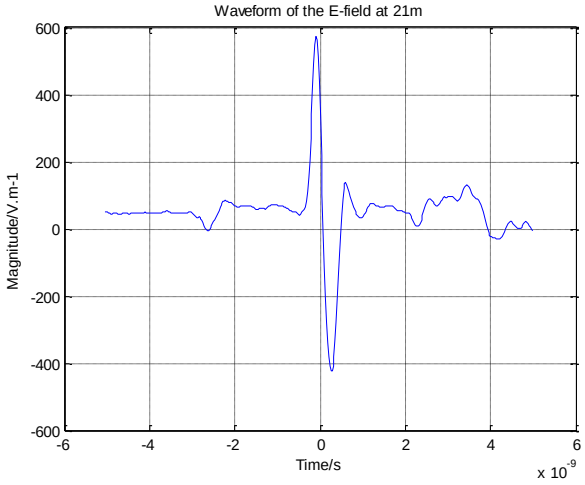

Figure 5. Waveform of the electric field

The rise time of the electric field at 21m from the aperture on the boresight is 130 ps, and the amplitude is Ep=574 V/m, which means the effective potential is about 12 kV, and the peak field strength coefficient is $k=rEp/U_0$=3.43.

4 Summary

A kind of IRA system with high PRF is developed, and the maximum PRF is 100 kHz. The rise time of the radiating field is 130ps, and the effective potential is about 12 kV. The field strength coefficient is 3.43. In the future, we would like to work on the design of array IRA so as to further improve the field strength coefficient.

Acknowledgements

The author would like to thank Dr. D. V. Giri for the valuable suggestions and experimental support by Yan-peng Ge and Wei Zhou during the development of the CHIRA-I.

References

[1] D. V. Giri. "High-Power Electromagnetic Radiators: Nonlethal Weapons and other Applications", *Harvard University Press*, 2004.

[2] Everett G. Farr, "Optimizing the Feed Impedance of Impulse Radiating Antennas Part I: Reflector IRAs", *Sensor and Simulation Notes*, 354, (1993).

The effect of rounding the corners on the transient response of scattering structures

P D Smith*, A J Markowskei*

**Department of Mathematics, Macquarie University, Sydney 2109 Australia;*
paul.smith@mq.edu.au, audrey.markowskei@mq.edu.au

Abstract

A numerical study of the scattering of transient plane wave excitation by an infinite cylindrical structure is reported. At its core is a rapidly convergent quadrature scheme for the solution of an integral equation formulation. A variety of boundary conditions including perfectly conducting structures are examined. The effect on the scattered field of rounding the corners is quantified as a function of the radius of curvature.

Keywords: Time-domain scattering, cylindrical structures, corners.

1 Introduction

In studying the scattering by transient electromagnetic waveforms, the choice of an appropriate canonical structure to model the dominant features of a scattering scenario can be very illuminating. The study in this paper was originally motivated by the influence that the corners of buildings and their surface cladding have on electromagnetic wave propagation. Rawlins [1] considered an approximate model relevant to the understanding of signal strength for mobile phones in this environment. It studied the diffraction of an E-polarised wave by an absorbing rectangular cylinder, based upon Keller's method of GTD and its extensions to deal with multiple diffraction.

In order to validate those results, Smith and Rawlins [4] undertook a numerical study of the scattering of an E-polarised plane wave by an infinite cylindrical structure in which an impedance boundary condition is enforced at all points on the cross-sectional boundary of the cylinder. It employed the frequency-domain integral equation formulation of [2] for the unknown surface distribution comprising a single-layer potential and the adjoint of the double-layer potential. A method similar to that of [3] for the perfectly conducting boundary was developed to obtain numerical solutions of this integral equation. The computed scattered far-fields were compared with the results of Rawlins in order to validate his solutions over the range of impedances and wavenumbers examined. The study concluded that results of [1] provide reasonably accurate patterns for rectangular structures for the range of wavenumbers and dimensions examined, but some divergences appear at higher frequencies. The divergences arise because – for the particular formulations employed - the cylindrical cross-sections are required to be smooth (having a continuously varying normal vector at each point), so that exactly rectangular structures are replaced by an appropriate "super-ellipse" approximating the rectangle with rounded corners. This limitation is common to both time-domain and frequency-domain integral formulations of the scattering problem.

2 Problem formulation and results

In order to quantify the effect of corner rounding on the scattering by transient electromagnetic waveforms this paper examines cylindrical scatterers which possess corners, that is, points at which the normal changes discontinuously. Specifically we develop a numerical method for the scattering of an E-polarised plane wave by such cylindrical structures with a variety of boundary conditions. It relies on the highly efficient numerical approach developed in [5] which is essential in obtaining accurate results across the bandwidth of the incident transient pulsed plane wave. In each case the boundary condition is enforced at all points on the cross-sectional boundary of the cylinder. We implement the Nystrom method expounded in [3] for perfectly conducting structures to obtain numerical solutions of an appropriate integral equation, and extend it for other boundary conditions.

We examine the difference between a test structure with a corner and a rounded corner to assess the impact on near and far field scattering, as a function of the radius of curvature in the vicinity of the rounded corner point. We then extend the numerical methods developed thus far to examine various test structures with two and four corners. The use of an appropriate graded mesh is seen to be essential in obtaining efficient and accurate solutions. We conclude by examining the effect on the scattered field of rounding these corners as a function of the radius of curvature in the vicinity of the rounded corner points. The differences become more pronounced as the incident transient pulse width narrows and is most visible in the early-time response.

References

[1] A.D. Rawlins, High frequency diffraction of electromagnetic plane wave by an imperfectly conducting rectangular cylinder, *J. Eng. Math.* **76**, pp. 157-180, (2012).

[2] D. Colton and R. Kress, *Integral equation Methods in Scattering Theory*, Krieger Pub. Co., Florida, 1992.
[3] D. Colton and R. Kress, *Inverse Acoustic and Electromagnetic Scattering Theory*, 3rd Ed., Springer-Verlag, New York, 2013.
[4] P.D. Smith and A.D. Rawlins, "Diffraction from structures with an impedance boundary", *Proc. International Conference on Electromagnetics in Advanced Applications (ICEAA '13)*, Torino, Italy, pp. 1036-1039, (2013).
[5] P.D. Smith and A. J. Markowskei, What effect does rounding the corners have on diffraction from structures with corners? In *Advanced Electromagnetic Waves, ed.* S.O. Bashir, pp. 1-28. Intech, 2015.

Development of an IEC HEMP/IEMI installation hardening guideline document

W. A. Radasky

Metatech Corporation, U.S.A, wradasky@aol.com

Abstract

Since 1989 the International Electrotechnical Commission (IEC) has been developing a series of basic standards, generic standards, protection publications and technical reports that provide information to protect systems and equipment from the threats of high altitude electromagnetic pulse (HEMP) and intentional electromagnetic interference (IEMI). There are now 21 publications in the IEC 61000 series produced by IEC SC 77C covering specific topics to include the description of the environments, test methods, measurement techniques and protection methods. A new publication IEC 61000-5-10 is now being developed to provide a guide to all of the existing publications for those who wish to protect installations from either one or both of these threats.

Keywords: high altitude electromagnetic pulse (HEMP), intentional electromagnetic interference (IEMI), installation hardening

1 Introduction

IEC SC 77C has developed a wide variety of HEMP and IEMI protection reports and standards over 25 years, and the growth of these publications has been organic, responding to the needs of industry. In addition, some of the existing standards are being revised to be more specific and useful to industry. IEC SC 77C publications are currently found in many parts of the IEC 61000 series including:

1: General – 2 publications
2: Environment – 4 publications
4: Testing and measuring techniques – 6 publications
5: Installation and mitigation guidelines – 7 publications
6: Generic standards – 1 publication

As the aim of the entire work program in IEC SC 77C is to determine the likely environments from the HEMP and IEMI threats and to develop protection and test methods to protect electronics from these environments, it is felt that a comprehensive guide to consolidate this work will be of great help to industry.

The proposal to prepare IEC 61000-5-10, "Guide to the Application of IEC SC 77C HEMP and IEMI Publications," has been approved and will include several specific categories of how to apply the basic and generic publications in the IEC SC 77C series. The cases covered are intended to include:

1) application of a protection and testing scheme for a new facility, and
2) application of a protection and testing scheme for an existing facility.

For both applications, protection and testing schemes need to be identified for three cases: a HEMP environment protection and testing scheme; an IEMI environment protection and testing scheme; and a HEMP+IEMI protection and testing scheme. This means there could be up to 6 schemes covered in this publication.

2 Basic protection approach

As indicated in Figure 1 the best approach for new construction of a facility is to use the shielding approach for the main installation with shielded cables extending to other critical equipment. This approach is valid for both HEMP and IEMI.

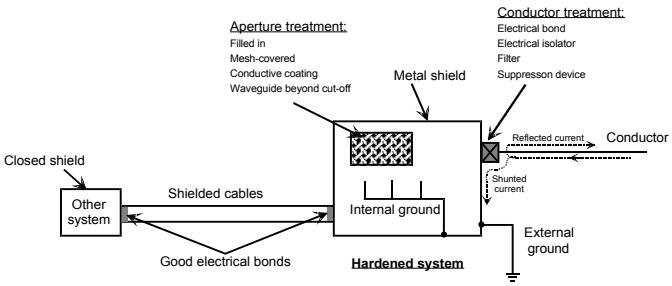

Figure 1. Illustration of a typical shielding approach for HEMP and IEMI [IEC 61000-1-5]

3 Presentation details

The presentation will present technical details of the development of this publication to include the proposed hardening concept levels and the resultant levels of testing that will be required for each concept. Also variations in test requirements due to variations in how the commercial power enters a facility will be presented. In addition, advantages and disadvantages of different types of test techniques will be reviewed.

An Overview: MIL-STD-4023 HEMP Protection for Military Surface Ships

M. R. Rooney, Defense Threat Reduction Agency, USA

Abstract

MIL-STD-4023 High-Altitude Electromagnetic Pulse (HEMP) Protection for Military Surface Ships is the first standard that can be used to certify the survivability of U.S. surface ships to the HEMP threat environment in MIL-STD-2169. The protection (hardening) practices and testing protocols in the standard are built on a decades-long legacy of experimental testing of military ships using the EMPRESS I and II EMP pulse simulators [1]. This paper discusses the strategy employed in the standard to leverage and build upon existing ship design and construction practices to create a system of electro-magnetic barriers with controls on points of entry where HEMP-induced fields and currents can penetrate into protected ship spaces and upset or damage mission-critical systems and subsystem equipment (MCS). It then provides an overview of the integrated testing protocols used to establish MCS immunity levels, verify stress reduction measures, and demonstrate ship surviv-ability through full-ship testing to the HEMP threat environment.

Keywords: HEMP, full-ship testing, simulator

1 Introduction

The electromagnetic effects of HEMP on electrical systems were first realized during the "Fishbowl" nuclear effects test in the 1960's. It was soon realized that the only technically sound way of testing large ships was to simulate the radiated nuclear HEMP threat environment and use it to illuminate an entire ship. In the 1970s, the EMPRESS I sub-threat level HEMP simulator was developed and used to test ships. But it was not until the early 1990s that the EMPRESS II was developed and used to test entire ships to full-threat level HEMP. EMPRESS I and II testing and analysis showed that the expected level of coupling to ship cables and antennas from an HEMP event can range from a few amps to thousands of amps. Unmitigated, these currents can cause significant damage to the ships' mission critical systems including communications, navigation, radars and weapons.

2 Discussion

In tandem with development of the standard, DTRA conducted experimental tests on active and de-activated ships to investigate alternative test methods. However, none of this experimental testing has identified a viable substitute for a full-ship, threat-level HEMP simulator test for verifying the HEMP survivability of a ship. The main issue with other assessment methods is that only a small fraction of the MCS can actually be tested due to test time and cost constraints. Whereas a properly designed, full-ship HEMP simulator test (Fig.1) exposes all ship mission-critical systems and

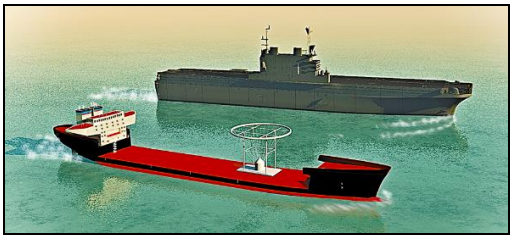

Figure 1. Ship with the starboard toward radiating vertical-polarization simulator.

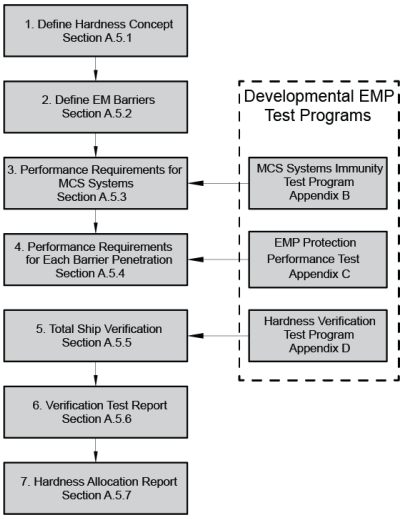

Figure 2. The seven steps of a typical Hardness Allocation Procedure.

subsystems equipment simultaneously to threat-level HEMP, other methods can only result in a partial ship assessment performed on a limited number of MCS.

Fig. 2 shows a block diagram of the chronological steps in the Hardness Allocation Procedure and its interrelationship with to the testing program. The presentation will provide an overview of each of these steps.

Summary

In conclusion, MIL-STD-4023 provides HEMP hardening schema and full-ship testing protocols with margin-based pass/ fail criteria for demonstrating hardness to the HEMP threat environment in MIL-STD-2169. Successful compliance with the standard will result in low-risk survivability. Based on recent studies, it offers the most timely and cost effective test methods. Employing alternative methods that do not rely on total ship illumination with the HEMP threat waveform will not result in a high-confidence hardness statement on full-ship EMP survivability.

Acknowledgments

The authors wish to thank the members of the MIL-STD-4023 Tri-Service Technical Working Group who contributed to the development of this standard.

References

[1] John M. Nelson et al, "USS *Anzio* EMPRESS II Trial," Naval Engineering Journal, May 1996

Advances in all-metal metamaterial slow wave structure design for high power microwave generation

E Schamiloglu, S C Yurt, S D Prasad, and M I Fuks

Dept. of Electrical and Computer Engineering, University of New Mexico, Albuquerque, NM 87131 USA edls@unm.edu

Abstract

Interest in all-metal metamaterial slow wave structures (MSWSs) has increased in recent years with the goal of engineering dispersion curves that are unattainable using conventional materials. This paper describes recent advances in optimizing a broadside-coupled split ring resonator SWS for L-band high power microwave (HPM) generation. The structure driven by a 400 kV relativistic electron beam generates 250 MW output power at 1.4 GHz frequency with 15% efficiency in a TE_{21}-like mode. Experimental plans to validate the simulation results will also be discussed.

Keywords: BWO; metamaterial; slow-wave structure; high power microwaves.

1 Introduction

The unusual properties of metamaterials [1] have motivated investigations of their use as SWS elements in microwave vacuum electron devices [2]. When combined with the large amplitude of the longitudinal electric field (and, hence, ensuring large Pierce parameter values), MSWSs could find a unique place in the field of HPM electronics. In this work, we present the design of a MSWS based on a broadside-coupled split ring resonator. The MAGIC particle-in-cell code and HFSS were used in the investigations. Experiments are planned to validate the design.

2 SWS Design

We aim to achieve optimum coupling of the electron beam to the MSWS, and thus, optimum microwave generation at the output by designing a broadside-coupled split ring resonator MSWS. We designed a structure that can produce a backward wave with a negative dispersion mode and has negative refraction index, which is one of the fundamental metamaterial properties. The MSWS consists of split rings (Fig. 1) where the broadside-coupled rings are 180° out of phase. Each split ring is electrically connected to the output waveguide with a conducting tab and each ring has a slit in one side except for the last 3 rings (Fig. 2). When driven by a 400 kV electron beam, 250 MW at 1.4 GHz is generated in a TE_{21}-like output mode with 15% electronic efficiency.

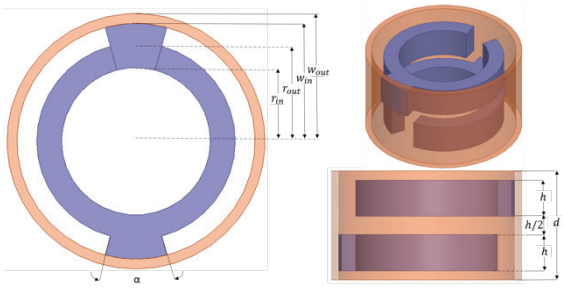

Figure 1. Geometry of a unit cell of the MSWS in different angles of view.

Table 1: Dimensions corresponding to Fig. 1.

r_{in}	r_{out}	w_{in}	w_{out}	α	h	d
1.5 cm	2 cm	2.4 cm	2.8 cm	30 degree	1 cm	3 cm

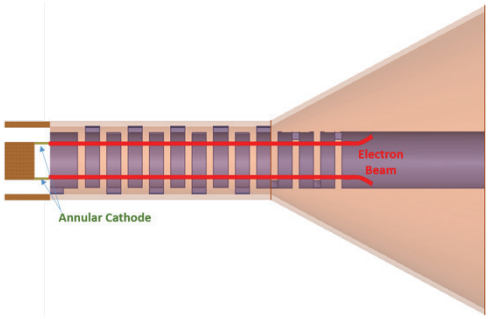

Figure 2. Drawing of the entire structure design.

Acknowledgements

This research was supported by AFOSR MURI Grant FA9550-12-1-0489.

References

[1] R. Marques, F. Martin, and M. Sorolla, *Metamaterials with Negative Parameters: Theory, Design, and Microwave Applications* (John Wiley and Sons, New York, NY, 2008).

[2] S.C. Yurt, S. Prasad, M. Fuks, and E. Schamiloglu, "Designing of an O-Type BWO with a Metamaterial Slow-Wave Structure," to be presented at *IVEC 2016* (Monterey, CA, April 19-21, 2016).

Measurements and Modelling of Planar Periodic Lattices for Electromagnetic Applications

A. J. MacLachlan, A. R. Phipps*, C. W. Robertson*, I. V. Konoplev†, A. W. Cross*, and A. D. R. Phelps**

*Department of Physics, SUPA, University of Strathclyde, Glasgow, G4 0NG, Scotland, UK
†JAI, Department of Physics, University of Oxford, Oxford, OX1 3RH, England, UK
a.d.r.phelps@strath.ac.uk

Abstract

Theory, modelling and measurements of periodic surface lattice (PSL) structures are reported. This work is in the developing area of 'transformational electromagnetics'. One of the aims of this work is to support the design of novel sources of radiation. In situations where a structure may support several modes, volume and surface wave coupling can result in the formation of a cavity eigenmode. The formation of such eigenmodes is relevant to improved mode selectivity and the realization of high power mm-wave and THz coherent sources.

Keywords: Periodic lattices, surface waves, metadielectric.

1 Introduction

Transformational electromagnetics is important for the realization of improved high-power coherent sources [1-3], operating in the GHz-THz frequency range. The cavity dimensions of traditional electromagnetic sources tend to decrease as the wavelength of the source radiation decreases, to keep the excited cavity mode a single low order mode thus avoiding less efficient multi-mode excitation. This in turn limits the output power of mm-wave and THz sources, compared with corresponding RF and microwave sources. An approach that can be used to mitigate this is to introduce novel methods of mode selection in over-moded cavities. The novel method studied here uses periodic surface lattices (PSLs) [4]. Such a PSL can be created by manufacturing shallow periodic perturbations on a metal surface. Periodic structures can be one, two or three dimensional. The present study employs two dimensional (2D) periodic perturbations. Such 2D PSLs can be used for several applications exploiting different physical phenomena, [1-7]. This 2D PSL study aims to observe and understand the role of PSLs in the coupling between volume and surface fields, resulting in the formation of a cavity eigenmode. In previous work, a dispersion relation describing coupling of volume and surface fields inside a 2D PSL of cylindrical topology was derived [6]. Under certain conditions, when driven by a suitable electron beam this structure can support a Cherenkov instability. Hence PSLs show potential for use in electron-beam-driven high power, coherent sources [4,6,7].

A planar structure with a shallow chessboard corrugation is considered. This basic planar geometry rather than a cylindrical geometry is used here to investigate the fundamental 'proof of principle' coupling between the volume and surface fields. It is important to note that it is not intended to deploy these present planar PSLs within electron-beam-driven, high power coherent vacuum electronic sources. Conformal mapping allows PSLs in planar geometry to be mapped into PSLs in cylindrical geometry that are compatible with the construction of high power electron-beam-driven vacuum electronic sources. In the cylindrical geometry, the PSL is formed by structuring the inside of the metallic outer vacuum wall of the cylindrical cavity [8] and so unlike the present proof-of-principle experiments no dielectric materials are required. The cylindrical PSL structures are compatible with vacuum conditions and the use of energetic electron beams. Since the corrugation height is much smaller than the operating wavelength, the lattice may be described as a high-impedance surface or effective 'meta-dielectric'. The lattice acts as one reflecting surface mounted on a dielectric waveguide, with a thin copper foil backing acting as another reflecting surface. The volume mode trapped inside this volume enables synchronization of individual PSL elements.

2 Results

Several PSLs have been constructed by chemical etching printed circuit board (PCB) with a 35μm copper coating and FR-4 dielectric (Fig.1). PSLs with periods $d_z = 1.50$mm, 1.62mm, 1.74mm and 1.94mm have been etched onto PCBs of various thicknesses (0.4mm, 0.8mm and 1.6mm) both with and without a copper backing.

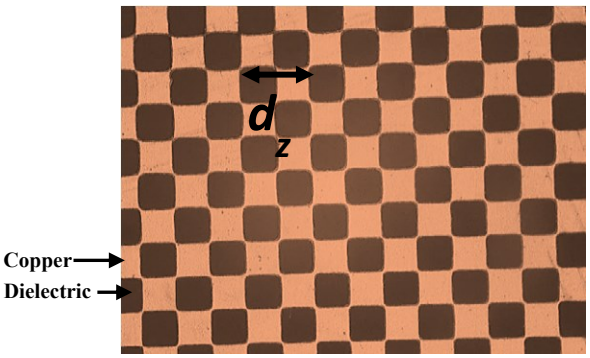

Figure 1. Copper planar PSL, constructed by chemical etching a PCB. PSL has d_z=1.74 mm and FR-4 dielectric.

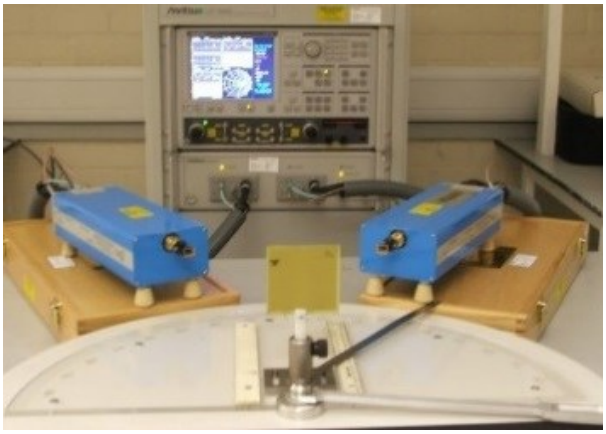

Figure 2. PSL measurements made at various incident angles using a pair of G-band horns connected to 140-220 GHz heads of a Vector Network Analyzer (VNA).

The experimental measurement set-up is shown in Fig. 2 and Fig. 3 shows the formation of a single, sharp resonance, demonstrating eigenmode formation. The excellent reproducibility was confirmed by completely re-assembling the experiment and repeating the VNA measurements on three separate occasions over intervals of months. Such a high-Q cavity, when created using a PSL mapped into cylindrical geometry can form the basis of a novel coherent source when excited by a suitable electron beam [9-12].

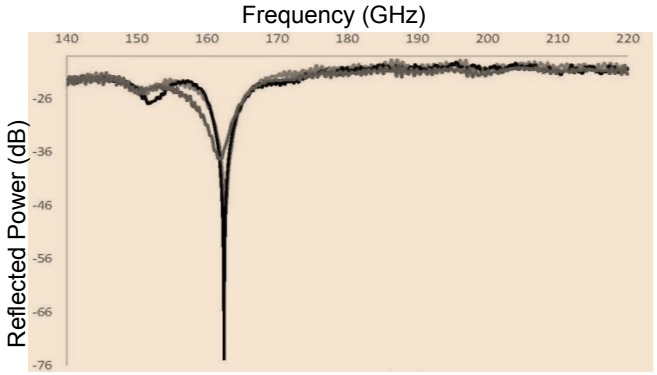

Figure 3. Coherent eigenmode formation for a PSL with lattice period dz = 1.62 mm, on FR-4 dielectric substrate of thickness 0.8 mm, with a 35 µm copper foil backing.

Numerical modelling is being carried out to further understand the coupling of volume and surface modes at the lattice interface and the effect of varying the dielectric and lattice parameters. Using the modelling software 'CST Microwave Studio', a single unit cell is irradiated by plane waves over a range of angles and the scattering parameters measured by a "Floquet" port. An alternative approach involves modelling a small section of the structure to provide a more realistic representation taking account of phenomena such as edge effects.

Going forward new samples have been constructed to operate in the 325-500 GHz band. The PSLs are scalable and so these principles apply at frequencies throughout the microwave, mm-wave and THz ranges.

3 Summary

Coupling between volume and surface modes and coherent eigenmode formation in PSL structures has been successfully demonstrated experimentally for planar 2D PSL structures. The parameters were carefully chosen to facilitate the resonant coupling of modes. When the necessary conditions are met, PSL structures have the potential to provide effective interaction regions for novel, coherent sources of radiation**.**

Acknowledgements

Amy J. MacLachlan and A. R. Phipps thank the EPSRC for supporting their postgraduate studentships.

References

[1] N. S. Ginzburg, et al., "Theory of free-electron maser with two-dimensional feedback driven by an annular electron beam", *J. Appl. Phys*., **92**, pp. 1619-1629, (2002).

[2] N. S. Ginzburg, et al., "The use of a hybrid resonator consisting of one dimensional and two-dimensional Bragg reflectors for generation of spatially coherent radiation in a co-axial free-electron laser", *Phys. Plasmas*, **9**, pp. 2798-2802, (2002).

[3] I. V. Konoplev, et al., "Experimental and theoretical studies of a coaxial free-electron maser based on two-dimensional distributed feedback", *Phys. Rev. E*, **76**, 056406, (2007).

[4] I. V. Konoplev, et al., "Surface wave Cherenkov maser based on a periodic lattice", *Appl. Phys. Lett*., **96**, 261101, (2010).

[5] A. W. Cross, et al., "Studies of surface two-dimensional photonic band-gap structures", *J. Appl. Phys*., **93**, pp. 2208-2218, (2003).

[6] I. V. Konoplev, et al., "Cylindrical, periodic surface lattice – Theory, dispersion analysis and experiment", *Appl. Phys. Lett*., **101**, 121111, (2012).

[7] I. V. Konoplev, et al., "Cylindrical periodic surface lattice as a metadielectric: concept of a surface-field Cherenkov source of coherent radiation", *Phys. Rev. A*, **84**, 013826, (2011).

[8] I. V. Konoplev, et al., "Surface field excitation by an obliquely incident wave", *Appl. Phys. Lett*., **102**, 141106, (2013).

[9] I. V. Konoplev, et al., "High-current oversized annular electron beam formation for high-power microwave research", *Appl. Phys. Lett.,* **89**, 171503, (2006).

[10] H. Yin, et al., "Pseudospark-based electron beam and Cherenkov maser experiments", *Phys. Plasmas*, **7**, pp. 5195-5205, (2000).

[11] A. W. Cross, et al., "Generation and application of pseudospark-sourced electron beams", *J. Phys. D: Appl. Phys*., **40**, pp. 1953-1956, (2007).

[12] H. Yin, et al., "Millimeter wave generation from a pseudospark-sourced electron beam", *Phys. Plasmas*, **16**, 063105, (2009).

Dielectric Characteristics of As-Prepared Carbon Black-Epoxy Nanocomposites in Medium Frequency Range

Rahim Jan*[†, ††], ***Akhtar Hussain***[††]

[†]*School of Chemical and Materials Engineering, National University of Sciences and Technology, Islamabad, Pakistan*
[††]*Centre for Excellence in Science and Technologies (CESAT), Islamabad, Pakistan*
**rahimjan@scme.nust.edu.pk*

Abstract

The dielectric properties of carbon black-epoxy nanocomposites have been the focus of the present work in the frequency range 100 kHz-5 MHz. An interesting behaviour is experienced for the composites with the different nano filler loading. Various parameters (dielectric constant, tangent loss and AC conductivity) are measured and 2% loading of carbon black (CB2) showed the maxima for all mentioned parameters. This is in line with our earlier results for the same formulation of the composites meant for the microwave absorption in Ku-band, making it a very good candidate for the above mentioned application over a broad band of frequency. Scanning electron microscopy of the composites reveal a homogeneous dispersion of the nano fillers in the matrix.

Keywords: Dielectric constant; Interface; Polarization

1 Introduction

Nano particles play an important role in altering the properties of base polymers due to the small size leading to the increase in surface area [1]. Polymeric nano composites (PNCs) based on conducting nano fillers have been widely studied. Electrical properties have been the core of the many scientific and technological explorations. Epoxy resin has been extensively used worldwide due to the variety of properties it possess like its use in elevated voltage applications as insulation, high temperature applications and for structural applications. Of late it has been used for EMI shielding purpose with a considerable success. Conductive fillers such as carbon black, carbon nano tubes, graphene and other metallic nano inclusions are dispersed in epoxy for applications like charge dissipation, mechanical reinforcements and to enhance the thermal behaviour of the nanocomposite. At a certain increment of conducting filler, polymer turns from an insulating to conducting composite; the transition is termed as percolation effect which is mainly dependent on the interfacial interaction of filler with the matrix. In the current work, carbon black is homogeneously dispersed in epoxy matrix by using solution processing route for the fabrication of nanocomposites. The focus is on the outcome of dielectric spectroscopic analysis with respect to filler concentration as a function of frequency (100 Hz – 5 MHz) which predicts the interfacial effects of the filler and matrix. The trend is such that the dielectric properties are enhanced till a certain level of loading after which we experience a lowering effect of the dielectric properties when the concentration of carbon black is increased.

2 Results and Discussion

The dielectric performance of the base polymer (epoxy only) and the CB/epoxy nanocomposite dielectric films (CB weight % 1-4) is measured with impedance analyser (Wayne Kerr 6500B) at an applied voltage of 10 mV and frequencies in the range of 100 kHz to 5MHz. Figure 1 (a-c) show the dielectric constant, tangent loss and AC conductivity response for CB/epoxy nano composites with different CB weight % as a function of frequency at room temperature. For the dielectric complex permittivity, the expression is given as

$$\varepsilon^* = \varepsilon'(\omega) - \varepsilon''(\omega) = \frac{C^*(\omega)}{C_0} \quad (1)$$

Where ε' represents the dielectric constant, ε'' denotes the dielectric loss value, C^* shows the complex capacitance and C_0 is the vacuum capacitance. The dielectric constant is calculated using the well-known relation [2-3]

$$\varepsilon' = \frac{Ct}{\varepsilon_0 A} \quad (2)$$

Where *'C'* is the capacitance of the sample in farad, *'t'* is the thickness of the sample in meters, *'A'* is the cross sectional area in m^2 and ε_o is the permittivity of free space. The dielectric dissipation factor can be expressed in terms of the dielectric constant and dielectric loss as

$$\tan\delta = D = \frac{\varepsilon''}{\varepsilon'} \quad (3)$$

The expressions for ac conductivity measurements is given in equation (4) as under

$$\sigma_{ac} = \omega\varepsilon'\varepsilon_0 \tan\delta \quad (4)$$

From the above parameters, capacitance *'C'* and dissipation factor *'D'* are measured directly from the impedance analyser while the dielectric constant, dielectric tangent loss and ac conductivity are calculated by using equations (2-4). The dielectric constant of the pure epoxy is found to be around 3. With the addition of 1% carbon black by weight, CB1, dielectric constant increases up to 3 folds of pure polymer as shown in Fig. 1 (a). Dielectric constant accounts for the ability of the dipoles formation inside the nanocomposites and its orientation with respect to the applied electric field as a function of frequency [4]. At 2% weight carbon black, CB2, the dielectric constant reaches to almost 20 at lower frequency region as clearly evident from Fig. 1 (a). With further increase of the CB concentrations (CB3 and CB4), the dielectric constant tends to lower down as compared to CB2.

The interesting behaviour can be well explained on the basis of molecular mobility. With the increment of nanofiller inside the polymer matrix, dielectric constant is increased due to the dipoles formation which are oriented along the direction of the applied field. But at the same time the nanofiller increment causes the decrease in the molecular mobility at the polymer-nanofiller interface. The general trend of dielectric constant, for all concentrations of CB, is such that at lower frequencies it is of the maximum values and decreases with the increase in frequency. A ‘’low frequency dispersion’ behavior is experienced due to the ionic movement to the vacant sites via hopping. It is believed that clusters are formed inside the composites with the addition of nano fillers and the intermolecular motions for long times is the reason for the high dielectric constant values at low frequency. For high frequency regions, dielectric constant tends to lower down relatively due to the intra-molecular motions for short times. The tan delta value in the carbon nano particles filled epoxy remains almost constant as a function of frequency with a little down wards humps at the lower frequency range caused due to the interfacial polarization. Tan delta values reaches a minimum value at lower frequency and then tend to increase and remains unchanged afterwards. Dielectric tangent loss value ranges from 0.02 to 0.2 for pure epoxy and CB2 respectively. For CB3 and CB4, the tangent loss values are on the decline (Fig. 1 (b)). The ac conductivity response is linear as a function of frequency and is on the increase constantly as the frequency is increased for all the weight fractions; and behaves similar to the dielectric constant response as a function of weight fraction. At CB2, the insulator-conductor transition takes place which is mentioned as percolation threshold (Fig. 1 (c)). The enhancement in dielectric characteristics for CB2 as a function of medium frequency range adds to the already found microwave absorption results [1] for the same set of CB-epoxy nanocomposites in the Ku-band (11-18 GHz). Functionalization of carbon nano particles can improve its adhesion with the matrix and also can avoid the aggregation effect, making them a good choice for broad band electromagnetic wave absorbers.

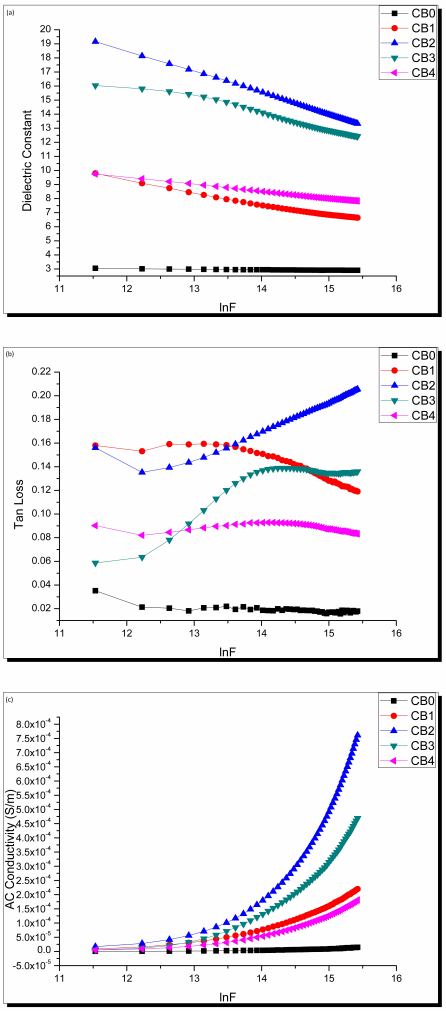

Fig. 1: Dielectric constant (a), Dielectric tangent loss (b) and AC conductivity (c) as a function of frequency for the CB-Epoxy composites with respect to different carbon black concentrations.

3 Conclusion

Carbon black-epoxy nanocomposites are synthesized and characterized for dielectric properties as a function of different filler concentration and frequency. The dielectric constant, loss and ac conductivity all are increased considerably up to carbon black concentration of 2% weight. Dielectric constant experiences an increase up to 6 fold of base polymer with a subsequent increase in the loss and ac conductivity as well, making it a good candidate for electromagnetic waves dissipation. The most promising part of this report is the trend of the results which follows our earlier work (reference1) in which the same kind of composites were tested for the microwave absorption in the Ku-band (11-18 GHz) and the best results in terms of absorption were found for CB2. The current work emphasizes on the use of such composites for broad band microwave absorption applications.

References

[1] R. Jan, Z. M. Khan, M. B. Khan, Synthesis and electrical characterization of “carbon particles reinforced epoxy-nanocomposite” in Ku-band, *Materials Letters*, **70**, 155–159 (2012).

[2] E. Arslan, Y. Safak, I. Tascioglu, H. Uslu, E. Uzbay, Frequency and temperature dependence of AC electrical and dielectric properties of hetrostructures. *Microelectronic Engineering*, **87**, 1997–2001 (2010).

[3] K. Khan, A. Maqsood, Synergistic microwave and structural studies of C-type of $Ho_2Si_2O_7$. *Journal of Alloys and Compounds*. **509**, 6649–6651 (2011).

[4] V. Kosmidou, A. S. Vatalis1, C. G. Delides, E. Logakis, P. Pissis, G. C. Papanicolaou: Structural, mechanical and electrical characterization of epoxy-amine/carbon black nanocomposites, *eXPRESS Polymer Letters*, **2**, 364–372 (2008).

Computational Comparison of bow-tie and notch arrays fed via notional PCSS Signal

S. Nickolas, J. Roos, P. Collins, J. Petrosky, A. J. Terzuoli, T. Zens

Institute of Electrical and Electronics Engineers; Dayton, Ohio, USA; a.j.terzuoli@ieee.org

Abstract

Linear mode Photo Conductive Semiconductor Switch (PCSS) devices offer low jitter and small size compared to spark gap switches. The benefit of using the PCSS in the pulse forming stage of HPEM systems allows for arrayed antenna operation. Arrayed operation allows for power distribution and electronic steering. Power distribution allows for circumvention of gas breakdown. Electronic steering is performed with the true time delay method, where time delays are potentially controlled with computer cycles rather than physical delay lines. In an effort to minimize array space and maximize the effect of the electric field, a mesoband signal is desired. The paper focuses on the antenna portion of the HPEM system, with design emphasis on two-dimensional antenna structures capable of radiating a notional mesoband signal with power levels derived from recent iron-doped GaN experiments. CST MWS is used to optimize variations of notch antennas and bow-tie antennas with design goals of small form factor and mesoband frequency response. The antennas are arrayed and the performance extrapolated for N distributed elements. The far-field electric fields are studied, and the field generated per size is taken into account.

Keywords: HPEM, Mesoband, PCSS.

1 Introduction

The bow-tie and notch antennas exhibit two dimensional compact form factors. The aforementioned traits of the antenna compliment the small nature of the PCSS, and lead to the possibility of covert operation. The two antennas offer differing radiation characteristics: the bow-tie relies on resonance whereas the notch creates an end fire traveling wave. The antennas are designed to permit 10 kV prior to air breakdown, assuming a 1.0 MV/m flashover field strength.

In addition to small size, the antennas are versatile with respect to placement on structures or printable substrates, and may be used as conformal antennas.

2 Methods

The input signal, representative of a potential PCSS signal, is generated in MATLAB. The signal is described by

$$V(t) = A\sin(2\pi f t)e^{-\alpha t}, \qquad (1)$$

which is representative of an ideal decaying oscillatory signal generated by a quarter wave oscillator, paired with a higher impedance antenna.

With regard to the bow-tie and notch antennas, the researchers executed parametric optimization routines with focus on bandwidth and size reduction. The targets included 25% FBW with a centre frequency of 665 MHz, and minimization of S_{11} parameters throughout the relevant frequency range. The antennas simulations used the FDTD solver in CST MWS. The FDTD method matches the semi-impulse like nature of the mesoband input signal.

Far field electric field probes placed at known locations captured the transient electric fields. The absolute maximums extracted from the probes provided the inputs for calculating transient antenna gains. The simulations were repeated with linear arrays employing true time delay steering.

3 Results

The bow-tie performed best on boresight and the notch returns better off-boresight, which is an effect of using an atypically short notch. The short notch offers a 27% greater maximum field than the bow-tie, but encompasses 67% more area than the bow-tie.

The arrays were designed and tested to steering angles of 0, 30, and 60 degrees. For the five element case, the short notch maintains 102%, 98% and 110% of the element factor respectively. This result can be explained by constructive mutual coupling. The bow-tie returned 114%, 93%, and 74% which shows a trend of destructive mutual coupling as steering angle increases.

3 Conclusion

The bow-tie offers superior performance in electric field generated per size, but the notch shows better steering performance. The bow-tie and notch offer similar results in terms of generated electric field in an arrayed case, with the bow-tie trending slightly higher as the number of elements increases.

Compact and lightweight PCI generator for HEMP shelter and filter verification

Jin-Ho Shin*, Kyu-Ho Son*, Yeong-Kyung Jung*, Dong-Gi Youn*

**HPEM Application Laboratory, Seoul, Republic of Korea, hpett@replex.co.kr*

Abstract

This paper presents 80kV short Pulsed Current Injection (PCI) generator corresponding to Mil-Std-188-125 1/2. The designed pulse generator was developed focused on being compact/lightweight and operating with ease. This generator can produce double exponential current of a rise time of <20ns, pulse width (FWHM) of 500ns~550ns and peak current of 1.3kA.

Keywords: HEMP, Pulsed Current Injection generator, Mil-Std-188-125 1/2, Short PCI

1 Introduction

The concern of electronic devices vulnerability to high power electromagnetic (HPEM) threats is increasing recently in South Korea. This is the reason why South Korea is facing nuclear threats associated with North Korea. But existing generator for testing high-altitude electromagnetic pulse is import-dependent and not easy to operate due to heavyweight and a complicated procedure. For such a reason, we developed and improved HEMP generator focused on user friendliness side.

2 Development

The designed 80kV short PCI generator consists of high voltage (HV) pulse generator and controller. The output current of HV pulse generator satisfies demand of short PCI standard. The spark-gap switch of HV pulse generator has external-triggered spark gap for minimizing output deviation. This trigger method is beneficial to stability than self-triggered method. The controller have embedded PC and touch screen, so operator can control generator by graphic user interface easily. Also the operator can check generator status like self-check and refer to report with test set-up.

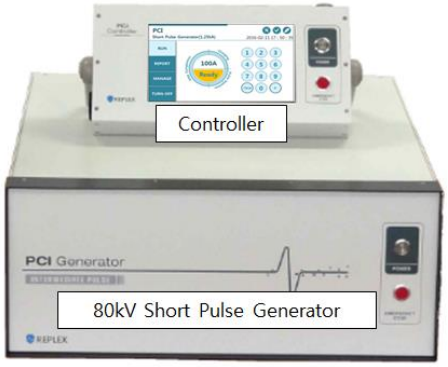

Figure 1. 80kV Short PCI generator

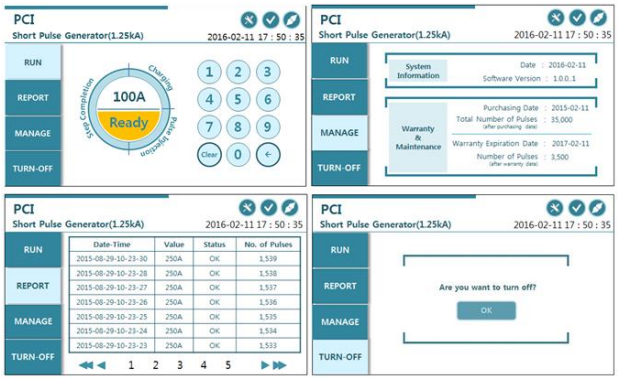

Figure 2. Graphic user interface of controller

The 80kV short PCI generator with 62Ω impedance was able to deliver 1.3kA to short load and 80kV to open load, also this specifications are satisfied with related standard.

3 Results

Overall dimensions of the manufactured HEMP 80kV short PCI generator are 65cm in length, 55cm in width and 25cm in height and the weight is less than 40kg. The generator in this work can be utilized for testing HEMP shelter and filter verification. Compact, lightweight and GUI can make user to check the test procedure easily and control instinctively.

References

[1] Montena, http://www.montena.com/system/generators/pulsed-current-injection-pci-generators/

Development of a Damped Sinusoidal Pulse Radiator with a High Stability for the IEMI testing

Kyung-Tae Lee, Young-Kyung Jeong, Dong-Gi Youn

Replex Co., Ltd., Seoul, Korea
admin@replex.co.kr

Abstract

In this paper, we proposed a DS(Dampled Sinusoidal) pulse radiator based on a Marx generator and a Fat dipole antenna which can be used for MIL-STD 464 testing. The radiator is mounted in a suitcase for a portable use, and compact and lightweight. A differentiated circuit design was applied to the inner structure of the Marx generator, which made a high stability in the radiator's operation though it operates with self-triggered spark-gap switches. In the test results, the radiator generated 14.5 kV/m of electric field strength at 10 m distance and showed highly stable operations.

Keywords: IEMI, MIL-STD 464, DS pulse radiator, Marx generator

1 Introduction

The electromagnetic susceptibility of electronic equipments is an important issue for their stability, and many ultra-wide band electromagnetic pulse radiators have been developed for the IEMI(Intentional Electromagnetic Interference) testing[1]. DS pulse radiators were developed to generate damped sinusoidal pulses for the IEMI testing, and some of them were made in a compact size[2,3] in order that they can be used under less limit of operating places and circumstances than other ones. But it was not easy to make high stabilities in the compact radiators' operations because they commonly used self-triggered spark-gap switches for the compactness and simplicity.
The radiator in this paper was developed for the purpose of being used for the IEMI tests and making sure the high stabilities in operations.

2 DS pulse radiator design

The radiator consists of a battery powered Power supply, a Marx generator, and a Fat dipole antenna, they are all mounted in a suitcase. The Marx generator and the Fat dipole antenna operate under high pressure N_2 gas, then a Gas supplier also included in the suitcase with a Gas container.
The Power supply generates up to 35 kV and supplies it to the Marx generator, and can operate with 20 Hz pulse repetition rate.
The Marx generator consists of 10 capacitor stages then can multiply voltage 10 times from supplied. Each stage consists of a capacitor, a spark-gap switch, and inductors. The capacitance of the capacitor is 940pF. Spark-gap switches operate with the self-triggered method which needs no external triggering, and set to discharge when charged voltage reaches up to 30 kV. The inductors isolate each stage in the spark-gaps' discharging.
The Marx generator made by a new circuit structure design described in Figure 1. Conventional Marx generators normally have one row of capacitors. Some have two rows but they need two powers to charge up the rows. The proposed Marx generator has two rows of capacitors but needs only one power to charge them up.

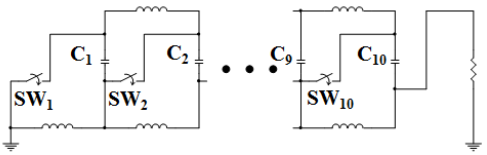

(a) Circuit A; a conventional Marx generator.

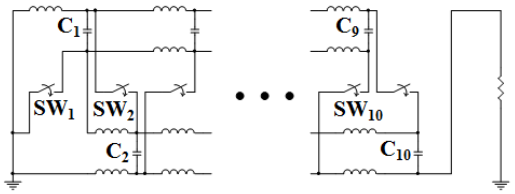

(b) Circuit B; Proposed Marx generator in this paper.

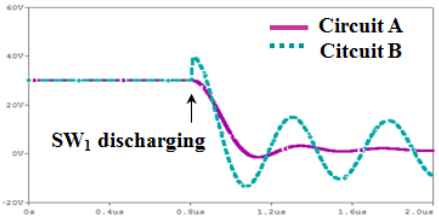

(c) Simulated voltage waveforms of SW_2 when SW_1 discharging.

Figure 1. Equivalent circuits and simulated voltage waveforms of SW_2 when SW_1 discharging in a conventional Marx generator and proposed one.

Especially the circuit structure is designed to raise a voltage spike at the next stage's spark-gap when the previous one discharging, this voltage spike leads a simultaneous discharge of the next spark-gap. The effect sequentially occurs from the

first spark-gap to the final, all spark-gaps can discharge at the almost same time. This makes the Marx generator operates with high stability without any external triggering method.
The Fat dipole antenna includes a spark-gap that discharges when the pulse power is supplied from the Marx generator.

3 DS pulse radiator produce and test

Figure 2 shows the radiator mounted in a suitcase, whose size is 540 mm × 410 mm × 210 mm and the weight is 24.6 kg.

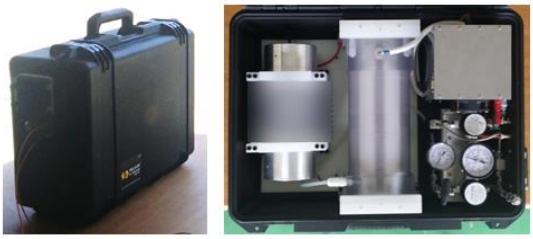

Figure 2. DS pulse radiator.

Figure 3 shows electric field waveforms that overlapped 100 times measured at 10 m distance, which shows the radiator operates highly stable. The average value of the maximum electric field strengths is 14.5 kV/m.

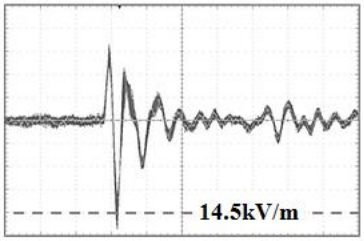

Figure 3. Electric field waveforms measured at 10 m distance(overlapped 100 waveforms).

4 Conclusion

A compact DS pulse radiator based on a new circuit design applied Marx generator was developed.
The size of the radiator is 540 mm × 410 mm × 210 mm and the weight is 24.6 kg. The average value of the maximum electric field strength is 14.5 kV/m at 10 m distance.
The radiator operates highly stable and can be used for the IEMI tests, including MIL-STD 464.

References

[1] J. R. Mayes, C.W. Hatfield, M.G. Mayes, W.C. Nunnally, M.B Lara, T.A. Holt. “A Compact High Power Wideband System”, *Power Modulator and High Voltage Conference*, pp. 612-616, (2010).
[2] DIEHL BGT Defence GmbH. “HPEMcase Standard F”, *Brochure.*
[3] J. R. Mayes, W. J. Carey. “The Marx Generator As An Ultra Wideband Source”, *IEEE International Pulsed Power Conference*, (2001).

Radiation pattern and scattering parameter on finite cylindrical loop antenna using the iterative method WCIP

Jarboua Ines[1], Ammar Noemen[1], Aguili Taoufik[1], Baudrand Henri[2]

Jarboua.ines@gmail.com, ammar.noemen@gmail.com , taoufik.aguili@enit.rnu.tn, henri.baudrand@gmail.com
[1]*System of communications laboratory (SYSCOM), ENIT, University of Tunis el Manar, 1068, Tunis, Tunisia,*
[2]*Laboratory of Laplace, Toulouse.*

Abstract

This paper presents the characteristics of cylindrical loop antenna on finite structure such as the radiation pattern and the scattering parameter using the integral equation method based on the wave Concept iterative process (WCIP) formulation
Keywords: WCIP method, cylindrical loop antenna, Radiation pattern, Scattering parameter.

1 Introduction

Loop antenna are widely used in Wireless Communications systems because they can eliminate multipath interferences and relax the alignment requirement for the transmitting and received antennas [1,2]. Cylindrical loop antenna has been resolved by many numerical methods such as the integral method (MoM method…) and the differential method. A new formulation based on wave Concept iterative process known as WCIP is presented in many research studies [3,4].
This method has many advantages compared to other electromagnetic modelling methods. Indeed, it ensures the convergence, optimizes calculated time and then it is applied in all structures forms [5]. In this paper, we present the principle of the Wave Concept Iterative Process (WCIP) applied to a finite cylindrical loop antenna in order to calculate the admittance parameter, the scattering parameter and to evaluate the radiation pattern in different plans.

2 Formulation of the problem and basic equations

2.1 The Wave Concept Iterative Method (WCIP)

The Wave Concept Iterative Process 'WCIP' is an integral method based on generalized concept of waves defined by the incident wave and the reflected wave according to the following relationships:

$$\begin{cases} \vec{A}_T = \dfrac{1}{2\sqrt{Z_0}}\left(\vec{E}_T + Z_0\left(\vec{H}_T \wedge \vec{n}\right)\right) \\ \vec{B}_T = \dfrac{1}{2\sqrt{Z_0}}\left(\vec{E}_T - Z_0\left(\vec{H}_T \wedge \vec{n}\right)\right) \end{cases} \quad (1)$$

$\vec{E}_T$, $\vec{H}_T$ represent respectively the tangential electric field and the tangential magnetic field. Z_0 is the environment impedance in which the waves are defined. $\vec{n}$ is the outward normal vector to the scattering surface S. The iterative process consists in establishing a recurrence relationship between incident and reflected waves through the diffraction operators defined in spatial and modal domain [4,5]. The diffraction operator in spatial domain $\hat{S}$ provides the relationships between incident and reflected waves by (2):

$$\vec{A} = \hat{S}.\vec{B} \quad (2)$$

The diffraction operator in the modal domain denoted $\hat{\Gamma}$ is given by the following expression:

$$\vec{B} = \hat{\Gamma}.\vec{A} \quad (3)$$

Thus, (2) and (3) will be repeated until the convergence of iterative process [4, 5].

2.2 Definition of cylindrical loop antenna structure

We consider the cylindrical loop antenna structure presented by figure 1. Two coaxial cylinders named C1 and C2 form this antenna. C1 is a perfectly conducting cylinder. C2 contains metallic and dielectric cylindrical rings excited by bilateral source. The distance between each two metal rings is rated h. This structure is periodic of period d.

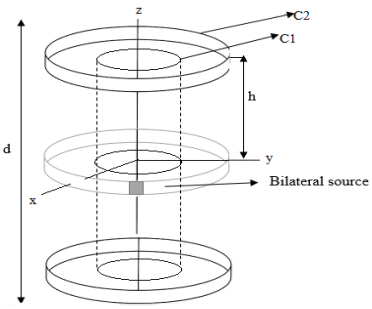

Figure 1. The structure of cylindrical loop antenna

2.3 Scattering Parameter S

The parameter Y depends of the current density $\vec{J}_T$ and the tangential electric field $\vec{E}_T$ according to the following relation:

$$Y = \frac{\int_{\Delta S} \vec{J}_T dS}{\int_{\Delta S} \vec{E}_T dS} \quad (4)$$

Where ΔS represents the definitions of source.
The scattering parameter S can be deduced from the admittance Y by the following expression:

$$S = \frac{(1 - Z_0.Y)}{(1 + Z_0.Y)} \quad (5)$$

2.4 Radiation Pattern *in* θ *plan*

To determine the radiation pattern according to theta, we must be placed on a cylinder of large radius. Therefore, we present the infinite diffraction operator denoted by $\hat{\Gamma}_{\inf}$.

2.5 Radiation Pattern in ϕ plan

The radiation pattern in ϕ plan is obtained where $\theta = 0^{\circ}$, the analytical expression is given by (2).

$$f_p(\phi) = d \sum_{n=-\frac{N}{2}}^{\frac{N}{2}-1} \sum_{m=-\frac{P}{2}}^{\frac{P}{2}-1} \vec{A}_{nm}^{p} \sin_c\left((k_0 \cos(\phi) - k_m) \frac{d}{2} \right) \quad (6)$$

Where N and M respectively the number of mode according to θ and ϕ plans, $k_m = k_0 \cos(\phi_m)$, $\vec{A}_{nm}^{p}$ represent the modal emitted wave from the exterior of the cylindrical structure.

3 Numerical results

This section present numerical result of iterative process applied on cylindrical loop antenna structure defined in the previous section. The iterative process is validated for this configuration: N=M=128pixels,R_1=0.01, R_2=1.2*R_1, iteration number=100. The variation of parameter S in terms of frequency is presented by figure 2. The radiation pattern according to theta and phi plans are presented respectively by figure 3 and 4. Two polarisations of the loop antenna are defined in each plan of radiation pattern: Horizontal polarisation and vertical polarisation.

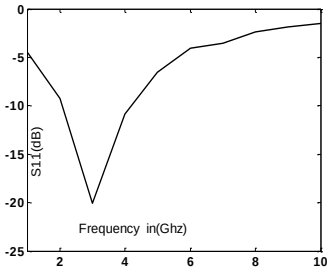

Figure 2: Scattering parameter S11 in dB

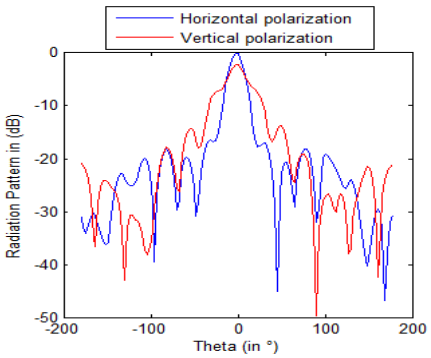

Figure 3: Radiation pattern in theta plan

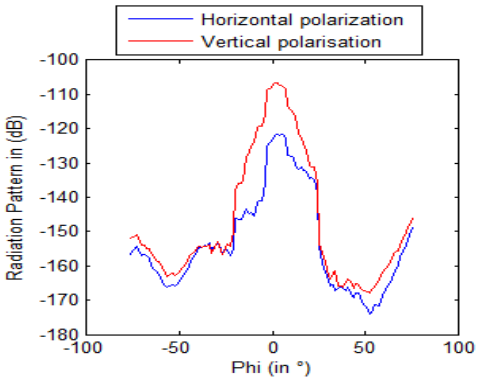

Figure 4: Radiation pattern in phi plan

4 Conclusion

In this paper, we have calculated the scattering parameter S and resolved the radiation problem of finite cylindrical loop antenna structure using the Wave Concept Iterative Process method.

Acknowledgment

This work was supported by the system of communications laboratory (LR-99-ES21).

References

[1]. W. Wei Li, K. Wa Leung , "Omnidirectional Circularly Polarized Dielectric Resonator Antenna With Top-Loaded Alford Loop for Pattern Diversity Design," *IEEE TRANSACTIONS ON ANTENNAS AND PROPAGATION*, VOL.61, NO.8, (AUGUST 2013).

[2]. John T. Conway, "New Exact Solution Procedure for the Near Fields of the General Thin Circular Loop Antenna," *IEEE TRANSACTIONS ON ANTENNAS AND PROPAGATION*, VOL.53, NO. 1, (JANUARY 2005).

[3]. N. Ammar, T. Bdour, T. Aguili and H. Baudrand, "Investigation of Electromagnetic Scattering by Arbitrarily Shaped Structures Using the Wave Concept Iterative Process Journal of Microwaves," *Optoelectronics and Electromagnetic Applications*, vol.7, NO.1, pp. 26-43, (June 2008).

[4]. N. Ammar, T. Aguili and H. Baudrand, "Modelling of Wave Penetration through Multilayered Cylindrical Aperture Using an Iterative Method Based on Transverse Wave Concept International," *Journal of Microwave and Optical Technology IJMOT*, Vol.4, NO.1, pp.27- 34, (January 2011).

[5]. N. Ammar, T. Aguili, H. Baudrand, B. Sauviac and B. Ounnas, ''Wave Concept Iterative Process method for Electromagnetic or Photonic Jets: Numerical and Experimental Results," *IEEE Trans. Antennas Propag*ation, vol.63, NO.11, (November 2015).

Heuristic Approach to Evaluate the Occurrence of IEMI Sources in Criminal Activities

F. Sabath*, H. Garbe †

* *Bundeswehr Research Institute for Protective Technologies and NBC-Protection (WIS) Munster, Germany, FrankSabath@bundeswehr.org,*

† *Department of Electrical Engineering, Leibniz Universität Hannover, Hannover, Germany, Garbe@geml.uni-hannover.de*

Abstract

This paper discusses a technique which enables the assessment of key parameter of various intentional electromagnetic environments (IEME) for electronic systems, including the likelihood of their occurrence. The technique starts with a categorization of aspects, including non-technical aspects like availability of components, required knowledge and costs. Based on this categorization the likelihood that an offender has access to such an IEMI source is determined by a heuristic approach. In a second assessment step the possibility that a considered IEMI source might occur in the ambient of a given target system is estimated.

Keywords: intentional electromagnetic interference (IEMI); IEMI source; EM environment; likelihood of occurence.

1 Introduction

The initial step of an IEMI risk analysis is the identification and characterization of the threat scenario and the generated EM environment. In a naive attempt one could simply use the maximum threat level of known HPEM sources to specify the IEM environment. As this attempt ignores the likelihood that criminal and terrorist offender obtains access to such sources and the ability of the sources to come close to the system under consideration (target) it will result in an overestimation of the existing threat and consequently in the requirement of an oversized protection.

In [1] we introduced the risk assessment cube, consisting of the aspects threat level, mobility and technological challenge. We indicated that the mobility and the technological challenge enable the determination of the likelihood of occurrence of a given IEM environment. This paper is intended to close this gap by presenting a heuristic technique which enables the assessment of the likelihood that criminal and terrorist offender get access to IEMI sources.

2 Likelihood of Occurrence

The likelihood of occurrence expresses how likely a considered IEMI source will occur during an IEMI attack in the vicinity of the target system. It became common practice for risk assessment to express the likelihood in relation to a small number of categories.

The likelihood of occurrence of a considered IEMI source can be divided into two parts: (1) the likelihood (P_{CU}) that a (criminal or terrorist) offender gets access to it and (2) the likelihood (P_{ACC}) that the source appears in the vicinity of the target system, i.e. it is capable to enter a defined accessibility zone. The first part P_{CU} depends on the technological challenge and is mainly determined by the availability of the system and its components, the required knowledge and the cost.

One approach to map the availability, knowledge and cost categories to categories for the likelihood that an offender gets access to a source of this availability is the category rating by experts. To enable a basic mapping, without expert's involvement, we approximated the experts rating for

- Availability (AV_C):

$$P_A = 11 - 2AV_C \tag{1}$$

- Knowledge (K_D):

$$P_K = 10 - \frac{7}{5} K_D \tag{2}$$

- Cost (C_{EXP}):

$$P_C = 1 + \frac{(5{,}3 - C_{EXP})^2}{2{,}25} \tag{3}$$

The discussed likelihood contributions P_A, P_K, P_{EXP} must be compiled to the demanded likelihood of criminal use (P_{CU}) of a considered IEMI source.

$$P_{CU} = \sqrt[3]{P_A \cdot P_K \cdot P_C} \tag{4}$$

The values determined by (4) are index numbers that enable a ranking of various IEMI sources (or source classes) with regard to its possible use in an IEMI attack [2].

References

[1] Sabath, F.; Garbe, H., "Risk potential of radiated HPEM environments," in 2009 IEEE International Symposium on Electromagnetic Compatibility, pp.226-231, 17-21 Aug. 2009

[2] Sabath, F.; Garbe, H., "Assessing the likelihood of various intentional electromagnetic environments the initial step of an IEMI risk analysis," 2015 IEEE International Symposium on in Electromagnetic Compatibility (EMC), pp.1083-1088, 16-22 Aug. 2015

Analysis of Transient in Buildings Grounding System Using a Modified Image Method

Z. GOUICHICHE, J. ROUDET*, E. CLAVEL*, P.JOYEUX***

**G2ELab, 21 avenue des Martyrs 38031 Grenoble, France*
***Hager Group,* 132, Boulevard d'Europe, 65210 *Obernai, France*

Abstract: This paper treats the analysis of transient in grounding system of building. The modeling is done using a recently proposed hybrid model. The proposed models are frequency dependent. The transient simulation is achieved by means of a fitted model.
Keywords: Grounding system, Modified Image Method, Green function.

1 Introduction

The grounding system is of a major importance in building safety. More and more high frequency equipment are introduced in buildings. The EMC troubles generated need to be taken into account in models. Many works have been done [1,3] to achieve this kind of modeling.
In this paper, we present a modeling method based on equivalent circuit representation. The analytical model, as presented in [1] is based on the integration of the Green function on the conductor's paths, geometrical configuration.
In section 2, we present the proposed model. For this case, details are given for one earth layer. The case of two layers is given in [1].
Then a circuit representation of the calculated model will be detailed taking into account the frequency dependence.
The validation of the model will be presented in section 3.

2 The proposed model

2.1Principle of the analytical expressions

The voltage on a conductor *j* due to a leaking current in *i* is given by V_{ij}^{ϕ} and that due of longitudinal current V_{ij}^{A}.

$$V_{ij}^{\phi} = \int_i \int_j G_{\phi}(r,r') \frac{dI'}{l_j} \frac{dI}{l_i} \qquad V_{ij}^{A} = \int_i \int_j \overline{G_A}(r,r') \vec{dI'} \vec{dI} \qquad (1)$$

Where G_{ϕ} and $\overline{G_A}$ represent the scalar and the vector Green functions. *r* and *r'* are the source and the observation vectors.
In this paper we treat only the impedance due to leaking current in the earth. The impedance due to the longitudinal current is not to be presented in this paper, but introduced for simulation using the partial inductance formulation[2].
For the case of punctual injection in *i* below a uniform earth, Fig. 1, the scalar Green function in (1) is given by:

$$G_{\phi}(r,r') = \frac{1}{4\pi\bar{\sigma}_1}\left(\frac{1}{R} + \frac{\bar{\sigma}_1 - \bar{\sigma}_0}{\bar{\sigma}_1 + \bar{\sigma}_0}\frac{1}{R'}\right) \qquad (2)$$

The first term, called Zm1, represents the direct influence of conductor *i* on *j*. The second term, Zm2, represents the influence of the image of *i,* called *i',* on *j*.

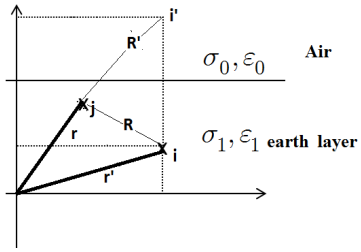

Figure 1 Source and observation configuration

The previous Green function gives the potential for a punctual injection at any point of the earth layer. To calculate (1), it is necessary to assume current I constant along the path of conductor. But since the current in the conductors varies along it, a meshing of conductor's length is achieved. Current density of small segments is considered as constant. The results in a matrix of impedance [Z] describe all self and mutual impedances between segments.
This principle of modelling is generalised to take into account the case of coefficients in two layers earth. Green function for this case taking into account multiple images [1]. The analytical expressions used in the remaining paper are identified for the case of two layers earth model.

2.2 Implementation of the circuit

The aim of the work is to determine the propagation of signals in grounding systems. A time domain simulation, is achieved using an equivalent circuit model.
The equation (2) can be decomposed into a real and imaginary part, giving a *(G//C)* circuit. For the case of Zm1 *G&C* are constant. For the case of Zm2, *G&C* are frequency dependent.
In Fig. 2 & Fig. 3, we present the frequency dependence of the equivalent circuit for the case of two layers earth.

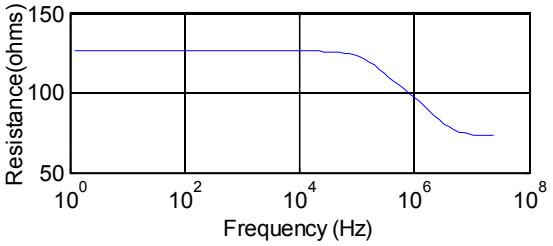

Figure 2 Frequency dependent of equivalent resistance

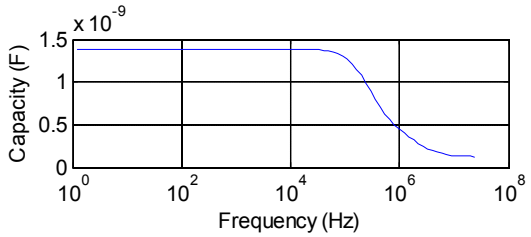

Figure 3 Frequency dependent of equivalent capacity C

We note a large variation according to the frequency domain. For the case of two segments, (i) and (j), in the first layer of a two layers earth, (Fig. 1 with two layers earth), the interpretation of the calculated matrix to circuit representation can be achieved by the circuit in Fig. 4. Where r, L are the parasitic characteristics of conductors [2], and G, C are the characteristics linked to leaked current.

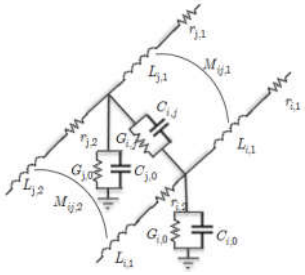

Figure 4 equivalent circuit between two segments.

In order to take into account this frequency dependence during the time simulation, an equivalent circuit based on basic and constant elements to reproduce this frequency behaviour is developed. The usual technique is a vector fitting method VFIT as described in [3].

In the case of a fitted model, all the parallel elements G and C are replaced by the fitted transfer function model. r, L are independent of frequency. The developed model is implemented on spice®.

3 Model validation

3.1. Frequency domain simulation

To validate the presented approach, a comparison of our model is carried out with a so-called full-wave electromagnetic model presented in paper [4].

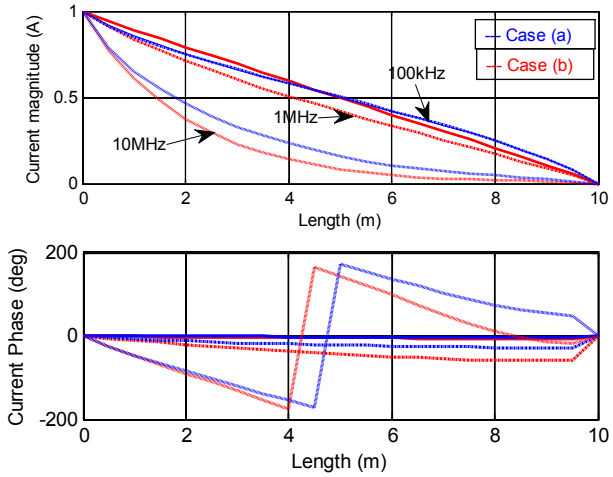

Figure 5 Longitudinal current along 10 m conductor in a two-layers soil.

The numerical example presented in [4] consists of 5mm radius horizontal cooper conductor, 10m length, buried at 0.75m depth in a two-layers earth. The upper layer is of 1m depth and of resistivity of $100\,\Omega m$. Two cases of resistivity for the bottom layer are treated: a) $1000\,\Omega m$, b)$10\,\Omega m$. The permittivity of both soils is of 10 at one end of the conductor. A current of 1A is injected into its one end. The results are presented in Figure 5 for 3 frequencies: 100kHz, 1MHz, 10MHz.

A good agreement between results presented in Figure 5 and those presented in [4] could be established.

3.2. Time domain simulation

A time domain simulation is carried out for simulation of one segment of 1m. The configuration is the same as the previously presented conductor of 10m. Fig. 6, shows the injected current as well as the resulted voltage.

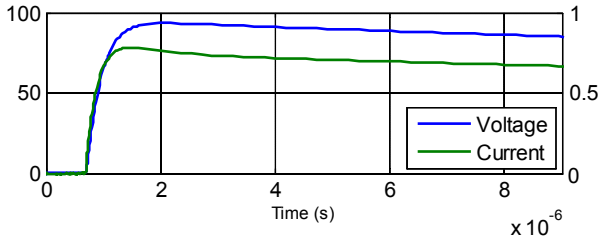

Figure 6 Voltage and current on the segment.

4 Conclusion

In this paper, a modeling of interface impact on earth conductor's impedance is presented. This method based on the use of modified images method to estimate the influence of soils parameter on the frequency dependent of parameters. The simulation in time domain is given for one segment, in future work, this method can be generalized for a conductor with considerable number of segments.

References

[1] T. Kawase, "Calculation of earth resistance for a deep-driven rod in a hulti-layer earth structure," vol. 6, no. 2, pp. 608–614, 1991.

[2] A. E. Ruehli, "Inductance Calculations in a Complex Integrated Circuit Environment," *IBM J. Res. Dev.*, vol. 16, no. 5, pp. 470–481, 1972.

[3] B. Gustavsen and A. Semlyen, "Rational approximation of frequency domain responses by vector fitting," *IEEE Trans. Power Deliv.*, vol. 14, no. 3, pp. 1052–1061, 1999.

[4] V. Arnautovski-Toseva, L. Grcev, and K. El Khamlichi Drissi, "High frequency electromagnetic analysis of horizontal grounding conductor and near-by passive parallel conductor within two-layer soil," *2007 15th Int. Conf. Software, Telecommun. Comput. Networks, SoftCOM 2007*, pp. 111–115, 2007.

Analysis of HPEM Effects on an Automobile by Using Ultra-Wideband Pulse Generators

Jeong-Hyeon Kuk, Kung-Han Yun*, Jongwon Lee*, Jin Soo Choi**

**Agency for Defense Development, Republic of Korea*

Abstract

This paper describes analysis of HPEM (High-Power Electromagnetic) effects on an automobile by using two kinds of ultra-wideband pulse generators. An electric field strength, a repetition rate, and a duration time are changed during tests. Three D-dot sensors to measure the electric fields radiated from the ultra-wideband pulse generator are installed in front of, inside, and behind the automobile, respectively. Malfunctions of automobile are inspected by the shielded camera installed inside the automobile to view a dashboard. From the electric fields measured by the D-dot sensors and the images recorded by the camera, Malfunctions of an automobile are analysed.

Keywords: Electromagnetic Pulse, Frequency Band, Electromagnetic Effect, Ultra Wideband, Automobile.

1 Introduction

HEMP (High-altitude EMP) effects generated from nuclear explosion on crucial civil communications and installations have been researched during the past many years. In recent years, electronic equipment and automobiles with high-tech features and a variety of HPEM pulse generators have been developed, accordingly interest in HPEM effects on those has been increased. In this background, HPEM effects on a universal automobile by using ultra-wideband pulse generators have been experimentally studied and the test results are described in this paper.

2 Experimental Setup

Ultra-wideband pulse generators used in this study are two kinds of parabolic reflector-based integrated antenna-source (IAS) systems with different frequency bands [1, 2]. The setup for the tests is illustrated in Figure 1. As shown in Figure 1, three D-dot sensors to measure the electric fields radiated from the IAS are installed in front of, inside, and behind the automobile.

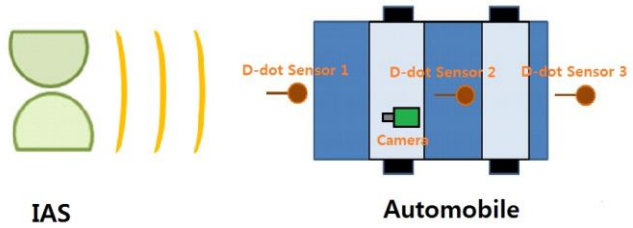

Figure 1. Setup for HPEM effects on an automobile.

The shielded camera inside the automobile is fixed on a tripod to see the dashboard. The electric field strength of EMP incident on the automobile is adjusted by the distance between the IAS and the automobile. The electric field strength at the D-dot sensor 1 is in the range of 10 ~ 160 kV/m. The repetition rate of EMP radiation is set to 1, 40, and 100 Hz and the duration time of radiation is changed from 1 second to 30 seconds.

3 Experimental Results

The representative frequency waveforms measured by the D-dot sensors are shown in Figure 2 and 3. The D-dot sensor 2 in Figure 2 and 3 is located at a distance of 22 m and 30 m from the IAS, respectively. The malfunctions of the dashboard taken with the shielded camera are shown in Figure 4.

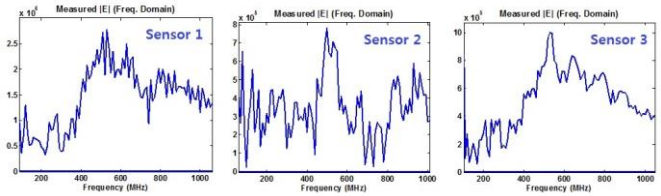

Figure 2. Frequency waveforms in IAS model-1 tests.

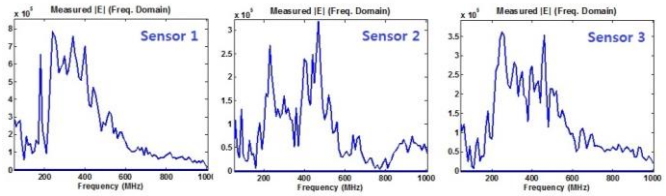

Figure 3. Frequency waveforms in IAS model-2 tests.

Figure 4. Dashboard photographs.

In the Figure 2 and 3, it can be seen that the centre frequencies of IAS model-1 and model-2 are in the range of 500 ~ 800 MHz and 200 ~ 500 MHz, respectively. From the frequency waveforms of the D-dot sensor 2 in Figure 2 and 3, the electromagnetic waves of the range 600 ~ 800 MHz and 300 ~ 400 MHz are greatly reduced. In the tests of HPEM effects on the automobile by using the IAS model-1, the malfunctions of the automobile were not shown on the recording data taken by the camera. However, when the IAS model-2 was used in the tests, various malfunctions of the automobile were observed as shown in Figure 4. From the test

results, the resonant frequency inside the automobile used in the tests seems to be in the range of 300 ~ 400 MHz and the range of 600 ~ 800 MHz is considered to be a multiple of the resonant frequency. The electric field strengths measured by the D-dot sensor 2 were in the range of 27 ~ 36 kV/m when the malfunctions appeared on the dashboard.

4 Conclusion

The tests of HPEM effects on the universal automobile have been carried out by using two kinds of ultra-wideband pulse generators. From the test results, the malfunction of an automobile seems to be occurred well when the centre frequency of an ultra-wideband pulse generator is in accordance with the resonant frequency inside an automobile rather than an electric field strength and a repetition rate are high. If an electric field strength and a repetition rate increase when the centre frequency of a pulse generator accords with the resonant frequency inside an automobile, the malfunction and the physical damage of the automobile will be getting worse and worse.

References

[1] J. Ryu, and J. Lee, "An Integrated Antenna-Source System of Very High Ultra Wide-Band Gain for Radiating High-Power Wide-Band Pulses," *IEEE Transactions on Plasma Science,* **vol.40, no.4,** pp. 1019-1027, Apr. 2012.

[2] J. Ryu, J. Lee, H. Chin, J. Yeom, H. Kim, H. Kwon, S. Han, and J. Choi, "A High Directive Paraboloidal Reflector Antenna for High Far Voltage in an Ultra Wideband Source System," *IEEE Transactions on Plasma Science,* **vol.41, no.8,** pp. 2283-2290, Aug. 2013.

Destruction Rate Analysis of CMOS Logic IC under the Condition of Various Pulse and PRF

J.W. Park, J.J. Bang*, R.W. Kim*, C.S. Huh *, J.S. Choi †, S.M. Hwang††*

**Department of Electrical Engineering, Inha University, Incheon, Korea, ginook83@naver.com*
†Agency for Defence Development, Dajeon , Korea
††Hanhwa Corporation, Gumi, Korea

Abstract

The logic ICs based on the CMOS are becoming miniaturization, low power consumption and high integration due to advances in technology. However, these factors have very weak characteristics under the Electromagnetic environment. In this paper, the vulnerability of the logic IC (Integrated Circuit) in accordance with pulse current injection and PRF (Pulse repetition frequency) was estimated by the Pulse injection test. As a result, device destruction was more influenced by the PRF in low voltages. However, as the voltage increase, device destruction is more influenced by the pulse voltage.

Keywords: EM environment, Logic IC, Pulse Injection, PFR.

1 Introduction

Modern society has quickly changed because of the development of the semiconductor devices. In particular, logic IC based on the CMOS is essential in electronic systems requiring logical operations. Logic ICs that have recently been released are becoming miniaturization, low-power consumption and high integration. In other hands, these factors make IC more vulnerable to the EM environment. Therefore, this study confirms the destruction characteristic of the Logic IC caused by the injection pulse and PRF. Furthermore this study analyzes which factor severely affects ICs. In addition, by using the DFR (Destruction failure Rate) curve, it was quantified on the vulnerability of the Logic IC in EM environment. [1]

2 Test setup

In the test, CMOS NAND gate IC was used. Test setup is shown in Fig. 1. 0V was applied to the input 1 pin and input 2 pin of IC, and consequently output was on. Pulse injection method was to inject two kinds of pulse into input 1 pin with three kinds of PRF, which was implemented by 60 times, respectively. Also using the oscilloscope, the voltage fluctuation of the input 1 pin and output 1 pin was observed. If output was off during pulse injection, reset IC and operate it. If IC did not resume normal operation, it was considered device destruction. [1-2]

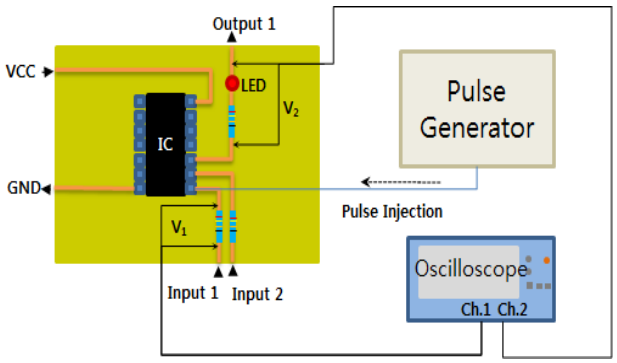

Figure 1 Test configuration

Table 1 Injected Pulse

	Pulse Repetition frequency	Pulse width(ns)	Rise time(ns)
Pulse 1	1[Hz] 10[Hz] 100[Hz]	1.1	0.75
Pulse 2	1[Hz] 10[Hz] 100[Hz]	1.2	0.75

3 Result

The DFR curve of NAND gate by pulse 1 is shown in Fig 2. After pulse with PRF of 1[Hz] and 10[Hz] is injected at 1100 [V] 11 to 12 times, device is destroyed. On the other hands, device destruction occurs after pulse with PRF of 100[Hz] is injected 4 to 5 times at 1100[V]. However, as the voltage of injection pulse increase, the number of pulse is being similar

to regardless of PRF of pulse until the device is destroyed. If the voltage of injection pulse is greater than 1125[V], device destruction occur at the same number of pulse. Therefore, when pulse voltage is low, PRF of pulse influence on device destruction.

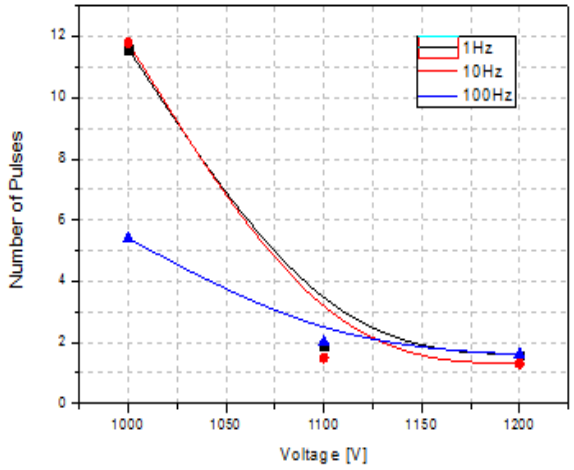

Figure 2 DFR curve by pulse 1 injection

DFR curve of NAND gate by the pulse 2 is shown in Fig 3. In case of pulse 2, device destruction occurred at lower voltage than that of pulse 1. If the injection pulse voltage was 1000[V], the number of pulse 2 that make device destroyed is one third of the number of pulse 1. Consequently, if the energy of injection pulse is higher than the other (pulse width is wider than the other), device destruction voltage is more affected by voltage than PRF.

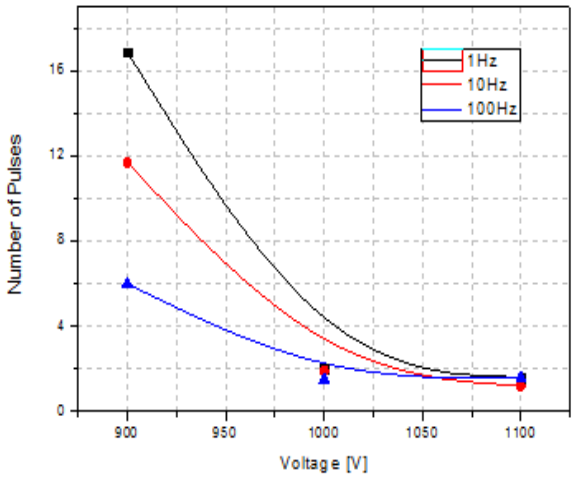

Figure 3 DFR curve by pulse 2 injection

References

[1] Hwang, S.M., J.I. Hong, S.M. Han, C.S. Huh, and J.S. Choi, "Susceptibility and coupled waveform of microcontroller devioce by impact of UWB-HEMP", *Journal of Electromagnetic Waves and Applications*, **vol. 24**, no.8-9, 1059-1067, 2010

[2] M. Camp, H. Garbe, D. Nitsch, "Influence of the Technology on the Destruction Effects of Semiconductors by Impact of EMP and UWB Pulses", *2002 IEEE International Symposium on Electromagnetic Compatibility*, **Vol. 1**, pp. 87-92, 2002.

Analysis of Mobile Targets in the Presence of High-Power Electromagnetic Energy using Multiscale,Multiphysics Techniques

Thomas J. Arcuri, Irina Kasperovich, Andrew L. Drozd

ANDRO Computational Solutions, LLC. Rome NY, 13440. United States

Abstract

This paper describes multiscale and multiphysics techniques for performing analyses of complex structures subjected to high-powered electromagnetic (HPEM) interference. We focus on recent advances in Uniform Theory of Diffraction (UTD) codes using facet-based techniques for antenna analysis that are hybridized with finite difference and partial element equivalent circuit methods, which have greatly improved the computational efficiency.

Keywords: Electromagnetic Effects, High Power Microwaves, UTD, facet models.

1 Introduction

Modern aircraft, ships, and land vehicles employ many on-board antennas and sensors. As these vehicles become more dependent on these on-board sensors and transmitters the task of mitigating electromagnetic vulnerability (EMV) becomes essential. EMV analysis is used to verify that various components on a given platform can tolerate external interference sources. This problem is exacerbated in the presence of high-power fields that add further requirements to the analysis tool and approach.

2 HPEM Analysis

The *E³Expert* EMC analysis toolkit has recently integrated the uCAST (UTD Complex Antenna Simulation Toolkit) engine (developed by Applied EM) to augment its multiscale and multiphysics capability for performing exterior EM coupling analysis, specifically in the high-power EM regime. Other suitable tools are being used to determine accurate energy penetration of the exterior structures, and interior propagation down to a component/device level using Finite-Difference Time-Domain (FDTD) techniques. FDTD solutions are then employed for the energy penetration domain, while innovative statistical approaches can be implemented for cavity problems [1]. Domain decomposition principles are used to partition the problem such that individual tools can address a subset of the problem for which they are best suited [2]. For circuit level analysis the PEEC tool can be used to generate a comprehensive fault tree.

*E³Exper*t's innovation is that it pulls these various techniques into a single tool to perform a comprehensive susceptibility analysis. Rather than perform disparate analysis and manually interfacing the output from one tool to another, *E³Expert* integrates these techniques under a user-friendly interface and provides expert system guidance to refine computational models.

3 High-Power EM Vulnerability

E³Expert has traditionally been employed in relatively low-frequency regimes with interfering emitters mostly comprised of standard RF equipment and other environmental effects. *HPEM-Expert* is a new version of the tool that is designed to handle the high-power EM fields that are characteristics of directed energy interferers. The uCAST tool's high-frequency ray tracing capabilities can be directly applied to the external coupling problems inherent in this regime.

4 Mobile Platforms

The computational efficiency provided by the aforementioned tools allows the implementation of a time-step based approach to moving targets. By taking full advantage of the parallel processing capabilities inherent in the uCAST engine, *E³Expert* can quickly calculate antenna coupling as a target moves relative to the source(s). The calculated rays can then be drawn to show how the incident RF coupling changes as the target moves over time to study both exterior as well as interior failure effects.

References

[1] V. Raamani, J.C. West, and C.F. Bunting. "Measurement and Simulation of the Induced Current on a Wire Using S-Parameter Method". *IEEE Trans. Electromagn. Compat.*, vol. 56, no. 2, pp. 382-390 2007.

[2] Xiaochuan Wang, Zhen Peng, Kheng-Hwee Lim, J.F. Lee. "Multisolver Domain Decomposition Method for Modeling EMC Effects of Multiple Antennas on Large Air Platform". *IEEE Trans. Electromagn. Compat.*, vol. 54, no. 2, pp. 375-388 2012.

Antennas and Wireless Device Interference Simulations within a Vehicle

D.Edgar[1], O.Donadio,[1]A.Moknache[2] , F. Bocquet [3]

[1]ANSYS UK, 97 Milton Park Abingdon, OX14 4RW, david.edgar@ansys.com
[2]ANSYS France SAS, 15, place Georges Pompidou Montigny Le Bretonneux, amazir.moknache@ansys.com
[3]ANSYS France SAS, 15, place Georges Pompidou Montigny Le Bretonneux, frederic.bocquet@ansys.com

Abstract

For vehicles, including electric car, higher powers, voltages and the use of fast switching converters can lead to perturbation of the antennas, and other wired or wireless systems. In this publication, it is proposed to demonstrate the relevance of simulation to predict the impacts. This article is structured in three parts: Firstly, an illustrative example of the problem and validating the methods put in place: disruption of the AM/FM antennas by signals from small or large electric motors with their control/command parts and wiring. Secondly, the integration of wireless automotive equipment (example: remote keyless entry device) or personal ones (example: mobile phone) in the cockpit and in the presence of a human body model. Finally, two types of analysis of the results: a health component with calculations of SAR and another one for the diagnosis and/or design with an assessment of interference using a dedicated system tool.

Keywords: EMC, WIRELESS, SAR, CONNECTED OBJECTS, VEHICLE.

1 Simulation of the AM/FM antenna interference due to the power electronics of the car

The FM antenna in the rear window of the vehicle receives a signal from a distant radio station. A wiper motor, or the power converter emits spurious signals due to fast switching transient currents through cables, which radiate and couple to the AM/FM antennas, disrupting the received signals. The vehicle environment is simulated with a finite element method (FEM) or combined integral equation/finite element method (IE or FEBI). The wiring is taken into account in the FEM tool and will eventually be done by an approximate method like Transmission Line Method (TLM). A model of the transmitting and receiving circuitry of the radio will be made by a circuit/system co-simulation (see Fig. 1; Fig.2 and Fig.3). Converter and control-command part will be simulated with a system tool for power electronics and eventually the electric motor will be taken into account with a quasi-static time domain FEM model to include the 3D effects of non-linear materials and the rotation of the rotor on the outputs in voltage-current in the coils that are the sources of disturbance of the RF case. All of these methods are linked and form a complex system simulation, the outputs can be response curves or E-H fields (and derived data) in 2D or 3D.

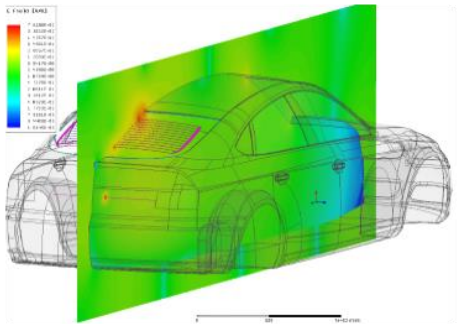

Fig. 1. Vehicle, Antenna and Wiring.

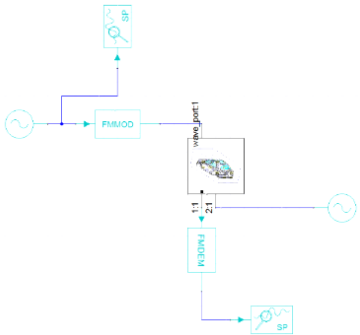

Figure 2. RF System including 3D simulation.

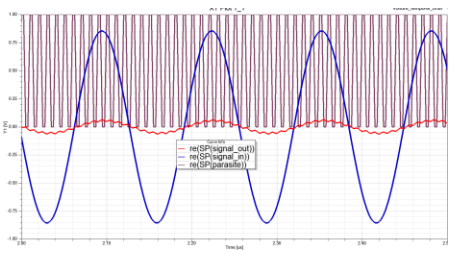

Figure 3. Interference results on FM.

A first test case has been made, the work will be completed by including signals, a realistic system (baseband) with a control / command and more complex wiring model.

2 Consideration of wireless objects in the presence of a human body

To the previous case, there will be added some electronic wireless equipment such as a handset, badge, tyre pressure sensor or a DVD player in the head support of seats. Also, a human body will be present in the cockpit. It will be a phantom: human body with a permittivity defined in the standards (see Fig. 4).

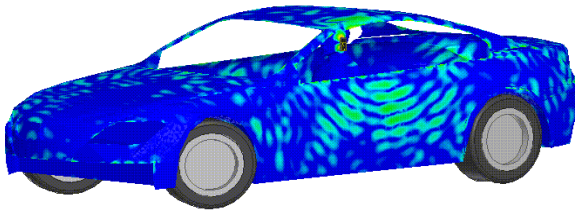

Figure 4. E fields from the mobile phone.

3 Health analysis and Design/Diagnosis aid

3.1 SAR simulation

For this analysis, the formula (1) is the one recommended [2] when an FEM method is used. A person (phantom) in the vehicle is subject to various electromagnetic emissions (see Fig.5).

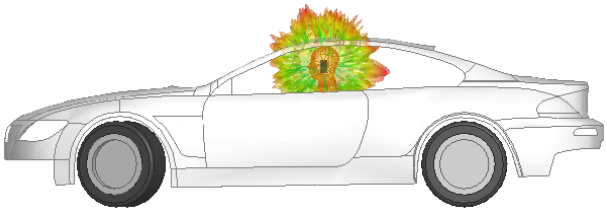

Figure 5. Gain plot of the phone in the car with phantom.

$$DAS : \sigma * E^2/(2\rho) \qquad (1)$$

Where

σ = conductivity defined as: $\sigma_{bulk}+\omega\varepsilon_0\varepsilon_r tg\delta$

ρ = mass density of the dielectric material in volume mass unit.

3.2 System analysis and interferences simulations

Using a system simulator, the interference calculations will be made by considering all intentional and unintentional sources in the cockpit. The results will give the possible interferences with identification of interference sources and the possibility of rapid correction incorporating a relevant filter (see Fig. 6).

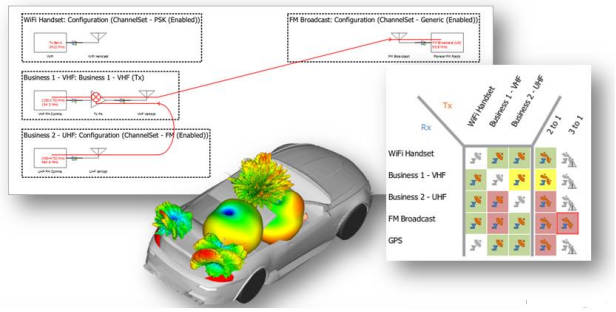

Figure 6. Result examples.

4 Conclusion

4.1 Simulation flow

The coupling of simulations like 3D FEM using system tools enables modelling of complex simulation cases of various wireless connected electronic devices, disrupted by emissions from vehicle power electronics over an ever increasing frequency range.

4.2 Health and Design/diagnosis Analysis

For 3D calculations performed with a human body model (phantom type), two types of analysis are carried out:
1/ Health: SAR calculation to see if the levels are acceptable according to the relevant standards. 2/ Diagnosis and design assistance with system analysis allowing identification of the disturbing and disturbed devices, including applying suitable correction to mitigate the interference risk for the device(s).

References

[1] J.F. Mologni, M. Kopp, F. Bocquet & A. Colin, *"Advanced Techniques for Efficient Automotive EMC/EMI Simulations"*, IEEE Proceedings, Automotive EMC, EMC Europe, Gothenburg, 2014

[2] IEEE P1528.4™/D1.0 Recommended Practice for Determining the Peak Spatial Average Specific Absorption Rate (SAR) Devices, 30 MHz - 6 GHz: Requirements for Using the Finite-Element Method for SAR Calculations, specifically involving Vehicle Mounted Antennas and Personal Wireless Devices.

Study of Transient Disturbance on Secondary Cable due to VFTO

Zhang Weidong

Beijing Key Lab of High Voltage and Electromagnetic Compatibility,
North China Electric Power University, Beijing 102206, China. zwd@ncepu.edu.cn

Abstract

In gas insulated substation (GIS), when the disconnect switcher is operated, the electric arc breakdown and reigniting between switchgear contacts will produce very fast transient overvoltage (VFTO). VFTO is characterized by high peak value, short rise time and wide frequency range. The transient electromagnetic field that generated by VFTO would coupling on the secondary cable. This paper gives introduction for our measurement and simulation of the disturbance on secondary cable due to the VFTO.

Keywords: gas insulated substation, very fast transient overvoltage, disturbance, secondary cable.

1 Introduction

During the past ten years, the ultra-high voltage (UHV) power transmission technology has been developed rapidly in China. In 2009, the first 1000kV UHV power transmission system was built up and start to work. Then, more and more UHV GIS were set up in China. When GIS disconnect switcher is operated, the electric arc breakdown and reigniting between switchgear contacts will produce VFTO characterized by high peak value, short rise time and wide frequency range. The main problem associated with the VFTO are not only the possible dielectric breakdown in primary system, but also the possible failure of electronic control circuits in secondary system because of electromagnetic interference due to VFTO. In order to research on the VFTO and its effects, a 1:1 real 1000kV GIS test platform was set up in Wuhan UHV Test Base in China 2010. Using the test platform, we obtained thousands of measured disturbance waveforms on the secondary cables. Meanwhile we tried to study the coupling mechanism of the VFTO to cable base on simulation.

2 Measurement

In GIS, the secondary cable is a kind of multi-line cable with shielding. The cables connect the two sides: sensors in switch yard (SY) and the secondary equipment in the control room (CR) usually. In order to study how the disturbance depending on the grounding style of the cable's shielding, we setup four grounding styles 1) both sides grounding; 2) only CR side grounding; 3) only SY side grounding; 4) both sides non-grounding. A test system was developed to measure the disturbances in situ. From thousands measured waveforms, the characteristic were analysed as in Table 1 [1]. The results show that the lowest disturbance is with grounding style 2).

Table 1: Summary of measurement results.

Grounding style	DS operations	Max peak voltage/V	Pulse duration/μs
Both sides grounding	closing	394.9	9.2
	opening	295.8	9.4
Only CR side grounding	closing	295.3	9.8
	opening	203.1	8.9
Only SY side grounding	closing	4557.0	68.7
	opening	4387.0	66.4
Both sides non-grounding	closing	4617.0	61.1
	opening	4472.0	53.2

3 Simulation

The frequency domain model of the shielded cable that combining transmission line method with field-to-line theory is established. The model is divided into three transmission line systems based on loss telegraph equations. One of simulated result is shown in Fig.1

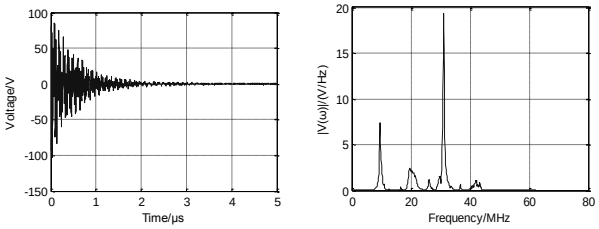

Figure 1. Simulated waveform and spectrum.

4 Conclusion

Base on more than one thousand measured waveforms, the characteristic of the disturbances on the secondary cable due to VFTO was analysed. The simulated result show good agreement with measured waveform.

Acknowledgements

Project Supported by the National Basic Research Program of China (2011CB209405).

References

[1] Zhang Weidong, Chen Peilong, et al.. "Measurement and Simulation of Disturbance Voltage Generated by VFTO in UHV GIS Substation on the Secondary Cables", *Proceedings of CSEE*, **volume 33**, pp. 187-196, (2013).

Periodic structures for novel electromagnetic sources manufactured by 3D printing

A. R. Phipps, A. J. MacLachlan*, C. W. Robertson*, I. V. Konoplev†, A. D. R. Phelps*, and A. W. Cross**

*Department of Physics, SUPA, University of Strathclyde, Glasgow, G4 0NG, Scotland, UK

†JAI, Department of Physics, University of Oxford, Oxford, OX1 3RH, England, UK

a.d.r.phelps@strath.ac.uk

Abstract

In the field of 'transformational electromagnetics' there is a requirement to create intricate structures to control and manipulate electromagnetic fields. The specific motivation for the work reported here is to create improved electron-beam-driven, vacuum electronic mm-wave and sub-THz sources by exploiting dispersion engineering. The successful manufacture is reported of electrically conducting cylindrical structures with a two dimensional periodic perturbation applied to the inner surface of the cylinder. Although such structures can be manufactured by other techniques, additive manufacturing has proven to be quick, reliable and cost-effective. This research is facilitating the realization of novel mm-wave and sub-THz coherent sources.

Keywords: Periodic structures, 3D printing, transformational electromagnetics.

1 Introduction

Additive manufacture [1] also known as "3D printing" is becoming more widely available as a method for manufacturing rapidly and cost-effectively small quantities of intricate structures. Such structures are of great interest because the application of smart dispersion engineering and transformational electromagnetics is having a positive impact on research leading to improved high-power coherent sources [2-4]. Two dimensional periodic surface lattices (PSLs) [5]. can be created by manufacturing shallow periodic perturbations on the inner surface of a hollow electrically conducting cylinder. Such 2D PSLs can be used for several applications exploiting different physical phenomena, [2-8]. A dispersion relation describing the coupling of the volume and surface fields inside a 2D PSL of cylindrical topology was derived by Konoplev et al. [7]. Under certain conditions, when driven by a suitable electron beam this structure can support a Cherenkov instability that provides a coherent source of electromagnetic radiation. These cylindrical 2D PSLs show potential for use in electron-beam-driven high power, coherent sources [5,7,8].

The cylindrical PSL structures need to be compatible with vacuum conditions and the use of energetic electron beams, while also providing the required boundary conditions for the electromagnetic fields. Manufacturing the cylindrical PSLs out of a suitable metal usually provides a good vacuum envelope and the electrical conductivity allows electrical charges impacting on the surfaces to be conducted away. A reasonably high thermal conductivity coefficient is another desirable property for PSLs intended for use in high power sources.

In our earlier years of research on high power mm-wave sources the technique employed to manufacture the cylindrical PSLs was to mill sinusoidal perturbations on the outer wall of an aluminium former and then to electrodeposit copper directly onto the surface [8,9]. The aluminium was then dissolved in a strong alkaline solution, leaving the copper PSL with the perturbations on the inner surface.

2 Results

The 3D printing technology used has reasonably high resolution, producing objects that have resolutions on the ±16 micron scale. The dimensional errors achievable with 3D printing are projected to decrease over time as the technology develops. Fig. 1(a) shows a photograph of a cylindrical silver-chromium alloy 2D periodic surface lattice, cast using a primary mandrel manufactured by 3D printing. The perturbations on the inner surface of the metallic cylinder are sinusoidal, whereas the virtual schematic of the mandrel seen in Fig. 1(b) just to indicate the dimensions has rectangular perturbations.

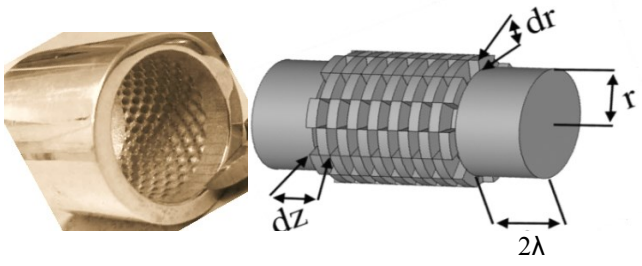

(a) **(b)**

Figure 1. (a) Cylindrical silver-chromium alloy 2D periodic surface lattice manufactured for a Cherenkov coherent source (b) Cylindrical CAD virtual mandrel that when 3D printed provided a mold for casting the cylindrical 2D PSL.

This cylindrical metallic 2D PSL is designed for a Cherenkov source to operate in the W-band (75-110 GHz) and the values of the parameters shown in Fig. 1 are r = 10.0mm, dz = 3.0mm, dr = 0.40mm and $2r/\lambda \sim 7$.

Fig. 2 shows measurements, made using a VNA, of the electromagnetic properties of this W-band cylindrical PSL and for comparison two simulations, made using CST Microwave Studio. The results show the potential of this structure for creating a novel coherent source when excited by a suitable electron beam [10-14].

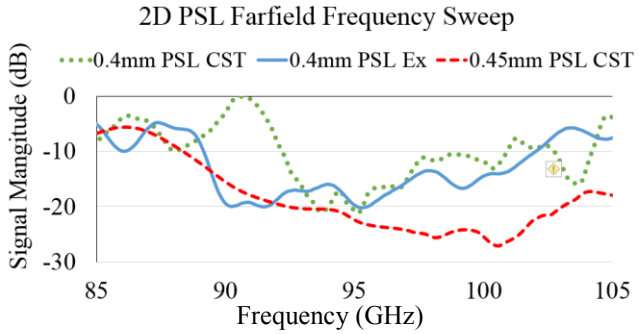

Figure 2. The on-axis frequency sweep for the 0.1 THz 2D PSL. The solid line represents the experimental measurements. The other two lines represent simulations of the structure, one with a perturbation amplitude of 0.4 mm (dotted line) and one with 0.45 mm (dashed line).

This 3D-printing method of manufacture has potential for use in a variety of dispersive structures and complex components [15,16] of growing significance in high power electromagnetics.

3 Summary

Cylindrical 2D PSL structures have been successfully manufactured using 3D printing to create the primary mold. This primary mold was then used to cast successfully the metallic cylindrical 2D PSL. This work is ongoing and it is intended to extend the research to higher frequencies.

Acknowledgements

Alan R. Phipps and Amy J. MacLachlan thank the EPSRC for supporting their postgraduate studentships. D. Barclay provided valuable technical assistance.

References

[1] I. Gibson, D. Rosen and B. Stucker, "Additive Manufacturing Technologies: 3D Printing, Rapid Prototyping, and Direct Digital Manufacturing", 2nd Edition, Springer, New York, USA, (2015).

[2] N. S. Ginzburg, et al., "Theory of free-electron maser with two-dimensional feedback driven by an annular electron beam", *J. Appl. Phys*., **92**, pp. 1619-1629, (2002).

[3] N.S. Ginzburg, et al., "The use of a hybrid resonator consisting of one dimensional and two-dimensional Bragg reflectors for generation of spatially coherent radiation in a co-axial free-electron laser", *Phys. Plasmas*, **9**, pp. 2798-2802, (2002).

[4] I. V. Konoplev, et al., "Experimental and theoretical studies of a coaxial free-electron maser based on two-dimensional distributed feedback", *Phys. Rev. E*, **76**, 056406, (2007).

[5] I. V. Konoplev, et al., "Surface wave Cherenkov maser based on a periodic lattice", *Appl. Phys. Lett*., **96**, 261101, (2010).

[6] A.W. Cross, et al., "Studies of surface two-dimensional photonic band-gap structures", *J. Appl. Phys*., **93**, pp. 2208-2218, (2003).

[7] I. V. Konoplev, et al., "Cylindrical, periodic surface lattice – Theory, dispersion analysis and experiment", *Appl. Phys. Lett*., **101**, 121111, (2012).

[8] I. V. Konoplev, et al., "Cylindrical periodic surface lattice as a metadielectric: concept of a surface-field Cherenkov source of coherent radiation", *Phys. Rev. A*, **84**, 013826, (2011).

[9] I. V. Konoplev, et al., "Surface field excitation by an obliquely incident wave", *Appl. Phys. Lett*., **102**, 141106, (2013).

[10] I. V. Konoplev, et al., "High-current oversized annular electron beam formation for high-power microwave research", *Appl. Phys. Lett.,* **89**, 171503, (2006).

[11] H. Yin, et al., "Pseudospark-based electron beam and Cherenkov maser experiments", *Phys. Plasmas*, **7**, pp. 5195-5205, (2000).

[12] A. W. Cross, et al., "Generation and application of pseudospark-sourced electron beams", *J. Phys. D: Appl. Phys*., **40**, pp. 1953-1956, (2007).

[13] H. Yin, A. W. Cross, et al., "Millimeter wave generation from a pseudospark-sourced electron beam", *Phys. Plasmas*, **16**, 063105, (2009).

[14] W. He, L. Zhang, et al., "Generation of broadband terahertz radiation using a backward wave oscillator and pseudospark-sourced electron beam", *Appl. Phys. Lett.,* **107**, 133501, (2015).

[15] D. Shiffler, J. Luginsland, et al., "A Cerenkov-like maser based on a metamaterial structure", *IEEE Trans. Plasma Sci.*, **38**, pp. 1462-1465, (2010).

[16] D. Shiffler, R. Seviour, et al., "Study of split-ring resonators as a metamaterial for high-power microwave power transmission and the role of defects", *IEEE Trans. Plasma Sci.,* **41**, pp. 1679-1685, (2013).

Development of Non Linear Transmission Lines for HPEM Applications

Dr Nigel Seddon MBE*

**MBDA UK Ltd, UK, nigel.seddon@mbda-systems.com*

Abstract

This paper reviews the operating principles of Non Linear Transmission Lines (NLTLs) and highlights their suitability for HPEM transmitter applications. Several types of NLTL are discussed, including nonlinear dielectric and nonlinear magnetic circuits, each with their particular pros and cons. Generally, NLTL technology lends itself to operation in arrays which can produce very large Effective Radiated Power (ERP) when coupled to a suitable antenna. Also, NLTLs allow for some electronic control of the phase and frequency of each element in an array; thus providing electronic beam steering and frequency agility from an HPEM source. Examples of high power NLTL phased arrays are described.

Keywords: Non Linear Transmission Line, NLTL.

1 Introduction

From the late 1950's to early 1970's NLTLs were extensively investigated, primarily in the Former Soviet Union, to create fast rising voltage and current waveforms (electromagnetic shock waves), but rarely to produce oscillatory signals. Over the past 20 years several types of NLTL have been developed specifically to produce powerful RF and microwave signals for HPEM applications. These include devices incorporating nonlinear magnetic, dielectric and semiconductor materials. Although these devices can operate over a broad range of power levels (<1MW to >500MW) and frequencies (10'sMHz to several GHz) they share fundamental characteristics that define their use in HPEM transmitters.

2 NLTL Characteristics

NLTLs are almost exclusively pulse modulation devices; they require a high power electrical input pulse and produce an RF/microwave signal by modulating the amplitude of this input pulse as it propagates along the transmission line. RF signal formation is the result of a complex interaction between the electrical pulse and the nonlinear and dispersive properties of the transmission line. The key to producing a useful NLTL is to select materials with the most appropriate nonlinear characteristics and to incorporate these into the design of a dispersive transmission line in order to give the required RF output pulse.

Nonlinear materials including saturating magnetic materials, gyromagnetic materials, nonlinear dielectric materials and semiconductor materials and devices have been used in high power NLTLs. Dispersion in these circuits has been provided by low pass LC ladder networks, modified LC ladder networks and by gyromagnetic behaviour of materials. Options for NLTL designs will be reviewed, highlighting their typical operating parameters and the advantages and disadvantages of each approach. These will include high power soliton generation in nonlinear dielectric transmission lines, quasi monochromatic RF generation in nonlinear magnetic transmission lines and very high power microwave generation using gyromagnetic transmission lines.

Irrespective of the specific nonlinear and dispersive properties, NLTLs are solid state devices and are capable of producing RF signals with very good phase and frequency stability. Consequently they are suitable for use in phased arrays, provided that each NLTL can be driven with a stable and repeatable input pulse. One of the most attractive features of NLTL devices is the possibility to adjust the precise timing (phase) of its output signal by varying the nonlinearity of the device with an external control signal. This offers the opportunity to create an electronically controlled phased array, and for some types of NLTL the opportunity to steer a very high power RF beam on a pulse to pulse basis.

3 Architectures for NLTL Phased Arrays

As the NLTL is a modulator, which requires a well-controlled input pulse, the development of an electronically steered, high power NLTL system depends not only on the design of the NLTL but is critically dependent on the performance of the pulsed power sources that are used to create the electrical input pulses and also on the selection of a suitable antenna.

Assuming identical NLTL devices in an array, each should be driven by an identical electrical input pulse in order to ensure phase and frequency control of the array. It is the generation of large numbers of identical input pulses that usually limits the size (and output power) of an NLTL transmitter array. Three approaches to input pulse generation for NLTL arrays will be described and compared, these are

a. Very low jitter pulse generators that allow each NLTL to be driven by a separate pulse generator.

b. A single large pulse generator whose output is split to provide an input to each NLTL in the array.

c. A mixing scheme in which a number of sources produce high voltage pulses outputs with similar, but not identical characteristics. The various pulses are combined order to produce a single electrical pulse which is the split in order to produce a number of identical output pulses

The second and third of these schemes have been used as the basis for developing very high power NLTL transmitters and examples of these high power array systems will be described.

The presentation will conclude with a discussion on future development of NLTL technology and prospects for HPEM transmitters based on this technology.

History of High-Power Electromagnetics (HPEM) with Illustrative Examples of HPEM Systems

Dr. D. V. Giri
Pro-Tech, 11-C Orchard Court, Alamo, CA 94507, USA
Dept. of ECE, Univ. of New Mexico, Albuquerque, NM 87130, USA
E-mail: Giri@DVGiri.com: URL: www.dvgiri.com

Abstract

In this presentation, we will discuss some illustrative examples of HPEM systems along with a historical sketch of HPEM (see Figure below). The first atomic test took place in Alamogordo, NM, USA on July 16, 1945. Nobel laureate physicist Enrico Fermi tried to calculate the possible electromagnetic fields that would be produced from the nuclear explosion. This can be considered as the birth of the study of HPEM.

Keywords**:** HPEM, NEMP, HPM, Hyper band

1. Introduction

HPEM is a comprehensive acronym to include EM waveforms such as natural lightning, nuclear electromagnetic pulse (NEMP), High-Power Microwaves (HPM) etc. [D. V. Giri and F. M. Tesche, "Classification of Intentional Electromagnetic Environments (IEME)", *IEEE Trans. EMC*, Volume 46, Aug. 2004, pp. 322-328]. Dr. Baum played an important role in the evolution of HPEM [C. E. Baum, "Reminiscences of High-Power Electromagnetics", *IEEE Trans. EMC*, Volume 49, May 2007, pp. 211-218]. The major Milestones of HPEM, especially in the last 5 decades can be summarized as shown in Figure 1.

The first decade of the 21st century has seen real and anecdotal evidence of RF terrorism and IEMI. HPEM source/antenna systems are being developed in many nations and are also becoming commercially available. HPEM systems have been classified into four categories based on percentage bandwidth (pbw). They are a) narrow band (pbw < 1.01, b) mesoband (1.01 < pbw < 100), c) ultra-moderate band (100 <pbw < 163.64) and d) hyper band (163.64 < pbw ≤ 200). This classification is driven by technological developments. We will present example systems in each of the four categories along with their capabilities.

Developments in pulse-power technologies driving conventional and newer RF devices will lead to improved and more powerful source/ antenna systems. An EMP attack is an example of RF terrorism by rogue countries and non-state actors, and the national infrastructure can be at risk. Infrastructure is a hyper system or a system of systems such as electric power, telecommunications, banking & finance, energy, transportation, food, water, emergency, space, and Government. In addition, cyber threats from hostile governments, terrorist groups and disgruntled employees are on the increase as well. It is prudent for civilized societies to asses such threats and take pro-active and precautionary actions.

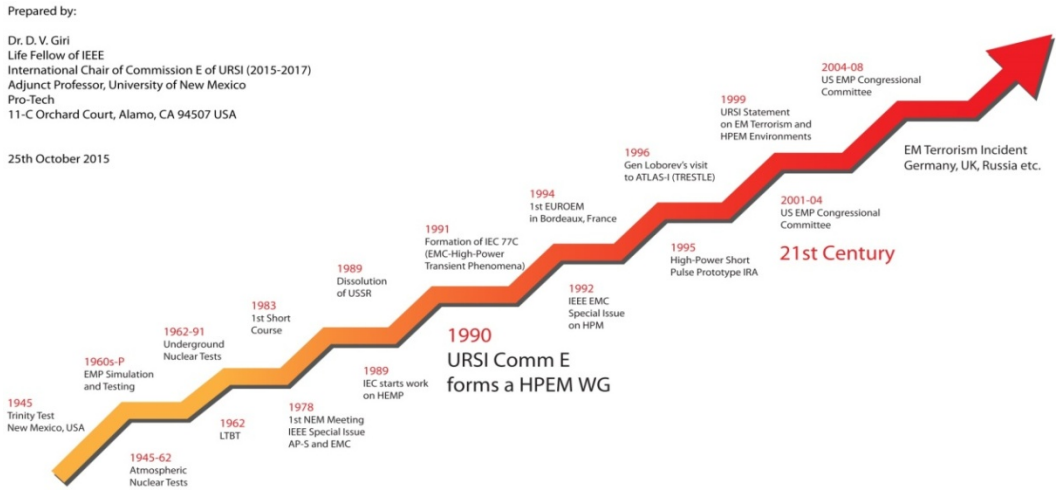

Figure 1. Graphical representation of the major milestones of HPEM

HPEM Activities in Switzerland Over the Last 50 Years

M Nyffeler*, D.V.Giri†

**armasuisse Science and Technology, Switzerland, markus.nyffeler@armasuisse.ch*
†Dept of ECE, University of New Mexico and Pro-Tech, Alamo, CA, USA , Giri@DVGiri.com

Abstract

The first paper about EMP protection in Switzerland was written in 1966 at the research institute for military construction technology (FMB) at ETH Zurich. In 1978 the EMP simulator GESIBAN was set into operation at the NBC laboratory in Spiez and used for the first test. Theoretical and practical experience evolved over the past 50 years up to today's sources and protection measures. About 400 test were performed with a total of about 20 people during this period. The knowledge grew with support of recognized experts as well as with the continuous collaborations with international organizations and the two technical universities EPFL and ETHZ who organized the EMC Zurich over years.

Keywords: armasuisse, HPE-laboratory, VERIFY

1 Introduction

EMP activities in Switzerland started in the late sixties at ETHZ by giving courses about this new threat for future army leaders. These technical universities mainly performed theoretical studies whereas the governmental organizations for public protection and procurement of army goods preferred to verify the knowledge with practical experiments and tests of buildings and systems using their simulators.

Both interest groups have always been small which might be the reason for having high flexibility in forming international networks and collaborations with private and public organizations who helped to become a known and valuable part of the HPEM community.

2 50 years of HPEM activities in Switzerland

Swiss army activities have been restricted to defence since Switzerland has been founded. Therefore EMP as a threat was always recognized as high-altitude EMP only because of the overall size of the country and the fact of having more serious problems with a surface burst than electromagnetic disturbances. Nevertheless ETH people visited public and private organizations in USA to get an idea whether the self-developed protection measures for example the so called "Swiss panel" (overlapped metal sheets) for shielded rooms are sufficient. US specialists rated them as insufficient and indicated their own protection measures against surface burst.

Back in Switzerland the new knowledge was used to write mitigation notes. Different commissions with representatives from government and economy were established to discuss these issues. Critical infrastructure including communication, banks, transportation systems, energy production, and hospitals etc., took the risk of EMP into account. The EMP simulator GESIBAN of HPE-lab was replaced by HEISS and plans for a HPD simulator raised for the EMP-test of Tiger F-5 airplane (Fig. 1). This was the most complex and impressive EMP test which was ever performed by the HPE-lab. After many pre-tests, the airplane was excited with tens of pulses in real mission condition including pilot and hidden landing gear.

Figure 1. EMP test of Swiss Tiger F-5 in MEMPS facility

Existing and new facilities of the army were upgraded or well protected against this electromagnetic threat.
With the fall of the Berlin wall and the end of the cold war in 1989, most of the Swiss commissions disappeared and the budgetary constraints started. At the same time the privatisation of some of the government institutions became popular. Therefore many organisations and companies reduced their EM- risk against more short time profit and the personnel knowledgeable in EMP looked for other jobs.

For tests of bigger mobile systems with vertical polarized E-fields, EMP simulator VEPES was procured from Israel in early nineties. This was the time when knowledge of non-nuclear sources reached Switzerland. With support of HPEM specialists [1] our lab built some self-made IEMI sources and used them to get experience with their effects. **V**ertical **E**mp **R**adiating **I**ndoor **F**acilit**Y** VERIFY from US, one of the world's fastest EMP- simulators, replaced HEISS in 1999 [2].

Over many years of its existence until now HPE-lab of armasuisse got an annual budget for research tasks. Since Switzerland is not a member of NATO there is still no knowledge about the actual restricted NEMP threat. Therefore it was always a goal to find the required information. This was done by defining strong research goals or specifications. As long as the industry was able to fulfill our goals, it was proven that we found the answer looked for. But the funding has been used too for studies, attendance of complex tests by mentioned consultants, as well as for writing international standards. A lot of analytical work has been done by EPFL because of personnel shortages at the HPE-lab.

With the death of Rüdiger Vahldiek of ETHZ in 2011 the HPEM community lost, beside Carl Baum in 2010, another famous key player in the team.

3 Current tasks

Like probably in other countries, HPE-lab's most important task today is to keep gathered knowledge and civil as well as military critical infrastructure protected against EM threats, knowing too that such protection has become an important economic issue. All the experience of more than 400 HPEM tests has shown that smaller infrastructure and systems are more resistant against the threats which are discussed during this conference than expected when they were introduced more than fifty years ago. A top modern test object containing COTS communication components has been tested with several EM threats including HPM using simulator SUPRA of German Bundeswehr in Munster [3]. Beside packet lost and a hang-up with need for personal intervention, no other reaction was observed. Someone might argue that Swiss HPE-lab has only toy/low-power sources for IEMI simulation which is really the case. But when monitoring the IEMI source market, one is not able to observe any success during the past decade.

As already mentioned, Switzerland recognizes only high altitude instead of surface burst EMP. Conductors for power distribution and communication are buried in urban areas almost without exception. The SPD's (surge protection devices) which are used for decades protect against overvoltage by lightning and HEMP at the same time. Recent studies have shown that the same SPDs are able to limit overvoltage of IMEI signals as well. This work is presented within the conference [4].

Shielding effectiveness tests of many facilities and containers have been performed in the past [5]. It is astonishing that natural coverage of systems like reinforced concrete structures, rocks of mountains and soil are hardly found in standards. Systems in buried facilities (Fig. 2) protected by 80 dB faraday cages can therefore reach easily shielding effectiveness of more than 120 dB or be far outside of the ability of today's powerful measurement systems.

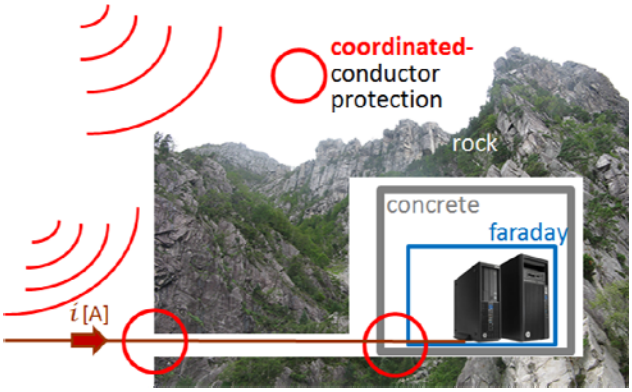

Figure 2. Multiple shield application

Although the crisis on the world did not decrease there might be a reason for adapting the Swiss protection measures which included EMP surface burst until now to HEMP only. It might be a challenge to find the individual difference between the threat or the systems protection requirement and the already given protection by its coverage. The protection of conducting wires is solved with Swiss SPD when applied the correct way. With appropriate reduction of the protection measures to what is necessary instead of what is best, more facilities and systems might be well protected with the same amount of resources.

Acknowledgements

Thank goes to all people of the HPEM community for supporting HPE-lab.

References

[1] A. W. Kaelin, B. Reusser, D. V. Giri. "Design, Fabrication and Testing of a Prototype Impulse Radiating Antenna (IRA)", *EUROEM 1998 conference, London*, UK.

[2] M. Nyffeler, A. Jaquier, B. Reusser, P-F. Bertholet, A. W. Kaelin. "VERIFY, a Threat-Level NEMP Simulator With 1 ns Risetime ", *AMEREM 2006 conference, Albuquerque NM*, USA.

[3] M. Nyffeler, A. W. Kaelin. "HPM-Testing of COTS Network Equipment", *AMEREM 2014 conference, Albuquerque NM*, USA.

[4] A. W. Kaelin. "UWB-IEMI laboratory tests of single-stage and multi-stage HEMP-protection devices", *EUROEM 2016 conference, London*, UK.

[5] F. M. Tesche. "CW Test Manual" (1994), *Measurements Notes, Note 64.*

Electromagnetics in Emerging Medical Technologies

Jayanti Venkataraman[1] and D. V. Giri[2]

[1]*Department of Electrical Engineering, Rochester Institute of Technology Rochester, NY 14623 USA* jnvee@rit.edu
[2]*Dept. of ECE, Univ of New Mexico Albuquerque, NM, USA and Pro-Tech, Alamo,CA 94507, USA* Giri@DVGiri.com

Abstract

The rapid advances in analog and digital technology have enabled electromagnetics to be applied in a wide range of medical therapies related to oncology, gastroenterology, ophthalmology, endocrinology etc. These are based on a variety of methodologies such as non-invasive diagnosis, continuous monitoring of physiological data, communication between implanted devices, communication to external devices, microwave imaging etc. In this paper, the state-of-art of electromagnetics in emerging medical technologies will be summarized. A few applications will be discussed in greater detail based on research at RIT.

Keywords: Non-invasive, real time, imaging, implanted

1 Introduction

In the past decade there have been some remarkable strides made by electromagnetic applications implemented in medical technologies as a result of rapid advances in the electronic and digital technologies. Most of the work is still in the clinical trial stages. The challenges are primarily because of well-known competing technologies. The objective of this paper is to summarize some significant developments with electromagnetics in emerging medical technologies.

2 Electromagnetics and Endocrinology

Recently here have been several approaches for non-invasive glucose concentration measurement that include interstitial fluid chemical analysis, breath chemical analysis, infrared spectroscopy, optical coherence tomography, spectroscopy (thermal, ocular, impedance). None to date have been accepted by the medical community. Some promising success has been shown by the RIT ETA Lab research for estimating blood glucose level in real time [1].

The technique utilizes a planar dipole to measure input impedance and resonant frequency. The antenna strapped on the arm of a patient is connected to a network analyzer automated to make measurements every 15 seconds. Figure 1 shows the resonant frequency vs. time for a diabetic patient after a eating a meal. It is seen that the resonant frequency of the antenna (dashed line) tracks changes in the glucose level measured by a traditional glucose meter (solid line). Analytical method is being developed for estimating the glucose level from changes in the resonant frequency.

Figure 1. Antenna System inserted into Arm Band

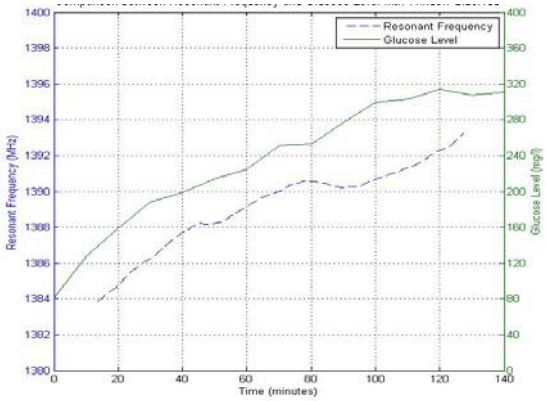

Figure 2. Increase in blood glucose level for diabetic patient: Resonant Frequency and Blood Glucose Level vs. Time

A clinical study, with a larger number of patients, is also being pursued. Work by other researchers includes the GlucoTrack that uses ultrasound, electromagnetic and thermal techniques to estimate glucose levels. Another non-invasive system is by Google, which is a contact lens that measures the glucose level in tears and extracts the data wirelessly.

3. Electromagnetics and Oncology

It is known that the dielectric properties of tissues change significantly when they become diseased. This property has allowed for microwave sensing and microwave imaging to be used in the detection of cancerous tissues.

At RIT, we have studied the feasibility of tissue characterization using an implanted LC sensor and querying it by an external antenna. The resonant frequency of the sensor is monitored by measuring the input impedance of the antenna, Figure 3. Analytical expressions have been derived for extracting the dielectric permittivity and conductivity of the tissue to determine if it is diseased [2]. Bio-compatible sensors have been fabricated and the methodology has been validated with phantom models. Microwave imaging is also, based on the change in the dielectric permittivity of cancer affected regions.

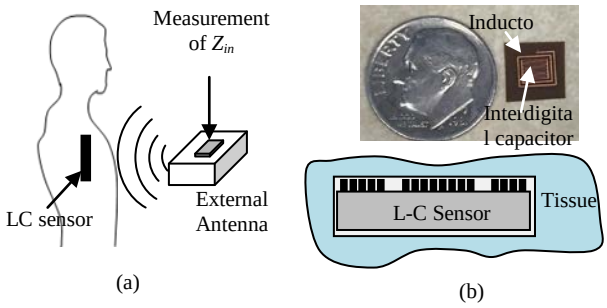

Figure 3 (a) RF Telemetry (b) L-C Sensor embedded in tissue

4. Electromagnetics and Real time Continuous Monitoring of Physiological Data

Body sensor networks (BSN) provide a continuous monitoring of physiological data with an integrated hardware and software platform [4]. Wearable or implanted wireless sensors containing antennas gather data and are either locally processed or encrypted and transmitted to a server. BSN has the potential of revolutionizing healthcare. Some examples of continuous monitoring devices that have proved to be very effective are management of acute diabetes with implanted insulin delivery, implanted multi-programmable brain stimulators, implanted cardio-defibrillator for prevention of life threatening events such as sudden cardiac arrest, or arrhythmia. At RIT, we have considered on-body, off-body, and body-to-body channels in wireless body area networks utilizing creeping wave antennas (Figure 4). Experimental setups are used to gather measurements in the 2.4 GHz band with body area networks operating in an office environment. Data packets containing received signal strength indicators are used to assess the performance of the creeping wave antenna in reducing interference at a neighboring on-body access point while supporting reliable on-body communications [3].

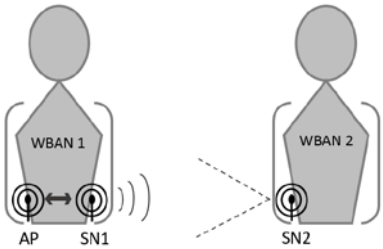

Figure 4- Experimental setup for capturing reflections and transmission

Results demonstrate that creeping wave antennas provide reliable on-body communications while significantly reducing inter-network interference; the inter-network interference is shown to be 10dB weaker than the on-body signal. In addition, the inter-network interference when both networks utilize creeping wave antennas is shown to be 3 dB weaker than the interference when monopole antennas are used. Yet another option is to use magnetic antennas and the magnetic fields can go through the body rather than around, since the human body is non-magnetic.

5. Electromagnetics and Ophthalmology

Innovative methodologies for monitoring intra-ocular pressure (IOP) are being pursued at RIT. We have designed and fabricated an implanted microelectromechanical systems (MEMS) device that has a novel LC tank structure in which post assembly and wafer bounding is not required. Pressure variations in the eye, induce the deflection of a thin diaphragm that causes a change in capacitance and hence the resonant frequency of the device. With inductive coupling, an external coil records changes in IOP. A methodology has been developed for correlating the measured data to IOP [4].

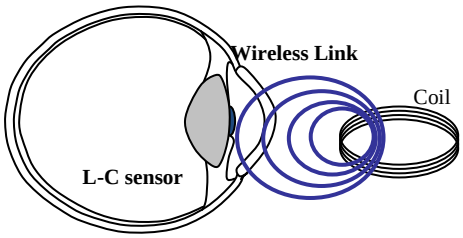

Figure 5 -Telemetry System for monitoring IOP pressure

5. Electromagnetics and Gastroenterology

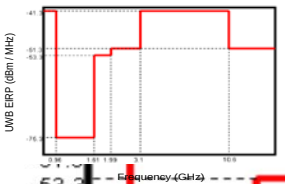

Figure 6. UWB

FCC has classified UWB which is defined as signals having a percent bandwidth more than 20%, or an absolute bandwidth of at least 500 MHz. Characteristics of UWB are: [3.1 to 10.6 GHz] band-width of 7500 MHz. High data rate capability and spectral power density limits (80 nW/MHz) on emission have opened up many technologies including medical applications ex: implantable devices; Wireless Capsule Endoscopy (WCE) is a “camera in a pill” the size of a large vitamin pill is a diagnostic tool. The application is described in this paper.

References

[1] Adhyapak A., Sidley M. and Venkataraman J., “Analytical model for real time, non-invasive estimation of blood glucose level”, Intl. IEEE Engg in Medicine and Biology Conference, Chicago, Aug 25-29, 2014.

[2] Yvanoff M, Venkataraman J, “A feasibility Study of Tissue Characterization using LC sensors” IEEE Transactions on Antennas and Propagation, Special Issue on Antennas and Propagation for Body-Centric Wireless Comm. Vol. 57, No 4, April 2009, pp 885-893.

[3] Tsouri, G., Zambita S., and Venkataraman J,” On the Benefits of Creeping Wave Antennas in Reducing Interference between Neighboring Wireless Body Area Networks”, IEEE Trans on Biomedical Circuits and Systems (accepted, to appear 2016)

[4] Yvanoff M., Fuller L. and Venkataraman J *“Implantable Micro-Transceiver Wireless Link for Intra-Ocular Pressure Measurement”* IEEE AP-S Intl Sym. Honolulu, Hawaii, June 2007.

Heuristic Approach to Evaluate the Occurrence of IEMI Sources in Criminal Activities

F. Sabath*, H. Garbe †

* *Bundeswehr Research Institute for Protective Technologies and NBC-Protection (WIS) Munster, Germany, FrankSabath@bundeswehr.org,*

† *Department of Electrical Engineering, Leibniz Universität Hannover, Hannover, Germany, Garbe@geml.uni-hannover.de*

Abstract

This paper discusses a technique which enables the assessment of key parameter of various intentional electromagnetic environments (IEME) for electronic systems, including the likelihood of their occurrence. The technique starts with a categorization of aspects, including non-technical aspects like availability of components, required knowledge and costs. Based on this categorization the likelihood that an offender has access to such an IEMI source is determined by a heuristic approach. In a second assessment step the possibility that a considered IEMI source might occur in the ambient of a given target system is estimated.

Keywords: intentional electromagnetic interference (IEMI); IEMI source; EM environment; likelihood of occurence.

1 Introduction

The initial step of an IEMI risk analysis is the identification and characterization of the threat scenario and the generated EM environment. In a naive attempt one could simply use the maximum threat level of known HPEM sources to specify the IEM environment. As this attempt ignores the likelihood that criminal and terrorist offender obtains access to such sources and the ability of the sources to come close to the system under consideration (target) it will result in an overestimation of the existing threat and consequently in the requirement of an oversized protection.

In [1] we introduced the risk assessment cube, consisting of the aspects threat level, mobility and technological challenge. We indicated that the mobility and the technological challenge enable the determination of the likelihood of occurrence of a given IEM environment. This paper is intended to close this gap by presenting a heuristic technique which enables the assessment of the likelihood that criminal and terrorist offender get access to IEMI sources.

2 Likelihood of Occurrence

The likelihood of occurrence expresses how likely a considered IEMI source will occur during an IEMI attack in the vicinity of the target system. It became common practice for risk assessment to express the likelihood in relation to a small number of categories.

The likelihood of occurrence of a considered IEMI source can be divided into two parts: (1) the likelihood (P_{CU}) that a (criminal or terrorist) offender gets access to it and (2) the likelihood (P_{ACC}) that the source appears in the vicinity of the target system, i.e. it is capable to enter a defined accessibility zone. The first part P_{CU} depends on the technological challenge and is mainly determined by the availability of the system and its components, the required knowledge and the cost.

One approach to map the availability, knowledge and cost categories to categories for the likelihood that an offender gets access to a source of this availability is the category rating by experts. To enable a basic mapping, without expert's involvement, we approximated the experts rating for

- Availability (AV_C):

$$P_A = 11 - 2AV_C \tag{1}$$

- Knowledge (K_D):

$$P_K = 10 - \frac{7}{5} K_D \tag{2}$$

- Cost (C_{EXP}):

$$P_C = 1 + \frac{(5{,}3 - C_{EXP})^2}{2{,}25} \tag{3}$$

The discussed likelihood contributions P_A, P_K, P_{EXP} must be compiled to the demanded likelihood of criminal use (P_{CU}) of a considered IEMI source.

$$P_{CU} = \sqrt[3]{P_A \cdot P_K \cdot P_C} \tag{4}$$

The values determined by (4) are index numbers that enable a ranking of various IEMI sources (or source classes) with regard to its possible use in an IEMI attack [2].

References

[1] Sabath, F.; Garbe, H., "Risk potential of radiated HPEM environments," in 2009 IEEE International Symposium on Electromagnetic Compatibility, pp.226-231, 17-21 Aug. 2009

[2] Sabath, F.; Garbe, H., "Assessing the likelihood of various intentional electromagnetic environments the initial step of an IEMI risk analysis," 2015 IEEE International Symposium on in Electromagnetic Compatibility (EMC), pp.1083-1088, 16-22 Aug. 2015

Recent Advances in HPEM Standards - 2016

R. Hoad* & W. A. Radasky†

**QinetiQ Ltd., Cody Technology Park, Farnborough, Hampshire, GU14 0LX, UK; †Metatech Corp., 358 S. Fairview Ave., Suite E, Goleta, CA 93117, USA*
rhoad@qinetiq.com

Abstract

Standardisation of High Power Electromagnetic (HPEM), environments, protection design and test methods is becoming increasingly important particularly as the perceived risk to society from HPEM is growing. Many generic standards and some application or product specific standards are now available which address Lightning, High Altitude Electromagnetic Pulse (HEMP) and Intentional Electromagnetic Interference (IEMI) phenomena. This paper will provide an overview of some recent developments in HPEM standards.

Keywords- *HPEM, IEMI, HEMP and Lightning*

1. Introduction

Standards provide a useful resource for those wishing to provide consistent approaches and solutions to important problems. They are often produced by a committee of recognised experts within niche technical disciplines in response to real or perceived need by the user community [1]. Chronologically, standardisation effort has progressed through HPEM phenomena Lightning, High Altitude EMP (HEMP) and then IEMI, with IEMI being the latest phenomena to be considered. However, work continues on the improvement of standardisation for the other phenomena mentioned above. In the specific area of HPEM, standards have been used to provide clear, consistent and often simplified information and guidance pertaining to three key areas;

- Protection design
- Environment definition
- Immunity test methods

This paper will highlight some recent developments in these areas of HPEM standardisation.

2. Protection Design Standards

Hardening and protection design standards generally formalize the process of hardening systems and provide a considered rationale for hardening design. In general the design principles for Lightning, HEMP and IEMI protection are similar in many ways to those used for Electromagnetic Compatibility (EMC). However, there are of course some important differences between the system interactions of electromagnetic transients from Lightning, HEMP [2] and IEMI and from the other EMC phenomena.

A common feature of HPEM effects on victims is that they tend to induce non-linear responses in victim systems. However, the nonlinear response to a given HPEM environment may not be the same because of differences in essential parameters such as rise-time, rate of change, energy and frequency content of the transient waveform. These considerations lead to special requirements for HEMP, Lightning and IEMI hardening design which HPEM hardening design standards seek to address.

Lately it has been identified that managing or controlling the distance between IEMI sources and victim systems perhaps by maintaining a physical security barrier such as a fence or other attenuating barrier at some distance from a victim installation can be very beneficial in terms of IEMI protection. Standards have been developed to provide guidance on this issue [3 and 4].

Recent developments in Lightning protection scheme design for fixed installations utilise a novel risk based approach in order to qualify the risk and the degree of protection required [5].

HPEM protection design standards generally cover a diverse range of topics such as specifying the performance level of a particular item of protective equipment to more generalized guidance on grounding, bonding and earthing techniques.

3. Environment Definition Standards

Standardized descriptions of the Lightning and HEMP environment have evolved over time. The Lightning environment definition continues to be analysed as improved understanding from modelling and measurement data becomes available [6].

Recently there has been increased focus on understanding the HEMP E3 environment in an effort to understand the similarities and differences between HEMP E3 and Geomagnetic storm type disturbances [7].

The standards committee International Electrotechnical Committee (IEC) SC 77C [8] has arguably done the most to characterise IEMI environments. IEC 61000-1-5 [9] provides a mathematically based waveform classification scheme which is now internationally recognised. In an important development the US military recently took steps to include

IEMI (actually, High Power Microwave (HPM)) environments within their primary Electromagnetic Environmental Effects (E3) standard [10].

A simplified composite HPEM environment has been produced [11] and is shown in Figure 1.

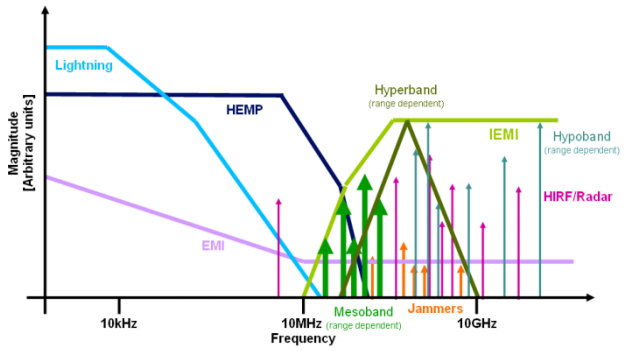

Figure 1. Simplified composite HPEM environment

4. Immunity Test Methods

HEMP and Lightning test standards tend to cover equipment level, system/platform level and fixed installation level test methods. There are also standards which act as directories to identify HEMP and IEMI simulators, so called simulator compendia [12 and 13] and others that provide guidance on measurement, instrumentation and calibration. All of the test standards simplify to a certain extent the HPEM interaction and coupling process.

In general civilian HPEM test standards try to make use of existing and common EMC test methods such as IEC 61000-4-4 [14] and 61000-4-20 [15] in order to reduce the burden on test houses from procuring specialist test equipment. As such civilian test standards are a compromise.

Recent developments in HEMP conducted protection testing methods and test levels have introduced a graduated approach in order to allow some flexibility for the performance of protection measures [16].

Work is currently underway in IEC SC 77C to produce a test method specifically for Mesoband and Hyperband type disturbances.

5. Summary

An important feature which appears to be emerging is the development of product or system specific or tailored Lightning [17], HEMP [18] and IEMI [19] test standards. These product standards are often based on the basic or generic standards exemplified by those provide by IEC SC 77C.

This paper will therefore provide examples of recent developments in HPEM standardisation.

References

[1] HIPOW project website, www.hipow-project.eu/, accessed Feb. 2016

[2] Vance, E. F., Uman, M. A., 'Differences Between Lightning and Nuclear Electromagnetic Pulse Interactions', IEEE Transactions on Electromagnetic Compatibility, Vol. 30, No. 1, February 1988

[3] IEC 61000-4-36 Ed. 1.0 (2014-12): Electromagnetic compatibility (EMC) - Part 4-36: IEMI immunity test methods for equipment and systems

[4] ITU-T K.81, SERIES K: PROTECTION AGAINST INTERFERENCE, 'High-power electromagnetic immunity guide for telecommunication systems', November 2009

[5] BS EN 62305-1:2011, 'Protection against Lightning. General principles'

[6] Yazhou Chen; Haojiang Wan; Xing Zhou, 'Simulation of Lightning Electromagnetic Fields and Application to Immunity Testing', IEEE Transactions on Electromagnetic Compatibility, Volume: 57, Issue: 4, 2015, Pages: 709 - 718,

[7] Radasky, W. A., J. Kappenman and R. Pfeffer, "Nuclear and Space Weather Effects on the Electric Power Infrastructure," NBC Report, Fall/Winter 2001, pp. 37-42.

[8] Radasky W. A. and Hoad R., 'Status and Progress of IEC SC 77C High-Power Electromagnetics Publications in 2015', Proceedings of IEEE EMC Europe 2015, Dresden, Germany

[9] IEC 61000-1-5: High Power Electromagnetic (HPEM) Effects on Civil Systems, PD IEC/TR 61000- 1-5:2004

[10] Mil-Std-464C, Military Standard, Electromagnetic Environmental Effects, Requirements for Systems, 1 Dec 2010

[11] Giri, D.V.; Tesche, F.M., 'Classification of intentional electromagnetic environments (IEME)', IEEE Transactions on Electromagnetic Compatibility, Volume: 46, Issue: 3, 2004, Pages: 322 – 328

[12] IEC 61000-4-32: 2002, 'HEMP simulator compendium'

[13] IEC 61000-4-36: 2009, 'HPEM simulator compendium'

[14] IEC 61000-4-4 Ed 3.0, 'Electrical fast transient/burst immunity test' 2012

[15] IEC 61000-4-20 Ed 2.0, 'Emission and immunity testing in transverse electromagnetic (TEM) waveguides', 2010

[16] IEC 61000-4-25 Ed 2.0, 'HEMP immunity test methods for equipment and systems', 2015

[17] EUROCAE ED-105A – 'Aircraft Lightning Test Methods', Issued in July 2013.

[18] ITU-T, K.78. 'High altitude electromagnetic pulse immunity guide for telecommunication centres', June 2009

[19] CIGRE C.600, Protection of High Voltage Power Network Control Electronics Against Intentional Electromagnetic Interference (IEMI), November 2014

Advances in Transient Response Modelling of Multi-conductor Transmission Lines

Yan-zhao Xie, Zi-weihua Du, Jun Guo, Zhan-yu Li †

State Key Laboratory of Electrical Insulation and Power Equipment,
School of Electrical Engineering, Xi'an Jiaotong University,
Xi'an, 710049, China
Yanzhao.xie@gmail.com

Abstract

Many researchers have proposed many approaches for the transient response modelling of multi-conductor transmission lines (MTLs) excited by electromagnetic pulse (EMP). There are yet some tough issues to be solved. This paper introduces some recent work in modelling methods of EMP coupling to MTLs at Xi'an Jiaotong University. The advances include distributed analytical representation and iterative technique (DARIT) method, an equivalent circuit model using SPICE software and random field coupling to MTLs, etc. The proposed methods have been validated in different ways for the cases of UHV transmission lines and buried oil pipes, etc.

Keywords: modelling methods; multi-conductor transmission lines; overhead lines; buried cables.

1 Introduction

To predict the effects of EMP coupling to MTLs, extensive researches have devoted to this field [1]-[4]. Some researchers have made significant progresses in the field of modelling of EMP coupling to MTLs [1-11]. There are yet some issues need to be further investigated for some special applications including the computation efficiency, treatment of non-linear termination loads and the response of buried cables surrounded by lossy and frequency-dependent medium, etc. Some new approaches have been proposed at State Key Laboratory of Electrical Insulation and Power Equipment (SKLEIPE). This talk will briefly review the existing modelling methods and then introduce some recent modelling approaches and the related application examples.

2 Advances of the modelling methods and application examples

2.1 DARIT method

In 2010, Y.Z. Xie, F. Canavero, et al. proposed an approach using the distributed analytical representation and an iterative technique (DARIT) for the crosstalk computation between MTLs[12]. Henceforth, this approach is named as the DARIT-crosstalk method. This method makes use of the strong points of the WCA method and the idea of the waveform relaxation with transverse partitioning (WR-TP) method. Based on the previous study, the DARIT method was developed to the area of EMP radiated field interaction with MTLs. The method employs Jacobi iterative technique method which is based on the WR-TP for the response computation of MTLs illuminated by the incident EMP field (Jacobi-DARIT-field) [13]. This algorithm can eliminate the need for inversing the matrix when solving MTLs equations and lead to high computational efficiency. And it has been validated that Jacobi-DARIT-field method is effective in dealing with many complex circumstances including different symmetry, cable structure and loads. Then, to further speed up the convergence rate of the DARIT-field method, the Gauss-Seidel Iteration Algorithm (Seidel- DARIT -field) was proposed [14], and the convergence rate is faster compared with Jacobi-DARIT-field. More recently, the model of DARIT-field in the time domain was proposed for the calculation of EMP coupling to MTLs with non-linear loads.

2.2 Equivalent SPICE circuit model

An equivalent SPICE circuit model using SPICE code was proposed for the calculation of the induced voltage and current in time domain by circuit simulation software,e.g. PSPICE software. The frequency-dependent parameters can be equivalent to circuit model by vector fitting (VF) method. Apparently, the circuit model method has advantages that both time dependent and frequency dependent parameters can be easily considered, at the same time, nonlinear loads such as transistors and digital devices, as well as dynamic loads, such as inductors and capacitors, may be easily incorporated using the existing elements in the SPICE code. And most of all, the circuit of a segment of transmission lines can be packaged as a sub-circuit of the whole transmission line network. The improved approach combined with delay extraction algorithm not only has the above advantages but also has higher efficiency in computation speed. Therefore, this method has been employed in EMP radiated field coupling to MTLs above lossy ground efficiently, as well as the response of buried conductor excited by external electromagnetic field.

2.3 Random variables impact on EMP coupling to MTLs

In recent years, a new approach called Polynomial Chaos (PC) has been introduced to deal with the problem of uncertainty-aware analysis because there exist some random variables when doing the simulation of EMP coupling to MTLs. The basic idea of the PC approach is to expand the random system outputs in terms of suitable orthogonal polynomials. Next, a Galerkin projection process is carried out to construct a deterministic system of equations in the coefficients of the polynomials. Compared to the traditional Monte Carlo (MC) method, PC's solution can capture the statistical information much faster than running a large number of MC simulations. And it has been applied in characterizing the variability analysis of EMP coupling to MTLs. Some examples will be presented during EUROEM 2016.

3 Conclusion and challenges

This paper reviews the existing modelling methods in the field of EMP radiated field coupling to MTLs. The advances of modelling methods in recent years were introduced to show their advantages and applications. However, there are also many challenges to be faced in this field. Future work will improve the method to be more accurate and efficient.

References

[1] Paul, CR. "Analysis of Multi-conductor Transmission Lines," New York: John Wiley and Sons, 1994.

[2] F.M.Teshe, M.V.Ianoz, T.Karlsson. "EMC analysis methods and computational models," New York: Wiley Interscience, 1997.

[3] F Rachidi，S Tkachenko. "Electromagnetic Field Interaction with Transmission Lines. From Classical Theory to HF Radiation Effects," Wit Press, 2008.

[4] Parmantier J P, Gobin V, Issac F, et al. ETE III: Application of the electromagnetic topology theory on the EMPTAC. Interaction Notes 527. 1996.

[5] F. M. Tesche, "On the Analysis of a Transmission Line With Nonlinear Terminations Using the Time-Dependent BLT Equation," in IEEE Transactions on Electromagnetic Compatibility, vol. 49, no. 2, pp. 427-433, May 2007.

[6] Haase, H. , Nitsch, J. , Full-wave transmission line theory (FWTLT) for the analysis of three-dimensional wire-like structures, 14th International Zurich Symposium on Electromagnetic Compatibility, 235-240, Feb. 2001.

[7] Nitsch J. , Tkachenko S. , Global and Modal Parameters In the Generalized Transmission Line Theory and Their Physical Meaning, Radio Science Bulletin, 312, March 2005, 21-31.

[8] Nitsch, J. , Tkachenko, S. , ,Physical Interpretation of the Parameters in the Full-Wave Transmission Line Theory, ISTET 2009–15th International Symposium on Theoretical Electrical, Engineering (ISTET 2009), Lübeck, Germany.

[9] Nitsch, J. , Tkachenko, S. , "Physical Interpretation of the Parameters in the Full-Wave Transmission Line Theory," Theoretical Engineering (ISTET), 2009 XV International Symposium on, Germany, 2009, pp. 1-5.

[10] M. Brignone, F. Delfino, R. Procopio, M. Rossi and F. Rachidi," A semi-analytical formula for the evaluation of the indirect lightning performance of overhead power lines," Electromagnetic Compatibility (EMC Europe), 2014 International Symposium on, Gothenburg, 2014, pp. 560-564.

[11] J. Paknahad, K. Sheshyekani, F. Rachidi, M. Paolone and A. Mimouni, "Evaluation of Lightning-Induced Currents on Cables Buried in a Lossy Dispersive Ground," in IEEE Transactions on Electromagnetic Compatibility, vol. 56, no. 6, pp. 1522-1529, Dec. 2014.

[12] Y.-Z. Xie, F. Canavero, T. Maestri, and Z.-J. Wang, "Crosstalk analysis of multiconductor transmission lines based on distributed analytical representation and iterative technique," IEEE Trans. Electromagn. Compat., vol. 52, no. 3, pp. 712–727, Aug. 2010.

[13] Y. Z. Xie, J. Guo and F. Canavero, "Analytic iterative solution of electromagnetic pulse coupling to multi-conductor transmission lines," IEEE Transactions on Electromagnetic Compatibility, vo1.55, no.3, pp.451-466, June 2013.

[14] J. Guo, Y. Z. Xie and F. Canavero, "Gauss-Seidel Iterative Solution of Electromagnetic Pulse Coupling to 3-Conductor Transmission Lines," IEEE Transactions on Electromagnetic Compatibility.